FLUID MECHANICS AND ITS APPLICATIONS

Tom Mullin and Rich Kerswell (Eds.)

IUTAM Symposium on

Laminar-Turbulent Transition and Finite Amplitude Solutions

IUTAM

Springer

IUTAM Symposium on Laminar-Turbulent
Transition and Finite Amplitude Solutions

FLUID MECHANICS AND ITS APPLICATIONS
Volume 77

Series Editor: R. MOREAU
MADYLAM
Ecole Nationale Supérieure d'Hydraulique de Grenoble
Boîte Postale 95
38402 Saint Martin d'Hères Cedex, France

Aims and Scope of the Series

The purpose of this series is to focus on subjects in which fluid mechanics plays a fundamental role.

As well as the more traditional applications of aeronautics, hydraulics, heat and mass transfer etc., books will be published dealing with topics which are currently in a state of rapid development, such as turbulence, suspensions and multiphase fluids, super and hypersonic flows and numerical modelling techniques.

It is a widely held view that it is the interdisciplinary subjects that will receive intense scientific attention, bringing them to the forefront of technological advancement. Fluids have the ability to transport matter and its properties as well as transmit force, therefore fluid mechanics is a subject that is particulary open to cross fertilisation with other sciences and disciplines of engineering. The subject of fluid mechanics will be highly relevant in domains such as chemical, metallurgical, biological and ecological engineering. This series is particularly open to such new multidisciplinary domains.

The median level of presentation is the first year graduate student. Some texts are monographs defining the current state of a field; others are accessible to final year undergraduates; but essentially the emphasis is on readability and clarity.

For a list of related mechanics titles, see final pages.

IUTAM Symposium on Laminar-Turbulent Transition and Finite Amplitude Solutions

Edited by

TOM MULLIN
University of Manchester, U.K.

and

RICH KERSWELL
University of Bristol, U.K.

Springer

A C.I.P. Catalogue record for this book is available from the Library of Congress.

ISBN-10 1-4020-4048-2 (HB)
ISBN-13 978-1-4020-4048-1 (HB)
ISBN-10 1-4020-4049-0 (e-book)
ISBN-13 978-1-4020-4049-8 (e-book)

Published by Springer,
P.O. Box 17, 3300 AA Dordrecht, The Netherlands.

www.springeronline.com

Printed on acid-free paper

All Rights Reserved
© 2005 Springer
No part of this work may be reproduced, stored in a retrieval system, or transmitted
in any form or by any means, electronic, mechanical, photocopying, microfilming, recording
or otherwise, without written permission from the Publisher, with the exception
of any material supplied specifically for the purpose of being entered
and executed on a computer system, for exclusive use by the purchaser of the work.

Printed in the Netherlands.

TABLE OF CONTENTS

Preface vii

Modeling the Direct Transition to Turbulence 1
Paul Manneville

Dynamical Systems and the Transition to Turbulence 35
Bruno Eckhardt and Holger Faisst

Nonlinear Solutions of Simple Plane Shear Layers with and without a System Rotation 51
M. Nagata, G. Kawahara, T. Itano, D.P. Wall, T. Mitsumoji and R. Nakamura

Co-Supporting Cycle: Sustaining Mechanism of Large-Scale Structures and Near-Wall Structures in Channel Flow Turbulence 71
Sadayoshi Toh, Tomoaki Itano and Kai Satoh

Transition Threshold and the Self-Sustaining Process 85
Fabian Waleffe and Jue Wang

Turbulent-Laminar Patterns in Plane Couette Flow 107
Dwight Barkley and Laurette S. Tuckerman

Subcritical Turbulent Transition in Rotating and Curved Shear Flows 129
Pierre-Yves Longaretti and Olivier Dauchot

The Karhunen–Loève Decomposition of the Autonomous Minimal Flow Unit 145
D. Desmidts and D. Carati

Coherent States in Transitional Pipe Flow 163
Maria Isabella Gavarini, Alessandro Bottaro and Frans T.M. Nieuwstadt†

Instability, Transition and Turbulence in Plane Couette Flow with System Rotation 173
P. Henrik Alfredsson and Nils Tillmark

Transition *to* Versus *from* Turbulence in Subcritical Couette Flows 195
A. Prigent and O. Dauchot

Transition to Turbulence in Pipe Flow 221
B. Hof

Threshold Amplitudes in Subcritical Shear Flows 233
Dan S. Henningson and Gunilla Kreiss

Non-Linear Optimal Perturbations in Subcritical Instabilities 251
Carlo Cossu

A Bypass Scenario of Laminar-Turbulent Transition in the Wind-Driven Free-Surface Boundary Layer 267
Victor I. Shrira, Guillemette Caulliez and Dmitry V. Ivonin

Viscoelastic Nonlinear Traveling Waves and Drag Reduction in Plane Poiseuille Flow 289
Wei Li, Philip A. Stone and Michael D. Graham

Subcritical Instabilities in Plane Couette Flow of Visco-Elastic Fluids 313
Alexander N. Morozov and Wim van Saarloos

Subject Index 331

PREFACE

This volume collects together papers presented at the LMS*-sponsored IUTAM Symposium on "Non-Uniqueness of Solutions to the Navier–Stokes Equations and Their Connection with Laminar-Turbulent Transition" held in Bristol, UK on August 9th–11th 2004. The meeting brought together theoreticians and experimentalists to discuss exciting new developments in the study of transition to turbulence in shear flows. Over 3 days and 21 lectures, various groups from around the world presented their latest results ranging from identifying the initial optimal disturbances which can trigger transition, through pattern formation in transitional processes and self-sustaining mechanisms in shear flows. Issues such as the re-laminarisation of turbulence and transition processes in non-Newtonian flows were also debated. Theoretical approaches included the construction of low-order models, Newton–Raphson searches for new nonlinear solutions and full numerical simulation of the Navier–Stokes equations. The experimental work was primarily concerned with plane Couette and pipe flows where substantial recent progress has been made. The debate in this focused meeting was lively and this is reflected in the contributions to this volume.

The overarching achievement of the symposium was to highlight the increasing evidence for the appearance of disconnected states, that is, alternative solutions to the Navier–Stokes equations which are not connected in any simple way to the well known simple exact solutions for pipe and Couette flows. The principal outcome of the meeting is to highlight the increasing amount of evidence for the relevance and importance of finite amplitude solutions in structuring laminar-turbulent transition in shear flows. The challenge for the future is to develop and exploit this realisation.

The financial support of the LMS and IUTAM is gratefully acknowledged.

T. Mullin & R.R. Kerswell

*London Mathematical Society

MODELING THE DIRECT TRANSITION TO TURBULENCE

Paul Manneville
Laboratoire d'Hydrodynamique, École Polytechnique, F-91128 Palaiseau, France
paul.manneville@ladhyx.polytechnique.fr

Abstract After a brief summary of experimental results focussed on plane Couette flow and contrasting the low-Reynolds numbers transition between laminar flow and the turbulent spot regime, with its high-Reynolds counterpart between homogeneous turbulence and turbulent stripes, we introduce a hierarchy of models from *conceptual* models designed to answer the most basic questions to *semi-realistic* models more adapted to the study of specific topics.

Among conceptual models we distinguish between low-dimensional deterministic dynamical systems apt to analyze problems linked to attractor coexistence and basin boundaries, stochastic models more appropriate to studying the role of noise in the natural transition, and models derived from statistical mechanics focussed on the "macroscopic" growth of turbulent patches in the triggered transition. Semi-realistic models separating cross-stream and in-plane variables are designed in view of concrete analysis of processes at a more "microscopic" scale, related to pattern formation and space-time chaos studies.

Keywords: subcritical bifurcation, plane Couette flow, turbulent spots, modeling.

1. INTRODUCTION

The transition to turbulence in shear flows along solid walls ("wall flows" for short) is a problem of tremendous importance in a large number of engineering situations. When compared to the transition in closed flows, especially convection due to buoyancy effects, difficulties accumulate. A first reason is that mechanisms are not easy to apprehend since inertia and dissipation effects may play counterintuitive roles. A second reason is the fact that the downstream advection introduces complications in the very understanding of perturbation growth. A third one is that nonlinearities may or may not make this growth saturate, so that the supercritical cascade of instabilities leading to turbulence may be by-passed by other processes ending in a direct transition from a regular (laminar) base state to an irregular (turbulent) regime as the Reynolds number R, the usual control parameter, is increased. Such a transition may be termed

T. Mullin and R.R. Kerswell (eds), Laminar Turbulent Transition and Finite Amplitude Solutions, 1–33.
© 2005 *Springer. Printed in the Netherlands.*

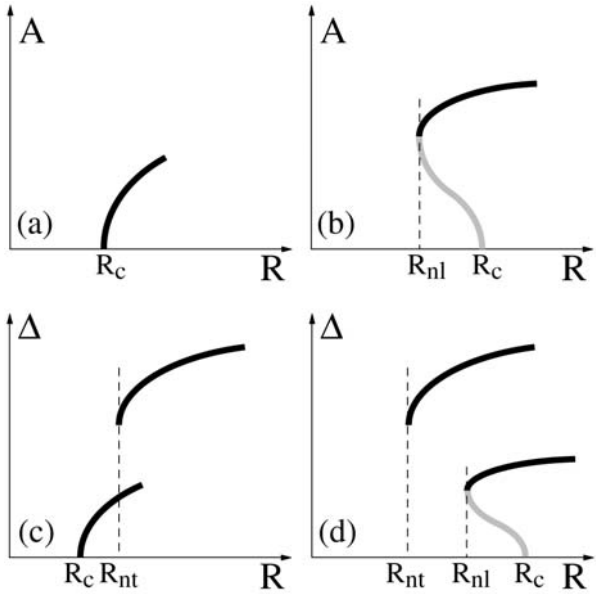

Figure 1. (a, b) Standard bifurcation diagram for supercritical and subcritical bifurcations, Axis $A \equiv 0$ features the base state, R_c is the linear instability threshold, R_{nl} the saddle-node bifurcation threshold beyond which coexistence of solutions, stable and unstable, is observed. (c,d) Δ now measures the distance to the base state, nontrivial states can either arise from instabilities or emerge from other processes possibly difficult to identify; these states are usually time dependent so that Δ measures some time-averaged distance. The unstable modes can be more "dangerous" than states on the nontrivial branch (c) or on the contrary less dangerous (d). The plane Couette flow represents the extreme case when no states derive from linear instabilities so that the corresponding branch is pushed away to infinity, while the branch of nontrivial states stays in place.

globally subcritical by contrast with the better understood *globally supercritical* case where the bifurcated states stay close to each other (Dauchot and Manneville, 1997). The latter situation occurs especially at a primary bifurcation issued from a linear instability (threshold R_c), so that the distance between the bifurcated state and the base state can be measured by the amplitude A of the corresponding critical mode as sketched in Figures 1(a, b).

Like any typical nonlinear system, flows governed by the Navier–Stokes (NS) equations may adopt one out of several possible solutions under given external conditions. Besides the trivial base state that derives by continuity from thermodynamic equilibrium upon increasing applied stresses, one can indeed find nontrivial solutions. In the globally supercritical case these solutions can be obtained by successive perturbation analyses. Otherwise roundabout approaches have to be followed to obtain them by continuation from situations

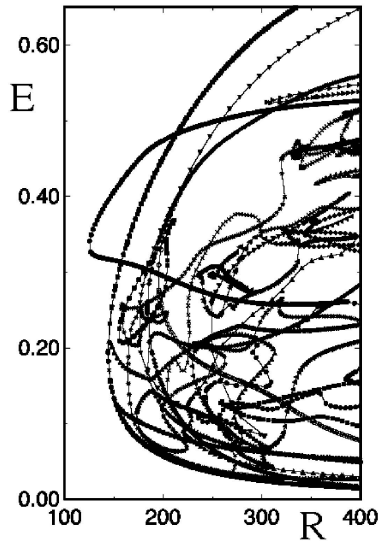

Figure 2. Energy of stationary plane Couette flow states found by Schmiegel as functions of the Reynolds number (box with aspect ratio $1 : 2\pi : \pi$, periodic in the streamwise and spanwise directions). Only nontrivial solutions belonging to the Nagata–Busse–Clever symmetry class are displayed (see Schmiegel, 1999, for details).

where they can more easily be computed (Nagata, 1990; Clever and Busse, 1992). In practice, many special solutions with given symmetries can be obtained in that way, generically emerging from blue sky through saddle-node bifurcations, see Figure 2 taken from Schmiegel (1999). As far as the global stability threshold R_{g} of the base flow is concerned, i.e. the value of the control parameter below which it is unconditionally stable, the determination of the minimum value $R_{\mathrm{nl,min}}$ at which these special solutions begins to exist is of little helps since they are usually unstable.[1] Though mathematically well defined, R_{g} is therefore difficult to determine since a complete exploration of phase space has to be performed to detect when at least one nontrivial solution becomes an attractor able to compete with the base state. Forthcoming details about the transition to turbulence in plane Couette flow will hopefully help us to better understand the original nature of the problem. In the following we shall replace the abstract (but unpractical) unconditional stability condition defining R_{g} by the concrete (and practical) condition that, for the largest possible set of experimentally achievable situations, the base state is systematically recovered in the long-time limit.

For the present introductory discussion, we only need to postulate the existence of a branch of nontrivial solutions, in addition to the possible presence of other solutions arising from linear instabilities. The distance from the

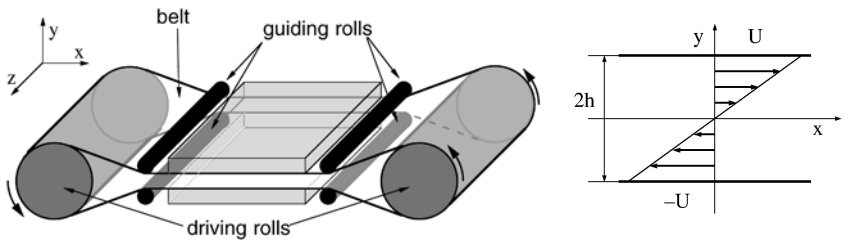

Figure 3. Left: experimental set-up used by the Saclay group. Driven by large rolls, a circulating belt is immersed in a container. It shears the fluid within the gap maintained between parallel parts of it guided by smaller rolls. Right: velocity profile of the laminar base flow.

base state to these unspecified remote, usually chaotic, states can be measured by some observable Δ. One is then led to the conceptual pictures in Figure 1(c,d) illustrating the general case. Figure 1(d) would correspond to plane Poiseuille flow for which Tollmien–Schlichting (TS) waves bifurcate subcritically at a threshold $R_c = 5772$ (Orszag, 1971) much larger than the corresponding $R_{nl} \approx 2900$ (Herbert, 1983) and even more than the experimentally determined global stability threshold $R_g \sim 1000$ beyond which turbulent spots coexist with, and travel within laminar flow without decaying (Carlson et al., 1982). Figure 1(c) would instead account for transitional boundary layer flows, with TS waves bifurcating supercritically at $R_c \approx 530$ next evolving into localized "spikes" from which turbulent spots nucleate and eventually merge to form a fully turbulent boundary layer, with the supplementary complications arising from the fact that R is not constant but increases downstream (for reviews, see Schmid and Henningson, 2001, chapter 9; or Manneville, 2004b, chapter 6).

As sketchy as Figure 1 might be, it already raises the most important questions about the transitional problem, namely how the branch of nontrivial states is reached from the laminar base flow, depending on the value of R and how the turbulent flow decays to the laminar state as R is decreased. During the last decade, this specific problem has been extensively studied experimentally and numerically in the case of the plane Couette flow. This system represents the most extreme case since it was known to be linearly stable for all R (Romanov, 1973), though sustained turbulent flow regimes could be observed down to some $R_g < \infty$. Here, we focus on results obtained by the Saclay group, using the set-up described in Figure 3. For a more complete review of these results, see Manneville and Dauchot (2001). Other studies include those of the Stockholm team that used a comparable experimental configuration, e.g. Tillmark and Alfredsson (1992).

The laminar plane Couette velocity profile is a linear function of the cross-stream coordinate y (Figure 3, right). It can be characterized by a single parameter, the Reynolds number, usually defined as $R = Uh/\nu$. At this point, notice that a better choice would probably be using shear rate U/h and gap $2h$, which would make $R = (U/h)(2h)^2/\nu = 4Uh/\nu$, i.e. four times the usual value. This scaling would then be more representative of processes at work in the flow since important structures in the flow occupy the full gap. Immediate comparisons would then be allowed with other wall flows, after scaling by some appropriate effective shear: channel flow, boundary layers, Couette–Taylor and torsional Couette experiments, etc.

Several kinds of experiments have been performed. The natural *relaxation* from turbulent to laminar flow has been studied by preparing an initial turbulent state at some high value of R and suddenly quenching the system at variable smaller values of R. By contrast, since the ideal basic profile is linearly stable for all R, the *natural* transition towards the nontrivial branch is sensitive to the amount of residual noise. To avoid uncertainties linked to this experimental difficulty, more controlled conditions have been chosen, either by triggering specific initial states, or else by slightly but permanently modifying the basic profile. The first strategy was achieved by nucleating turbulent spots from tiny jets impulsively launched through the gap (Figure 4, left), the second one by introducing small obstacles in the gap and decreasing their sizes in the spirit of a continuation method. Most of the time, the observable was the ratio of the surface occupied by turbulent flow to the surface of the total observation field at a given time, which defines an instantaneous *turbulent fraction* F_t further averaged in time to get the corresponding statistical quantity $\langle F_t \rangle$ (Figure 4, right). The main conclusion was that, whatever the kind of experiment (quench from turbulent flow, spot-triggering, basic flow deformation), below $R_g \approx 325$ no sustained flow regime departing from laminar Couette flow can be observed.

The nature of the different flow regimes in the range of Reynolds numbers corresponding to the transition to turbulence in plane Couette flow is specified in Figure 5, as can be inferred from experiments at finite but large aspect ratio (streamwise and spanwise sizes of the set up large when compared to the gap). This diagram can be more easily interpreted by distinguishing its low-R part from its high-R part. At the low-R end, below $R_u \simeq 312$, all perturbations to the laminar flow *rapidly* relax. Accordingly this value might represent the lower limit below which nontrivial solutions alluded to previously (see Figure 2) are unable to influence the dynamics because their inset in phase space cannot be accessed from typical initial conditions corresponding to turbulent flow or spot germs. Beyond R_u turbulent spots are seen to nucleate and grow but all of them eventually decay for $R < R_g \approx 325$. For $R > R_g$ some no longer decay as long as the experiment is pursued. When turbulent spots grow, they often form oblique turbulent patches. When the set-up has

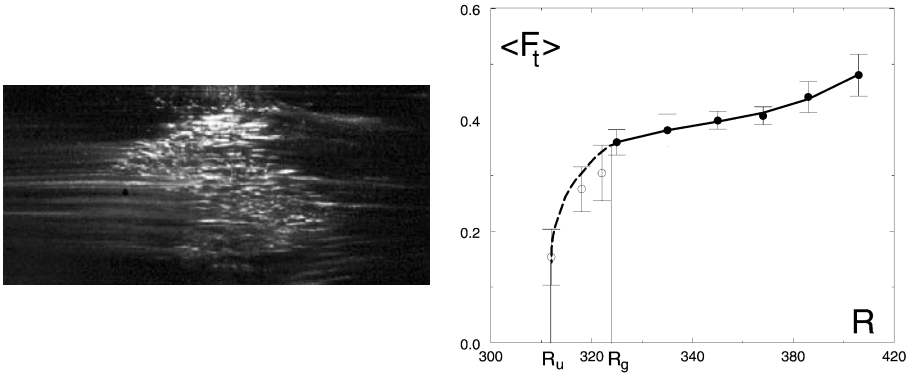

Figure 4. Left: Mature turbulent spot in plane Couette flow (courtesy, S. Bottin). Right: Time-averaged turbulent fraction as a function of R from a compilation of quench experiments. Below R_g, turbulence eventually decays. The time statistics shown (dashed line) is accordingly performed only during the chaotic transient stage before final decay; see also Figure 13. After Bottin et al. (1998).

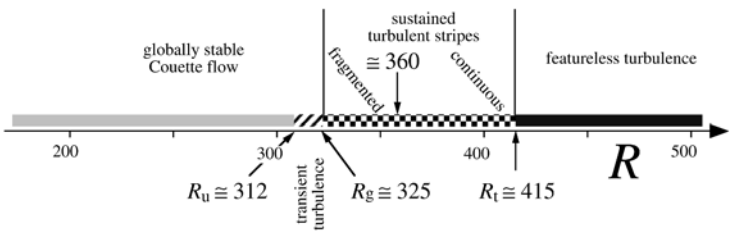

Figure 5. Full bifurcation diagram of plane Couette flow as a function of R.

sufficiently large aspect ratio, these patches evolve into discontinuous oblique turbulent stripes as depicted in the left panel of Figure 6. Beyond $R \simeq 360$ they subsequently merge to form continuous bands as shown in the right panel of Figure 6. This value of R thus roughly marks the frontier between low and high Reynolds numbers. Turbulent bands are present between $R = 360$ and $R = 415$. This steady spatial modulation of the turbulent regime progressively damps out and for $R > R_t \approx 415$ a spatially uniform turbulent flow is observed. Consult Bottin et al. (1998) and references therein for more details about original experimental findings and Manneville (2004b, pp. 257–262) for a review. The emerging global transition scenario is in all points similar to the one that takes place in circular Couette flow between counter-rotating cylinders, where spiral turbulence is observed (Coles, 1965), as reviewed at length by Prigent in this volume (see also Prigent, 2001).

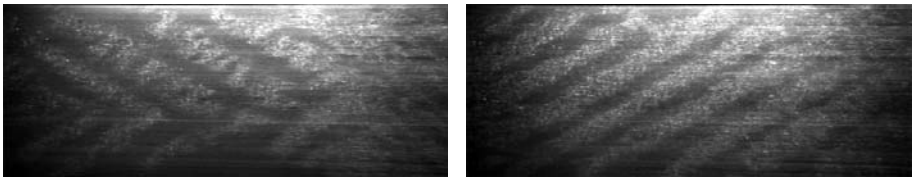

Figure 6. In large aspect ratio systems, turbulent spots evolve into oblique stripes, broken for $R < 360$ (left) and continuous beyond (right). Pictures: courtesy A. Prigent.

Current understanding of the transition to turbulence usually appeals to the theory of dynamical systems and the concept of chaos in line with early modeling by Landau (1944), further amended by Ruelle and Takens (1971). The actual transition problem in wall flows however displays specificities, both conceptual and practical. Questions relate in particular to the mechanisms sustaining nontrivial states and the fact that, by contrast with closed flows like convection, the spatially extended, open, character of the flow can never be neglected. In line with the seminal analysis/conjecture put forward in Pomeau (1986), further developed in Bergé et al. (1998), we organize the rest of this article as follows: In Section 2 we deal with "low-dimensional" conceptual aspects, trying to make explicit what can be learned from the analogy with thermodynamic phase transitions within the framework of dynamical systems. Section 3 focuses on *high-dimensional* features linked to space-time dependence, introducing Pomeau's concept of space-time intermittency (STI) and associated statistical tools. In fact, these interesting approaches remain too abstract and it is not clear how to use them in a given concrete context such as transitional plane Couette flow. This is the reason why we complete this presentation by an account of our personal semi-realistic modeling attempt in Section 4, before drawing some general conclusions in Section 5.

2. LOW-DIMENSIONAL CONCEPTUAL MODELS

Conceptual questions about the direct transition to turbulence were raised by Y. Pomeau using the analogy between subcritical bifurcations and first-order phase transition in thermodynamics, and pointing out the problem of nucleation of the turbulent state and fronts coexisting between laminar and turbulent domains.

In fact, the theory of elementary catastrophes already parallels the Landau theory of phase transitions since both rely on gradient-flow dynamical systems. For example, the bifurcations of a one-dimensional real vector field $\mathcal{F}_R$, depending on control parameter R are typically governed by a first-order dif-

ferential equation

$$\frac{\mathrm{d}}{\mathrm{d}t}A = \mathcal{F}_R(A) \equiv -\frac{\partial \mathcal{G}_R}{\partial A}\,, \tag{1}$$

where $\mathcal{G}_R$ is the potential from which $\mathcal{F}_R$ derives. Standard Landau theory rests on a Taylor expansion of $\mathcal{G}_R$ understood as a *free energy*, a function of variable A called the *order parameter*. Such an account of thermodynamic phase transitions is termed 'classical' since microscopic thermal fluctuations are neglected.

The characteristic feature of a first-order transition (a subcritical bifurcation) is phase (state) coexistence, i.e. the possibility of separated domains in physical space, homogeneously filled with one or another phase (state). A suggestion was then made in Pomeau (1986) to deal with nucleation and front propagation typical of such a coexistence by adding the space diffusion of the order parameter, thus converting (1) to a Ginzburg–Landau equation. When the direct transition to turbulence is considered, this simple formulation however does not account for the intrinsically random nature of the turbulent state. This led him to complete the picture by making a link with stochastic growth in terms of percolation processes. Before reviewing it in Section 3 let us keep the low-dimensional perspective opened by (1) and its extensions. Issues pertaining to non-normality, transient energy growth, and nonlinearity are first considered in Section 2.1. Nontrivial states and the self-sustaining process from which they originate are then examined in Section 2.2. The low-dimensional reduction follows from a *minimal flow unit* (MFU) assumption,[2] the possible short-comings of which are considered in Section 2.3. The role of noise in the thermodynamic analogy and the problem of nucleation understood as the escape from a potential well, or alternatively as resulting from a *crisis* are briefly evoked in Section 2.4.

2.1 Is transient energy growth triggering the transition?

Hydrodynamic stability theory has a long history basically relying on normal mode analysis and the implicit assumption that, as long as perturbations are sufficiently small, the dynamics can always be studied in terms of a direct sum of independent elementary dynamics of non-degenerate eigenmodes. This *modal* approach has more recently been challenged by the theory of *non-modal* energy growth in which the non-orthogonality of normal modes implies a transient amplification of perturbations able to trigger the by-pass transition to nontrivial states. The relevance of this linear point of view stems from the fact that the nonlinear advection term conserves the kinetic energy, as emphasized in Henningson and Reddy (1994). Low-dimensional differential models are particularly well designed to discuss such problems and in particular the respective roles of non-normality (non-orthogonality of eigenmodes)

(Trefethen et al., 1993) and nonlinearity (non-uniqueness of solutions) (Waleffe, 1995; Henningson, 1996).

The simplest possible illustration of non-normal interactions is obtained from the following two-dimensional model:

$$\tfrac{\mathrm{d}}{\mathrm{d}t}X_1 + a_1 X_1 = X_2\,, \qquad \tfrac{\mathrm{d}}{\mathrm{d}t}X_2 + a_2 X_2 = 0\,, \tag{2}$$

where, in a NS context, coefficients a_j are real and positive with $a_j \propto 1/R$, in order to account for viscous damping. Since the second mode is supposed to be more strongly damped than the first one, it is further assumed that $a_2 \gg a_1$. Accordingly, the base state at the origin $X_1 = X_2 = 0$ is a stable node. The kinetic energy $E = \frac{1}{2}\left(X_1^2 + X_2^2\right)$ is here the norm deriving from the canonical scalar product, and it is immediately seen that $\frac{\mathrm{d}}{\mathrm{d}t}E$ is a quadratic form that is not definite negative for all $a_j > 0$, but that there exists a sector in phase space where E is amplified when $\Delta = 1 - 4a_1a_2$ is positive, i.e. for R sufficiently large. The linear dynamics governed by (2) is illustrated in Figure 7. Anticipating over the nonlinear case, it should be emphasized that no qualitative difference can be observed between the situation when dissipation is sufficiently strong to drive a monotonic relaxation towards the base state ($\Delta < 0$, Figure 7, left) and the opposite situation ($\Delta > 0$, Figure 7, right) when inertia begins to win so that the energy can initially increase while eventually decaying. An appropriate variable change would yield a monotonic decrease of the exotic energy defined from the canonical inner product associated with the eigen-basis, but the understanding of this norm as a physical perturbation energy would be lost. The picture is typical of the relaxation towards a stable improper node, which in turn is due to eigenvalue degeneracy (Jordan block structure). Here degeneracy is to be found at the limit $R \to \infty$ when all viscous damping rates a_j go to zero. In this limit, converting the linear operator to diagonal form remains formally possible but near-degeneracy makes it an ill-posed problem and the search for the associated exotic energy irrelevant.

As long as the evolution of infinitesimal perturbations is considered, the long-term dynamics is controlled by the sign of the real part of the eigenvalues, so that relaxation is eventually observed. In the terminology of dynamical systems, the fixed point at the origin in phase space is a sink. To know how long conclusions from the linear analysis are valid, we must add nonlinearities. For model (2) a simple choice in line with the NS analogy is:

$$\tfrac{\mathrm{d}}{\mathrm{d}t}X_1 + a_1 X_1 = X_2 + X_1 X_2\,, \qquad \tfrac{\mathrm{d}}{\mathrm{d}t}X_2 + a_2 X_2 = -X_1^2\,. \tag{3}$$

Nonlinearities indeed conserve energy E and can be directly related to the advection term of a Burgers-like equation $V\partial_x V$ upon expansion in Fourier series $V = X_1 \sin x + X_2 \sin 2x + \cdots$ and appropriate amplitude rescaling. Phase portraits of the nonlinear system (3) are displayed in Figure 8. They

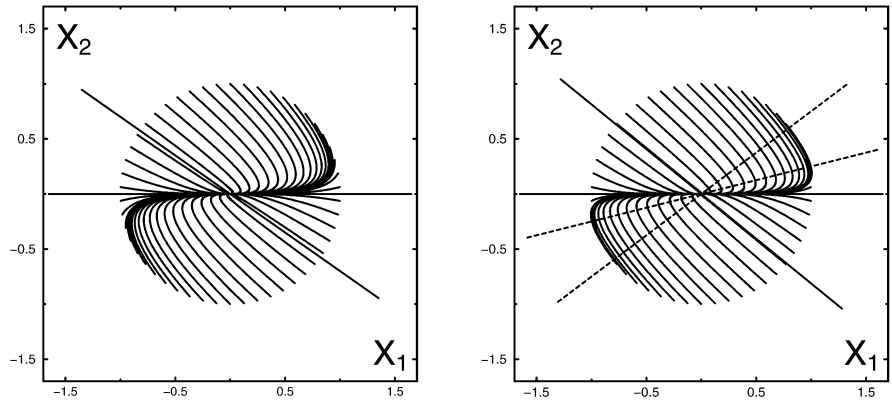

Figure 7. Phase portraits of system (2) for $\Delta < 0$ (left) and $\Delta > 0$ (right). Eigen-directions are the X_1 axis and the oblique continuous line. The sector where the perturbation energy E is amplified is indicated by dashed lines. Scales are arbitrary since the system is linear and thus invariant with respect to multiplication by any numerical factor.

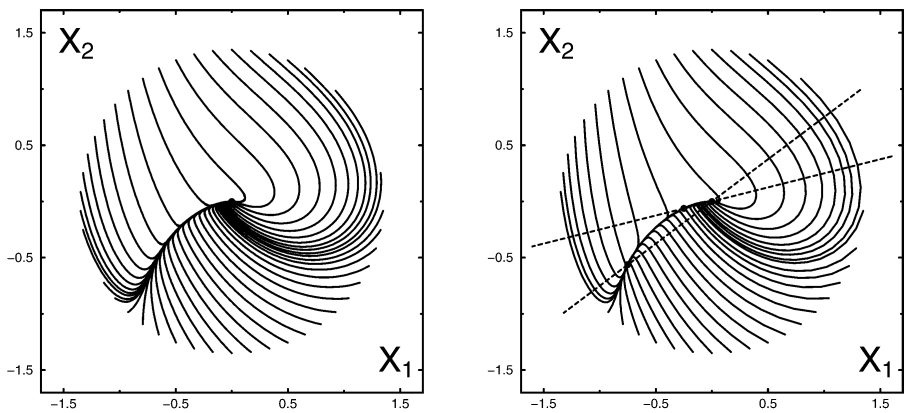

Figure 8. Phase portrait of (3) in the large. Scales are no longer arbitrary but on the contrary fixed by the numerical coefficients of the nonlinear system. The pictures in Figure 7 still hold but in an infinitesimal neighborhood of the origin.

are strikingly different from the linear phase portraits in Figure 7, which could be anticipated from the fact that nonlinear terms fix an amplitude scale, which was not the case of the tangent dynamics at the origin. Except very close to the origin, nonlinearities strongly distort the trajectories, destroy the $\mathbf{X} \to -\mathbf{X}$ symmetry and make the trajectories concentrate in a region of slow dynamics with parabolic shape, to the left of the origin. Fixed points are the trivial

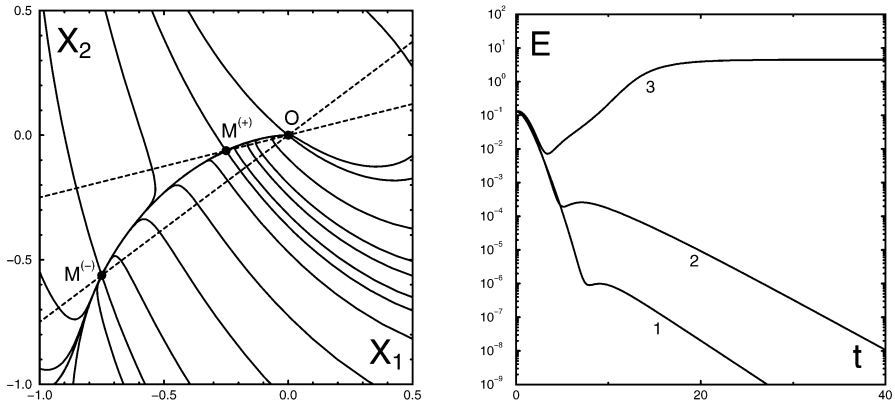

Figure 9. Left: Zoom on the neighborhood of the fixed points. The origin **O** is a stable node; nontrivial fixed points are $\mathbf{M}^{(-)}$, another stable node, and $\mathbf{M}^{(+)}$ a saddle. Dashed lines mark the sector where E increases. Thick continuous lines correspond to the invariant manifolds of the different fixed points. Thin lines represent typical orbits. The stable manifold of $\mathbf{M}^{(+)}$ serves as a frontier between the attraction basins of **O** and $\mathbf{M}^{(-)}$. Right: Evolution of E for three trajectories with same initial shape X_2/X_1 and increasing amplitude, 1 & 2 relax to the origin, 3 start on the other side of the stable manifold of $\mathbf{M}^{(+)}$ and terminates at $\mathbf{M}^{(-)}$.

solution $X_1 = 0$ and two nontrivial solutions ${X_1}^{(\pm)} = \frac{1}{2}(-1 \pm \sqrt{\Delta})$, and corresponding X_2 obtained from $X_2 = -X_1^2/a_2$, provided that $\Delta > 0$. A conventional saddle-node bifurcation takes place[3] at $\Delta = 0$. Another remarkable feature of the nonlinear phase portraits in Figure 8 is that differences between them are revealed only through a close inspection of the behavior along the slow parabolic manifold near the origin, as shown by the zoom on that region displayed in Figure 9 (left).

From these pictures, it is easily understood that, though relevant, the nonnormality of the linearized operator is not in itself responsible for the by-pass transition. The other essential ingredient is the nonlinearity of the perturbation equations. In particular, the main problem is that of computing the stable manifold of the unstable fixed point, which extrapolates the stable linear subspace close to the saddle point $\mathbf{M}^{(+)}$, since this manifold forms the boundary of the attraction basins of the stable nodes **O** and $\mathbf{M}^{(-)}$. Trajectories with initial perturbation energy less than the distance from the origin to the stable manifold return to it, while those with a larger energy may definitively depart from it (Figure 9, right). In the case of model (3), for R sufficiently large this critical distance is easily found to vary as R^{-3} by approximating the stable manifold of $\mathbf{M}^{(+)}$ by the stable eigendirection but this result is not generic. The scaling appropriate to plane Couette flow is a long standing theoretical and experimen-

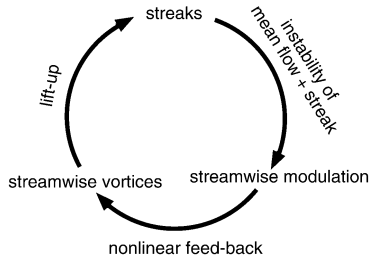

Figure 10. Self-sustaining process as it emerges from the detailed study of numerical simulations, see e.g. Hamilton et al. (1995): assume first the presence of weak streamwise vortices; by transporting fluid particles from regions where the flow velocity is different, they induce a spanwise modulation of the base flow, i.e. the streak component; in turn the superposition of the base and streak flows may become unstable, regenerating the streamwise vortices.

tal problem, see e.g. Schmid and Henningson (2001, chapter 9) for a review, Chapman (2002) for a recent analytical determination, and Cossu (2005) for further discussion. In spite of its shortcomings inherent in dimension two, consideration of Model (3) is enlightening. In particular it helps to weight (linear) non-normal and nonlinear features by showing that the issue of linear transient energy growth is overshadowed by the problem of finding the most critical part of the nonlinear boundary of the basin of attraction of the base flow. Shortcomings linked to dimension two are mainly that (i) monotonic stability is lost exactly when nontrivial solutions emerge at $\Delta = 0$, (ii) when non-trivial states appear, one is necessarily stable and the other unstable, and (iii) the stable manifold of $\mathbf{M}^{(+)}$ is one-dimensional and divides the two-dimensional phase space into attraction basins. All these specificities no longer hold in higher dimensions, which makes the search for the most dangerous perturbations much more tricky and forbids easy sizing up of the attraction basin of the base state (see next subsection and Cossu, 2005). Several other equally simple two or three-dimensional models have been proposed, for example in Trefethen et al. (1993) or Gebhardt and Grossmann (1994), with similar objectives and comparable limitations, see Waleffe (1995), Baggett and Trefethen (1997), Grossman (2000) for critical reviews.

2.2 Modeling the self-sustainment of nontrivial states

In addition to illustrating abstract considerations, models can also be devised to study specific processes in the flow and in particular the mechanisms by which nontrivial states can be sustained (Figure 10). Here we present such a model proposed in Waleffe (1997) and obtained by an appropriate truncation of a Galerkin expansion of the NS dynamics within the assumption of cross-

stream stress-free boundary conditions and in-plane periodic boundary conditions with wavelengths comparable to what was observed in realistic numerical simulations. Its interest lies in the fact that it should capture the essence of the mechanism, in spite of unrealistic boundary conditions and few supplementary assumptions. The model reads:

$$\begin{aligned}
\tfrac{\mathrm{d}}{\mathrm{d}t}X_1 + a_1 X_1 &= b_1^{44} X_4^2 + b_1^{23} X_2 X_3 + Z\,, \\
\tfrac{\mathrm{d}}{\mathrm{d}t}X_2 + a_2 X_2 &= b_2^{44} X_4^2 + b_2^{13} X_1 X_3\,, \\
\tfrac{\mathrm{d}}{\mathrm{d}t}X_3 + a_3 X_3 &= b_3^{44} X_4^2\,, \\
\tfrac{\mathrm{d}}{\mathrm{d}t}X_4 + a_4 X_4 &= b_4^{24} X_2 X_4 + b_4^{14} X_1 X_4 + b_4^{34} X_3 X_4\,.
\end{aligned}$$

Each mode X_j, $j = 1 \ldots 4$ can be related to a physical quantity in the flow. Variable X_1 represents the streamwise mean flow, X_2 is the *streak* component, i.e. a spanwise modulation of the mean flow velocity, X_3 corresponds to *streamwise vortices*, and X_4 to a fluctuation that accounts for the instability of the streak component, Z is the forcing that generates the base mean flow $X_1 = Z/a_1$. Viscous relaxation leads to $a_j \propto 1/R$ with $a_j > 0$, $j = 1 \ldots 4$. Energy conservation further implies relations between the nonlinear coefficients, namely $b_1^{44} = -b_4^{14}$, $b_1^{23} = -b_2^{13}$, $b_2^{44} = -b_4^{24}$, and $b_3^{44} = -b_4^{34}$. Properties of the model have been first studied in Waleffe (1997) and later in Dauchot and Vioujard (2000) from which Figure 11 is adapted. Like Model (3), Waleffe's model has only one stable node at the origin when R is small, the trivial solution corresponding to the base state BS. For R large enough, it has two supplementary nontrivial solutions called LB (*lower* solution branch) and UB (*upper* branch). At the value of R considered for Figure 11, UB is a stable spiral fixed point (hence a time independent solution) but, in association with the unstable limit cycle that has bifurcated from it, it is a remnant of the self-sustaining process (SSP). Another interesting feature of the model is that, at the saddle-node threshold, the pair (LB,UB) is unstable while UB becomes stable at larger R only. By contrast with Model (3) for which UB is stable and LB unstable right at threshold, this property is typical of systems in dimension larger than two since then there is enough room for unstable directions in phase space away from the manifold that supports the bifurcation set (see Note 1). Waleffe's four-dimensional model is thus a low-cost illustration of how phase space can be complicated, which is *a fortiori* expected to hold for the full NS problem (see, e.g., Figure 2). Approximations made in the course of its derivation oblige one to consider this model as a conceptual model of SSP rather than a semi-realistic model of it. Other attempts, in particular by the Marburg group (Schmiegel, 1999; Eckhardt and Mersmann, 1999; Moehlis et al., 2004), have taken more care to fulfill NS requirements, obtaining higher-dimensional models mostly used to study the sensitivity to initial conditions,

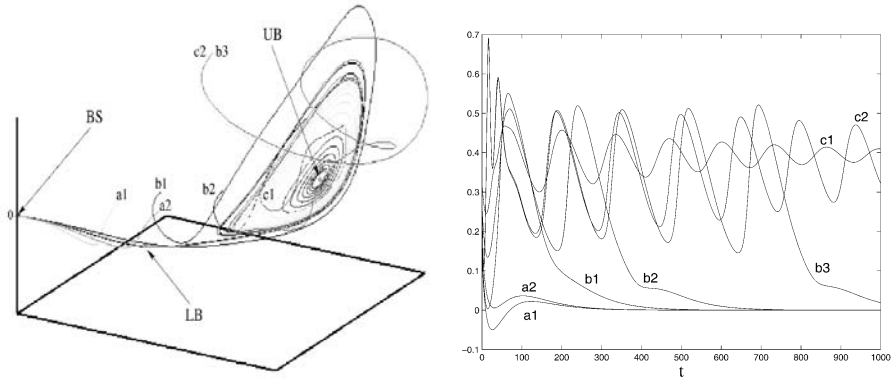

Figure 11. Left: three-dimensional projection of the phase portrait of Waleffe's model in a typical case relevant to attractor coexistence ($R = 160$). Besides the origin BS (stable node), two nontrivial fixed points are to be found: LB (saddle) and UB (stable focus). The boundary of the attraction basin of stable fixed points are already very complicated. Trajectories are guided by the stable manifolds of LB and of an invisible unstable limit cycle that has emerged from a subcritical Hopf bifurcation of UB. Trajectories emerging from a series of neighboring initial conditions are displayed. Some relax to the origin, others to UB, with possibly long, complicated, oscillatory transients. Right: time series corresponding to trajectories labeled on the left panel: immediate relaxation to BS (a1,a2), relaxation to BS after one or several turns around an unstable limit cycle (b1,b2,b3), oscillatory relaxation to UB (c1,c2,c3); notice that (b3) and (c2) start close to each other. For details, see Dauchot and Vioujard (2000).

chaotic transients, decay rates and the fractal character of the basin boundaries, e.g. Schmiegel and Eckhardt (1997).

2.3 The MFU assumption and size effects

As already mentioned in Note 2, it is often assumed that the number of degrees of freedom necessary to account for the transition to turbulence can be reduced by decreasing the flow domain to a size at which underlying mechanisms are too damped to sustain the nontrivial state. It is not easy to discuss the validity of this approach in the case of the NS equations but hints of possible shortcomings of the MFU assumption can be obtained from the consideration of a simple model, namely the Kuramoto–Sivashinsky equation (see Manneville, 1988). Resembling the NS equations to some extent, it is a partial differential equation for a scalar field whose one-dimensional version reads:

$$\partial_t w + w\partial_x w = -\partial_{xx} w - \partial_{xxxx} w \,. \tag{4}$$

This form is parameterless. When periodic boundary conditions are set at a distance ℓ in direction x, the nature of the solutions thus depends only on the value of ℓ, or equivalently on the aspect-ratio $\Gamma = \ell/\lambda_{\max}$. The linear part of the evolution operator indeed allows us to define an intrinsic length-scale $\lambda_{\max}$

from the most unstable wavevector $k_{\max} = 2\pi/\lambda_{\max} = 1/\sqrt{2}$ corresponding to the maximum growth rate $s_{\max} = 1/4$ of modes $\exp(st + ikx)$ as easily derived from their dispersion relation $s = k^2 - k^4$.

As Γ is increased, one obtains an alternation of sustained chaotic solutions and globally stable laminar states in the form of time-independent cellular solutions or nonlinear traveling waves (Hyman et al., 1986). Non-chaotic solutions exist for ℓ in narrow windows centered around the successive multiples of the basic length $\lambda_{\max}$, which corresponds to the fact that domains of such lengths can accommodate given numbers of stable pair of normal cells, simply repeated by periodicity. Other regular solutions can be constructed with anomalous cells made by gluing together single arches or/and making them slide to get traveling waves, which enlarges the set of possibilities as Γ increases. All these laminar states can be reached provided that geometrical resonance condition are fulfilled. However, though such solutions do exist as global attractors in narrow Γ-windows while chaos prevails elsewhere, the time τ necessary to reach them is observed to increase exponentially with the length.

Translating these results to the wall flow problem should sound as a warning since we may understand the size of the MFU as the intrinsic length scale in the KS equation below which the sole solution is the trivial one. Here it would just be the streamwise/spanwise size necessary to have a pair of streamwise vortices and associated streaks active in the flow. This may lead to an overestimate of the Reynolds number necessary to have a *sustained* turbulent state. The implicit periodic repetition at such a small size indeed plays the role of an effective confinement that should be relaxed by considering larger systems. In turn this would allow the possible excitation of subharmonics of the basic pattern *via* long-wavelength instabilities such as the Eckhaus instability, or the outbreak of dislocations in the pattern. Consideration of larger domains would also accommodate the counterpart of KS anomalous cells and propagating waves that play their part in the complexity of the phase space structure and the emergence of chaotic behavior. We will come back to this point later in Section 4, when dealing with semi-realistic models.

2.4 Escape from a metastable state

Let us come to a another facet of Pomeau's conjectures, namely the close connection between subcritical bifurcations and first-order thermodynamic transitions. In the present context, we have two possible out-of-equilibrium permanent states, the laminar flow and the turbulent regime. Two transitions can be considered, the *laminar* $\rightarrow$ *turbulent* natural (as opposed to triggered) transition due to experimental noise linked to set-up imperfections and residual turbulence, and the *turbulent* $\rightarrow$ *laminar* decay when R is low enough, so that dissipation is sufficiently strong to kill small scale turbulent fluctuations and

make the flow settle down. In the thermodynamic terminology, metastable states correspond to local minima of some relevant thermodynamic potential and potential barriers hinder the thermally activated transition from one minimum to the other, while the Maxwell plateau is defined by the condition that the two potential minima are equal. So, one would like to associate two minima of some potential to either the laminar flow or the turbulent regime and to understand the transition as an escape problem from one metastable state to another. The global stability threshold R_{g} would then be the value of the control parameter corresponding to the Maxwell plateau.

Following Graham (1989), one can extend the definition of thermodynamic potentials to the non-equilibrium case of interest here by converting the deterministic governing equations into stochastic equations. In the simplest possible case of additive white noise, model (3) becomes a Langevin system:

$$\tfrac{\mathrm{d}}{\mathrm{d}t}X_1 + a_1 X_1 = X_2 + X_1 X_2 + \eta_1\,, \qquad \tfrac{\mathrm{d}}{\mathrm{d}t}X_2 + a_2 X_2 = -X_1^2 + \eta_2\,, \tag{5}$$

where η_1 and η_2 are the two components of a delta correlated noise $\langle \eta_j(t)\rangle = 0$, $\langle \eta_j(t)\eta_{j'}(t')\rangle = 2\zeta\delta_{jj'}\delta(t-t')$, where ζ is a measure of the noise intensity. The probability of finding the system at a given place in phase space is then expressed as

$$P_\infty(\mathbf{X};\zeta) = Z(\mathbf{X})\exp(-\Phi(\mathbf{X})/\zeta)\,, \tag{6}$$

where $\Phi(\mathbf{X})$ plays the role of the thermodynamic potential and $Z(\mathbf{X})$ is a prefactor. As an example, Figure 12 displays the potential empirically obtained for system (5) as explained in the caption, which illustrates the thermodynamic analogy in this simple case.

According to this approach, one would interpret the exponential behavior of lifetimes of turbulent transients depicted in Figure 13 (left) as resulting from the escape from a potential well over a barrier according to some Arrhenius law $\exp(-\Delta\Phi/\zeta)$, where $\Delta\Phi$ would be a function of the Reynolds number. One could also determine optimal escape trajectories, according to some *minimal noise energy* principle (Kautz, 1988), i.e. upon minimization of the noise energy necessary to drive the system from an attractor out of its attraction basin. In the simple case of model (5), optimal escape trajectories correspond to heteroclinic trajectories of a *deterministic* four-dimensional system made of:

$$\tfrac{\mathrm{d}}{\mathrm{d}t}X_1 + a_1 X_1 = X_2 + X_1 X_2 + Y_1\,, \qquad \tfrac{\mathrm{d}}{\mathrm{d}t}X_2 + a_2 X_2 = -X_1^2 + Y_2\,, \tag{7}$$

and two *adjoint* equations:

$$\tfrac{\mathrm{d}}{\mathrm{d}t}Y_1 - a_1 Y_1 = -X_2 Y_1 + 2X_1 Y_2\,, \qquad \tfrac{\mathrm{d}}{\mathrm{d}t}Y_2 - a_2 Y_2 = -Y_1 - X_1 Y_1\,. \tag{8}$$

The sought-for heteroclinic trajectories connect the fixed points corresponding to the relevant attractors, either $(\mathbf{X}=\mathbf{0}, \mathbf{Y}=\mathbf{0})$ or $(\mathbf{X}=\mathbf{X}^{(-)}, \mathbf{Y}=\mathbf{0})$ to the saddle $(\mathbf{X}=\mathbf{X}^{(+)}, \mathbf{Y}=\mathbf{0})$ on the basin boundary. This approach, especially

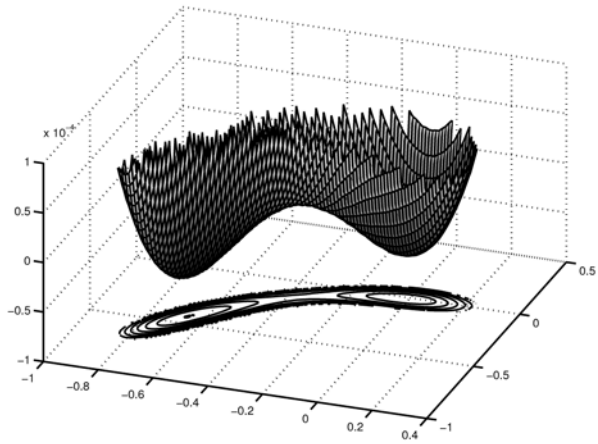

Figure 12. Potential $\Phi(\mathbf{X})$ as defined from (6) and computed from the statistics of arbitrarily long trajectories of (5) for $\Delta = 0.09$ and $a_2 = 1$ [we recall that $\Delta = 1 - a_1 a_2$] through pointwise elimination of $Z(\mathbf{X})$ between two box-counting estimates of the probability $P_\infty(\mathbf{X})$ for $\zeta = 10^{-4}$ and $\zeta = 5.10^{-5}$.

the introduction of (8) arising from the minimization of noise energy that plays the role of a cost function, is quite close to what is currently developed in *control theory*.

Limitations of this appealing perspective stem from the fact that, even if the reduction to so few variables were valuable, probabilities and subsequent potentials would likely be impossible to determine either analytically or practically, e.g. by box-counting which is ineffective in dimensions larger than two. For the same reason optimal escape trajectories would be out of reach since finding heteroclinic trajectories in a phase space with doubled dimension cannot be concretely achieved in general. At any rate, this would be of little help here because a singular variation of the potential barrier would have to be assumed as the global stability threshold R_g is approached from below since the average lifetime is observed to diverge roughly as $1/(R_g - R)$ as depicted in Figure 13 (right).

So, putting aside the thermodynamic analogy, one can instead find an apparently convincing interpretation of this phenomenon in terms of low-dimensional dynamical systems and chaotic transients at a *boundary crisis* (Grebogi et al., 1983). As a simple example to be reused later, let us consider the tent map defined by $X^{k+1} = rX^k$ for $X^k \leq 1/2$ and $X^{k+1} = r(1 - X^k)$ for $X^k > 1/2$, superscript k denoting (discrete) time, see Figure 14 (left). As long as $1 < r \leq 2$, the map is chaotic and the interval [0, 1] is invariant under the map. Beyond $r = 2$, this interval ceases to be invariant. Trajectories

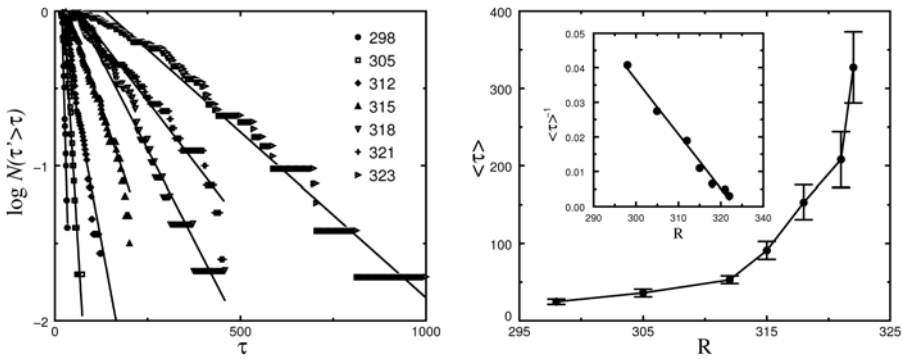

Figure 13. Study of transients in plane Couette flow experiments where the flow is suddenly quenched from some high-R turbulent regime to a given lower value of R. Left: Distribution of transients with duration larger than τ as a function of τ for different values of R below R_g. Right: Divergence of the mean duration of transients as $(R_g - R)^{-1}$. After Bottin et al. (1998).

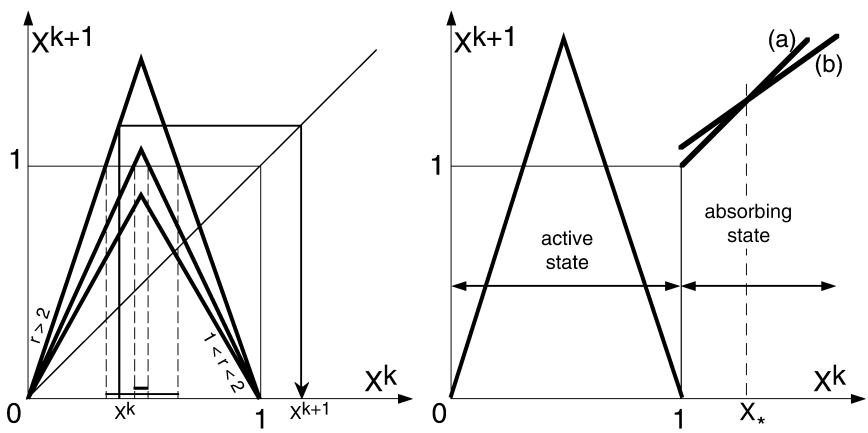

Figure 14. Left: Tent map. Interval [0, 1] is invariant and trajectories are chaotic provided that $1 < r \leq 2$. When $r > 2$ trajectories leak through a tiny hole around $X = 1/2$ and the mean lifetime of chaotic dynamics diverges as r is approached from above. Right: Local map used in the study of STI (Chaté and Manneville, 1990); instead of escaping to $-\infty$ trajectories remain "stuck" in some way for $X^k > 1$, which defines the laminar dynamics as (a) $X^{k+1} = X^k$, i.e. marginal stability, or (b) $X^{k+1} - X_* = p(X^k - X_*)$ with $0 < p < 1$ i.e. asymptotic stability of fixed point X_*.

all end at $-\infty$ after chaotic transients with durations depending on the initial conditions, except those belonging to a zero-measure Cantor set which, strictly speaking, is a *repellor*, i.e. an *unstable* set. By contrast, *metastability* was introduced above for a state which was *locally stable* (finite-measure inset and empty outset in the context of deterministic dynamical systems) but from which escape was possible due to additional random fluctuations. A simple calculation shows that the distribution of lifetimes of chaotic transients is exponential and that the average lifetime diverges as $1/(r-2)$ when r approaches 2 from above. As already mentioned, this viewpoint is currently adopted within the approach sketched earlier in this section, e.g. in Schmiegel and Eckhardt (1997). According to it, the transition *turbulent* $\rightarrow$ *laminar* is just the conversion of a chaotic attractor into a chaotic repellor riddled with holes belonging to the basin of attraction of the laminar flow at the crisis point R_{g}.

We believe that these two approaches do not faithfully account for the transitional problem. On the one hand, the naive *thermodynamic* approach sketched here takes the system as a whole and defines a potential that, at least formally, sets the laminar and turbulent states on an equal footing, which is not the case. Whereas it seems reasonable to accept that the natural *laminar* $\rightarrow$ *turbulent* transition can be triggered by a weak extrinsic noise, it is not at all clear that the reverse transition can be considered in the same way since turbulent flow on the nontrivial branch is not easily decomposed into a mean flow and fluctuations with the characteristics of a weak random noise. On the contrary, fluctuations are large and even seem to play an essential role. On the other hand, the *crisis* interpretation of the escape from a chaotic attractor neglects the intrinsic space-time dependence at intermediate scales pointed out when discussing the validity of the MFU assumption, which also seems to be an important feature. This is why we now turn to modeling attempts developed in terms of space-time intermittency (STI), which leads one to a different thermodynamic analogy based on the statistical physics of phase transitions and the theory of *critical phenomena*.

3. HIGH-DIMENSIONAL STOCHASTIC APPROACH AND STATISTICS

In the context of low-dimensional systems, the introduction of noise can be seen as an extrinsic way to take an infinity of hidden degrees of freedom into account. In this section, we consider rather an intrinsic way to do so by developing an approach that explicitly deals with space dependence. Here we follow another of Pomeau's proposals: to translate the state coexistence *in phase space* typical of subcritical bifurcations into a competition *in physical space*, and discuss the existence and motion of interfaces between domains occupied by each of the different possible states. A first possibility is to unfold

the space dependence of models such as (3) by allowing space diffusion of its order parameter, thus transforming an ordinary differential equation into a partial differential equation (PDE). The simplest variation on this theme is the real Ginzburg–Landau (GL) equation, here in one dimension:

$$\tau_0 \partial_t A = \xi_0^2 \partial_{xx} A - \frac{\partial \mathcal{G}_R}{\partial A}\,, \tag{9}$$

where the potential $\mathcal{G}_R(A)$, depending on the control parameter R, displays two local minima (stable) for $A = A_{1,3}$ separated by a relative maximum (unstable) at $A = A_2$, much like potential Φ defined in Section 2.4. Fronts separating locally stable domains of A_1 and A_2 are easily shown to move without deformation in the direction producing a decrease of $G(t) = \int \mathcal{G}(x,t)\,\mathrm{d}x$. The front stays at rest for $R = R_\mathrm{M}$ (Maxwell plateau) defined by $\mathcal{G}_{R_\mathrm{M}}(A_1) = \mathcal{G}_{R_\mathrm{M}}(A_2)$ and, except for this special value, one kind of state always "wins," while experiments leave the possibility of a (statistically) steady coexistence in finite ranges of R. More complicated models have thus been considered, with nonlinearities breaking the gradient character of (9), e.g. Bottin and Lega (1998), or adding nonlocal constraints, e.g. Hayot and Pomeau (1994), in an attempt to understand the domain-size problem, but without definitive answer.

In the Ginzburg–Landau approach, space dependence and subsequent front motion are treated with an emphasis on the *macroscopic* coherence implied by the introduction of the diffusion operator. Following Pomeau, one can think of coexistence implied by subcriticality at a *mesoscopic* scale. Let us consider a spatio-temporally discrete version of the primitive continuous model (i.e. in terms of PDE) in which a regular lattice of sites is defined with a dynamical system attached to each site. All the distributed local dynamical systems are identical with two possible states, one called *absorbing* corresponds to the laminar state and the other called *active* to the turbulent state. The rule of the game is that absorbing states can never become active by themselves but only by contamination from a neighboring active state, with a given probability ϖ. The control parameter is the contamination probability and the observable is the fraction of active states Π akin to the turbulent fraction used to study the plane Couette flow. This process, called *directed percolation* (DP), is thus modeled by a probabilistic cellular automaton, which is a common starting point in epidemics or forest-fire studies. It is characterized by a persistence of clusters of active sites beyond some percolation threshold ϖ_c and, below threshold, by the divergence of life-time and size of clusters triggered from small germs of active sites.

The remarkable fact is that, when analyzed within the framework of critical phenomena in phase transitions theory,[4] this process defines a *universality class* characterized by power law behaviors close to ϖ_c, e.g. $\Pi \propto (\varpi - \varpi_\mathrm{c})^\beta$, where the exponent β just depends on space dimension and other general char-

acteristics of the process (coupling range, short or long; number of absorbing states), just as in the case of second-order thermodynamic phase transitions. For a review of DP, see, e.g., Kinzel (1983).

The evolution of a DP lattice involves successive random drawings of contamination probabilities. In the transition-to-turbulence context, such an extrinsic stochasticity should be replaced by the intrinsic randomness due to the chaotic nature of the active (turbulent) state in competition with the absorbing (laminar) state. This idea is easily implemented in terms of a lattice of coupled maps (CML), as introduced in Kaneko (1985) to study STI:

$$X_j^{k+1} = gF(X_{j+1}^k) + (1-2g)F(X_j^k) + gF(X_{j-1}^k)\,, \tag{10}$$

where j and k denote space and time respectively, and g is a coupling constant. Here we briefly review past work performed in collaboration with Chaté; see Chaté and Manneville (1990) for a more extended presentation with references. For simplicity, one-dimensional lattices of diffusively coupled identical maps F were mostly considered. Contrasting with Kaneko's approach involving a local map F close to a type-I intermittency threshold, in order to test Pomeau's idea about universality we took the map depicted in Figure 14 (right) which has the advantage of making a clear cut definition of the active state, here governed by a tent map with $r > 2$ for $X < 1$, and the absorbing state, here simply taken as a neutrally stable fixed point for $X > 1$, case (a). The model thus depends on two parameters, the slope r of the tent map and the coupling constant g. As discussed earlier, when $r > 2$, chaos is only transient. Accordingly, the uncoupled system ($g = 0$) always return to the global laminar state in spite of local transient chaos. When a coupling $g > 0$ is introduced, local states at given nodes are perturbed by the states at neighboring nodes. These perturbations can hinder the relaxation to the local laminar state, so that, despite the local tendency, a global sustained turbulent state is obtained. Typical results are displayed in Figure 15 for values of g beyond the STI threshold g_c above which local transient temporal chaos is converted into global sustained space-time chaos.

The role of the local dynamics in the chaotic range (parameter r) is easily understood by considering a typical node and its immediate neighbors. Assume that the central node is active. When r is large, chaotic transients are typically short. Its neighbors thus rapidly become laminar and immediately exert a non-random force on it. This leaves little room for intrinsic stochasticity and, accordingly the lattice as a whole behaves in more deterministic way than for conventional DP. In particular, propagating structures are observed, in close analogy with Class IV automata (Wolfram, 1986), see the right panel of Figure 15. In contrast, when r is close to 2, transients are long. Any given node, that has already a marked tendency to stay chaotic, experiences a highly fluctuating force from its neighbors. This global dynamics is closer to the

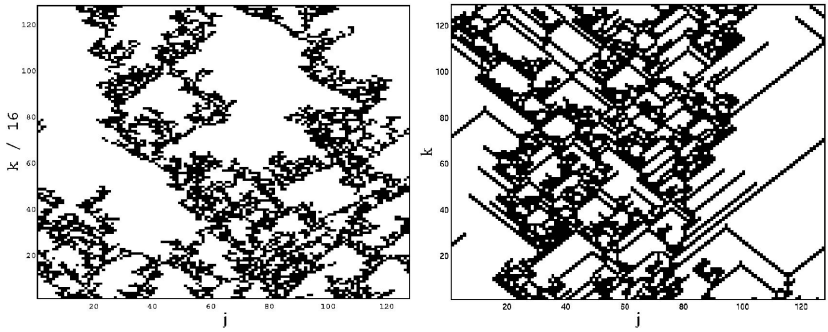

Figure 15. Typical evolution of the CML for $r = 2.1$ (left) and $r = 3$ (right). The evolution for $r = 2.1$ is reminiscent of DP (notice the slow time dependence and the random aspect of clusters of active nodes). By contrast a situation close to that occurring with cellular automata takes place when $r = 3$, especially class IV automata, owing to a stronger influence of deterministic dynamics and corresponding lesser role of (intrinsic) stochasticity.

stochastic archetype offered by DP as seen in Figure 15 (left). This visual difference has also a quantitative translation in terms of critical exponents, e.g. exponent β defined from the variation of the average turbulent fraction with the coupling constant g as $F_t \propto (g - g_c)^\beta$. For $r = 3$ one gets $\beta \approx 0.25$, significantly different from $\beta \approx 0.28$ for DP, which is almost exactly the value obtained for STI with $r = 2.1$.

Subsequent studies showed that the universality issue was tricky owing to anomalously persistent size effects. The problem was with reaching the *thermodynamic limit* of an infinitely large system observed at steady state after a supposedly infinitely long transient (Grassberger and Schreiber, 1991). The synchronous character of the dynamics defined by (10) was also questioned since DP universality class was systematically recovered when asynchronous dynamics was adopted, i.e. an update of nodes, not simultaneous as with (10), but one after another randomly-chosen one (Rolf et al., 1998).

These facts should however not lead us to dismiss STI as a key process in the understanding of the transition to turbulence of plane Couette flow and other globally subcritical systems in extended geometry since it is much more versatile than suggested above. Whereas universality is a requirement posed *a priori* for continuous transitions, when considering Figure 4 (right), it is clear that the transition at R_g is discontinuous. Furthermore this question of universality was discussed mainly in the one-dimensional case and for a neutrally stable laminar dynamics, case (a) in Figure 12 (right). But, already in the one-dimensional case, for the damped Kuramoto–Sivashinsky equation, i.e. (4) with a supplementary term $-\eta w$, $\eta > 0$, on the right-hand side, the transition *via* spatio-temporal intermittency at $\eta \approx 0.075$ was likely discontinuous (Manneville, 1990, chapter 10, §4. Even more convincingly, two-dimensional coupled map

lattices with asymptotically stable laminar dynamics, case (b) in Figure 12 (right), were known to display a discontinuous transition (Chaté and Manneville, 1988). Because two-dimensional systems are clearly more relevant to the experimental situation than one-dimensional systems, their study was resumed later on (Bottin and Chaté, 1998), pointing out the semi-quantitative validity of this analog modeling in which each lattice node is intended to represent a MFU and the coupling between them to deal with nontrivial space-time dependence in extended geometry. The most striking result was the existence of threshold fulfilling the characteristics of R_g, beyond which space-time chaos was sustained and below which it was only transient but with diverging lifetime in the limit $R \to R_g$, whereas the active fraction was finite at threshold, in exact correspondence with laboratory results for plane Couette flow.

The STI approach thus deserves further attention since it is capable of accounting for stochastic growth within the deterministic perspective supposed to be valid at the low-R end of the transition region for $R \lesssim R_g$ and a little beyond R_g. It also points to why the reasoning based on a strict MFU assumption might be misleading. We have seen that, in the CML context, only *transient* chaotic local dynamics is needed, and not *sustained* turbulence implicit in the definition of the MFU (see Note 2). Spatial coupling is then explicitly the cause of a conversion of the low-dimensional local dynamics of coherent structures inside the spots into turbulence understood as *space-time chaos*. This observation is precisely what substantiates our search for semi-realistic models to be described now.

4. SEMI-REALISTIC MODELS

The main idea behind our approach in terms of space-time chaos is the assumption of strong cross-stream coherence, which allows us to treat it in a low-dimensional spirit accounting for the local processes, while dropping the constraint of strict periodicity at short streamwise and spanwise distances, i.e. keep the MFU perspective but unfreeze it, hence rather focussing on what happens in the complementary directions. This idea was remarkably fruitful when dealing with the globally supercritical context of convection patterns. It should work also in the subcritical case provided that cross-stream coherence is indeed sufficiently preserved, and that a good account of it can be achieved with a small number of Galerkin modes. As already said, this should be the case at the low-R end of the transitional region. In convection, the analogue of Waleffe's model is the celebrated Lorenz model obtained by cleverly truncating a Galerkin expansion of Boussinesq equations. The Swift–Hohenberg model (Swift and Hohenberg, 1977), supplemented by drift-flow equations (Manneville, 1983) can be viewed as the space-unfolding of the Lorenz model close

to the convection threshold. The explicit derivation of our plane Couette flow model relies the same basic technique (Manneville and Locher, 2000).

As in Waleffe (1997) stress-free boundary conditions are considered and a bulk force is used to drive a sinusoidal base flow profile, consistent with a trigonometric Galerkin expansion. The difference with the standard MFU modeling approach (e.g. Waleffe, 1997; Eckhardt and Mersmann, 1999; Moehlis et al., 2004) is that now the expansion only deals with the cross-stream variable y and no longer assumes a specific periodic streamwise and spanwise dependence. Accordingly all the coefficients are now functions of x, z, and t. Perturbations to the base flow $u = u_{\mathrm{b}} = \sin(\beta y)$, with $\beta = \pi/2$ are then taken in the form

$$u' = U_0 + U_1 \sin(\beta y) + \sum_{n\geq 1} U_{2n} \cos(2n\beta y) + U_{2n+1} \sin((2n+1)\beta y)$$

with similar expressions for v' and w', and p'. Here we just give a glimpse at the equations at the lowest possible truncation order, i.e. including components $n = 0$ and $n = 1$. The projection of the continuity equation on this restricted subset reads

$$\partial_x U_0 + \partial_z W_0 = 0, \qquad \partial_x U_1 - \beta V_1 + \partial_z W_1 = 0. \tag{11}$$

The expression of the momentum equations are more cumbersome. We give here only that governing the streamwise velocity component with $n = 0$:

$$\begin{aligned} &\partial_t U_0 + N_{U_0} = -\partial_x P_0 - \tfrac{1}{2}\partial_x U_1 - \tfrac{1}{2}\beta V_1 + R^{-1}\Delta_2 U_0\,, \\ &N_{U_0} = U_0\partial_x U_0 + W_0\partial_z U_0 + \tfrac{1}{2}U_1\partial_x U_1 + \tfrac{1}{2}\beta V_1 U_1 + \tfrac{1}{2}W_1\partial_z U_1\,, \end{aligned} \tag{12}$$

with $\Delta_2 \equiv \partial_{xx} + \partial_{zz}$. Other equations have similar structures, with a clear viscous contribution (term with R^{-1}), linear non-normal terms arising from the expansion of cross-terms involving u_{b}, and nonlinear terms with the obvious quadratic expression expected for advection terms. The main features of NS plane Couette flow are preserved, in particular energy conservation by advection terms and linear stability for all Reynolds numbers.

Here, we recall preliminary simulation results obtained with the model truncated beyond lowest order (Manneville, 2004a), involving three fields Ψ_0, Ψ_1, and Φ_1, from which velocity components can be recovered through $U_0 = -\partial_z\Psi_0$, $W_0 = \partial_x\Psi_0$, $U_1 = \partial_x\Phi_1 - \partial_z\Psi_1$, $W_1 = \partial_z\Phi_1 + \partial_x\Psi_1$, and V_1 obtained from the second equation in (11). Figure 16 displays the results of quench experiments analogous to those performed in the laboratory. A detailed statistical study would show that the model's global stability threshold R_{g} is a little below $R = 50$.

In connection with the previous discussion about the significance of the MFU assumption, it should be noted that, when periodic boundary conditions

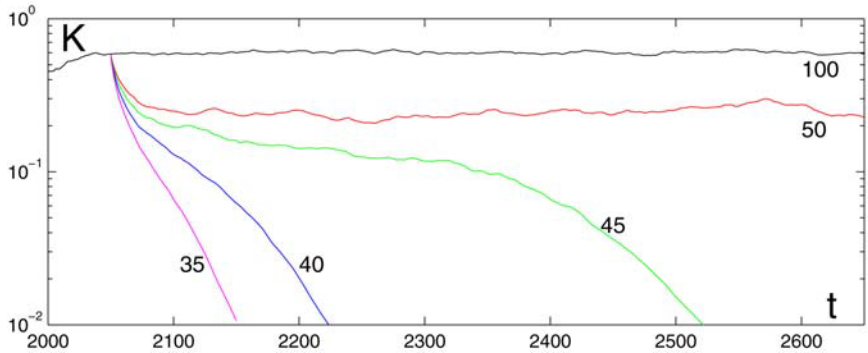

Figure 16. Simulation of the SH-like model for $L_x = 128$, $L_z = 64$ and decreasing values of R (quench experiment). A fully turbulent state is prepared with $R = 100$. At $t = 2050$, R is suddenly decreased. The observable here is the surface-averaged perturbation kinetic energy K. For $R = 50$ turbulence is still sustained, whereas it decays for $R = 45$ after a "long" turbulent transient. As R is further decreased, a direct relaxation to the laminar state is observed.

are imposed at the typical size of the MFU, nontrivial behavior is observed at roughly the same R values as those for Waleffe's model. An important difference is, however, observed: sustained chaos and chaotic transients are obtained instead of time-independent regimes and oscillatory transients, which is the consequence of an enlarged effective phase space. Furthermore, by successively doubling the size of our system, we have observed that, beyond some minimal domain size of the order to a few usual MFUs, the spatio-temporally chaotic (turbulent) regime is extensive in the sense that the average turbulent energy per unit surface is preserved upon changing the in-plane size. This suggests that instead of being related to the self-sustainment property, the MFU size could perhaps be better determined from extensivity property by demanding that *statistical* properties of the flow be no longer sensitive to actual size of the domain.

Let us give two additional examples of situations where the model might help us raise good questions about the dynamics of transitional wall flows. Then we will proceed to a discussion of shortcomings and possible improvements of our modeling.

The first example relates to spot nucleation. The experimental triggering procedure is easily reproduced numerically. Depending on the value of R, the same initial condition can relax or, on the contrary, promote the transition to fully turbulent flow as shown in Figure 17, the left panel of which is strikingly similar to the right panel of Figure 9. Parameterized by the "shape" of the initial condition, i.e. a direction in phase space, a threshold value can be determined which separates orbits that remain inside the basin of attraction of

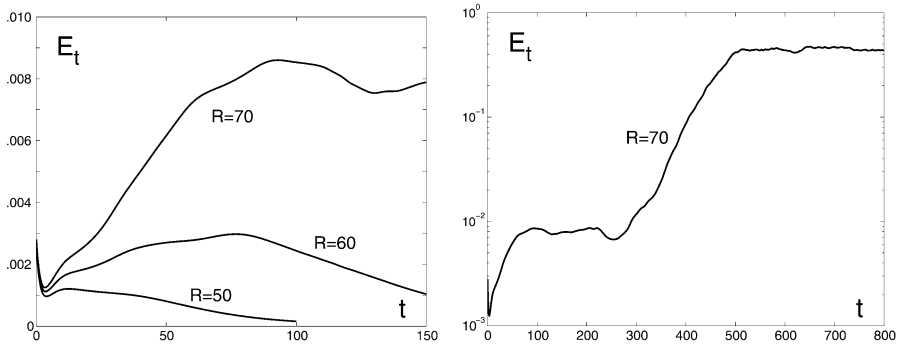

Figure 17. Total perturbation energy as a function of time. Left: $R = 50, 60, 70$, short term evolution in lin-lin scale. Right: $R = 70$, long term evolution in lin-log scale showing the fall-over to sustained turbulence for $R = 70$.

laminar flow and those that become turbulent, maybe after a long hesitation as seen from the plateau for $80 < t < 260$ in Figure 17 (right). This plateau corresponds to a reorganization of the flow around the spot into a streamwise turbulent bands that next expands regularly spanwise from $t \sim 300$ to $t \sim 500$, ending in a homogeneous turbulent state.

As our second example, we take the dynamics of fronts at different values of R. Figure 18 displays the expansion of a turbulent band for $R = 70$, which can clearly be interpreted in terms of a regularly advancing front. In contrast, at $R = 50$ the front also advances (at an insignificantly smaller speed) but the system is seen to relax to laminar flow because turbulence is no longer sufficiently self-sustained, which leads us back to an analysis of the competition between local chaos breakdown and spatial coupling close to R_g analogous to Pomeau's STI.

It might be disturbing that the global stability threshold R_g, below 50, is so far off the experimental value of 325. This can however partly be attributed to the stress-free boundary conditions that artificially decrease the gradients and the associated dissipation, thus lowering the thresholds, in exactly the same was as for convection. This deficiency can be corrected by using a functional expansion appropriate to physical no-slip boundary conditions.[5] For example, a polynomial cross-stream expansion similar to that used in Manneville (1984) is easily seen to yield a system of PDEs with essentially the same structure as the one considered above but with different coefficients. At lowest truncation order the most important modification is the addition of terms damping U_0 and W_0, that is the replacement of Δ_2 by $(\Delta_2 - \tilde{\beta}^2)$ in the equivalent of (12), since those flow components are no longer cross-stream independent. Energy dissipation in the streak flow component, a key mode of the self-sustaining process, should already raise the thresholds.

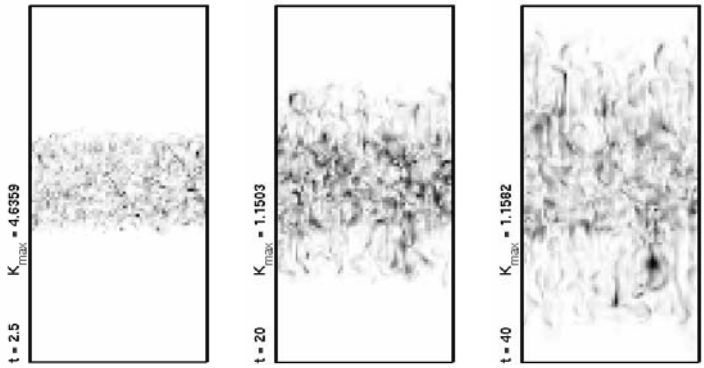

Figure 18. Widening of a spanwise turbulent band for $R = 70$ as depicted by a gray-level representation of the local total perturbation energy, $t = 2.5, 20, 40$. Here the vertical (horizontal) axis features the streamwise (spanwise) direction.

Returning to the stress-free case, the discrepancy in R can of course also be attributed to the small number of fields retained in the simulation since including more functions in the expansion allows for a transfer of energy towards smaller cross-stream scales where it can be dissipated. It is easily shown that higher order truncations have the same nice formal properties as the three-field model.[6] Recent work by M. Lagha with five, seven, and nine fields indeed shows a cascade of energy from large to small cross-stream scales (see Figure 19) but unfortunately little effect on the range of values of R in which interesting things happen, so that one should probably work out the no-slip case more extensively.

Despite its shortcomings, the modeling attempt sketched above already helps us to study local processes pertaining to the transition to turbulence at the low-R end of the laminar-turbulent coexistence region. In particular, work is in progress about the system's capability to propagate turbulence and/or to sustain it since the processes involved might not be the same and have different sensitivity to confinement and non-local effects. Accordingly, mechanisms by which small-scale fluctuations generate large-scale flows can be analyzed in detail, hopefully giving clues to the frequent symmetry breaking observed in the shape of turbulent patches and the subsequent formation of oblique bands from below, i.e. low-R ($R \gtrsim 325$). In addition, the reduced number of cross-stream modes makes it possible to perform numerical simulations in very large domains necessary to approach the limit considered by the thermodynamic arguments, namely the dynamics of fronts separating semi-infinite domains and what determines the apparent equilibrium extension of turbulent patches at large-but-finite aspect-ratios. Unfortunately, the very same reduced number of modes is likely to prevent any reliable interpretation of the formation of

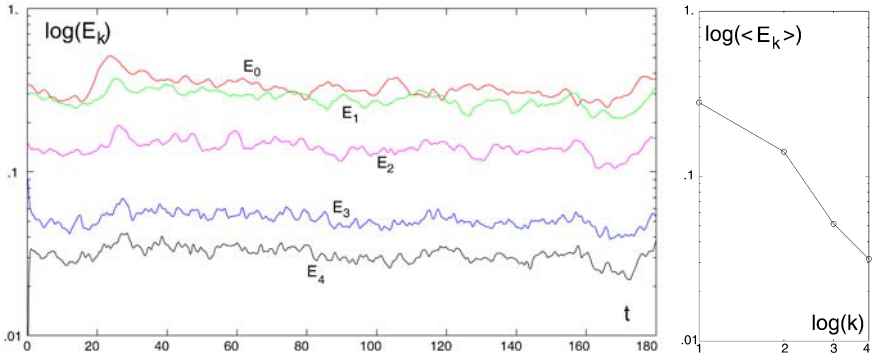

Figure 19. Sustained turbulent regime at $R = 70$ for the nine-field model, Ψ_0, (Ψ_k, Φ_k), $k = 1 \ldots 4$. Left: Spatially averaged kinetic energy contained in modes 0 to 4 as a function of time (lin-log scale). Right: An embryo of cascade toward small cross-stream scales is clearly visible from the plot of the time averaged energies in the left panel as a function of the index of the mode for modes 1 to 4 (log-log scale). Data: courtesy M. Lagha.

oblique turbulent bands from above, i.e. at the high-R end of the transition region ($R \lesssim 440$) since high cross-stream resolution (Barkley and Tuckerman, 2005a) is expected to be necessary to account for this empirical observation. A relevant extension of the present modeling attempt mimicking small-scale dissipation through explicit adiabatic elimination of the highest modes, or the introduction of supplementary variables in the spirit of k-ϵ methods, could however perhaps help us understand what is going on when the bands form out of uniform turbulence.

5. SUMMARY AND CONCLUDING REMARKS

Processes that control the transition to turbulence in wall flows develop at moderately high Reynolds numbers. Their study is made difficult by the globally subcritical character of the bifurcation, in turn linked to the irrelevance of standard low Reynolds number linear instability mechanisms of inertial origin and the existence of nontrivial fully nonlinear states in competition with the laminar base flow. It turns out that the transition has to be studied along two different lines depending on whether one considers the emergence of turbulence from the laminar flow by increasing R or the decay of turbulent flow while decreasing R. On practical grounds, it is illusory to think that one can understand what is going on directly from the primitive equations and we are obliged to resort to modeling. In this contribution we have mostly reviewed the modeling attempts relative to the *laminar* $\rightarrow$ *turbulent* transition. Before summarizing our conclusions about it let us first briefly consider the reverse case, i.e. the *turbulent* $\rightarrow$ *laminar* transition.

Two situations have to be distinguished: (i) the high Reynolds part marked by the emergence of turbulent stripes out of uniformly homogeneous small-scale turbulence, and (ii) the breakdown of the bands ending in the return to laminar flow. These situations are well documented for cylindrical Couette flow (spiral turbulence) as well as for plane Couette flow but they are likely to also take place in other wall flows, though it is certainly more difficult to prepare the corresponding statistically steady regimes in those cases owing to unavoidable downstream flow development. Very little of what we have discussed is relevant to problem (i) which has, up to now, received no clear explanation and is clearly a different challenge. A convincing phenomenological approach in terms of stochastic Ginsburg–Landau formulation has been proposed to interpret several aspects of the bifurcation *homogeneous turbulence* $\rightarrow$ *oblique bands* (Prigent et al., 2003) but the mechanism responsible for it is still open to physical explanation, though the numerical approach developed by Barkley and Tuckerman represents a most promising step in that direction (Barkley and Tuckerman, 2005a). As far as situation (ii) is considered, it should be more easily amenable to interpretation since it holds at lower R, so that the cross-stream coherence of the departure from laminar flow can be assumed, which makes low-dimensional approaches in terms of dynamical systems fully relevant. In these terms, some of the statistical features of the decay are most easily understood as arising from the chaotic-saddle nature of the turbulent regime. However, this neglects the basic coexistence in physical space of laminar and chaotic states, which point to an understanding of this *abstract* chaotic saddle as a *concrete* relaxing STI cluster.

The interest of the STI concept is that a clear separation is made between local processes of two kinds: first, generation and sustainment of chaotic behavior linked to the existence of local phase space with complicated structure allowing for nontrivial states, and second, couplings of local units underlying the idea of a transition due to contamination. An extensive research effort has been devoted to the first kind of process, unfolding the dynamics of the flow within a *minimal flow unit* and leading to a good understanding of the self-sustainment process as a cycle *streamwise vortices* $\rightarrow$ *streaks* $\rightarrow$ *streak breakdown* $\rightarrow$ *vortex regeneration* and several increasingly realistic models have been derived. The same cannot be said from the second kind of process, the coupling between units. There is indeed no reason to assume that the coupling is local and more or less diffusive. On the contrary, the underlying Navier–Stokes character of the dynamics would instead suggest nonlocal interactions and an inverse cascade towards ever larger in-plane structures, while the MFU assumption rather focuses on the small-scale and cross-stream direction. This is mostly the reason why we have attempted to develop 2D semi-realistic models in terms of partial differential equations governing amplitudes arising from a Galerkin expansion of the cross-stream dependence and respecting the speci-

ficities of Navier–Stokes equations. Such modeling allows detailed analysis of the relevant transition mechanisms since it accounts for flow coherence at the appropriate scales. That should help us overcome the limitations of the MFU approach in restoring space-time dependence in a less conceptual perspective than the statistical physics framework underlying percolation.

Beyond the specific case of plane Couette flow, the modeling perspective described here should be of interest to less academic wall flows. This is especially true since for all of them the transition, i.e. the emergence of sustained spots, subsequently merging in bands, eventually evolving into homogeneous small scale developed turbulence, lies in the same range of R when appropriately defined using some effective shear rate, as most easily checked for plane channel Poiseuille flow and counter-rotating Taylor–Couette flow. We hope that this open-minded review, confronting experimental results to approaches in terms of dynamical systems and to perspectives familiar to the statistical physics community, will serve its purpose of (i) reactivating studies that appeared to be conceptual advances but blind alleys from a practical viewpoint, and (ii) stimulating the use of models focussed on the spatio-temporal aspects of the transition to turbulence in open flows.

ACKNOWLEDGEMENTS

The author wishes to thank Y. Pomeau for introducing him to the field, D. Barkley, C. Cossu, B. Eckhardt, L. Tuckerman, for insightful discussions, S. Bottin, H. Chaté, O. Dauchot, F. Daviaud, A. Prigent for early work in common at Saclay on different subjects touched upon in this review, and finally M. Lagha and F. Locher for their collaboration to the most recent work.

Simulations of the semi-realistic model were performed thanks to a CPU time allocation on the NEC-SX5 computer of IDRIS at Orsay (grant 1462).

NOTES

1. The idea that, among the pair of limit sets that appear, one is stable and the other unstable, rests a one-dimensional argument, see Figure 1(b). This still holds in two dimensions as seen in Section 2.1 but not necessarily in higher dimensions, a counter-example is given by Waleffe's model in Section 2.2. We believe that overall instability is the rule in far-from-equilibrium situations corresponding to high-dimensional dynamics at large R.

2. This assumption formalizes the expectation that mechanisms can be analyzed by reducing the size of the flow domain of interest to some minimal value below which turbulence cannot be sustained. See Jiménez and Moin (1991) for one of the first explicit introductions of the MFU concept.

3. The value $\Delta = 1$ taken when a_1 goes through zero would correspond to a transcritical bifurcation of the origin from stable to unstable. This never happens in the plane Couette case.

4. As mentioned earlier, the Landau theory based on (9) neglects thermal fluctuations and only predicts an approximation to the set of critical exponents termed *classical*.

5. Full realism, which is not our purpose, is of course achieved by direct simulation of the NS equations, see e.g. Lundbladh and Johansson (1991) for the spot problem and Barkley and Tuckerman (2005b), or Barkley and Tuckerman (2005a), for the turbulent band problem.

6. At this stage, it should be noted that, with the stress-free model, at least seven fields must be kept in order to account for the mean flow correction pointed out in Moehlis et al. (2004) and thought to play an important role since the corresponding perturbation enters the model through Ψ_3.

REFERENCES

Baggett, J.S. and Trefethen, L.N. (1997). Low-dimensional models of subcritical transition to turbulence. *Phys. Fluids* **9**, 1043–1053.

Barkley, D. and Tuckerman, L. (2005a) Computational study of turbulent-laminar patterns in Couette flow. *Phys. Rev. Lett.* **94**, 014502.

Barkley, D. and Tuckerman, L.S. (2005b). Turbulent-laminar patterns in plane Couette flow. In *Laminar Turbulent Transition and Finite Amplitude Solutions*, Proceedings of the IUTAM Symposium, Bristol, UK, 9–11 August 2004, T. Mullin and R.R. Kerswell (eds), Springer, Dordrecht, pp. 107–127 (*this volume*).

Bergé, P., Pomeau, Y. and Vidal, Ch. (1998). *L'Espace Chaotique*. Hermann, Paris. [Unfortunately not available in English. Of specific interest here: Chapt. III: L'intermittence spatio-temporelle dans les écoulements structurés, and Chapt. IV: Transition vers la turbulence dans les écoulements parallèles.]

Bottin, S. and Chaté, H. (1998). Statistical analysis of the transition to turbulence in plane Couette flow. *Eur. Phys. J. B* **6**, 143–155.

Bottin, S. and Lega, J. (1998). Pulses of tunable size near a subcritical bifurcation. *Eur. Phys. J. B* **5**, 299–308.

Bottin, S., Daviaud, F., Manneville, P. and Dauchot, O. (1998). Discontinuous transition to spatiotemporal intermittency in plane Couette flow. *Europhys. Lett.* **43**, 171–176.

Carlson, D.R., Widnall, S.E. and Peeters, M.F. (1982). A flow visualization of transition in plane Poiseuille flow. *J. Fluid Mech.* **121**, 487–505.

Chapman, S.J. (2002). Subcritical transition in channel flows. *J. Fluid Mech.* **451**, 35–97.

Chaté, H. and Manneville, P. (1988). Continuous and discontinuous transition to spatiotemporal intermittency in two-dimensional coupled map lattices. *Europhys. Lett.* **6**, 591–595.

Chaté, H. and Manneville, P. (1990). Transition to turbulence via spatio-temporal intermittency. In *New Trends in Nonlinear Dynamics and Pattern-Forming Phenomena: The Geometry of Nonequilibrium*, P. Coullet and P. Huerre (eds), NATO ASI series, Series B: Physics, Vol. 237, Plenum Press.

Clever, R.M. and Busse, F.H. (1992). Three-dimensional convection in a horizontal fluid layer subjected to a constant shear. *J. Fluid Mech.* **234**, 511–527.

Coles, D. (1965). Transition in circular Couette flow. *J. Fluid Mech.* **21**, 385–425.

Cossu, C. (2005). An optimality condition on the minimum energy threshold in subcritical instabilities. *C.R. Acad. Sc. Paris* **333**, 331–336.

Dauchot, O. and Manneville, P. (1997). Local versus global concepts in hydrodynamic stability theory. *J. Phys. II France* **7**, 371–389.

Dauchot, O. and Vioujard, N. (2000). Phase space analysis of a dynamical model for subcritical transition to turbulence in plane Couette flow. *Eur. Phys. J. B* **14**, 377–381.

Eckhardt, B. and Mersmann, A. (1999). Transition to turbulence in a shear flow. *Phys. Rev. E* **60**, 509–517.

Gebhardt, Th. and Grossmann, S. (1994). Chaos transition despite linear stability. *Phys. Rev. E* **50**, 3705–3711.

Graham, R. (1989). Macroscopic potentials, bifurcations and noise in dissipative systems. In *Noise in Nonlinear Dynamical Systems*, Vol. 1: *Theory of Continuous Fokker–Planck Systems*, F. Moss and P.V.E. McClintock (eds), Cambridge University Press, pp. 225ff.

Grassberger, P. and Schreiber, T. (1991). Phase transitions in coupled map lattices. *Physica D* **50**, 177–188.

Grebogi, C., Ott, E. and Yorke, J.A. (1983). Crises, sudden changes in chaotic attractors, and transient chaos. In *Order in Chaos*, D. Campbell and H. Rose (eds), *Physica D* **7**, pp. 181ff.

Grossmann, S. (2000). The onset of shear flow turbulence. *Rev. Mod. Phys.* **72**, 603–618 (RPM Colloquia).

Hamilton, J.M., Kim, J. and Waleffe, F. (1995). Regeneration mechanisms of near-wall turbulence structures. *J. Fluid Mech.* **287**, 317–348.

Hayot, F. and Pomeau, Y. (1994). Turbulent domain stabilization in annular flows. *Phys. Rev. E* **50**, 2019–2221.

Henningson, D.S. (1996). Comment on "Transition in shear flows. Nonlinear normality versus non-normal linearity". *Phys. Fluids* **8**, 2257–2258.

Henningson, D.S. and Reddy, S.C. (1994). On the role of linear mechanisms in transition to turbulence. *Phys. Fluids* **6**, 1396–1398.

Herbert, T. (1983). Secondary instability of plane channel flows to subharmonic three-dimensional disturbances. *Phys. Fluids* **26**, 871–874.

Hyman, J.M., Nicolaenko, B., Zaleski, S. (1986). Order and complexity in the Kuramoto–Sivashinsky model of weakly turbulent interfaces. *Physica D* **23**, 265–292.

Jiménez, J. and Moin, P. (1991). The minimal flow unit in near-wall turbulence. *J. Fluid Mech.* **225**, 213–240.

Kaneko, K. (1985). Spatiotemporal intermittency in coupled map lattices. *Progress of Theor. Phys.* **74**, 1033–1044.

Kautz, R.L. (1988). Thermally induced escape: The principle of minimum available noise energy. *Phys. Rev. A* **38**, 2066–2080.

Kinzel, W. (1983). Directed percolation. In *Percolation Structures and Processes*, G. Deutscher et al. (eds), *Annals of the Israel Phys. Soc.* **5**, pp. 425ff.

Lundbladh, A. and Johansson, A.V. (1991). Direct simulations of turbulent spots in plane Couette flow. *J. Fluid Mech.* **229**, 499–516.

Manneville, P. (1983). A two-dimensional model for three-dimensional convective patterns in wide containers. *J. Physique* **44**, 759–765.

Manneville, P. (1984). Modelisation and simulation of convection in extended geometry. In *Cellular Structures in Instabilities*, Wesfreid and Zaleski (eds), Springer Lecture Notes in Physics, Vol. 210, Springer, Berlin, pp. 137–155.

Manneville, P. (1988). The Kuramoto–Sivashinsky equation: A progress report. In *Propagation in Systems Far from Equilibrium*, J.E. Wesfreid et al. (eds), Springer Series in Synergetics, Vol. 41, Springer, Berlin, pp. 265ff.

Manneville, P. (1990). *Dissipative Structures and Weak Turbulence* (Academic Press, 1990).

Manneville, P. (2004a). Spots and turbulent domains in a model of transitional plane Couette flow. *Theor. Comput. Fluid Dynam.* **18**, 169–181.

Manneville, P. (2004b). *Instabilities, Chaos and Turbulence*, Imperial College Press/World Scientific.

Manneville, P. and Dauchot, O. (2001). Patterning and transition to turbulence in subcritical systems: The case of plane Couette flow. In *Coherent Structures in Classical Systems* D. Reguera, L.L. Bonilla and J.M. Rubi (eds), Springer Verlag, Berlin, pp. 58ff.

Manneville, P. and Locher, F. (2000). A model for transitional plane Couette flow. *C.R. Acad. Sc. IIb – Mécanique* **328**, 159–164.

Moehlis, J., Faisst, H. and Eckhardt, B. (2004). A low-dimensional model for turbulent shear flows. *New J. Phys.* **6**, pp. 56ff.

Nagata, M. (1990). Three-dimensional finite-amplitude solutions in plane Couette flow: Bifurcation from infinity. *J. Fluid Mech.* **217**, 519–527.

Orszag, S.A. (1971). Accurate solution of the Orr–Sommerfeld stability equation. *J. Fluid Mech.* **50**, 689–703.

Pomeau, Y. (1986). Front motion, metastability and subcritical bifurcations in hydrodynamics. *Physica D* **23**, 3–11.

Prigent, A. (2001). *La Spirale Turbulente: Motif de grande longueur d'onde dans les écoulements cisaillés turbulents*, PhD Dissertation, Orsay/Paris-Sud University.

Prigent, A., Grégoire, G., Chaté, H. and Dauchot, O. (2003). Long-wavelength modulation of turbulent shear flows. *Physica D* **174**, 100–113.

Rolf, J., Bohr, T. and Jensen, M.H. (1998). Directed percolation universality in asynchronous evolution of spatiotemporal intermittency. *Phys. Rev. E* **57**, R2503–R2506.

Romanov, V.A. (1973). Stability of plane parallel Couette flow (English transl.). *Funktsional'nyi Analiz i Ego Prilozhaniya* **7**, 62–73.

Schmid, P.J. and Henningson, D.S. (2001). *Stability and Transition in Shear Flows*, Springer, Berlin.

Schmiegel, A. (1999). *Transition to Turbulence in Linearly Stable Shear Flow Geometries*. PhD Dissertation, Philipps Universität, Marburg.

Schmiegel, A. and Eckhardt, B. (1997). Fractal stability border in plane Couette flow. *Phys. Rev. Lett.* **79**, 5250–5253.

Swift, J. and Hohenberg, P.C. (1977). Hydrodynamic fluctuations at the convective instability. *Phys. Rev. A* **15**, 319–328.

Tillmark, N. and Alfredsson, P.H. (1992). Experiments on transition in plane Couette flow. *J. Fluid Mech.* **235**, 89–102.

Trefethen, L.N., Trefethen, A.E., Reddy, S.C. and Driscoll, T.A. (1993). Hydrodynamic stability without eigenvalues. *Science* **261**, 578–584.

Waleffe, F. (1995). Transition in shear flows: Nonlinear normality versus non-normal linearity. *Phys. Fluids* **7**, 3060–3066.

Waleffe, F. (1997). On a self-sustaining process in shear flows. *Phys. Fluids* **9**, 883–900.

Wolfram, S. (1986). *Theory and Applications of Cellular Automata*, World Scientific.

DYNAMICAL SYSTEMS AND THE TRANSITION TO TURBULENCE

Bruno Eckhardt[1,2] and Holger Faisst[1,3]
[1]*Fachbereich Physik, Philipps-Universität Marburg, 35032 Marburg, Germany*
[2]*IREAP, IPST and Burgers Program, University of Maryland, College Park, MD 20742, USA*
[3]*Siemens VDO Automotive AG, 93055 Regensburg, Germany*
bruno.eckhardt@physik.uni-marburg.de

Abstract We discuss the theoretical, numerical and experimental evidence for the formation of a chaotic saddle in the transition region to turbulence in pipe flow and plane Couette flow.

Keywords: pipe flow, plane Couette flow, strange saddles, strange attractors.

1. INTRODUCTION

In 1942, Landau suggested that the transition to turbulence might hold some clues as to the nature of the turbulent state itself (Davidson, 2004). By this time the instabilities of fluids heated from below (the Rayleigh–Bénard problem) and of centrifugal instabilities between rotating concentric cylinders (the Taylor–Couette problem) had been studied experimentally and theoretically with satisfactory agreement between both (Drazin and Reid, 1981; Chandrasekhar, 1961). It was thus not unnatural to speculate that turbulence might emerge as the final result of a cascade of instabilities that lead from the laminar state to the vortex state and then on to states with more complicated spatial and temporal dependencies. Secondary and tertiary bifurcation studies in Rayleigh–Bénard and Taylor–Couette flows, together with insights from nonlinear dynamics and the routes to chaos have added plausibility to this picture (Drazin and Reid, 1981; Chandrasekhar, 1961; Cross and Hohenberg, 1993). But this approach rests on the presence of linear instabilities around which some sort of amplitude or Ginzburg–Landau-type expansion is possible. Therefore, it does not work for flows without a linear instability, such as pipe flow or plane-Couette flow.

In addition to the lack of a linear instability, which by itself might be considered just a mathematical nuisance, the transition in pipe flow and plane Couette

T. Mullin and R.R. Kerswell (eds), Laminar Turbulent Transition and Finite Amplitude Solutions, 35–50.
© 2005 *Springer. Printed in the Netherlands.*

flow differs from the other two paradigmatic examples in other aspects as well: the state that appears does not have a simple spatial or temporal structure, such as rolls or hexagons, but immediately becomes more complex. Furthermore, the transition does not seem to be well defined, as indicated by the huge variations in the critical flow parameters documente in the literature. Clearly, if the transition were subcritical in the usual sense, with a stable upper branch, then there should be a well-defined critical Reynolds number that has to be exceeded before an appropriate perturbation can trigger the transition. Finally, there are indications that the state that emerges may not be permanent but transient only (Reynolds, 1883; Brosa, 1989; Tillmark and Alfredsson, 1992; Daviaud et al., 1992; Dauchot and Daviaud, 1995; Bottin and Chaté, 1998; Bottin et al., 1998b).

As in the case of the usual bifurcation scenarios, nonlinear dynamics and dynamical system theory has a blueprint for such kind of behaviour as well. It is the transient chaos first described in the dynamics of chemical reactions (Rankin and Miller, 1971; Noid et al., 1986; Eckhardt and Jung, 1986; Eckhardt, 1988) which has become a paradigm for transient chaos in few-degree of freedom systems. For chemical reactions, transient chaos occurs when two molecules meet in a collision, stick together and perform some complicated dynamics before finally rearranging and decaying to the products of the chemical reaction. In a hydrodynamic context, such a behaviour can arise in the dynamics of point vortices (Manakov and Shchur, 1983; Eckhardt and Aref, 1988; Aref et al., 1988). Since a pair of vortices with opposite vorticity $(\kappa, -\kappa)$ will move in a straight line, one can take two pairs, with vorticities $(\kappa, -\kappa)$ and $(\kappa', -\kappa')$ and aimed them at each other for a collision. During the interaction they can regroup pairs $(\kappa, -\kappa')$ and $(\kappa', -\kappa)$, which will move on circles since their net pair-vorticity $\kappa - \kappa' \neq 0$ does not vanish. During their next encounter the vortices may regroup to the original pairs, in which case their interaction ends and they depart the interaction region, or they may continue in their current grouping and continue for another round (Figure 1). Numerical simulations show that tiny variations in the initial conditions are amplified during collisions and can lead to vastly different final states and trapping times.

Further exploration of systems with transient chaos has shown that one can embed a Smale horseshoe in their phase space (Tél, 1991; Eckhardt, 1988): this implies chaos in the mathematical sense, the presence of a countable infinite set of periodic states and an uncountable infinity of aperiodic states. The dynamics in phase space now has the features of a saddle (with attraction along stable manifolds and escape along some unstable ones) and those of a chaotic motion (horseshoes and positive Lyapunov exponents): it supports a chaotic saddle. With suitable limit processes an invariant density, Lyapunov exponents, and the mean escape rate can be defined (Tél, 1991; Ott, 1993). Among

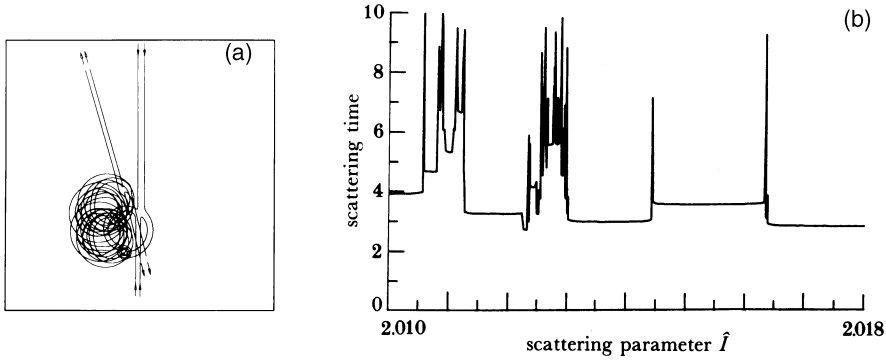

Figure 1. Chaotic scattering of colliding vortex pairs. Part (a) (from Aref et al., 1988) shows the tracks of two vortex pairs. Clearly visible are the approach along straight lines, the circular arcs of the newly formed pairs, several further encounters and the final rearrangement to the initial pairs and their escape along straight lines. Part (b) (from Eckhardt and Aref, 1988) shows the lifetimes, defined as the time the vortices stay within a finite distance of each other, as a function of the impact parameter. The peaks of very long lifetimes are connected with crossings of the stable manifolds of some trapped states.

the key signatures of a chaotic saddle are positive Lyapunov exponents for motion close to a saddle and an exponential distribution of lifetimes.

Most of the studies of transient chaos deal with finite dimensional phase spaces, ordinary differential equations or even discrete maps. The example of colloding vortices falls into this category, since it is possible to reduce the partial differential equations that govern the dynamics of vorticity to ordinary differential equations for the centres of the vortices. In the case studied here such an exact reduction is not possible. Nevertheless, the effective number of degrees of freedom, as measured, for instance, by the Lyapunov dimension, will be finite, and similar concepts should be applicable. Therefore, we will use similar tools and ideas in a study of pipe flow and plane Couette flow. The viability of such an approach is also backed up by experimental evidence (see in particular Dauchot and Daviaud, 1995; Bottin and Chaté, 1998; Bottin et al., 1998b).

The outline of this contribution is as follows. In Section 2 we will study the sensitive dependence of lifetimes on initial conditions. This will be followed by a statistical characterisation of the system, i.e. the distribution of lifetimes, in Section 3. In Section 4 we discuss the relevance of coherent states. Some open questions are summarised in Section 5.

2. SENSITIVITY TO INITIAL CONDITIONS

Sensitivity to initial conditions in dynamical systems is usually quantified in terms of the separation between neighbouring trajectories: in a chaotic sys-

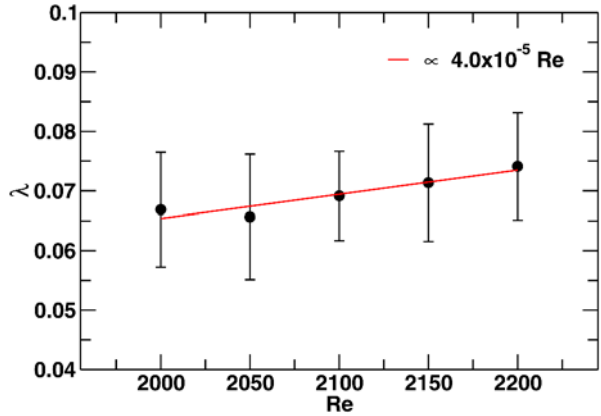

Figure 2. Largest Lyapunov exponent in pipe flow (from Faisst and Eckhardt, 2003a). The exponent was determined in direct numerical simulations.

tem this separation is exponential in time, with a rate given by the Lyapunov exponent,

$$\lambda = \lim_{T\to\infty} \lim_{||\delta x(0)||\to 0} \frac{1}{T} \ln \frac{||\delta x(T)||}{||\delta x(0)||} . \tag{2.1}$$

The limits are usually replaced with sufficiently small separations and long time segments (though there are ways of defining finite time Lyapunov exponents, e.g. Eckhardt and Yao, 1993). For the case of transient chaos, where typical trajectories will have finite lifetime, the chaotic dynamics and the decay of correlations on the invariant set assure the convergence of such finite time Lyapunov exponents to the asymptotic ones in the limit of infinite lifetime. For pipe flow, numerical estimates for the largest Lyapunov exponent give values of about 0.07 for Reynolds numbers around 2000. There seems to be a slight increase with Reynolds number, but the slope is small (see Figure 2).

As far as an experiment is concerned, a deviation between two initial states doubles in about every 10 time units. Since the scaling of the flow is such that time is made dimensionless by the mean speed and the diameter, this means that a perturbation going with the mean flow will double in amplitude every 10 diameters. Thus, in order to track the continuous evolution of the distance between two nearby sets of initial conditions for a distance of about 100 diameters, the initial conditions have to be controlled with an accuracy of 0.1%, well below todays possibilities.

A different sort of sensitive dependence on initial conditions was reported in Darbyshire and Mullin (1995), see Figure 3a. They introduced a perturbation to the flow and studied whether it was still turbulent when it reached the end of the pipe. They noticed that the border between the decaying and turbulent regime was not sharp but had a rather fragmented appearance.

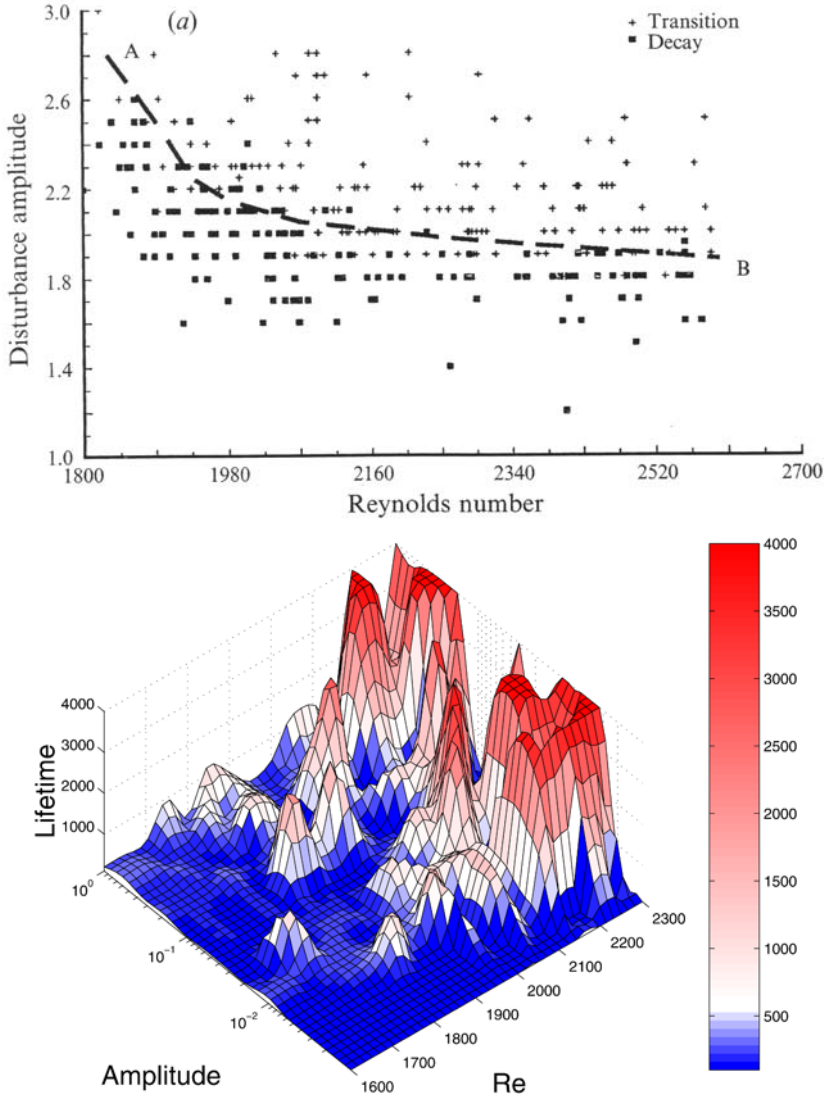

Figure 3. Lifetimes in pipe flow from experiments (Darbyshire and Mullin, 1995) (top) and numerical simulations (bottom). An experiment is labelled transition (cross) and decayed (full symbol) according to the state at the end of the pipe. The numerical lifetime landscape was calculated on a discrete grid. To compare to the experiment, cut the landscape at the height given by the observation time and label points according to the lifetimes being above (turbulent) or below (decayed) that level.

The numerical simulations reflect this kind of behaviour (see Figure 3b). Incidentally, the direct numerical simulations of Boberg and Brosa (1988), with

a different representation and resolution of the flow field, can in hindsight also be taken as evidence for some non-smooth dependence on initial conditions. Brosa later also noticed that all his initial conditions would decay when integrated for a long enough time (Brosa, 1989).

There is an obvious relation between the Lyapunov exponent and this kind of sensitivity. Suppose that an initial condition leads to a long living turbulent state. Suppose furthermore that a state a certain distance $d_0 \approx O(1)$ away decays to the laminar profile. Imagine now a perturbation in initial conditions that leads to this decaying state after a time T. Then, because of the exponential separation, an initial variation of the order of $d_0 \times \exp(-\lambda T)$ in the appropriate direction will suffice to bring this decay about. Therefore, varying initial conditions near a state with a very long lifetime, vary rapid changes in lifetimes can be expected. Indeed, under repeated magnifications of parameter windows, the variations with parameter values persist. This behaviour was found for plane Couette flow (Schmiegel and Eckhardt, 1997), pipe flow (Faisst and Eckhardt, 2004), and various low-dimensional models for shear flows (Eckhardt and Mersmann, 1999; Moehlis et al., 2004).

3. LIFETIME DISTRIBUTIONS

The sensitive dependence on initial conditions shows that tracking of individual trajectories is a fairly difficult, if not impossible, task. In such cases it is better to study ensembles of initial conditions, since they may show properties in their averages and distributions that in a statistical sense are more reproducible and reliable. One such ensemble quantity is the rate of escape from the chaotic saddle, first considered in Kadanoff and Tang (1984) (see also Kantz and Grassberger, 1985; Crutchfield and Kaneko, 1988; Tél, 1991; Ott, 1993). The theory of hyperbolic saddles shows this rate to be an intrinsic characteristic of the saddle. It can be determined from the evolution of initial conditions sprinkled close to it. Initial conditions further away will decay rapidly, and will have short lifetimes. But the closer they are the more their dynamics will reflect the properties of the chaotic saddle and the closer their escape rates will be to the characteristic one of the saddle. Thus, the asymptotic behaviour of the life time distribution reflects the intrinsic rate of escape. Empirically, just as with the calculation of Lyapunov exponents from finite trajectory segments, one does not have to go too far into the tail of the distributions to obtain stable and reproducible escape rates.

The operational description given above may raise concerns about a possible dependence of the lifetime distribution on the set of initial conditions. However, the longer a trajectory is trapped, the less memory of the initial conditions remains, so that again the long time behaviour is typical for the saddle and not for the initial conditions. The situation is not unlike the one found in normal

chaotic attractors, where, for instance, a judicious choice of initial conditions can select a periodic orbit with a Lyapunov exponent different from the typical one. The way this is dealt with is by appealing to the invariant measure in the presence of a little bit of noise, and then studying the unique invariant measure selected as the noise disappears. Similarly, one may here introduce a little bit of noise and end up with a unique invariant measure on the chaotic saddle. The escape from this saddle is then the relevant quantity. (The effects of noise on dynamical systems can be many. Its effect on lifetimes can be stabilising or destabilising, as the examples in Faisst and Eckhardt (2003a) show.)

The data in Figure 4 show the survival probability for pipe flow and plane Couette flow: $P(t)$ is the probability that a state is still turbulent after a time t. The data support an exponential distribution of lifetimes, compatible with the assumption of the presence of a chaotic saddle. The characteristic time in the exponential distribution increases rapidly with Reynolds number.

In cases when determination of lifetimes is truncated by a cut-off, the best characterisation of the distribution is not the mean (which would be influenced by the unknown longest lifetimes) but the median (for which we only need to know that the longest lifetimes exceed its value). The representation of the median in Figure 5 suggests that it diverges near a Reynolds number of about 2250. This would imply a transition from a chaotic saddle to a chaotic attractor. A mechanism by which this might occur is the inverse of the boundary crisis that results in the annihilation of basins of attraction (Grebogi et al., 1982). However, the data are insufficient to confirm this. One has to take into account that a number of studies show that, especially in high-dimensional systems, the lifetimes can increase dramatically with system parameters, i.e., algebraically (Kaneda, 1990), exponentially (Moehlis et al., 2004), or even super-exponentially (Crutchfield and Kaneko, 1988). This seems to be a typical behaviour for high-dimensional systems (Lai and Winslow, 1995; Braun and Feudel, 1996; Goren et al., 1998; Rempel and Chian, 2003). In addition to the hydrodynamic examples mentioned earlier, an exponential increase is also observed in superfluid turbulence, see Schoepe (2004) for the data and a convincing theoretical model. For flow down a pipe, a lifetime in excess of 1000 diameters is, for all practical purposes, longer than can be observed in any of todays set-ups, so that the a value of 2250 qualifies as a critical Reynolds number for the transition to sustained turbulence in pipe flow for all practical purposes.

4. COHERENT STATES

The presence of long lived turbulent states, a positive Lyapunov exponent and bounded fluctuations in energy suggests that the usual stretch-and-fold mechanism that gives rise to horseshoe maps and chaos should be present. If a

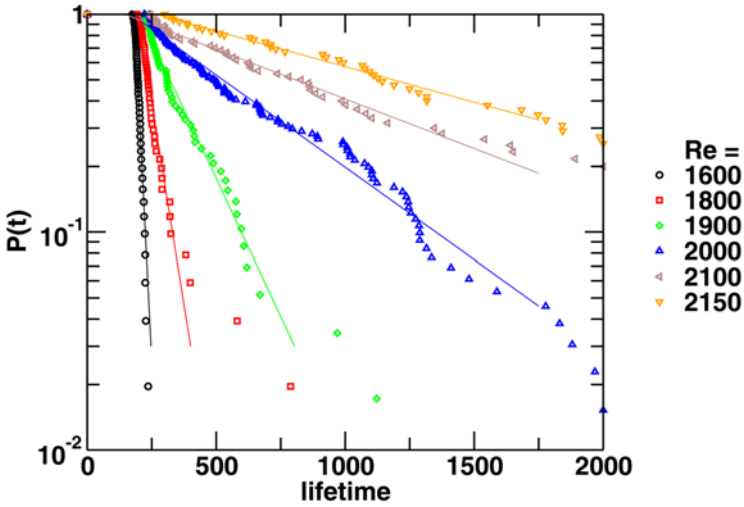

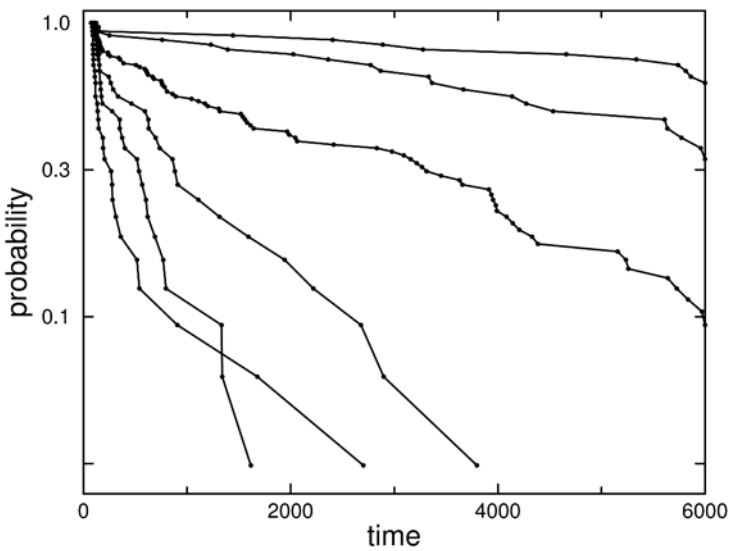

Figure 4. Lifetime distributions for pipe flow (top) and plane Couette flow (bottom). The ordinate in both cases is the probability to find an initial condition with lifetimes in excess of t. In the lower frame the Reynolds number (based on half the gap widths and half the velocity difference, as often used for plane Couette flow) ranges from 300 for the lowest curve to 350 for the upper most curve in steps of 10.

horseshoe can be embedded in the dynamics, then it implies the existence of an infinite number of periodic and aperiodic states that never leave turbulence.

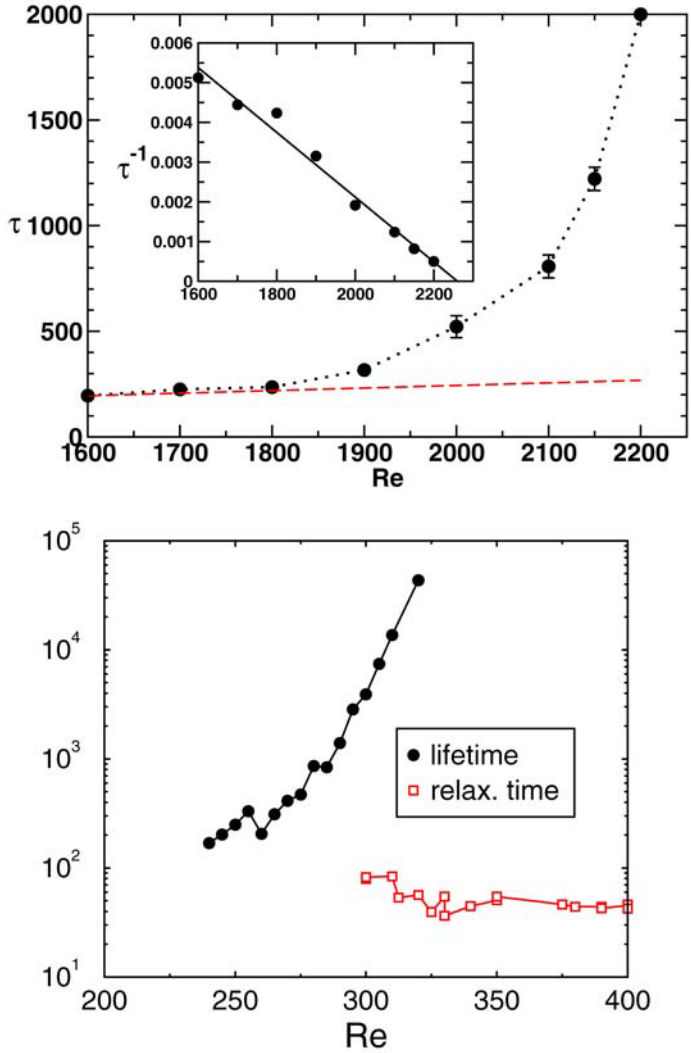

Figure 5. Median lifetimes for pipe flow (top) and plane Couette flow (bottom). The inset in the top diagram shows $1/\tau$ vs. Re, indicating a divergence near $Re_c = 2250$. The bottom diagram also contains the relaxation rate to the turbulent state, a measure relevant for adiabatic annealing to lower Reynolds numbers (see Schmiegel and Eckhardt, 2000, for further details).

Identifying a horsehoe map in high-dimensional systems is difficult, but as a beginning one may search for simple states, such as stationary states in the case of plane Couette flow or travelling waves in pipe flow (there are travelling waves in plane Couette flow as well, see Nagata, 1997; Eckhardt et al., 2002), but no stationary states in pipe flow, since the reflection symmetry that

allows the mean velocity to vanish does not exist in pipe flow). If these states are unstable, then their stable and unstable manifolds can intersect, forming a hyperbolic tangle in which a horseshoe map can be embedded.

There is a strong connection between the coherent states and the peaks in the lifetime distribution. Whenever the initial conditions are on the stable manifold of one of the states on the chaotic saddle, the lifetimes diverge. The presence of a countable infinity of periodic ones and an uncountable one of aperiodic provides the possibility of a dense set of initial conditions with infinite lifetimes, as observed in the data.

The divergence of the lifetime near a crossing of a stable manifold is controlled by the Lyapunov exponents near this state and is very sharp: in a simple model with a single hyperbolic fixed point the lifetime varies like $|\ln \epsilon|$, if ϵ denotes the distance from the stable manifold. In more realistic systems this may only hold for vanishingly small ϵ, and the finite ϵ-behaviour can be influenced by folds in the manifolds and the interactions between several states. Nevertheless, the very rapid increase remains.

An unguided search for travelling waves in the high-dimensional space of the Galerkin representation of the Navier–Stokes equation (typically several thousand degrees of freedom) does not work: the Newton-method is led astray too often by nearby minima and steep gradients. A more promising route is to embed the system under study into a larger class of flows where instabilities can be detected and then followed over. For instance, one may perturb the flow with a bead and study its behaviour as the bead size gets smaller (Bottin et al., 1997, 1998a; Barkley and Tuckerman, 1999, 2002). One can also combine plane Couette flow with a temperature gradient, to trigger vortices by buoyancy (Clever and Busse, 1997). Similarly, it can be combined with centrifugal forces to link it to Taylor–Couette flow (Nagata, 1990, 1997; Faisst and Eckhardt, 2000; Eckhardt et al., 2002). In the latter two cases the additional forces introduce a flow that has residual symmetry, e.g. straight convection rolls or azimuthal Taylor-vortices. When the forcing increases, these state undergo a symmetry breaking bifurcation to wiggly or modulated waves. In both cases the symmetric states do not carry over to the undriven shear flow, but the symmetry broken ones do (see Figure 6).

In pipe flow no physically realisable embedding with states that connect over to pure pipe flow is known (in particular the states for one likely candidate, pipe flow with rotation along the axis, do not connect to non-rotating pipe flow, see Barnes and Kerswell, 2000), but artificial body forces do the job just as well. The forces drive vortices that are translationally invariant along the axis. As their amplitude increases, the vortices become unstable, the translational symmetry is broken and a pair of modulated vortices appear. These vortices then survive when the Reynolds number is increased and the forcing decreased, and can be tracked all the way over to the case of pure pipe flow

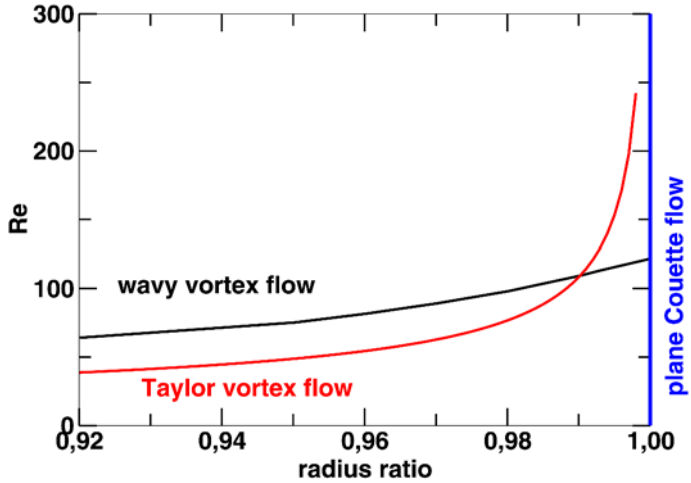

Figure 6. Variation of the instability to Taylor vortices and to the modulated vortices as a function of the radius ratio η as $\eta \to 1$. In this limit the linear instability to Taylor vortices moves out to infinite Reynolds number, but the modulated vortices, which appear in a secondary bifurcation from Taylor vortices for small η persist. For η close enough to the limit of plane Couette flow they appear in subcritical bifurcations.

without additional forces. Different forces which drive different numbers of vortices have been used. The vortices are still noticeable in the final travelling waves (Faisst and Eckhardt, 2003b), but their number does not uniquely specify it, as it has been possible to find different states with the same number of vortex pairs (Wedin and Kerswell, 2004).

Downstream vortices are known to have strong non-normal amplification properties and to drive strong streaks, but the strongest amplifier of them all, with just two vortices (Zikanov, 1996), does not give rise to a travelling wave for Re below 5000. The two vortex case differs from the others in that the velocity field does not vanish in the centre and this may introduce some rigidity against the 3-d azimuthal modulations that are essential for the travelling waves.

All states appear 'out-of-nowhere' in what appears to be a saddle-node type bifurcation. However, a closer investigation of their stability shows that already at the point of bifurcation they are dynamically unstable (Figure 8). Thus, they arise in pairs where the 'saddle'-state has not one but two unstable eigenvalues and the 'node'-state has one. In the case of plane Couette flow the situation is slightly different, in that at the point of bifurcation it is a traditional saddle-node bifurcation with one stable and one unstable state appearing (Clever and Busse, 1997). However, at Reynolds numbers slightly above the bifurcation the node looses its stability in what appears to be a Hopf bifurcation.

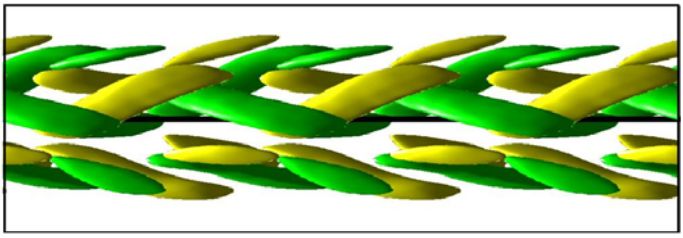

Figure 7. A representation of the C_3 travelling waves using vorticity iso-surfaces, at $\pm 40\%$ of the maximal downstream vorticity. The banana shaped surfaces have alternatingly positive and negative axial vorticity. The structures are travelling waves and move with constant speed without changing their form. The flow is from left to right, and the line in the center indicates the centerline of the pipe.

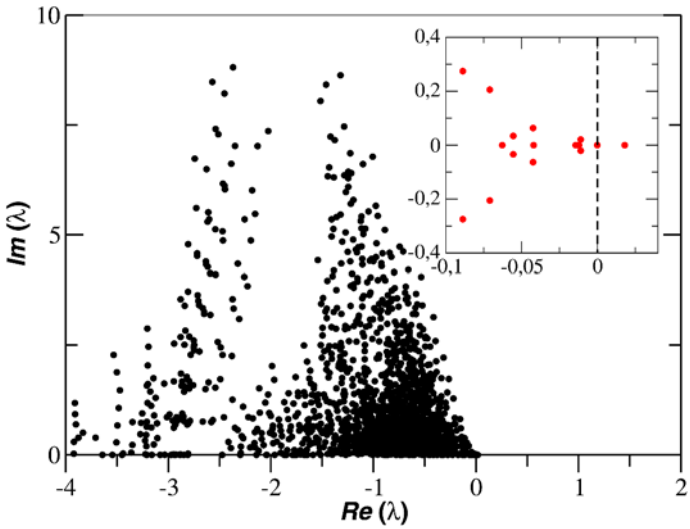

Figure 8. Eigenvalues of the C_3 state in pipe flow close to the point of bifurcation. The inset shows a magnification near the origin, clearly showing the one positive eigenvalue.

While so far only a few states have been identified (Faisst and Eckhardt, 2003b; Wedin and Kerswell, 2004; Hof et al., 2004), one has to expect many more. In plane Couette flow (Schmiegel, 1999; Eckhardt et al., 2002) and various low-dimensional models (Eckhardt and Mersmann, 1999; Moehlis et al., 2004, 2005) a multitude of steady states have been found. In plane Couette flow, in addition to the steady states, some travelling waves (Nagata, 1997; Eckhardt et al., 2002) and other periodic structures have been identified (Kawahara and Kida, 2001). There can be now doubt that further searches will reveal even more states, all being part of the chaotic saddle and the horseshoes

embedded in it. The situation for related flows, like plane Poiseuille flow, is similar, see Ehrenstein and Koch (1991) and Cherhabili and Ehrenstein (1997).

5. FINAL REMARKS

The experimental and numerical data for the transition in pipe flow and plane Couette flow are compatible with the formation of a chaotic saddle in phase space. Some key features, like the exponential distribution of lifetimes, and positive Lyapunov exponents have been identified.

The numerical simulations presented here are for a domain with periodic boundary conditions along the pipe. The length is adjusted to the wavelength of the coherent states or 10 diameter. Experimentally it is observed that turbulence appears in localised structures of about 50 diameter length. Since this is much larger than the typical wave lengths of the travelling waves, it should be possible to separate an internal dynamics governed by the coherent states from an external dynamics of an envelope that varies on much larger scales. In the case of plane Couette flow the corresponding features are localised patches of turbulence. While there is some progress in understanding their dynamics, many details remain to be worked out (Schumacher and Eckhardt, 2001; Barkley and Tuckerman, 2005b, 2005a).

The fit of the variation of the median lifetime with Reynolds number suggests a divergence of lifetimes near a Reynolds number of about 2250 in pipe flow. A true divergence would imply a transition from an open and transient structure to a true chaotic attractor. A mechanism by which this might happen is the inverse of the boundary crisis in which boundaries of basins of attraction meet and basins annihilate (Grebogi et al., 1982). Whether this happens here is an open problem; but it can be noted that for all practical purposes any lifetimes beyond several hundred radii are tantamount to infinity, given the finite length of the usual set up. This is different in a bounded geometry like Taylor–Couette, where the perturbations are not carried out of the system by the flow.

ACKNOWLEDGEMENTS

This work was prepared while the first author was visiting the University of Maryland as Burgers Professor. It is a pleasure to thank the Burgers board and in particular Dan Lathrop for the hospitality at the University of Maryland. Additional support was obtained from the Deutsche Forschungsgemeinschaft.

REFERENCES

Aref, H., Kadtke, J.B., Zawadzki, I., Campbell, L.J. and Eckhardt, B. (1988). Point vortex dynamics: Recent results and open problems. *Fluid Dyn. Res.* **3**, 63–74.

Barkley, D. and Tuckerman, L.S. (1999). Stability analysis of perturbed plane Couette flow. *Phys. Fluids* **11**, 1187–1195.

Barkley, D. and Tuckerman, L.S. (2002). Symmetry breaking and turbulence in perturbed plane Couette flow. *Th. Comp. Fluid Dyn.* **16**, 91–97.

Barkley, D. and Tuckerman, L.S. (2005a). Turbulent-laminar patterns in plane Couette flow. In *Proceedings of the IUTAM Symposium on Non-Uniqueness of Solutions to the Navier–Stokes Equations and Their Connection with Laminar-Turbulent Transition*, T. Mullin and R. Kerswell (eds), Springer, Dordrecht, pp. 107–127 (*this volume*).

Barkley, D. and Tuckerman, L.S. (2005b). Computational study of turbulent laminar patterns in Couette flow. *Phys. Rev. Lett.* **94**, 014502.

Barnes, D.R. and Kerswell, R.R. (2000). New results in rotating Hagen–Poiseuille flow. *J. Fluid Mech.* **417**, 103–126.

Boberg, L. and Brosa, U. (1988). Onset of turbulence in a pipe. *Z. Naturforsch.* **43a**, 697–726.

Bottin, S. and Chaté, H. (1998). Statistical analysis of the transition to turbulence in plane Couette flow. *Eur. Phys. J. B* **6**, 143–155.

Bottin, S., Dauchot, O. and Daviaud, F. (1997). Intermittency in a locally forced plane Couette flow. *Phys. Rev. Lett.* **79**, 4377–4380.

Bottin, S., Dauchot, O., Daviaud, F. and Manneville, P. (1998a). Experimental evidence of treamwise vortices as finite amplitude solutions in transitional plane Couette flow. *Phys. Fluids* **10**, 2597–2607.

Bottin, S., Daviaud, F., Manneville, P. and Dauchot, O. (1998b). Discontinuous transition to spatiotemporal intermittency in plane Couette flow. *Europhys. Lett.* **43**(2), 171–176.

Braun, R. and Feudel, F. (1996). Supertransient chaos in the two-dimensional complex Ginzburg–Landau equation. *Phys. Rev. E* **53**, 6562–6565.

Brosa, U. (1989). Turbulence without strange attractor. *J. Stat. Phys.* **55**, 1303–1312.

Chandrasekhar, S. (1961). *Hydrodynamic and Hydromagnetic Stability*, Oxford University Press, Oxford.

Cherhabili, A. and Ehrenstein, U. (1997). Finite-amplitude equilibrium states in plane Couette flow. *J. Fluid Mech.* **342**, 159–177.

Clever, R.M. and Busse, F.H. (1997). Tertiary and quaternary solutions for plane Couette flow. *J. Fluid Mech.* **344**, 137–153.

Cross, M.C. and Hohenberg, P.C. (1993). Pattern formation out of equilibrium. *Rev. Mod. Phys.* **65**, 851–1112.

Crutchfield, J.P. and Kaneko, K. (1988). Are attractors relevant to turbulence? *Phys. Rev. Lett.* **60**, 2715–2718.

Darbyshire, A.G. and Mullin, T. (1995). Transition to turbulence in constant-mass-flux pipe flow. *J. Fluid Mech.* **289**, 83–114.

Dauchot, O. and Daviaud, F. (1995). Finite amplitude perturbation and spot growths mechanism in plane Couette flow. *Phys. Fluids* **7**, 335–343.

Daviaud, F., Hegseth, J. and Bergé, P. (1992). Subcritical transition to turbulence in plane Couette flow. *Phys. Rev. Lett.* **69**, 2511–2514.

Davidson, P.A. (2004). *Turbulence*, Oxford University Press, Oxford.

Drazin, P.G. and Reid, W.H. (1981). *Hydrodynamic Stability*, Cambridge University Press, Cambridge.

Eckhardt, B. (1988). Irregular scattering. *Physica D* **33**, 89–98.

Eckhardt, B. and Aref, H. (1988). Integrable and chaotic motions of four vortices: II. Collision dynamics of vortex pairs. *Philos. Trans. Roy. Soc. London* **A326**, 655–696.

Eckhardt, B., Faisst, H., Schmiegel, A. and Schumacher, J. (2002). Turbulence transition in shear flows. In *Advances in Turbulence IX*, I.P. Castro, P.E. Hanock and T.G. Thomas (eds), Barcelona, p. 701.

Eckhardt, B. and Jung, C. (1986). Regular and irregular potential scattering. *J. Phys. A* **19**, L829–L833.

Eckhardt, B. and Mersmann, A. (1999). Transition to turbulence in a shear flow. *Phys. Rev. E* **60**, 509–517.

Eckhardt, B. and Yao, D. (1993). Local Lyapunov exponents. *Physica D* **65**, 100–1008.

Ehrenstein, U. and Koch, W. (1991). Three-dimensional wavelike equilibrium states in plane Poiseuille flow. *J. Fluid. Mech.* **228**, 111–148.

Faisst, H. and Eckhardt, B. (2000). Transition from the Couette-Taylor system to the plane Couette system. *Phys. Rev. E* **61**, 7227–7230.

Faisst, H. and Eckhardt, B. (2003a). Lifetimes of noisy repellors. *Phys. Rev. E* **68**, 026215.

Faisst, H. and Eckhardt, B. (2003b). Traveling waves in pipe flow. *Phys. Rev. Lett.* **91**, 224502.

Faisst, H. and Eckhardt, B. (2004). Sensitive dependence on initial conditions in transition to turbulence in pipe flow. *J. Fluid Mech.* **504**, 343–352.

Goren, G., Eckmann, J.-P. and Procaccia, I. (1998). Scenario for the onset of space-time chaos. *Phys. Rev. E* **57**, 4106–4134.

Grebogi, C., Ott, E. and Yorke, J.A. (1982). Chaotic attractors in crisis. *Phys. Rev. Lett.* **48**, 1507–1510.

Hof, B., van Doorne, C.W.H., Westerveel, J., Nieuwstadt, F.T.M., Faisst, H., Eckhardt, B., Wedin, H., Kerswell, R.R. and Waleffe, F. (2004). Experimental observation of nonlinear travelling waves in turbulent pipe flow. *Science* **305**, 1594–1598.

Kadanoff, L.P. and Tang, C. (1984). Escape from strange repellers. *Proc. Natl. Acad. Sci. USA* **81**, 1276.

Kaneda, Kunihiko (1990). Supertransients, spatiotemporal intermittency and stability of fully developed spatiotemporal chaos. *Phys. Lett. A* **149**, 105–112.

Kantz, H. and Grassberger, P. (1985). Repellers, semi-attractors, and long-lived chaotic transients. *Physica D* **17**, 75–86.

Kawahara, G. and Kida, S. (2001). Periodic motion embedded in plane Couette turbulence: Regeneration cycle and burst. *J. Fluid Mech.* **449**, 291–300.

Lai, Y.-C. and Winslow, Raimond L. (1995). Geometric properties of the chaotic saddle responsible for supertransients in spatiotemporal chaotic systems. *Phys. Rev. Lett.* **74**, 5208–5211.

Manakov, S.V. and Shchur, L.N. (1983). Stochastic aspects of two-particle scattering. *Sov. Phys. JETP* **37**, 54–58.

Moehlis, J., Faisst, H. and Eckhardt, B. (2004). A low-dimensional model for turbulent shear flows. *New J. Phys.* **6**, Article 56.

Moehlis, J., Faisst, H. and Eckhardt, B. (2005). Bifurcations in a low-dimensional model for shear flows. *SIAM J. Appl. Dyn. Syst.*, in press.

Nagata, M. (1990). Three-dimensional finite-amplitude solutions in plane Couette flow: Bifurcation from infinity. *J. Fluid Mech.* **217**, 519–527.

Nagata, M. (1997). Three-dimensional traveling-wave solutions in plane Couette flow. *Phys. Rev. E* **55**(2), 2023–2025.

Noid, D.W., Gray, S.K. and Rice, S.A. (1986). Fractal behaviour in classical collisional energy transfer. *J. Chem. Phys.* **85**, 2649–2652.

Ott, E. (1993). *Chaos in Dynamical Systems*, Cambridge University Press.

Rankin, C.C. and Miller, W.M. (1971). Classical S matrix for linear reactive collisions of $H+Cl_2$. *J. Chem. Phys.* **55**, 3150–3156.

Rempel, E.L. and Chian, A.C.-L. (2003). High-dimensional chaotic saddles in the Kuramoto–Shivashinsky equation. *Phys. Lett. A* **319**, 104–109.

Reynolds, O. (1883). An experimental investigation of the circumstances which determine whether the motion of water shall be direct or sinuous and the law of resistance in parallel channels. *Philos. Trans. Roy. Soc.* **174**, 935–982.

Schmiegel, A. (1999). *Transition to Turbulence in Linearly Stable Shear Flows*. Ph.D. Thesis, Philipps-Universität Marburg.

Schmiegel, A. and Eckhardt, B. (1997). Fractal stability border in plane Couette flow. *Phys. Rev. Lett.* **79**, 5250–5253.

Schmiegel, A. and Eckhardt, B. (2000). Persistent turbulence in annealed plane Couette flow. *Europhys. Lett.* **51**, 395–400.

Schoepe, W. (2004). Fluctuations and stability of superfluid turbulence at mK temperatures. *Phys. Rev. Lett.* **92**, 095301.

Schumacher, J. and Eckhardt, B. (2001). Evolution of turbulent spots in a parallel shear flow. *Phys. Rev. E* **63**, 046307.

Tél, T. (1991). Transient chaos. In *Directions in Chaos*, Volume 3, H. Bai-Lin, D.H. Feng and J.M. Yuan (eds), World Scientific, Singapore, p. 149.

Tillmark, N. and Alfredsson, P.H. (1992). Experiments on transition in plane Couette flow. *J. Fluid Mech.* **235**, 89–102.

Wedin, H. and Kerswell, R.R. (2004). Exact coherent structures in pipe flow: Travelling wave solutions. *J. Fluid Mech.* **508**, 333–371.

Zikanov, O.Y. (1996). On the instability of pipe Poiseuille flow. *Phys. Fluids* **8**(11), 2923–2932.

NONLINEAR SOLUTIONS OF SIMPLE PLANE SHEAR LAYERS WITH AND WITHOUT A SYSTEM ROTATION

M. Nagata, G. Kawahara, T. Itano, D.P. Wall, T. Mitsumoji and R. Nakamura
Department of Aeronautics and Astronautics, Graduate School of Engineering, Kyoto University, Japan

Abstract We analyse the bifurcation sequence of typical simple plane shear flows numerically by using a bifurcation analysis and also a DNS technique, considering flows with and without a system rotation about a spanwise axis. Our analysis is applied to (1) plane Couette flow, (2) plane Poiseuille flow, and (3) flow with a cubic velocity profile.

Keywords: bifurcation, plane shear flows, system rotation, Couette flow, Poiseuille flow.

1. INTRODUCTION

It is of considerable importance to applications in engineering and geophysics, among others, to understand the mechanism of the transition from laminar flow to early stages of turbulence in plane parallel shear layers. As the examples of such shear layers we consider (1) plane Couette flow, (2) plane Poiseuille flow, and (3) flow with a cubic velocity profile.

The rate of change of the basic vorticity across the fluid layer is homogeneous in case (1), has the same sign in case (2) and changes signs in case (3). Therefore, Rayleigh's inflection-point theorem applies only for the flow (3) and instabilities can be expected although the theorem is proved only in the inviscid limit. For viscous non-rotating case Squire's theorem is applicable, so that it is sufficient to analyse the stability of all the above flows with respect to two-dimensional (spanwise-independent) perturbations. It is known that (1) plane Couette flow is linearly stable at any finite values of the Reynolds number, thus indicating no bifurcation directly from the basic flow, (2) plane Poiseuille flow becomes unstable at some finite Reynolds number with a subcritical bifurcation, and (3) the cubic velocity profile flow undergoes a supercritical bifurcation from the basic state. When the system rotation is added Squire's theorem

T. Mullin and R.R. Kerswell (eds), Laminar Turbulent Transition and Finite Amplitude Solutions, 51–69.
© 2005 *Springer. Printed in the Netherlands.*

is not applicable and the flows may become unstable to perturbations which are independent in the streamwise direction.

(1) Plane Couette flow: Nagata (1990) analysed the nonlinear stability of the flow with a linear velocity profile when the system rotation was added and successfully continued a tertiary solution branch in the rotating system to the zero-rotation rate, finding 3D nonlinear solutions of the plane Couette system for the first time. Later, he showed the existence of Hopf bifurcation points on the tertiary solution branch at some rotation rate (Nagata, 1998). We present time-dependent solutions bifurcating from the Hopf bifurcation points. It is found that for a relatively small Reynolds number, R, the time-dependent motion is characterised by a periodic motion with a single frequency. As the system rotation, Ω, varies the periodic motion undergoes a period doubling bifurcation and eventually collides with a 2D streamwise independent solution forming a homoclinic connection. Tracing the branch of the periodic solution in the $R-\Omega$ space, we find that it intersects the Ω-axis, producing the periodic solution for the non-rotating plane Couette system.

(2) Plane Poiseuille flow: The linear stability of plane Poiseuille flow with a parabolic velocity profile subject to the system rotation is determined by streamwise independent disturbances (Lezius and Johnstone, 1976). We find 2D nonlinear solutions of a streamwise vortex character which arise in bifurcation from the basic flow. The secondary stability analysis indicates an adjustment of 2D multiple solutions with different spanwise wavenumbers. The analysis also predicts bifurcations of 3D tertiary flows. We present three different classes of full nonlinear solutions of 3D travelling-wave type.

(3) Cubic velocity profile flow: A flow between two vertical plates of infinite extent maintained at constant different temperatures provides a shear flow with a cubic velocity profile (Vest and Arpaci, 1969). The instability of this flow becomes purely hydrodynamic, provided a Boussinesq fluid with a small Prandtl number limit is considered (Nagata and Busse, 1983). We note that liquid metals could be approximated by a fluid with the vanishing Prandtl number. The only parameter that governs the flow is the Grashof number, G_r. Contrary to the cases (1) and (2), the velocity profile of this flow includes an inflection point. Nagata and Busse (1983) found that the primary bifurcation is described by a steady 2D transverse vortex flow whereas the secondary bifurcation is characterised by steady 3D subharmonic sinusoidal motions of the transverse vortex. After confirming the result of Nagata and Busse (1983), we show that as G_r is increased above its (third) critical value, a 3D periodic motion sets in as the quaternary flow. Observing that the DNS could capture several unstable periodic solutions representing a transient state, we find different types of motion coexist as stable or unstable solutions of the system at high Grashof numbers.

2. MATHEMATICAL FORMULATION

We consider a viscous incompressible fluid motion between two parallel plates separated by the distance $2L$. We take the origin of a Cartesian coordinate system on the mid-plane between the plates with the x- and y-axes along the plate and the z-axis in the direction normal to the plate. We impose a system rotation Ω_0 about the y-axis. The Coriolis force does not affect the basic parallel flow along the x-direction. For plane Couette flow the bottom plate moves along the x-axis with a constant speed U_0 whereas the top plate moves in the opposite direction with the same speed. For plane Poiseuille flow a constant pressure gradient is imposed along the x-axis inducing a parabolic velocity profile with the maximum value U_m on the z-axis. The basic flow with a cubic velocity profile can be realised by taking a Boussinesq fluid between vertical plates of infinite extent maintained at constant different temperatures, T_1 and T_2. The conductive state is represented by a linear temperature variation across the fluid layer, and buoyancy balances the viscous force. In the vanishing Prandtl number limit temperature perturbations become identically zero.

By taking an appropriate nondimensionalisation the basic laminar flows are described by

$$\text{plane Couette flow:} \qquad U_B(z) = -R\,z, \tag{1}$$

$$\text{plane Poiseuille flow:} \qquad U_B(z) = R\,(1 - z^2), \tag{2}$$

$$\text{cubic velocity profile flow:} \qquad U_B(z) = G_r\,z(1 - z^2). \tag{3}$$

The Reynolds number R is defined by $R = 4U_0L/\nu$ for (1) or $R = U_mL/\nu$ for (2) where ν is the kinematic viscosity. G_r in (3) is the Grashof number defined by $G_r = \gamma g L^3(T_2 - T_1)/(2\nu^2)$ where γ is the coefficient of thermal expansion and g is the acceleration due to gravity.

The stability of the basic state is governed by

$$\partial_t \nabla^2 \triangle_2 \tilde{\phi} + \{U_B(z)\partial_x - \nabla^2\}\nabla^2\triangle_2\tilde{\phi} - U_B''(z)\partial_x\triangle_2\tilde{\phi} + \Omega\partial_y\triangle_2\tilde{\psi} = 0, \tag{4}$$

and

$$\partial_t \triangle_2 \tilde{\psi} + \{U_B(z)\partial_x - \nabla^2\}\triangle_2\tilde{\psi} - U_B'(z)\partial_y\triangle_2\tilde{\phi} - \Omega\partial_y\triangle_2\tilde{\phi} = 0, \tag{5}$$

where $\tilde{\phi}$ and $\tilde{\psi}$ are the poloidal and toroidal components of an infinitesimal velocity perturbation $\tilde{\boldsymbol{u}}$:

$$\tilde{\boldsymbol{u}} = \nabla \times \nabla \times (\tilde{\phi}\boldsymbol{k}) + \nabla \times (\tilde{\psi}\boldsymbol{k}). \tag{6}$$

superimposed on the basic flows (1)–(3). $\Omega = 2\Omega_0L^2/\nu$ is the rotation parameter. Note that the rotation number Ω is defined differently from that used by, for instance, Lezius and Johnstone (1976). Their rotation number R_o is

defined by $R_o = 4\Omega/R$ for rotting plane Couette flow and $R_o = \Omega/R$ for rotating Poiseuille flow.

We express $\tilde{\phi}$ and $\tilde{\psi}$ as

$$\tilde{\phi} = \sum_{\ell=0}^{\infty} \tilde{a}_l (1 - z^2)^2 T_l(z) \exp\{i\alpha x + i\beta y + \sigma t\}, \tag{7}$$

$$\tilde{\psi} = \sum_{ell=0}^{\infty} \tilde{b}_l (1 - z^2) T_l(z) \exp\{i\alpha x + i\beta y + \sigma t\}, \tag{8}$$

where α and β are the wavenumbers in the streamwise and the spanwise directions, respectively. $T_\ell(z)$ is the ℓ-th Chebyshev polynomial.

In order to analyse the nonlinear development of the perturbation we consider a velocity deviation $\hat{\boldsymbol{u}}$ from the laminar state and for convenience separate it into the average part $\check{U}(z)\boldsymbol{i} + \check{V}(z)\boldsymbol{j}$ and the residual $\check{\boldsymbol{u}}$, so that the total velocity $\boldsymbol{u}$ is given by

$$\boldsymbol{u} = U(z)\boldsymbol{i} + \check{V}(z)\boldsymbol{j} + \check{\boldsymbol{u}}, \tag{9}$$

where $U(z) = U_B(z) + \check{U}(z)$. The residual $\check{\boldsymbol{u}}$ is further decomposed into the poloidal and toroidal parts:

$$\check{\boldsymbol{u}} = \nabla \times \nabla \times (\phi \boldsymbol{k}) + \nabla \times (\psi \boldsymbol{k}). \tag{10}$$

In (9) and (10) $\boldsymbol{i}$, $\boldsymbol{j}$ and $\boldsymbol{k}$ stand for the unit vectors in the x-, y- and z-directions, respectively.

The nonlinear state is governed by

$$\begin{aligned} \partial_t \nabla^2 \triangle_2 \phi \quad &+ \quad \{U(z)\partial_x - \nabla^2\}\nabla^2\triangle_2\phi - U''(z)\partial_x\triangle_2\phi \\ &+ \quad \check{V}(z)\partial_y\nabla^2\triangle_2\phi - \check{V}''(z)\partial_y\triangle_2\phi + \Omega\partial_y\triangle_2\psi \\ &+ \quad \delta[(\check{\boldsymbol{u}}\cdot\nabla)\check{\boldsymbol{u}}] = 0, \end{aligned} \tag{11}$$

$$\begin{aligned} \partial_t \triangle_2 \psi \quad &+ \quad \{U(z)\partial_x - \nabla^2\}\triangle_2\psi - U'(z)\partial_y\triangle_2\phi \\ &+ \quad \check{V}(z)\partial_y\triangle_2\psi + \check{V}'(z)\partial_x\triangle_2\phi - \Omega\partial_y\triangle_2\phi \\ &+ \quad \epsilon[(\check{\boldsymbol{u}}\cdot\nabla)\check{\boldsymbol{u}}] = 0, \end{aligned} \tag{12}$$

$$\check{U}'' + \partial_z \overline{\triangle_2\phi(\partial^2_{xz}\phi + \partial_y\psi)} = \partial_t \check{U}, \tag{13}$$

$$\check{V}'' + \partial_z \overline{\triangle_2\phi(\partial^2_{yz}\phi - \partial_x\psi)} = \partial_t \check{V}, \tag{14}$$

where the differential operators ϵ in (11) and δ in (12) are defined by

$$\epsilon \equiv \boldsymbol{k}\cdot(\nabla\times \quad \text{and} \quad \delta \equiv \boldsymbol{k}\cdot(\nabla\times\nabla\times\,. \tag{15}$$

and the overline in (13) or (14) stands for the x, y-average. In the above, the possibility of induced average flow $\check{V}(z)$ in the spanwise direction is incorporated (see cubic velocity profile flow in Section 4). We express ϕ, ψ, $\check{U}$ and $\check{V}$ as follows:

$$\begin{aligned}
\phi &= \sum_{l=0}^{\infty} \sum_{\substack{m=-\infty \\ (m,n)\neq(0,0)}}^{\infty} \sum_{n=-\infty}^{\infty} a_{lmn} \left(1-z^2\right)^2 T_l(z) \\
&\quad \times \exp(im\alpha(x-c_x t) + in\beta(y-c_y t)) \qquad (16) \\
\psi &= \sum_{l=0}^{\infty} \sum_{\substack{m=-\infty \\ (m,n)\neq(0,0)}}^{\infty} \sum_{n=-\infty}^{\infty} b_{lmn} \left(1-z^2\right) T_l(z) \\
&\quad \times \exp(im\alpha(x-c_x t) + in\beta(y-c_y t)) \qquad (17) \\
\check{U} &= \sum_{l=0}^{\infty} c_l \left(1-z^2\right) T_l(z) \qquad (18) \\
\check{V} &= \sum_{l=0}^{\infty} d_l \left(1-z^2\right) T_l(z). \qquad (19)
\end{aligned}$$

In the expressions (16)–(17) the phase velocities, c_x and c_y, are included in order to deal with a travelling-wave type of nonlinear equilibrium states. For a steady state time-derivatives are omitted in Equations (11)–(14) and c_x and c_y are both zero. As a measure of nonlinearity we choose the momentum transport τ on the plates normalised by its value for the basic state:

$$\tau = U'(z)/U'_B(z)|_{z=\pm 1} \qquad (20)$$

In order to investigate the stability of the equilibrium state, we superimpose arbitrary three-dimensional infinitesimal perturbations on the nonlinear state. The stability equations linearised with respect to the perturbations are given by

$$\begin{aligned}
\partial_t \nabla^2 \triangle_2 \tilde{\phi} &+ \{U(z)\partial_x - \nabla^2\}\nabla^2\triangle_2\tilde{\phi} - U''(z)\partial_x\triangle_2\tilde{\phi} \\
&+ \check{V}(z)\partial_y\nabla^2\triangle_2\tilde{\phi} - \check{V}''(z)\partial_y\triangle_2\tilde{\phi} + \Omega\partial_y\triangle_2\tilde{\psi} \\
&+ \delta[(\check{\boldsymbol{u}}\cdot\nabla)\tilde{\boldsymbol{u}} + (\tilde{\boldsymbol{u}}\cdot\nabla)\check{\boldsymbol{u}}] = 0, \qquad (21)
\end{aligned}$$

$$\begin{aligned}
\partial_t \triangle_2 \tilde{\psi} &+ \{U(z)\partial_x - \nabla^2\}\triangle_2\tilde{\psi} - U'(z)\partial_y\triangle_2\tilde{\phi} \\
&+ \check{V}(z)\partial_y\triangle_2\tilde{\psi} + \check{V}'(z)\partial_x\triangle_2\tilde{\phi} - \Omega\partial_y\triangle_2\tilde{\phi} \\
&+ \epsilon[(\check{\boldsymbol{u}}\cdot\nabla)\tilde{\boldsymbol{u}} + (\tilde{\boldsymbol{u}}\cdot\nabla)\check{\boldsymbol{u}}] = 0. \qquad (22)
\end{aligned}$$

$\tilde{\phi}$ and $\tilde{\psi}$ are expressed by

$$\tilde{\phi} = \sum_{l=0}^{\infty} \sum_{m=-\infty}^{\infty} \sum_{n=-\infty}^{\infty} \tilde{a}_{lmn} \left(1-z^2\right)^2 T_l(z)$$

$$\times \exp\{i(m\alpha + d)(x - c_x t) + i(n\beta + b)(y - c_y t) \quad + \quad \sigma t\}, \tag{23}$$

$$\tilde{\psi} = \sum_{l=0}^{\infty} \sum_{m=-\infty}^{\infty} \sum_{n=-\infty}^{\infty} \tilde{b}_{lmn} \left(1 - z^2\right) T_l(z)$$

$$\times \exp\{i(m\alpha + d)(x - c_x t) + i(n\beta + b)(y - c_y t) \quad + \quad \sigma t\}, \tag{24}$$

where d and b are Floquet parameters.

3. NUMERICAL METHODS

In the present analysis we use three different numerical schemes as described below.

1 Newton–Raphson method is used for steady and travelling-wave type equillibrium states. Substitution of the expansions (16)–(19) with appropriate truncation to the basic equations (11)–(14) leads to to a set of nonlinear algebraic equations for the expansion coefficients, $a_{\ell mn}$, $b_{\ell mn}$, c_ℓ, d_ℓ, combined with the Chebyshev collocation method.

With similar truncation and substitution, the linearised perturbation equations (21) and (22) provide the eigenvalue problem for the growth rate σ of the perturbations as the eigenvalue by applying Floquet's theorem.

2 The time development of the disturbance is followed by a direct numerical simulation (DNS) by performing the time integration on the wall-normal components, w for the velocity and ω_z for the vorticity, derived from the full Navier–Stokes equation by using a pseudo-spectral and Chebyshev-tau methods. The dealiased Fourier expansions are employed in the streamwise and spanwise directions, while the Chebyshev-polynomial expansion is employed in the direction normal to the plates. For the time integration we use Adams–Bashforth scheme for convective terms and Crank–Nicolson scheme for viscous terms.

3 Newton–Raphson method is employed in order to find a periodic motion as a fixed point in a Poincaré map. The return map on the Poincaré section where one of the expansion coefficients, $a_{\ell mn}$, $b_{\ell mn}$, c_ℓ, d_ℓ, is constant, is calculated by the DNS. In order to evaluate the Jacobian matrix numerically the other expansion coefficients are changed slightly one by one. Their return maps are also created by the DNS and used to approximate the Jacobian matrix by a linear finite-difference scheme. We first take a 'stable' periodic state, which is available in the DNS, as an initial guess for the Newton–Raphson iteration. The existence of the periodic solution is explored even in a region in the parameter space where it is unstable.

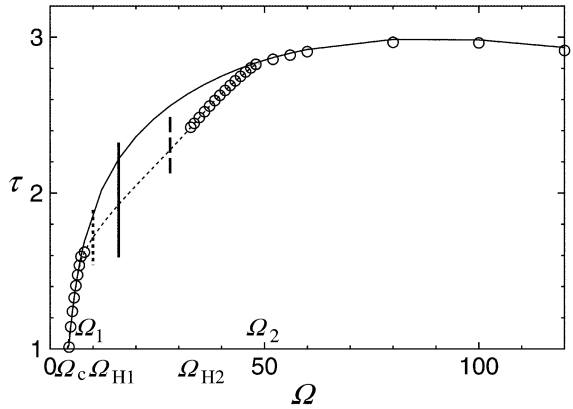

Figure 1. The momentum transport τ against the system rotation Ω for various types of motion at $Re = 400$.

4. ANALYSIS

4.1 Rotating and non-rotating plane Couette flow

Background. Recently, Nagata (1998) investigated the stability of the steady tertiary flow in the rotating plane Couette system with the result that the tertiary flow, which bifurcate from the steady 2D streamwise vortex flow, is stable within a certain interval of the system rotation, Ω, when the Reynolds number, R, is relatively small, say $R = 200$, with its stability boundaries being determined by perturbations which are subharmonic in the streamwise direction. As the Reynolds number is increased to $R \simeq 250$, another type of instabilities begins to emerge in the middle of the stability interval at $\Omega \simeq 20$. These instabilities are characterised by an oscillatory nature. As R is further increased, the oscillatory instabilities spread in the directions of both increasing and decreasing Ω, gradually contaminating the stability interval. It is expected that the tertiary flow is totally overtaken by time-dependent motions for large Reynolds numbers. In this report we examine the development of the time-dependent motions in rotating and non-rotating plane Couette flow numerically.

Results. The momentum transport on the plates, τ, against Ω for various types of motion is shown in Figure 1 when $R = 400$. The solid curve indicates the steady 2D streamwise vortex flow with the streamwise wavenumber $\alpha = 0$ and the spanwise wavenumber $\beta = 3.117$ (this value of β corresponds to the critical wavenumber obtained by linear theory), whereas the dotted curve indicates the steady three-dimensional solution with $\alpha = 1.0$ and $\beta = 3.117$ (This wavenumber combination corresponds to that of the perturbation with

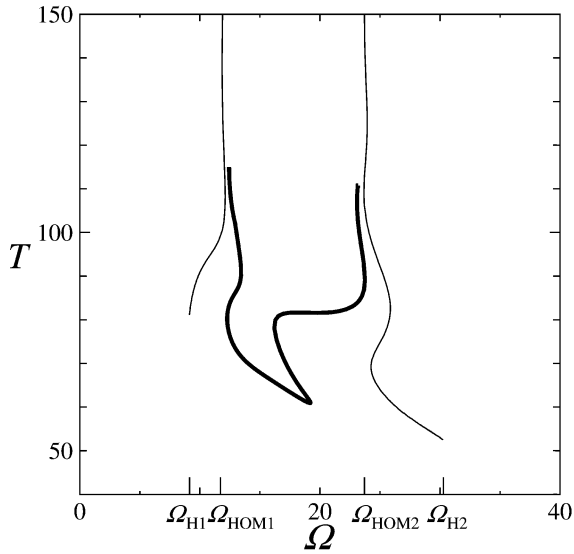

Figure 2. The period T of the periodic solutions for $R = 400$. The thin curves indicate the single periodic solutions bifurcating at the Hopf bifurcation points Ω_{H1} and Ω_{H2}. Half the period for the double periodic solution is also shown by the thick curve.

the largest growth rate.) They are obtained by the Newton–Raphson method. The vertical lines indicate a single periodic motion (the dotted line for the smaller Ω side and the dashed line for the larger Ω side) and a doubly periodic motion (the thick solid line) obtained by the DNS. Also the DNS reproduces two-dimensional and three-dimensional steady flows indicated by open circles.

From Figure 1 it can be seen that as Ω is increased the streamwise vortex flow, which bifurcates from the basic flow at $\Omega_C = 4.3$, is taken over by the steady three-dimensional flow at $\Omega_1 = 6.5$. The stable steady three-dimensional flow persists over a small range of Ω above Ω_1 before a periodic motion due to a Hopf bifurcation sets in at $\Omega_{H1} = 8.4$. It has been confirmed by DNS that the time development of the periodic motion at $\Omega = 10$ in the phase space has a single period, whereas at $\Omega = 16$ the period of the motion is doubled. When the system rotation is increased to and over $\Omega = 24$ the motion becomes single periodic again, until the periodic motion shrinks to a steady three-dimensional flow at $\Omega_{H2} = 32$. The three-dimensionality vanishes at $\Omega_2 = 47$ and the streamwise vortex flow is obtained for larger Ω values and finally the basic state is recovered although it is not shown in the figure.

Figure 2 shows the period of the periodic motion obtained as a fixed point on the Poincaré section. It can be seen that the period T of the periodic solutions which bifurcate from the Hopf bifurcation points $\Omega = \Omega_{H1}$ (Ω_{H2}) increase sharply and approach infinity as Ω is increased (decreased). The infinitely

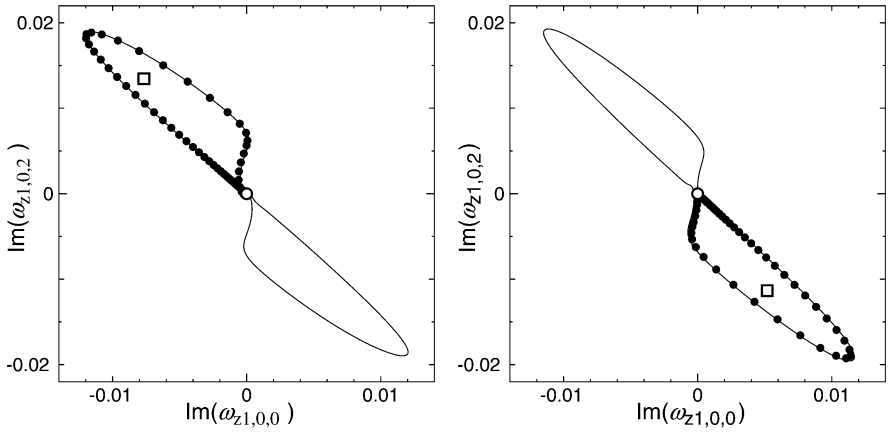

Figure 3. The orbits of the single periodic motion indicated by dots and the double periodic motion by a curve in the phase space at (a) $\Omega \approx \Omega_{\mathrm{HOM1}}$ and (b) $\Omega \approx \Omega_{\mathrm{HOM2}}$. The circle at the centre represents the steady streamwise independent motion and the square represents the steady three-dimensional solution.

long period is also speculated by the accumulation of the dots near the centre of Figure 3, where we plot the points on the periodic orbit (not shown) at a constant time interval, where the streamwise dependency is absent. Therefore, we conclude that there exists a homoclinic orbit originating from the streamwise independent steady solution. Figure 3 also shows the trajectory of the double periodic motion. Half its period is plotted by the thick curve in Figure 2.

We also explore the existence of the single periodic solution branch in the $\Omega - R$ space. The periodic solution detected at $\Omega = 10$ is traced by keeping its period T constant. It is found that the solution branch extends to a smaller Ω, crossing the line of $\Omega = 0$ at $R = 774$. Then, the periodic solutions are followed along the $\Omega = 0$ in the direction of decreasing R. The momentum transport calculated by DNS in Figure 4 for the non-rotating plane Couette system shows that the periodic motion merges with the steady three-dimensional flow at $R \approx 600$.

4.2 Rotating plane Poiseuille flow

Background. The linear stability of rotating plane Poiseuille flow is considered by Lezius and Johnstone (1976), who found a minimum critical Reynolds number, R_c, of many orders of magnitude less than the corresponding value for non-rotating case. Alfredsson and Persson (1989) found experi-

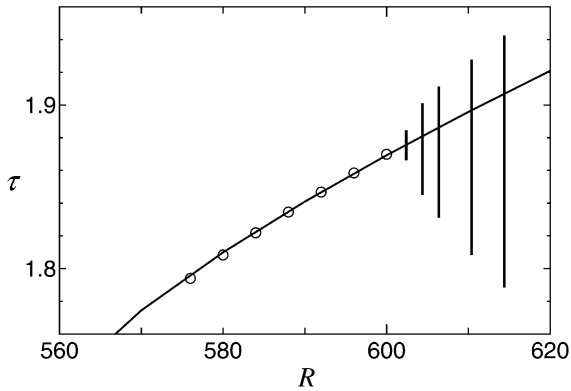

Figure 4. The momentum transport τ periodic solutions indicated by vertical lines for non-rotating plane Couette system. The curve and the circles indicate the steady three-dimensional flow calculated by Newton–Raphson method and the DNS, respectively.

mentally the setting up of streamwise-oriented vortices for $R > R_c$ when the rotation number, Ω lies in a certain range. At higher values of R, a secondary instability sets in as Ω is increased and this leads to a three-dimensional travelling-wave type tertiary flow. Alfredsson and Persson (1989) identified the instability with streamwise wavelength of the order of the spanwise vortex wavelength usually characterized by a twisting of the vortices. Alfredsson and Persson (1989) also observed another secondary instability consisting of the splitting and merging of the streamwise vortices. Using a direct numerical simulation approach, Finlay (1990) found that the twisting-mode exists for a wide range of R and first appears for values of R between $2R_c$ and $3R_c$. Both Finlay (1990), and Yang and Kim (1991) found the twisting-mode to have the largest growth rate, and so it would be expected to dominate in practice in flows. Matsubara and Alfredsson (1998) reported experimentally that the most rapidly growing disturbance responsible for the twisting-mode instability is an out of phase sinuous mode. Guo and Finlay (1991) considered an Eckhaus-type instability causing merging and splitting of vortices by performing a linear stability analysis of a DNS-generated two-dimensional vortex flow to two-dimensional streamwise-independent disturbances. They found this instability to be important in selecting the wavenumber of the streamwise vortices. The aim of the present study is to find the two-dimensional secondary flow using a global bifurcation approach which would allow the solution to be accurately computed away from the bifurcation point to large amplitude. We also set out to examine the stability of these solutions so that we can find the solutions bifurcating from the secondary flow, which enables us to compare with the previous experimental and DNS results described above.

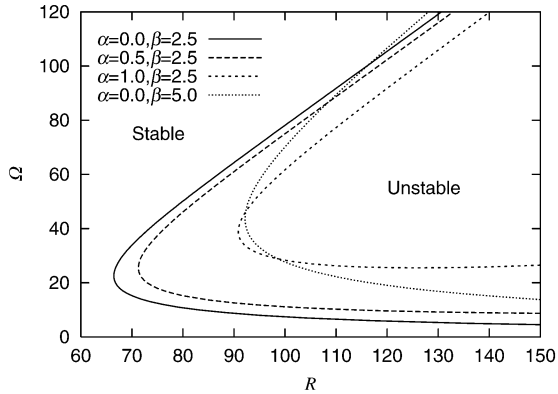

Figure 5. Marginal stability curves in the $\Omega - Re$ space for a various combination of wavenumbers (α, β).

Results. Marginal stability curves in the $R - \Omega$ plane are plotted in Figure 5 for a various combination of the streamwise wavenumber α and the spanwise wavenumber β with instability occurring to the right of a given curve and stability to the left. For a fixed value of Ω it is a two-dimensional mode with $\alpha = 0$ that first becomes unstable with increasing R. It may be seen from Figure 5 that for $\Omega > 100$ the basic flow loses stability to the $(\alpha = 0, \beta = 5)$ mode before the $(\alpha = 0, \beta = 2.5)$ as R increases, whereas this situation is reversed for $\Omega < 100$. Although we obtain the minimum critical Reynolds number to be $R_c = 66.448$ for $\beta_c = 2.459$ we select two-dimensional modes with $(\alpha, \beta) = (0, 2.5)$ and (0,5) for convenience to facilitate an easier understanding of the one-two modal interactions.

In Figure 6 we plot values of the L_2 norm of the ϕ amplitude coefficients a_{l0n} against R for streamwise-independent solutions (2DLR: two-dimensional longitudinal rolls) $(\alpha, \beta) = (0.2.5)$ and (0, 5) at $\Omega = 22.1325$. The marginal stability points derived by the linear stability analysis correspond to the bifurcation points of the nonlinear solutions from the basic flow. It may be observed that the solution for $\beta = 2.5$ bifurcates from the basic flow in a supercritical bifurcation, with the amplitude of the bifurcating solution increasing with increasing R until a turning point is reached ar $R \approx 374$. The amplitude then decreases as R reduces until the solution appears to merge with that of the upper branch of the $\beta = 5$ solution at $R \approx 153$. A visualisation of the contours of ϕ has illustrated the transition from the $\beta = 5$ solution to the $\beta = 2.5$ solution branch via this bifurcation . Such a bifurcation, in which the spanwise wavelength of the flow doubles, corresponds to a merging of some of the vortical structures present in the $\beta = 5$ case. Not shown in the figure are the branches of the solution for $\beta = 1.25$ and $\beta = 3.75$. The bifurcation points

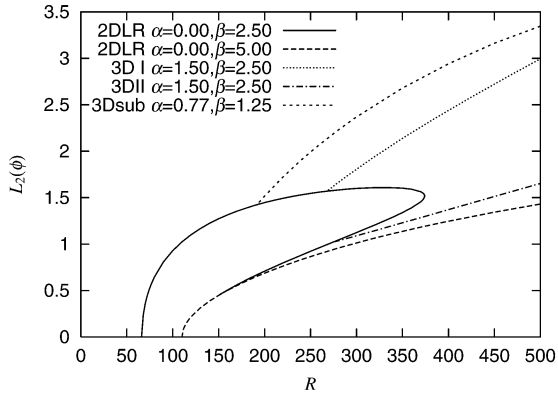

Figure 6. The bifurcation diagram at $\Omega = 22.1325$.

from the basic flow lie between those for $\beta = 2.5$ and $\beta = 5$. Therefore, the merging and splitting picture would be more complicated if we would add these solutions.

In order to fully understand the stability of the streamswise-independent flow, we consider stability to disturbances of all Floquet parameter values within the semi-infinite strip $0 \leq d, 0 \leq \beta$. Figure 7 shows the contours of the real part of the most unstable eigenvalue in Floquet parameter space (d, b) for the secondary flow with $\beta = 2.5$ at a sequence of points along the upper and lower solution branches. It may be seen that the secondary flow is stable to all disturbances when $R = 70$ (see Figure 7(a)). The present analysis indicates that the flow first loses stability at $R = 80$ to a two-dimensional disturbance mode with vanishing b. As R increases, the flow rapidly becomes unstable to all values of $b \in (0, \beta)$ for zero d with the subharmonic secondary disturbance mode $b = \beta/2$ possessing the largest growth rates (see Figure 7(b)). When R has reached 220 on the upper branch, a disjoint region of instability centred around $d \approx 0.75$ and $b = 1.25$ appears (see Figure 7(c)). As R increases it may be seen that such a three-dimensional spanwise-subharmonic disturbance $(d \neq 0, b = \beta/2)$ then becomes the disturbance of largest growth rate. This mode consists of a single complex eigenvalue, and so would be expected to produce a travelling-wave tertiary flow. With reference to Figures 7(d)–(f), it can be seen that this region of unstable Floquet parameters eventually extends to include all spanwise Floquet parameters. It can also be seen that the mode with largest growth rate then becomes one with $b = 0, d > 0$. This mode is consistent with Finlay's (1990) WVF1 (wavy vortex flow 1) mode or the twisting mode observed in Alfredsson and Persson's (1989) study. As we progress down the lower branch from the turning point of the nonlinear branch it may be seen in Figures 7(g) and (h), that the region of instability then collapses

to a single region which is bounded by a finite value of d. The flow remains unstable everywhere on the lower branch.

The stability analysis on the secondary flow as described above serves to give the bifurcation points for tertiary flows (see Wall and Nagata, 2005). Recently, we identify three distinct three-dimensional travelling-wave solutions: one of them (3Dsub) is subharmonic in the spanwise wavenumber and the other two (3DI and 3DII) harmonic flows, that is, flows with the primary spanwise wavenumber unchanged. These solution branches have been included in Figure 6.

4.3 Cubic velocity profile flow

Background. Nagata and Busse (1983) found numerically that the bifurcation from the basic state is described by two-dimensional transverse vortex flow. As the Grashof number, which measures the temperature difference between the plates, increases above its critical value, this secondary flow becomes unstable first to three-dimensional perturbations with a steady subharmonic nature, and then, at a slightly larger Grashof number, to those with a harmonic oscillatory nature. After confirming the findings by Nagata and Busse (1983), we extend their analysis to flows above the second critical Grashof number. It is found that the steady tertiary flow which bifurcates from the two-dimensional secondary flow at the second critical Grashof number becomes unstable in turn, losing its stability to time-dependent quaternary flows.

Results. The basic state becomes unstable at $G_r = 500$ (see the circle in Figure 8) to a two-dimensional perturbation where the 2D transverse vortex flow (2DTV) as a steady secondary solution bifurcates supercritically (see the dotted line in Figure 8(b)). The 2DTV becomes unstable first at $G_r = 534$ (triangle) to 3D subharmonic three-dimensional perturbation and at $G_r = 545$ (black triangle) to a harmonic three-dimensional perturbation with a complex conjugate pair of eigenvalues. The real eigenvalue corresponding to the 3D subharmonic perturbation increases first as G_r is increased, has a maximum at $G_r \approx 610$, and then decreases. It crosses zero at $G_r = 664$ (inverted triangle) and merges with another real eigenvalue to form a complex conjugate pair with a negative real part. The real part of the complex conjugate pair becomes positive at $G_r = 676$ (inverted black triangle).

We find that the 3D steady subharmonic flow (3DSS), which bifurcates at $G_r = 534$ (triangle) as a tertiary solution, loses its stability against two different types of three dimensional perturbations, one at $G_r = 680$ (open square) and the other at $G_r = 700$ (black square). The other 3DSS bifurcating at $G_r = 664$ (inverted triangle) never gains stability.

For DNS we restricted the wavenumber pair (α, β) for the computation domain $(L_x = 2\pi/\alpha L_y = 2\pi/\beta)$ to (1.25, 1.00) for the harmonic case and to

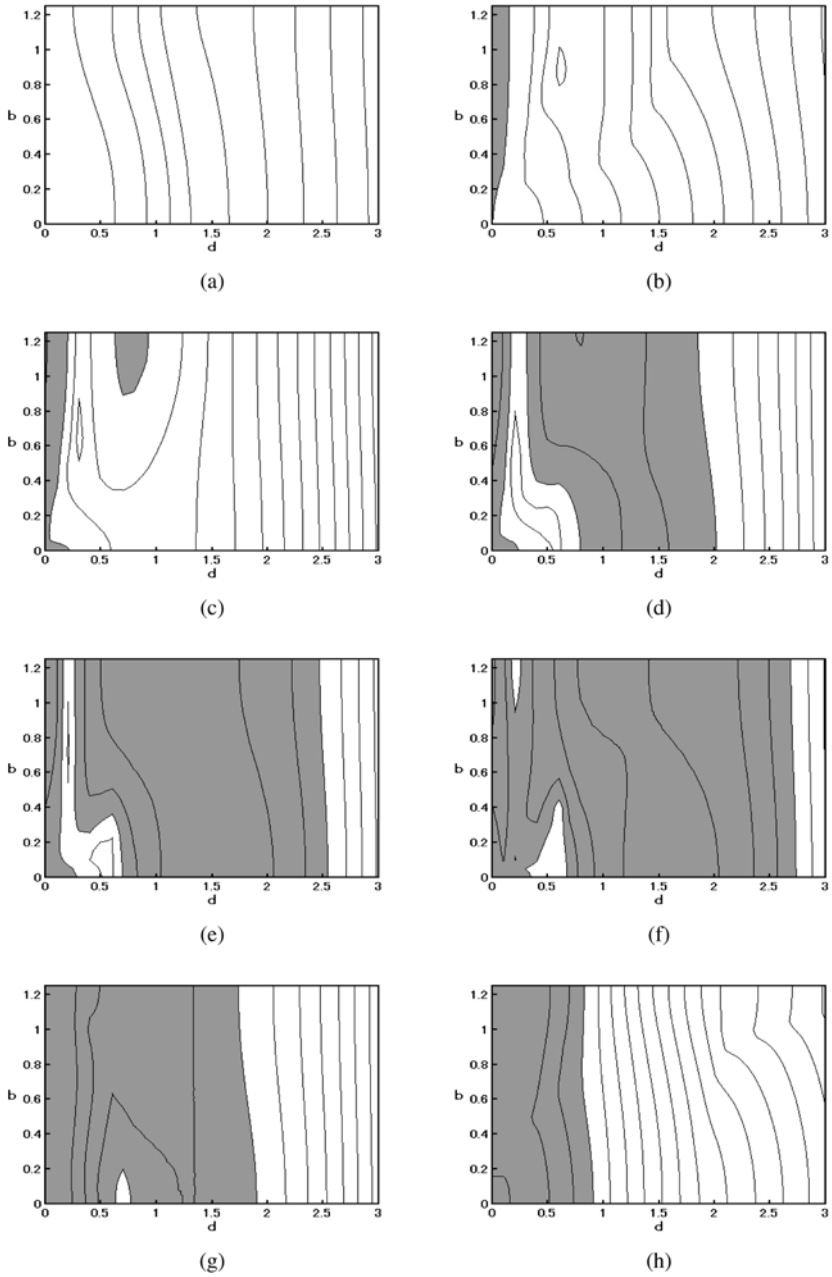

Figure 7. Contours of the real part of the most unstable eigenvalue in Floquet parameter space (d, b) for the secondary flow with $\beta = 2.5$, $\Omega = 22.1325$ on the upper branch at (a) $R = 70$, (b) $R = 100$, (c) $R = 200$ (d) $R = 300$ (e) $R = 350$ and (f) $R = 374.1$ and on the lower branch at (g) $R = 300$ and (h) $R = 160$. The horizontal axis ranges $0 \leq d \leq 3$. The vertical axis ranges $0 \leq b \leq 1.25$. Contour intervals are 2.0.

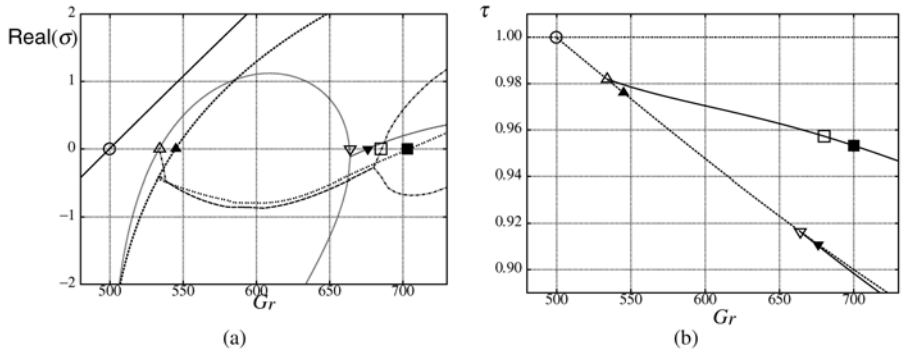

Figure 8. (a) The real part of the growth rate σ as a function of G_r indicated by the solid line for the basic flow, the thin-dotted curve for 2DTV with $(\alpha, \beta) = (1.25, 0)$ in the subharmonic case $(d, b) = (0.625, 1.0)$, The thick-dotted curve for 2DTV in the harmonic case $(d, b) = (0.0, 1.0)$. The dash-dotted curve and the thick two-dotted curve correspond to the stability of 3DSS with $(\alpha, \beta) = (0.625, 1.0)$ in the case of $(d, b) = (0, 0)$ and $(0, 0.5)$, respectively. (b) The momentum transport τ of the basic state (thin horizontal line), 2DTV (dotted line) and 3DSS (thick line) by nonlinear analysis. Marks on each line indicate points where the stability changes.

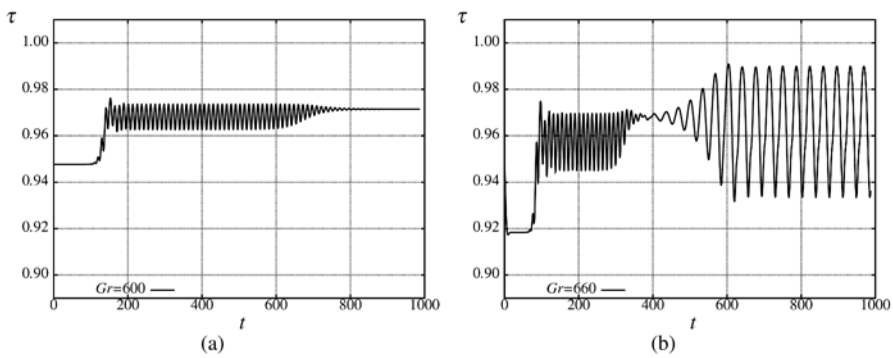

Figure 9. The time development of the momentum transport τ. (a) $G_r = 600$. (b) $G_r = 660$.

(0.625, 1.0) for the subharmonic case. Figure 9 shows the time development of the momentum transport τ by DNS in the harmonic calculation domain. We notice that the flow passes through several stages with relatively long intervals before it reaches its final state in general. Each transient stage is characterised by a distinct flow property. Therefore, we suppose that the DNS could capture an unstable solution as long as the point representing the flow in the phase space stays near a stable manifold. However, because the solution itself is unstable the point is repelled eventually and possibly attracted towards a different state in the phase space as soon as it moves on an unstable manifold.

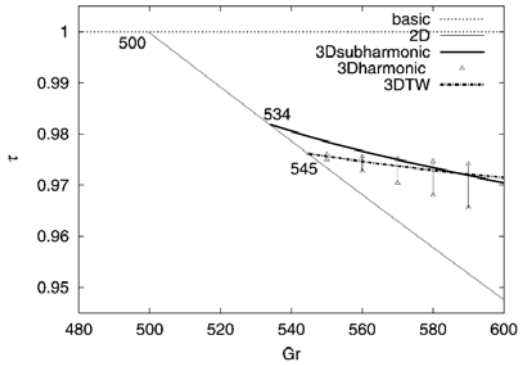

Figure 10. The bifurcation in the harmonic case.

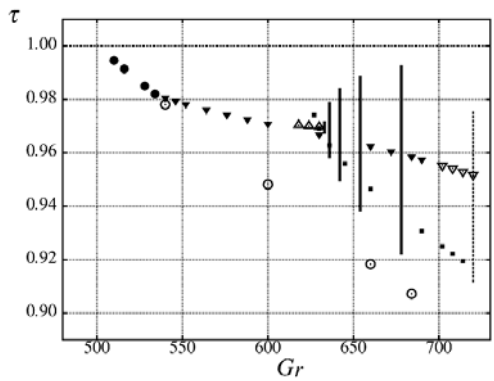

Figure 11. The momentum transport of steady and time-dependent solutions by DNS.

Since the three-dimensional subharmonic solution cannot manifest itself by DNS in the harmonic domain we expect some three-dimensional periodic flows to bifurcate directly from the 2DTV in the harmonic case. However, it turns out that the periodic flows exist only as a transient state and the solution in the final state is actually a three-dimensional travelling-wave (3DTW) instead (see Figure 9(a), for example). The 3DTW does not change its flow pattern in a frame moving with the spanwise phase speed c_y and keeps a constant momentum transport on the plates. The existence of the 3DTW is also confirmed by the calculation by Newton–Raphson method as shown in Figure 10. It is interesting to note that the 3DTW has a non-zero average velocity $\check{V}(z)$ in the spanwise direction. It should be noted that the solutions in the harmonic case constitute a subset of the solutions in the subharmonic case.

Clear distinction between transient states and the final state has been observed by DNS in the subharmonic domain as well. Figure 11 shows the momentum transport τ for the subharmonic case. The stable solution which

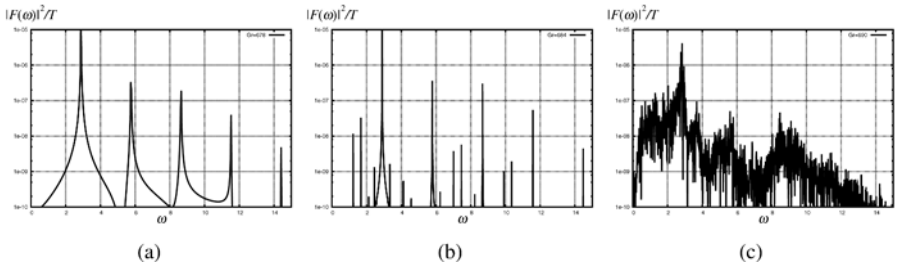

Figure 12. The spectrum of the momentum transport. (a) $G_r = 678$. (b) $G_r = 684$. (c) $G_r = 690$.

bifurcates from the 2DTV (black circles for final states and open circles for transient states) is the 3DSS (black inverted triangles). The 3DSS persists up to $G_r \approx 680$ as the final state and they can be realised only as a transient state for $G_r > 680$ (open inverted triangles). Depending on the initial condition, the final state can also be reached by a time-dependent state with periodic nature for $630 < G_r < 680$ as indicated by the thick lines in Figure 11. (The open triangles at around $G_r \approx 620$ in the figure indicate the three-dimensional travelling-wave solutions detected as a transient state.) As the Grashof number increases further, the periodic trajectory in the phase space undergoes quasi-periodic motions and eventually becomes chaotic. We observe that the discrete harmonic frequency exists at $Gr = 678$, the peaks of another frequency emerges at $G_r = 684$, and the peaks eventually form a continuous spectrum at $G_r = 690$ as shown in Figure 12.

We note that with other different initial conditions three-dimensional steady states are detected as the final state as can be seen by the black squares in Figure 11. These steady states are traced back to $G_r \approx 625$. Lastly, we add that a three-dimensional solution with a sporadic burst has been detected at $G_r = 720$ with yet another initial condition, which is indicated by the dotted line in Figure 11. The time development of its momentum transport is displayed in Figure 13.

5. SUMMARY

5.1 Rotating and non-rotating plane Couette flow

We have shown that the periodic motions, which bifurcate from the tertiary flow in the rotating plane Couette system, undergo a period doubling bifurcation.

We have traced the periodic motions in the parameter space and found that they exist even when the system rotation is absent. Preliminary investigation has indicated that the periodic motions obtained in the present study for non-

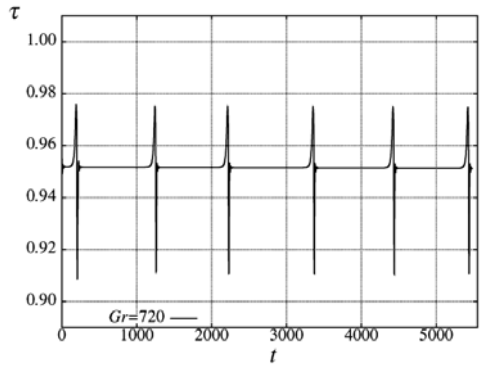

Figure 13. The time development of the burst.

rotating plane Couette system do not have connection with those periodic motions found by Clever and Busse (1997) or Kawahara and Kida (2001).

5.2 Rotating plane Poiseuille flow

This study has considered the flow through a channel subject to a system rotation about a spanwise axis. In contrast to previous studies, a global bifurcation approach has been undertaken which allows the structure of the bifurcating secondary flow to be fully elucidated, with both stable solution, unstable solution and also the relationship between the secondary-flow solutions investigated. We have further undertaken a stability analysis of the secondary flow which has identified stable flows, and also the location of tertiary-flow bifurcation points. Finally, three types of three-dimensional travelling-wave solution branches bifurcating from the predicted location of the bifurcation points are obtained. Overall, our findings are in good qualitative agreement with those of previous studies. The quantitative comparison with the previous studies will be reported separately (Wall and Nagata, 2005).

5.3 Cubic velocity profile flow

We have presented the stability and bifurcation analyses of flows of a Boussinesq fluid between vertical plates with different temperatures in the vanishing P_r limit. It is confirmed that the secondary and tertiary flows are the two-dimensional transverse vortex flow and the three-dimensional subharmonic steady flow, respectively. This is consistent with the result by Nagata and Busse (1983). The stability analysis on the tertiary flow indicates an oscillatory state as a possible quaternary motion.

We have also presented results obtained by the numerical experiment, where several unstable solutions representing a transient state are captured. We have

found that the final state for $630 < G_r < 680$ can be reached by a three-dimensional steady subharmonic motion or a three-dimensional periodic motion, depending on the initial condition. These two different types of motion coexist as a stable solution of the system. As the Grashof number is increased, the periodic motion becomes quasi-periodic and eventually a chaotic motion ensues.

REFERENCES

Alfredsson, P.H. and Persson, H. (1989). Instabilities in channel flow with system rotation. *J. Fluid Mech.* **202**, 543–557.

Clever, R.M. and Busse, F.H. (1997). Tertiary and quaternary solutions for plane Couette flow. *J. Fluid Mech.* **344**, 137–153.

Finlay, W.H. (1990). Transition to oscillatory motion in rotating channel flow. *J. Fluid Mech.* **215**, 209–227.

Guo, Y. and Finlay, W.H. (1991). Splitting, meerging and wavelength selection of vortices in curved and/or rotating channel flow due to Eckhaus instability. *J. Fluid Mech.* **228**, 661–691.

Kawahara, G. and Kida, S. (2001). Periodic motion embedded in plane Couette turbulence: Regeneration cycle and burst *J. Fluid Mech.* **449**, 291–300.

Lezius, D.K. and Johnstone, J.P. (1976). The structure and stability of turbulent boundary layers in rotating channel flow. *J. Fluid Mech.* **77**, 153–173.

Matsubara, M. and Alfredsson, P.H. (1998). Three-dimensional tertiary motion in a plane shear layer. *J. Fluid Mech.* **368**, 27–50.

Nagata, M. (1990). Three-dimensional finite-amplitude solutions in plane Couette flow: Bifurcation from infinity. *J. Fluid Mech.* **217**, 519–527.

Nagata, M. (1998). Tertiary solutions and their stability in rotating plane Couette flow. *J. Fluid Mech.* **358**, 357–378.

Nagata, M. and Busse, F.H. (1983). Three-dimensional tertiary motions in a plane shear layer. *J. Fluid Mech.* **135**, 1–26.

Vest, C.M. and Arpaci, V.S. (1969). Stability of natural convection in a vertical slot. *J. Fluid Mech.* **36**, 1–15.

Wall, D.P. and Nagata, M. (2005). Nonlinear secondary flow through a rotating channel. *J. Fluid Mech.*, submitted.

Yang, K.S. and Kim, J. (1991). Numerical investigation of instability and transition in rotating plane Poiseuille flow. *Phys. Fluids* **A3**, 633–641.

CO-SUPPORTING CYCLE: SUSTAINING MECHANISM OF LARGE-SCALE STRUCTURES AND NEAR-WALL STRUCTURES IN CHANNEL FLOW TURBULENCE

Sadayoshi Toh[1], Tomoaki Itano[2] and Kai Satoh[1]
[1]*Department of Physics and Astronomy, Graduate School of Science, Kyoto University, Kitashirakawa, Sakyo-ku, Kyoto 606-8502, Japan*
[2]*Department of Aeronautics and Astronautics, Graduate School of Engineering, Kyoto University, Yoshida-Honmachi, Sakyo-ku, Kyoto 606-8501, Japan*

Abstract Direct numerical simulation of a turbulent channel flow in a periodic domain of relatively wide spanwise extent, but minimal streamwise length, is carried out at Reynolds numbers $Re_\tau = 137$ and 349. The large-scale structures previously observed in studies of turbulent channel flow using huge computational domains are also shown to exist even in the streamwise-minimal channel of the present work. In the system, it is also clearly observed how the large-scale structures and the near-wall structures affect each other. While the collective behavior of near-wall structures enhance a large-scale structure, the resulting large-scale structure in turn activates the generation and drift of the latter. Hence near-wall and large-scale structures interact in a co-supporting cycle. The preliminary numerical results suggesting the existence of traveling wave solutions that correspond to large-scale structures are reported.

Keywords: turbulent channel flow, coherent structure, generation mechanism, numerical simulation, large-scale structure, traveling wave solution.

1. INTRODUCTION

In the vicinity of the wall, including the viscous and buffer layers which together constitute the near-wall region, a pair of streamwise vortices induces a low-speed streaky region, 'wall streak', the instability of which makes the near-wall region energetic, and regenerates the streamwise vortices. This cyclic process, which was first recognized as self-sustaining process (SSP) in plane Couette flow by Hamilton et al. (1995) and Waleffe (1997), is thought to be common in many types of wall-bounded turbulent flows. SSP was recently confirmed by the find of exact solutions (cf. Waleffe, 1998; Kawahara and

T. Mullin and R.R. Kerswell (eds), Laminar Turbulent Transition and Finite Amplitude Solutions, 71–83.
© 2005 *Springer. Printed in the Netherlands.*

Kida, 2001) for the minimal flow unit proposed by Jiménez and Moin (1991). Although SSP may largely account for turbulent fluctuations in the near-wall region, the minimal flow unit is a small subspace of the huge computational domain which is required to simulate 'real' or practical turbulence. In the real turbulence therefore, large-scale structures in the outer region and a huge number of these near-wall structures in the near-wall region, interacting and developing spatially, participate in the production and transfer toward the outer region of turbulent fluctuation (Miyake et al., 1987; Lee and Kim, 1987; Komminaho et al., 1996).

In the present work, our main interest is in understanding the collective behavior of the near-wall structures, and investigating how the behavior could be associated with the large-scale structures from a physical point of view. To prevent the near-wall and large-scale structures from evolving spatially in the streamwise direction as a first step, we restrict the streamwise length of the computational box to the minimal length in direct numerical simulations of channel flow. Because this channel still has large spanwise extent comparable to the extent of huge computational domains used previously, we call this box a 'streamwise-minimal' channel. We will show that large-scale structures can exist even in the streamwise-minimal channel, and propose a mechanism for the sustenance of large-scale structures based on the observation of the dynamical behaviors of a large-scale structure and near-wall structures. It should be noted that in the streamwise-minimal channel plane Poiseuille flow is stable for all values of the Reynolds number. We expect that this restriction may make large-scale structures much more visible in turbulence flow.

In Section 5, we will introduce the preliminary work on traveling wave solutions that appear to correspond to large-scale structures. These solutions are on the basin boundary of the turbulence attractor and thus considered to be the lower branch of traveling wave solutions, while the upper branch of them, not found yet, is believed to represent the turbulence generation process in the near-wall region. The Reynolds number dependence of these solutions also confirm their relation to large-scale structures and Waleffe's theory presented at the symposium.

2. STREAMWISE-MINIMAL FLOW

The numerical scheme we used to simulate channel flow is the same as used in Toh and Itano (2003), which is based on that of Kim et al. (1987). The origin of coordinate system is taken on the mid-plane of the channel with the x, y, z axes in the streamwise, wall-normal and spanwise directions, respectively. The no-slip boundary condition is imposed at the top ($y = +h$) and bottom ($y = -h$) walls, where h is half the channel width. Flow is driven by constant streamwise volume flux per unit spanwise length Q. We define the characteristic velocity

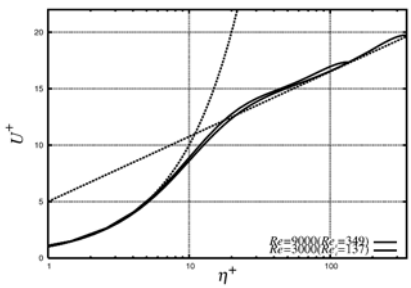

Figure 1a. Mean streamwise velocity of the present channels in wall units. Thick curve, $Re_\tau = 349$; thin curve, $Re_\tau = 137$. Dashed lines are $U^+ = 2.5 \log \eta^+ + 5$ and $U^+ = \eta^+$, where η is distance from the wall, $\eta = h - |y|$.

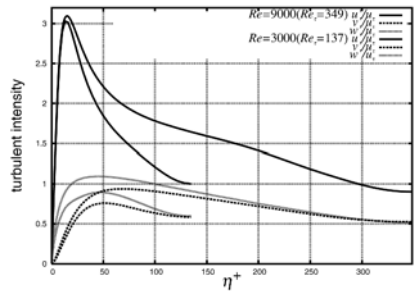

Figure 1b. Turbulent intensity profiles. Thick curves correspond to streamwise (solid), wall-normal (dashed), and spanwise (dotted) velocity profiles in the $Re_\tau = 349$ case. Thin curves correspond to those in the $Re_\tau = 137$ case.

U_c as $3Q/4h$; for laminar Poiseuille flow U_c is just the centerline velocity. In the present work, we fix the Reynolds number based on U_c, h and the kinematic viscosity ν at 3000 and 9000. The Reynolds number based on the friction velocity, $Re_\tau = U_\tau h/\nu$, is 137 and 349 for our streamwise-minimal channel, where $U_\tau = \sqrt{\langle \tau \rangle_T}$,

$$\langle \tau \rangle_T = \frac{1}{T} \int_0^T \nu \frac{\partial U}{\partial y}(t')|_{\text{wall}} \mathrm{d}t'$$

and $U(y, t)$ is the streamwise velocity averaged over the horizontal plane at y.

In the present work, the streamwise length of our streamwise-minimal channel is set to be approximately minimal by reference to the domain sizes of the minimal flow units used by Jiménez and Pinelli (1999). Thus, it is obvious that the streamwise length of our domain, L_x, is much shorter than that used in the earlier studies which suggested the existence of large-scale structures in the turbulent channel flow. On the other hand, the spanwise extent of the domain is relatively wide; since it is more than 800 in wall units in the $Re_\tau = 349$ case, about six to eight wall streaks could survive in the near-wall region in our domain. The spanwise extent of the domain, L_z, is $2.39h$ in the $Re_\tau = 349$ case and $3.78h$ in the $Re_\tau = 137$ case. Therefore, L_z exceeds just the critical value, $2h$, necessary for large-scale structure to exist in the outer region, as described by Jiménez (1998).

As seen in Figure 1a, the empirical law of the wall and log-law velocity profile whose description has been obtained by many researchers (for example, see Schlichting, 1979), appears to offer a good approximation. Figure 1b shows the turbulent intensity obtained for our channels. Note that the peak value of the turbulent intensity of streamwise velocity fluctuation is somewhat larger than that obtained from direct numerical simulations with not only min-

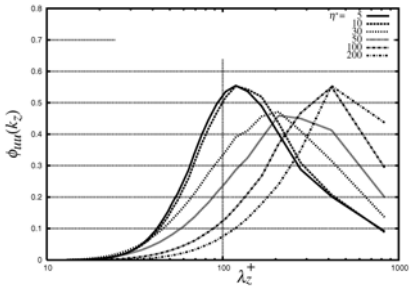

Figure 2a.

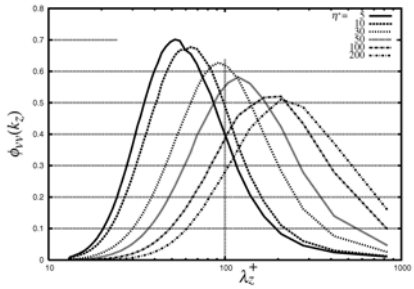

Figure 2b.

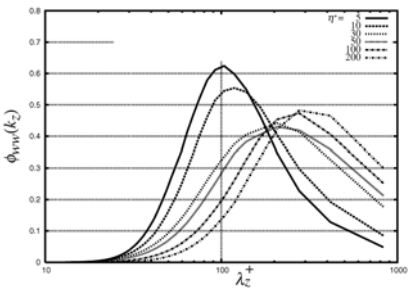

Figure 2c.

Figure 2. Pre-multiplied power spectrum, $\phi(k_z)$, as a function of $\lambda_z = 2\pi/k_z$. (a) ϕ_{uu}; (b) ϕ_{vv}; (c) ϕ_{ww} in the case of the streamwise-minimal channel at $Re = 9000$ ($Re_\tau = 349$). Increasing distance from the wall, $\eta = h - |y|$, corresponds to a rightward shift towards the long-wavelength end of the spectrum. All the spectra are normalized to unit area under the curve in the log-lin plots, to emphasize their frequency content.

imal flow unit but also huge domains. Thus, the large peak value is probably due to our domain size; the large spanwise extent of our domain allows large-scale structures to exist in the outer region, while the short streamwise length of our domain may reinforce the interaction between near-wall structures and large-scale structures.

3. LARGE-SCALE STRUCTURE

The pre-multiplied power spectra have been often used to suggest the existence of large-scale structures in channel flow, e.g., Jiménez (1998) or Abe et al. (2001). Specifically, we define the pre-multiplied power spectra as follows:

$$\phi_{ff}(k_z)|_\eta = k_z E_{ff}(k_z, y) / \sum_{k_z=2\pi/L_z}^{\max(k_z)} E_{ff}(k_z, y) \tag{1}$$

$$E_{ff}(k_z, y) = \frac{1}{TL_x} \int_0^T \int_0^{L_x} (|f_{k_z}(x, y, t)|^2 + |f_{-k_z}(x, y, t)|^2) \mathrm{d}x\mathrm{d}t, \tag{2}$$

where $f_{k_z}(x, y, t)$ is the Fourier coefficient for a spanwise wave number k_z of velocity component $f(x, y, z, t)$, $f = u_x, u_y, u_z$ and distance from the wall $\eta = h - |y|$. We use pre-multiplied spectra $\phi(k_z) \equiv k_z E(k_z)$ so that areas

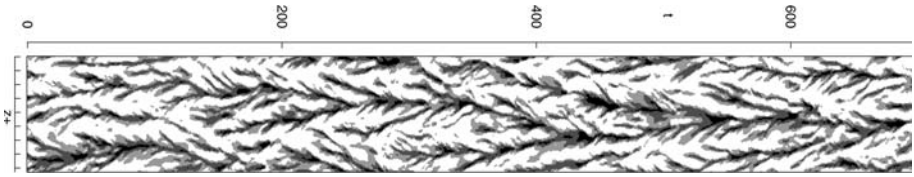

Figure 3a. Shaded regions represent the low-speed zone, $u_x^{2D}(t, y, z) < U(t, y)$ at $\eta^+ = 5$ (near-wall region) in the lower half domain ($-h < y < 0$) in the interval $0 < t < 720$. The vertical axis z^+ is scaled by 100 wall units.

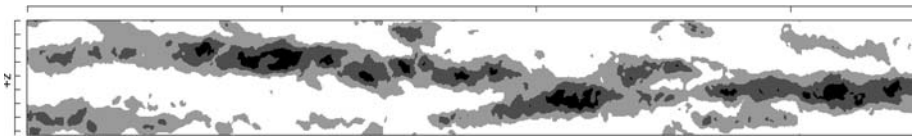

Figure 3b. Same as in (a) but at $\eta^+ = 200$ in the outer region.

under the curve in log-lin plots correspond to the actual energy content, i.e., $E(k_z)\mathrm{d}k_z = \phi(k_z)\mathrm{d}(\ln k_z)$. Figures 2a–2c are pre-multiplied power spectra obtained in the $Re_\tau = 349$ case. The characteristic length giving the spectrum peak is dependent on distance from the wall and is thought to correspond to the spanwise scale of a relatively dominant structure at each distance in the flow. In the case of the streamwise-minimal channel, $\phi_{u_x u_x}$ and $\phi_{u_z u_z}$ at $\eta^+ = 5$ peak approximately at $\lambda_z^+ = 100$, which corresponds to the accepted mean spacing of the wall streaks in the near-wall region. With increasing η in both cases, the peaks move to a longer wavelength corresponding to the outer length.

In this section, it is shown that the pre-multiplied power spectra of streamwise and spanwise velocities have two specified peaks corresponding to the mean intervals of near-wall structure in the near-wall region and large-scale structure in the outer region. These characteristics have been also reported in many studies using direct numerical simulation with more practical huge channel (for example Jiménez, 1998). The similarities between the streamwise-minimal channel and a huge channel suggest that the former contains a large-scale structure quite close to that in the latter. If this is so, we will then be interested in what makes a large-scale structure and, how the large-scale structure contributes to turbulence, in the streamwise-minimal channel.

4. CO-SUPPORTING CYCLE

The streamwise-minimal channel allows for only one near-wall and one large-scale structure with respect to the streamwise direction. This artificial restriction inhibits some of the rich spatio-temporal properties observed in huge domains, for example, the spatial growth of structures and the interaction between structures aligned in the streamwise direction (Adrian et al., 2000). Still, this

simplified system appears to include fundamental dynamics of both the large-scale structure and near-wall structures.

The structures interact with each other while moving around in a streamwise cross-section and repeating their own dynamical processes. In order to understand the dynamics of the structures as a whole, we below represent the location of a near-wall structure or a large-scale structure simply as the low-speed zone at $\eta^+ = 5$ (near-wall region) or 200 (outer region) respectively. The low-speed zone is defined as z satisfy $u_x^{2D}(t, y, z) < U(t, y)$ at time t and the distance from the lower wall $\eta = h - |y|$, where

$$u_x^{2D}(t, y, z) = \frac{1}{L_x}\int_0^{L_x} u_x(t, \boldsymbol{x})\mathrm{d}x \quad \text{and} \quad U(t, y) = \frac{1}{L_z}\int_0^{L_z} u_x^{2D}(t, y, z)\mathrm{d}z.$$

Time-development of low-speed zones in both regions are shown in Figures 3a and 3b, which allow us to trace the spanwise movement and generation processes of near-wall and large-scale structures. In fact, the characteristic spanwise wavelength λ_z^+ at the peak of $\phi_{u_x u_x}$ mentioned in the previous section finds reasonable agreement with the mean spanwise interval between two adjacent minima; as may be seen from the figure, $\Delta z^+ \approx 100$ and 400 for $\eta^+ = 5$ and 200, respectively.

Moreover, from Figure 3a we can see that the branches may be classified into two types: dominant branches, which survive for a relatively long time, and weak branches. As time elapses, weak branches are successively merged into a few dominant branches in almost all of the merging events in the near-wall region, while some weak branches emerge from structure-free areas. The branches in Figure 3a are reminiscent of rivers in a map of a mountainy area and thus we call the regions where branches gather 'valley' and the structure-free regions where branches emerge 'watershed'. It is also significant to note that large-scale structures in Figure 3b appear to be located always above a valley, that is, a long-lived dominant branch in Figure 3a, while a watershed in Figure 3a separates two adjacent large-scale structures in Figure 3b.

The dynamics of the large-scale structures and near-wall structures in the streamwise-minimal channel is described as follows (see Figure 5): Immature near-wall structures are continually generated through a local instability near a watershed between two adjacent large-scale circulations and slowly move toward either of the two. Moreover, a dominant near-wall structure continually attracts and merges weaker structures into itself, beneath the low-speed region of a large-scale structure. These facts suggest a tight coupling between a large-scale structure and near-wall structures, which consists of the following three elementary processes (see Figure 5):

1 Sweeping of near-wall structures by a large-scale circulation in the spanwise direction toward the area under the low-speed region.

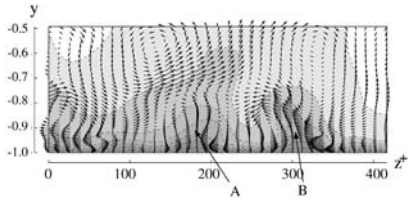

Figure 4a. Snapshots of flow in the $Re = 9000$ ($Re_\tau = 349$) case in a z-y cross-section at $t = 120$. Vector field indicates (u_z^{2D}, u_y^{2D}). Shaded region indicates $u_x^{2D} < 0.7U_c$ and contour levels are $0.6U_c, 0.5U_c, ..., 0.1U_c$.

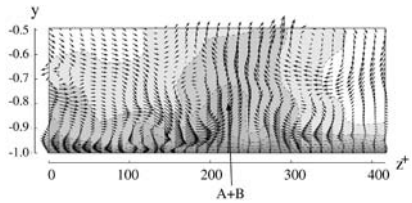

Figure 4b. Same as in (b) but $t = 140$ A concentrated eruption follows a merging event of near-wall structures A and B in the panel (a).

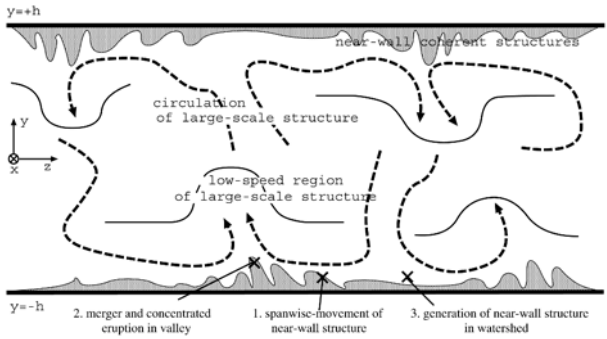

Figure 5. Schematic view of a snapshot in our channel in a z-y cross-section, where three elementary processes of the co-supporting cycle are described. Thin solid curves indicate contours of u_x^{2D} in the outer region, each bulge of which corresponds to the low-speed region of a large-scale structure. The circulation of a large-scale structure is represented by thick dashed curve. Shaded regions near the walls denote wall streaks.

2 Enhanced or collective bursting (called eruption here) through the merging of two near-wall structures which causes an influx of fluid from the near-wall region into the outer region (see Figures 4a and 4b). This eruption brings about strong suction from both sides which acts to maintain the large-scale circulation and the low-speed region of the large-scale structure.

3 Formation of near-wall structures through some instability around the downward flow of a circulation of the large-scale structure.

The coupling with the near-wall structures through the three processes above probably enables the large-scale structure to survive. However, in the cycle the large-scale structure is not just passive, but active enough to contribute to the generation, spanwise-movement and merger of near-wall structures, which reactivate the large-scale structure itself. Therefore, we denote the whole cycle

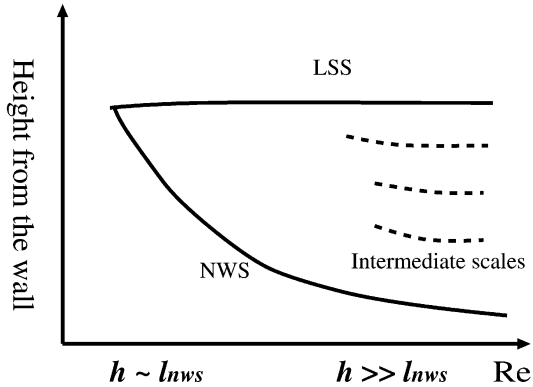

Figure 6. Schematic bifurcation diagram of traveling wave solutions. The upper branch (in this figure the lower one) corresponds to near-wall structure (NWS). The lower one (the upper one) is expected to represent large-scale structure (LSS).

as 'co-supporting cycle' of a large-scale structure and near-wall structures, to distinguish this from the self-sustaining process of a single near-wall structure.

5. ORIGIN OF LARGE-SCALE STRUCTURES

In the previous section, we have shown that large-scale structures are sustained through the co-supporting cycle so that one may deduce that they are not self-sustained. This, however, could not be the case.

Large-scale structures are characterized by their streamwise low-speed regions similar to streaks in the near-wall region; The average interval of them is estimated about $1.2h$ to $2h$ by the pre-multiplied spectra so far. According to Del Álamo and Jiménez (2003), their streamwise extent is almost infinite in practical turbulence. The large-scale structures, thus, are nearly homogeneous in the streamwise direction and scaled by the outer scale. Although large-scale structures are observed at high enough Reynolds numbers in experiments where the separation of the outer and inner scale is noticeable, they can be detected even at low Reynolds numbers where the two scales are comparable. These facts suggest that a large-scale structure has an origin at a low Reynolds number accompanied by its counterpart, i.e., a near-wall structure. As the Reynolds number increases further, the large-scale and near-wall structures may separate out gradually. Note that large-scale structures can exist even over rough walls which tend rather to suppress near-wall structures. In this case, large-structures should be self-sustained.

Waleffe (2001, 2003) found that for plane Couette and Poiseuille flows a pair of traveling wave solutions emerge through a saddle-node bifurcation and both the upper and lower branch solutions have spatial structures similar to those of near-wall structure observed in direct numerical simulations and experiments.

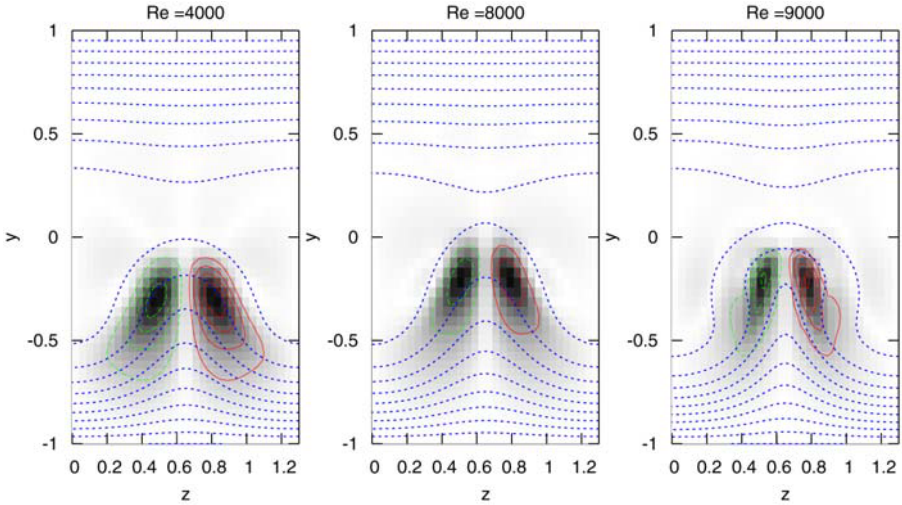

Figure 7. Traveling wave solutions for $Re = 4000$, 8000 and 9000. Their streamwise extents, L_x are π, π and 0.35π, respectively. Dashed line, tow dimensional streamwise velocity u_x^{2D}; solid lines, tow dimensional streamwise vorticity ($\omega_x^{2D} > 0$); broken lines, $\omega_x^{2D} < 0$. The shaded regions show ω_x^{2D}.

Whereas the upper branch corresponds to near-wall structures, the lower one is scaled in the outer scale.

All the circumstantial evidences mentioned above indicate that a large-scale structure can be described by the lower branch of a couple of traveling wave solutions while near-wall structures are represented by the upper branch. Figure 6 shows this view schematically. There we assume that each branch experiences bifurcations successively. Through the bifurcations traveling wave solutions in intermediate scales might emerge and constitute hierarchical structure corresponding to the log layer.

At the symposium, Waleffe reported that an asymptotic behavior of the lower branch solution with respect to the Reynolds number is approximated by a formal perturbation expansion with the small parameter Re^{-1} based on the self-sustaining process for Couette flow. With this expansion, he almost succeeded to explain the Re^{-1} scaling of the amplitude of disturbances needed for excitation of turbulence. It is easy to apply this formal expansion to Poiseuille flow; The lower branch solution is expected to extend in the full channel even at high Reynolds numbers and get two-dimensional as the x dependences are weaken against the Reynolds number. These characteristics are just those of large-scale structures. We, therefore, infer that large-scale structure is represented by the lower branch of traveling wave solutions.

Plane Poiseuille flow in a streamwise-minimal box is stable for all values of the Reynolds number because the streamwise extent of the channel is shorter

than the wavelengths of any linearly-unstable modes for plane Poiseuille flow (Drazin and Reid, 1981). In this sense, this flow is subcritical. Thus we can apply the shooting method (Toh and Itano, 2003) to obtain a traveling wave solution which is stable on the basin boundary separating the turbulence attractor and the laminar solution.

In Figure 7, we show traveling wave solutions obtained at $Re = 4000$, 8000 and 9000, respectively: The streamwise dimensions of them are π, π, and 0.35π. The last one is the same as that of the streamwise-minimal box dealt with in this paper. It should be noted that these results are nothing but preliminary ones because they are not sufficiently converged in the sense that the control parameter used is settled in only first three digits. We need further numerical works to confirm these solutions. Anyway, these preliminary solutions show that they occupy the outer layer and thus are scaled in the outer scale. Furthermore, these solutions are dominated in the lower half region so that they are asymmetric in the wall-normal direction unlike traveling wave solutions obtained so far.

The Reynolds number dependence of two- and three-dimensional (2D and 3D) energy components of the traveling wave solutions are shown in Figure 8. Here,

$$E_*^{2D} = \int_V (u_*^{2D})^2/2\mathrm{d}V, \quad E_*^{3D} = \int_V (u_* - u_*^{2D})^2/2\mathrm{d}V,$$

$* = x$, y and z, and V is the volume of the computational box. All the energy components except for E_x^{2D} which is the energy of the mean flow, are multiplied by Re^2 and are roughly constant. This is consistent with Waleffe's Re^{-1} expansion where the first order components of the spanwise and wall-normal velocities and the second order components are the order of Re^{-1}.

6. CONCLUDING REMARKS

In this paper, we have shown by direct numerical simulations that large-scale structures exist even in a streamwise-minimal box whose streamwise dimension is confined to the minimal length required for the sustenance of turbulence. Furthermore, we obtained the preliminary results suggesting that these large-scale structures are described by traveling wave solutions. A large-scale structure has spatial form quite similar to that of near-wall structures. It involves a streak-like low-speed region and two counter-rotating large-scale circulations, although the circulations, i.e., (u_z^{2D}, u_y^{2D}) and the streamwise modulation of the streak, $u_x^{3D} = u_x - u_x^{2D}$, seem to be scaled in Re^{-1} and thus diminish as the Reynolds number increases.

Two open questions, however, arise. One is why and how the solutions on the basin boundary can affect turbulence. The other one is the fate of the lower branch in the case of the streamwise extent of a computational box larger than

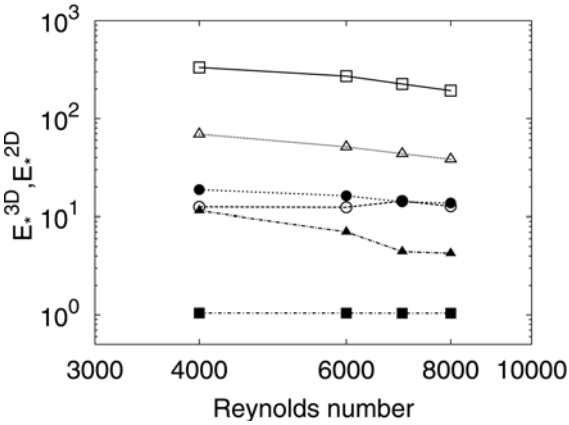

Figure 8. Reynolds number dependence of the modal energy of traveling wave solutions for $L_x = \pi$: filled square, E_x^{2D}; square $E_x^{3D} \times Re^2$; filled circle, $E_y^{2D} \times Re^2$; circle, $E_x^{3D} \times Re^2$; filled triangle, $E_z^{2D} \times Re^2$; triangle, $E_z^{3D} \times Re^2$.

the critical length for the instability of plane Poiseuille flow. These questions must be essential in considering the substantial role of large-scale structures in practical wall-bounded turbulence.

Large-scale structures are coupled tightly with near-wall structures and sustained by their direct interaction in the streamwise-minimal flow. We have, therefore, called this sustaining process of the large-scale and near-wall structures a co-supporting cycle. If large-scale structures are really self-sustained and described by some exact solutions, the feedback from the dynamics of large-scale structures to that of near-wall structures, i.e. the turbulence generation process, may be much more significant than expected.

Finally, it would remain to make it convincing that the co-supporting cycle can be realized even in the huge computational box. Del Álamo and Jiménez (2001, 2003) reported that the pre-multiplied power spectrum of the streamwise velocity, which characterizes the large-scale structure, decomposes into two components: quasi-isotropic modes of relatively short streamwise length scales and (maybe infinitely) long modes deeply penetrated into the near-wall region. They suggested that the latter modes interact with the near-wall region. In this work, we have seen that our large-scale structures are dominated by modes with $k_x = 0$, i.e., with infinitely long streamwise length. Furthermore, the traveling wave solutions suggest that a large-scale structure is getting homogeneous in the streamwise direction as the Reynolds number goes infinity. We conclude, therefore, that our large-scale structure corresponds to their long, deep modes and thus reflect some properties of the large-scale structure observed in practical turbulence. Thus, since streamwise-minimal channel may accommodate large-scale structure, the collective motion of wall streaks and

deep modes and thus reflect some properties of the large-scale structure observed in practical turbulence. Thus, since streamwise-minimal channel may accommodate large-scale structure, the collective motion of wall streaks and their interactions as well as the self-sustaining processes of individual near-wall structures, the present study will contribute significantly to the elucidation of practical wall-bounded turbulent flow.

ACKNOWLEDGEMENTS

S.T. is supported by a Grant-in-Aid for the 21st Century COE 'Center for Diversity and Universality in Physics'. T.I. was supported in part by Center of Excellence for Research and Education on Complex Functional Mechanical Systems (COPE program of the Ministry of Education, Culture, Sports, Science and Technology, Japan).

REFERENCES

Abe, H., Kawamura, H. and Matsuo, Y. (2001). Direct numerical simulation of a fully developed turbulent channel flow with respect to Reynolds number dependence. *Trans. ASME J. Fluids Engrg.* **123**, 382–393.

Adrian, R.J., Meinhart, C.D. and Tomkins, C.D. (2000). Organization of vortical structure in the outer region of the turbulent boundary layer. *J. Fluid Mech.* **422**, 1–51.

Del Álamo, J.C. and Jiménez, J. (2001). Direct numerical simulation of the very large anisotropic scales in a turbulent channel. *Center for Turbulence Research Annual Research Briefs*, 329–341.

Del Álamo, J.C. and Jiménez, J. (2003). Spectra of the very large anisotropic scales in turbulent channels. *Phys. Fluids* **15**, L41–44.

Draizin, P.G. and Reid, W.H. (1981). *Hydrodynamic Stability*, Cambridge University Press.

Hamilton, J.M., Kim, J. and Waleffe, F. (1995). Regeneration mechanisms of near-wall turbulence structures. *J. Fluid Mech.* **287**, 317–348.

Hof, B. et al. (2004). Experimental observation of nonlinear traveling waves in turbulent pipe flow. *Science* **305**, 1594–1598.

Jiménez, J. and Moin, P. (1991). The minimal flow unit in near-wall turbulence. *J. Fluid Mech.* **225**, 213–240.

Jiménez, J. and Pinelli A. (1999). The autonomous cycle of near wall turbulence. *J. Fluid Mech.* **389**, 335–359.

Jiménez, J. (1998). The largest scales in the turbulent wall flows. *Center for Turbulence Research Annual Research Briefs*, 137–154.

Komminaho, J., Lundbladh, A. and Johansson, A.V. (1996). Very large structures in plane turbulent Couette flow. *J. Fluid Mech.* **320**, 259–285.

Kawahara, G. and Kida, S. (2001). Periodic motion embedded in plane Couette turbulence: Regeneration cycle and burst. *J. Fluid Mech.* **449**, 291–300.

Kim, J., Moin, P. and Moser, R. (1987). Turbulence statistics in fully developed channel flow at low Reynolds number. *J. Fluid Mech.* **177**, 133–166.

Lee, M.J. and Kim, J. (1991). The structure of turbulence in a simulated plane Couette flow. In *Proceedings of the 8th Symposium on Turbulent Shear Flows*, Paper No. 5-3.

Miyake, Y., Kajishima, T. and Obana, S. (1987). Direct numerical simulation of plane Couette flow at transitional Reynolds number. *JSME Int. J.* **30**, 57-65.

Moser, R.D., Kim, J. and Mansour N.N. (1999). Direct numerical simulation of turbulent channel flow up to $Re_\tau = 590$. *Phys. Fluids* **11-4**, 943–945.

Shlichting H. (1979). *Boundary-Layer Theory*, 7th edn., McGraw-Hill.

Toh, S. and Itano, T. (2003). A periodic-like solution in channel flow. *J. Fluid Mech.* **481**, 67–76.

Toh, S. and Itano, T. (2005). Interaction between a large-scale structure and near-wall structures in channel flow. *J. Fluid Mech.* **524**, 249–262.

Waleffe, F. (1997). On a self-sustaining process in shear flows. *Phys. Fluids* **9**(4), 883–900.

Waleffe, F. (1998). Three-dimensional coherent states in plane shear flows. *Phys. Rev. Lett.* **81**(19), 4140–4143.

Waleffe, F. (2001). Exact coherent structures in channel flow. *J. Fluid Mech.* **435**, 93–102.

Waleffe, F. (2003). Homotopy of exact coherent structures in plane shear flows. *Phys. Fluids* **15**(6), 1517–1534.

TRANSITION THRESHOLD AND THE SELF-SUSTAINING PROCESS

Fabian Waleffe[1,2,3] and Jue Wang[1]
[1]*Department of Mathematics, University of Wisconsin, Madison, USA*
[2]*Department of Engineering Physics, University of Wisconsin, Madison, USA*
[3]*CNLS, CCS-2 and IGPP, Los Alamos National Laboratory, USA*
waleffe@math.wisc.edu, wang@math.wisc.edu

Abstract The self-sustaining process is a fundamental and generic three-dimensional nonlinear process in shear flows. It is responsible for the existence of non-trivial traveling wave and time-periodic states. These states come in pairs, an upper branch and a lower branch. The limited data available to date suggest that the upper branch states provide a good first approximation to the statistics of turbulent flows. The upper branches may thus be understood as the "backbone" of the turbulent attractor while the lower branches might form the backbone of the boundary separating the basin of attraction of the laminar state from that of the turbulent state. Evidence is presented that the lower branch states tend to purely streaky flows, in which the streamwise velocity has an essential spanwise modulation, as the Reynolds number R tends to infinity. The streamwise rolls sustaining the streaks and the streamwise undulation sustaining the rolls, both scale like R^{-1} in amplitude, just enough to overcome viscous dissipation. It is argued that this scaling is directly related to the observed R^{-1} transition threshold. These results also indicate that the exact coherent structures never bifurcate from the laminar flow, not even at infinity. The scale of the key elements, streaks, rolls and streamwise undulation, remain of the order of the channel size. However, the higher x-harmonics show a slower decay with R than naively expected. The results indicate the presence of a warped critical layer.

Keywords: wall-bounded turbulence, coherent structures, self-sustaining process, transition threshold, critical layers.

1. INTRODUCTION

Recent pipe flow experiments by Hof et al. (2003) provide clear evidence that the transition threshold, i.e. the smallest perturbation amplitude ϵ that triggers transition from laminar to turbulent flow, scales like R^{-1} as $R \to \infty$, where R is the Reynolds number. Some numerical results also indicate that scaling in plane Couette-like flows and models (e.g. Eckhardt and Mersmann, 1999).

T. Mullin and R.R. Kerswell (eds), Laminar Turbulent Transition and Finite Amplitude Solutions, 85–106.
© 2005 *Springer. Printed in the Netherlands.*

The concept of transition threshold was introduced by Trefethen et al. (1993) who conjectured that $\epsilon \sim R^a$ with $a < -1$, strictly. Their argument rests on linear transient algebraic growth of some perturbations before exponential viscous decay, i.e. a behavior of the form $\epsilon\, t\, e^{-t/R}$ where ϵ is the initial perturbation amplitude and t is time. Such perturbations grow to a maximum amplitude of order ϵR at a time of order R before the final viscous decay. A simple scaling argument balancing the quadratic nonlinear interaction (since the Navier–Stokes nonlinearity is quadratic) of maximally amplified disturbances with the linear viscous decay of the original disturbance then suggests a transition threshold exponent $a = -3$,

$$(\epsilon R)^2 \sim \frac{\epsilon}{R} \;\Rightarrow\; \epsilon \sim R^{-3}. \tag{1}$$

On the other hand, the balance

$$(\epsilon)^2 \sim \frac{\epsilon}{R} \;\Rightarrow\; \epsilon \sim R^{-1}, \tag{2}$$

suggests that $a = -1$ would correspond to a nonlinear transition where linear transient growth does not play a role. Furthermore, the linear transient growth, which in shear flows primarily results from the redistribution of streamwise velocity by streamwise rolls, is accompanied by a mean shear reduction of order $(\epsilon R)^2$ (Waleffe, 1995a, 1995b, 1997; Reddy et al., 1998). Therefore, for $\epsilon \sim R^{-1}$, that mean shear reduction would invalidate linear theory, since the latter assumes that the mean shear is fixed at its laminar value. Hence, the understated importance of the restriction $a < -1$, *strictly*, in the original conjecture.

A lower bound on the transition threshold was derived by Kreis et al. (1994). That lower bound clearly involves transient growth but leads to the scaling exponent $a = -21/4$, much smaller even than the $a = -3$ suggested by the simple scaling argument above (1). Numerical simulations suggest scaling exponents that are much closer to $a = -1$. Reddy et al. (1998) report $a \approx -1$ for streamwise vortices perturbations and $a \approx -5/4$ for oblique roll perturbations, in plane Couette flow, and $a \approx -7/4$ for both type of perturbations in plane Poiseuille flow. However, those exponents are deduced from small and low Reynolds number ranges and may therefore not correspond to the true asymptotic values. Chapman (2002) presents an asymptotic scaling analysis of the two transition scenarios studied in Reddy et al. (1998)) and suggests that the true scaling exponents are in fact $a = -1$ for both types of perturbations in plane Couette flow, and $a = -3/2$ and $-5/4$ for the streamwise vortices and oblique perturbations, respectively, in plane Poiseuille flow.

Chapman's study contains a detailed asympotic analysis of the linear dynamics about the laminar flow using WKB methods.[1] However, the rest of his formal analysis consists only of scaling estimates and is incomplete. His

analysis of oblique perturbations calls on intricate initial disturbances with relatively large vorticity of $O(R^{-2/3})$ in plane Couette flow and $O(R^{-11/12})$ in plane Poiseuille flow and specific nonlinear interactions to create channel-size streamwise rolls.[2] His analysis of the streamwise vortex scenario leads to plausible thresholds for streak instability, but those cannot be considered as thresholds for transition since his formal analysis does not address feedback.[3] Transition is not possible without feedback. The instability of a transient perturbation, e.g. the instability of transient streaks, is not sufficient for transition, since that instability would necessarily extract energy from the streaks and therefore could simply accelerate the return to the laminar flow. Transition claims require demonstrating that disturbances are sustained.

The *self-sustaining process* (SSP) is a weakly nonlinear theory about a spanwise varying shear flow that incorporates feedback. It is a synthesis of experimental studies of coherent structures in the near-wall region of turbulent flows (particularly the nicely illustrated work of Acarlar and Smith (1987)) and theoretical ideas due to Benney (1984). The main elements of the SSP (Figure 1) are streamwise rolls of $O(R^{-1})$ that redistribute the streamwise velocity to create $O(1)$ streaks whose streamwise undulation of $O(R^{-1})$ directly feeds back onto the streamwise rolls (Waleffe, 1990, 1995a, b, 1997; Waleffe et al., 1993). The validity and relevance of the SSP was established by Hamilton et al. (1995) using Direct Numerical Simulations which strongly suggested the existence of time-periodic solutions in plane Couette flow that have been isolated by Kawahara and Kida (2001). The process and the proposed scalings have served as the basis for a method to compute three-dimensional traveling wave solutions of the Navier–Stokes equations. In that method (Waleffe, 1998), an artificial forcing of $O(R^{-2})$ is introduced to sustain $O(R^{-1})$ streamwise rolls, these rolls redistribute the mean shear to create $O(1)$ streaks. The resulting new steady state, called the streaky flow, is linearly unstable because of the strong spanwise inflections. This instability is subcritical in terms of the artificial forcing because the direct nonlinear effect of the streak instability is to feedback on the streamwise rolls. The nonlinear self-interaction of an $O(R^{-1})$ streak eigenmode provides an $O(R^{-2})$ nonlinear forcing that replaces the artificial forcing to sustain the rolls against viscous decay. That approach was used successfully in plane Couette and Poiseuille flow with both free-slip and no-slip boundary conditions (Waleffe, 1998, 2001, 2003) and has also been used to compute analogous traveling waves in pipe flow by Faisst and Eckhardt (2003) and Wedin and Kerswell (2004). Itano and Toh (2001) use a related shooting method where the starting point is a suitably selected x-averaged flow (i.e. a streaky flow) obtained from a direct numerical simulation. These works demonstrate that the SSP is robust and generic for shear flows.

The more recent and farther-reaching work on transient growth (e.g. Reddy et al., 1998; Chapman, 2002) has moved closer to the self-sustaining process

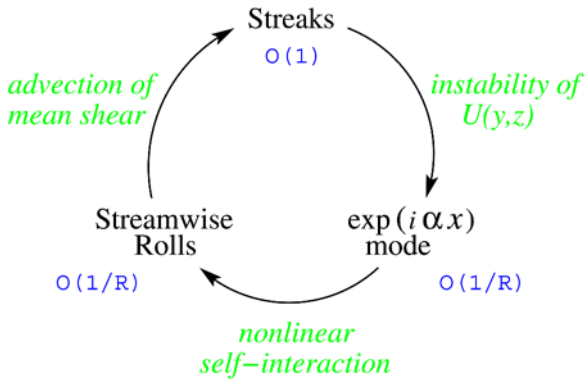

Figure 1. The key elements of the Self-Sustaining Process with their presumed scalings.

theory. Those papers do not focus anymore on which laminar flow perturbations lead to maximum transient energy growth but instead on those perturbations that lead to the most unstable streaks.[4] However that line of work has not yet addressed the feedback issue which is key for transition. Work on the self-sustaining process includes the complete and exact representation of the redistribution of streamwise velocity by streamwise rolls, including the modification of the mean shear, and seeks to construct streamwise rolls leading to streaks whose spanwise inflectional instability leads *directly* to the regeneration of the *same* streamwise rolls, thereby demonstrating self-sustenance and transition potential.

Here, motivated by Hof, Juel and Mullin's recent outstanding evidence that $a = -1$ in pipe flow, we look back at the presumed scalings for the self-sustaining process and provide numerical evidence that such scalings are asymptotically exact as $R \to \infty$. We illustrate the ideas using a simple 4th order model, follow with a sketch of an asymptotic theory and finally present fully resolved calculations of the lower branch exact coherent states in plane Couette flow. Our Cartesian coordinates follow the usual choice with x streamwise, y shearwise (wall-normal) and z spanwise, and corresponding velocity components u, v and w, respectively.

2. SCALING IN A SIMPLE MODEL OF THE SSP

A simple model of the self-sustaining process was proposed in Waleffe (1995a, 1995b) and later "derived" from a systematic Galerkin projection of the Navier–Stokes equations (Waleffe, 1997). The simplest non-trivial Galerkin model consists of 8 modes, but that model is pathological as explained in Waleffe (1997, sect. IV). An *ad hoc* reduction to a 4-mode model was made in Waleffe (1997). Moehlis et al. (2004) have considered a 9-mode model

that cures the pathological behavior of the 8-mode model, to some extent. Their surgical modification of the 8-mode model is along the lines suggested in Waleffe (1997, sect. IV), namely, to increase the resolution in the wall-normal direction, but they do this in a very economical way that only adds one mode and slightly modifies the shearwise structure of a few other modes. Their 9-mode models illustrates some of the nonlinear dynamics of shear flow transition such as chaotic repellors and the fractal nature of the transition boundary. However, from the point of view of the gross features of self-sustaining process and the associated non-trivial fixed points, the original 4th order model is sufficient and simpler.

The 4th order model[5] consists of the 4 real ODEs

$$\begin{aligned}
\left(\frac{d}{dt}+\frac{\kappa_m^2}{R}\right)M &= \tfrac{\kappa_m^2}{R} \quad -\sigma_u\, UV \qquad\qquad\qquad\qquad +\sigma_m\, W^2 \\
\left(\frac{d}{dt}+\frac{\kappa_u^2}{R}\right)U &= \qquad\quad \sigma_u\, MV \quad -\sigma_w\, W^2 \\
\left(\frac{d}{dt}+\frac{\kappa_v^2}{R}\right)V &= \qquad\qquad\qquad\qquad\qquad\quad \sigma_v\, W^2 \\
\left(\frac{d}{dt}+\frac{\kappa_w^2}{R}\right)W &= \qquad\qquad\qquad\quad \sigma_w\, UW \quad -\sigma_v\, VW \quad -\sigma_m\, MW
\end{aligned} \tag{3}$$

In this model, the κ^2/R terms on the left-hand side represent viscous dissipation, all σ coefficients on the right-hand side are considered to be positive. We do not need to consider specific numerical values for the κ's and σ's. The right-hand side terms are organized in columns to emphasize that the nonlinear terms are energy-conserving and to clearly identify the various parts of the SSP. The first column κ_m^2/R is the external forcing of the mean shear amplitude $M(t)$. The 2nd column correspond to the redistribution of the mean shear by streamwise rolls of amplitude $V(t)$ to create streaks of amplitude $U(t)$. The flip-side of that redistribution is the Reynolds stress $-\sigma_u UV$ in the M-equation. The third column represents the streak instability. $W(t)$ is the amplitude of a three-dimensional streak eigenmode, sinusoidal in the streamwise x-direction, that would grow exponentially on sufficiently large amplitude (frozen) streaks U. This is accompanied by a Reynolds stress arising from the nonlinear self-interaction of the streak eigenmode, $-\sigma_w W^2$, that destroys the streaks as discussed in the introduction. The 4th column is the key nonlinear feedback on the streamwise rolls, $\sigma_v W^2$, that arises from the nonlinear self-interaction of the streak eigenmode. The fifth column was overlooked in the original write-up of the SSP model (Waleffe, 1995a, 1995b), since it is not essential for the SSP. Its existence was revealed by the Galerkin derivation and it turns out to be essential for the lower branch scaling discussed in this article, as already discussed in Waleffe (1997, eqn. (23)). Its physical origin is simply the

shearing by the mean of x-dependent disturbances. This shearing is important and tied to the reduction of the mean shear by the streaks-rolls Reynolds stress. Indeed if $\sigma_w U - \sigma_m M < 0$, i.e. if the streaks are not sufficiently large compared to the mean shear, then the streak instability (the exponential growth of W) cannot occur. Note that the rolls V also reduce the streak instability growth rate, but they are typically much weaker than the streaks U and the mean shear M.

Model (3) has a laminar fixed point $(M, U, V, W) = (1, 0, 0, 0)$ that is linearly stable for all R, as in plane Couette flow. It can be shown in general, i.e. for any κ's and σ's provided that all σ's are positive, that model (3) has a critical Reynolds number $R_{sn} > 0$ above which two non-trivial fixed points exist as long as $\sigma_u \sigma_v \sigma_w > 0$. The complete derivation is sketched in Waleffe (1997, sect. III D); here we only state the asymptotic balance for the lower branch fixed point. For large R, the lower branch fixed point (indicated by the subscript ℓ) corresponds to the balance

$$\begin{aligned}
\frac{\kappa_m^2}{R} M_\ell &\sim \frac{\kappa_m^2}{R} \quad -\sigma_u U_\ell V_\ell \\
\frac{\kappa_u^2}{R} U_\ell &\sim \qquad \sigma_u M_\ell V_\ell \\
\frac{\kappa_v^2}{R} V_\ell &\sim \qquad\qquad \sigma_v W_\ell^2 \\
\sigma_w U_\ell &\sim \sigma_m M_\ell
\end{aligned} \tag{4}$$

specifically,

$$\lim_{R\to\infty} M_\ell = \frac{1}{1 + \dfrac{\kappa_u^2 {\sigma_m}^2}{\kappa_m^2 \sigma_w^2}} < 1, \qquad \lim_{R\to\infty} U_\ell = \frac{\sigma_m/\sigma_w}{1 + \dfrac{\kappa_u^2 {\sigma_m}^2}{\kappa_m^2 \sigma_w^2}} > 0, \tag{5}$$

$$\lim_{R\to\infty} (R\, V_\ell) = \frac{\sigma_m \kappa_u^2}{\sigma_u \sigma_w}, \qquad \lim_{R\to\infty} (R\, W_\ell) = \sqrt{\frac{\sigma_m \kappa_u^2 \kappa_v^2}{\sigma_u \sigma_v \sigma_w}} \tag{6}$$

so the lower branch fixed point tends to a streaky flow, not to the laminar point as $R \to \infty$, $(M_\ell, U_\ell, V_\ell, W_\ell) \to (M_\infty, U_\infty, 0, 0) \neq (1, 0, 0, 0)$. This is only true if $\sigma_m \neq 0$. Thus the key physical effect responsible for the R^{-1} scaling of streamwise rolls and streak eigenmode, and the need for $O(1)$ streaks, is the shearing of the x-dependent streak eigenmode by the mean shear.[6]

2.1 Transition threshold in the 4th order model

The transition threshold is the smallest distance to the stable manifold of the lower branch coherent state.[7] Therefore we want to estimate the smallest initial condition that will bring the system in the neighborhood of the lower branch

fixed point. Our postulate is that we can obtain a good estimate of that threshold from the lower branch coherent state combined with our mechanistic understanding of the self-sustaining process.

A look at the 4th order model (3) shows that $W = 0$ is an invariant manifold. This follows from the fact that W represents the amplitude of the only x-dependent 3D mode in that model. The streaks U and rolls V correspond to x-independent 2D modes and the mean shear M is a 1D mode with no streamwise or spanwise variation. Therefore this $W = 0$ invariant manifold directly correspond to the 2D x-independent invariant manifold for the Navier–Stokes equations. It is clear that the laminar fixed point is the global attractor in the $W = 0$ invariant manifold, since V is not sustained and will decay viscously back to zero, in which case the streamwise velocity redistribution ceases and $U \to 0$, $M \to 1$. This is true also for the 2D invariant manifold in shear flows, as first shown in Joseph and Tao (1963). Therefore, to trigger transition in model (3), the initial conditions must be such that $W(0) \neq 0$. This is a first key observation and constraint for transition.

Besides the need for $W(0) \neq 0$, it is rather clear that an efficient way to jumpstart the SSP is to start with streamwise rolls $V(0) \sim V_\ell = O(R^{-1})$ with $V(0) \gg W(0) \neq 0$ and $V(0) > V_\ell$ since the rolls will suffer some viscous decay while creating streaks. This is the strategy that has always been employed to study the SSP (e.g. Waleffe, 1995a, sect. 4.1; Waleffe, 1997, sect. II A) as well as to calculate self-sustained 3D traveling waves in the Navier–Stokes equations by bifurcation from a streaky flow. Another good candidate perturbation is to start with a $W(0) \sim W_\ell = O(R^{-1})$. However such initial condition is subjected to shearing by the mean ($-\sigma_m MW$ term) which destroys W rapidly. Therefore we expect this type of perturbation to be much less effective in triggering transition, requiring $W(0)$ significantly larger than W_ℓ although still scaling like R^{-1} asymptotically as $R \to \infty$.

3. ASYMPTOTIC THEORY OF THE SSP

The original presumed scalings for the SSP was that streamwise rolls of $O(R^{-1})$ create inflectionally unstable streaks of $O(1)$, and that the nonlinear self-interaction of $O(R^{-1})$ streak eigenmode, sinusoidal in x, sustains the rolls.

To formalize these scaling presumptions we begin with the postulate that lower branch traveling wave states correspond to the following naive asymptotic scaling for each of the Cartesian velocity components and the pressure:

$$\begin{aligned} u &= u_0 + R^{-1} u_1 e^{i\theta} + R^{-2} u_2 e^{2i\theta} + c.c. + \cdots \\ v &= R^{-1} v_0 + R^{-1} v_1 e^{i\theta} + R^{-2} v_2 e^{2i\theta} + c.c. + \cdots \\ w &= R^{-1} w_0 + R^{-1} w_1 e^{i\theta} + R^{-2} w_2 e^{2i\theta} + c.c. + \cdots \\ p &= R^{-2} p_0 + R^{-1} p_1 e^{i\theta} + R^{-2} p_2 e^{2i\theta} + c.c. + \cdots \end{aligned} \tag{7}$$

where $\theta = \alpha(x - ct)$, $c = c(\alpha, R)$ is a real phase velocity and $c.c.$ stands for complex conjugate. Every modal amplitude function, e.g. $u_0 = u_0(y, z; \alpha, R)$ is a 2D function of both y and z. The streamwise wavenumber α and the Reynolds number R are the controlling parameters.

This asymptotic *ansatz* is very similar to that postulated by Benney (1984). Benney's original formulation was for time-dependent inviscid flow with an amplitude parameter ϵ in lieu of R^{-1} and long time and space modulations, $T = \epsilon t$, $X = \epsilon x$. Benney and Chow (1989) later re-introduced the Reynolds number, which requires the semi-implicit assumption that $\epsilon = O(R^{-1})$.

Substituting expansion (7) into the Navier–Stokes equations leads to the following coupled equations at lowest order:

Streaky flow

$$\nabla^2 u_0 = v_0 \frac{\partial u_0}{\partial y} + w_0 \frac{\partial u_0}{\partial z} \quad + \; F_0, \tag{8}$$

First x-harmonic

$$\begin{aligned} (u_0 - c)\frac{\partial \boldsymbol{v}_1}{\partial x} + (\boldsymbol{v}_1 \cdot \nabla u_0)\hat{\boldsymbol{x}} &= -\nabla\left(p_1 e^{i\theta}\right), \\ \nabla \cdot \boldsymbol{v}_1 &= 0, \end{aligned} \tag{9}$$

Streamwise rolls

$$\begin{aligned} \nabla^4 \Psi_0 = J(\nabla^2 \Psi_0, \Psi_0) \quad + \\ 2\frac{\partial^2}{\partial y \partial z}\left(v_1 v_1^* - w_1 w_1^*\right) + \left(\frac{\partial^2}{\partial z^2} - \frac{\partial^2}{\partial y^2}\right)\left(v_1 w_1^* + v_1^* w_1\right), \end{aligned} \tag{10}$$

where $\Psi_0(y, z)$ is the streamfunction for the streamwise rolls $(0, v_0, w_0)$ with

$$v_0(y, z) = \frac{\partial \Psi_0}{\partial z}, \quad w_0(y, z) = -\frac{\partial \Psi_0}{\partial y}, \tag{11}$$

$J(A, B) = \partial A/\partial y \;\; \partial B/\partial z - \partial A/\partial z \;\; \partial B/\partial y$ is the usual Jacobian and $\boldsymbol{v}_1 = e^{i\theta}(u_1\hat{\boldsymbol{x}} + v_1\hat{\boldsymbol{y}} + w_1\hat{\boldsymbol{z}})$ is the first harmonic with $\hat{\boldsymbol{x}}$, $\hat{\boldsymbol{y}}$ and $\hat{\boldsymbol{z}}$ the unit vectors in the respective coordinate directions. The streaky flow equation (8) contains the non-dimensionalized driving pressure gradient F_0. For channel (plane Poiseuille) flow, $F_0 = -2$ with $-1 \le y \le 1$ and $u_0(\pm 1, z) = 0$, while $F_0 = 0$ with $u_0(\pm 1, z) = \pm 1$ for plane Couette. Equations (8), (9), (10) are the equations for the lowest order terms in a Reynolds number expansion of the modal amplitudes, e.g. for the u_{00} term in the expansion

$$u_0(y, z; \alpha, R) = u_{00}(y, z; \alpha) + \frac{1}{R} u_{01}(y, z; \alpha) + \cdots \tag{12}$$

but we write u_0 for brevity. The lowest order problem consists of three coupled two-dimensional (y and z) problems (8), (9), (10).

The lowest order contribution to the 2nd harmonic would arise at order R^{-2}

$$\begin{aligned}(u_0 - c)\frac{\partial \boldsymbol{v}_2}{\partial x} + (\boldsymbol{v}_2 \cdot \nabla u_0)\hat{\boldsymbol{x}} &= -\nabla\left(p_2 e^{i2\theta}\right) - \nabla \cdot (\boldsymbol{v}_1 \boldsymbol{v}_1) \\ \nabla \cdot \boldsymbol{v}_2 &= 0\end{aligned} \tag{13}$$

where $\boldsymbol{v}_2 = e^{i2\theta}(u_2\hat{\boldsymbol{x}} + v_2\hat{\boldsymbol{y}} + w_2\hat{\boldsymbol{z}})$ is the 2nd harmonic.

Equations (8), (9), (10) are the Navier–Stokes equivalent of the asymptotic balance (4) for the lower branch of the 4th order model. Equation (8) corresponds to the first two equations of that model, and to the advective redistribution of the streamwise velocity by streamwise rolls to induce an essential spanwise modulation. Equation (10) directly corresponds to the 3rd equation in (4), with the streamwise rolls maintained by the quadratic self-interaction of the streak eigenmode. Equations (9) correspond to the linearized equations – if $u_0(y, z)$ was fixed – for the stability of the 2D streaky flow $u_0(y, z)$ to a 3D perturbation, $\boldsymbol{v}_1$, sinusoidal in x. Since we demand that c be real, these equations correspond to the *marginal* inviscid stability of a pure streaky flow, just as the 4th equation of (4). Note that equations (8) and (10) are viscously balanced (formally corresponding to $R = 1$ in fact), while Equation (9) is inviscid, with $\boldsymbol{v}_1$ corresponding to a marginally stable mode, and requires only inviscid boundary conditions. In a wall-bounded domain, this suggests that viscous boundary layers of $O(R^{-1/2})$ will be required to satisfy the no-slip boundary conditions. There is also the possibility that a *critical layer* will arise from the

$$u_0(y, z) - c = 0 \tag{14}$$

singularity in the 1st harmonic equation (9). In two dimensions, linear critical layers scale like $R^{-1/3}$ while nonlinear critical layers scale like $\epsilon^{1/2}$ where ϵ is a measure of the disturbance amplitude (e.g. Maslowe, 1986). These scalings are for small 2D perturbation of the 1D laminar shear flow. In our case, our critical layer $u_0(y, z) - c = 0$ would be a warped surface, our perturbation is 3D and its amplitude is directly tied to the Reynolds number as $\epsilon = R^{-1}$. Nonetheless, by analogy with 2D critical layers we can expect a warped critical layer of thickness δ with

$$\epsilon^{1/2} = R^{-1/2} \lesssim \delta \lesssim R^{-1/3}. \tag{15}$$

Such critical and boundary layers seriously complicate the expansion, both theoretically and computationally. Looking at the right-hand side of the 2nd harmonic equation (13), the nonlinear forcing term arising from the the 1st harmonic, $\nabla \cdot (\boldsymbol{v}_1 \boldsymbol{v}_1)$, could contribute at order $R^{-5/3}$ or $R^{-3/2}$ instead of R^{-2} as postulated. This is because if the first harmonic has amplitude of order R^{-1}, then its nonlinear self-interaction term, $\boldsymbol{v}_1 \boldsymbol{v}_1$, would indeed be of order R^{-2}, but if a critical layer of thickness δ is present, then the nonlinear forcing term $\nabla \cdot (\boldsymbol{v}_1 \boldsymbol{v}_1)$ could generate a 2nd harmonic of order $\delta^{-1}R^{-2}$. For δ as in (15) this gives 2nd harmonic amplitudes between $R^{-5/3}$ and $R^{-3/2}$.

4. NUMERICAL CONTINUATION OF LOWER BRANCH STATES

Here we present fully-resolved numerical solutions of the Navier–Stokes equations that consist of lower branch 'exact coherent structures' in plane Couette flow with no-slip boundary conditions. These particular solutions have $c = 0$ by symmetry in a Galilean frame such that the average flow velocity is zero. These solutions were obtained in two ways, (1) by homotopy from free-slip to no-slip solutions (Waleffe, 2003), the free-slip solutions having been obtained using the bifurcation from streaky flow approach (Waleffe, 1998), and (2) by direct bifurcation from a streaky flow in the no-slip case. These no-slip solutions belong to the same family as the solutions originally obtained by Nagata (1990) by continuation of wavy Taylor vortices solutions in rotating plane Couette flow.

4.1 Bifurcation from streaky flow in no-slip plane Couette

For the SSP approach of tracking solutions that bifurcate from a streaky flow, we begin by adding an artificial forcing of the streamwise rolls to the Navier–Stokes equations. The forcing is chosen to correspond to the slowest decaying linear streamwise rolls appropriate to the shear layer. In the no-slip plane Couette case, these correspond to x-independent vertical velocity of the form

$$V(y,z) = \frac{F_r}{R}\frac{\hat{v}(y)}{\hat{v}_m}\cos\gamma z = \frac{1}{R}\frac{\partial\Psi_0}{\partial z} \tag{16}$$

with

$$\hat{v}(y) = \frac{\cos\beta y}{\cos\beta} - \frac{\cosh\gamma y}{\cosh\gamma} \tag{17}$$

where $\hat{v}_m = \max_y\left[\hat{v}(y)\right]$ and β is the smallest positive solution of $\beta\tan\beta + \gamma\tanh\gamma = 0$. For $\gamma = 5/3$, $\beta \approx 2.604189715$. The functions (17) solve the Stokes eigenvalue problem $(D^2-\gamma^2)^2\hat{v} = \lambda(D^2-\gamma^2)\hat{v}$, with $\hat{v} = D\hat{v} = 0$ at $y = \pm 1$, where $D = d/dy$. The streamwise rolls are normalized so that $\max V(y,z) = F_r/R$ where R is the Reynolds number and F_r is an $O(1)$ forcing parameter. These are the same streamwise rolls as used in Waleffe (1997). The free-slip rolls used in Waleffe (1998) have the same form and scaling except that $\hat{v}(y) = \cos\pi y/2$ in that case.

In that formulation, the initial roll forcing must balance the viscous term in the streamwise rolls equation (10). For $v = V(y,z)$ as in (16)

$$\nabla^4\Psi_0(y,z) = F_r\,\frac{(\beta^2+\gamma^2)^2}{\hat{v}_m}\frac{\cos\beta y}{\cos\beta}\,\frac{\sin\gamma z}{\gamma}, \tag{18}$$

and we therefore add the right-hand side of this equation as a forcing term to the RHS of the streamwise rolls equation (10) (the R^{-2} scaling of the forcing term

is implicit in that equation). In the free-slip case, the Jacobian $J(\nabla^2\Psi_0, \Psi_0)$, corresponding to the nonlinear self-advection of the zeroth harmonic in (10) vanishes identically. That nonlinear term does not vanish in the no-slip case with the forcing (18), however it is small and has little effect. In the no-slip case, that forcing generate rolls that are only approximately described by (16). This is of no consequence, since the forcing is merely an educated guess for the streamwise rolls.

The roll forcing sustains weak streamwise rolls that redistribute the streamwise velocity and the base state now consists of a two-dimensional, three-component "streaky flow" $[u_0(y, z), R^{-1}v_0(y, z), R^{-1}w_0(y, z)]$ instead of the one-dimensional, one-component laminar flow $[U(y), 0, 0]$. That streaky flow is linearly unstable and we can track the bifurcating solution from the marginal stability point. The bifurcation is subcritical in term of the roll-forcing parameter, confirming that the first-harmonic nonlinear self-interaction terms on the RHS of (10) positively feedback on the rolls and take over the role of the artificial roll forcing. For that continuation of 3D solutions from the bifurcation point of the streaky flow, F_r is a dependent variable that must be computed and we select

$$A_x = \Re\langle \eta e^{-i\alpha x}\rangle \tag{19}$$

as the new control parameter where $\langle\cdot\rangle$ denotes an average over the domain and $\Re$ denotes real part. Hence, A_x is the y-average of the $(\alpha, 0)$ Fourier component of the y-vorticity η. That control parameter is chosen because it is a key component of the sinusoidal streak instability mode. Figure 2 shows the resulting bifurcation diagrams for several (α, γ) and R. The key objective is to obtain a 3D self-sustained solution at $F_r = 0$. Once a solution has been obtained, it can be continued in the self-sustained parameter space (α, γ, R) with $F_r = 0$. Details of the mathematical and numerical formulation can be found in Waleffe (2003) and the resolution parameters quoted below correspond to the numerical parameters $[L_T, M_T, N_T]$ in that reference.

4.2 Continuation of lower branch solutions to high R

We pick the fundamental wavenumbers $\alpha = 1.14$ and $\gamma = 2.505$, corresponding to spatial periods $L_x = 2\pi/\alpha$ and $L_z = 2\pi/\gamma$. These parameter values follow from our earlier studies of the SSP and exact coherent states in plane Couette flow. The value $\gamma = 5/3 \approx 1.67$ was selected and $\alpha \approx 1.14$ obtained by "annealing" studies of plane Couette turbulence in Hamilton et al. (1995) that confirmed the validity of the SSP and suggested the existence of a time-periodic solution for those parameter values at $R = 400$ extracted in Kawahara and Kida (2001). A continuation study of 3D steady states in Waleffe (2002) found that these states exist only for $\alpha \lesssim 1.08$ when $\gamma = 1.67$ and for $1.7 \lesssim \gamma$ when $\alpha = 1.14$, at small Reynolds numbers $\lesssim 400$. In

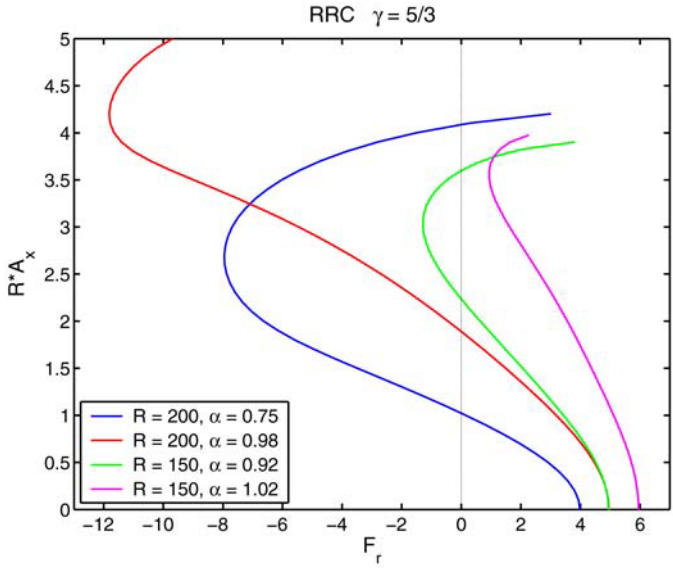

Figure 2. Bifurcation diagrams for no-slip streaky plane Couette flow with $\gamma = 1.67$ (resolution [9,21,9]). Vertical axis is A_x defined in (19) multiplied by R.

particular, 3D steady states were found to exist at $R = 400$ when $\alpha = 1.14$ for $\gamma = 1.5 \times 1.67 = 2.505$ and $\gamma = 2 \times 1.67 = 3.34$. The latter corresponds to the 2nd z-harmonic in a box of fundamental spanwise wavenumber $\gamma = 1.67$, while the former is intermediate between the fundamental and the 2nd harmonic. We selected $\alpha = 1.14$ and $\gamma = 2.505$ for our initial lower branch continuation to large Reynolds numbers but have also considered other parameter values such as $(\alpha, \gamma) = (1.14, 2.5)$, $(1.39, 2.5)$ and $(1, 2)$, all with similar results.

Figure 3 visualizes the typical structure of the lower branch steady state at high R. The streaks (visualized by the green isosurface of total streamwise velocity u) appear completely straight, i.e. x-independent. The red isosurfaces correspond to $Q = 0.6 \max(Q) = 3.46\,10^{-4}$ where $Q = \nabla^2 p/2$ is the 2nd invariant of the velocity gradient tensor. Note that although the red Q-isosurfaces are prominent in the figure, they correspond to very low values of max Q, consistent with the presumption that rolls and streak undulation are of $O(R^{-1})$. The yellow isosurface is $u = 0$ and this correspond to the critical surface $u_0(y, z) - c = 0$, since $c = 0$ by symmetry for these plane Couette flow steady states and $u \approx u_0(y, z)$. It is remarkable how the Q isosurface straddles that $u = 0$ surface, suggesting that it is indeed a critical layer.

Figure 4 shows the mean velocity profile (i.e. the x and z average streamwise velocity) for the lower branch steady states for $(\alpha, \gamma) = (1.14, 2.505)$ at $R =$

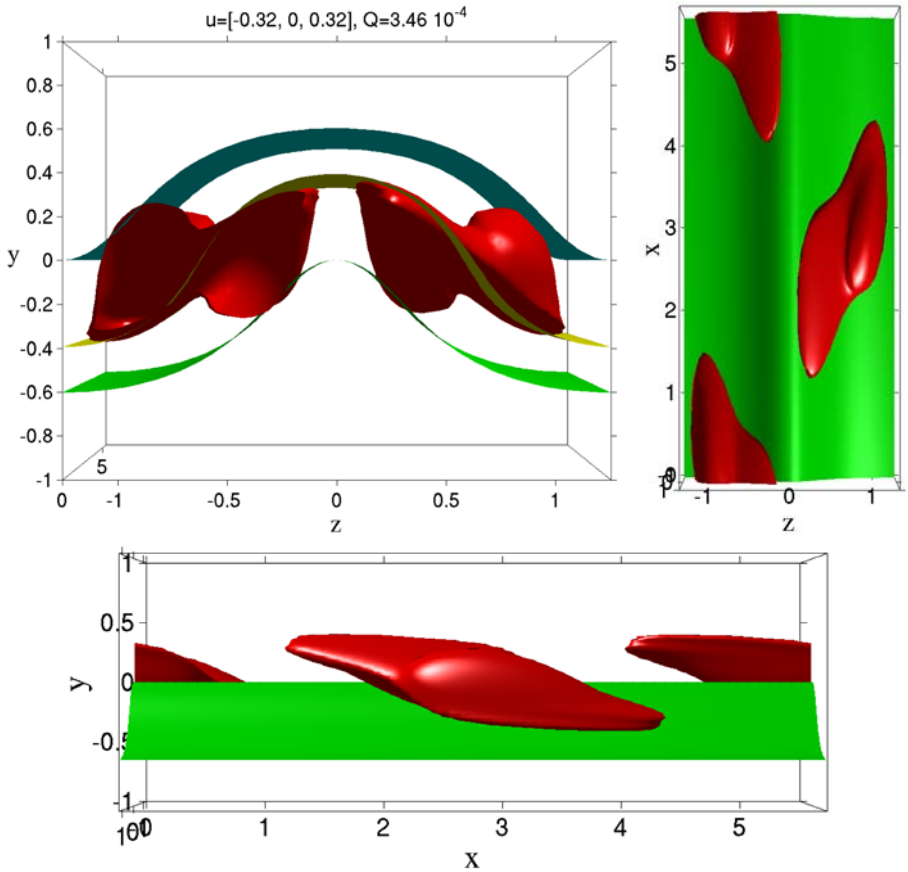

Figure 3. Isosurfaces $u = -0.32$ (green), 0 (yellow), 0.32 (cyan) and $Q = \nabla^2 p/2 = 0.6\max(Q) = 3.46 \times 10^{-4}$ (red) for $(\alpha, \gamma, R) = (1.14, 2.505, 6196)$, resolution [9, 75, 21]. Clockwise: Front, top and side views. Top and side show Q and $u = -0.32$ only.

400, 897 and 7050. Although the higher R profiles are closer to laminar they do not seem to tend to the laminar flow as $R \to \infty$, in fact the profiles are very weakly dependent on R, which is why we jump from $R = 897$ to 7050 in the figures. The mean profiles for $(\alpha, \gamma) = (1, 2)$ at $R = 400$, 867 and 7014 are also shown.

Figure 5 shows the x-averaged, z-rms velocity fluctuation profiles, i.e. the rms of the streaks, defined as the x-averaged streamwise velocity minus the mean velocity, and of the streamwise rolls. The latter are scaled by a factor of R. Those profiles show that the streaks appear to be converging to an $O(1)$ profile, while the rolls scale like R^{-1}. The z-rms velocity profiles for the 1st harmonic, scaled by R, are shown in Figure 6. These R-compensated profiles appear to show convergence, confirming the R^{-1} scaling of the first harmonic.

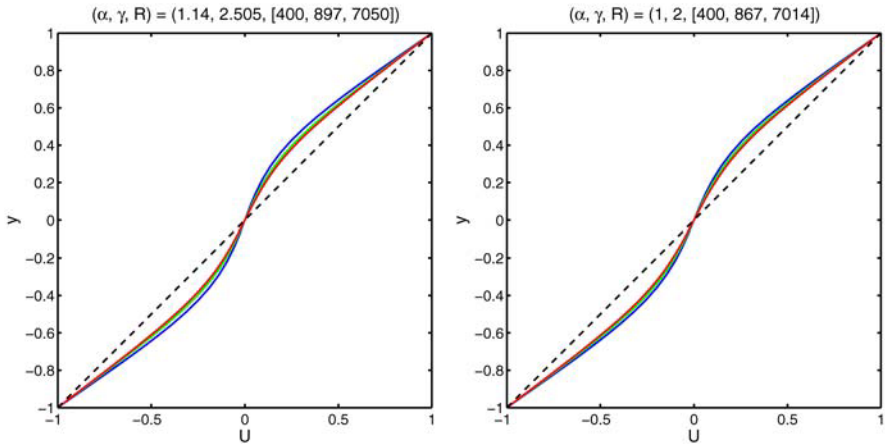

Figure 4. Mean velocity profiles for lower branch steady states in no-slip plane Couette. Left: $(\alpha, \gamma) = (1.14, 2.505)$ for $R = 400, 897, 7050$ (higher R closer but not converging to laminar), resolution [13, 27, 13], [9, 45, 17] and [9, 75, 21], respectively. Right: $(\alpha, \gamma) = (1, 2)$ for $R = 400, 867, 7014$.

Although, there are signs of boundary layers near the walls in the u_1 and w_1 profiles, the most dramatic feature is the rapid rise of the profiles away from the walls near $y = \pm 0.4$. This roughly corresponds to the extreme y-locations of the critical surface $u_0(y, z) - c = 0$ show in Figure 3. That critical surface is very weakly dependent on the Reynolds number R as confirmed by the mean and rms-streak profiles in Figures 4 and 5. This critical layer interpretation is confirmed by the rms profiles of the 2nd harmonic shown in Figure 7. Those profiles are scaled by $R^{3/2}$ and appear to be converging. The most dramatic feature is that they are close to zero near the walls but then shoot up abruptly near $y = \pm 0.4$ again. This behavior, together with the apparent $R^{-3/2}$ scaling instead of the naive R^{-2}, strongly suggest that critical layer behavior is taking place. Log-log plot of the peak rms values for the streamwise rolls, the 1st, 2nd and 3rd harmonics are shown in Figure 8 together with a lin-lin plot of the peak rms streak amplitude. These plots provide a global visual confirmation that the rolls and the first harmonic scale like R^{-1}. The 2nd harmonic appears to scale like $R^{-3/2}$ and the 3rd like R^{-2}. This is in contrast to the R^{-2} and R^{-3}, respectively, in the naive expansion (7) and an indication that critical and/or boundary layers are occuring. The earlier figures suggest the key importance of the critical surface $u_0(y, z) - c = 0$. We have verified that $R^{-3/2}$ and R^{-2} are better fits than $R^{-5/3}$ and $R^{-7/3}$ for the 2nd and 3rd harmonic, respectively. The bottom plots in Figure 8 show the peak rms streak amplitude for $(\alpha, \gamma) = (1.14, 2.505)$, $(1.39, 2.5)$, $(1, 2)$ and strongly suggest convergence

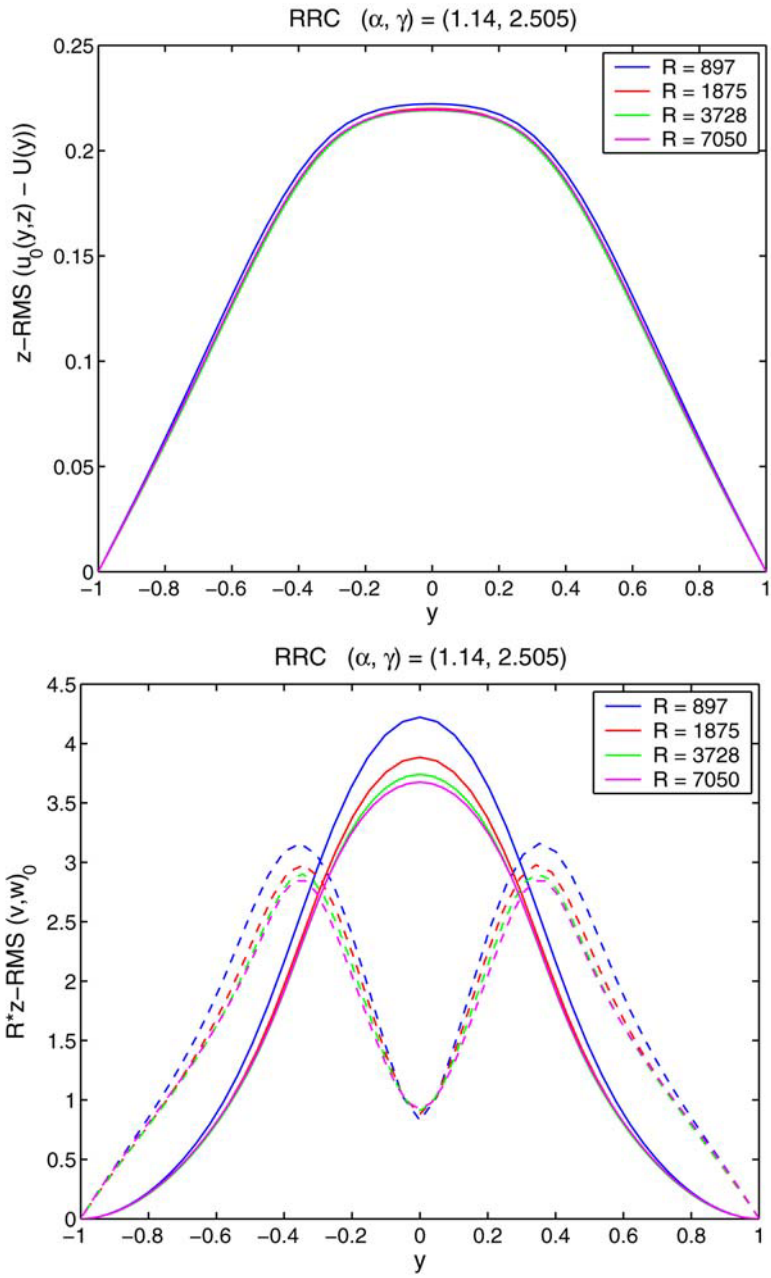

Figure 5. z-RMS of x-averaged velocity fluctuation profiles. Top: streaks $u_0(y, z) - \bar{u}(y)$. Bottom: rolls scaled by R, v_0 solid, w_0 dash. Peak rms values decrease with increasing R.

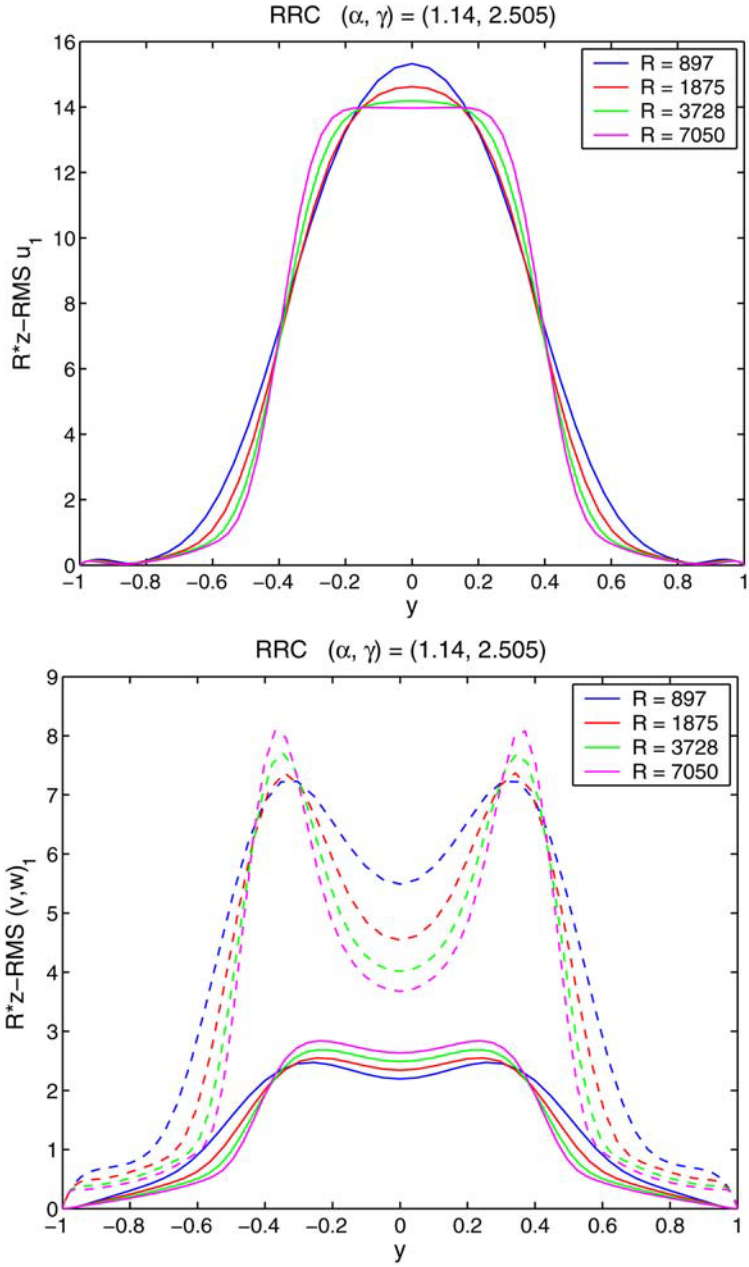

Figure 6. z-RMS velocity profiles scaled by R for the 1st harmonic $\boldsymbol{v}_1$. Top: streamwise velocity $u_1(y, z)$. Bottom: v_1 solid, w_1 dash. Peak scaled rms decreases for u_1 but increases for v_1, w_1 as R increases.

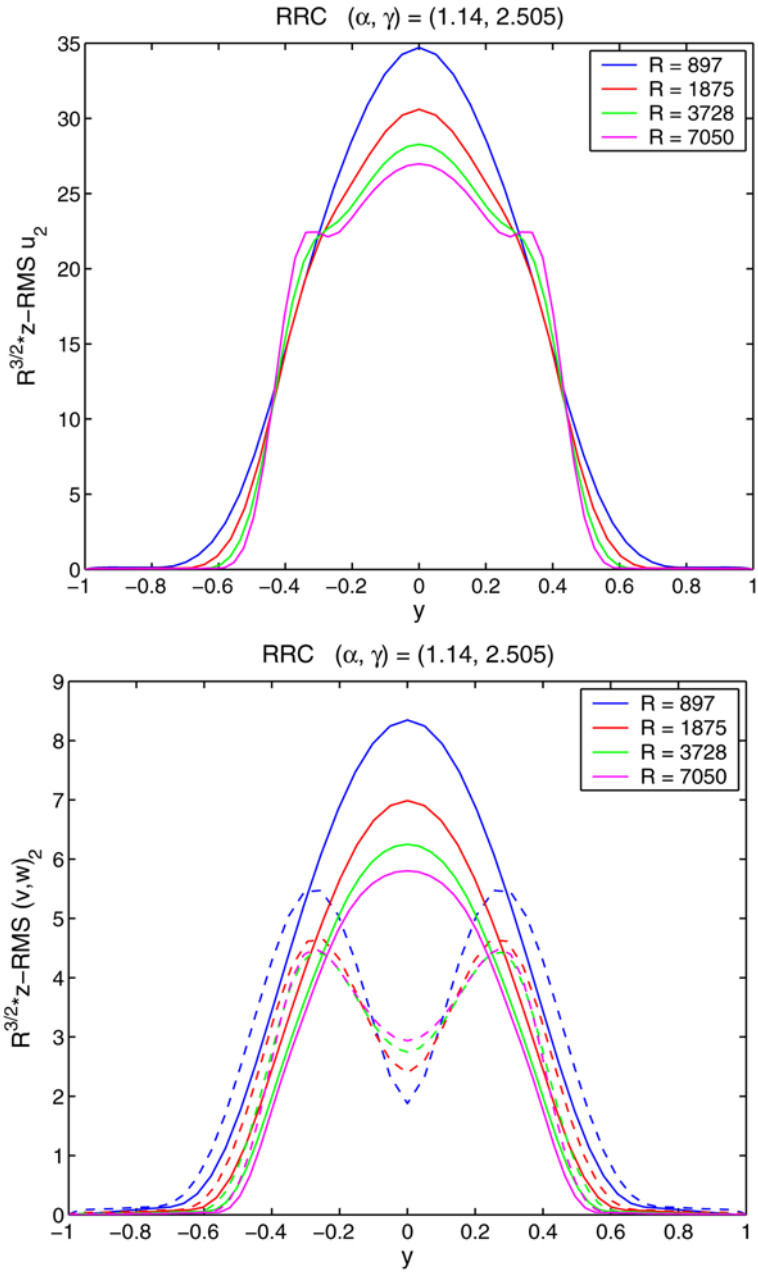

Figure 7. z-RMS velocity profiles scaled by $R^{3/2}$ for the 2nd harmonic $\boldsymbol{v}_2$. Top: $u_2(y, z)$. Bottom: v_2 solid, w_2 dash. Peak scaled rms decreases with increasing R for all three components.

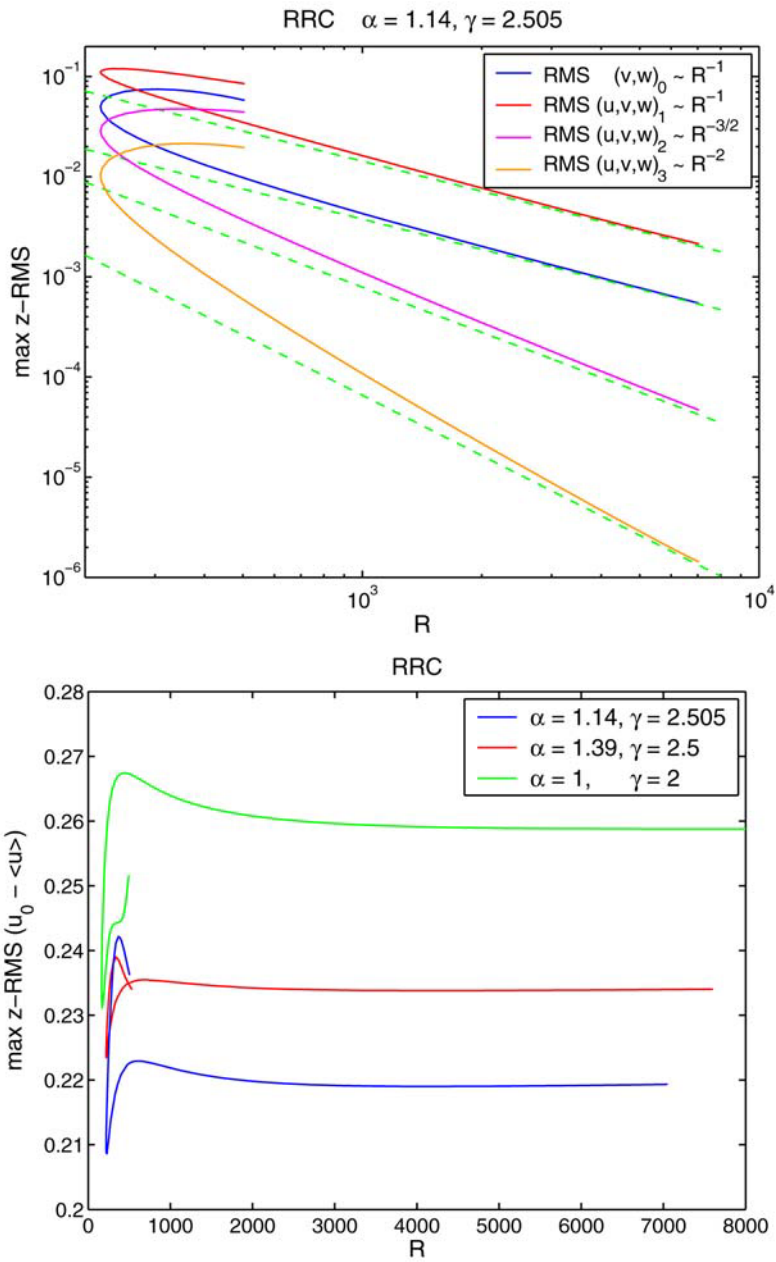

Figure 8. Peak z-rms velocity fluctuation profiles *vs.* R. Top: 1st harmonic, streamwise rolls, 2nd and 3rd harmonics (highest to lowest curve) for $(\alpha, \gamma) = (1.14, 2.505)$. Dashed lines: R^{-1} fits for $\boldsymbol{v}_1$ and rolls (v_0, w_0), $R^{-3/2}$ for $\boldsymbol{v}_2$ and R^{-2} for $\boldsymbol{v}_3$. Bottom: streaks $u_0(y, z) - \bar{u}(y)$ for $(\alpha, \gamma) = (1.14, 2.505)$ (lowest curve), (1.39,2.5) (middle), (1,2) (top curve). Composite of several resolutions, [9,75,21] for highest R.

to a finite value confirming that streaks remain $O(1)$ as $R \to \infty$. Other results for these other (α, γ) are similar to those reported here for (1.14, 2.505).

5. CONCLUSIONS

We have continued lower branch exact coherent structures in no-slip plane Couette flow to high Reynolds number, up to about 20 times higher than the Reynolds number ($\approx$ 320) where turbulence is first observed to occur. Our results support earlier presumptions that the lower branch coherent states have streaks of $O(1)$ supported by streamwise rolls and a streak eigenmode of $O(R^{-1})$. The numerical results show that the higher harmonics do not follow the naive scaling where the n-th harmonic would scale like R^{-n}. There is instead clear evidence for the importance of a critical layer determined by $u_0(y, z) - c = 0$ where $u_0(y, z)$ is the x-averaged streamwise velocity and c is the traveling velocity of the structure. This critical layer reduces the decay rate of the higher harmonics. The 2nd harmonic appears to decay like $R^{-3/2}$ and the 3rd harmonic like R^{-2}. Nonetheless, this suggests that the various harmonics separate as $R \to \infty$ and that the limiting state of the flow is given by a "mean flow-first harmonic theory" similar to that proposed by Benney (1984). In other words, the self-sustaining process (Figure 1) becomes exact for the lower branch states as $R \to \infty$. The flow retains an essential spanwise variation, sustained by ever weaker rolls and a single x-harmonic eigenmode of the streaky flow. The streaky flow never connects to the laminar flow, not even at infinity.

On the transition threshold question, we expect that all *lower branch* nontrivial states based on the self-sustaining process will have the same asymptotic scaling: $O(1)$ streaks supported by $O(R^{-1})$ rolls and streak eigenmode. This suggests that the best perturbations to trigger turbulence probably consist of channel size $O(R^{-1})$ streamwise rolls of streamwise extent of the order of a few channel sizes as well to trigger a first harmonic of the proper wavelength and strength (Figure 3). The relevant length scale ℓ is the full width in plane Couette, the half-width in plane Poiseuille and the radius in pipe flow, i.e. the width of the laminar shear layer. The jet perturbation used in Hof et al. (2003) precisely generates a disturbance of that form, i.e. a pair of counter-rotating vortices whose axes are aligned in the streamwise direction, provided the duration of the jet is at least of the order of the convective time scale ℓ/U. The SSP suggests that very short jets will not be very effective at triggering turbulence, since they would trigger α's that are too large and would not set up sufficiently long streaks. On the other hand, the SSP suggests there will be little sensitivity to the length of the pulse once it is longer than a few ℓ's, since sufficiently long rolls will have been excited leading to sufficiently long

naturally unstable streaks. This is entirely consistent with the results of Hof et al. (2003, fig. 3).

ACKNOWLEDGEMENTS

FW thanks Tom Mullin and Rich Kerswell for organizing the Bristol workshop and Julian Scott for discussions about critical layers at that workshop. This work was partially supported by the US NSF through grant DMS-0204636. FW thanks Beth Wingate, Susan Kurien and Bob Ecke for setting up an extended visit to Los Alamos National Laboratory where this article was written [LA-UR-04-8916].

NOTES

1. For transient growth, the essence of the WKB results can be obtained by considering the linear evolution of Kelvin modes, i.e. Fourier modes with time-dependent wavevectors, on an unbounded plane Couette flow.

2. Chapman assumes the predominance of nonlinear interactions between oblique streaks (rapidly oscillating in y) that would generate large scale streamwise rolls and between oblique streaks and streamwise streaks to sustain the oblique rolls (this is more clearly illustrated by his "toy model" (2.6)-(2.9) and his figures 19 and 20). This is an excitation of subharmonic-type where oblique modes with horizontal wavenumbers $(\pm\alpha, \gamma)$ would create a pair of streamwise rolls with spanwise wavenumber $(0, 2\gamma)$. In Chapman's oblique transition scenario, the oblique streaks are induced by velocity perturbations of $O(R^{-1})$ and $O(R^{-5/4})$, in Couette and Poiseuille flows, respectively, that rapidly oscillate in y on a $R^{-1/3}$ lengthscale. Such perturbations correspond to rather intricate initial perturbations with vorticity of $O(R^{-2/3})$ and $O(R^{-11/12})$, much larger than the corresponding vorticity perturbations for the streamwise vortex scenario.

3. Chapman's "toy model" does incorporate feedback but his formal asymptotic study merely estimates the size of streamwise streaks necessary to perturb the laminar flow eigenvalues at lowest order, assuming but not demonstrating that this would lead to streak instability. His entire analysis ignores the modification of the mean shear. His nonlinear system (3.6), (3.12) is not complete since it lacks the equation for the mean flow. As recalled in the introduction, the mean shear perturbation is of order $(\epsilon R)^2$ which is of order unity for $a = -1$ and these mean flow modifications play an important role in the streak instability, at least in plane Couette flow (as discussed in Waleffe, 1995a, 1995b, 1997; Reddy et al., 1998).

4. Chapman's Couette analysis focuses on streamwise rolls of amplitude $\epsilon \sim R^{-1}$, as in the SSP (Figure 1), but that implies an order 1 reduction of the mean shear that invalidates linear theory about the laminar flow. Chapman's Poiseuille analysis suggests that large scale streamwise rolls of $O(R^{-3/2})$ are the most efficient to lead to streak instability. That threshold corresponds to odd-in-y streamwise rolls, that do *not* correspond to the largest transient growth. Although instability of the resulting $O(R^{-1/2})$ streaks is plausible, it has not been shown that instability of such streaks would lead to some feedback able to trigger transition.

5. The 4th order model is derived for a sinusoidal shear flow $(\sin \pi y/2, 0, 0)$ maintained by a body force. $M(t)$ represents the amplitude of that shear flow, $U(t)$ is the amplitude of a pure streak mode of the form $(\cos \gamma z, 0, 0)$ whose z-average vanishes, $V(t)$ is the amplitude of a streamwise roll of the form $(0, \gamma \cos \beta y \cos \gamma z, \beta \sin \beta y \sin \gamma z)$ while $W(t)$ is the amplitude of a streak eigenmode sinusoidal in x, but whose minimum representation involves 5 Stokes modes (see Waleffe, 1997, eqns. 8, 9 and sect. III, C). In the context of Section 3 and Equations (8), (9) and (10), $M(t)$ would represent a measure of the mean shear (i.e. y-derivative of the x and z averaged streamwise velocity, $\overline{u}^{xz}$, which is identical to $\overline{u_0}^z$, the z-average of $u_0(y, z)$) in a neighborhood of the critical layer $u_0(y, z) - c = 0$ (not near the no-slip walls), $U(t)$ would represent the amplitude of the streaks (i.e. of $u_0(y, z) - \overline{u_0}^z$), $V(t)$ would represent the amplitude of the unscaled rolls (i.e. $R^{-1}\psi_0(y, z)$) and $W(t)$ the amplitude of the unscaled streak eigenmode $(R^{-1}\boldsymbol{v}_1(x, y, z) + c.c.)$.

6. Since the Navier–Stokes numerical results indicate the presence of a critical layer, it is interesting to note that the scaling of the lower branch fixed point in the 4th order model would not change even if the decay rate of W was order $R^{-1/3}$, typical of linear critical layers and shear-induced diffusion, instead of R^{-1}.

7. The lower branch coherent state is a saddle fixed point with many stable but a few unstable directions. Its 'stable' manifold is the set of all initial conditions that will end up at the fixed point in forward time, but that manifold is unstable in the sense that initial conditions near but not on the 'stable' manifold will move away from that manifold.

REFERENCES

Acarlar, M.S. and Smith, C.R. (1987). A study of hairpin vortices in a laminar boundary layer. *J. Fluid Mech.* **175**, 1–41 and 45–83.

Benney, D.J. (1984). The evolution of disturbances in shear flows at high reynolds numbers. *Stud. Appl. Math.* **70**, 1–19.

Benney, D.J. and Chow, K.A. (1989). A mean flow first harmonic theory for hydrodynamic instabilities. *Stud. Appl. Math.* **80**, 37–73.

Chapman, S.J. (2002). Subcritical transition in channel flows. *J. Fluid Mech.* **451**, 35–97.

Eckhardt, B. and Mersmann, A. (1999). Transition to turbulence in a shear flow. *Phys. Rev. E* **60**, 509–517.

Faisst, H. and Eckhardt, B. (2003). Traveling waves in pipe flow. *Phys. Rev. Lett.* **91**, 224502.

Hamilton, J., Kim, J. and Waleffe, F. (1995). Regeneration mechanisms of near-wall turbulence structures. *J. Fluid Mech.* **287**, 317–348.

Hof, B., Juel, A. and Mullin, T. (2003). Scaling of the turbulence transition threshold in a pipe. *Phys. Rev. Lett.* **91**, 244502.

Itano, T. and Toh, S. (2001). The dynamics of bursting process in wall turbulence. *J. Phys. Soc. Japan* **70**, 703–716.

Joseph, D.D. and Tao, L.N. (1963). Transverse velocity components in fully developed unsteady flows. *J. Appl. Mech.* **30**, 147–148.

Kawahara, G. and Kida, S. (2001). Periodic motion embedded in plane Couette turbulence: Regeneration cycle and burst. *J. Fluid Mech.* **449**, 291–300.

Kreiss, G., Lundbladh, A. and Henningson, D.S. (1994). Bounds for threshold amplitudes in subcritical shear flows. *J. Fluid Mech.* **270**, 175–198.

Maslowe, S.A. (1986). Critical layers in shear flows. *Ann. Rev. Fluid Mech.* **18**, 405–432.

Moehlis, J., Faisst, H. and Eckhardt, B. (2004). A low-dimensional model for turbulent shear flows. *New Journal of Physics* **6**, 56+17.

Nagata, M. (1990). Three-dimensional finite-amplitude solutions in plane Couette flow: Bifurcation from infinity. *J. Fluid Mech.* **217**, 519–527.

Reddy, S.C., Schmid, P.J., Baggett, J.S. and Henningson, D.S. (1998). On stability of streamwise streaks and transition thresholds in plane channel flows. *J. Fluid Mech.* **365**, 269–303.

Trefethen, N., Trefethen, A.E., Reddy, S.C. and Driscoll, T.A. (1993). Hydrodynamic stability without eigenvalues. *Science* **261**, 578–584.

Waleffe, F. (1990). Proposal for a self-sustaining process in shear flows. Working paper, available at http://www.math.wisc.edu/∼waleffe/ECS/sspctr90.pdf.

Waleffe, F. (1995a). Hydrodynamic stability and turbulence: Beyond transients to a self-sustaining process. *Stud. Applied Math.* **95**, 319–343.

Waleffe, F. (1995b). Transition in shear flows: Nonlinear normality versus non-normal linearity. *Phys. Fluids* **7**, 3060–3066.

Waleffe, F. (1997). On a self-sustaining process in shear flows. *Phys. Fluids* **9**, 883–900.

Waleffe, F. (1998). Three-dimensional coherent states in plane shear flows. *Phys. Rev. Lett.* **81**, 4140–4148.

Waleffe, F. (2001). Exact coherent structures in channel flow. *J. Fluid Mech.* **435**, 93–102.

Waleffe, F. (2002). Exact coherent structures and their instabilities: Toward a dynamical-system theory of shear turbulence. In *Proceedings of the International Symposium on Dynamics and Statistics of Coherent Structures in Turbulence: Roles of Elementary Vortices*, S. Kida (ed.), National Center of Sciences, Tokyo, Japan, pp. 115–128.

Waleffe, F. (2003). Homotopy of exact coherent structures in plane shear flows. *Phys. Fluids* **15**, 1517–1543.

Waleffe, F., Kim, J. and Hamilton, J. (1993). On the origin of streaks in turbulent shear flows. In *Turbulent Shear Flows 8: Selected Papers from the Eighth International Symposium on Turbulent Shear Flows*, Munich, Germany, September 9–11, 1991, F. Durst, R. Friedrich, B.E. Launder, F.W. Schmidt, U. Schumann and J.H. Whitelaw (eds), Springer-Verlag, Berlin, pp. 37–49.

Wedin, H. and Kerswell, R.R. (2004). Exact coherent structures in pipe flow. *J. Fluid Mech.* **508**, 333–371.

TURBULENT-LAMINAR PATTERNS IN PLANE COUETTE FLOW

Dwight Barkley[1] and Laurette S. Tuckerman[2]
[1]*Mathematics Institute, University of Warwick, Coventry CV4 7AL, UK*
[2]*LIMSI-CNRS, BP 133, 91403 Orsay, France*
barkley@maths.warwick.ac.uk, www.maths.warwick.ac.uk/∼barkley;
laurette@limsi.fr, www.limsi.fr/Individu/laurette

Abstract Regular patterns of turbulent and laminar fluid motion arise in plane Couette flow near the lowest Reynolds number for which turbulence can be sustained. We study these patterns using an extension of the minimal flow unit approach to simulations of channel flows pioneered by Jiménez and Moin. In our case computational domains are of minimal size in only two directions. The third direction is taken to be large. Furthermore, the long direction can be tilted at any prescribed angle to the streamwise direction. We report on different patterned states observed as a function of Reynolds number, imposed tilt, and length of the long direction. We compare our findings to observations in large aspect-ratio experiments.

1. INTRODUCTION

In this chapter we consider plane Couette flow – the flow between two infinite parallel plates moving in opposite directions. This flow is characterized by a single non-dimensional parameter, the Reynolds number, defined as $Re = hU/\nu$, where $2h$ is the gap between the plates, U is the speed of the plates and ν is the kinematic viscosity of the fluid (see Figure 1). For all values of Re, laminar Couette flow $\mathbf{u_C} \equiv y\hat{\mathbf{x}}$ is a solution of the incompressible Navier–Stokes equations satisfying no-slip boundary conditions at the moving plates. This solution is linearly stable at all values of Re. Nevertheless it is not unique. In particular, for Re greater than approximately 325 (Dauchot and Daviaud, 1995), turbulent states are found in experiments and numerical simulations. Our interest is in the flow states found as one decreases Re from developed turbulent flows to the lowest limit for which turbulence exists.

Our work is motivated by the experimental studies of Prigent and coworkers (2001, 2002, 2003, 2005) on flow in a very large aspect-ratio plane Couette apparatus. Near the minimum Re for which turbulence is sustained, they find

T. Mullin and R.R. Kerswell (eds), Laminar Turbulent Transition and Finite Amplitude Solutions, 107–127.
© 2005 *Springer. Printed in the Netherlands.*

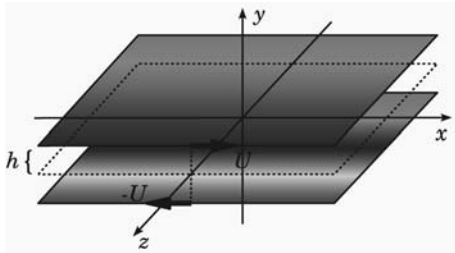

Figure 1. Plane Couette geometry. Plates separated by a gap $2h$ move at speeds $\pm U$. The coordinate system we use is as shown, with $y = 0$ corresponding to midgap.

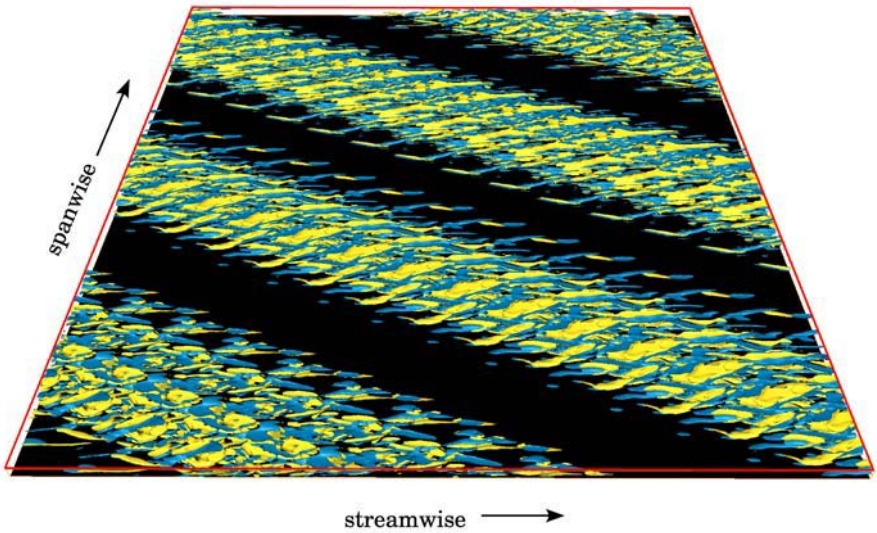

Figure 2. Turbulent-laminar pattern at Reynolds number 350. Isosurfaces of streamwise vorticity ($\omega = \pm 0.5$) are shown at one instant in time. For clarity the bottom plate is shown in black while the top plate is transparent. The streamwise and spanwise extent of the region shown are 60 times the plate separation $2h$.

remarkable, essentially steady, spatially-periodic patterns of turbulent and laminar flow. These patterns emerge spontaneously from featureless turbulence as the Reynolds number is decreased. Figure 2 shows such a pattern from numerical computations presented in this chapter. Two very striking features of these patterns are their large wavelength, compared with the gap between the plates, and the fact that the patterns form at an angle to the streamwise direction.

Fluid flows exhibiting coexisting turbulent and laminar regions have a significant history in fluid dynamics. In the mid 1960s a state known as spiral turbulence was first discovered (Coles, 1965; van Atta, 1966; Coles and van Atta, 1966) in counter-rotating Taylor–Couette flow. This state consists of a

turbulent and a laminar region, each with a spiral shape. The experiments of Prigent et al. (2001, 2002, 2003, 2005) in a very large aspect-ratio Taylor–Couette system showed that in fact the turbulent and laminar regions form a periodic pattern, of which the original observations of Coles and van Atta comprised only one wavelength. Cros and Le Gal (2002) discovered large-scale turbulent spirals as well, in the shear flow between a stationary and a rotating disk. When converted to comparable quantities, the Reynolds-number thresholds, wavelengths, and angles are very similar for all of these turbulent patterned flows.

2. METHODS

Our computational technique (Barkley and Tuckerman, 2005) extends the minimal flow unit methodology pioneered by Jiménez and Moin (1991) and by Hamilton et al. (1995) and so we begin by recalling this approach. Turbulence near transition in plane Couette and other channel flows is characterized by the cyclical generation and breakdown of streaks by streamwise-oriented vortices. The natural streak spacing in the spanwise direction is about 4–5h. In the minimal flow unit approach, the smallest laterally periodic domain is sought that can sustain this basic turbulent cycle. For plane Couette flow at $Re = 400$, Hamilton et al. (1995) determined this to be approximately $(L_x, L_y, L_z) = (4h, 2h, 6h)$. This domain is called the minimal flow unit (MFU). The fundamental role of the streaks and streamwise vortices is manifested by the fact that the spanwise length of the MFU is near the natural spanwise streak spacing. Figure 3(a) shows the MFU in streamwise-spanwise coordinates.

We extend the MFU computations in two ways. First we tilt the simulation domain in the lateral plane at angle θ to the streamwise direction [Figure 3(b)]. We use x' and z' for the tilted coordinates. We impose periodic lateral boundary conditions on the tilted domain. To respect the spanwise streak spacing while imposing periodic boundary conditions in x', the domain satisfies $L_{x'} \sin\theta \simeq 4h$ for $\theta > 0$. (For $\theta = 0$, we require $L_{x'} \gtrsim 6h$.) Secondly, we greatly extend one of the dimensions, $L_{z'}$, past the MFU requirement [Figure 3(c)], in practice between 30h and 220h, usually 120h.

This approach presents two important advantages, one numerical and the other physical. First, it greatly reduces the computational expense of simulating large length-scale turbulent-laminar flows. Our tilted domains need only be long perpendicular to the turbulent bands. In the direction in which the pattern is homogeneous, the domains are of minimal size, just large enough to capture the streamwise vortices typical of shear turbulence. Second, the approach allows us to impose or restrict the pattern orientation and wavelength. We can

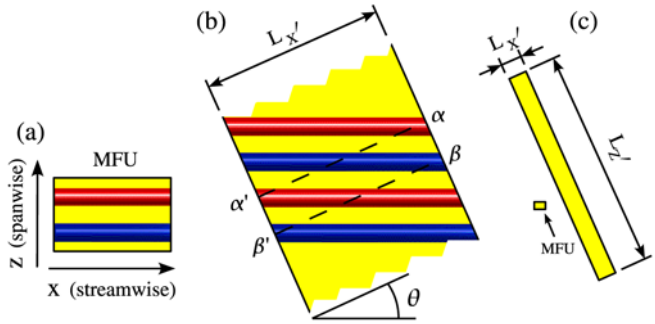

Figure 3. Simulation domains. The wall-normal direction y is not seen; $L_y = 2h$. The bars represent streamwise vortex pairs with a spanwise spacing of $4h$. (The vortices are schematic; these are dynamic features of the actual flow.) (a) MFU domain of size $6h \times 4h$. (b) Central portion of a domain [on the same scale as (a)] tilted to the streamwise direction. α, α' and β, β' are pairs of points identified under periodic boundary conditions in x'. (c) Full tilted domain with $L_{x'} = 10h$, $L_{z'} = 120h$, $\theta = 24°$. On this scale the MFU domain, shown for comparison, is small.

thereby investigate these features and establish minimal conditions necessary to produce these large-scale patterns.

We now present some further details of our simulations. We consider the incompressible Navier–Stokes equations written in the primed coordinate systems. After nondimensionalizing by the plate speed U and the half gap h, these equations become

$$\frac{\partial \mathbf{u}'}{\partial t} + (\mathbf{u}' \cdot \nabla')\mathbf{u}' = -\nabla' p' + \frac{1}{Re}\nabla'^2 \mathbf{u}' \quad \text{in } \Omega, \tag{1a}$$

$$\nabla' \cdot \mathbf{u}' = 0 \quad \text{in } \Omega, \tag{1b}$$

where $\mathbf{u}'(\mathbf{x}', t)$ is the velocity field and $p'(\mathbf{x}', t)$ is the static pressure in the primed coordinate system, and ∇' is used to indicate that derivatives are taken with respect to primed coordinates. Ω is the computational domain. In these coordinates, the no-slip and periodic boundary conditions are

$$\mathbf{u}'(x', y = \pm 1, z') = \pm(\cos\theta, 0, \sin\theta) \tag{2a}$$

$$\mathbf{u}'(x' + L_{x'}, y, z') = \mathbf{u}'(x', y, z') \tag{2b}$$

$$\mathbf{u}'(x', y, z' + L_{z'}) = \mathbf{u}'(x', y, z') \tag{2c}$$

The equations are simulated using the spectral-element (x'-y) – Fourier (z') code `Prism` (Henderson and Karniadakis, 1995). We use a spatial resolution consistent with previous studies (Hamilton et al., 1995; Waleffe, 2003; Waleffe and Wang, 2005). Specifically, for a domain with dimensions $L_{x'}$ and $L_y = 2$, we use a computational grid with close to $L_{x'}$ elements in the x' direction and

5 elements in the y direction. Within each element, we usually use 6th order polynomial expansions for the primitive variables. Figure 4 shows a spectral element mesh used for the case of $L_{x'} = 10$. In the z' direction, a Fourier representation is used and the code is parallelized over the Fourier modes. Our typical domain has $L_{z'} = 120$, which we discretize with 1024 Fourier modes or gridpoints. Thus the total spatial resolution we use for the $L_{x'} \times L_y \times L_{z'} = 10 \times 2 \times 120$ domain can be expressed as $N_{x'} \times N_y \times N_{z'} = 61 \times 31 \times 1024$.

We shall always use (x, y, z) for the original streamwise, cross-channel, spanwise coordinates (Figure 1). We obtain usual streamwise, and spanwise components of velocity and vorticity using $u = u' \cos\theta + w' \sin\theta$ and $w = u' \sin\theta - w' \cos\theta$, and similarly for vorticity. The kinetic energy reported is the difference between the velocity $\mathbf{u}$ and simple Couette flow $\mathbf{u_C}$, i.e. $E = \frac{1}{2}((u - u_C)^2 + v^2 + w^2)$.

We have verified the accuracy of our simulations in small domains by comparing to prior simulations (Hamilton et al., 1995). In large domains we have examined mean velocities, Reynolds stresses, and correlations in a turbulent-laminar flow at $Re = 350$ and find that these reproduce experimental results from Taylor–Couette (Coles and van Atta, 1966) and plane Couette (Hegseth, 1996) flow. While neither experimental study corresponds exactly to our case, the agreement supports our claim that our simulations correctly capture turbulent-laminar states.

The procedure we use to initiate turbulence is inspired by previous investigations of plane Couette flow in a perturbed geometry. We recall that laminar plane Couette flow is linearly stable at all Reynolds numbers. It has been found, experimentally (Bottin et al., 1998) and numerically (Barkley and Tuckerman, 1999; Tuckerman and Barkley, 2002), that the presence of a wire (Bottin et al., 1998) or a ribbon (Barkley and Tuckerman, 1999; Tuckerman and Barkley, 2002) oriented along the spanwise direction causes the flow in the resulting geometry to become linearly unstable to either a steady or a turbulent state containing streamwise vortices. We simulate such a flow with a ribbon which is infinitesimal in the x' direction, occupies 30% of the cross-channel direction y and spans the entire z' direction. At $Re = 500$, the effect of such a ribbon is to produce a turbulent flow quickly without the need to try different initial conditions. Once the turbulent flow produced by the ribbon is simulated for a few hundred time units, the ribbon can be removed and the turbulence remains. This is the procedure we use to initialize turbulent states for the simulations to be described below.

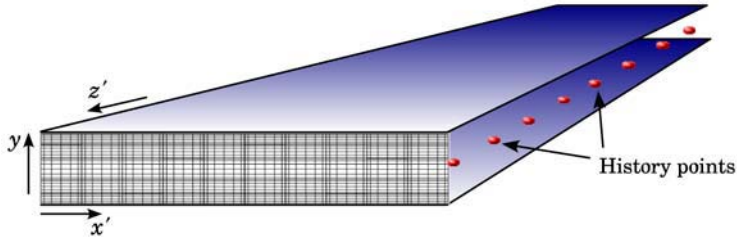

Figure 4. Simulation domain. The (x', y) grid is the actual spectral-element mesh used for the case $L_{x'} = 10$. Only part of the z' direction is shown. In practice we use 32 history points in the z' direction.

3. APPEARANCE OF TURBULENT-LAMINAR BANDS

3.1 Basic phenomenon

We begin with one of our first simulations, in a domain tilted at angle $\theta = 24°$. This angle has been chosen to be close to that observed experimentally near pattern onset. The simulation shows the spontaneous formation of a turbulent-laminar pattern as the Reynolds number is decreased. We initiated a turbulent flow at $Re = 500$ by perturbing laminar Couette flow with a ribbon as described in Section 2. Time zero in Figure 5 corresponds to the removal of the ribbon. The flow is simulated for 500 time units at $Re = 500$ and the kinetic energy E is measured at 32 points equally spaced in z' along the line $x' = y = 0$ in the mid-channel shown in Figure 4. The corresponding 32 time series are plotted at the corresponding values of z'. At $Re = 500$, there is no persistent large-scale variation in the flow, a state which we describe as uniform turbulence. (This is not the homogeneous or fully developed turbulence that exists at higher Reynolds numbers or in domains without boundaries.) At the end of 500 time units, Re is abruptly changed to $Re = 450$ and the simulation continued for another 500 time units. Then Re is abruptly lowered to $Re = 425$ and the simulation is continued for 1000 time units, etc. as labeled on the right in Figure 5.

At $Re = 350$ we clearly see the spontaneous formation of a pattern. Out of uniform turbulence emerge three regions of relatively laminar flow between three regions of turbulent flow. (We will later discuss the degree to which the flow is laminar.) While the individual time traces are irregular, the pattern is itself steady and has a clear wavelength of 40 in the z' direction. This Reynolds number and wavelength are very close to what is seen in the experiments.

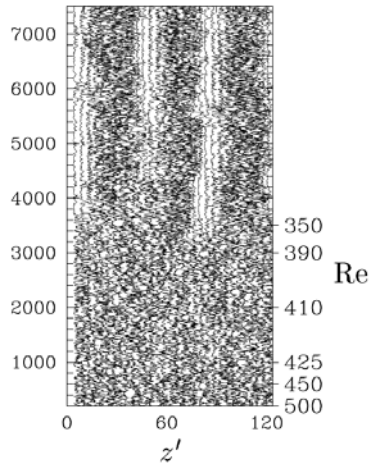

Figure 5. Space-time diagram. Kinetic energy $E(x' = 0, y = 0, z')$ at 32 equally spaced points in z' in a domain with $L_{x'} \times L_y \times L_{z'} = 10 \times 2 \times 120$ with tilt $\theta = 24°$. The Reynolds number is decremented in discrete steps (right). Three long-lasting and well-separated laminar regions emerge spontaneously from uniform turbulence as Re is decreased.

3.2 Visualizations

Figure 6 shows visualizations of the flow at the final time in Figure 5. Shown are the kinetic energy, streamwise velocity, and streamwise vorticity in the midplane between the plates. The computational domain is repeated periodically to tile an extended region of the midplane. The angle of the pattern is dictated by the imposed tilt of the computational domain. The wavelength of the pattern is not imposed by the computations other than that it must be commensurate with $L_{z'} = 120$. The vorticity isosurfaces of this flow field were shown in Figure 2. Spanwise and cross-channel velocity components show similar banded patterns.

Clearly visible in the center figure are streamwise streaks typical of shear flows. These streaks have a spanwise spacing on the scale of the plate separation but have quite long streamwise extent. We stress how these long streaks are realized in our computations. A streak seen in Figure 6 typically passes through several repetitions of the computational domain, as a consequence of the imposed periodic boundary conditions. In the single tilted rectangular computational domain, a single long streak is actually computed as several adjacent streaks connected via periodic boundary conditions.

Figure 7 shows the streamwise vorticity and velocity fields between the plates. The two leftmost images correspond to the same field as in Figure 6. The streamwise vorticity is well localized in the turbulent regions. Mushrooms of high- and low-speed fluid, corresponding to streamwise streaks, can be seen

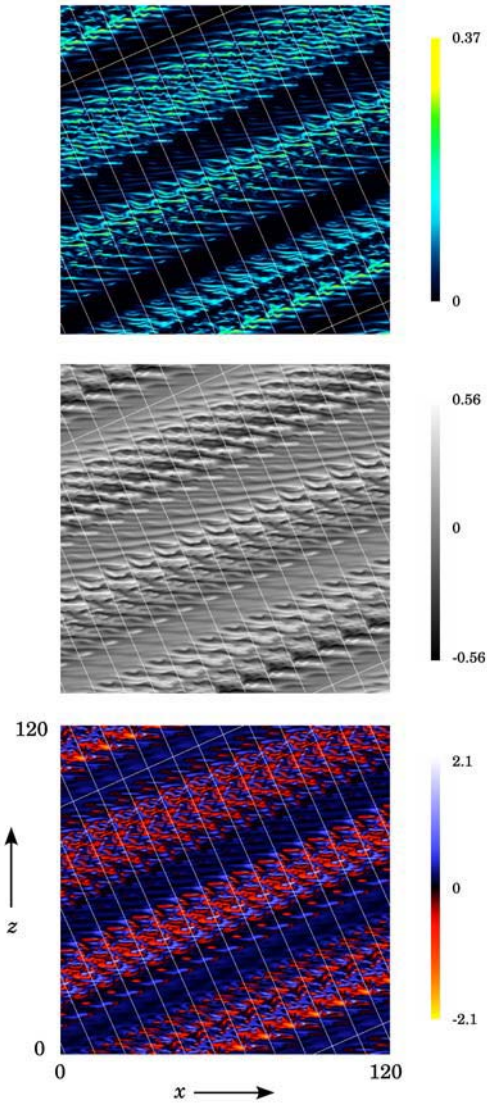

Figure 6. Turbulent-laminar pattern at $Re = 350$. The kinetic energy, streamwise velocity, and streamwise vorticity are visualized in the $y = 0$ plane, midway between and parallel to the moving plates. The computational domain (outlined in white, tilted at angle $\theta = 24°$) is repeated periodically to tile an extended region in x-z coordinates. Streamwise streaks, with spanwise separation approximately $4h$, are visible at the edges of the turbulent regions.

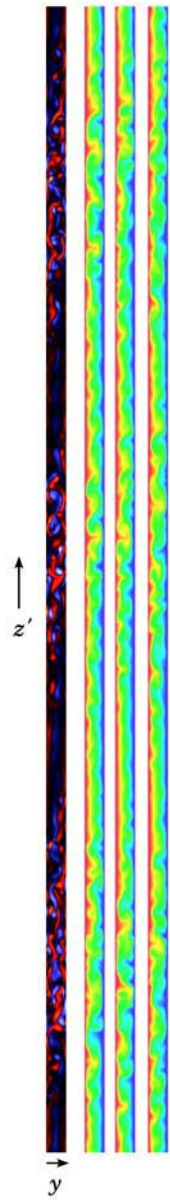

Figure 7. Turbulent-laminar pattern at $Re = 350$ viewed between the moving plates ($x' = 0$ plane). Left plot shows streamwise vorticity. The other three plots show contours of streamwise velocity at three times separated by 100 time units (time increasing left to right). The vorticity plot and the first velocity plot correspond to the field seen in Figure 6.

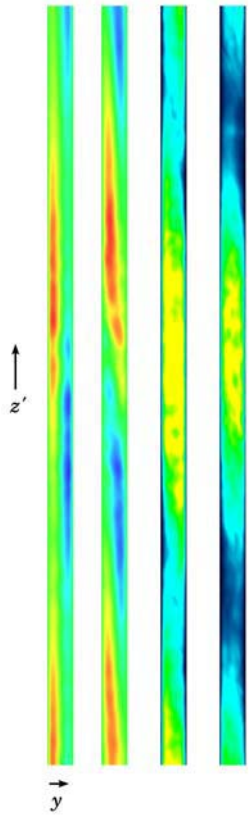

Figure 8. Mean and rms velocity fields for the turbulent-laminar pattern. From left to right: mean streamwise velocity, mean spanwise velocity, rms streamwise velocity and rms spanwise velocity. The rms velocities are maximal in the lightest regions. Only the central half ($30 \leq z' \leq 90$) of the computational domain is shown.

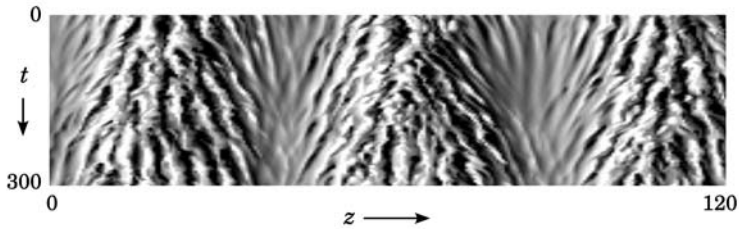

Figure 9. Space-time plot showing dynamics of the turbulent-laminar pattern. Streamwise velocity is sampled along a spanwise cut through the flow field (the line $x = y = 0$ in the reconstructed flows in Figure 6). Time zero corresponds to the time of Figure 6. The streaks propagate away from the center of the turbulent regions toward the laminar regions.

in the turbulent regions of flow. Dark velocity contours, corresponding to fluid velocity approximately equal to that of the lower and upper moving plates, are seen to reach into the center of the channel in the turbulent regions. In the center of the laminar regions, where the flow is relatively quiescent (Figure 5), there is very little streamwise vorticity and the streamwise velocity profile is not far from that of laminar Couette flow. In particular, no high- or low-speed fluid reaches into the center of the channel in these laminar regions.

In Figure 8 we show the mean and rms of the streamwise and spanwise velocity components obtained from averages over $T = 2000$ time units. These results show that the mean flow is maximal at the boundaries separating the turbulent and laminar regions while the fluctuations are maximal in the middle of the turbulent bands. This agrees with the experimental observations of Prigent et al. (2001, 2002, 2003, 2005). Note further that the regions of high fluctuation have approximately the same rhombic shape as the turbulent regions shown by Coles and van Atta (1966) in experiments on Taylor–Couette flow.

Finally, Figure 9 shows a space-time plot of streamwise velocity along the spanwise line $x = y = 0$. Specifically, data is taken from reconstructed flows as in Figure 6. Time zero in Figure 9 corresponds to the field in Figure 6. Time is taken downward in this figure to allow for comparison with a similar figure from the experimental study by Hegseth (1996: figure 6) showing the propagation of streaks away from the center of turbulent regions. Our results agree quantitatively with those of Hegseth. We find propagation of streaks away from the center of the turbulent regions with an average spanwise propagation speed of approximately 0.054 in units of the plate speed U. Translating from the diffusive time units used by Hegseth, we estimate the average spanwise propagation speed of streaks in his data to be approximately 0.060 at Reynolds number 420. This space-time plot again shows the extent to which there is some small activity in the regions we refer to as laminar.

3.3 Average spectral coefficients

We have determined a good quantitative diagnostic of the spatial periodicity of a turbulent-laminar pattern. We use the same data as that presented in Figure 5, i.e. velocities at 32 points along the line $x' = y = 0$ in the midplane along the long direction, at each interval of 100 time steps: $100\Delta t = 1$. We take a Fourier transform in z' of the spanwise velocity w, yielding $\hat{w}_m$. We take the modulus $|\hat{w}_m|$ to eliminate the spatial phase. Finally, we average over a time T to obtain $\langle|\hat{w}_m|\rangle$. Figure 10 shows the evolution of $\langle|\hat{w}_m|\rangle$ for wavenumbers $m = 3$, $m = 2$, $m = 1$, and $m = 0$ during one of our simulations (shown below in Figure 11, which is a continuation of that shown in Figure 5). As before, the vertical axis corresponds to time, and also to Reynolds number, which was decreased in steps of $\Delta Re = 10$. We average successively over $T = 10$,

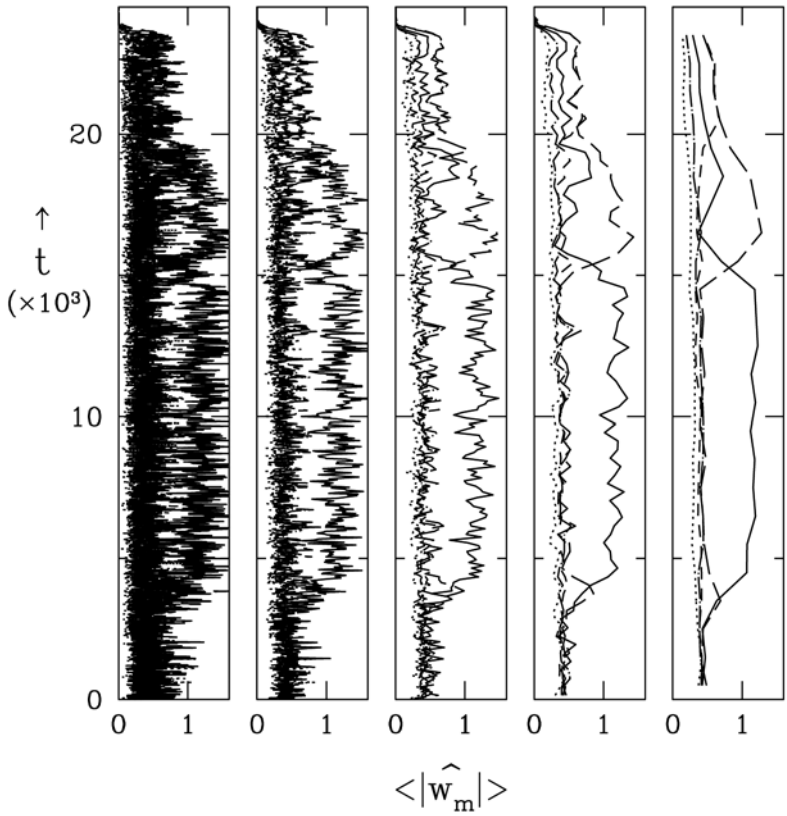

Figure 10. Evolution of $\langle|\hat{w}_m|\rangle$, which is an average over time T of the modulus of the Fourier transform in the z' direction of 32 spanwise velocity samples taken along the line ($x' = 0$, $y = 0$). The components with wavenumber $m = 3$ (solid curve), $m = 2$ (long-dashed curve), $m = 1$ (short-dashed curve) and $m = 0$ (dotted curve) can be used as a quantitative diagnostic of a turbulent-laminar pattern. For example, the dominance of the $m = 3$ component indicates a pattern containing three turbulent bands. From left to right, the average is taken over $T = 10$, $T = 30$, $T = 100$, $T = 300$, and $T = 1000$.

$T = 30$, $T = 100$, $T = 300$, and $T = 1000$ and observe the short-term fluctuations gradually disappear, leaving the long-term features which will be discussed in the next section. We have chosen $T = 500$ as the best compromise between smoothing and preserving the detailed evolution.

4. DEPENDENCE ON REYNOLDS NUMBER

We have investigated in detail the Reynolds-number dependence of the $\theta = 24°$ case. To this end, we have carried out two simulations, shown in Figure 11. In each the Reynolds number is lowered at discrete intervals in time,

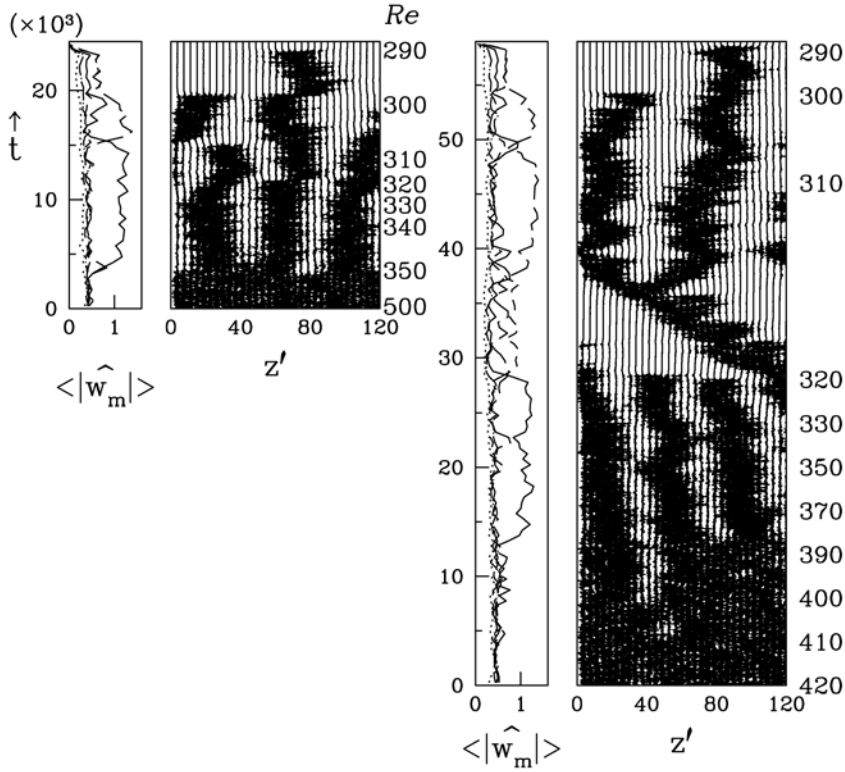

Figure 11. Two time series at $\theta = 24°$. The Reynolds number is lowered in steps, but at different instants to generate the two evolutions shown. For each case, we show w at 32 points along the z' direction on the right and the spectral components $\langle|\hat{w}_m|\rangle$ on the left. Left: uniform turbulence is succeeded by the formation of three bands, then two, then a single band (a localized state) and finally by laminar Couette flow. Right: two bands disappear almost simultaneously at $Re = 320$. The remaining band moves toward the left, periodically emitting turbulent spurs, of which one finally becomes a second turbulent band.

but following a different sequence in the two cases. For each case, we present a space-time diagram of $E(x' = 0, y = 0, z', t)$ at 32 values of z'. The Reynolds-number sequence is shown on the right of each diagram and the time (up to $T = 59,000$) on the left. Each space-time diagram is accompanied by a plot showing the evolution of its average spectral coefficients, as defined above.

Careful observation of Figure 5 already shows a laminar patch beginning to emerge at $Re = 390$, consistent with experimental observations: Prigent et al. (2001, 2002, 2003, 2005) observed a turbulent-laminar banded pattern with wavelength 46 and angle 25° when they decreased Re below $Re = 394$. The space-time diagram on the left of Figure 11 shows a continuation of this simulation. (Here, the Reynolds numbers intermediate between 500 and 350

are not shown to reduce crowding.) We see a sequence of different states: uniform turbulence and the three-banded turbulent-laminar pattern already seen are succeeded by a two-banded pattern (at $Re = 310$), then a state containing a single localized turbulent band (at $Re = 300$), and finally laminar Couette flow. These features are reflected in the average spectral coefficients. The flow evolves from uniform turbulence (all components of about the same amplitude) to intermittent turbulence, to a pattern containing three turbulent bands (dominant $m = 3$ component) and then two turbulent bands (dominant $m = 2$ component), then a single band (dominant $m = 1$ and $m = 2$ components), and finally becomes laminar (all components disappear).

In the simulation on the right, the Reynolds number is decreased more slowly. A state with three bands appears at $Re = 390$. (Although a laminar patch already appears at $Re = 400$, it is regained by turbulence when Re is maintained longer at 400; this is not shown in the figure.) Based on the previous simulation shown on the left, we had expected the three turbulent bands to persist through $Re = 320$. However here, instead, we see a rapid loss of two bands, leaving only a single turbulent band. This band moves to the left with a well-defined velocity, emitting turbulent spurs toward the right periodically in time. Finally, after a time of $T = 36000$, one of these spurs succeeds in becoming a second turbulent band and the two bands persist without much net motion. It would seem that the loss of the second band was premature, and that at $Re = 320$ one band is insufficient. We then resumed the simulation on the left, maintaining $Re = 320$ for a longer time, and found that two bands resulted in this case as well. Both simulations show two bands at $Re = 310$, one band at $Re = 300$, and laminar Couette flow at $Re = 290$.

4.1 Three states

The turbulent-laminar patterned states shown in Figure 11 are of three qualitatively different types (Barkley and Tuckerman, 2005). We demonstrate this by carrying out three long simulations, at three different Reynolds numbers, that are shown in Figure 12. In this figure, the energy along the line $x' = y = 0$ for the 32 points in z' has been averaged over windows of length $T = 500$ to yield a value shown by the shading of each space-time rectangle.

The simulations at $Re = 350$ and $Re = 300$ are carried out by increasing the long direction of our domain, $L_{z'}$, in regular discrete increments of 5 from $L_{z'} = 50$ to $L_{z'} = 140$. At $Re = 350$, a single turbulent band is seen when $L_{z'} = 50$. This band divides into two when $L_{z'} = 65$ and a third band appears when $L_{z'} = 130$: the periodic pattern adjusts to keep the wavelength in the range 35–65. This is close to the wavelength range observed experimentally by Prigent et al., which is 46–60. When the same protocol is followed at $Re = 300$, no additional turbulent bands appear as $L_{z'}$ is increased. We call the state

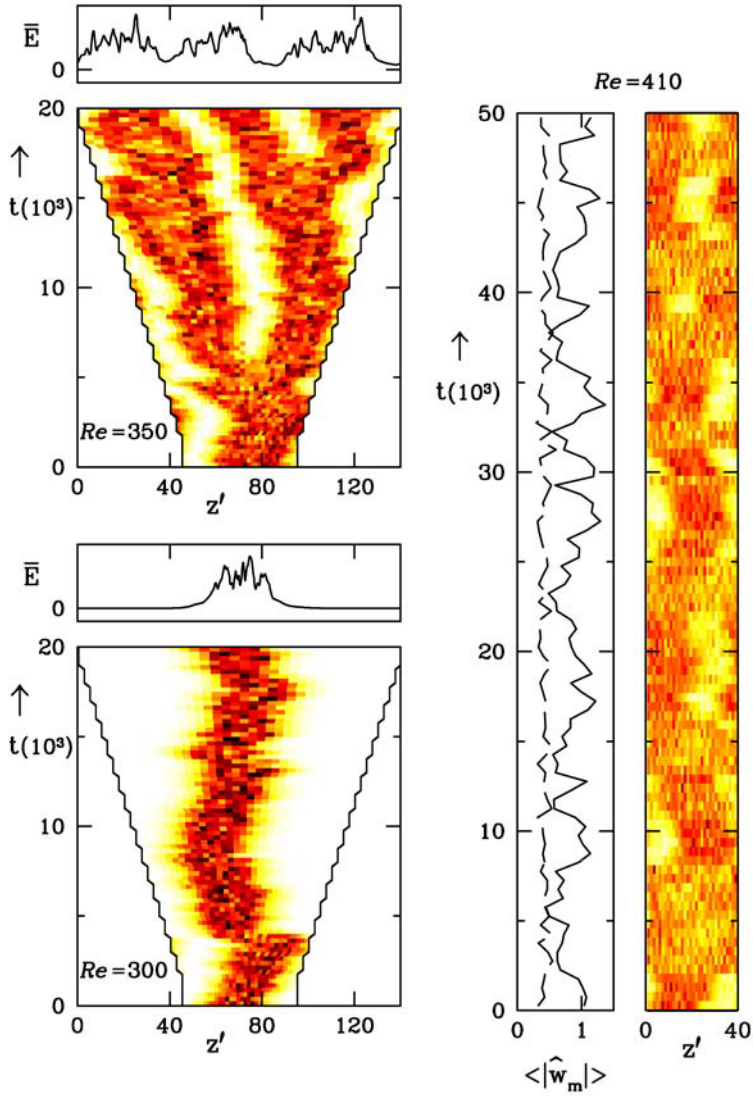

Figure 12. Simulations at $Re = 350$, $Re = 300$, and $Re = 410$ illustrating three qualitatively different regimes. For the simulations at $Re = 350$ and $Re = 300$, $L_{z'}$ is increased from 50 to 140. The state at $Re = 350$ is periodic: the turbulent band divides as $L_{z'}$ is increased to retain a wavelength near 40. The final kinetic energy profile $\bar{E}(z')$ is bounded away from zero. The state at $Re = 300$ is localized: a single turbulent band persists, regardless of domain size and $\bar{E}(z')$ decays exponentially to zero away from the band. The simulation at $Re = 410$ is carried out at $L_{z'} = 40$. The state is intermittent: laminar regions appear and disappear and the average spectral coefficients corresponding to $m = 1$ (solid) and $m = 0$ (dashed) oscillate erratically.

at $Re = 300$ localized and note that turbulent spots are reported near these values of Re in the experiments. The small $L_{x'}$ of our computational domain does not permit localization in the x' direction; instead localized states must necessarily take the form of bands when visualized in the x-z plane.

The instantaneous integrated kinetic energy profile

$$\bar{E} \equiv \int dx'\, dy\; E(x', y, z')$$

is plotted at the final time for both cases. For $Re = 350$, $\bar{E}$ does not reach zero and the flow does not revert to the simple Couette solution between the turbulent bands, as could also be seen in the earlier visualizations (Figures 7, 9). In contrast, for $Re = 300$, $\bar{E}$ decays to zero exponentially, showing that the flow approaches the simple Couette solution away from the turbulent band. In this case, there is truly coexistence between laminar and turbulent flow regions.

The simulation at $Re = 410$ illustrates another type of behavior. In a domain of length $L_{z'} = 40$, laminar or, rather, weakly-fluctuating regions appear and disappear. The spectral coefficients corresponding to $m = 1$ (wavelength 40) and $m = 0$ oscillate erratically. Similar states at similar Reynolds numbers are reported experimentally by Prigent and coworkers (2001, 2002, 2003, 2005), where they are interpreted as resulting from noise-driven competition between banded patterns at equal and opposite angles, a feature necessarily absent from our simulations.

5. DEPENDENCE ON ANGLE

5.1 Angle survey

We have explored the angles with respect to the streamwise direction at which a turbulent-laminar pattern may exist. The results are plotted in Figure 13. We keep $L_{z'} = 120$ and $L_{x'} = 4/\sin\theta$. The transition from uniform turbulence to laminar Couette flow occurs via intermediate states which occupy a decreasing range of Re as θ is increased. The sequence of states seen for increasing θ at $Re = 350$ is qualitatively the same as that for decreasing Re at $\theta = 24°$: uniform turbulence at $\theta = 0°$, a turbulent-laminar pattern with three bands at $\theta = 15°$ to $\theta = 24°$, two bands for $\theta = 30°$ and $\theta = 45°$, a localized state for $\theta = 66°$, and laminar Couette flow for $\theta° \geq 72$. Thus far we have obtained patterns for angles between 15° and 66° and the number of bands decreases with angle.

Experimental data from Prigent and coworkers (2001, 2003, 2005) is also shown in Figure 13. The wavelengths, angles, and Reynolds numbers reported ranged from $\lambda_{z'} = 46.3$ and $\theta = 25.3°$ at $Re = 394$ to $\lambda_{z'} = 60.5$ and $\theta = 37°$ at $Re = 340$. In these ranges of angle and Reynolds number, we observe a similar trend, since our wavelength (constrained here to be a divisor

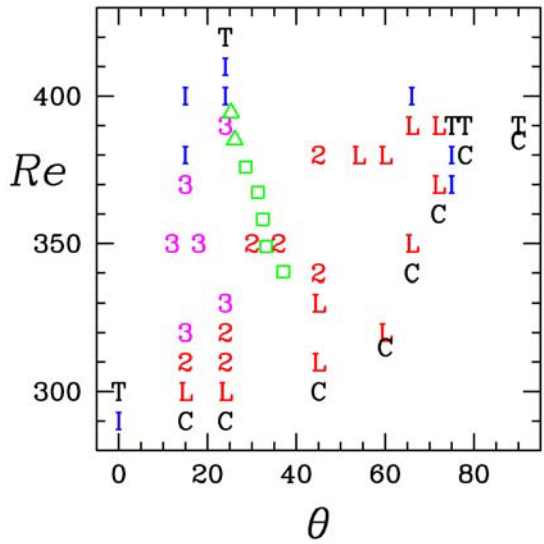

Figure 13. Patterns as a function of Reynolds number Re and θ, the angle between the $L_{x'}$ direction of our rectangular computational domain and the streamwise direction. The domain is of size $L_{x'} \times L_y \times L_{z'} = (4/\sin\theta) \times 2 \times 120$. For each angle, upper and lower limits in Re are shown for each regime. T: uniform turbulence (lower limit in Re). I: intermittent turbulence. 3: pattern containing three turbulent-laminar bands, each of approximate wavelength 40. 2: pattern containing two bands of approximate wavelength 60. L: pattern containing one turbulent region, possibly localized. C: laminar Couette flow (no patterns observed below this Re). Open symbols show experimental observations of Prigent et al. Triangles: patterns with wavelength between 46 and 50. Squares: patterns with wavelength between 50 and 60.

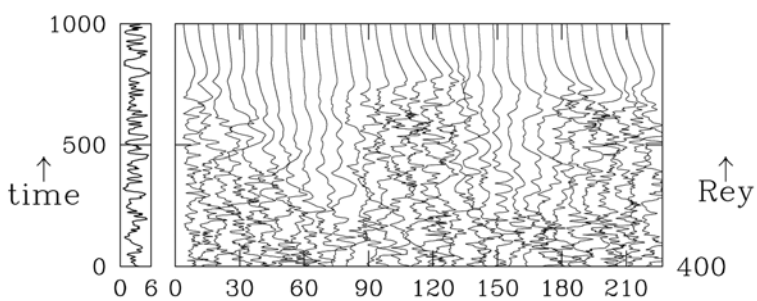

Figure 14. Evolution for $\theta = 90°$. Two simulations at $Re = 400$ are shown, in domains with $L_{x'} = L_z = 4$. The domain shown on the right has $L_{z'} = L_x = 220$; that on the left has $L_{z'} = L_x = 6$, close to the minimal flow unit (the two are not shown to scale). The large domain supports a transient pattern as an intermediate state between uniform turbulence and laminar Couette flow, whereas the turbulence persists in the small domain.

of $L_{z'} = 120$) increases from 40 to 60 as the number of bands decreases from 3 to 2. Between $Re = 325$ and $Re = 280$, experiments showed spots, which may correspond to some of the states we have labeled as localized in Figure 13. At present, we do not systematically distinguished localized states from others containing one turbulent region but which may not behave like Figure 12. The threshold for intermittency is also difficult to define and to determine.

The most striking difference between our computations and the experimental data is that the range of angles over which we find periodic turbulent-laminar patterns (from $\theta = 15°$ to at least $\theta = 45°$) is far greater than that seen in the experiment. Patterns with angles outside of the experimental range are likely to be unstable in a large domain in which the angle is unconstrained.

Our computational technique requires that the size of the domain be increased as θ decreases according to $L_{x'} = 4/\sin\theta$ in order to respect the spanwise vortex or streak spacing; see Figure 3. Hence the computational cost increases with decreasing θ and for this reason we have not as yet investigated θ between 15° and 0°. For θ exactly 0°, this trigonometric constraint is lifted, since the streamwise vortices and streaks would not extend diagonally across the rectangular domain, but parallel to its boundaries. As θ increases, the domain size $L_{x'} = 4/\sin\theta$ decreases, as does the computation cost. For θ between 45° and 90°, for which $L_{x'}$ is between 5.7 and 4, we reduce the number of spectral elements in the x' direction from 10 to 4 (see Figure 4).

5.2 Long streamwise direction

For $\theta = 90°$, the domain has a long streamwise direction $L_{z'} = L_x$ and a short spanwise direction $L_{x'} = L_z$. Figure 13 shows that, for $\theta = 90°$ and $L_x = 120$, we obtain direct decay from uniform turbulence to laminar Couette flow at $Re = 385$. We have varied L_x and show the results in Figure 14. When $L_x = 220$, the turbulence is extinguished at $Re = 400$; a transient pattern of wavelength 110 can be seen. But when $L_x = 6$, we find that the turbulence persists down to a value of $Re \approx 370$. We recall that the minimal flow unit was proposed by Hamilton et al. (1995) as the smallest which can support the streak and streamwise-vortex cycle and maintain turbulence; the flow becomes laminar when either of the dimensions are reduced below their MFU values. However, Figure 14 shows that turbulence can also sometimes be extinguished by increasing L_x. Simulations in domains with a long streamwise and a short spanwise dimension have also been carried out by Jiménez et al. (2005) with the goal of understanding the role of the streamwise dimension, e.g. streak length.

5.3 Long spanwise direction

In the case $\theta = 0°$, the domain has a long spanwise direction ($L_z = L_{z'} = 120$) and a short streamwise direction ($L_x = L_{x'} = 10$). In decreasing the Reynolds number by $\Delta Re = 5$ after each interval of $T = 1000$, we observe turbulent regions far below $Re = 300$, terminating only at $Re = 210$, as shown in Figure 15. At several times, the turbulence seems ready to disappear, only to spread out again. In order to confirm this surprising result, we have carried out longer simulations at each of these low values of Re. Turbulence persisted over $T = 4200$ (in the usual advective time units) at $Re = 220$, over $T = 3000$ at $Re = 225$, and even over $T = 15000$ for $Re = 230$.

Experiments (Dauchot and Daviaud, 1995) and numerical simulations in large domains ($L_x \times L_y \times L_z = 128 \times 2 \times 64$) (Lundbladh and Johansson, 1991) and numerical simulations in periodic minimal flow units ($L_x \times L_y \times L_z = 4 \times 2 \times 6$) (Hamilton et al., 1995) have produced long-lived turbulence only for $Re > 300$. A number of studies (Schmiegel and Eckhardt, 1997, 2000; Faisst and Eckhardt, 2004; Eckhardt and Faisst, 2005) have examined turbulent lifetimes as a function of initial perturbation amplitude, Reynolds number, and quenching rate (rate of Reynolds number decrease) in minimal flow units. In these studies, turbulence with a lifetime greater than $T = 2000$ was counted as sustained; experiments (Dauchot and Daviaud, 1995), however, are carried out on timescales several orders of magnitude longer than this. Schmiegel and Eckhardt (2000) studied the effect of quenching rate on turbulent lifetimes. For rates of Reynolds number decrease comparable to ours, they found that turbulence could in some cases subsist to $Re = 280$ or 290 for times on the order of $T = 1000$ to 10000; for rates that were ten times faster than ours, turbulence was occasionally sustained to $Re = 240$.

If we compare our results to the previous simulations, then the conclusion would be that turbulence is favored by a short streamwise direction $L_x = 10$ and a long spanwise direction $L_z = 120$. When either of these two conditions are lifted, the turbulence disappears. We note, however, that our simulations do not systematically vary the initial conditions and thus do not determine the probability of long-lived turbulence at these low Reynolds numbers near 220.

We also note that Toh and colleagues (Toh and Itano, 2005; Toh et al., 2005) have recently reported results from simulations of Couette flow in domains with long spanwise extent compared with the MFU geometry. These simulations are for higher values of Re than those considered here.

We observe an approximately periodic oscillation in time, shown on the right of Figure 15. The oscillation period of about 200 time units has the same order of magnitude as the minimum turbulent cycle (Hamilton et al., 1995), but further analysis of our results is required before we can identify the streak and streamwise-vortex cycle in our flow.

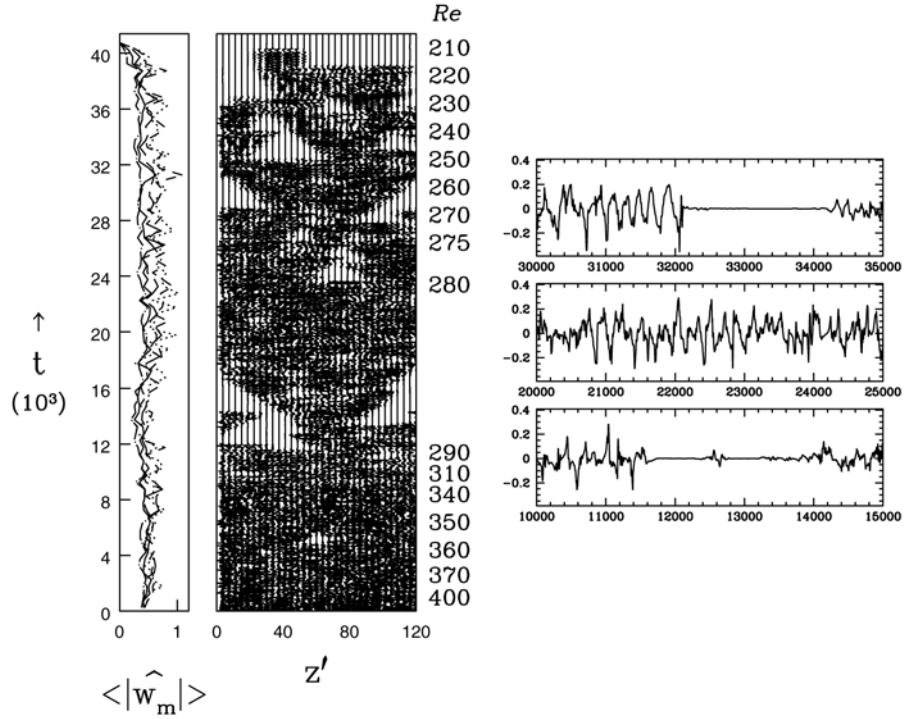

Figure 15. Evolution for $\theta = 0°$ with $L_{x'} = L_x = 10$ and $L_{z'} = L_z = 120$. Re is lowered by steps of $\Delta Re = 5$; not all intermediate values of Re are shown. The flow continues to have turbulent regions far below $Re = 300$. Left: evolution over the entire domain, showing the formation and disappearance of turbulent domains. Right: evolution of $w(x = 0, y = 0, z = 60, t)$, showing irregular periodic cycles.

6. SUMMARY

We have used an extension of the minimal-flow-unit methodology to study large-scale turbulent-laminar patterns formed in plane Couette flow. Turbulent-laminar patterns are obtained as solutions to the Navier–Stokes equations in domains with a single long direction. The other dimensions are just large enough to resolve the inter-plate distance and to contain an integer number of longitudinal vortex pairs or streaks. We have presented various visualizations of the computed turbulent-laminar patterns as well as space-time plots illustrating the formation and dynamics of these patterns. The time-averaged modulus of the spatial Fourier spectrum is shown to provide a quantitative diagnosis of the patterns. Periodic, localized, and intermittent states occur in our simulations where similar states are observed experimentally.

We have explored the patterns' dependence on Reynolds number, domain length and tilt angle. The patterned states do not appear to depend sensitively

on how the turbulence is initialized nor on the route taken to a particular point in parameter space. It is, however, possible that some parameter combinations may support different numbers of turbulent bands (although we have not yet observed this). All states are bistable with respect to laminar Couette flow and if parameters are changed too abruptly, then reversion to laminar Couette flow occurs.

It appears that large-scale patterns are inevitable intermediate states on the route from turbulent to laminar flow in large aspect-ratio Couette flow. A key open question is what mechanism causes laminar-turbulent patterns. These patterns are not only interesting in and of themselves, but may provide clues to the transition to turbulence in plane Couette flow.

ACKNOWLEDGEMENTS

We thank Olivier Dauchot for valuable discussions and Ron Henderson for the use of `Prism`. We thank the CNRS and the Royal Society for supporting this work. The two CPU decades of computer time used for this research were provided by the IDRIS-CNRS supercomputing center under project 1119, and by the University of Warwick Centre for Scientific Computing (with support from JREI grant JR00WASTEQ).

REFERENCES

Barkley, D. and Tuckerman, L.S. (1999). Stability analysis of perturbed plane Couette flow. *Phys. Fluids* **11**, 1187–1195.

Barkley, D. and Tuckerman, L.S. (2005). Computational study of turbulent laminar patterns in Couette flow. *Phys. Rev. Lett.* **94**, 014502.

Bottin, S., Dauchot, O., Daviaud, F. and Manneville, P. (1998). Experimental evidence of streamwise vortices as finite amplitude solutions in transitional plane Couette flow. *Phys. Fluids* **10**, 2597–2607.

Coles, D. (1965). Transition in circular Couette flow. *J. Fluid Mech.* **21**, 385–425.

Coles, D. and van Atta, C.W. (1966). Progress report on a digital experiment in spiral turbulence. *AIAA J.* **4**, 1969–1971.

Cros, A. and Le Gal, P. (2002). Spatiotemporal intermittency in the torsional Couette flow between a rotating and a stationary disk. *Phys. Fluids* **14**, 3755–3765.

Dauchot, O. and Daviaud, F. (1995). Finite-amplitude perturbation and spots growth-mechanism in plane Couette flow. *Phys. Fluids* **7**, 335–343.

Eckhardt, B. and Faisst, H. (2005). Dynamical systems and the transition to turbulence. In *Laminar Turbulent Transition and Finite Amplitude Solutions*, Proceedings of the IUTAM Symposium, Bristol, UK, 9–11 August 2004, T. Mullin and R.R. Kerswell (eds), Springer, Dordrecht, pp. 35–50 (*this volume*).

Faisst, H. and Eckhardt, B. (2004). Sensitive dependence on initial conditions in transition to turbulence in pipe flow. *J. Fluid Mech.* **504**, 343–352.

Hamilton, J.M., Kim, J. and Waleffe, F. (1995). Regeneration mechanisms of near-wall turbulence structures. *J. Fluid Mech.* **287**, 317–348.

Hegseth, J.J. (1996). Turbulent spots in plane Couette flow. *Phys. Rev. E* **54**, 4915–4923.

Henderson, R.D. and Karniadakis, G.E. (1995). Unstructured spectral element methods for simulation of turbulent flows. *J. Comput. Phys.* **122**, 191–217.

Hof, B., Juel, A. and Mullin, T. (2003). Scaling of the turbulence transition threshold in a pipe. *Phys. Rev. Lett.* **91**, 244502.

Jiménez, J. and Moin, P. (1991). The minimal flow unit in near-wall turbulence. *J. Fluid Mech.* **225**, 213–240.

Jiménez, J., Kawahara, G., Simens, M.P. and del Alamo, J.C. (2005). The near-wall structures of turbulent wall flows. In *Proceedings of the IUTAM Conference on Elementary Vortices and Coherent Structures*, S. Kida (ed.), Springer, Dordrecht, forthcoming.

Lundbladh, A. and Johansson, A.V. (1991). Direct simulation of turbulent spots in plane Couette flow. *J. Fluid Mech.* **229**, 499–516.

Prigent, A. (2001). La spirale turbulente: Motif de grande longueur d'onde dans les écoulements cisallés turbulents. PhD Thesis, University Paris-Sud.

Prigent, A. and Dauchot, O. (2005). Transition to versus from turbulence in subcritical Couette flows. In *Laminar Turbulent Transition and Finite Amplitude Solutions*, Proceedings of the IUTAM Symposium, Bristol, UK, 9–11 August 2004, T. Mullin and R.R. Kerswell (eds), Springer, Dordrecht, pp. 195–219 (*this volume*).

Prigent, A., Grégoire, G., Chaté, H., Dauchot, O. and van Saarloos, W. (2002). Large-scale finite-wavelength modulation within turbulent shear flows. *Phys. Rev. Lett.* **89**, 014501.

Prigent, A., Grégoire, G., Chaté, H. and Dauchot, O. (2003). Long-wavelength modulation of turbulent shear flows. *Physica D* **174**, 100–113.

Schmiegel, A. and Eckhardt, B. (1997). Fractal stability border in plane Couette flow. *Phys. Rev. Lett.* **79**, 5250–5253.

Schmiegel, A. and Eckhardt, B. (2000). Persistent turbulence in annealed plane Couette flow. *Europhys. Lett.* **51**, 395–400.

Toh, S. and Itano, T. (2005). Interaction between a large-scale structure and near-wall structure in channel flow. *J. Fluid Mech.* **524**, 249–262.

Toh, S., Itano, T. and Satoh, K. (2005). Co-supporting cycle: Sustaining mechanism of large-scale structures and near-wall structures in channel flow turbulence. In *Laminar Turbulent Transition and Finite Amplitude Solutions*, Proceedings of the IUTAM Symposium, Bristol, UK, 9–11 August 2004, T. Mullin and R.R. Kerswell (eds), Springer, Dordrecht, pp. 71–83 (*this volume*).

Tuckerman, L.S. and Barkley, D. (2002). Symmetry breaking and turbulence in perturbed plane Couette flow. *Theoret. Comput. Fluid Dynam.* **16**, 43–48.

van Atta, C.W. (1966). Exploratory measurements in spiral turbulence. *J. Fluid Mech.* **25**, 495–512.

Waleffe, F. (2003). Homotopy of exact coherent structures in plane shear flows. *Phys. Fluids* **15**(6), 1517–1534.

Waleffe, F. and Wang, J. (2005). Transition threshold and the self-sustaining process. In *Laminar Turbulent Transition and Finite Amplitude Solutions*, Proceedings of the IUTAM Symposium, Bristol, UK, 9–11 August 2004, T. Mullin and R.R. Kerswell (eds), Springer, Dordrecht, pp. 85–106 (*this volume*).

SUBCRITICAL TURBULENT TRANSITION IN ROTATING AND CURVED SHEAR FLOWS

Pierre-Yves Longaretti[1] and Olivier Dauchot[2]
[1]*LAOG, BP 53X, F-38041 Grenoble, France*
[2]*GIT/SPEC/DRECAM/DSM CEA Saclay, F-91191 Gif-sur-Yvette, France*

Abstract The effects of global flow rotation and curvature on the subcritical transition to turbulence in shear flows are examined. The relevant time-scales of the problem are identified by a decomposition of the flow into a laminar and a deviation from laminar parts, which is performed for rotating plane Couette and Taylor–Couette flows. The usefulness and relevance of this procedure are discussed at the same time. By comparing the self-sustaining process time-scale to the time-scales previously identified, an interpretation is brought to light for the behavior of the transition Reynolds number with the rotation number and relative gap width in the whole neighborhood (in parameter space) of the non-rotating plane Couette flow covered by the available data.

1. INTRODUCTION

In the last decade or so, a number of breakthroughs have been achieved in the understanding of the onset of turbulence in subcritical shear flows, such as the plane Couette flow and Poiseuille flow, both from an experimental point of view (e.g., Bottin et al., 1998), and a numerical and theoretical one (e.g., Nagata, 1990; Clever and Busse, 1997; Hamilton et al., 1995; Waleffe, 1997, 1998, 2003; Faisst and Eckardt, 2003). In this context, the present contribution has two main objectives: characterize the effects of global flow rotation and curvature in subcritical flows from the available data, and show that these characteristics can be understood at a semi-quantitative level from time-scale considerations. Understanding these questions is essential for geophysical and astrophysical applications, which is one of the motivations of this work. Data on rotating plane Couette flows and Taylor–Couette flows are used in this investigation.

Section 2 is devoted to the identification of rotation and curvature characteristic quantities, and relating them to the gross dynamics of the flow. Not surprisingly, the associated dimensionless numbers reduce to the shear-based Reynolds number, the rotation number, and the relative gap width (for Taylor–

T. Mullin and R.R. Kerswell (eds), Laminar Turbulent Transition and Finite Amplitude Solutions, 129–144.
© 2005 *Springer. Printed in the Netherlands.*

Couette flows); the novel point is that the relative gap width is interpreted in terms of a ratio of dynamically relevant time-scales. The experimental data are then reviewed in section 3, and the characterization of the available data in terms of the previously defined dimensionless numbers is performed in section 4. The last section briefly summarizes the most important results, and discusses their astrophysical implications.

2. THE PHYSICS OF THE ADVECTION TERM REVISITED

The main objective of this section is to pinpoint the relevant time-scales in globally subcritical, rotating and curved flows, and to relate them to the various contributions of the advection/acceleration term. This turns out to be essential to develop a semi-quantitative understanding of the available data on such flows. In practice, we consider only rotating plane Couette and Taylor–Couette flows. Incompressibility is assumed throughout.

2.1 Equations of motions

The relevant time-scales are well-known in rotating plane Couette flows, and follow immediately from the expression of the Navier–Stokes equation in the rotating frame, which reads

$$\frac{\partial \mathbf{u}}{\partial t} + \mathbf{u}.\nabla\mathbf{u} = -\frac{\nabla\pi}{\rho} - 2\Omega \times \mathbf{u} + \nu\Delta\mathbf{u}, \tag{1}$$

with obvious notations (in particular, the centrifugal term has been included in the pressure gradient). They are the shear[1] time-scale $t_s = |S^{-1}|$, the viscous one $t_\nu = d^2/\nu$ (d is the gap in the experiment), and the rotation time-scale related to the Coriolis force $t_\Omega = (2\Omega)^{-1}$ (Ω is the rotation velocity of the flow in an inertial frame), and relate to the advection term, the viscous term, and the Coriolis force, respectively. Correlatively, the flow is described by two dimensionless numbers, the Reynolds number[2] $Re = t_\nu/t_s = |S|d^2/\nu$, and the rotation number $R_\Omega = \mathrm{sgn}(S)t_s/t_\Omega = 2\Omega/S$.

The situation is less straightforward for Taylor–Couette flows, where the dimensionless number usually associated to the flow geometry, $\eta = r_i/r_o$ (r_i is the inner cylinder radius, r_o the outer one) does not obviously correspond to a ratio of time-scales of the flow. However, on closer inspection, it appears that this situation arises from a partially incorrect assimilation of the shear time-scale to the advection term. Indeed, in the case of solid body rotation, the shear vanishes, while the advection term does not, due to the global curvature of the flow. One must therefore devise a way to isolate the global shear contribution to the advection term from other contributions.

It turns out that one convenient way to operate such a distinction is to decompose the total flow into its laminar part, and a (not necessarily small) deviation:

$$\mathbf{u} = \mathbf{u}_L + \mathbf{w}. \tag{2}$$

Although the dynamical relevance of the laminar flow to the turbulent one is not a priori obvious, this procedure is suggested and justified by the following considerations:

- Inasmuch as this is feasible, a distinction between global shear, rotation and curvature cannot be operated by a tensorial decomposition of the advection term. For example, it is well-known that both a pure global shear and a global rotation, such as the ones present in rotating plane Couette flows, contribute to the vorticity tensor. In fact, a direct Taylor expansion of the deformation for small displacements shows that one needs to go at least to second order to distinguish the two contributions. Therefore, no tensor constructed from the flow velocity first derivatives will establish the required distinction, by construction.

- The global characteristics of the flow are the same for the laminar and turbulent solutions (geometry, global time-scales, nature of the boundary condition, etc). Therefore, one way to make them appear explicitly in the Navier–Stokes equation is precisely to make the proposed decomposition, as the laminar solution depends everywhere explicitly on these global characteristics. In particular, the laminar and turbulent flows share the same boundary conditions (velocity difference on the boundary, gap width, etc), so that the relative difference between the laminar and turbulent solution is of order unity. This means that the laminar solution is a convenient measure of the turbulent one, although their detailed mechanisms and characteristics are of course essentially different. For example, it turns out that the transition Reynolds number is highly sensitive to various global and/or qualitative characteristics of the laminar flow, such as time-scales, or "distance" in parameter space to the linear stability limits (see section 3).

It is useful to point out where this decomposition leads to for the rotating plane Couette flow. This is most naturally done in the rotating frame, so that Equation (1) becomes

$$\frac{\partial \mathbf{w}}{\partial t} + \mathbf{w}.\nabla\mathbf{w} = S \cdot y\frac{\partial \mathbf{w}}{\partial x} + (2\Omega + S)w_y\mathbf{e}_x - 2\Omega w_x\mathbf{e}_y - \frac{\nabla\delta\pi}{\rho} + \nu\Delta\mathbf{w}, \tag{3}$$

where the pressure gradient balancing the laminar flow Coriolis force has been subtracted out to form the effective generalized pressure $\delta\pi$. Note that on the walls, which specify the global characteristics of the flow, the boundary

condition becomes $\mathbf{w} = 0$, quite a featureless constraint: the effect of these boundaries is now explicitly included in the Navier–Stokes equation through the dynamical linear forcing terms on the right-hand side. The real usefulness of this change of point of view comes out when considering Taylor–Couette flows, as we shall now argue.

In this flow, the laminar solution takes the form $\mathbf{u}_L(\mathbf{r}) = r\Omega(r)\mathbf{e}_\theta$. Note that the rotating plane Couette flow can be viewed as a limit of small relative gap width $d/\bar{r} \to 0$ ($\bar{r}$ is some characteristic radius of the flow), at constant shear, and constant rotation. Then, the effect of the global curvature and rotation will be more easily distinguished from one another if one chooses a formulation of the Navier–Stokes equation which makes the difference with Equation (3) explicit. To this effect, one must define a characteristic rotation velocity $\bar{\Omega}$, and a characteristic shear[3] $\bar{S}$ of the laminar flow. A convenient way to do this is to choose a characteristic radius $\bar{r}$, and impose $\bar{\Omega} = \Omega(\bar{r})$, $\bar{S} = S(\bar{r})$; the choice of $\bar{r}$ does not need to be further specified for the time being (this point is discussed in the next subsection). Defining $\delta\Omega = \Omega(r) - \bar{\Omega}$ and $\delta S = S(r) - \bar{S}$, the decomposition of the Navier–Stokes equation of the Taylor–Couette flow leads to (r, ϕ, z is the coordinate system in the rotating frame)

$$\frac{\partial \mathbf{w}}{\partial t} + \mathbf{w}.\nabla\mathbf{w} = -\,\delta\Omega\partial'_\phi\mathbf{w} - (2\bar{\Omega} + \bar{S})w_r\mathbf{e}_\phi + 2\bar{\Omega}w_\phi\mathbf{e}_r - \frac{\nabla\delta\pi}{\rho} + \nu\Delta\mathbf{w}$$
$$- (2\delta\Omega + \delta S)w_r\mathbf{e}_\phi + 2\delta\Omega w_\phi\mathbf{e}_r, \tag{4}$$

where one has used $\partial_\phi\mathbf{w} = \partial'_\phi\mathbf{w} + \delta\Omega w_r\mathbf{e}_\phi + 2\delta\Omega w_\phi\mathbf{e}_r$, with $\partial'_\phi\mathbf{w} \equiv (\partial_\phi w_r)\mathbf{e}_r + (\partial_\phi w_\phi)\mathbf{e}_\phi + (\partial_\phi w_z)\mathbf{e}_z$; this definition is introduced so that the contributions of order $1/\bar{r}$ of the derivatives in the linear terms are separated from the contributions of order $1/d$. This equation is similar[4] to Equation (3), except for the last two terms, which consequently are connected to the global flow curvature. Note that, although the definition of $\delta\Omega$ and δS depends on the choice of $\bar{r}$, the overall variation of these quantities throughout the flow, $\Delta(\delta\Omega)$ and $\Delta(\delta S)$, does not. In fact, $|\Delta(\delta\Omega)| \sim |\Delta(\delta S)| \sim |\bar{S}|d/\bar{r}$, as can be checked from the laminar flow profile $\Omega(r) = A + B/r^2$. In the process, four time-scales of the incompressible Taylor–Couette flow have been identified: they are the shear time-scale $t_s = |\bar{S}^{-1}|$, the rotation time-scale $t_\Omega = (2\bar{\Omega})^{-1}$, a curvature-related time-scale that one can define as $t_C = |\bar{S}^{-1}|\bar{r}/d$, and, of course, the viscous time-scale $t_\nu = d^2/\nu$. This also shows that the dimensionless geometric number η can be related to the ratio of the shear and curvature time-scales. Taking the limit $d/\bar{r} \to 0$ ($\eta \to 1$), one recovers the rotating plane Couette relation Equation (3).

2.2 Characteristic quantities, dimensionless numbers, and the curvature and rotation concepts

Taylor–Couette flows possess three dimensionless control parameters, which are usually chosen as the Reynolds numbers associated to the inner and outer cylinder rotation velocities, R_i and R_o, and η, the ratio of their two radii. The preceding discussion suggests that one should use instead ratios of time-scales, which have a more direct dynamical meaning. This defines the shear-based Reynolds number[5] $Re = t_\nu/t_s$, the rotation number $R_\Omega = \mathrm{sgn}(S)t_s/t_\Omega$, and a "curvature" number $R_\mathcal{C} = t_s/t_\mathcal{C}$. Once a choice of $\bar{r}$ is operated (see below), the procedure is completely specified. This three-dimensional parameter space, in which notable curves and surfaces are drawn, is represented in Figure 1.

However, the physical meaning of this procedure is less straightforward than one would like, and this is related to an obvious weakness of Equation (4): the distinction between the rotation and curvature terms is not absolute when the related time-scales are both dynamically significant. Indeed, any change of definition of $\bar{\Omega}$ and $\bar{S}$ results in a correlative change of $\delta\Omega$ and δS. Nevertheless, the physical meaning is to a large extent unambiguous in at least two different contexts:

- If one changes the rotation velocity of the inner and outer cylinders by the same quantity, this will change $\bar{\Omega}$ by the same amount (independently of the choice of $\bar{r}$), while leaving all other quantities ($\bar{S}$, $\delta\Omega$, δS) unchanged. Such changes are obviously an effect of changes in the flow rotation.

- On the other hand, when changes in the flow are operated while maintaining $t_\Omega \lesssim t_\mathcal{C}$, the physical meaning of the distinction between the characteristic quantities ($\bar{\Omega}$, $\bar{S}$) and the deviations from these ($\delta\Omega$, δS) is blurred. This is the case in particular when the cylinders are counter-rotating, or when one cylinder is at rest, for *any* choice of $\bar{r}$. In such a context, changes in both parameters (the rotation number and the curvature number) describe the effect of a change in the flow curvature, as they are both proportional to $d/\bar{r}$, and vanish if the limit of vanishing global curvature is taken while enforcing the $t_\Omega \lesssim t_\mathcal{C}$ relation.

This clearly shows that rotation and curvature are not interchangeable concepts, although they have a non-negligible overlap. In this context, the denominations "rotation number" and "curvature number" are somewhat conventional and partially misleading, even if justified to some extent by the preceding considerations. In the (R_Ω, $R_\mathcal{C}$) plane, changes along lines of constant $R_\mathcal{C}$ correspond to changes of rotation, but there are infinitely many paths involving changes of both parameters and corresponding to changes of curvature from a physical point of view. Furthermore, most paths do not lead to any clear-cut

distinction between curvature and rotation changes in the flow. Of course, once a reference curvature path is chosen (e.g., the path with the inner cylinder at rest, corresponding to the inviscid linear stability limit on the cyclonic side, shown as curve (4) on Figure 1), every point in the (R_Ω, $R_\mathcal{C}$) plane can be connected to the non-rotating plane Couette flow (the origin in the plane), first through a change of curvature along the chosen curvature path until the desired curvature number is reached, and then through a change of rotation at constant $R_\mathcal{C}$. However, this distinction is only relative.

Obviously, this situation is intrinsic, as one cannot curve a straight flow, without at the same time making it rotate. The procedure outlined here nevertheless leads to the definition of well-defined parameters, which have a dynamical interpretation. It is their physical meaning in terms of rotation and curvature which is partially ambiguous. Furthermore, these parameters turn out to be useful to understand basic features in the data on the subcritical transition to turbulence, as discussed in the next section.

The remaining point to be addressed relates to the choice of $\bar{r}$. The preceding discussion makes it clear that this choice is not unique. The definition we have adopted here is $\bar{r} \equiv (r_i r_o)^{1/2}$, as suggested in Dubrulle et al. (2005) (r_i and r_o are the inner and outer radius, respectively). This choice is partially motivated by the compactness of the resulting expressions for the dimensionless numbers introduced above:

$$Re = \frac{2\bar{r}}{r_o + r_i} \frac{\bar{r}|\Omega_o - \Omega_i|d}{\nu} = \frac{2}{1+\eta}|\eta R_o - R_i|, \tag{5}$$

$$R_\Omega = \frac{r_i\Omega_i + r_o\Omega_o}{r_o r_i} \frac{d}{\Omega_o - \Omega_i} = (1-\eta)\frac{R_i + R_o}{\eta R_o - R_i}, \tag{6}$$

$$R_\mathcal{C} = \frac{d}{\bar{r}} = \frac{1-\eta}{\eta^{1/2}}. \tag{7}$$

Note that, for the range of values of η explored in the available experiment, $Re \simeq \bar{r}|\Delta\Omega|d/\nu$, and $R_\Omega \simeq (2\bar{\Omega}/\bar{r})(d/\Delta\Omega)$ (within a few percents).

3. SUBCRITICAL TRANSITION IN ROTATING PLANE COUETTE AND TAYLOR–COUETTE FLOWS

Considering a laminar flow of given dimensionless numbers (rotation, curvature, and Reynolds), two different things can happen when increasing the Reynolds number: either the flow will undergo a linear instability first (supercritical transition), or it will undergo a laminar-turbulent transition first (globally subcritical transition). The second option may happen whether the flow is linearly unstable or not.

The Reynolds number characterizing subcritical transition in a system is not a quantity that can be measured with absolute precision, as it depends to some extent on the experimental protocol used in its determination. For example, the laminar-turbulent transition Reynolds number is generically larger than the turbulent-laminar one. Furthermore, the flow is intermittent over a range of Reynolds numbers in the vicinity of this transition. This leads to some differences in the determined Reynolds transition values, even when the same data are used by different authors; however, the dispersion of the data in a given author's choice is much smaller. Overall, the resulting range of values (at given dimensionless numbers) is uncertain within less than a factor of ~ 2; we shall ignore this problem here, as we are only interested in characterizing qualitative trends and orders of magnitude.

With this convention, both supercritical ($Re = R_c$) and globally subcritical ($Re = R_g$) transitions are characterized by surfaces in the three dimensional space (R_Ω, $R_\mathcal{C}$, Re). Only particular lines on these surfaces have been probed by the available experiments. Obviously, the supercritical and subcritical surfaces meet somewhere in this space, so that one needs to characterize both surfaces.

It turns out, from a practical point of view, that the supercritical surface (manifold (1) in Figure 1) is sufficiently well captured by the analytic approximation derived by Esser and Grossmann (1996), for Taylor–Couette flows, although it relates only to axisymmetric perturbations (in other words, the non-axisymmetric perturbations seem to play little role in the definition of the supercritical transition). The rotating plane Couette flow is included in the limit $\eta \to 1$. For the relatively high Reynolds numbers of interest for subcritical transitions to turbulence (> 1000), the dependence of the supercritical surface on the Reynolds number is very steep, and the surface is well-approximated by the inviscid linear stability limit (curves (2) of Figure 1). This explains that the limit of the subcritical regime in the (R_Ω, $R_\mathcal{C}$) plane is well-approximated by the inviscid limit. Linear instability follows somewhere in the fluid in this limit if

$$-1 \leqslant \frac{2\Omega(r)}{S(r)} \leqslant 0, \tag{8}$$

at this location (this is equivalent to the constraint put by the Rayleigh discriminant). Asking that the fluid is everywhere stable with respect to this criterion translates into $R_\Omega < -1$, or $R_\Omega > (1-\eta)/\eta$.

The data on subcritical transition discussed here are those of Wendt (1933), Taylor (1936), Tillmark and Alfredsson (1996), and Richard (2001); they are represented on Figure 2. One could also include data on counter-rotating cylinders (Andereck et al., 1986; Prigent et al., 2003), but these occupy only a small area in the (R_Ω, $R_\mathcal{C}$) plane, and bring little constraint on the trend of the transi-

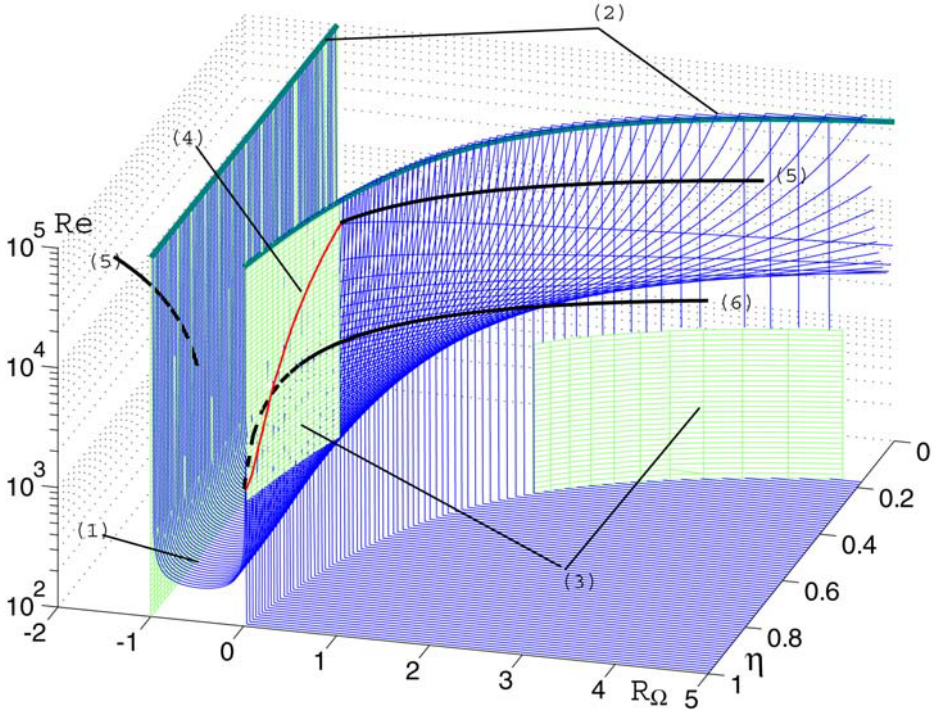

Figure 1. Stability boundaries in the $(Re, R_\Omega, R_\mathcal{C})$ parameter space (η is used as a measure of $R_\mathcal{C}$ on this graph). Manifold (1): linear stability threshold. Dark curves (2): linear stability threshold in the inviscid limit. Manifold (3): extrapolation of the inviscid criteria throughout the full Reynolds space (partially shown for readability). Curve (4): globally subcritical threshold obtained with inner cylinder at rest (see text). Other curves: globally subcritical thresholds obtained at fixed value of η [(5): $\eta = 0.7$; (6): $\eta = 1$] (see text).

tion Reynolds number with the rotation and curvature numbers (see Longaretti and Dauchot, 2005, for a discussion o couter-rotating data).

The data are well parameterized by the following approximate formula (the $+$ and $-$ sign refer to cyclonic and anticyclonic flows, respectively)

$$R_g^{\pm}(R_\Omega, R_\mathcal{C}) = R_{PC}^{\pm} + a^{\pm}(\eta)|R_\Omega - R_\Omega^{\infty,\pm}| + b^{\pm}R_\mathcal{C}^2, \tag{9}$$

with $R_{PC}^{+} \simeq 1400$, $R_{PC}^{-} \simeq 1100 \sim R_{PC}^{+}$, $21000 \lesssim a^{\pm} \lesssim 61000$, $2 \times 10^5 \lesssim b^{+} \lesssim 6 \times 10^5$, $b^{-} \ll b^{+}$, and where $R_\Omega^{\infty,+} = (1-\eta)/\eta$, and $R_\Omega^{\infty,-} = -1$. This is discussed in detail in Longaretti and Dauchot (2005) and Dubrulle et al. (2005).

The most notable characteristics of this dependence are the following:

- The linear dependence on the rotation number, and quadratic one on the curvature number.

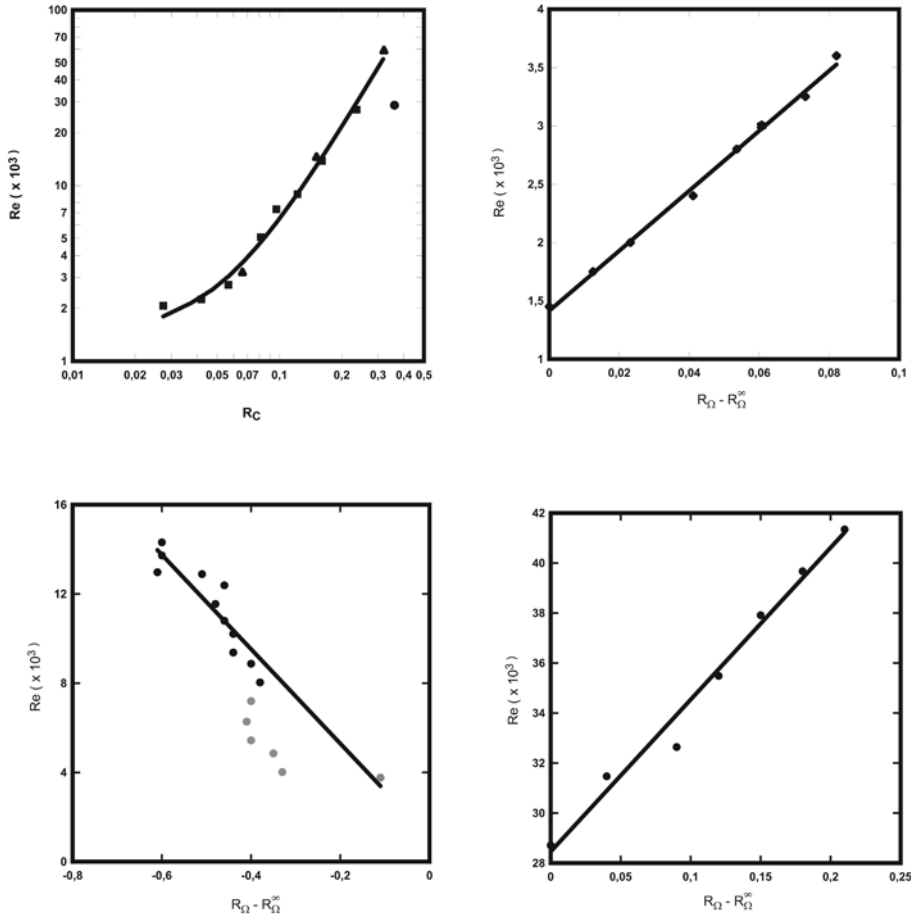

Figure 2. Data on subcritical transition. Upper left: data of Wendt (1933) and Taylor (1936), for cyclonic rotation, with the inner cylinder at rest, for varying η; this shows the dependence on the curvature number in cyclonic flows. Upper right: data of Tillmark and Alfredsson (1996) for rotating plane Couette flows ($\eta = 1$). Lower left and lower right: data of Richard (2001), for anticyclonic and cyclonic rotation, respectively ($\eta = 0.7$). On the last three graphs, the curvature number is held fixed, so that the data show the dependence of the transition Reynolds number on the rotation number. The solid lines represent best quadratic or linear fits to the data. $R_\Omega^\infty = (1-\eta)/\eta$ for cyclonic flows, and $R_\Omega^\infty = -1$ for anticyclonic ones.

- The rather steep dependence with both numbers ($a^\pm$ and b^+ are large numbers).
- The apparent symmetry between cyclonic and anticyclonic rotation number dependence, and the absence of dependence on the curvature on the anticyclonic side ($b^- \simeq 0$).

The next section discusses these features; in particular, the strength of this dependence is explained in order of magnitude on the basis of time-scale considerations.

4. DATA INTERPRETATION

The linear and quadratic dependence just pointed out can be viewed as the result of a Taylor expansion. For cyclonic rotation, this expansion is performed around the non-rotating plane Couette flow, first in terms of R_C along curve (4) on Figure 1, and then away from it, at constant R_C, in terms of R_Ω. For anticyclonic rotation, the expansion depends only on R_Ω, at least for $\eta > 0.7$, and is performed from the marginal stability state, at $R_\Omega \simeq -1$.

4.1 Linear dependence

The linear dependence with R_Ω is neater on the cyclonic data than on the anticyclonic one, but the data extend less far on the cyclonic side, unfortunately. The increased dispersion on the anticyclonic side has several reasons:

- Both cylinders need to be rotating at much higher speed than on the cyclonic side to reach the subcritical turbulent transition. This automatically reduces the precision of the measurements.
- The quantity R_Ω amplifies the uncertainty due to small errors in the determination of the cylinder angular velocities at transition.
- There is an important intrinsic difference between the cyclonic and anticyclonic marginal stability limits. On the cyclonic side, instability begins at a single location (the inner radius), whereas on the anticyclonic side, marginal stability applies throughout the fluid (this follows because the constant angular momentum solution is a laminar solution of the Taylor–Couette flow). Equivalently $2\delta\Omega(r) + \delta S(r) = 0$ at the anticyclonic marginal stability limit. Therefore, the fluid is much more sensitive to a potential linear instability. In particular, the unavoidable Eckmann circulation can much more easily make the criterion Equation (8) satisfied somewhere in the flow on the anticyclonic side than on the cyclonic one. We believe that this feature most likely explains why Richard's data show only a weak dependence of the transition Reynolds number on the rotation number out to $|1 + R_\Omega| \simeq 0.35$, and then a sharp increase to reach back the linearly varying regime. The related data points are shown as thin dots in the lower left quadrant of Figure 2, and not used in the linear fit.

Note that the mutual cancellation of a part of the curvature terms in Equation (4) at the anticyclonic marginal linear stability limit just pointed out also

provides a natural explanation for the apparent absence of dependence of the anticyclonic data on the curvature number.

4.2 Quadratic dependence

The quadratic dependence of the data on the gap width when keeping the inner cylinder at rest has already been pointed out by Zeldovich (1981), and (Richard and Zahn, 1999). At least three explanations of this behavior have been put forward in the literature (Zeldovich, 1981; Dubrulle, 1993; Longaretti, 2002). These will be commented below.

Let us first note that, in plane Couette flows, transition occurs at a constant Reynolds number $Re = \bar{S}d^2/\nu$. Therefore, at a given shear $\bar{S}$, the scale d is the characteristic scale of turbulence in such a system. Conversely, in the quadratic asymptotic regime, $[Re \propto (d/\bar{r})^2]$, transition occurs at constant $Re^* = \bar{S}\bar{r}^2/\nu$ $(= b^+)$, a point already made by Richard and Zahn (1999). Consequently, the characteristic radius $\bar{r}$ instead of the gap d characterizes the transition at a given shear. This unambiguously points out curvature and not rotation as the source of this behavior, consistently with the discussion of Section 2.

Dubrulle (1993): explains the quadratic behavior by considering the growth of finite amplitude local defects in the laminar profile. However, only WKB modes of instability created by the defects are considered, for which the scale $\bar{r}$ cannot play any role. This is why we believe that this analysis cannot capture the transition mechanism.

Zeldovich (1981): phenomenological explanation is based on the following two ideas:

- The transition Reynolds number may depend on the single time-scale ratio $Ty(r) = 4\kappa^2(r)/S^2(r)$ at some appropriately chosen radius in the flow: $R_g = f(Ty)$; $\kappa(r) = [2\Omega(2\Omega + S)]^{1/2}$ is the epicyclic frequency, i.e., the frequency of oscillation of the whole fluid, under the combined action of the shear and the Coriolis force.

- A "split-régime" of instability may occur, in which the inner portion of the flow undergoes a transition to turbulence at lower Reynolds number than the whole flow, once a large enough relative gap width is reached.

Considering the relative ambiguity in the distinction between the rotation and curvature time-scale discussed in Section 2, one may indeed ask whether a single time-scale would be sufficient to understand the data. This would imply that Taylor–Couette flows possess a hidden redundancy, and could be described by two appropriately chosen parameters, and not three. However, the extended set of data used here does not support this idea, although a larger body of experimental results is probably needed to ascertain this result.

Longaretti (2002) has developed an alternate phenomenology of subcritical shear flow turbulence. It relies on the one hand on a turbulent viscosity description, in which the characteristic length is identified to the top of the Kolmogorov cascade; on the other hand it makes use of the constraint that a subcritical shear flow is out of thermodynamic equilibrium and tries to restore equilibrium by transporting momentum across the shear, and, to do so, chooses the most efficient of the two means at its disposal (laminar or turbulent transport). This provides scaling laws for the characteristic length and velocity of turbulent eddies, by relating them to the Reynolds number of transition to turbulence. By further noting that for large enough gap widths, the turbulent eddies must unavoidably scale with the radius and not the gap, the quadratic régime is recovered.

4.3 Orders of magnitude

The last point we wish to address is the origin of the large values the coefficients a and b which appear in the characterization of the data performed in Equation (9). We mostly consider cyclonic flows, for which the physics is best understood

As mentioned in the introduction, an important breakthrough in the understanding of subcritical turbulence in non-rotating plane Couette flow comes from the work of Waleffe (1997), who analyzed by the means of quasi-linear theory a turbulent self-regeneration process previously observed in the numerical simulations of Hamilton et al. (1995). These last authors have tracked down turbulence to the smallest unit where it is self-sustained by reducing appropriately the simulation box size and the Reynolds number. A very important feature of the identified self-sustaining process is that it has a rather long time-scale compared to the shear:

$$t^{+}_{ssp} \sim 100\bar{S}^{-1}. \tag{10}$$

and that the scales involved in the self-regeneration mechanism are comparable to the flow width. This time-scale is the shortest of all the mechanisms found in the systematic reduction of the flow, and thus corresponds to the most robust one, which involves two streamwise rolls in the spanwise direction. These streamwise rolls, first observed by Dauchot and Daviaud (1995), typically scale on the gap width. Accordingly, it is very likely that such a long time-scale is a generic feature in non rotating plane Couette flows, because of the large ($R^{+}_{PC} \sim 1500$) Reynolds number of transition to turbulence which are always observed in these systems. Such a large Reynolds number constrains the viscous diffusion time at the scales involved in the self-regeneration mechanism. Typically for a length-scale $d/4$, the equality of the viscous time $t_\nu = (d/4)^2/\nu$ with t^{+}_{ssp} would indeed leads to $R_g = 1600$. Such a scale $(d/4)$ is characteristic

of the thickness of the streaks, apparently the smallest characteristic scale of the process.

From a physical point of view, one expects that the contributions of either rotation or curvature become comparable to R^+_{PC} in Equation (9) when the rotation or curvature time-scales decrease to become comparable to t^+_{ssp}. Correlatively, the fact that this happens when the rotation and curvature numbers are $\simeq 1/20$ comes as no coincidence. Indeed, the timescale associated with the Coriolis term is $t_\Omega \simeq (2\bar{\Omega})^{-1}$, while the timescale associated with the curvature terms is $t_\mathcal{C} \simeq (\delta\Omega)^{-1} \sim \bar{S}\bar{r}/d$. They become comparable to t^+_{ssp} as defined in Equation (10) when R_Ω or $R_\mathcal{C}$ exceeds 10^{-2}, which is remarkably close to the actual value of $1/20$, considering the qualitative nature of the argument. This physical constraint is also what primarily determines the magnitude of a^+ and b^+ (once the form of the dependence on R_Ω and R_c is known). Indeed, in rotating plane Couette flows, requiring $a^+ R_\Omega \gtrsim Re^+_{PC}$ when $R_\Omega \gtrsim 1/20$, implies that $a^+ \sim 10^4$. Similarly, in Taylor–Couette flows, requiring that $b^+ R^2_\mathcal{C} \gtrsim Re^+_{PC}$ when $R_\mathcal{C} \gtrsim 1/20$ leads to $b^+ \sim 10^5$.

One can see that the rather large values of the transition Reynolds number, as well as of the coefficients characterizing the effect of rotation (a^+) and curvature (b^+) can be ascribed to a single origin: the rather large ratio of the turbulence self-regeneration process to the shear time scale. Still, we do *not* infer that the self-sustaining mechanism proposed by Waleffe is valid in the presence of rotation. We just use the fact that in order to modify or even suppress this mechanism, the rotation or curvature effects must have timescales of the same order. On the contrary, the above analysis clearly indicates that a better understanding of this process in the framework of curved shear flows, and identifying it in the presence of rotation, is of primary importance for future progress.

The self-sustaining process has not yet been identified at the anticyclonic marginal stability limit, and its nature is not known. However, one can reverse the reasoning expressed right above to reach the conclusion that its characteristic time-scale is also $\sim 100\bar{S}^{-1}$. Testing this conjecture would bring support to the framework developed here to analyze and understand the data.

5. CONCLUSIONS AND IMPLICATIONS

We feel that this work brings to light a few important points, which we believe to be of potentially more general applicability than what was done here:

- It is both meaningful and useful to decompose the Navier–Stokes equation into a laminar part of the flow, and a deviation from the laminar flow. This helps identifying the relevant time-scales in the flow, and isolating which "portion" of the advection term is directly related to the physics

described by the Reynolds number. The same procedure is also useful to relate various flows to one another.

- The general trends and features of the transition Reynolds number data can be understood with the help of the previously identified time-scales, and over a reasonably extended fraction of the parameter space, once the turbulence self-sustaining process time-scale is identified at one point in the parameter space. The procedure in turns constrains to some extent the time-scale of the self-sustaining process in the domain where data are available, a point we have only briefly touched upon in the preceding section.

In the process, we have tried to elucidate a little more the relation between the flow global rotation and its global curvature. We found that rotation and curvature effects most probably cannot be accounted for by a single time-scale, as suggested by Zeldovich (1981), but that two time-scales are required, in accordance with the fact that Taylor–Couette flows are characterized by two dimensionless numbers besides the Reynolds number.

The data described here, and the analysis we have developed, have some bearing to a related astrophysical problem, namely, the existence of subcritical turbulence in Keplerian accretion disks, a question which has been the object of an important debate in the astrophysical community over the three or four past decades. Such disks are observed in relation to the formation of young stars; they are also believed to be present in a variety of other astrophysical objects, such as active galactic nuclei, microquasars, and so on. A large scale Keplerian profile ($\Omega(r) \propto r^{-3/2}$) follows if the disk is cold enough. The profile can nevertheless stochastically deviate from Keplerian on scales comparable to the disk scale height $h \ll r$. Young (proto-)star disks are also probably not ionized enough for MHD processes to be relevant over a significant fraction of their extent.

The microscopic transport in these disks is known to be many orders of magnitude smaller than the one inferred from the observations, so that these disks are believed to be turbulent. Hydrodynamic Keplerian disks are linearly stable in their most simple flavors. It was believed until the mid-90s that they were nevertheless hydrodynamically turbulent, on the basis of the experimental evidence of subcritical turbulence in non-rotating Couette flows.

This belief was challenged by the numerical simulations of Balbus et al. (1996) and Hawley et al. (1999). These authors have studied whether Keplerian disks are locally turbulent, by reducing the Navier–Stokes equation in the disk to Equation (3), with "shearing-sheet" boundary conditions (they ignore the disk vertical stratification), thus asking the question in a framework which is extremely close to the one studied here. They found that a dynamically significant and stabilizing Coriolis force prevents the appearance of turbulence for

Keplerian-like flows ($R_\Omega = -4/3$), up to to the highest resolution achieved in the simulation (256^3 with finite-difference codes; see the referenced papers for detail).

These simulations have had a very large impact in the astrophysics community, where the now most largely spread opinion is that a linear instability is needed for turbulence to show up, a somewhat excessive position. However, the experimental results of Richard (2001), seem to imply that Keplerian-like flows should be turbulent at very modest (in astrophysical standards) Reynolds numbers. The problem is currently reinvestigated from a numerical point of view (Lesur and Longaretti, *in preparation*). Preliminary results indicate that the Coriolis force does not prevent the existence of turbulence in rotating plane Couette flows, but of course alters the turbulence properties, as one would expect. However, the relevance of subcritical hydrodynamic turbulence to accretion disk transport remains to be more precisely investigated.

NOTES

1. The convention adopted here is that the sign of S is chosen to be positive when the flow is cyclonic, i.e., when the contributions of shear and rotation to the flow vorticity have the same sign. With the usual choice of axes in plane Couette flows, this implies that $S = -2S_{xy}$, where S_{ij} is the usual deformation tensor.

2. This definition differs from the usual one by a factor of 4; this convention is adopted here for consistency with the treatment of Taylor–Couette flows.

3. The shear of the laminar flow is defined as $S = rd\Omega/dr = 2S_{r\phi}$ in order to maintain the sign convention adopted for rotating plane Couette flows for cyclonic and anticyclonic rotation.

4. In the identification of the two equations, note that $r \longleftrightarrow y$ and $\phi \longleftrightarrow -x$. Also, $\delta\Omega \simeq \bar{S}(r-\bar{r})/\bar{r}$, an approximation which holds to $\sim 10\%$ for the range of η explored in the available experiments, a feature needed in the comparison of Equations (3) and (4).

5. We use the same Reynolds number definition for rotating plane Couette and Taylor–Couette flows, based on the total gap width and total velocity difference. Consequently, the quoted Reynolds numbers for plane Couette flows differ from the ones in the literature by a factor of 4.

REFERENCES

Andereck, C.D., Liu, C.C. and Swinney, H.L. (1986). Flow regimes in a circular Couette system with independently rotating cylinders. *J. Fluid Mech.* **164**, 155–183.

Balbus, S.A., Hawley, J.F. and Stone, J.M. (1996). Nonlinear stability, hydrodynamical turbulence, and transport in disks. *Astrophys. J.* **467**, 76–86.

Bottin, S., Dauchot, O., Daviaud, F. and Manneville P. (1998). Experimental evidence of streamwise vortices as finite amplitude solutions in transitional plane Couette flow. *Phys. Fluids* **10**(10), 2597–2607.

Clever, R.M. and Busse, F.H. (1997). Tertiary and quaternary solutions for plane Couette flow. *J. Fluid Mech.* **344**, 137–153.

Dauchot, O. and Daviaud, F. (1995). Finite amplitude perturbation and spot growth mechanism in plane Couette flow, *Phys. Fluids* **7**, 335–343.

Dubrulle, B. (1993). Differential rotation as a source of angular momentum transfer in the Solar Nebula. *Icarus* **106**, 59–76.

Dubrulle, B., Dauchot, O., Daviaud, F., Longaretti, P.-Y., Richard, D. and Zahn, J.-P. (2005). Stability and turbulent transport in rotating shear flows: prescription from analysis of cylindrical and plance Couette flow data. *Phys. Fluids*, accepted for publication.

Esser, A. and Grossmann, S. (1996). Analytic expression for Taylor–Couette stability boundary. *Phys. Fluids* **8**, 1814–1819.

Faisst, H. and Eckardt, B. (2003). Travelling waves in pipe flow. *Phys. Rev. Lett.* **91**, 224502.

Hamilton, J.H., Kim, J. and Waleffe, F. (1995). Regeneration mechanisms of near-wall turbulence structures. *J. Fluid Mech.* **287**, 317–348.

Hawley, J.F., Balbus, S.A. and Winters, W.F. (1999). Local hydrodynamic stability of accretion disks. *Astrophys. J.* **518**, 394–404.

Longaretti, P.-Y. (2002). On the phenomenology of hydrodynamic shear turbulence. *Astrophys. J.* **576**, 587–598.

Longaretti, P.-Y. and Dauchot, O. (2005). Global rotation-curvature time-scales, and the subcritical transition to turbulence in shear flows. *Phys. Fluids*, submitted.

Nagata, M. (1990). Three-dimensional finite-amplitude solutions in plane Couette flow: Bifurcation from infinity. *J. Fluid Mech.* **217**, 519–527.

Prigent, A., Grégoire, G., Chaté, H. and Dauchot, O. (2003). Long wavelength modulation of turbulent shear flows. *Physica D* **174**, 100–113.

Richard, D. (2001). *Instabilités hydrodynamiques dans les écoulements en rotation différentielle*. PhD Thesis, Université de Paris VII.

Richard, D. and Zahn, J.-P. (1999). Turbulence in differentially rotating flows. *Astron. Astrophys.* **347**, 734–738.

Taylor, G.I. (1936). Fluid friction between rotating cylinders. *Proc. Roy. Soc. London A* **157**, 546–564.

Tillmark, N. and Alfredsson, P.H. (1996). Experiments on rotating plane Couette flow. In *Advances in Turbulence VI*, Gavrilakis et al. (eds), Kluwer, Dordrecht, pp. 391–394.

Waleffe, F. (1997). On a self-sustaining process in shear flows. *Phys. Fluids* **9**, 883–900.

Waleffe, F. (1998). Three-dimensional coherent states in plane shear flows. *Phys. Rev. Lett.* **81**, 4140–4143.

Waleffe, F. (2003). Homotopy of exact coherent structures in plane shear flows. *Phys. Fluids* **15**, 1517–1534.

Wendt, G. (1993). Turbulente Strömung zwischen zwei rotierenden konaxialen Zylindern. *Ing. Arch.* **4**, 577–595.

Zeldovich, Y.B. (1981). On the friction of fluids between rotating cylinders. *Proc. Roy. Soc. London A* **374**, 299–312.

THE KARHUNEN–LOÈVE DECOMPOSITION OF THE AUTONOMOUS MINIMAL FLOW UNIT

D. Desmidts and D. Carati
Université Libre de Bruxelles, Statistical and Plasma Physics, Bld. du Triomphe, Campus Plaine – CP 231, B-1050 Brussels, Belgium

Abstract We propose to examine the effects of restricting the interaction between near-wall turbulence and the outer flow on the structure and dynamics of the empirical eigenfunctions functions determined using the proper orthogonal decomposition (POD). This research is motivated by the fact that standard POD-based low-dimensional models for the near-wall region have been derived for empirical eigenfunctions computed for an unbiased channel flow. However, under the present truncation of the flow dynamics, the POD basis may be significantly affected so that the common assumption that effective reduced-order models can be constructed from the POD basis of an unaltered flow may be suspect. This issue is explored for plane, incompressible, turbulent channel flow at Reynolds number, $Re_\tau = 180$. Based on direct numerical simulations, POD basis functions are constructed for an unbiased and four truncated minimal channel flows. The POD eigenfunctions which characterize these modified flows are associated to a travelling-wave solution which undergoes a series of bifurcation until settling into a turbulent regime. A POD-based two-mode model is also derived for the near-wall layer and is evaluated. It is shown that travelling-wave solutions appear as a backbone to the low-dimensional dynamics of the autonomous near-wall region.

Keywords: coherent structures, near-wall turbulence, POD.

1. INTRODUCTION

It is now well-established that near-wall coherent structures that have been studied experimentally for about 50 years play a major role in transport mechanism of wall turbulence. It has been found that the increased drag and heat transfer in turbulent boundary layers are due to streamwise velocity streaks and quasi-streamwise vortices which dominate the near-wall region. The near-wall vortical coherent structures are observed to burst, transferring energy from the large to the small scales and producing turbulent fluctuations. This bursting

T. Mullin and R.R. Kerswell (eds), Laminar Turbulent Transition and Finite Amplitude Solutions, 145–161.
© 2005 *Springer. Printed in the Netherlands.*

process is responsible for the production of most of the turbulent kinetic energy in turbulent boundary layer.

Even if coherent structures have deeply changed our views on the statistical nature of turbulence, their description has been limited to a qualitative level for a long time. A first quantitative approach has been initiated by Aubry et al. (1988) who developed a mathematical model of the coherent structures under the scope of finite-dimensional dynamical-systems theory. This was achieved by projecting Navier–Stokes equations on the most energetic empirical eigenfunctions issued from the proper orthogonal decomposition (POD) of the near-wall region. It was found that turbulence is sustained not by a random process but by a quasi-cyclic process passing quiescent and activated periods in turn. Moreover, this low-dimensional model predicted values of the bursting period which are resonably similar to measurements.

The eigenfunctions of the POD were extracted from hot film anemometry data provided by Herzog's (1986) experiment for a pipe flow. However, such experiments required collection of large amounts of data. A more affordable tool for studying near-wall turbulent flow was introduced by Jiménez and Moin (1991). This so-called "minimal flow unit" corresponds to the smallest such computational box in which turbulence may be sustained. Accordingly, reduced dynamical models based on this approach have been formulated to examine the elementary processes of turbulent generation in the near-wall region.

A somewhat different model, but again based on orthogonal modes, has been developed by Waleffe (1997). This model also exhibits a self-sustaining process in which an interaction between streamwise rolls and the mean shear leads to the development of streaks. The streaks then become unstable and break down to recreate rolls. This so-called self-sustaining process (SSP) seems to reproduce most of the features of near-wall turbulence.

More recently, traveling-wave solutions (TWS) in minimal channel flow were identified by Waleffe (1998) and Toh and Itano (1999), suggesting a dynamical reformulation of the bursting process, that is, turbulent generation in the near-wall region. Jiménez and Pinelli (1999) showed, by means of numerical experiments which mask the influence of the outer flow, that this generation cycle is autonomous, in the sense that it can run by itself without any input from the exterior. Moreover, the autonomous region is able to run on a single copy of the fundamental TWS solution in a minimal channel (Jiménez and Simens, 2001).

In the present work, the Proper Orthogonal Decomposition (POD) (see Lumley, 1971) is applied to a set of datafields extracted from a DNS of a minimal autonomous-wall turbulent channel flow in order to investigate the spatiotemporal properties of the velocity field and to extract information on coherent structures in the autonomous near-wall region. Characteristic struc-

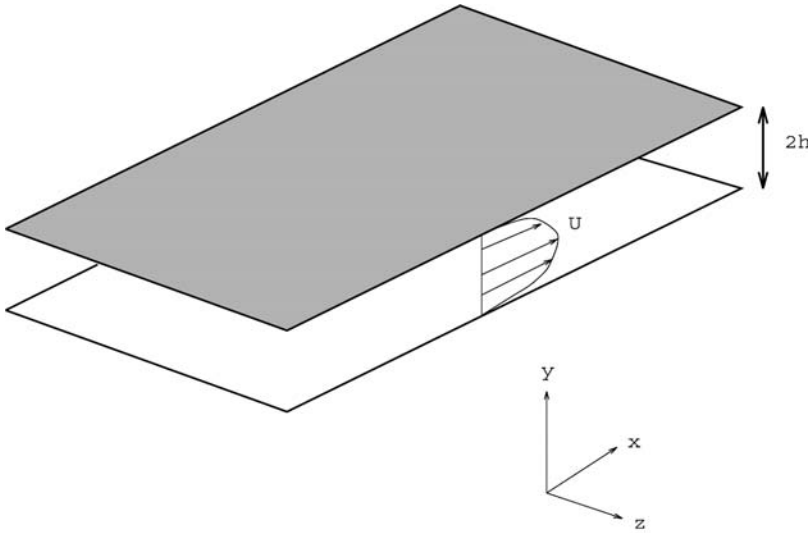

Figure 1. The flow configuration.

tures are computed in terms of POD eigenfunctions which are used to derive a two-mode model for the autonomous near-wall region.

2. NUMERICAL METHOD

2.1 Minimal channel flow

Let us consider the pressure-driven turbulent flow between two infinite parallel plates as shown schematically in Figure 1. In the present study, x, y and z denote the streamwise, the wall-normal and the spanwise coordinates, respectively. The corresponding velocities are u, v and w. Alternatively an index is used to denote a coordinate direction x_i, or a velocity component u_i.

The governing equations are the Navier–Stokes equations for an incompressible flow between two parallel plates and driven by a uniform pressure gradient can be expressed in the following dimensionless form:

$$\nabla \cdot \mathbf{u} = 0, \tag{1}$$

$$\frac{\partial \mathbf{u}}{\partial t} + (\mathbf{u} \cdot \nabla)\,\mathbf{u} = -\nabla p + \frac{1}{Re_\tau}\nabla^2 \mathbf{u}. \tag{2}$$

Here, velocities u_i are scaled by the friction velocity $u_\tau = \sqrt{\nu \partial U/\partial y}$,where ν is the kinematic viscosity, and coordinates x_i are scaled by the half width of the channel, h. Time is scaled by h/u_τ, and the friction Reynolds number is defined as $Re_\tau = u_\tau h/\nu$. We can also refer to velocity, length, and time in

local wall units expressed as $u_i^+ = u_i/u_\tau$, $x^+ = x_i/\delta_\tau$, $t^+ = tu_\tau/\delta_\tau$ where $\delta_\tau = \nu/u_\tau$ denotes the viscous length scale.

The numerical method used in the present study of Equations (1–2), is the same as that of Moin et al. (1987). The Navier–Stokes equations are integrated in the form of evolution equations for the wall-normal vorticity ω_y and for $\phi = \nabla^2 v$, using a pseudospectral code with Fourier expansions in the two wall-parallel directions and Chebychev polynomials in the wall-normal direction y:

$$\mathbf{u}(\mathbf{x}, t) = \sum_{m=-\frac{n_x}{2}}^{\frac{n_x}{2}-1} \sum_{n=-\frac{n_z}{2}}^{\frac{n_z}{2}-1} \sum_{p=0}^{P} a_{mnp}(\mathbf{x}, t)\ T_p(y) \exp(ik_x x) \exp(ik_z z),$$

where $T_p(y)$ denotes the Chebyshev polynomials, $k_x = 2\pi m/L_x$, and $k_z = 2\pi n/L_z$, where L_x and L_z are the domain lengths in the x and z directions, respectively. A third-order Runge–Kutta scheme and a second-order Crank–Nicholson scheme are used for the discretization of the nonlinear terms and the viscous terms, respectively.

In this paper, we consider turbulence in a minimal channel flow (called hereafter MCF), i.e. the narrowest channel for fixed length in which turbulence is maintained on both walls. In our simulations, the box lengths were set to $L_x = 2\pi h/3\ \left(\simeq 360^+\right)$ and $L_z = \pi h/3\ \left(\simeq 180^+\right)$, and the resolution was in $32 \times 129 \times 32$ the wall normal, streamwise, and spanwise directions, respectively. The friction Reynolds number Re_τ is fixed to 180 and the mass flow rate is kept constant.

2.2 Autonomous solutions

The solutions described below as "autonomous" are computed using the numerical scheme described by Jiménez and Simens (2001). At each time step, the right-hand sides of the two evolution equations for the wall-normal vorticity ω_y and for $\phi = \nabla^2 v$, are multiplied by a damping filter

$$F(y) = 1 \qquad \text{if } y^+ \le \delta_1^+$$
$$F(y) = F_0 < 1 \ \text{ if } y^+ \ge \delta_2^+.$$

with the two limits connected smoothly by a cubic spline. For the solutions considered in this paper $\delta_2^+ = 1.5\,\delta_1^+$. Because the filter is very effective in damping the vorticity fluctuations, we use $F_0 = 0.95$, and the damping is effective approximately midway between δ_1^+ and δ_2^+. Higher values for F_0 were tested and were shown to have negligible impact on the dynamics of the flow. The evolution equations are not modified below the mask lower limit δ_1^+, but F_0 is large enough for all the vorticity fluctuations to be effectively damped above $y \simeq \left(\delta_1^+ + \delta_2^+\right)/2$. The autonomous solutions are initialized from a statistically converged instantaneous field from the minimal channel

Table 1. Characteristics of minimal channels used. U_0 is the bulk flow velocity, and h the channel half-width. L_x and L_z are the streamwise and spanwise lengths of the periodic computational box. Δ_x and Δ_z the horizontal grid spacings after dealiasing, and Δ_y the distance to the wall from the first y grid collocation point. N_x and N_z are Fourier modes after dealiasing. t is the time over which statistics are collected, after discarding the initial transient.

Simulation	$\frac{U_0 h}{\nu}$	$\frac{u_\tau h}{\nu}$	L_x^+	L_z^+	Δ_x^+	Δ_y^+	Δ_z^+	N_x	N_y	N_z	$\frac{U_0 t}{h}$	$\frac{u_\tau t}{\delta_\tau}$
Minimal Flow Unit	15000	180	377	188	11.78	5.89	0.0542	48	129	48	2375	27000
Autonomous Run 1	8000	104.94	230	115	7.20	3.60	0.0316	48	129	48	5120	36300
Autonomous Run 2	9000	116.53	240	120	7.52	3.76	0.0351	48	129	48	5120	37950
Autonomous Run 3	10000	119.17	250	125	7.85	3.93	0.0359	48	129	48	5120	39600
Autonomous Run 4	11000	123.42	260	130	8.18	4.09	0.0362	48	129	48	5120	41250

Simulation	δ_1^+	δ_2^+	F_0
Autonomous Run 1	49	72	0.95
Autonomous Run 2	69	119	0.95
Autonomous Run 3	72	127	0.95
Autonomous Run 4	83	153	0.95

flow simulation described above. Direct numerical simulations were made for a range of values between the minimal filter height $\delta_1^+\big|_{\min} \simeq 49$ under which the flow relaminarizes and an upper value $\delta_1^+\big|_{\max} \simeq 83$ for which we start to get self-sustaining bursting turbulence.

The parameters of the simulations presented in this paper are summarized in Table 1.

3. TURBULENCE STATISTICS

3.1 Standard MCF

Using the methods defined here above, we have simulated turbulence in a standard minimal channel for a time of approximately $150\,h/u_\tau$ at $Re_\tau = 180$. We find fully developed turbulent activity on both walls for the box size considered. Even if the activity on one wall tended to dominate over the other through some portions of the simulation, this effect did not cause a noticeable asymmetry in the mean velocity profile or any other statistics that we examined.

3.2 Autonomous MCF

In the case of the filtered channel, the volumetric flux is adjusted so that its Reynolds number would have been equal to the $Re_\tau = 180$ of the undamped minimal flow unit. As can be seen in Figure 3(a), the flow relaminarizes in

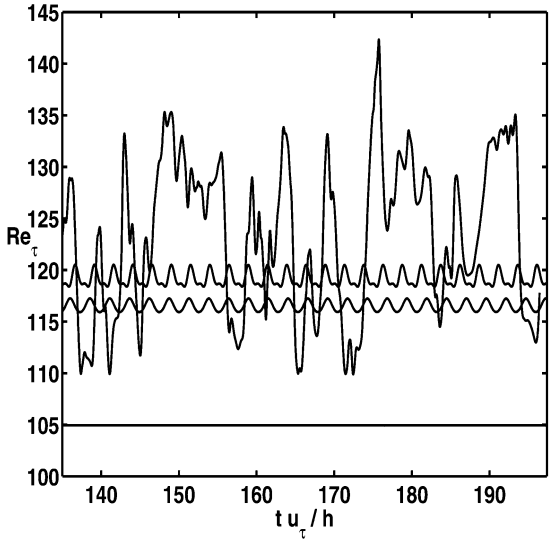

Figure 2. Wall friction time series.

the region in which the filter is active and displays a parabolic mean velocity profile which carries much of the total mass flux. In the autonomous near-wall region, the flow stabilizes after a substantially long transient to a relatively low final Reynolds number which ranges between $Re_\tau = 110$ and $Re_\tau = 125$ (see Table 1). Since no turbulent flow extends to the far wall, the relevant turbulent Reynolds number is the one based on the filter height of the damping function $\delta_1^+ = u_\tau \delta_1 / \nu$.

The mask acts as a relaminarizing filter which induces a kink in the vorticity profiles (see Figures 3(b) and 3(c)) due to reconnection of vortex filaments in the irrotational region. Figure 3(d) shows that the mean velocity profiles are in good agreement with the linear scaling of the inner region while they exhibit an abortive logarithmic layer in which the velocity decreases slightly before recovering the laminar profile. The time behaviour of the flow is monitored by the evolution of the averaged wall-shear histories. As seen in Figure 2, we observe a stationary friction coefficient for $\delta_1^+ = 49$. As described in Jiménez and Simens (2001), the flow in the near-wall region is a travelling wave (see Figure 5(a)) moving at constant speed. As the mask height increases, the dynamics of the travelling wave switches to a periodic and quasi-periodic motion for $\delta_1^+ = 69$ and 72 respectively. For higher values of the filter, the flow metastable states of bursting turbulence appear.

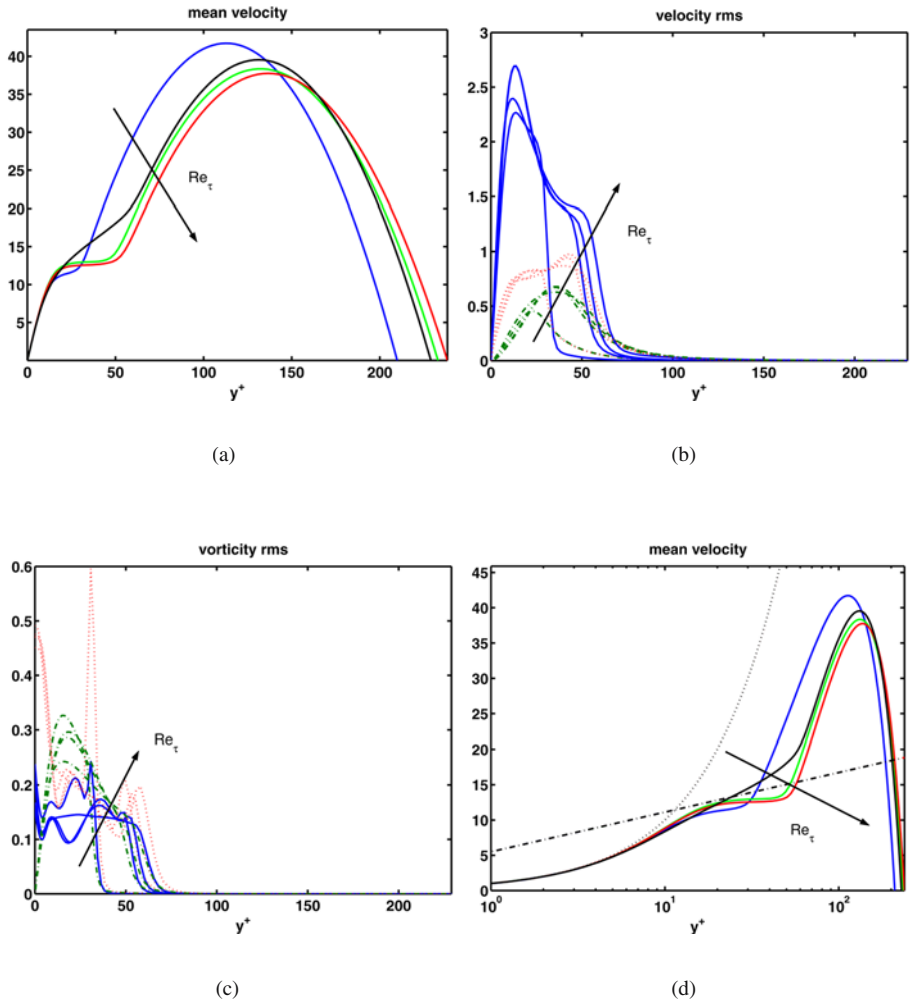

Figure 3. (a) Mean streamwise velocity. (b) RMS velocity fluctuations. Solid line: u^{rms}, dashdotted line: v^{rms}, small dotted line: w^{rms}. (c) RMS vorticity fluctuations. Solid line: ω_x^{rms}, dashdotted line: ω_y^{rms}, small dotted line: ω_z^{rms}. (d) Mean streamwise velocity (logarithmic plot).

4. PROPER ORTHOGONAL DECOMPOSITION

The results of our DNS in standard and autonomous minimal channels are analyzed by the POD. The ideas stem from Lumley's (1971 suggestion of decomposing the flow into a sum of eigenfunctions ϕ_i of the two-point correlation tensor. In homogeneous directions, POD eigenmodes are simply Fourier modes. In the wall-normal direction and in Fourier space, the eigenfunctions

ϕ^n associated with the eigenvalue λ^n are solutions of

$$\int \left\langle \widehat{u}^i_{\mathbf{k}}(y,t)\, \widehat{u}^{*j}_{\mathbf{k}}\left(y',t\right)\right\rangle \phi^{nj}_{\mathbf{k}}\left(y'\right)\, dy' = \lambda^n_{\mathbf{k}} \phi^{ni}_{\mathbf{k}}(y)\,, \tag{3}$$

where $\widehat{u}^i_{\mathbf{k}}(y,t)$ and $\left\langle \widehat{u}^i_{\mathbf{k}}(y,t)\, \widehat{u}^{*j}_{\mathbf{k}}\left(y',t\right)\right\rangle$ represent the Fourier transform in the homogeneous directions of respectively the velocity field and the spatial autocorrelation tensor at zero time lag $R_{ij}\left(x-x', y, z-z'\right)$ and $\langle\ \rangle$ denotes an ensemble average. Let $\mathbf{k} = (k_1, k_3)$. The velocity field is then decomposed as follows:

$$\widehat{u}^i_{k_1,k_3}(y,t) = \sum_{k_1,k_3,n} a^n_{k_1,k_3}(t)\, \phi^{ni}_{k_1,k_3}(y). \tag{4}$$

We chose to normalize the eigenfunction such that

$$\int_{domain} \phi^{ni}_{k_1,k_3}(y)\, \phi^{*ni}_{k_1,k_3}(y)\ dy = 1 \tag{5}$$

so that, by definition (4) of the eigenfunction,

$$\left\langle a^n_{k_1,k_3}(t)\, a^{*n}_{k_1,k_3}(t)\right\rangle = \lambda^n_{k_1,k_3}. \tag{6}$$

represents the energy in each KL mode. Consequently, the eigenfunctions can be sorted according to their contribution to the turbulent kinetic energy. In this paragraph we solve Equation (3). Our procedure is very similar to Moin and Moser's (1989) who applied the POD to the simulation of a fully developed turbulent channel flow. To compute the kernel, i.e. the Fourier transform of the autocorrelation tensor, we used an ensemble average over velocity fields taken at sufficiently large time intervals to be uncorrelated. The database consists of 3000 time samples for the standard minimal channel, and 4000 time samples for the autonomous case.

4.1 POD eigenvalues

Figure 4 displays the energy spectra for the streamwise-independent eigenmodes for each simulation, after having discarded the contribution of the mean flow $k_x = 0, k_z = 0$ to the Karhuenen–Loève expansion. The main conclusion that can be drawn from these results is that the effect of the filter is to reduce strongly the contribution from higher k_z modes. This result supports the expectation that the autonomous wall-region has less structural complexity making the fundamental turbulent mechanisms easier to identify.

4.2 POD eigenfunctions

In Figures 4(a) and 4(b), we show the y-dependence of the first streamwise-independent eigenfunctions for $k_x = 0, k_z = 1, n = 1$ and for $k_x = 0, k_z =$

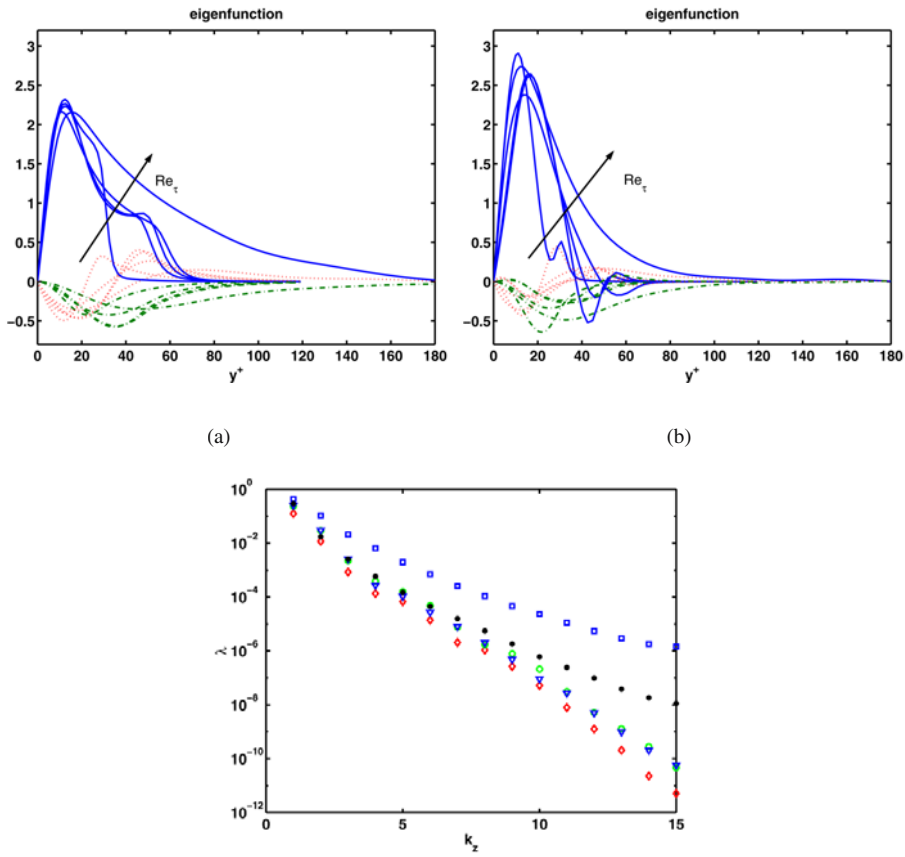

Figure 4. Spatial structure of the first eigenfunctions: (a) Solid line: $\phi^1_{k_x=0,k_z=1,n=1}$, dashed dotted line: $\phi^2_{k_x=0,k_z=1,n=1}$, small dotted line: $\phi^3_{k_x=0,k_z=1,n=1}$. (b) Solid line: $\phi^1_{k_x=0,k_z=2,n=1}$, dashed dotted line: $\phi^2_{k_x=0,k_z=2,n=1}$, small dotted line: $\phi^3_{k_x=0,k_z=2,n=1}$. Energy spectrum for the most energetic eigenmode: (c) Diamonds: $\delta_1^+ = 49$, circles: $\delta_1^+ = 69$, triangles: $\delta_1^+ = 72$, dots: $\delta_1^+ = 72$, squares: unfiltered channel.

$2, n = 1$ for the standard and autonomous case. We have chosen to present these particular modes since we intend to develop a two-mode model by projecting the Navier–Stokes onto the most energetic eigenfunctions of the $k_x = 0$ subspace as done in Podvin and Lumley (1998).

We still note the appearance of a kink in the eigenfunctions just above the filter height δ_1. The most significant feature to observe for each case study is that the most energetic empirical eigenfunctions are strongly affected by

the filtering above $y^+ = 20$, in agreement with the mean velocity profiles in Figure 3(d). The bifurcations observed in the flow dynamics are thus closely linked to the parametric modulation of the mean profile in the pseudo-log region connecting the viscous layer to the laminar region for the different filter heights considered.

4.3 POD plane wave modes

As a result of the fact that the flow is unbounded in the x and z directions, the eigenfunctions take on the following form in the physical space

$$\psi^n_{k_1,k_3}(\mathbf{x}) = \phi^n_{k_1,k_3}(y)\exp(ik_x x)\exp(ik_z z) \tag{7}$$

so that the empirical eigenfunctions can naturally be regarded as plane waves. The POD eigenfunctions can be divided into two categories: roll modes, which have no streamwise dependence ($k_x = 0$) and propagating modes, which have streamwise dependence ($k_x \neq 0$). Figure 5(b) and 5(c) show the structure of the most energetic roll ($k_x = 0, k_z = 1, n = 1$) and propagating mode ($k_x = 1, k_z = 1, n = 1$) respectively. A study by Keefe et al. (1990) has showed that roll modes dominate the energetics of the flow. As a result we will only consider the contribution of roll modes to the dynamics of the travelling wave solution. As seen in Figure 5(a), this wave consists of a low-velocity streak associated to a pair of quasi-streamwise vortices.

The projection of the flow along the roll modes is used to characterize their contribution to the travelling wave solution. In Figures 6(a)–(b) and Figures 6(c)–(d), we plot the history of the modulus and phase for the amplitude $a^n_{k_x,k_z}$ coefficient of the first two roll modes. Since the phase is defined by

$$\theta^n_{k_x,k_z} = \tan^{-1}\left[Im\left(a^n_{k_x,k_z}\right)/Re\left(a^n_{k_x,k_z}\right)\right], \tag{8}$$

it is clear that both modes have a secular time course described by a characteristic frequency

$$\omega^n_{k_x,k_z}(\mathbf{x}) = \lim_{t\to\infty}\frac{\theta^n_{k_x,k_z}}{t}. \tag{9}$$

This result reveals the existence of propagating plane waves moving along the spanwise direction for the roll modes considered. In physical space, these travelling waves correspond to a pair of streamwise vortices drifting in the transverse z-direction. In addition to the modulus time series, phase portraits in Figures 7(a)–(b) show that, for $\delta_1^+ = 69$, the roll-mode components bifurcate to a solution winding quasi-periodically on a torus, that is a modulated travelling wave.

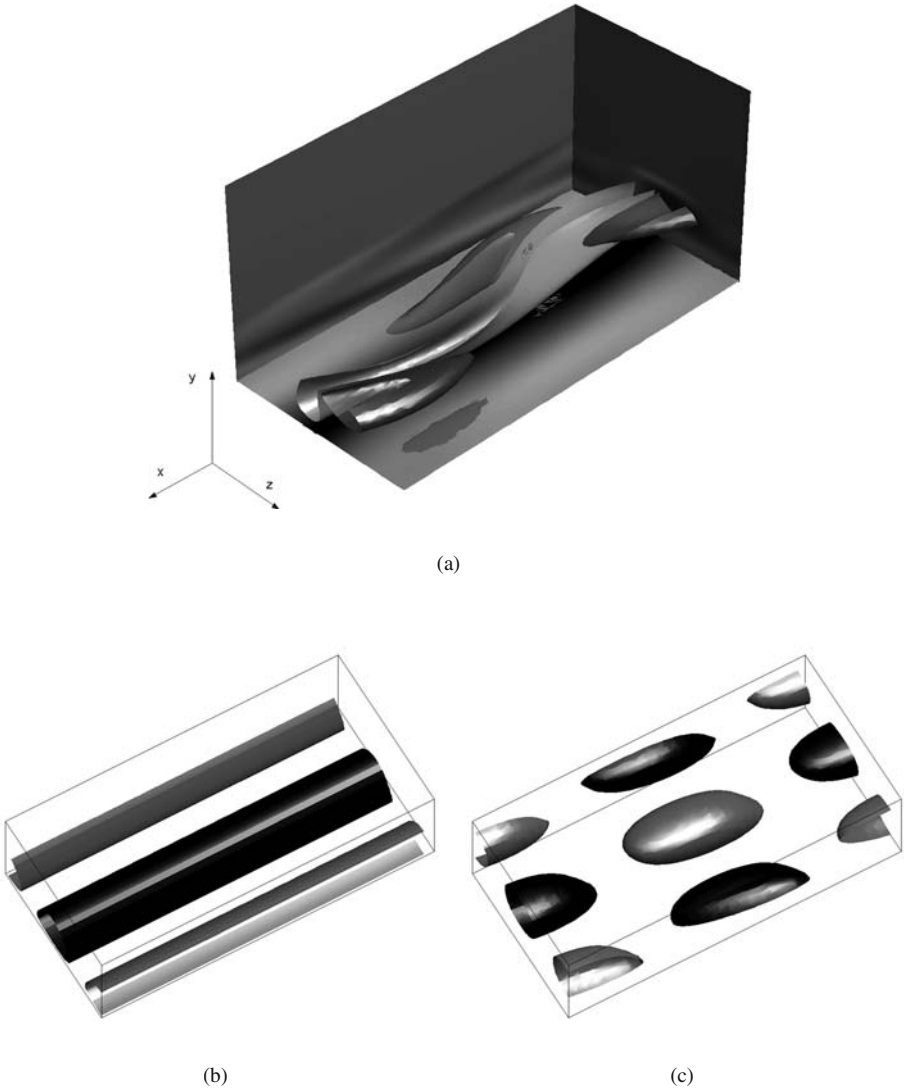

Figure 5. (a) Flow visualization for $\delta_1^+ = 69$, dark grey: vorticity isosurface for $\omega_x^+ = \pm 0.12$, light grey: velocity isosurface for $u'^+ = -2$. (b) Most energetic roll mode, grey: velocity isosurface for $u'^+ = -2$, black: velocity isosurface for $u'^+ = 2$. (c) Most energetic propagating mode. Same legend as (b).

4.4 Low dimensional model

In this section, we analyse the prediction of a two-mode model for the amplitude of the POD modes. This severely truncated model results from the

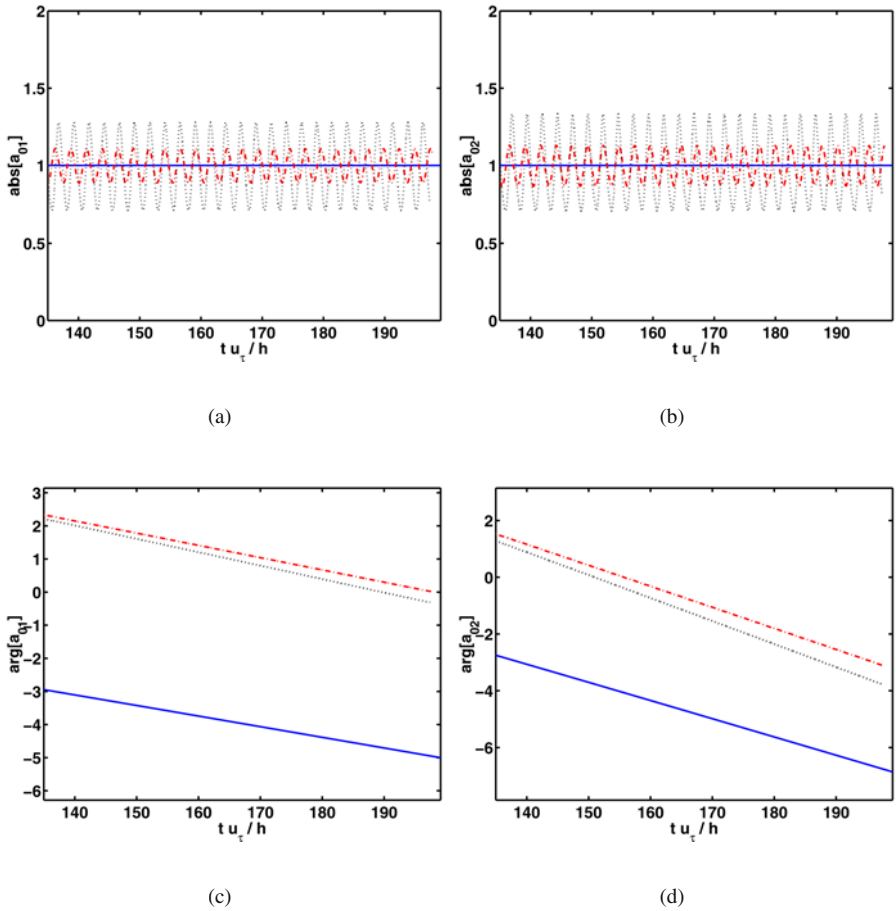

Figure 6. Time histories of the POD modes computed from DNS. Solid line: $\delta_1^+ = 49$, Dashed line: $\delta_1^+ = 69$, Dotted line: $\delta_1^+ = 72$.

projection of the Navier–Stokes equations onto the finite set of POD modes

$$T_{0,1,2} = \left\{ a^n_{k_x,k_z} \mid |k_x| \leq 0, |k_z| \leq 2, n \leq 1 \right\}$$

which represents the first two most energetic roll modes and was introduced by Podvin and Lumley (1998) as the simplest POD-derived model for the low-dimensional dynamics in a minimal flow unit.

It belongs to the class of four-dimensional systems with SO(2) symmetry, which corresponds in physical space to invariance by horizontal translations and invariance by reflection with respect to a plane parallel to the directions x

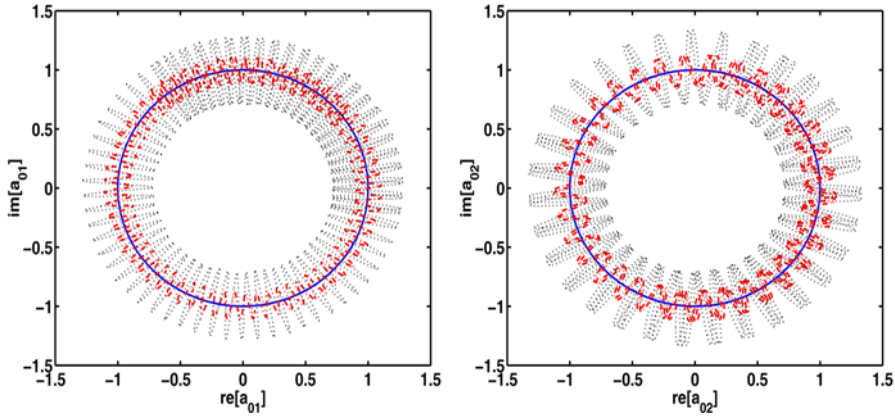

(a) (b)

Figure 7. Phase portraits of the POD modes computed from DNS . Solid line: $\delta_1^+ = 49$, Dashed line: $\delta_1^+ = 69$, Dotted line: $\delta_1^+ = 72$.

and z. In our particular case, the system of ODEs can be written as

$$\dot{a}_1 = \mu_1 a_1 + c_{-1,2} a_1^* a_2 + \left(d_{11} \left|a_1\right|^2 + d_{12} \left|a_2\right|^2\right) a_1, \tag{10}$$

$$\dot{a}_2 = \mu_2 a_2 + c_{1,1} a_1^2 + \left(d_{21} \left|a_1\right|^2 + d_{22} \left|a_2\right|^2\right) a_2, \tag{11}$$

where $\mu_k = b_k^1 - (1 + \alpha \nu_T)\, b_k^2$ and $a_k = a_{0,k}^1$. The bifurcation parameter μ_k represents the balance between the supply from the mean shear and the dissipation to smaller scales.

If we pose $a_j = r_j\, e^{i\theta_j}$, Equations (10–11) can be reduced to

$$\dot{r}_1 = r_1 r_2 cos\, \phi + \left(\mu_1 + e_{11} r_1^2 + e_{12} r_2^2\right) r_1, \tag{12}$$

$$\dot{r}_2 = -r_1^2 cos\, \phi + \left(\mu_2 + e_{21} r_1^2 + e_{22} r_2^2\right) r_2, \tag{13}$$

$$\dot{\phi} = \left(-2r_2 - r_1^2/r_2\right) sin\, \phi, \tag{14}$$

where $e_{11} = d_{11}/\left|c_{11} c_{-1,2}\right|$, $e_{12} = d_{12}/\left|c_{-1,2}\right|^2$, $e_{21} = d_{11}/\left|c_{11} c_{-1,2}\right|$, $e_{22} = d_{22}/\left|c_{-1,2}\right|^2$. In the case when $c_{11} c_{-1,2} < 0$, possible equilibrium solutions for this system include fixed points coexisting over a finite domain in (μ_1, μ_2) with travelling waves (see Armbruster et al., 1988).

We will focus on the qualitative aspects of the comparison, i.e. we examine if and how two-mode models can generally reproduce the dynamical behavior of the POD modes. We describe below the behavior of the two-mode model for $\delta_1^+ = 49$, 69, and 72 respectively. The adjustable parameter α accounting for

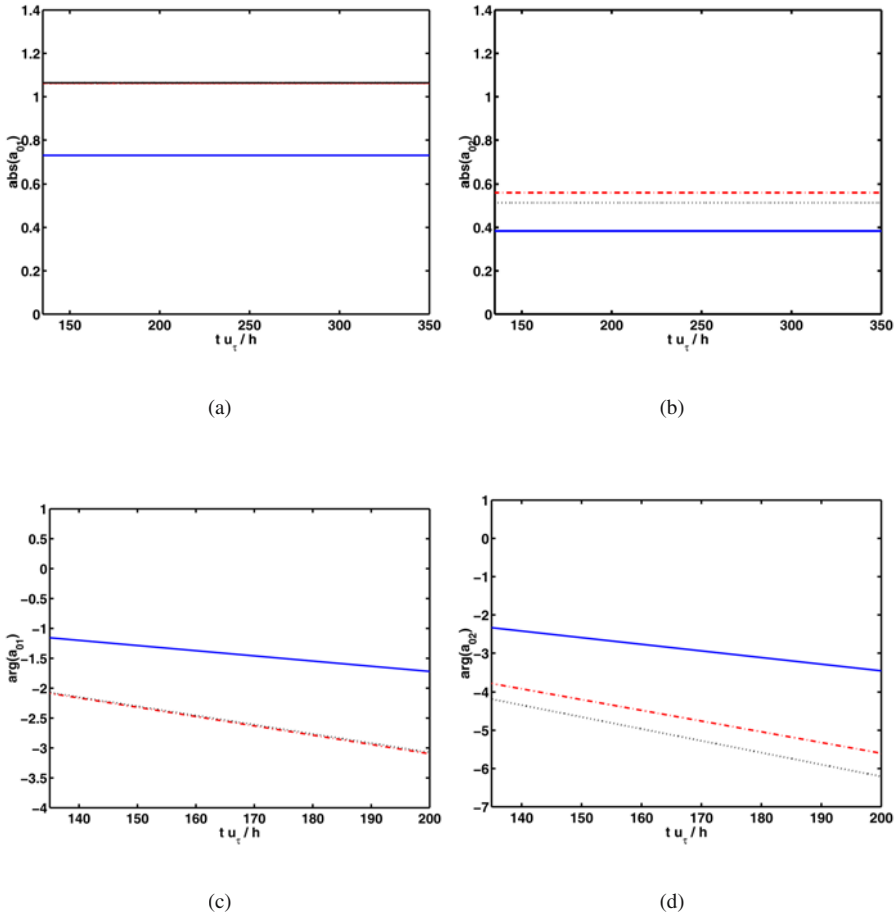

Figure 8. Time series of the POD modes computed from the two-mode model. Solid line: $\delta_1^+ = 49$, Dashed line: $\delta_1^+ = 69$, Dotted line: $\delta_1^+ = 72$.

energy losses to unresolved modes was fixed to zero in our computations. This particular choice is motivated by the results of the Aubry et al. (1988) model for which travelling waves solutions occur for low values of this bifurcation parameter.

Results from the time histories for both modes are shown in Figures 8(a)–(d). Phase portraits are shown in Figures 9(a)–(c). Travelling wave solutions clearly appear as a backbone for the dynamics of the autonomous near-wall region for all the cases considered. However, the restriction of the model to a two-mode interaction does not succeed to catch the bifurcation from a periodic to quasi-periodic behavior as observed in DNS time series. The model predicts

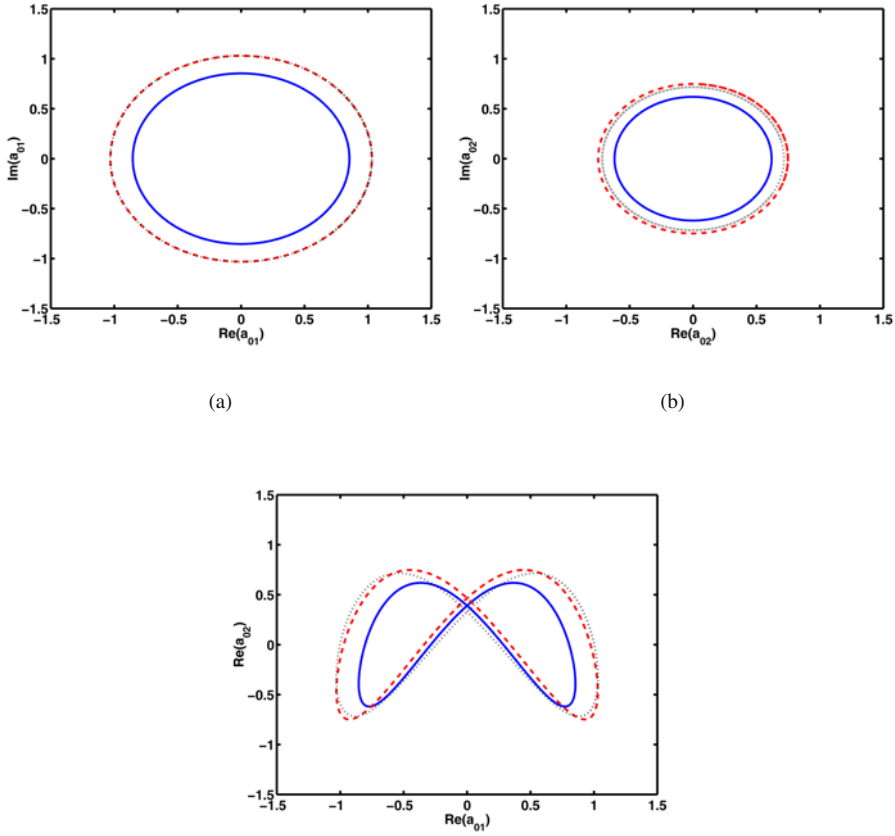

Figure 9. Phase portraits of the POD modes computed from the two-mode model. Solid line: $\delta_1^+ = 49$, Dashed line: $\delta_1^+ = 69$, Dotted line: $\delta_1^+ = 72$.

instead an increase in the energy content for both modes as the filter hight rises without any loss of structural stability while we observe a decrease in the contribution from the first mode computed from the DNS. Other discrepancies are also noted for the spanwise speed of the solution which is underestimated seen the absence of triadic interactions in a two-mode truncature. Our results are to compare with studies by Moehlis et al. (2002) and Smith et al. (2004) on the derivation of a POD-model for the plane Couette flow which revealed the crucial need to incorporate streamwise-independent modes and operate a decoupling between rolls and streaks, as suggested before by Waleffe (1995), in order to catch the relevant dynamical features in the phase space.

5. CONCLUSIONS

An analysis of different autonomous minimal channel flow datasets has been performed, each revealing the existence of travelling wave solutions in the near-wall region. Differences between each flow have been described and quantified through the POD. An evaluation of a POD-based two-mode model for the wall layer revealed its ability to recover such solutions for the cases considered. However the severe truncation in the number of degrees of freedom as well as the artificial coupling between the streamwise rolls components to the streamwise velocity do not allow to recover the bifurcation of the solution towards a modulated travelling wave for higher filter values.

ACKNOWLEDGEMENTS

The first author is extremely grateful to Professor John Lumley and his co-workers, specially Peter Blossey, Berengere Podvin and John Gibson for their support. Special thanks are also due to Professor Fabian Waleffe and Dr. Laurette Tuckerman for their useful suggestions and discussions.

REFERENCES

Armbruster D., Guckenheimer J. and Holmes P. (1988). Heteroclinic cycles and modulated traveling waves in systems with O2 symmetry. *Physica D* **29**, 257.

Aubry N., Lumley J.L., Holmes P. and Stone E. (1988). The dynamics of coherent structures in the wall region of the wall boundary layer. *J. Fluid Mech.* **192**, 115–173.

Herzog, S. (1986). The large scale structure in the near wall region of a turbulent pipe flow. Ph.D. Thesis, Cornell University.

Jiménez, J. and Moin, P. (1991). The minimal flow unit in near-wall turbulence. *J. Fluid Mech.* **225**, 213–240.

Jiménez, J. and Pinelli, A. (1999). The autonomous cycle of near wall turbulence. *J. Fluid Mech.* **389**, 335–359.

Jiménez, J. and Simens, M.P. (2001). Low-dimensional dynamics in a turbulent wall flow. *J. Fluid Mech.* **435**, 81–91.

Keefe, L.R., Sirovich L. and Ball, K.S. (1990). Plane waves and structures in turbulent channel flow. *Phys. Fluids* **A2**, 2217.

Lumley, J.L. (1971). *Stochastic Tools in Turbulence*. Academic Press, New York.

Moehlis, J., Smith, T.R., Holmes, P.J. and Faisst, H. (2002). Models for turbulent plane Couette flow using the proper orthogonal decomposition. *Phys. Fluids* **14**, 2493.

Moin, P. and Moser, R. (1989). Characteristics-eddy decomposition of turbulence in a channel. *J. Fluid Mech.* **200**, 471–509.

Moin, P., Kim, J. and Moser, R. (1987). Turbulence statistics in fully developed channel flow at low Reynolds number. *J. Fluid Mech.* **177**, 133–166.

Podvin, B. and Lumley, J.L. (1998). A low-dimensional approach for the minimal flow unit. *J. Fluid Mech.* **362**, 121.

Smith, T.R., Moehlis, J. and Holmes, P.J. (2004). Low-dimensional models for turbulent plane Couette flow in the minimal flow unit, in preparation.

Toh, S. and Itano, T. (1999). Low-dimensional dynamics embedded in a plane Poiseuille flow turbulence. Traveling-wave solution is a saddle point? Preprint physics/9905012.

Waleffe, F. (1995). Transition in shear flows. Nonlinear normality versus non-normal linearity. *Phys. Fluids* **7**, 3060.

Waleffe, F. (1997). On a self-sustaining process in shear flows. *Phys. Fluids* **9**, 883–900.

Waleffe, F. (1998). Three-dimensional coherent states in plane shear flows. *Phys. Rev. Lett.* **81**, 4140–4143.

COHERENT STATES IN TRANSITIONAL PIPE FLOW

Maria Isabella Gavarini[1], Alessandro Bottaro[2] and Frans T.M. Nieuwstadt[1,†]
[1]*J.M. Burgers Centre, Delft University of Technology, The Netherlands*
[2]*DIAM, Università di Genova, Italy*

Abstract A numerical simulation of the early nonlinear stages of transition in a pipe flow, for which the base profile presents a small defect, reveals the formation of coherent states reminiscent of the recently found non-linear travelling waves.

Keywords: transition in pipe flow, coherent structures, streamwise vortices and streaks.

1. INTRODUCTION

The causes of transition in pipe flow have been debated for a long time and have been considered to be unrelated to the linear stability of the underlying, parabolic base flow. It is, in fact, accepted that Hagen–Poiseuille flow is stable to all infinitesimal disturbances. Finite amplitude disturbances are necessary to provoke transition, which is generally believed to take place for a Reynolds number Re around 2000. The observed transition "point" moves to higher Re when the magnitude of the inflow disturbance field decreases, pointing to the role of the *receptivity* in deciding the fate of the flow. Since transition is eventually observed in any experimental set-up (including those with exceptional low level of flow disturbances), and since all eigenmodes of the linearized stability operator are damped for all values of Re, there must be a mechanism for the amplification of ambient noise, leading to the subsequent breakdown of the motion. Via such a mechanism the system filters the environmental disturbances and transforms them into instability waves.

Current interpretation of the results of linear stability theory points in the direction of transient growth of disturbances as the likely candidate for the initial phase of transition (Schmid and Henningson, 2001). The argument goes that in subcritical conditions the initial/inflow disturbance field can be amplified (transiently) to such a level that eventually nonlinear phenomena kick

†Deceased on May 17th, 2005.

T. Mullin and R.R. Kerswell (eds), Laminar Turbulent Transition and Finite Amplitude Solutions, 163–172.
© 2005 *Springer. Printed in the Netherlands.*

in causing transition of the flow, thus superseding the asymptotic modal behaviour of exponential decay. The weak point of the argument appears to be the – as yet unclearly defined – generic nonlinear mixer responsible for maintaining large amplitude disturbances during transition. It has been argued that such a generic mixer, which is needed to turn streamwise streaks into streamwise vortices in the self-sustaining cycle of near-wall turbulence, begins with the secondary, inviscid and modal instability of the streaks (Waleffe, 2003). Recent results demonstrate that a streaky base flow can support a strong algebraic amplification of perturbations (Hoepffner et al., 2005) so that a scenario of transition is emerging based on a succession of transient phenomena (see also Grossmann, 2000). There is as yet little experimental/numerical evidence to show what precisely these transients states are, and how they follow one another (i.e. what the phase-space trajectory is, in dynamical systems terminology). The influence of the environment in deciding the states which prevail and their space-time evolution is undoubtedly crucial.

More recent work has focussed on the possible presence of defects in the base flow (eventually caused and/or maintained by the transient growth) which can give rise to exponential amplification of perturbations (Dubrulle and Zahn, 1991; Bottaro et al., 2003; Gavarini et al., 2004). Here the argument goes that defects of small (albeit finite) amplitude would cause a distorted base flow that is linearly unstable. The unlimited growth provided by exponential amplification represents an initial stage of transition, which does not require any speculation on subsequent processes (the generic nonlinear mixing) for a high level of disturbances to be maintained. Furthermore, the existence of defects does not hamper the possibility of transient growth, which remains unaltered. It is hence likely, as argued by Biau and Bottaro (2004), that transient growth and flow defects cooperate in defining the initial stages of transition in shear flows of the Poiseuille, Hagen–Poiseuille or Couette type.

As far as the nonlinear stages are concerned, there has been some excitement recently over the discovery of unstable travelling wave solutions which could constitute the "skeleton" of states around which transitional and perhaps turbulent flows organize. Such solutions have been identified theoretically for pipe flow by Faisst and Eckhardt (2003) and Wedin and Kerswell (2004) with the help of continuation techniques; for example, Faisst and Eckhardt imposed an initial body force on the momentum balance equations, capable of generating streamwise vortices in the pipe cross-section. The amplitude of the driving force was then decreased (while simultaneously increasing Re) until eventually a finite amplitude solution (with vanishing body force) was reached. The chosen domain was streamwise periodic, implying that the receptivity of the flow was unaccounted (and unaccountable) for. The excitement arose when experimenters in Delft observed coherent states in a pipe very similar to the computed ones (Hof et al., 2004). The experiments were carried out by inject-

ing fluid through a hole in the pipe for a short time, and observing the puffs generated by the injection as it passed through the observation window 150 diameters downstream of the injection point. The temporal observations of the puff were then translated into spatial observations by the use of Taylor's hypothesis, showing that at $Re = 2000$ the puff is about $12R$ long (with R the cylinder radius), with three high speed streaks near the wall at the downstream (leading) edge of the puff, that transform into six near-wall high speed streaks at the upstream edge of the puff. At the center of the pipe a large low speed streak was observed, with arms stretching radially towards the walls. Not only did the experimental flow states present a remarkable similarity to some of the computed ones, also features of the solutions such as the amplitudes, wavelengths and phase speeds were in good agreement, supporting a scenario that describes transition to turbulence through the self-organization of the flow around some dominant travelling waves.

Recent direct numerical simulations (in a streamwise periodic domain) by Priymak and Miyazaki (2004) support the existence of equilibrium puffs at Re as low as 2200, propagating in the direction of the mean flow at a speed of the order of the bulk velocity, while maintaining their spatial downstream length equal to about 40 cylinder radii. The disagreement in the puff's length between experiments and simulations could perhaps be explained by the difficulty in identifying properly the leading and trailing edges of the puff, by the characteristics of the forcing employed to trigger the puff, and by the fact that simulations in streamwise periodic domains (even very long ones, as in the present case where a domain $50R$ long was employed) can only mimic the real, spatially developing situation. When periodic conditions are employed, perturbations exiting the domain are continuously fed into the inflow plane thus providing energy for the sustainment of the puff.

The present paper aims at presenting further evidence for the existence of flow states such as those computed by Faisst and Eckhardt (2003) and Wedin and Kerswell (2004). It has been chosen here to focus on a transition scenario with *spatially developing* disturbances and to capture both linear and nonlinear stages through a numerical computation in which the fast initial development of perturbations is caused by the linear instability of a mildly distorted Hagen–Poiseuille flow. Hence, the present simulation does not describe the evolution of a puff induced by a Dirac-like perturbation, rather it describes the patterns produced when transition is triggered and sustained by a permanent inflow forcing.

2. THE TRAVELLING WAVES

The existence of families of finite-amplitude coherent states in shear flows has been known for some time (Nagata, 1990; Clever and Busse, 1997; Waleffe,

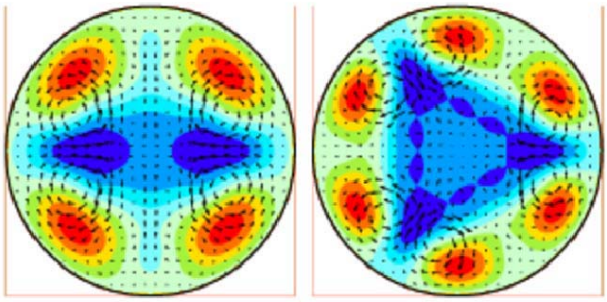

Figure 1. Downstream averaged travelling waves of the C_2 and C_3 families (after Faisst and Eckhardt).

2001). However, the symmetry properties of these families were such that no straightforward connection could be established with the coherent structures observed in turbulent shear flows. In pipe flow the solutions found by Faisst and Eckhardt (2003) and Wedin and Kerswell (2004) are travelling waves (TW), moving downstream at wave speeds larger than the bulk velocity. Although the stability/instability of such states is currently not known, they are thought to be unstable solutions of the Navier–Stokes equations. It is speculated that they form a chaotic repellor with the system's trajectory wandering in phase space among mutually repelling solutions; thus the flow would remain in the vicinity of a given TW state for a while before going elsewhere. No formal mathematical justification has ever been given for this behaviour, although Christiansen et al. (1997) have shown results on the one-dimensional Kuramoto–Sivashinsky system endorsing the so-called "Hopf's description of chaos", with a dynamics based on unstable recurrent patterns. Just as the theory of finite amplitude TW was being developed, the above speculative picture of the early stages of transition received experimental support by the measurements conducted by Hof et al. (2004) and van Doorne (2004).

The TWs that appear earliest (in terms of the Reynolds number) are those denoted as C_2 and C_3 by Faisst and Eckhardt, where the subscripts 2 and 3 refer to the azimuthal rotation symmetry, for example a C_3 state is invariant under rotation around the pipe axis by an angle $2\pi/3$. Streamwise averaged C_2 and C_3 states are displayed in Figure 1; they appear for Re as low as 1250. Notable characteristics of such states (at their saddle-node bifurcation points) are the streamwise wavelengths (scaled with the pipe radius), which equal 4.19 and 2.58 for the C_2 and C_3 states, respectively, and the phase speeds (scaled with $U_{\max}$, the maximum velocity on the pipe axis in the laminar case), which equal 0.71 and 0.64, also for the C_2 and C_3 states, respectively. Furthermore, the streamwise velocity disturbance (with respect to the laminar state) is found to be one order of magnitude larger than the transverse velocity, and the dimen-

sionless peaks are found at 0.19 (C_2) and 0.17 (C_3), and 0.017 (C_2) and 0.023 (C_3). Although such peak disturbance values increase with increasing of Re, the qualitative picture of the states changes little, with rather static high speed streaks near the wall and low speed streaks which change shape and position near the center of the cross-section.

3. THE PRESENT SIMULATION

A direct numerical simulation has been conducted for the flow in a pipe of streamwise extent equal to 80 cylinder radii, with inflow and outflow boundaries and at a Reynolds number $Re = 3000$. The incompressible Navier–Stokes equations written in cylindrical coordinates are discretized by a second order finite volume technique (for details, see Eggels et al., 1994); after numerical tests it has been decided that a resolution of $64 \times 32 \times 640$ grid points in the radial, azimuthal and axial directions, respectively, is adequate for our purposes. The underlying axisymmetric base motion consists of the Hagen–Poiseuille flow plus a *minimal defect* (Gavarini et al., 2004), which is forced via an appropriate source term in the governing equations throughout the whole length of the pipe. We do not dwell on the possible physical origins of the imposed mean flow deflection; we simply assume that it is due to environmental effects. Due to the presence of the defect an axisymmetric mode of the linear stability operator becomes unstable. Such a mode – with a given initial amplitude – is prescribed at the inflow section of the pipe; it grows exponentially and is responsible for the early stages of transition. For further details on the choice of the defect and its stability characteristics refer to Gavarini et al. (2004).

In Figure 2 we have plotted the energy of the various modes produced by nonlinear interactions against the streamwise distance x. The modes are indicated be a number pair (m, n) with m the azimuthal wave number of the disturbance and n denoting its frequency ω_n. The exponentially unstable disturbance is noted as $(0, 2)$ in Figure 2. We further observe that small amplitude random noise has been introduced at $x = 0$ to permit rapid growth of other modes due to the subharmonic instability of the primary axisymmetric pattern. The subharmonic mode labelled $(2, 1)$ dominates the spectrum around $x \approx 50$.

It is precisely the $(2, 1)$ mode, and to some extent also the $(0, 0)$ and the $(4, 0)$ modes (the latter is shown by a thin solid line in Figure 2) which define the structure of the motion in downstream regions of the pipe, i.e. for x around 60. In Figure 3, the pipe has been unfolded in a plane, and an instantaneous plan view at $r = 0.7$ is shown. It should be noticed that axisymmetry is gradually broken and that the subharmonic disturbance $(2, 1)$ dominates until $x \approx 60$, from which point on the mean flow correction, i.e. mode $(0, 0)$, becomes more energetic and individual high-frequency, high-wavenumber structures become more blurred. The length of each individual Λ structure is about

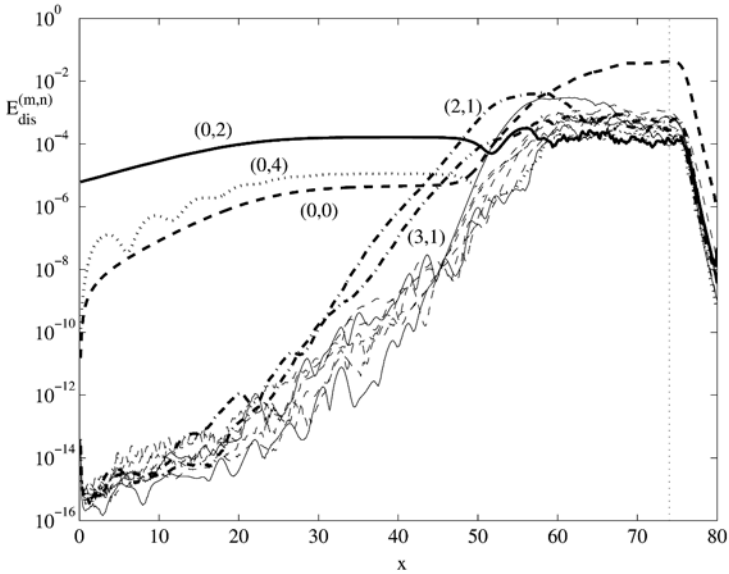

Figure 2. Evolution of the different Fourier components of the disturbance energy density with x. The number pair (m,n) next to each line defines the azimuthal wavenumber m of the mode and its frequency ω_n. For example, the initial condition, which consists only of the $(0, 2)$ mode, aside from small amplitude random noise, is axisymmetric since $m = 0$ and is characterised by a frequency number $n = \pm 2$ (that is $\omega_2 = 1$); similarly, the notation $(2, 1)$ denotes the mode with $m = 2$ (a wave with two periods along the circumference) and $n = \pm 1$ (that is $\omega_1 = 0.5$, the fundamental frequency). The dotted vertical line at $x \approx 75$ indicates the start of the fringe region near the outflow plane, from which point on the equations are gradually rendered parabolic.

5 pipe radii (in the x-range where they are visible; this is quite close to the optimal wavelength found in the C_2 case by Faisst and Eckhardt), which translates to a phase speed of 0.4 (in units of $U_{\max}$) for $\omega = 0.5$.

Aside from the C_1 state which exists only at values of Re exceeding 3000 (Wedin and Kerswell, 2004), the theory predicts that as Re increases past 1250 successively new TWs with C_n symmetries make their appearance (the index n increasing monotonically with Re), i.e. finer and finer scales should emerge downstream in our spatial simulation. In the late transitional and turbulent regimes the problem becomes that of discerning each repelling state from one another in every given experimental/numerical data set, a task which could possibly be pursued by wavelet transform or by POD analysis.

In the qualitative approach pursued here, we will satisfy ourselves with showing that in the cross-section of the pipe flow structures exist resembling those found theoretically. In Figure 4, the instantaneous flow patterns at $x = 54$ and 56.6 are shown. Large scale streaks similar to those of the C_2 state are

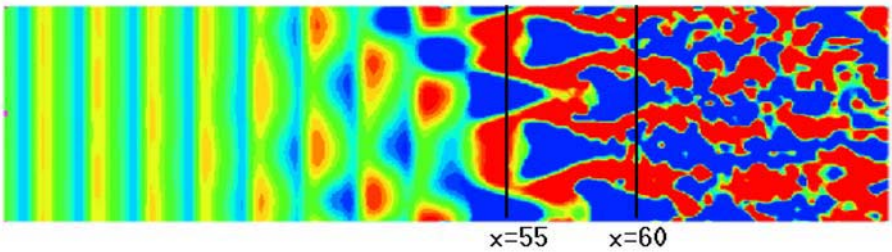

Figure 3. Instantaneous streamwise disturbance velocity in a $(x, r\theta)$ plane, with $r = 0.7$ The azimuthal modulation of the flow and the formation of staggered arrays of Λ vortices is strongly reminiscent of the so-called H*-type* transition in the flat plate boundary layer. The axes are not to scale; the horizontal axis spans from $x = 35$ to $x = 70$.

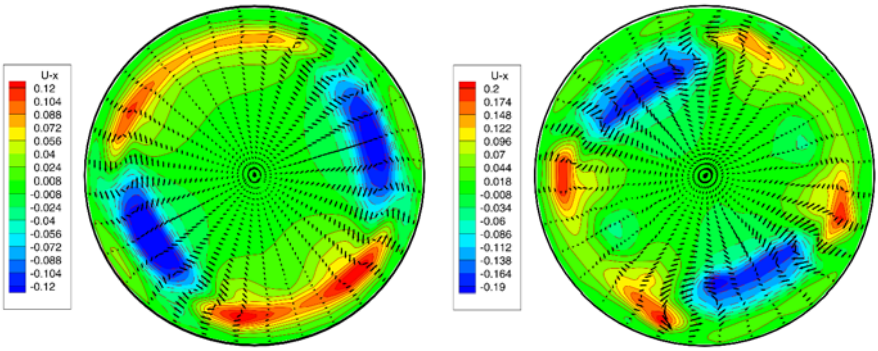

Figure 4. Instantaneous isocontours of the streamwise disturbance velocity, and velocity vector plots of the secondary flow, at $x = 54$ (left) and $x = 56.6$. The states resemble the travelling wave solution with C_2 symmetry. The colour scale to the left of each figure refers to the streamwise disturbance speed. The full range of disturbance velocity values is given only for the figure on the right.

present near the pipe walls: the largest transverse velocity is around 0.07, whereas the streamwise disturbance velocity peaks at 0.2. The latter value is in line with theory (at a smaller Re), whereas the secondary speed is four times as large. The discrepancy could be attributed to a number of factor, e.g. to the presence of many harmonics in the flow. In fact, when we superpose only the three dominant modes present at $x = 56.6$, i.e. modes $(2, 1)$, $(0, 0)$ and $(4, 0)$, the resulting solution (Figure 5) is much less energetic than the full solution, besides displaying a remarkable similarity to the C_2 state.

In the streamwise interval shown in Figure 4 (which corresponds to roughly half a wavelength) the slow streaks appear to have rotated half a wavelength in the azimuthal direction. In reality this is not the case, since in the two cases

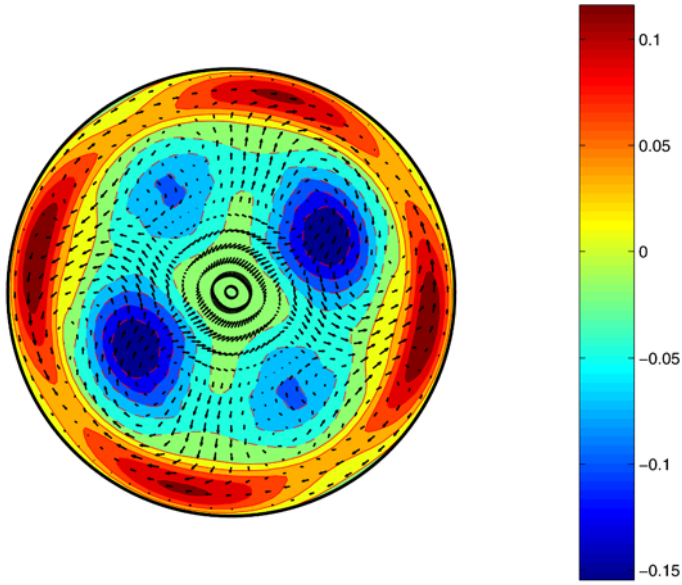

Figure 5. Sum of the three dominant Fourier modes at $x = 56.6$.

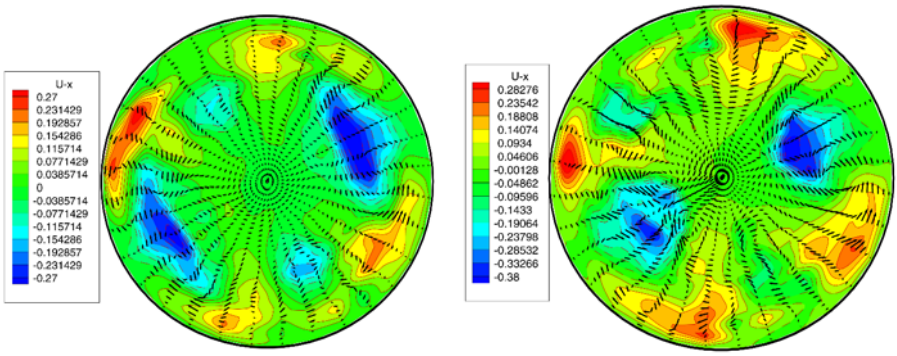

Figure 6. Instantaneous isocontours of the streamwise disturbance velocity, and velocity vector plots of the secondary flow, at $x = 59$ (left) and $x = 60$. The full range of disturbance velocity values is given only for the figure on the right.

we are at x-positions centered on different (and staggered) Λ vortices (cf. Figure 3). As we proceed downstream (Figure 6), high and low speed streaks are intensified (the latter more, cf. the colour scale for the figure corresponding to $x = 60$), although the qualitative picture remains that of Figure 1 (left frame).

Even further downstream, the picture in Figure 3 would suggest that coherence is almost lost. However, inspection of the flow at the cross-sections $x = 74$ and 75 (the latter value already in the fringe region), reveal a configur-

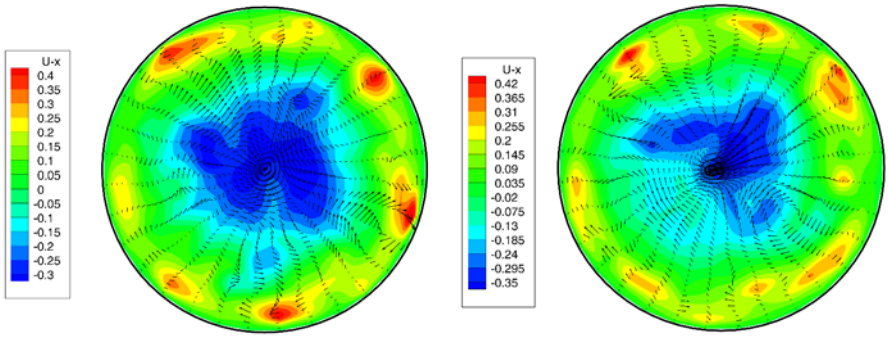

Figure 7. Instantaneous isocontours of the streamwise disturbance velocity, and velocity vector plots of the secondary flow, at $x = 74$ (left) and $x = 75$.

ation which matches well both the experimental observation of a puff by Hof et al. (2004) and theoretical predictions In particular, we observe in Figure 7 the presence of several high speed streaks near the wall, likely to result in increased values of the friction factor. At these streamwise positions the disturbance velocity peaks at $0.5U_{\max}$, with a maximum transverse speed exceeding $0.1U_{\max}$. The states depicted resemble the TW solution with C_3 symmetry.

4. CONCLUSIONS

A qualitative analysis of the instantaneous flow patterns observed in a transitional pipe flow at $Re = 3000$ has been presented. In contrast to previous numerical studies, transition has been triggered by the exponential amplification of small disturbances, evolving in a mildly distorted base flow, which have been followed in their spatial evolution. The path to transition considered is not necessarily that which is universally followed by all pipe flow experiments, it is just a plausible scenario which displays sufficiently generic features. Other scenarios exist (Gavarini et al., 2004). In the present case, central to transition is the formation of large Λ vortices which form staggered arrays, before small scale structures grow enough to destroy the coherence of such vortices. It can be argued that Λ structures constitute the basic units of transition; within them, low speed fluid is contained so that, in a cross-section, two large scale slow speed streaks appear. This corresponds to the C_2 travelling state of the theory. Along the flanks of the Λ structures high speed streaks of smaller dimensions can be observed. Downstream of the position where the Λ vortices break down, the cross-sectional picture of the flow displays a large patch of slow velocity fluid at the center of the pipe, with several small scale high-speed streaks near the wall. This picture is highly suggestive of the C_3 state of Faisst and Eckhardt.

Although these results are preliminary, they are sufficiently promising to warrant a more detailed analysis of the available data base. In particular, it would be interesting to decompose the results of the DNS to extract the states – bound to satisfy specific azimuthal symmetry constraints – which maximise the rate of dissipation energy, following the lead of recent results in this direction by Plasting and Kerswell (2005).

REFERENCES

Biau, D. and Bottaro, A. (2004). Transient growth and minimal defects: Two possible initial paths of transition to turbulence in plane shear flows. *Phys. Fluids* **16**, 3515.

Bottaro, A., Corbett, P. and Luchini, P. (2003). The effect of base flow variation on flow stability. *J. Fluid Mech.* **476**, 293.

Christiansen, F., Cvitanovic, P. and Putkaradze, V. (1997). Spatiotemporal chaos in terms of unstable recurrent patterns. *Nonlinearity* **10**, 55.

Clever, R.M. and Busse, F.H. (1997). Tertiary and quaternary solutions for plane Couette flow. *J. Fluid Mech.* **344**, 137.

van Doorne, C.W.H. (2004). *Stereoscopic PIV on transition in pipe flow*. PhD Thesis, Delft University of Technology, the Netherlands.

Dubrulle, B. and Zahn, J.-P. (1991). Nonlinear instability of viscous plane Couette flow. Part 1. Analytical approach to a necessary condition. *J. Fluid Mech.* **231**, 561.

Eggels, J.G.M., Unger, F., Weiss, M.H., Westerweel, J., Adrian, R.J., Friedrich, R. and Nieuwstadt, F.T.M. (1994). Fully developed turbulent pipe flow: A comparison between direct numerical simulation and experiment," *J. Fluid Mech.* **268**, 175.

Faisst, H. and Eckhardt, B. (2003). Travelling waves in pipe flow. *Phys. Rev. Lett.* **91**, 224502.

Gavarini, M.I., Bottaro, A. and Nieuwstadt, F.T.M. (2004). The initial stage of transition in pipe flow: role of optimal base-flow distortions. *J. Fluid Mech.* **517**, 131.

Grossmann, S. (2000). The onset of shear flow turbulence. *Rev. Modern Phys.* **72**, 603.

Hoepffner, J., Brandt, L. and Henningson, D.S. (2005). Transient growth on boundary layer streaks. *J. Fluid Mech.*, accepted for publication.

Hof, B., van Doorne, C.W.H., Westerweel, J., Nieuwstadt, F.T.M., Faisst, H., Eckhardt, B., Wedin, H., Kerswell, R.R. and Waleffe, F. (2004). Experimental observation of nonlinear travelling waves in turbulent pipe flow. *Science* **305**, 1594.

Nagata, M. (1990). Three-dimensional finite-amplitude solutions in plane Couette flow: Bifurcation from infinity. *J. Fluid Mech.* **217**, 519.

Plasting, S.C. and Kerswell, R.R. (2005). A friction factor bound for transitional pipe flow. *Phys. Fluids* **17**, 011706.

Priymak, V.G. and Miyazaki, T. (2004). Direct numerical simulation of equilibrium spatially localized structures in pipe flow. *Phys. Fluids* **16**, 4221.

Schmid, P.J. and Henningson, D.S. (2001). *Stability and Transition in Shear Flows*, Springer.

Waleffe, F. (2001). Exact coherent structures in channel flow. *J. Fluid Mech.* **435**, 93.

Waleffe, F. (2003). Homotopy of exact coherent structures in plane shear flows. *Phys. Fluids* **15**, 1517.

Wedin, H. and Kerswell, R.R. (2004). Exact coherent structures in pipe flow: Travelling wave solutions. *J. Fluid Mech.* **508**, 333.

INSTABILITY, TRANSITION AND TURBULENCE IN PLANE COUETTE FLOW WITH SYSTEM ROTATION

P. Henrik Alfredsson and Nils Tillmark
KTH Mechanics, Royal Institute of Technology, SE-100 44 Stockholm, Sweden
hal@mech.kth.se, nt@mech.kth.se

Abstract System rotation may have either stabilizing or destabilizing effects on shear flows depending on the direction of rotation vector as compared to the vorticity vector of mean flow. This study describes experimental results of laminar, transitional and turbulent plane Couette flow with both stabilizing and destabilizing system rotation. For laminar flow with destabilizing rotation roll cells appear in the flow which may undergo several different types of secondary instabilities, especially interesting is a repeating pattern of wavy structures followed by breakdown, thereafter roll cells reappear in a cyclic pattern. For higher Reynolds number roll cells appear also in a turbulent environment. It is also shown how stabilizing rotation may quench the turbulence completely.

Keywords: transition, turbulence, system rotation.

1. INTRODUCTION

It has been known for a long time that effects due to body forces, such as curvature (centrifugal effects) or rotation (Coriolis effects), may have strong influence on boundary layer development. In cases with system rotation, if there is a component of the rotation vector that is parallel to the wall and normal to the mean flow direction, the Coriolis effects may lead to an unstable "stratification". As in cases where unstable stratification is set up by density differences (due to temperature or concentration gradients for instance) the flow may develop streamwise oriented vortices. If the flow experiences system rotation the Coriolis force may be stabilizing or destabilizing depending on the direction of rotation. If the mean vorticity is of the opposite sign as compared to the system rotation vector then the flow becomes destabilized (anticyclonic rotation), whereas the flow becomes stabilized if they have the same sign (cyclonic rotation) (see Figure 1).

T. Mullin and R.R. Kerswell (eds), Laminar Turbulent Transition and Finite Amplitude Solutions, 173–193.
© 2005 *Springer. Printed in the Netherlands.*

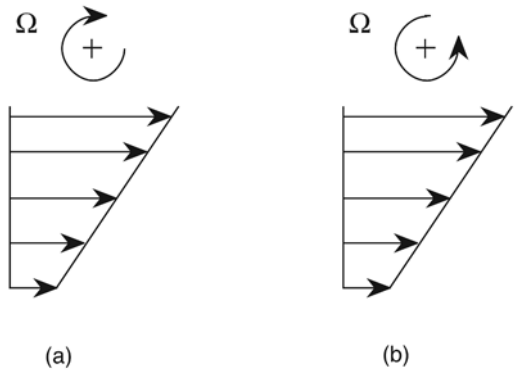

Figure 1. Superposition of rotation on a shear flow (a) Stabilizing (cyclonic) rotation, (b) Destabilizing (anti-cyclonic) rotation.

In plane Poiseuille flow subjected to spanwise rotation the Coriolis force acts in such a way that in the part of the channel where the system rotation has opposite sign compared to the mean flow vorticity the flow becomes destabilized whereas in the other part of the channel it becomes stabilized. Alfredsson and Persson (1989) showed that the instability takes the form of streamwise oriented roll cells and demonstrated good agreement between linear theory and experiments. In plane Couette flow with system rotation the Coriolis force will either be stabilizing or destabilizing across the full channel width (Figure 2).

Plane Couette flow with and without rotation. Plane Couette flow may be viewed as a paradigm of wall bounded flows, conceptually one of the simplest non-trivial fluid dynamics systems where the flow is solely driven by the shear at the moving walls. According to linear stability theory all disturbances are stable even for an infinite Reynolds number (see e.g. Schmid and Henningson, 2001), although the transitional Reynolds number (defined as $Re = U_w h/\nu$, see Figure 2), i.e. the Reynolds number below which there is no self sustained

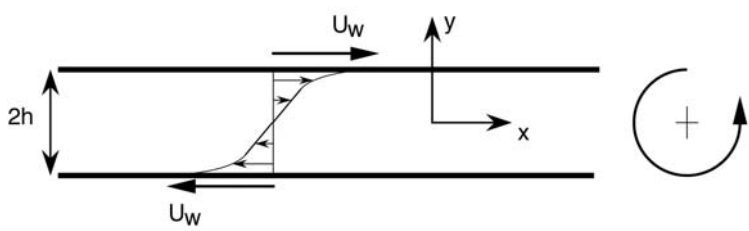

Figure 2. Flow definition of rotating plane Couette flow. U_w is the wall velocity with respect to the centreline. Rotation direction is here anti-cyclonic.

turbulence, has been observed to be in the range 320–360 both experimentally and numerically (Lundblad and Johansson, 1991; Tillmark and Alfredsson, 1992; Tillmark, 1995; Daviaud et al., 1992; Dauchot and Daviaud, 1994). Fully developed turbulence on the other hand is obtained only for Reynolds numbers above about 500.

Experiments and simulations (see e.g. Bech et al., 1995, and references therein) have shown that turbulent plane Couette flow exhibits a central core region with an almost linear mean velocity profile, so that the mean shear is uniform there. Also other properties of the flow, such as Reynolds stresses, production and dissipation are homogeneous in the core region. However this is only true in the long-time sense, instantaneous velocity distributions show long-lived streamwise oriented structures with a cross flow diameter of the order of the channel width. In the simulation of Komminaho et al. (1996) these structures gave rise to spanwise variations in the streamwise velocity of the order of $0.3U_w$.

There have been a few numerical studies made on plane Couette flow rotating around its spanwise axis. Bech and Andersson (1996, 1997) made simulations with destabilizing rotation and found that secondary flow in form of streamwise oriented vortices occurs also in this case both for weak and strong rotation. The paper by Komminaho et al. (1996) was mainly devoted to the non-rotating case, however they also showed that the flow can be relaminarized by weak cyclonic rotation.

Nagata (1998) studied stationary flow solutions which bifurcate from the two-dimensional streamwise vortex flow in rotating Couette flow. He showed that such a stationary solution may exist within a rather limited Reynolds number range and that for high Reynolds numbers these solutions would become time-dependent.

1.1 Layout of paper

In the present work we have experimentally studied the effects of system rotation on plane Couette flow mainly through flow visualization. Some of the experiments described in the present paper have also been presented in preliminary form by Tillmark and Alfredsson (1996). The parameter space covered includes both stabilizing and destabilizing rotation in the laminar, transitional and turbulent flow regimes. Destabilizing rotation in the laminar regime gives rise to elongated roll cells, which may develop secondary instabilities, breakdown and regeneration of the roll cells in a cyclic process. Rotating plane turbulent Couette flow contains strong streamwise oriented roll cells even in an otherwise turbulent flow, with a sharp demarcation between the rolls cells. With stabilizing rotation the turbulent flow can be relaminarised. This is an amazingly strong effect (to anyone who has seen it in the laboratory) and a hy-

pothesis is that the rotation strongly affects an important part of the turbulence generation chain.

Section 2 gives some theoretical background, whereas Section 3 describes the experimental set-up. Section 4 describes the results in the various parameter regions and the results are summarized in Section 5.

2. THEORETICAL BACKGROUND

Equations of motion. The momentum and continuity equations for a plane Couette flow which is rotating with an angular velocity $\Omega = \Omega(t)$ are

$$\frac{\partial \mathbf{u}}{\partial t} + \mathbf{u} \cdot \nabla \mathbf{u} = -\frac{1}{\rho}\nabla P + \nu \nabla^2 \mathbf{u} + 2\mathbf{u} \times \Omega + \dot{\Omega} \times \mathbf{r} \tag{1}$$

$$\nabla \cdot \mathbf{u} = 0 \tag{2}$$

where $\mathbf{u} = (U + u, v, w)$, U is the mean velocity in the streamwise direction (x) and u, v and w are the fluctuating components in x, y and z (see Figure 2 for a definition of the coordinate system). ρ is the fluid density and ν is the kinematic viscosity, which both are assumed to be constant. The static pressure P^* and the centrifugal acceleration are combined to give

$$P = P^* - \frac{\rho}{2}|\Omega \times \mathbf{r}|^2$$

and $\mathbf{r}$ is a position-vector from the axis of rotation. In the following we assume that the walls are countermoving with a velocity difference of $2U_w$, that the distance between the walls is $2h$ and that the rotation vector is in the spanwise direction, i.e. $\Omega = \Omega \mathbf{e}_z$. The basic velocity profile for laminar flow becomes linear also in the case with system rotation so that

$$U(y) = U_w \frac{y}{h} \tag{3}$$

For the flow under study there are two non-dimensional parameters of interest, namely

$$\begin{aligned} Re &= U_w h/\nu && - \text{ Reynolds number} \\ Ro &= 2\Omega h/U_w && - \text{ Rotation number} \end{aligned}$$

Linear stability results. For plane Couette flow with spanwise system rotation, the Coriolis force will either be stabilizing or destabilizing across the full channel width giving rise to spanwise periodic disturbances in the form of roll cells. Lezius and Johnston (1976) showed that for rotating plane Couette flow the critical Reynolds number for such disturbances is given by the following

expression

$$Re_c = \frac{10.3}{\sqrt{Ro(1 - Ro)}} \tag{4}$$

which gives the lowest Re_c as 20.6 for a rotation number $Ro = 0.5$. The corresponding critical spanwise wave number is $\beta_c = 1.56$, i.e. the spanwise size of each roll cell is equal to the channel height ($2h$). For $Ro \leq 0$ and $Ro \geq 1$ the flow is stable as seen from Equation (4).

Rotation effects on turbulence. It is well known that system rotation also affects turbulent shear flows. The equations for the Reynolds stresses are obtained by taking the i-th component of Equation (1) and multiplying by u_j and thereafter taking the ensemble average (here denoted by overbar) to get

$$\left(\frac{\partial}{\partial t} + U_k \frac{\partial}{\partial x_k}\right) R_{ij} = P_{ij} + \Pi_{ij} - \epsilon_{ij} + D_{ij} + G_{ij} \tag{5}$$

where $R_{ij} = \overline{u_i u_j}$. The first four terms on the right hand side represent turbulent production (P_{ij}), pressure strain redistribution (Π_{ij}), viscous dissipation (ϵ_{ij}), turbulent and viscous diffusion (D_{ij}) and are the same as for the non-rotating case. The last term G_{ij} is a term stemming from the system rotation which can be written as

$$G_{ij} = -2\Omega_k (R_{jm}\epsilon_{ikm} + R_{im}\epsilon_{jkm}) \tag{6}$$

where ϵ_{ijk} is the permutation tensor. As is well known, the Coriolis term does not perform work, so the physical interpretation of this term is a redistribution of energy between the velocity components. It is noteworthy that the term $\dot{\Omega} \times \mathbf{r}$ in Equation (1) does not contribute to Equation (5).

For unidirectional flows (as e.g. channel flows) there is no variation of mean quantities in the $x_1 = x$ and $x_3 = z$ directions and the mean velocity components $U_2 = U_3 = 0$. This simplifies Equation (5) significantly (see for instance Johnston et al., 1972) and we can write

$$\frac{\partial}{\partial t}(\overline{u^2}) = -2\overline{uv}\left(\frac{dU}{dy} - 2\Omega\right) + \Pi_{11} - \epsilon_{11} + D_{11} \tag{7}$$

$$\frac{\partial}{\partial t}(\overline{v^2}) = -4\overline{uv}\Omega + \Pi_{22} - \epsilon_{22} + D_{22} \tag{8}$$

$$\frac{\partial}{\partial t}(\overline{w^2}) = \Pi_{33} - \epsilon_{33} + D_{33} \tag{9}$$

$$\frac{\partial}{\partial t}(-\overline{uv}) = \overline{v^2}\frac{dU}{dy} + 2(\overline{u^2} - \overline{v^2})\Omega + \Pi_{12} - \epsilon_{12} + D_{21} \tag{10}$$

For a steady flow, i.e. U and Ω are both independent of t, Equations (7)–(10) can be further simplified since then the left hand side is equal to zero.

In the case that Ω and $\partial U/\partial y$ have the same sign (i.e. anticyclonic rotation), the production of energy in the streamwise component will be reduced. On the other hand since the production of $\overline{v^2}$ increases it is not clear what the overall result will be on the turbulence, except that it will lead towards an equalization of the various components. On the other hand negative rotation will give an increased production of $\overline{u^2}$ but a decrease in $\overline{v^2}$ and lead towards a more two-dimensional turbulence. Since the normal velocity is important for turbulence production it can be intuitively understood that this will lead to a stabilizing of the turbulence or even to laminarization.

3. EXPERIMENTAL SET-UP AND TECHNICAL DETAILS

Experimentally it turns out to be quite complicated to realize plane Couette flow. From the fluid dynamics point of view the easiest way is to use an apparatus with counter-moving walls. The fully developed laminar state is reached through the diffusion of vorticity from the walls across the channel and the influence of the inlet region at both ends of the channel is estimated to be only a few channel widths. Having counter moving walls the net transport of fluid through the channel is zero. In such a system only non-intrusive measurement methods, such as flow visualization or Laser Doppler Velocimetry (LDV), are suited since measurement probes inserted in the channel give rise to disturbances propagating in both directions and hence changing the flow conditions.

The present Couette flow apparatus has been used in a number of reported experiments and its basic technical details are found in Tillmark and Alfredsson (1992), which justifies that only a brief description will be given here.

The Couette apparatus itself consists of two open tanks connected by a 1500 mm long open plane channel with vertical parallel glass walls. The channel has a rectangular cross section, its vertical extent is 400 mm and the distance between the walls is adjustable between 10 mm and 70 mm. The flow in the channel is set up by a transparent polyester plastic belt (360 mm wide) which runs along the facing inner glass surfaces of the channel. Vertical cylinders in each tank drives and steers the belt loop. A feedback controlled DC-motor drives one of the large cylinders and a tacho-generator on the other large cylinder, which is driven by the belt itself, monitors the band speed. The working fluid is water and for flow visualization it is seeded with light reflecting platelets (Merck, Iriodin 120).

In the present experiments the approximately 2.5 m long and 300 kg heavy apparatus is placed on a rigid plate mounted on a turntable (see Figure 3). The turntable is driven by a DC motor with a tacho generator in a feed back system. A second tacho generator measures the tangential velocity of the turntable at

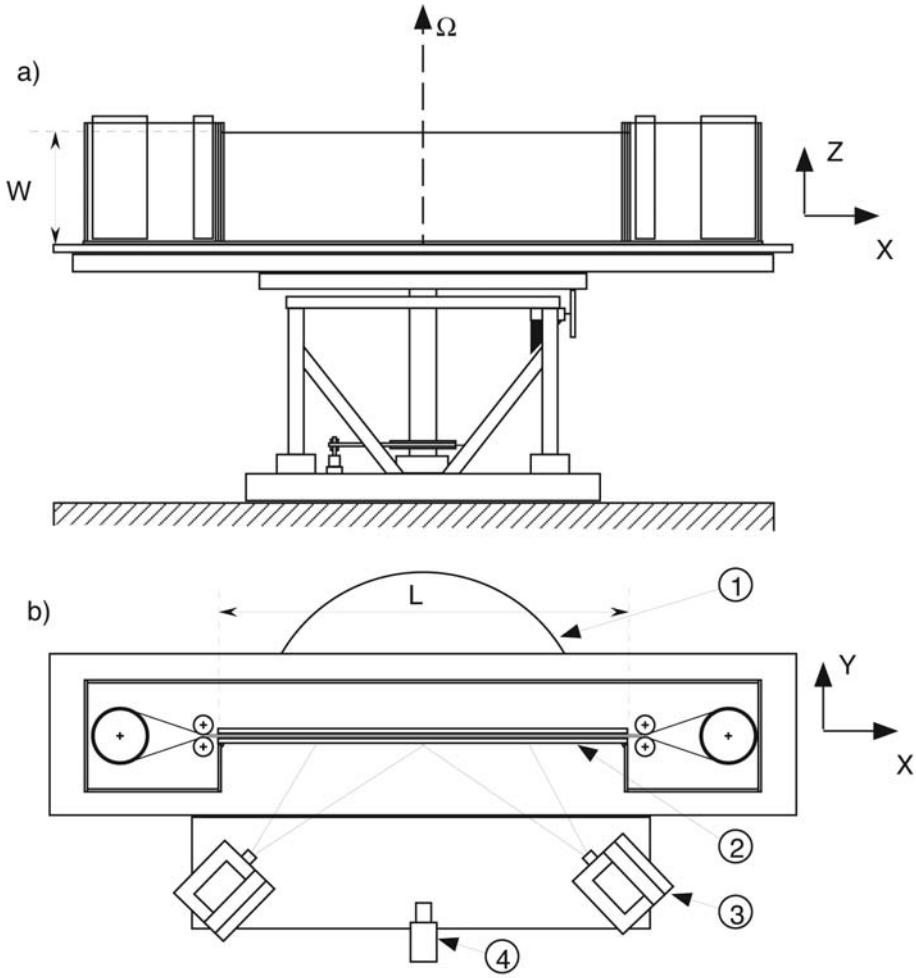

Figure 3. Schematic of the rotating plane Couette flow apparatus. (a) side view and (b) top view. 1) turntable; 2) Couette channel; 3) light source (slide projector); 4) CCD camera. $L = 1500$ mm, $W = 360$ mm.

a fixed radius. The maximum angular velocity of the system is $\Omega = 0.53\ \mathrm{s}^{-1}$ and the angular velocity variation is about 1%. The equipment on the turntable is connected to the surrounding lab through swirl connectors. One connector (mounted above the apparatus and not shown in the figure), supplies the electric power and a second connector, mounted in the bottom end of the main shaft, handles the signal transmission.

The techniques used in the experiments have been video recordings for the visualization studies and LDV for the velocity measurements. The flow visualizations studies initially used a standard CCD-camera connected to a video

tape recorder but were later changed to a digital video (DV) system (Sony DCR-TRV900E). The video recordings give a time resolution of 25 frames per second in the non-interlaced mode. As compared to the standard CCD camera the video gives an improved picture quality as well as a simplified digital image analysis in the post processing stage. The major part of the pictures shown is from such recordings. In the velocity measurements a DANTEC FlowLite LDV system consisting of a one component fiber optic probe head, a 10 mW HeNe laser and a DISA traversing system (57G10) were used. The main lens has a focal length of 160 mm giving an approximately ellipsoidal measuring volume (0.075 mm$\times$0.63 mm (diameter$\times$length) in air). All equipment as well as the LDV-computer were placed on the turntable.

4. EXPERIMENTS AND RESULTS

Several different rotation experiments have been performed, and the equipment and channel configuration on the turntable have varied with the different types of studies carried out. In the velocity measurements and in the major part of the visualization experiments a channel height of 20 mm was used. Such a channel height gives reasonable width and length aspect ratios ($W/2h = 18$, $L/2h = 300$), ensuring small undesired boundary influences, clear visualizations of the flow but unfortunately also severely restricts the range of Reynolds numbers at high rotation rates. As can be easily shown the angular velocity is

$$\Omega = RoRe\frac{\nu}{2h^2}$$

and since the rotational speed of the experimental apparatus is limited, it is necessary to have a large channel width (h) to obtain large Ro and Re simultaneously. To be able to make visualization studies at moderate Reynolds numbers (790 and 1000) and $|Ro| = \mathcal{O}(1)$, the channel height was chosen to 70 mm at the expense of a proper aspect ratio.

The results have been structured in two sections:

(a) A general survey of the flow characteristics at different constant destabilizing rotation rates and for low Reynolds numbers ($Re = 50, 100, 200$) showing different forms of primary and secondary instabilities. We also try to determine the stability boundaries in the $RoRe$-plane.

(b) The effect of destabilizing and stabilizing rotation on turbulent flow.

4.1 Flow regimes for Reynolds numbers below 300 (laminar flow)

The low Reynolds number flows, described in this section, were first established before the rotation was started. During the start up the rotation rate usually reached steady state before any changes in the laminar flow were ob-

served. Here we only describe destabilizing rotation, since no effect on the laminar flow for stabilizing rotation was observed (or expected).

According to the results of linear theory presented in Section 2 the flow is fully stable at all rotation rates if Re is less than 20.6. An exact value of the critical Re was not possible to determine experimentally from the visual observations. A number of rotation numbers in the span $0 \leq Ro \leq 1$ were tried, at and slightly above the critical Re, without any changes in the seemingly homogenous laminar flow. At around $Re = 26$ the flow started to contain visually weak structures. To be able to capture the various flow structures photographically which were readily seen by a naked eye, the Reynolds number had to be increased to more than twice the critical.

***Re* = 50.** In Figure 4, photographs of the flow are shown for various rotation rates at a constant Reynolds number of 50. The size of the illuminated region in the picture is approximately 0.45×0.32 m^2 and the belt motion is in the horizontal direction.

At zero rotation rate (Figure 4(a)) the flow is homogeneous though the unevenly distributed light in the photograph may confuse. At very low rotation rates (Figure 4(b)) the first structures that are observed are found in the upper part of the channel and consist of weak horizontal, alternately light and dark streaks or bands of varying width. The bands are slightly curved with the radius of curvature directed upwards. The wider bands are subsequently split into equally spaced light and dark zones each about $2h$ wide, which is the width of the most unstable disturbances according to linear theory. The character of the zones is not clear from the flow visualization but is consistent with a roll-cell structure. For higher rotation numbers the structures in the flow becomes clearer but also less ordered and the flow is seen to contain a number of merging and splitting roll-cells of different length as in Figure 4(c). For still higher rotation rate the cells become again less pronounced and above $Ro = 1$ the flow is homogeneous (Figure 4(d)) as in the non-rotating case (Figure 4(a)). This is in accordance with the results from linear theory which show that the flow should be stabilized above $Ro = 1$.

***Re* = 100.** If the Reynolds number is increased to 100 while keeping the rotation rate low ($Ro = 0.05$) the flow character changes with time and new intermediate unstable structures appear (Figure 5). Initially, unequally spaced weak horizontal bands develop which through mergings and splittings develop a pattern of horizontal roll-cell pairs of varying spanwise scale (as in the left hand side of Figure 5(a)). The growth of the wider roll-cells continues at the expense of the slender cells. Thereafter a wavy appearance of the cells are observed (Figure 5(b)), with an amplitude which is of the order of the streak width itself and with a streamwise wavelength approximately twice the original

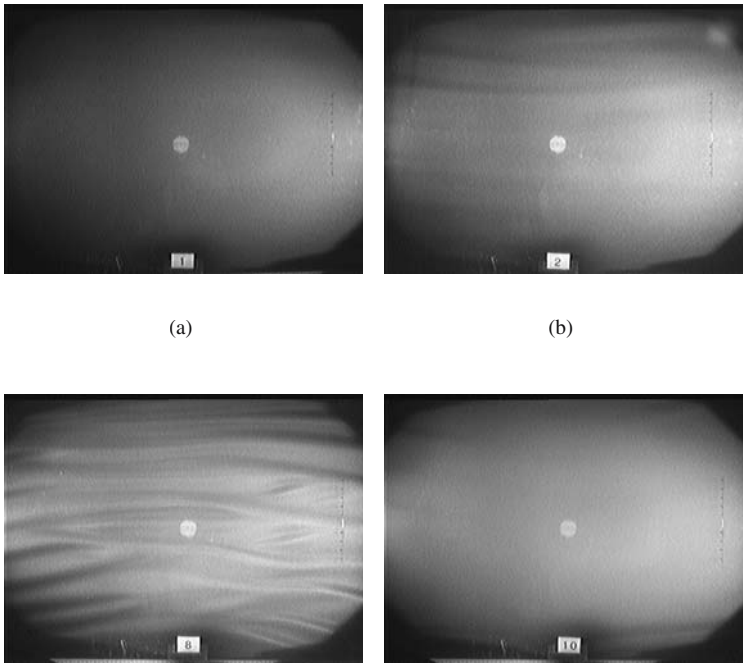

(a) (b)

(c) (d)

Figure 4. Different modes of the laminar flow at $Re = 50$. $U_w = 0.005$ m/s, $h = 10$ mm. Pictures taken of the flow in the xz-plane. The circular bright spot in the centre is behind the moving surface and does not interfere with the flow. (a) Unperturbed flow, $Ro = 0$; (b) Slightly curved bands in the upper part of the channel, $Ro = +0.04$; (c) Strong rotation and mismatched roll-cells, $Ro = +0.74$; (d) Homogeneous flow due to high rotation rate, $Ro = +1.11$. Vertical dimension of photographs is approximately $32h$.

spanwise width of the cells. The wavy structure is not stable but disintegrate and a pattern of nearly straight cells is again formed. Eventually the flow pattern becomes wavy again and the sequence repeats itself. The timescale of such a cycle is several minutes.

At higher rotation rates a secondary instability in the form of spirals appears on the roll-cells (see Figure 6). This secondary mode is confined to a certain domain of the $RoRe$-plane and the dividing-line between this mode and the primary roll-cell mode has been mapped and is shown in Figure 7. This instability is only observed up to $Re \approx 300$ where the flow becomes turbulent.

The flow visualization experiments do not reveal the strength of the apparent roll-cell structures. To obtain a measure of the amplitude simultaneous video and LDV recordings were made. We chose to show a case for which $Re = 140$ and $Ro = 0.16$ which gives a relatively stable roll-cell structure with a span-

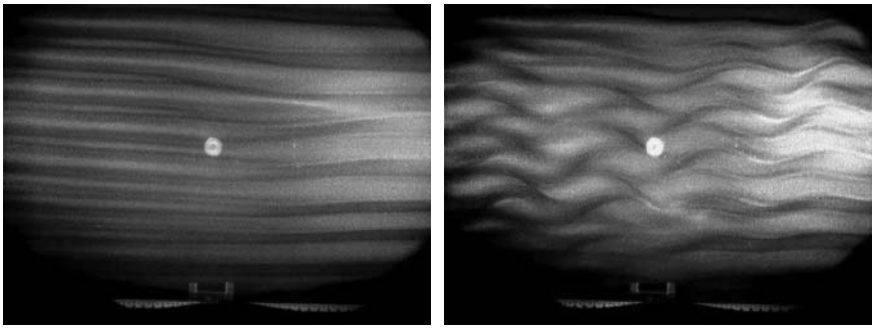

(a) (b)

3

Figure 5. The development of wavy structures in rotating plane Couette flow. $U_w = 0.010$ m/s, $h = 10$ mm, $Re = 100$, $Ro = +0.05$. Rotation started at $t = 0$. (a) Roll-cells established at $t = 165$ s; (b) Slowly transformation of straight roll-cells to a large-scale wavy pattern ($t = 295$ s). Vertical dimension of photographs is approximately $32h$.

Figure 6. Roll-cells developing secondary disturbances as spiral windings. $U_w = 0.011$ m/s, $h = 10$ mm. $Re = 100$, $Ro = +0.44$.

wise size of the order of the channel width. The flow visualization shows light and dark bands which are not stationary but drift slowly in the spanwise direction, sometimes also merging with each other. The LDV-measurements show (see Figure 8) that the streamwise velocity at $y/h = -0.5$ actually changes sign periodically (note that the mean streamwise velocity should be negative at this position). The peak-to-peak amplitude is roughly 10 mm/s which can be compared with the wall velocity of U_w =14 mm/s. This pattern is due to the slow drift of the vortices across the measurement volume. It is hence clear that the vortices drastically change the streamwise velocity distribution

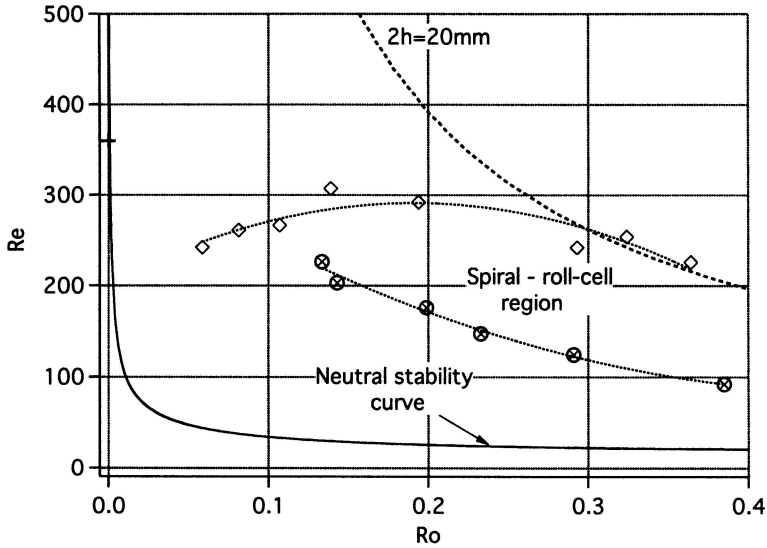

Figure 7. Different modes of the flow in the $RoRe$-plane. ⊗: demarcation between roll-cells and roll-cells with spiral winding; ◇: demarcation between roll-cells with spiral winding and "turbulent" flow.

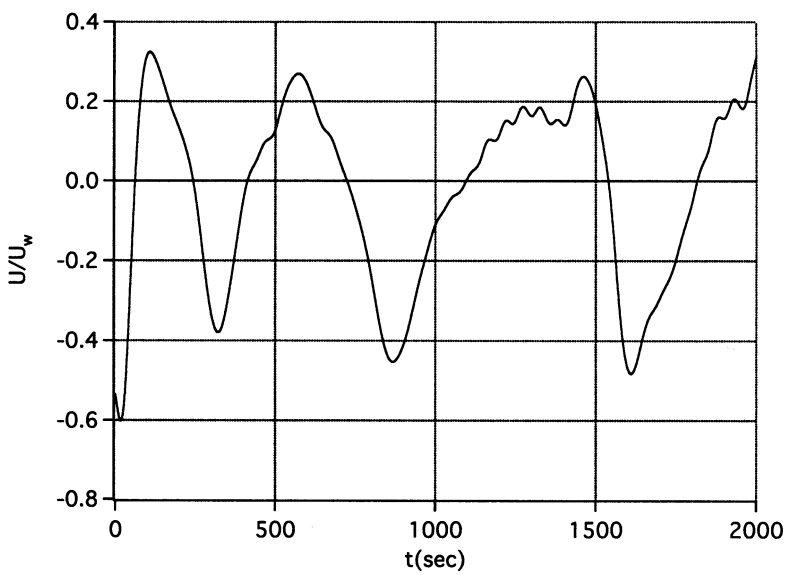

Figure 8. The evolution in time of the normalized streamwise velocity $U(t)/U_w$ at $y = -h/2$, $h = 10$ mm. $U_w = 0.014$ m/s, $Re = 140$, $Ro = +0.16$.

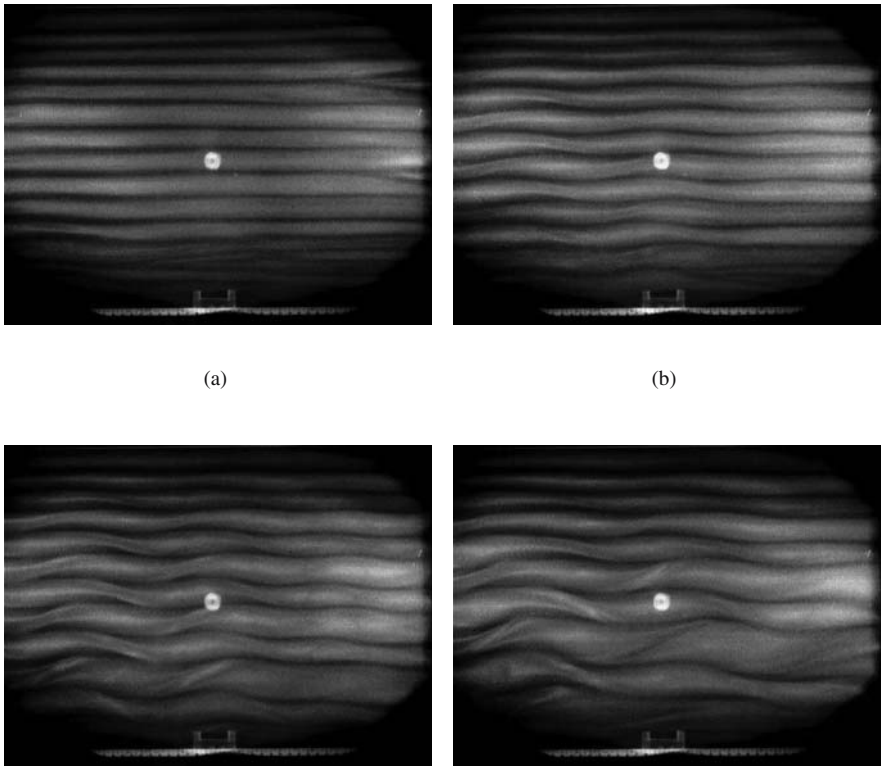

(a) (b)

(c) (d)

Figure 9. Development in time of a spiral secondary disturbance on slightly wavy roll-cells $U_w = 0.021$ m/s, $h = 10$ mm. $Re = 200$, $Ro = +0.10$. Rotation started at $t = 0$. (a) Almost straight streamwise roll-cells, $t = 65$ s; (b) Mismatch causes the rolls to start to wind $t = 110$ s; (c) A secondary twine mode appear on the roll-cells, $t = 300$ s; (d) Increase in the spanwise wavelength and a clear twine mode, $t = 590$ s. Vertical dimension of photographs is approximately $35h$.

in the channel. Similar measurements of the spanwise velocity component (not shown) show variations of this component of the order of ± 3 mm/s.

***Re* = 200.** For still higher Reynolds numbers other modes appear. In Figure 9 at $Re = 200$, $Ro = 0.10$ the initial phase is similar to what is found at $Re = 100$. The regular pattern of cylindrical roll-cells breaks up and the cells become wavy at the same time as the spanwise wavelength increases (Figures 9(a)–9(c)). Finally the spiral secondary disturbance arises which twine the individual roll-cells (Figure 9(d)).

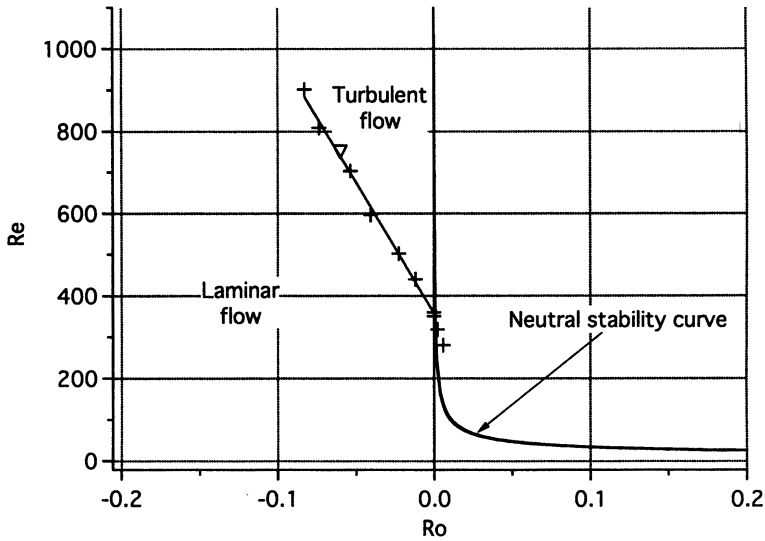

Figure 10. The boundary between laminar and turbulent flow as a function of the stabilizing rotation rate. The + symbols indicate experiments (Tillmark and Alfredsson, 1996) and the ▽ show numerical simulation results by Komminaho et al. (1996).

4.2 Flow regimes for Reynolds numbers above 300

Turbulence at high rotation numbers. We have previously shown that stabilizing rotation (negative Ro) can make a turbulent flow laminar (Tillmark and Alfredsson, 1996). The experiments were done by setting the rotation rate and then decreasing the Reynolds number until laminarization occurred. As seen in Figure 10 the higher the Re, the higher the $|Ro|$ for which laminarization occurs.

In order to reach both high Re and high Ro it is necessary to operate the channel with a large distance between the walls. Some experiments were therefore made with $2h = 70$ mm. This gives the channel a rather low spanwise aspect ratio (approximately 5) and also its length will be only about 20 channel heights. Two Reynolds numbers were documented, namely 790 and 1000. They showed similar behaviour and only results for $Re = 790$ are described here. For $Re = 790$ we show a sequence of six photographs (Figure 11) spanning both negative and positive Ro. At a high negative rotation rate ($Ro = -1.20$, Figure 11(a)), the flow is stable and laminar. Decreasing the rotation in steps the flow remains laminar and steady although at $Ro = -0.05$, weak intermittent disturbances from the inlets penetrate into the channel but the flow can still be considered laminar (see Figure 11(b)). This is different

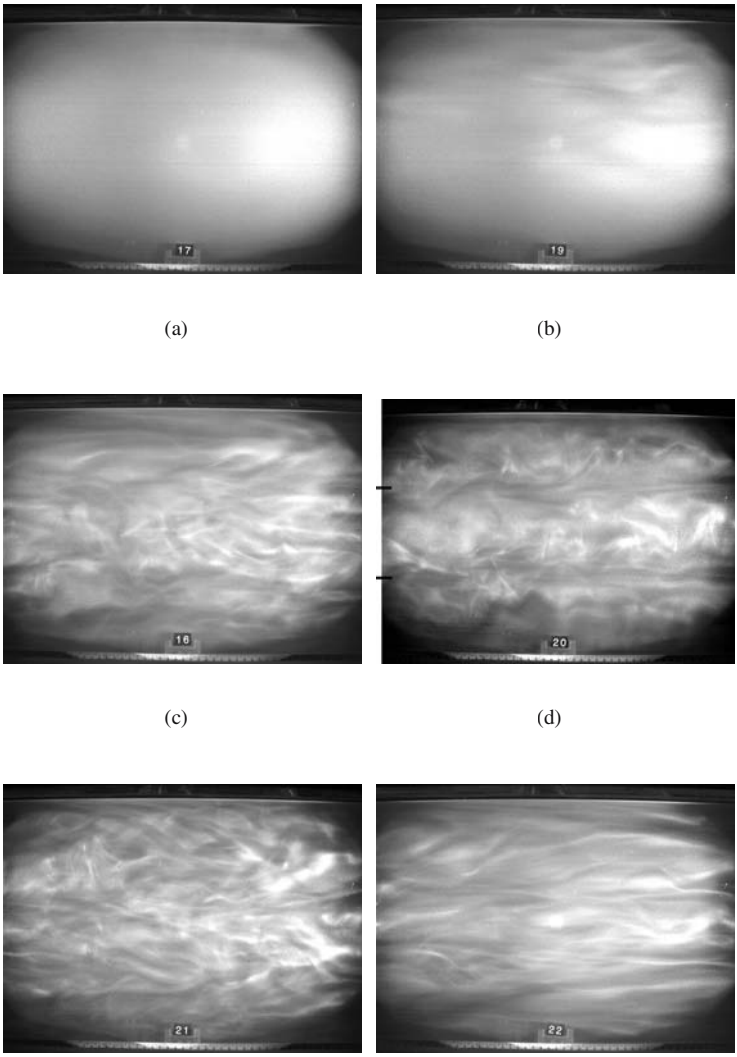

Figure 11. Views of the large gap plane Couette flow at constant Reynolds number and varying constant rotation rates. $Re = 790$, $h = 35$ mm, $U_w = 0.024$ m/s. (a) High negative rotation, completely homogeneous laminar flow, $Ro = -1.20$; (b) Low negative rotation rate, tendency to perturbed laminar flow, $Ro = -0.05$; (c) Large scale turbulent flow, $Ro = 0.0$; (d) Large roll-cell structures superpositioned on the turbulent flow at $Ro = +0.05$ and at $Ro = +0.50$ in (e). The width of a single roll-cell is marked in the left hand side of figure (d) and corresponds to $3.3h$; (f) High positive rotation rate, elongated turbulent structures and weaker roll-cells of varying spanwise extent, $Ro = +0.75$. At high positive rotation ($Ro = +1.10$) turbulence and roll-cells are completely suppressed and photograph looks like in (a). Vertical dimension of photographs is approximately $10h$.

from what was observed for similar parameters in the narrow gap situation where the flow becomes turbulent at these Re and Ro values.

At zero rotation the flow is turbulent as expected (Figure 11(c)). Due to the increased spacing between the walls the turbulent scales are significantly larger compared to the narrow channel case. When starting to rotate the channel in positive sense, i.e. destabilizing rotation, the flow almost instantaneously develops streamwise roll-cells. They are stationary and extend in the streamwise direction over the whole visible area ($\Delta x = 14h$). They are difficult to recognize in still pictures (Figure 11(d)) but are easily identified if the video recording is played at an increased speed. In this figure we have marked the spanwise width of what seems to be one roll cell, and the width is $3.3h$.

Increasing the rotation the turbulent structures get elongated in the streamwise direction and the cells become unsteady, weaker and also shorter. At rotation numbers above 0.75 the predominant cell structures have vanished and the elongation of the turbulent structures is significant (Figure 11(f)). For $Ro > 1$ the turbulence is quenched, no roll-cells are seen and the flow is fully relaminarized and photographs are indistinguishable from Figure 11(a).

Figure 12 summarizes the experiments regarding the different flow regimes in the $RoRe$-plane.

Effects of destabilizing rotation on turbulent flow. For low positive (destabilizing) rotation rates we observe that the plane Couette flow becomes turbulent at Reynolds number around and above 300. However, the demarcation between laminar flow with large structures discussed earlier and turbulent flow is not distinct. In Figure 7 we attempted to estimate the border between these regions based on visualization data. The border is seen to be located around $Re = 300$ for $0.05 < Ro < 0.4$. In order to study the effect on rotation on fully developed turbulence the visualization study was made at Reynolds numbers well above the transition range.

The experiments show that for a large range of Reynolds numbers above the transitional range the steady state flow exhibits large streamwise oriented vortical structures superimposed on the turbulent flow with destabilizing rotation. If the system has constant rotation rate and the belt is accelerated to its final speed the flow passes a series of transitional stages. Such a sequence is shown in Figure 13 for $Re = 740$ and $Ro = 0.10$. The first photo is taken 4 seconds after the start and shows a pattern of thin streamwise streaks over the whole channel width and length. Their spanwise wavelength is about $1h$. The streaks immediately begin to merge, doubling the wavelength (see Figure 13(a)). The very rapid transition to fully turbulent flow is initiated by local breakdown seen in Figures 13(b),(c) as 3–5 parallel transverse stripes with a spacing of about $1h$. After the breakdown the flow becomes fully turbulent (Figure 13(d)) with no evident roll-cell structures. After some time the roll-

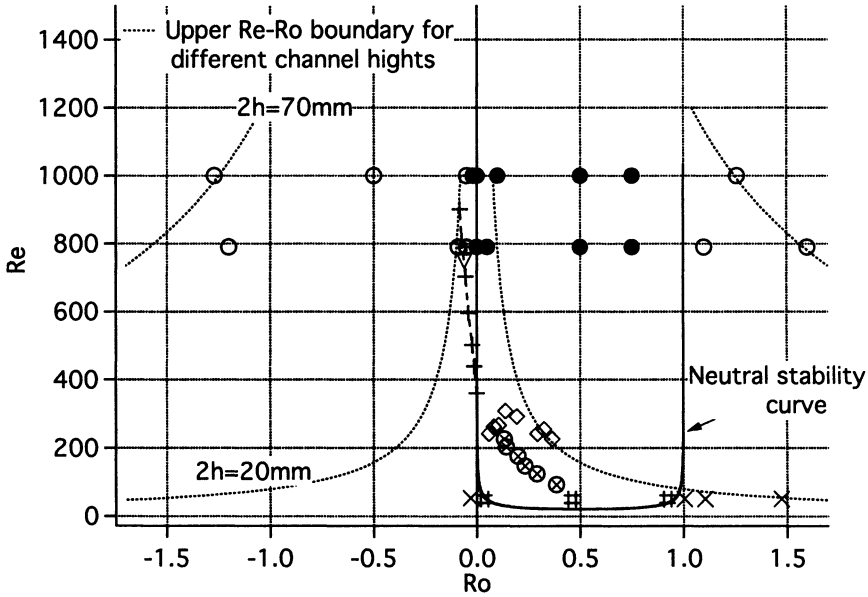

Figure 12. The neutral stability curve (——), the upper limit for present experimental set-up (·····) and selected measurement points. The symbols indicate the following: ○: laminar flow, $2h = 70$ mm; •: turbulent flow with imbedded roll cells, $2h = 70$ mm; ⊕: disturbed flow, $2h = 70$ mm; ×: laminar flow, $2h = 20$ mm; #: turbulent flow, $2h = 20$ mm. Included in the figure are also data presented in Figures 7 and 10. The + symbol shows the demarcation between laminar and turbulent flow obtained in experiments and (▽) in the numerical simulation by Komminaho et al. (1996), respectively. The demarcation between roll-cells and roll-cells with spiral winding has the symbol ⊗ and between roll-cells with spiral winding and "turbulent" flow ◇ are used.

cells appear (Figure 13(e)) and initially the spanwise wave length (i.e. the width of two counter-rotating vortices) is about $4h$. Typically a roll-cell pair is seen as two cells with different width. In Figure 13(f) the flow has reached a steady state with a roll-cell pair having a spanwise wave length of $5h$. The same final cell spacing is also found at $Re = 740$ for a larger (0.15) and a smaller (0.05) rotation number.

From the flow visualizations it seems that the turbulence is "contained" within each streamwise vortex and the width of the dark bands is much smaller than in the laminar case. A low pass filtered time signal obtained by LDV is shown in Figure 14. Here the flow shows regions where the velocity fluctuates around zero (which one expects for a fully turbulent flow in the central region of the channel) and short duration periods of negative velocities. This shows that the streamwise roll cells move slowly in the spanwise direction also in the turbulent case. The peak-to-peak values are about $0.8U_w$ which is larger than typical spanwise variations observed in the non-rotating case (Komminaho et

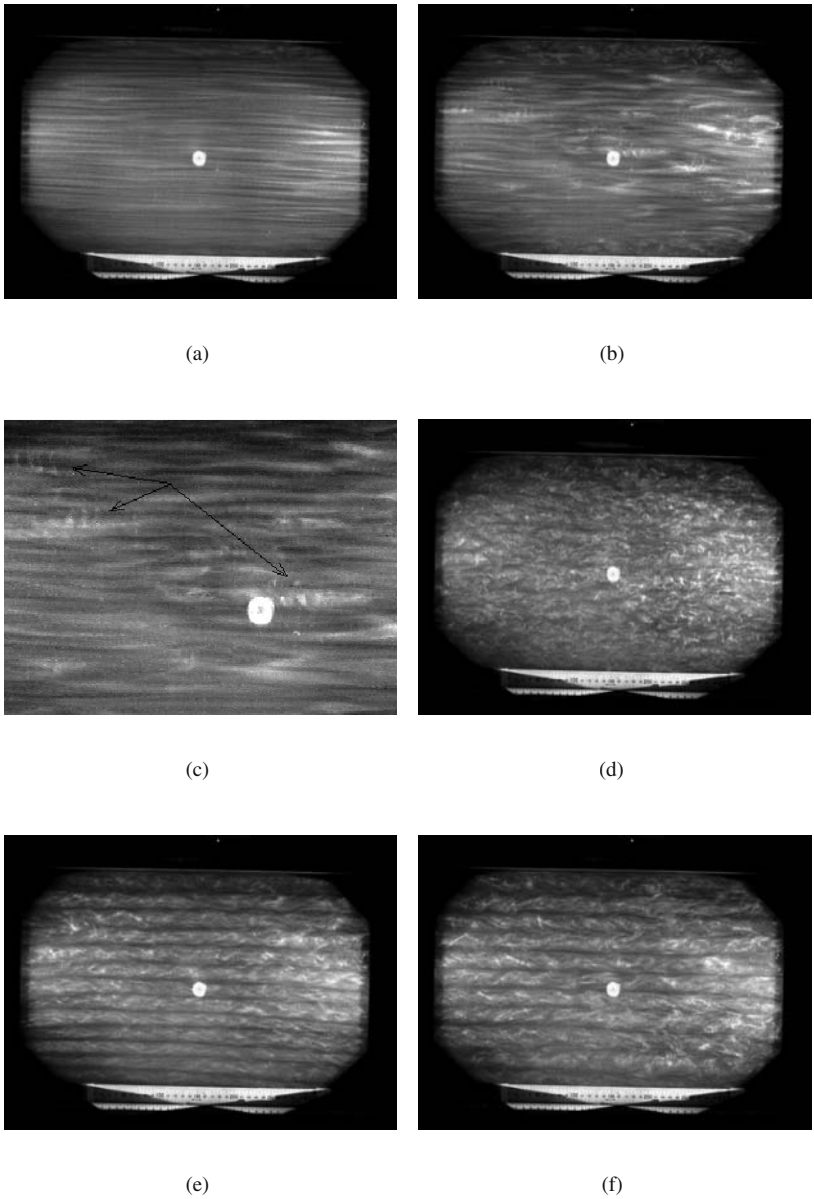

Figure 13. The development in time of the plane Couette flow at constant rotation rate during instantaneous start of the walls. $U_w = 0.076$ m/s, $h = 10$ mm, $Ro = +0.10$ and final $Re = 740$. Belt started at $t = 0$. (a) Streaky pattern at $t = 8$ s; (b) Merged streaks and initial stages of break down of the laminar flow to turbulence, $t = 9$ s; (c) Blow up of the central part of the previous picture. The arrows point out the breakdown zones on the streaks (periodic spanwise lines); (d) Fully turbulent flow without clear roll-cell structures, $t = 13$ s; (e) The development of streamwise roll-cells, $t = 34$ s; (f) Steady state roll-cell structures. $t = 113$ s. Vertical dimension of photographs is approximately $40h$ except for (c).

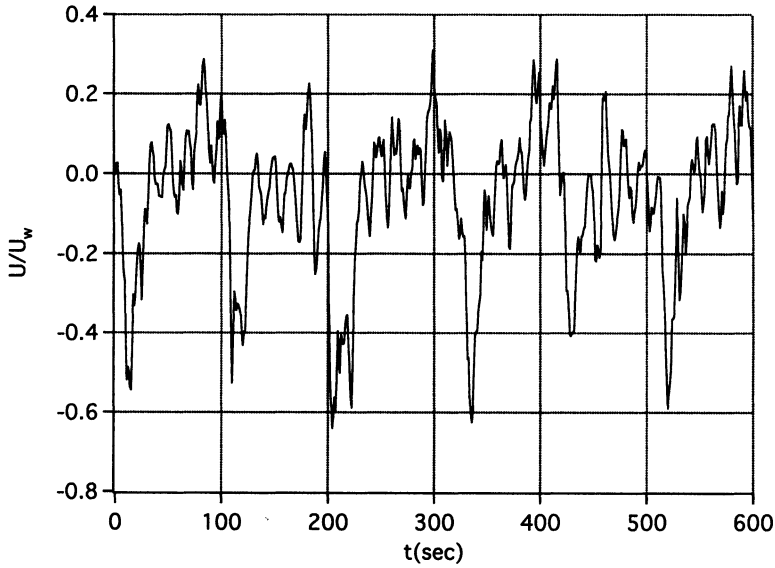

Figure 14. The evolution in time of the low pass filtered streamwise velocity $U(t)/U_w$ at $y = -h/2$, $h = 10$ mm. $U_w = 0.073$ m/s, $Re = 730$, $Ro = +0.10$.

al., 1996) showing that the roll cell structure is stronger here. It should be noted that the intermediate scale fluctuations in the LDV-recording with a period of about 17 seconds is the same as the period of one revolution of the system for this case. This may be an effect of "pumping", i.e. there is a flow between the two sides of the apparatus due to a slight inclination of the apparatus with regard to the horizontal plane.

5. SUMMARY

The present work deals with the effect of spanwise rotation on laminar and turbulent plane Couette flow. The flow shows many visual similarities with Taylor–Couette flow both in the laminar and turbulent case (cf. Coles, 1965).

In the laminar case the development of primary instability in the form of roll cells is striking. We were able to verify the stability boundaries obtained from linear stability theory, for instance that strong enough rotation ($Ro > 1$), stabilizes the flow. We observed several dynamically interesting phenomena, such as merging and splitting of streamwise vortices as well as wavy type of secondary instability. The latter was found to reach high amplitudes, disintegrate, thereafter the roll cells were reestablished and the process repeated itself. One may also notice that the photograph also strongly resemble the finite amplitude solutions obtained by Nagata (1998). Another type of secondary

instability was a spiral motion of the roll cells. Velocity measurements showed that the roll cells change the velocity distribution significantly, changes in the streamwise velocity of the order of half the velocity difference between the walls were observed.

Also for Reynolds numbers where plane Couette flow is turbulent in the non-rotating case a strong influence of the rotation is observed. We showed that negative rotation (cyclonic rotation) can completely suppress turbulence. High positive rotation also stabilizes the flow and may for $Ro > 1$ suppress turbulence completely. For turbulent flows the roll cell structures go straight through the full length of the channel and the spacing is quite regular. After the roll cell structure is established it persists and no merging or splitting of cells were observed. An observation, which cannot at this stage be quantified, is that the turbulence seems to be confined within the roll cells and that there is little interaction between neighboring roll cells.

An observation for both the laminar and the turbulent cases is that the roll cells slowly drift towards the upper side of the channel, i.e. towards the air-water interface. The reason for this drift may be different boundary conditions, where the lower side of the channel is a rigid wall and the upper a free surface. In the laminar case at low Reynolds numbers we also note that the first signs of roll cell structures occur at the upper surface.

The rotating Couette flow shows a rich variety of interesting flow phenomena, some of which are described in this paper. The unsteady character of the flow makes it hard to make velocity measurements however with the use of PIV it should be possible to correlate the measurements with the flow structures themselves. Such measurements are planned for the future.

REFERENCES

Alfredsson, P.H. and Persson, H. (1989). Instabilities in channel flow with system rotation. *J. Fluid Mech.* **202**, 543–557.

Bech, K.H. and Andersson, H.I. (1996). Secondary flow in weakly rotating turbulent plane Couette flow. *J. Fluid Mech.* **317**, 195–214.

Bech, K.H. and Andersson, H.I. (1997). Turbulent plane Couette flow subject to strong system rotation. *J. Fluid Mech.* **347**, 289–314.

Bech, K.H., Tillmark, N., Alfredsson, P.H. and Andersson, H.I. (1995). An investigation of turbulent plane Couette flow at low Reynolds numbers. *J. Fluid Mech.* **286**, 291–325.

Coles, D. (1965). Transition in circular Couette flow. *J. Fluid Mech.* **21**, 385–425.

Dauchot, O. and Daviaud, F. (1994). Finite amplitude perturbations in plane Couette flow. *Europhys. Lett.* **28**, 225–230.

Daviaud, F., Hegseth, J. and Bergé, P. (1992). Subcritical transition to turbulence in plane Couette flow. *Phys. Rev. Lett.* **69**, 2511–2514.

Johnston, J.P., Halleen, R.M. and Lezius, D.K. (1972). Effects of spanwise rotation on the structure of two-dimensional fully developed turbulent channel flow. *J. Fluid Mech.* **56**, 533–557.

Komminaho, J., Lundblad, A. and Johansson, A.V. (1996). Very large structures in plane turbulent Couette flow. *J. Fluid Mech.* **320**, 259–285.

Lezius, D.K. and Johnston, J.P. (1976). Roll-cell instabilities in rotating laminar and turbulent channel flows. *J. Fluid Mech.* **77**, 153–175.

Lundblad, A. and Johansson, A.V. (1991). Direct simulation of turbulent spots in plane Couette flow. *J. Fluid Mech.* **229**, 499–516.

Nagata, M. (1998). Tertiary solutions and their stability in rotating plane Couette flow. *J. Fluid Mech.* **358**, 357–378.

Schmid, P.J. and Henningson, D.S. (2001). *Stability and Transition in Shear Flows*, Springer.

Tillmark, N. (1995). On the spreading mechanisms of a turbulent spot in plane Couette flow. *Europhys. Lett.* **32**, 481–485.

Tillmark, N. and Alfredsson, P.H. (1992). Experiments on transition in plane Couette flow. *J. Fluid Mech.* **235**, 89–102.

Tillmark, N. and Alfredsson, P.H. (1996). Experiments on rotating plane Couette flow. In *Proceedings of the Sixth European Turbulence Conference 1996, Advances in Turbulence VI*, S. Gavrilakis, L. Machiels and P.A. Monkewitz (eds), Kluwer, Dordrecht, pp. 391–394.

TRANSITION *TO* VERSUS *FROM* TURBULENCE IN SUBCRITICAL COUETTE FLOWS

A. Prigent[1] and O. Dauchot[2]
[1]*Laboratoire de Mécanique, Physique et Géosciences, Université du Havre, 25 Rue Philippe Lebon, 76600 Le Havre, France*
[2]*Groupe Instabilités et Turbulence, DSM / SPEC, CEA Saclay, 91191 Gif sur Yvette, France*
arnaud.prigent@univ-lehavre.fr, olivier.dauchot@cea.fr

Abstract We report experiments conducted in Taylor–Couette and plane Couette flows considering both the transition from laminar to turbulent flow and the reverse transition from turbulent to laminar flow. In the first case, the transition is discontinuous and is characterized by laminar-turbulent coexistence. The transition is controlled by the existence of finite amplitude solutions. In the second case, unexpectedly, the transition is continuous and leads to a periodical stripes pattern whose wavelength is large compared to the shear scale. This pattern can even be described in a generalized noisy Ginzburg–Landau formalism. In this context, the intermittent and disordered laminar-turbulent coexistence can be seen as the ultimate stage of the modulation of the turbulent flows.

1. INTRODUCTION

When studying the transition to turbulence one usually considers the transition from the laminar *to* the turbulent flow. In many flows, this transition is supercritical. The bifurcated state exists only above the linear stability threshold and remains close to the basic state. In other flows, as in the plane Couette flow, this transition is subcritical. It generally proceeds abruptly by the appearance of turbulent domains coexisting with laminar ones. As illustrated in Figure 1 these domains may take more or less regular shapes and the laminar-turbulent coexistence regime that sets in is often characterized by a complex spatio-temporal dynamics called intermittency. In that case the transition is governed by the properties of the phase space at finite distance from the basic state. Accordingly the description of the transition is out of reach of any perturbative method. Alternatively, one may consider the reverse transition *from* the turbulent to the laminar flow. It turns out that the intermittent regime is preceded by a modulation of the homogeneous turbulent state, which can be described within a weakly nonlinear formalism.

T. Mullin and R.R. Kerswell (eds), Laminar Turbulent Transition and Finite Amplitude Solutions, 195–219.
© 2005 *Springer. Printed in the Netherlands.*

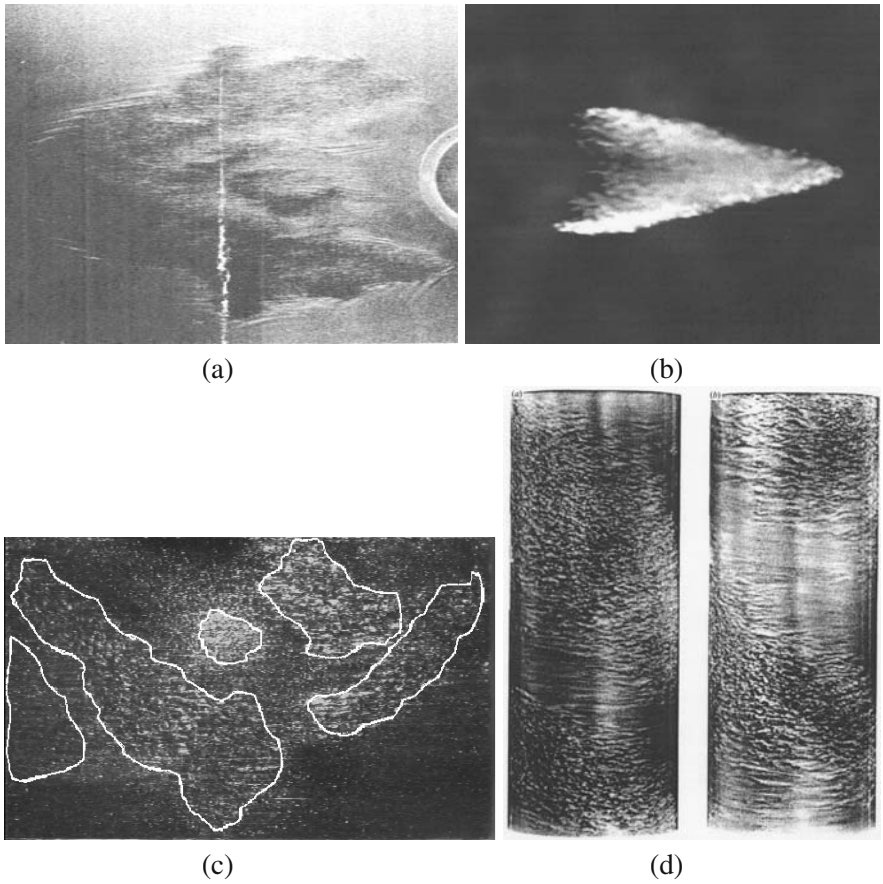

Figure 1. Laminar-turbulence coexistence regime in the plane Poiseuille flow (a) from Alavyoon et al. (1986), in the boundary layer (b) from Gad-El-Hak (1981), in the plane Couette flow (c) from Bottin (1998) and in the Taylor–Couette flow (d) from Andereck et al. (1986).

In the present paper, we review experimental results on the transition to turbulence obtained during the last decade in the Saclay group. We first report experiments conducted in the plane Couette flow which is stable for all Reynolds numbers (Romanov, 1973) whereas direct transition to turbulence is experimentally observed and therefore is a good prototype to study the subcritical transition. We then report experiments conducted in the plane Couette flow and the Taylor–Couette flow in large aspect ratios configuration. In the Taylor–Couette flow, the intermittency regime turns into an ordered laminar-turbulent pattern called spiral turbulence (see Figure 1(d) from Andereck et al., 1986). Here we consider the reverse transition from the turbulent flow and

Table 1. Geometrical characteristics of the plane Couette device for the three gap widths. $\Gamma_z^{PC} = L_z/\delta$ and $\Gamma_x^{PC} = L_x/\delta$. PC_i refers to the plane Couette device according to its gap width.

Device	δ (mm)	Γ_z^{PC}	Γ_x^{PC}
PC_1	7.0	36	83
PC_2	3.5	85	193
PC_3	1.5	170	385

show that the spiral turbulence is actually a long wavelength modulation of the turbulent flow which also occurs in the plane Couette flow.

The paper is organized as follows. The first part presents the two experimental setup. The second part reports experiments conducted in the plane Couette flow on the laminar-turbulent transition. The third part is devoted to experiments conducted in large aspect ratios Taylor–Couette and plane Couette flows on the turbulent-laminar transition. The last part presents concluding remarks and perspectives.

2. EXPERIMENTAL SETUP

2.1 The plane Couette apparatus

Our plane Couette apparatus (Daviaud et al., 1992) is made of an endless transparent plastic film belt (363.0 cm long, 25.4 cm wide, 0.15 mm thick) driven by two pairs of small guiding rotating cylinders and one pair of large rotating cylinders as shown in Figure 2. The guiding cylinders fix the gap width δ between the walls. Table 1 gives the characteristics of the plane Couette device PC_i according to the three different gap widths used for the works reported here: PC_1, or PC_2 if specified, for those on the laminar-turbulent transition and PC_3 otherwise. The belt is also guided by two glass plates 3 mm apart and strictly parallel to the walls. The entire set up is placed in a tank filled with water. The temperature is controlled within 0.5° K. The gap size is controlled with an accuracy of 0.1 mm, that is 1.5% of the largest gap width and 6.5% of the smallest. Accordingly, the accuracy on the Reynolds number is between 2.5% and 7.5%.

The study is based on flow visualizations and quantitative velocity measurements by laser Doppler velocimetry (LDV). For visualizations, the flow is seeded with Kalliroscope AQ 1000 ($6 \times 30 \times 0.07 \mu$m platelets) or iriodin flakes and lighted on its whole width with a thin laser sheet. In a laminar flow, the reflected light is steady and rather weak, because of the averaged orientation of the flakes parallel to the laser sheet. In a turbulent flow, the reflected light intensity is larger and fluctuating. Images and spatio-temporal diagrams (tem-

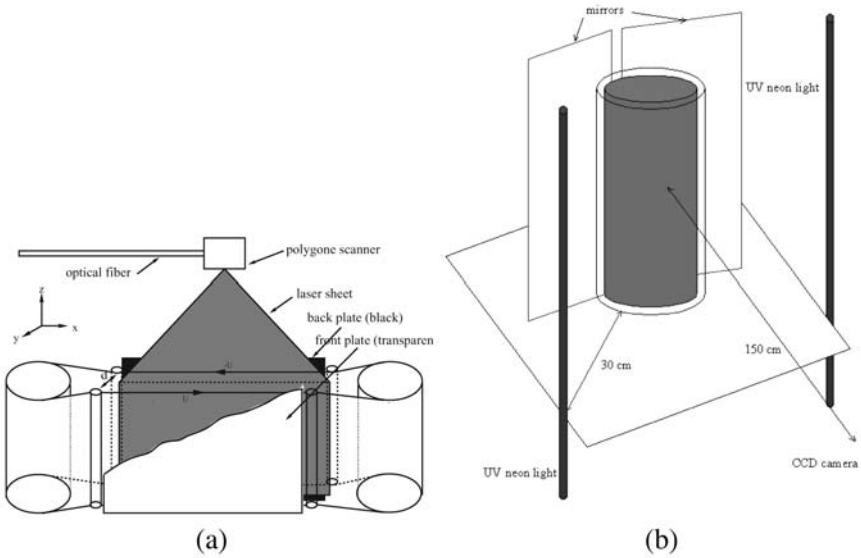

Figure 2. Schematic drawing of the plane Couette (a) and Taylor–Couette apparatus (b).

Table 2. Geometrical characteristics of the Taylor–Couette device for the two inner cylinders. $\eta = r_i/r_o$, $\Gamma_z^{\mathrm{TC}} = L_z/d$ and $\Gamma_\theta^{\mathrm{TC}} = \pi(r_i + r_o)/d$. TC_{η_i} refers to the Taylor–Couette device according to its inner radius.

Device	r_i (mm)	d (mm)	η	Γ_z^{TC}	$\Gamma_\theta^{\mathrm{PC}}$
TC_{η_1}	49.09	0.87	0.983	431	358
TC_{η_2}	48.11	1.85	0.963	203	167

poral recording of one line along the spanwise direction) are recorded by a CCD camera.

2.2 The Taylor–Couette apparatus

Our Taylor–Couette apparatus (Prigent and Dauchot, 2000) is made of two independently rotating coaxial cylinders. The useful length is $L_z = 375 \pm 0.1$ mm and the glass outer cylinder has an inner radius $r_o = 49.96 \pm 0.005$ mm. Two inner cylinders of radius r_i can be used and Table 2 gives the geometrical characteristics of the Taylor–Couette device TC_{η_i} according to the used inner cylinder.

The aspect ratios are large and the radius ratios η are very close to 1. Once the geometry is fixed, the flow is governed by the inner and outer Reynolds numbers $R_{i,o} = r_{i,o}\Omega_{i,o}d/\nu$, with $\Omega_{i,o}$ the angular velocities, and ν the kinematic viscosity of water. The flow is thermalized by water circulation inside

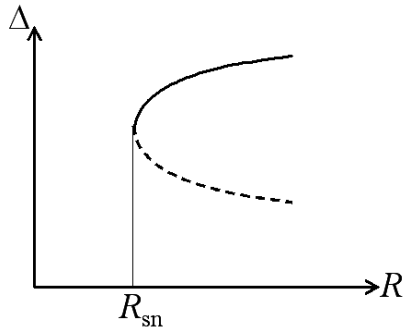

Figure 3 Globally subcritical bifurcation with a non-trivial branch of solution fully disconnected from an ever linearly stable basic state. Δ is some "distance" to the basic state.

the inner cylinder. At thermal equilibrium the temperature is uniform in space up to 0.1° K and does not vary more than 0.1° K/hour. As a result, the accuracy on $R_{\mathrm{i,o}}$ is of the order of 3%. The flow is visualized using a "fluorescent lighting" technique (Prigent and Dauchot, 2000) developed for the purpose of this study. The water flow is seeded with Kalliroscope AQ 1000. The inner cylinder is covered by a fluorescent film and the entire apparatus is UV-lighted. The fluorescent film re-emits a uniform visible lighting, transmitted through the fluid layer: the more turbulent the flow is, the brighter it appears. Images and spatio-temporal diagrams (temporal recording of one line along the cylinder axis) are recorded by a CCD camera. Two plane mirrors reflect the two thirds of the flow hidden to the camera so that the whole cylindrical flow can be reconstructed. The $\mathrm{TC}_{\eta 2}$ apparatus allows to perform LDV measurements of the velocity.

For the purpose of comparison between the two flows, we define the Reynolds number R equivalently in both flows as the ratio of the viscous time scale to the shear time scale. The length scale h is chosen to be half the gap, as usually done in the plane Couette flow context, so that

$$R^{\mathrm{PC}} = \frac{U}{h} \times \frac{h^2}{\nu} = \frac{Uh}{\nu}$$

(with U the belt velocity), and

$$R^{\mathrm{TC}} = \frac{r_{\mathrm{i}}\Omega_{\mathrm{i}} - \eta r_{\mathrm{o}}\Omega_{\mathrm{o}}}{(1+\eta)h} \times \frac{h^2}{\nu} = \frac{(r_{\mathrm{i}}\Omega_{\mathrm{i}} - \eta r_{\mathrm{o}}\Omega_{\mathrm{o}})h}{(1+\eta)\nu}.$$

3. THE TRANSITION *TO* TURBULENCE

3.1 Unstable finite amplitude solutions

Figure 3 is a schematic view of the bifurcation diagram corresponding to the plane Couette flow. For more details, see Dauchot and Manneville (1997) and

the paper of Manneville in the present book (Manneville, 2005) and references therein. The basic state is linearly stable for all Reynolds numbers (Romanov, 1973). The upper branch corresponds to a bifurcated state such as the turbulent one which coexists with the basic one. It appears at R_{sn} through a saddle-node bifurcation fully disconnected from the basic state. Accordingly, nontrivial solutions have to be searched in the full phase space, hence this kind of transition is called "globally subcritical". In that context, Dauchot and Manneville (1997) have studied a simple two ordinary differential equations model with the same key properties of the Navier–Stokes operator, namely the non normality of the linearized operator and the energy conservation by the nonlinear terms. In particular, they show the importance of the role played by the unstable finite amplitude solutions which are also the key elements of more realistic models (Waleffe, 1995, 1997; Hamilton et al., 1995; Schmiegel and Eckhardt, 1997; Eckhardt and Mersmann, 1999; Manneville and Dauchot, 2000).

These solutions are observable either temporarily in the laminar-turbulent coexistence regime, either in a more stabilized form when forcing the base flow. Figure 4 from Bottin et al. (1998a) shows the relaxation from the turbulent plane Couette flow ($R > 500$) to the laminar flow at $R = 250$ below the transition threshold. One distinguishes clearly the presence of more or less spaced streamwise stripes. As shown in Figure 5(a) these structures are also present around and inside a spot obtained at $R \simeq 320$ using a tiny jet through the gap as an instantaneous localized perturbation (Dauchot and Daviaud, 1994; Dauchot and Daviaud, 1995a). Cuts in the spanwise direction (Figure 5(b)) reveal that these structures correspond to paired streamwise vortices extending over the gap and, though more disorganized, still present inside the spot. In such experiments, the vortices are not stable enough to allow their quantitative study. An alternative method adopted here is to introduce a thin wire in the zero-velocity plane perpendicularly to the flow (Dauchot and Daviaud, 1995b).

Figure 6 presents two sets of spanwise cuts for two different wire diameters. The counter-rotating streamwise vortices appear clearly. When reducing the wire diameter their size remains almost constant but they become more independent. Vortices still exists for wire diameter smaller than 0.5% of the gap width.

As confirmed by Barkley and Tuckerman (1999) these coherent structures are representative of a family of unstable finite amplitude solutions of the non modified plane Couette flow. Similar approaches have also been considered in several numerical studies of the plane Couette flow (Nagata, 1986, 1990; Busse and Clever, 1995; Cherhabili and Ehrenstein, 1996; Clever et al., 1997) which all, except Cherhabili and Ehrenstein (1996), lead to the observation of streamwise vortices.

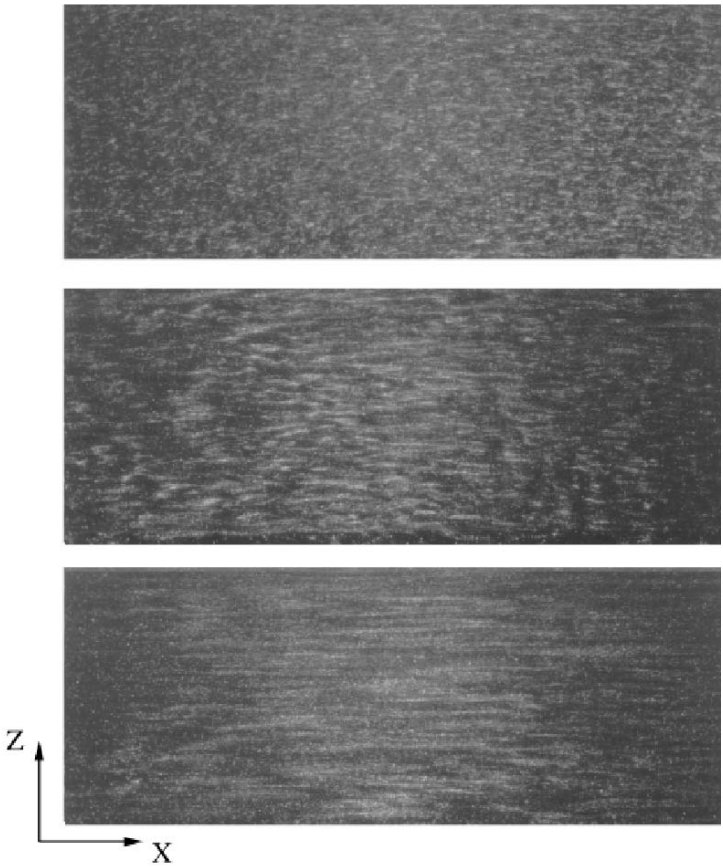

Figure 4. Snapshots of the relaxation of the turbulent plane Couette flow after a brutal quench from $R > 500$ to $R = 250$, $t = t_0$, $t = t_0 + 5s$, $t = t_0 + 10s$.

The knowledge of these finite amplitude solutions, their properties of stability and the observation of the underlying hydrodynamic mechanisms have suggested various modellings (Waleffe, 1995, 1997; Hamilton et al., 1995; Schmiegel and Eckhardt, 1997; Eckhardt and Mersmann, 1999; Manneville and Dauchot, 2000) for which the streamwise vortices are the elementary bricks of the dynamics. The study of these models has revealed that several families of unstable solutions fill the phase space even before the apparition of the first stable solution other than the basic state. The trajectory in phase space might visit the vicinity of these unstable fixed points leading to long transients very sensitive to the initial consition. As a result the dynamics is strongly conditioned by these numerous unstable finite amplitude solutions.

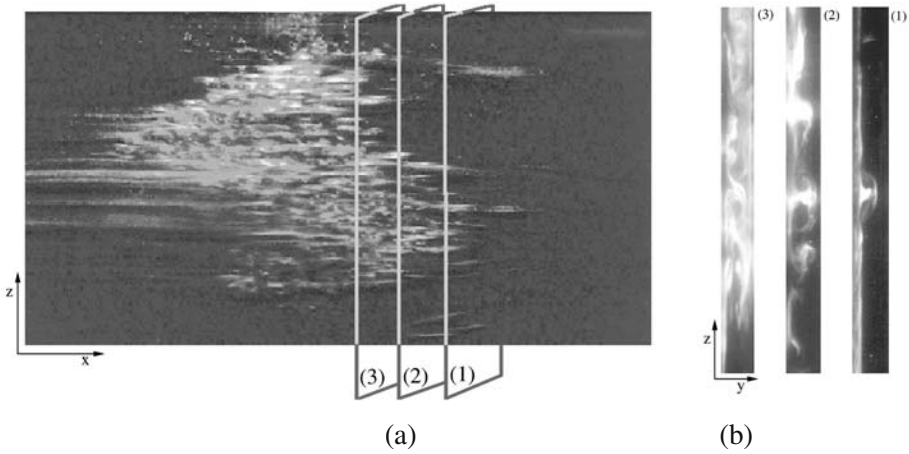

Figure 5. Structure of the flow inside and around a spot for $R = 340$. (a) Snapshot of the flow. (b) (y, z) cuts at three different positions.

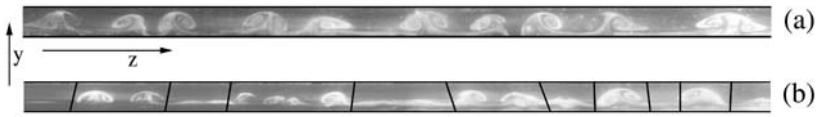

Figure 6. (y, z) cuts of the coherent structures observed in the modified plane Couette flow. The modification is realized with a wire of diameter ρ. (a) $\rho/h = 0.057$, (b) $\rho/h = 0.014$.

3.2 Long transients and laminar-turbulent coexistence

We describe now the response of the plane Couette flow to a finite amplitude perturbation as well as its relaxation during quench experiments from the fully turbulent flow. As the laminar velocity profile is linearly stable for all Reynolds numbers, only finite amplitude perturbations are able to induce a transition leading to the observation of turbulent domains or spots (Daviaud et al., 1992) (Figure 1). In the present case, these perturbations are realized using a jet through the gap (Dauchot and Daviaud, 1994; Dauchot and Daviaud, 1995a), their dimensionless amplitude being given by $A = v/U$ where v is the mean velocity of the jet flow. They are called effective if their amplitude is such that the disturbance is sustained for a long time. Hence one defines, for a given perturbation, a critical amplitude A_c function of the Reynolds number and below which the perturbation is ineffective.

The simplest way to follow the evolution of a perturbation is to measure the ratio of the surface occupied by turbulence to the total surface. This ratio called turbulent fraction F_t is displayed in Figure 7(a). One distinguishes three ranges of Reynolds number. For $R < R_u \simeq 310$, all perturbations relax monotonously on a viscous time-scale. For $R_u < R < R_g \simeq 325$, all per-

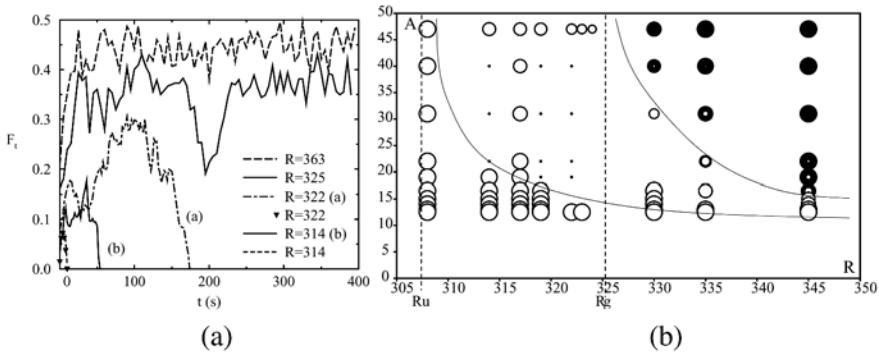

Figure 7. (a) Typical time evolutions of F_t. (b) Probability that a perturbation of amplitude A in an experiment at Reynolds number R destabilizes permanently the flow (dark disks), or relaxes monotonously (white disks). The disks size is proportional to the considered probability. The curves separate the domains of the (R, A) plane dominated by one of the three possible dynamical regimes.

turbations relax but those having the largest amplitude exhibit long transients with large fluctuations of F_t. For $R > R_g$, the large amplitude perturbations may destabilize the laminar flow permanently, whereas the others exhibit one or the other relaxational dynamics. Observing a particular evolution strongly depends on the perturbation, even at given Reynolds number and operating protocol. It is impossible to decide on the basis of a single experiment whether perturbations of a given amplitude lead to sustained turbulence or not. As a matter of fact, the only meaningful quantities are the probabilities, estimated from a large number of experiments, to exhibit one or the other dynamics. Figure 7(b) show these probalities in the (R, A) plane. It is in good qualitative aggreement with similar observations obtained within the Waleffe's model by Dauchot and Vioujard (2000), as well as within numerical simulations by Eckhardt and Mersmann (1999).

The threshold R_g can also be approached from above by quenching the homogeneous turbulent flow at high Reynolds number $R_{\text{init}} > R_g$ to a smaller Reynolds number R_{final} (Bottin et al., 1998b; Bottin and Chaté, 1998). Such experiments have the advantage of not requiring the choice of some type of initial perturbation but they must be averaged over initial conditions representative of the turbulent flow (Figure 8). For $R > R_g$, the turbulent fraction rapidly decreases towards a constant mean value. For $R_u < R < R_g$, the flow asymptotically relax to the laminar flow, presenting long transients for which a mean value of F_t can still be defined. The duration τ of the decay of the sustained turbulence strongly fluctuates and has to be described via a probability distribution. The transition is then defined by the observed divergence of its first moment when $R_{\text{final}} \to R_g$. Finally for $R < R_u$, the relaxation is

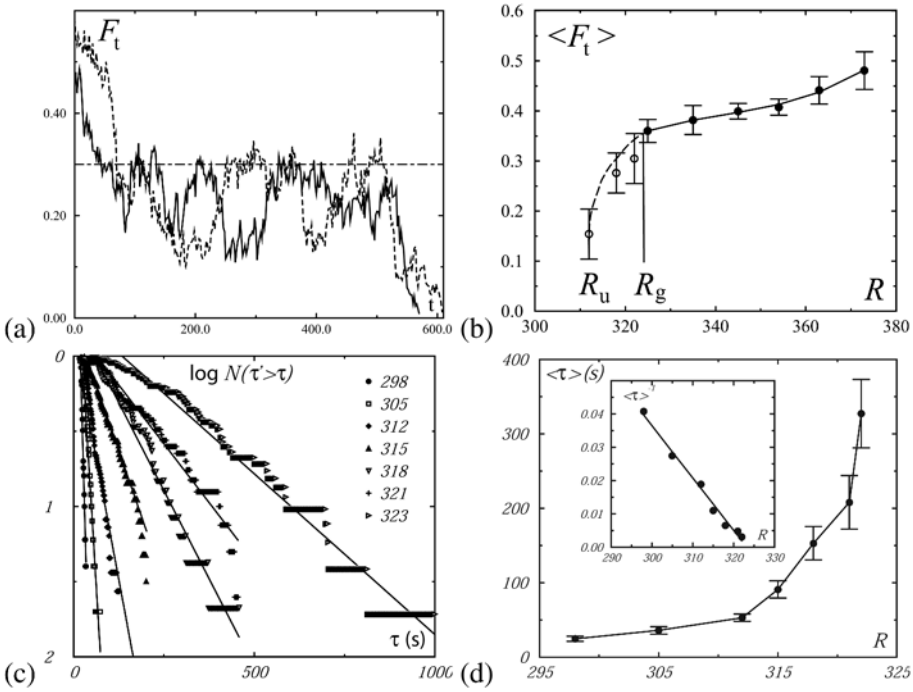

Figure 8. (a) Evolution of F_t in quench experiment. (b) Mean turbulent fraction $\langle F_t \rangle$ for a permanent regime (solid line) and a transient regime (dotted line). (c) Logarithms of cumulated distributions $N(\tau' > \tau)$ of transient lifetimes τ' longer than a given value τ for various Reynolds numbers. (d) Mean lifetimes obtained as the slope of the exponential tails or the mean of these distributions. Insert: divergence of $\langle \tau \rangle$ as $(R_g - R)^{-1}$ with $R_g \simeq 325$.

instantaneous. One may notice a strong similarity with the simulations of the Swift–Hohenberg type model of Manneville and Dauchot (2000).

Taking into account all of the above facts, one is led to the following general picture for the transition to turbulence in the plane Couette flow. For $R < R_g$, The laminar flow is the only attractor of the system. For $R < R_u$, the possibly existing unstable non laminar solutions do not influence the dynamics and the monotonous relaxation to the laminar flow. For $R > R_u$, these unstable solutions give rise to a complex dynamics as their stable directions strongly influence the trajectory in phase space. This suggests the emergence of a chaotic repellor, which for $R > R_g$, turns into a turbulent attractor, the laminar state not being anymore the only asymptotic state. Depending on the position of initial conditions with respect to the complex boundary separating the two basins of attraction, one reaches either the statistically-steady turbulent state or decays to the fully laminar flow (Dauchot and Chaté, 1999).

Let us finally consider the spatio-temporal structure of the laminar-turbulent coexistence regime. Figure 1(c) displays a typical snapshot of the flow regime

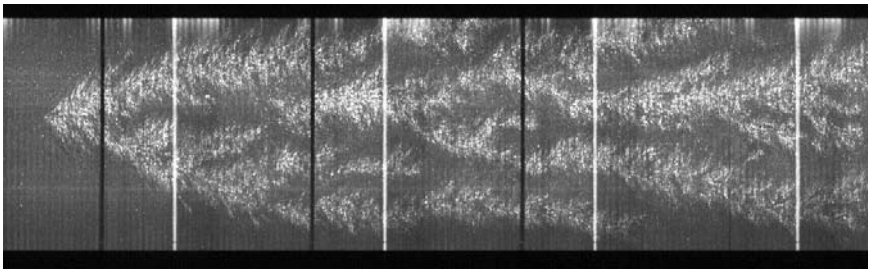

Figure 9. Spatio-temporal diagram of a spanwise line displaying the contamination of the flow from its extremities (PC_2 device).

above R_g where the turbulent regions have been delimited by white lines. The turbulent spots move, grow or decay, split or merge in an erratic way. This dynamics is characteristic of the spatio-temporal intermittency (STI) (see, e.g., Chaté and Manneville, 1987, 1994). The linear stability of the laminar flow guarantees that turbulent spots can only grow by contamination of laminar regions (Figure 9). This suggests to look at the subcritical transition to turbulence as an out of equilibrium phase transition of the type of the directed percolation as proposed by Pomeau (1986).

For that purpose, one has to consider two locally defined states (laminar and turbulent) and two phases in a thermodynamical spirit (an homogeneous laminar one and a spatio-temporally intermittent one). Then one has to choose an order parameter M, which has to be zero in the homogeneous laminar phase and non zero in the STI phase.

In the present case, the mean turbulent fraction $\langle F_t \rangle$ is a good candidate for such an order parameter. Far from the threshold, the two phases dynamics can be modelized by a reaction-diffusion equation (Bergé et al., 1998):

$$\frac{\partial M}{\partial t} = D \triangle M - \frac{\delta \Phi(M)}{\delta M}$$

where D is a positive coefficient of diffusion and Φ is a potential depending on the control parameter (the Reynolds number in our case). Its minima indicate the values of M for possible homogeneous stable phases, M_L standing for the laminar phase and M_{STI} for the STI phase. The most stable phase is the one for which $\Phi(M)$ is the lowest. Notice that, far above threshold, M_{STI} is generally close to 1 and the STI phase is often abusively called turbulent phase. In one dimension system, a front separating two phases moves in the direction allowing the most stable phase to substitute for the other phase. A threshold value of the control parameter R_μ appears, for which the two minima of Φ have the same value and the front moves in the opposite direction. In the context of the plane Couette flow modeling, $R_\mu = R_g$. In a two-dimensional system, one adds to the description the Gibbs–Vollmer model of nucleation, which takes

into account the interfacial energy between the two phases (Bergé et al., 1998). Below threshold, the STI phase asymptotically vanishes but the lifetime of the turbulent spots diverges at threshold. Above threshold, the critical amplitude A_c can be interpreted as the amplitude necessary for the creation of a turbulent domain with a size greater than the critical nucleus. However, close to threshold, the fronts width shall increase and their propagating velocity goes to zero so that the fluctuations in the STI phase strongly increase. A mean field type description as the one above can not handle such fluctuations so that one must consider more "microscopic" models including a probabilistic or deterministic local dynamics. In that context, similarities have been found by Bottin et al. (1998b) between experimental results obtained in the plane Couette flow and simulations of a coupled map lattices minimal model. In such a description, Figure 8(b) can be interpreted as the variation of the order parameter for a discontinuous first order transition.

4. THE TRANSITION *FROM* TURBULENCE

In the first part we have studied the laminar to turbulence transition in the plane Couette flow. It appears subcritical, strongly conditionned by finite amplitude solutions and displays a complex spatio-temporal dynamics. Such transition is also known to exhibit hysteresis. In the following, we investigate the reverse transition from the turbulent to the laminar flow in large aspect ratios plane Couette (PC_3) and Taylor–Couette flows.

4.1 Qualitative description of the transition

Figures 10 and 11 display snapshots of each flow for decreasing values of the Reynolds number (internal Reynolds number in the Taylor–Couette case).

The deceleration rate is as small as $0.1\% R\ \mathrm{s}^{-1}$ and the flow is let to stabilize before each snapshot is taken. At high enough Reynolds number, both flows are homogeneously turbulent. Decreasing R, there is a critical value below which a periodic structure appears with two preferred opposite inclinations. The pattern occurs simultaneously in the whole flow and does not appear to be triggered by end effects. Close to threshold, nucleation of competing domains of both orientations occurs. For lower R, a regular pattern is eventually reached after a transient during which domains, separated by wandering fronts, again compete. The oblique stripes have a wavelength of the order of 50 times the gap. The pattern is stationary in the plane Couette flow case, and rotates at the mean angular velocity of both cylinders (see further) in the Taylor–Couette flow case. For even lower Reynolds number, the stripes pattern breaks down, leaving a spatiotemporally intermittent regime of turbulent patches evolving in an otherwise laminar flow.

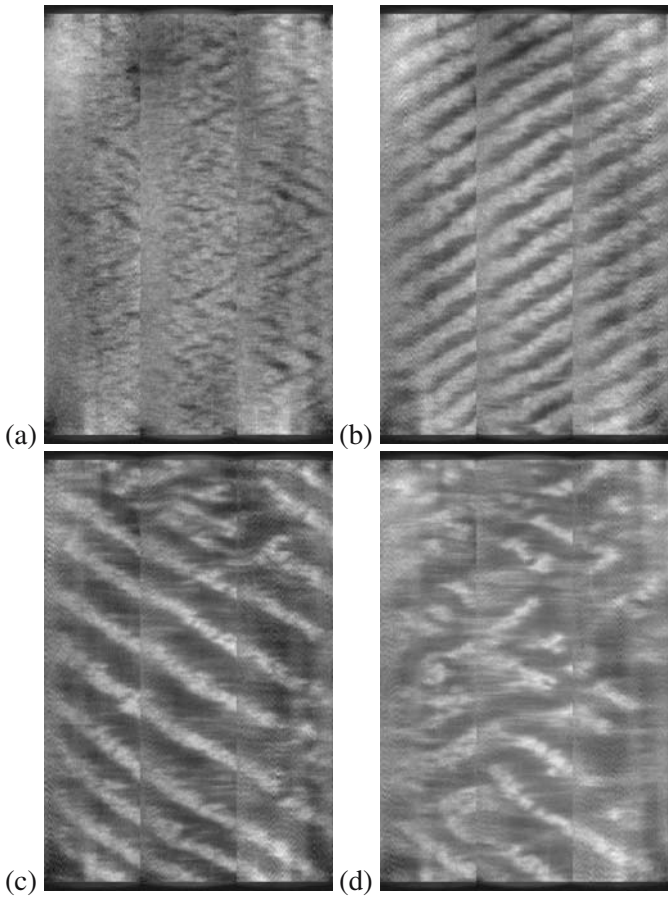

Figure 10. Turbulent spots and stripes along path F, (see Figure 12). $R^{\mathrm{TC}} =$ (a) 391; (b) 368; (c) 340; (d) 331. Each picture displays a 360° view of the whole flow (38 cm high and 31.4 cm wide). The vertical lines are dued to the image reconstruction.

The pattern is observed for $340 < R < 415$ in the plane Couette flow, and in the so-called "spiral turbulence" region of the bifurcation diagram in the Taylor–Couette flow (see Figure 12). This diagram, obtained by following the procedure introduced by Coles (1965) is similar to the one obtained by Andereck et al. (1986) for a different geometry ($\eta = 0.878$ and much smaller aspect ratio). The same regimes are observed, but the linear instabilities thresholds are shifted to higher R values and the subcritical character of the flow is "enhanced" (the laminar-turbulent coexistence regions "INT" and "SPT" are larger). In agreement with the azimuthal aspect ratio ($\Gamma_\theta = 55$) of their apparatus, the spiral turbulence regime described by Van Atta (1966) and later by Andereck et al. (1986), corresponds to one wavelength of the regular pattern observed here. For azimuthal aspect ratios as small as 20 no spiral

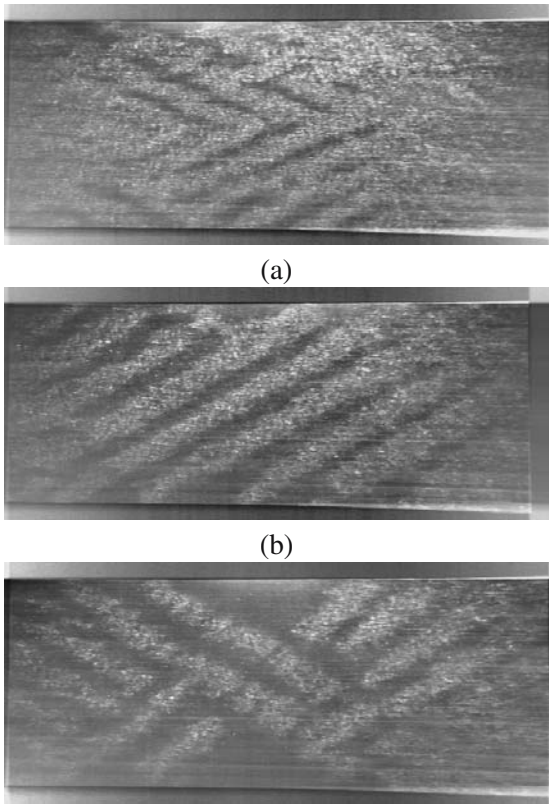

(a)

(b)

(c)

Figure 11. Turbulent stripes in plane Couette flow (PC_3 device). R^{PC} = (a) 393; (b) 358; (c) 340. Each picture displays a view of the whole flow (25.4 cm high and 57.7 cm wide).

turbulence takes place and, similarly, plane Couette flow studies with small aspect ratios, as PC_1 and PC_2, can only produce one or two turbulent spots taking sometimes the shape of an inclined stripe.

4.2 Comparison between both flows

As it can be noticed in Figure 12 the path E defined by $R_i = -\eta R_o$, where $\mu = \Omega_0/\Omega_i = -1$, crosses the spiral turbulence regime, in contrast with smaller-η experiments where spiral turbulence occurs only below this straight line. We take advantage of this opportunity to develop a full comparison with the plane Couette flow, since in this case both patterns are stationary and governed by only one control parameter. As shown in Figure 13, the similarity between the two flows goes beyond the above qualitative description. Both patterns have the same Reynolds number range of existence and exhibit the same wavelengths at any R, the only difference being that the azimuthal wavenum-

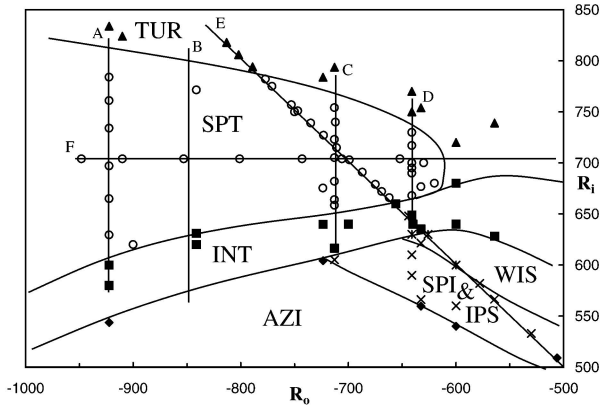

Figure 12. Zoom on the region of interest of the experimental phase diagram ($\eta = 0.983$). The labels (see Andereck et al., 1986, for details) stand for AZI: azimuthal flow; SPI&IPS: spiral and interpenetrating spiral vortices; WIS: wavy inter-penetrating spiral vortices; INT: intermittency; SPT: spiral turbulence; TUR: turbulence. The solid straight lines show the paths along which measurements are conducted.

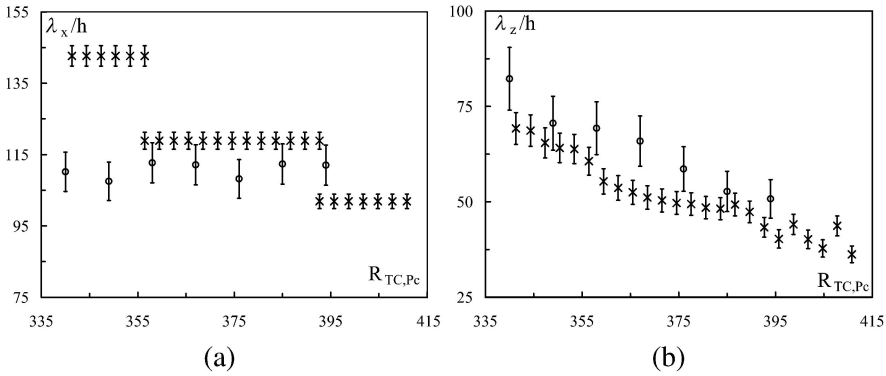

Figure 13. (a) streamwise/azimuthal wavelengths and (b) spanwise/axial wavelengths vs. the Reynolds numbers R^{PC} in PC (∘) and $R^{\mathrm{TC}} = \frac{R_i+R_o}{2(1+\eta)\nu}$ along path E in TC (×).

ber is quantized by the circumference in the Taylor–Couette case. We can now investigate the transition in more details on data collected solely with the Taylor–Couette apparatus for which the mechanical control is the best. We are nevertheless confident that most of our findings apply to both flows.

4.3 A modulation of the turbulence strength

Given that the azimuthal wave number is constant in most of the "spiral turbulence" region of the (R_{i}, R_{o}) plane, it is convenient to record the light intensity I along the cylinders axis z only and analyze the spatiotemporal diagrams $I(z, t)$.

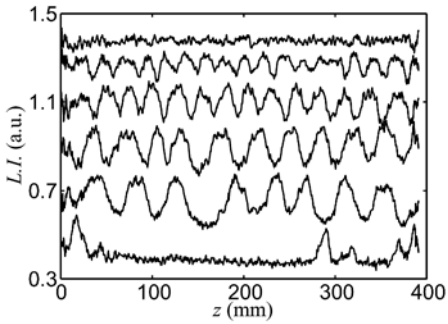

Figure 14. Axial light intensity profiles in the Taylor–Couette flow, decreasing R_i from 900 to 550, at fixed $R_o = -1055$. (The mean value of each profile has been arbitrarily fixed for the purpose of clarity.)

Figure 14 displays typical light intensity profiles $I(z)$ for various Reynolds numbers. Keeping R_o fixed and decreasing R_i from the fully-turbulent to the intermittent regime, a modulation gradually appears along $I(z)$, indicating the continuous nature of the transition. The amplitude and wavelength of the modulation increase until the modulation minima saturate at the light intensity corresponding to the laminar flow. Only then can one speak of coexistence of laminar and turbulent domains. At still lower Reynolds numbers, the pattern loses its coherence and the turbulent stripes become "independent" patches.

In TC_{η_2} apparatus, it is possible to perform laser Doppler velocimetry measurements in order to access directly hydrodynamical quantities and to relate them to the light intensity. Figure 15 displays $v_z(t)$ (dark line), its running average $\langle v_z \rangle(t)$ (white line) and $v_{rms}(t)$ the *rms* of previous average (bottom) for $R_o = -850$ and three different R_i values corresponding to the three different regimes identified by light intensity observation: the fully turbulent regime at $R_i = 2000$, the spiral turbulence regime at $R_i = 670$ and the laminar regime at $R_i = 0$. As expected given the symetries of the system, for both the fully turbulent regime (Figure 15(a)) and the laminar one (Figure 15(c)), the signals are stationnary in average. For the laminar regime, the mean value of v_{rms} is close to zero and indicates the experimental noise intensity. The fully turbulent regime is characterized by high fluctuations compared to the experimental noise. In the spiral turbulence regime, the velocity, its running average and its *rms* are modulated and share the same modulation frequency which corresponds to the mean angular rotation frequency times the azimuthal wavenumber ($n_\theta = 3$ in the present geometry). Furthermore, decreasing the inner Reynolds number down from the fully-turbulent regime to the spiral turbulence one, both the average velocity modulation and the velocity fluctuations modulation increase as does the light intensity modulation, the lighter regions being more turbulent. More specifically, the amplitude of the modulation of the light intensity

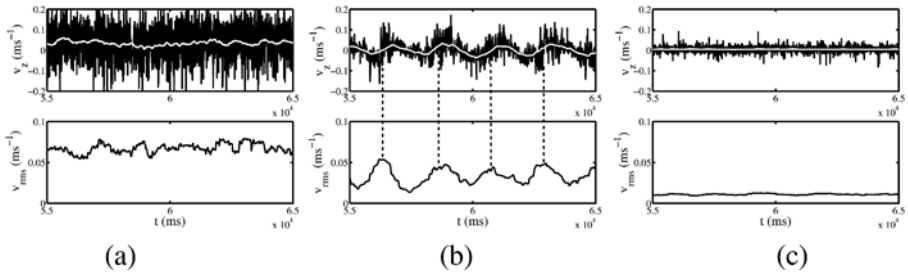

Figure 15. Axial velocity time series (v_z) at mid-gap and mid-height for $R_o = -850$, $R_i = 2000$ (a), $R_i = 680$ (b) and $R_i = 0$ (c). Velocities are given in m/s and the time is in ms. The top curve presents the instantaneous signal (dark line) with its running average (white line) calculated over windows of 400 time-steps. The bottom curve presents the *rms* of previous average.

$\mathcal{A}$ shows a linear dependance with the amplitude of the modulation of $v_{\rm rms}$ (see Prigent et al., 2002, for details). As a result $I(z,t)$ can be used to investigate the spatiotemporal dynamics of the modulation in the largest aspect ratio apparatus TC_{η_1}, in which LDV measurements are not accessible given the too small gap width.

Figure 16 displays the spatio-temporal diagrams $I(z,t)$ obtained for $R_{\rm o} = -850$ just below threshold for $R_{\rm i} = 785$ (Figure 16(a)) and in the core of the spiral turbulence regime for $R_{\rm i} = 720$ (Figure 16(b)). Close to threshold domains with one or the other inclination are constantly nucleated. Their sizes are exponentially distributed with a characteristic scale that rapidly reaches the size of the system as $R_{\rm i}$ is decreased. Below $R_{\rm i} = R^*$, no nucleation occurs and only transient fronts are observed. A Fourier analysis of the spatio-temporal diagrams allows an easy determination of the basic frequency and wavelength. As already mentioned, the angular velocity of the pattern (the measured frequency divided by the azimuthal wavenumber) is equal to $\Omega_{\rm m} = (\omega_{\rm i} + \omega_{\rm o})/2$ the mean angular velocity of both cylinders (see Figure 17(a)). The axial wavelength increases while decreasing $R_{\rm i}$ and slightly depends on $R_{\rm o}$ (see Figure 17(b)). At threshold the axial wavelength is independent of $R_{\rm o}$.

4.4 Description in terms of slowly varying amplitude

Applying now the standard complex demodulation technique to the spatio-temporal diagrams, the light intensity $I(z,t)$ is writen in terms of slowly varying complex fields A^+ and A^-:

$$\begin{aligned} I(z,t) &= A^-(z,t)\exp i(\omega_0 t - k_0 z) \\ &\quad + A^+(z,t)\exp i(\omega_0 t + k_0 z) + c.c. \end{aligned}$$

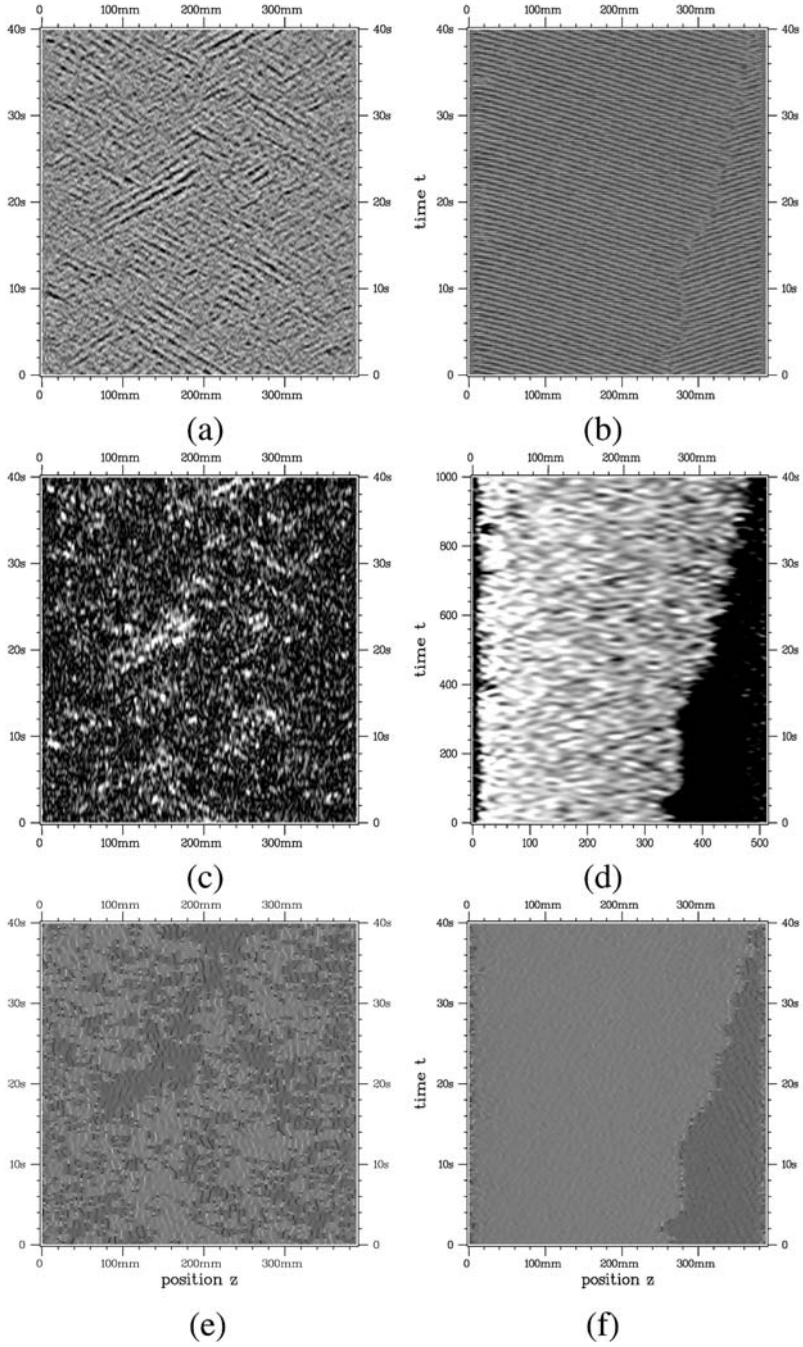

Figure 16. Spatio-temporal diagrams for $R_o = -850$ and $R_i = 785$ (left column) and $R_i = 720$ (right column). (a)(b): Intensity $I(z,t)$. (c)(d): module $|A^+(z,t)|$. (e)(f): frequency $\partial_z \arg A^{\pm}$.

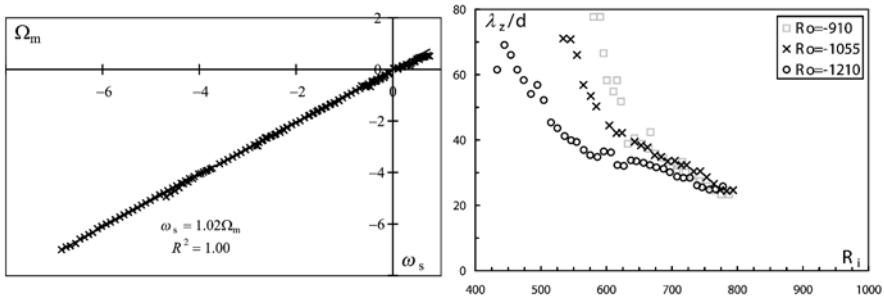

Figure 17. (a) Temporal frequency versus mean angular velocity of both cylinders Ω_m in units of viscous time d^2/ν. (b) Axial wavelength λ_z.

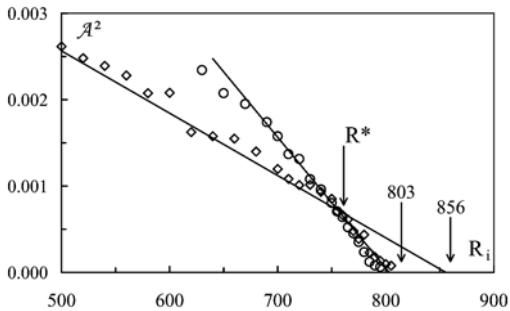

Figure 18. $\mathcal{A}^2$ versus R_i; ($\diamond$) $R_o = -1200$, ($\circ$) $R_o = -850$.

where k_0 and ω_0 are the basic wavenumber and frequency of the pattern. Figures 16(c, d, e, f) show the outputs of such demodulation on two typical spatiotemporal diagrams above and below R^*. Saptio-temporal diagrams (c) and (d) show the spacetime evolution of $|A^+|$, while the (e) and (f) ones give the local wavenumber.

The mean square modulus $\mathcal{A}^2 \equiv \langle |A^+|^2 + |A^-|^2 \rangle$ allows for a first quantitative determination of the threshold of modulated turbulence. Figure 18 shows that $\mathcal{A}^2$ increases linearly as R_i is decreased below R^*, as expected for a supercritical instability. However, in the nucleation regime, this usual variation breaks down and a dip of $\mathcal{A}^2$ can be observed. This one is directly linked to the large number of fronts separating the domains leading to a weaker amplitude of light intensity modulation. The threshold R_c is thus defined by extrapolating the region of linear variation of $\mathcal{A}^2$ in the nucleation regime, going towards $\mathcal{A} = 0$ beyond R^*.

The ordinary weakly nonlinear description of instabilities can not handle the nucleation dynamics observed for $R^* < R_i < R_c$ and the resulting damping of $\mathcal{A}$. This suggests that the intrinsic fluctuations of the turbulent basic state must be taken into account. We have, with Prigent et al. (2002, 2003), pro-

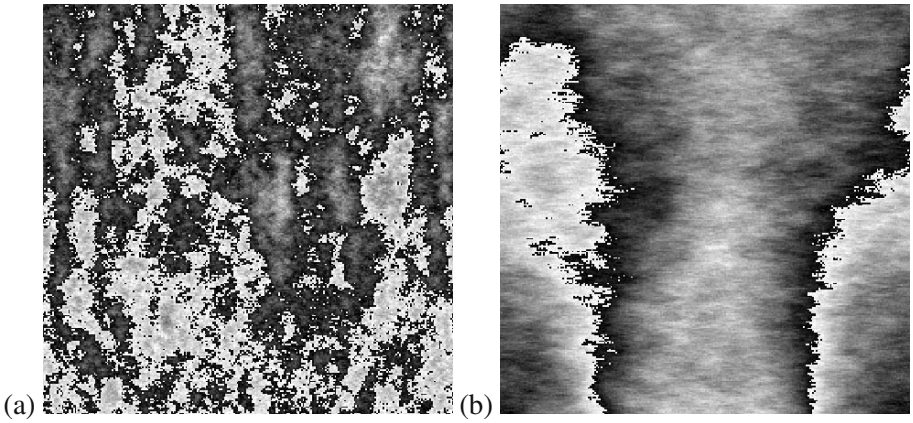

Figure 19. Numerical simulation with (a) and without (b) nucleation dynamics. ($L = 256 \times 0.5$ and $T = 256 \times 0.08$).

posed an heuristic modification of the usual amplitude equations by transposing the effect of the turbulent fluctuations into an additional constant-strength noise term. In the absence of further indication, this noise term is choosen to be additive at the amplitude level, leading to the following Ginzburg–Landau equations governing A^- and A^+:

$$\tau_0(\partial_t A^\pm \pm s_0 \partial_z A^\pm) = \epsilon A^\pm + \xi_0^2(1 + ic_1)\partial_z^2 A^\pm - g_3(1 - ic_3)\left|A^\pm\right|^2 A^\pm \\ -g_2(1 - ic_2)\left|A^\mp\right|^2 A^\pm + \alpha\eta^\pm \quad (1)$$

where τ_0 and ξ_0 are the characteristic time and length scales of amplitudes modulation, s_0 is the group velocity, $\varepsilon = (R_c - R_i)/R_c$ is the reduced distance to threshold, α is the noise strength and $\eta^\pm$ is a delta-correlated white noise. The cubic nonlinearities have been choosen to acount for the observed supercritical nature of the transition. The overall consistency of such a description has been checked by determining, through parallel numerical and experimental investigations, all the coefficients of these equations which appear to be real (see Prigent et al., 2003, for details). As an illustration, Figures 19 show numerical spatio-temporal diagrams displaying the nucleation dynamics close to threshold and the emergence of a regular pattern for larger ε.

For real Ginzburg–Landau equations, it is possible to propose a potential formulation of the transition:

$$\tau_0 \partial_t A^\pm = -\frac{\partial V}{\partial \overline{A^\pm}} + \xi_0^2 \partial_{zz} A^\pm + \alpha\eta^\pm$$

with

$$V = -\varepsilon\left(|A^+|^2 + |A^-|^2\right) +$$

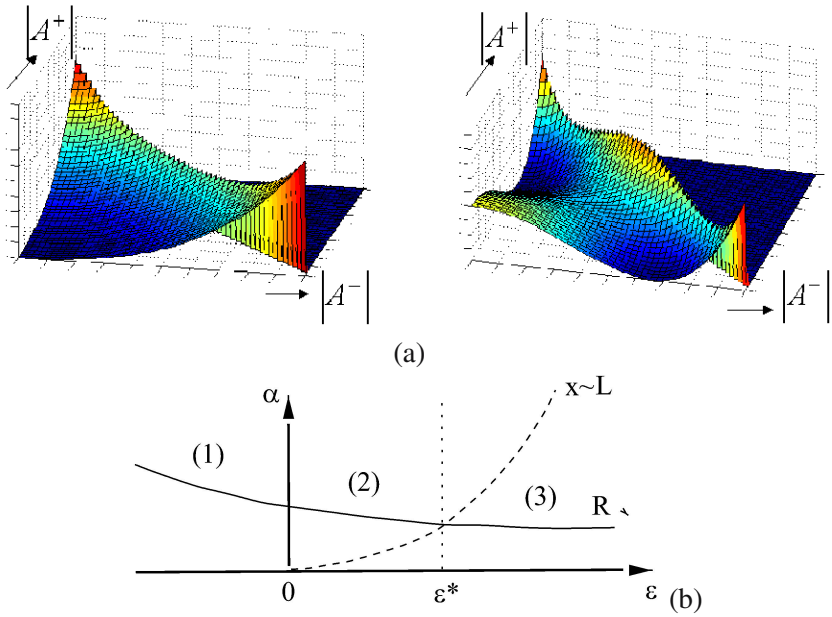

Figure 20. Potential formulation. (a) V for $\varepsilon < 0$ (left) and $\varepsilon > 0$ (right). (b) Schematic view of the transition. (1): homogeneous turbulent state regime. (2): regime of nucleation dynamics. (3): mono-domain regime. The dashed line indicate that the transition where domains A^+ and A^- reach the size of the system. The solid line is a typical path covered by the system when varying the Reynolds number.

$$\frac{g_3}{2}\left(|A^+|^4 + |A^-|^4\right) + g_2\left(|A^+|^2|A^-|^2\right)$$

For $\varepsilon < 0$, V has a single minimum $(|A^+|, |A^-|) = (0, 0)$. For $\varepsilon > 0$, V has two minima $(|A^+|, |A^-|) = (\sqrt{\varepsilon/g_3}, 0)$ and $(|A^+|, |A^-|) = (0, \sqrt{\varepsilon/g_3})$ and a saddle-node $(|A^+|, |A^-|) = (\sqrt{\varepsilon/(g_2+g_3)}, \sqrt{\varepsilon/(g_2+g_3)})$ (see Figure 20(a)).

Such a potential dynamics with noise provides a good framework to describe the different regimes of the transition. Here the potential must be understood as local in space. Its equilibrium states describe the local states of the spatio-temporal dynamics. For $\varepsilon < 0$, the minimum is the non-modulated turbulent state and for $\varepsilon > 0$ each minimum corresponds to one or the other possible orientation of the modulated pattern. The unstable saddle-node describes the superposition of these two states. Figure 20(b) presents the differents observed regimes when varying the symmetry-breaking parameter ε and the noise intensity α. When $\varepsilon < 0$, the unique stable state of the potential extends over all the space, corresponding to the homogeneous turbulent basic state. When $\varepsilon > 0$, domains of both inclinations compete in space. For small noise intensity, compared to the potential barrier, a domain of one or the other minimum

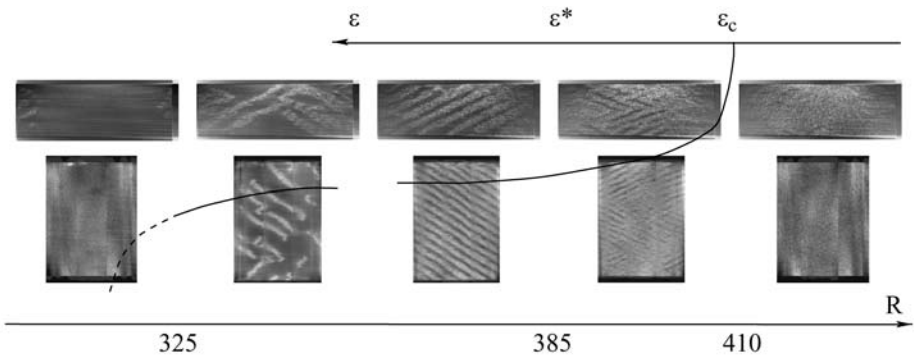

Figure 21. Global bifurcations of the plane Couette flow (upper sequence) and of the Taylor–Couette flow (lower sequence) in the " subcritical regime".

of the potential may grow until it reaches the system size and all fronts are eliminated. On the contrary for large noise intensity, a state of opposite inclination can locally be created leading to the nucleation of a new domain together with an associated pair of fronts. One may notice that within a front the total amplitude is not zero. This is related to the local state that corresponds to the saddle-node between the two wells of the potential, which is the superposition of both inclinations states and not the patternless state.

From an hydrodynamical point of view, not only the distance to threshold but also the strength of the turbulent fluctuations, depend on the Reynolds number, the single control parameter of the system. When varying R, the system follows a path in the (ε, α) plane as sketched in Figure 20(b) with the solid line. A first transition occurs from the homogeneous turbulent state to the multi-domains nucleation dynamics state for $R = R_c$ $(\varepsilon = 0)$, when the underlying potential symmetry is broken. It is followed by a second "transition" charactarized by the disparition of the nucleation dynamics $(\varepsilon = \varepsilon^*)$.

5. CONCLUSION

Figure 21 summarizes the general perception that we propose for the subcritical transition in Couette flows.

- For sufficiently large Reynolds number, i.e. $R > 400$, the turbulent flow is globally attractive, while the laminar one, though linearly stable, only attracts few initial conditions in the phase space. Decreasing the Reynolds number, a supercritical bifurcation (for $\varepsilon = 0$) gives rise to a long wavelength periodic pattern, which symetrical realizations "left" and "right" coexist in a multi-domains dynamics. This bifurcation is well described in the context of amplitude equations provided that the intrinsically fluctuating nature of the turbulent basic state is taken into

account by adding noise. Further decreasing the Reynolds number, one observes a transition at $\varepsilon = \varepsilon^*$ to the homogenization of the system into a single domain of one of the symetrical states in the same way as in a phase transition for a two states local potential when decreasing the thermal agitation.

- For a sufficiently small Reynolds number, i.e. $R < R_g = 325$, the laminar flow is the only global attractor of the system. Other solutions already fill the phase space but are all linearly unstable. They only induce long turbulent transients, that asymptotically relax towards the laminar flow. Beyond R_g, an *ad hoc* perturbation, sufficiently strong, leads to disordered laminar-turbulent domains coexistence, which dynamics should belong to the directed percolation class. The order parameter of this transition, the turbulent fraction F_t, presents a discontinuous transition, then increases regularly towards 1. For a given small Reynolds number, the system seems to keep a well defined value of the turbulent fraction which does not depend on the form of the turbulent domains present within the flow.

- Between these two well defined regimes, one observes a cross-over which is characterized by elongated turbulent spots at small Reynolds number and a periodic pattern with the expected turbulent fraction within each period at large Reynolds number. In the light of the different experiments, we believe that the respective influence of both dynamics in that cross-over regime essentially depends on the aspect ratio of the considered flow.

Beyond this synthetic description of the transition *to* and *from* turbulence in subcritical Couette flows, important questions remain to be answered. One would like to know for instance what are the hydrodynamical mechanisms responsible for the stabilization of the laminar-turbulent fronts in the spatio-temporal intermitent regime as well as for the modulation of the homogeneous turbulent flow. In particular, what is the mechanism governing the lengthscale of this modulation? At this stage, we believe that direct numerical simulations of the Navier–Stokes equations, as the one performed by Barkley and Tuckerman (see Barkley and Tuckerman, 2005a and their paper in the present book Barkley and Tuckerman, 2005b) should be able to provide new insights.

REFERENCES

Alavyoon, F., Henningson, D.S. and Alfredsson, P.H. (1986). Turbulent spots in plane Poiseuille flow – Flow visualization. *Phys. Fluids* **29**(4), 1328.

Andereck, C.D., Liu, S.S. and Swinney, H.L. (1986). Flow regimes in a circular Couette system with independently rotating cylinders. *J. Fluid Mech.* **164**, 155.

Barkley, D. and Tuckerman, L.S. (1999). Stability analysis of perturbed plane Couette flow. *Phys. Fluids* **11**, 1187–1195.

Barkley, D. and Tuckerman, L.S. (2005a). Computational study of turbulent laminar patterns in Couette flow. *Phys. Rev. Lett.* **94**, 014502.

Barkley, D. and Tuckerman, L.S. (2005b). Turbulent-laminar patterns in plane Couette flow. In *Laminar Turbulent Transition and Finite Amplitude Solutions*, Proceedings of the IUTAM Symposium, Bristol, UK, 9–11 August 2004, T. Mullin and R.R. Kerswell (eds), Springer, Dordrecht, pp. 107–127 (*this volume*).

Bergé, P., Pomeau, Y. and Vidal, C. (1998). *L'espace chaotique*. Hermann Ed., Paris.

Bottin, S. (1998). *Structures cohérentes et transition vers la turbulence par intermittence spatio-temporelle dans l'écoulement de Couette plan*. PhD Thesis, Université Paris XI, CEA Saclay, France.

Bottin, S. and Chaté, H. (1998). Statistical analysis of the transition to turbulence in plane Couette flow. *Eur. Phys. J. B* **6**, 143.

Bottin, S., Dauchot, O. and Daviaud, F. (1998a). Experimental evidence of streamwise conter-rotating vortices as a finite amplitude solution in transitional modified Couette flow. *Phys. Fluids* **10**(10), 2597.

Bottin, S., Manneville, P., Daviaud, F. and Dauchot, O. (1998b). Discontinuous transition to spatiotemporal intermittency in plane Couette flow. *Europhys. Lett.* **43**(2), 171.

Busse, F.H. and Clever, R.M. (1995). *Bifurcation Sequences in Problems of Thermal Convection and of Plan Couette Flow*. Kluwer Academic Publishers, Dordrecht, 1995.

Chaté, H. and Manneville, P. (1987). Transition to turbulence via spatiotemporal intermittency. *Phys. Rev. Lett.* **58**, 2.

Chaté, H. and Manneville, P. (1994). Spatiotemporal intermittency. In *Turbulence: A Tentative Dictionary*, P. Tabeling and O. Cardoso (eds), Plenum Press, p. 111.

Cherhabili, A. and Ehrenstein, U. (1996). Finite-amplitude equilibrium states in plane Couette flow. *J. Fluid Mech.* **342**, 159–177.

Clever, R.M. and Busse, F.H. (1997). Tertiary and quartenary solutions for plane Couette flow. *J. Fluid Mech.*.

Coles, D. (1965). Transition in circular Couette flow. *J. Fluid Mech.* **21**(3), 385.

Dauchot, O. and Chaté, H. (1999). Deterministic vs. statistical description of the transition to turbulence in plane Couette flow. In *Stochastic and Chaotic Dynamics in the Lakes*, D.S. Broomhead, E.A. Luchinskaya, P.V.E. McClintock and T. Mullin (eds), Ambleside, UK, AIP 502, p. 524.

Dauchot, O. and Daviaud, F. (1994). Finite amplitude perturbation in plane Couette flow. *Europhys. Lett.* **28**, 225.

Dauchot, O. and Daviaud, F. (1995a). Finite amplitude perturbation and spots growth mechanism in plane Couette flow. *Phys. Fluids* **7**(2), 335.

Dauchot, O. and Daviaud, F. (1995b). Streamwise vortices in plane Couette flow. *Phys. Fluids* **7**(5), 901.

Dauchot, O. and Manneville, P. (1997). Local versus global concepts in hydrodynamic stability theory. *J. Phys. II France* **7**, 371.

Dauchot, O. and Vioujard, N. (2000). Phase space analysis of a dynamical model for the subcritical transition to turbulence in plane Couette flow. *Eur. Phys. J. B* **14**, 377–381.

Daviaud, F., Hegseth, J. and Bergé, P. (1992). Subcritical transition to turbulence in plane Couette flow. *Phys. Rev. Lett.* **69**, 2511.

Eckhardt, B. and Mersmann, A. (1999). Transition to turbulence in a shear flow. *Phys. Rev. E* **60**, 509–517.

Gad-El-Hak, M., Blackwelder, R.F. and Riley, J.J. (1981). On the growth of turbulent regions in laminar boundary layers. *J. Fluid Mech.* **110**, 73.

Hamilton, J.M., Kim, J. and Waleffe, F. (1995). Regeneration mechanisms of near-wall turbulence structures. *J. Fluid Mech.* **287**, 317–348.

Manneville, P. (2005). Modeling the direct transition to turbulence. In *Laminar Turbulent Transition and Finite Amplitude Solutions*, Proceedings of the IUTAM Symposium, Bristol, UK, 9–11 August 2004, T. Mullin and R.R. Kerswell (eds), Springer, Dordrecht, pp. 1–33 (*this volume*).

Manneville, P. and Dauchot, O. (2000). Patterning and transition to turbulence in subcritical systems: The case of plane Couette flow. In *Coherent Structures in Classical Systems*, Sitges, Spain, 2000, M. Rubi (ed.), Springer-Verlag.

Nagata, M. (1986). Three-dimensional finite-amplitude solutions in plane Couette flow: Bifurcation from infinity. *J. Fluid. Mech.* **169**, 229–250.

Nagata, M. (1990). Bifurcations in Couette flow between almost corotating cylinders. *J. Fluid. Mech.* **217**, 519.

Pomeau, Y. (1986). Front motion, metastability and subcritical bifurcations in hydrodynamics. *Physica D* **23**(1), 3.

Prigent, A. and Dauchot, O. (2000). Visualization of a Taylor–Couette flow avoiding parasitic reflexions. *Phys. Fluids* **12**(10), 2688.

Prigent, A., Grégoire, G., Dauchot, O., Chaté, H. and van Saarloos, W. (2002). Large-scale finite-wavelength instability within shear flows. *Phys. Rev. Lett.* **89**(1), 014501.

Prigent, A., Grégoire, G., Chaté, H. and Dauchot, O. (2003). Long wavelength modulation of turbulent shear flow. In *Papers from the Workshop on the Complex Ginzburg–Landau Equation: Theoretical Analysis and Experimental Application in the Dynamics of Extented Systems*, M. Bär and A. Torcini (eds), Instituto Nazionale di Ottica Applicata, Firenze, Italy, May 21–23, 2001. *Physica D* **174**, 100–113.

Romanov, V.A. (1973). Stability of plane Couette flow. *Funkcional Anal. i Prolozen* **7**.

Schmiegel, A. and Eckhardt, B. (1997). Fractal stability borders in plane Couette flow. *Phys. Rev. Lett.* **79**, 5250–5253.

Van Atta, C. (1966). Exploratory measurements in spiral turbulence. *J. Fluid Mech.* **25**(3), 495.

Waleffe, F. (1995). Hydrodynamic stability and turbulence: Beyond transcients to self-sustaining process. *Stud. Appl. Math.* **95**, 319–343.

Waleffe, F. (1997). On a self-sustaining process in shear flow. *Phys. Fluids* **9**(4), 883–900.

TRANSITION TO TURBULENCE IN PIPE FLOW

B. Hof
Laboratory of Aerodynamics and Hydrodynamics, Delft University of Technology, Leeghwaterstraat 21, 2628 CA Delft, The Netherlands

Abstract Transitional pipe flow is investigated in two different experimental set-ups. In the first the stability threshold and the initial growth of localized perturbations are studied.

Good agreement is found with an earlier investigation of the transition threshold. The measurement technique applied in the last part of this study allows the reconstruction of the streamwise vorticity in a turbulent puff.

1. INTRODUCTION

In pipe flow transition to turbulence occurs despite the linear stability of the laminar base flow. Investigations of this problem date back to the 19th century when the pioneering experiments of Reynolds (1883) were carried out. An explanation of why pipe flows become turbulent and a detailed understanding of the underlying transition mechanisms is still missing. Although the linear stability of the base flow has not been proven rigorously (Drazin and Reid, 1981) all theoretical and experimental work is in line with this assumption and confirms that finite amplitude perturbations are necessary to destabilize the laminar flow and that the transition is of subcritical nature.

One of the recent approaches to explain transition in pipe and related shear flows focuses on the non-normal nature of the linearized equations which permits perturbations to grow by several orders of magnitude before they eventually decay. It has been speculated that this so called transient growth (Trefethen et al., 1993) can trigger secondary instabilities causing transition to turbulence.

A mechanism that also takes nonlinear effects into account and focuses on how turbulence is sustained in shear flows has been proposed by Waleffe and co-workers (Hamilton et al., 1995; Waleffe, 1997). This so called self sustaining mechanism describes how certain flow configurations consisting of streamwise vortices, streaks and a wavelike modulation can maintain themselves against viscous decay. The streamwise vortices generate streamwise streaks through algebraic growth which in turn become inflexionally unstable. This instability can feed energy from the mean flow back into the streamwise

T. Mullin and R.R. Kerswell (eds), Laminar Turbulent Transition and Finite Amplitude Solutions, 221–231.
© 2005 *Springer. Printed in the Netherlands.*

vortices closing the feedback loop. Self sustained flow states which are exact but unstable solutions of the Navier–Stokes equations have recently been found by Faisst and Eckhardt (2003) and Wedin and Kerswell (2004). These solutions arise from saddle node bifurcations and have the form of waves travelling in the streamwise direction.

In a recent experimental study of pipe flow Hof et al. (2004) found evidence for the relevance of such unstable states to turbulent flows. The vortex streak configurations observed in the experiment were in striking agreement with those observed for the travelling waves in the computational studies. Furthermore the length scale of the streamwise modulation observed in the experiment is in very good agreement with the wavelength of the travelling waves.

A transition scenario which is based on the observation of such unstable solutions has been suggested. Here pipe flow is viewed as a dynamical system and the state of this system is governed by the Reynolds number. It has been suggested that as the Reynolds number is increased these unstable solutions undergo secondary bifurcations and form a chaotic saddle in phase space. Such a chaotic saddle can initially attract trajectories leading to long lived turbulent transients. Eventually however the system will return to the laminar state which is globally attracting. As the Reynolds number is increased further the chaotic saddle is believed to evolve into a turbulent attractor which gives rise to sustained turbulence. At this point the laminar state is reduced to a local attractor and it is believed that the basin of attraction of the laminar state decays while that of the turbulent state grows as the Reynolds number increases. Hence for increasing Reynolds numbers smaller and smaller perturbations will be sufficient to destabilize the laminar pipe flow.

I would here like to present results from two experimental investigations into the transition threshold, the initial growth rate of finite amplitude perturbations and flow structures observed in the turbulent flow. After a brief description of the two experimental set-ups in Section 2 the results will be presented in Sections 3 to 5 and their relation to the above theoretical models will be discussed.

2. EXPERIMENTAL METHODS

The results discussed in Sections 3 and 4 have been obtained in the 18 m long constant mass flux pipe situated at the Manchester Centre for Nonlinear Dynamics. A schematic diagram of the experiment is shown in Figure 1. The flow is driven by a piston that pulls the water at a constant mass flux from a reservoir through the pipe. The pipe is made of 150 mm long perspex sections with an inner diameter of 20 mm. These sections were aligned with a laser on a steel base and connected to the supply tank by a trumpet shaped inlet. Flows could be kept laminar up to $Re = 24000$. In the experiments the stability of the fully developed flow was probed by applying controlled perturbations which had

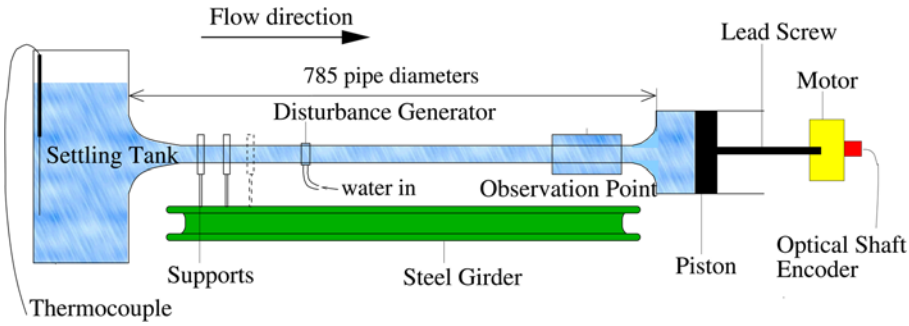

Figure 1. Schematic of the Manchester pipe setup. See text for details.

the form of either a single jet injected through a 1.5 mm hole or by injection of six jets through 0.5 mm holes. The six jets are equally spaced around the perimeter and injected tangentially to the pipe wall in the azimuthal direction, whereas the single jet is injected perpendicularly to the wall. A more detailed description of the pipe set-up and the perturbation mechanism can be found in Hof et al. (2003) and Darbyshire and Mullin (1995). Injections were applied at a constant rate over a short interval typically lasting between 0.2 and 4 s. As was discussed in Hof et al. (2003) the perturbation had the shape of a single boxcar pulse and the amplitude of the jet could be varied independently of its duration. The water was seeded with anisotropic flow visualization particles and the perturbed fluid section could be inspected with CCD cameras while progressing down the pipe.

The results I am presenting in Section 5 have been obtained in the 26 m long recirculation pipe at the Aero- and Hydrodynamics Laboratory in Delft. The pipe is made of 2 m long perspex sections with an inner diameter of 40 mm. A schematic diagram of the pipe setup is shown in Figure 2. The working fluid is water which is seeded with isotropic particles for visualization purposes. The flow was perturbed 350 diameters from the inlet by a single jet injected impulsively over a period of 1 s through a 1 mm hole into the pipe. The so created turbulent flow region was investigated 150 diameters downstream using a high speed PIV system with a maximum sampling rate of 1500 Hz. Here a cross-sectional plane of the pipe was illuminated with a pulsed high speed laser and the plane was viewed by two cameras positioned in forward scatter at 45° to the illuminated plane. By sampling images in rapid succession and correlation of the particles observed from two different view angles in the illuminated plane, all three velocity components of the flow can be reconstructed for the entire cross-section. A more detailed description of the experimental apparatus and the measurement technique can be found in Hof et al. (2004).

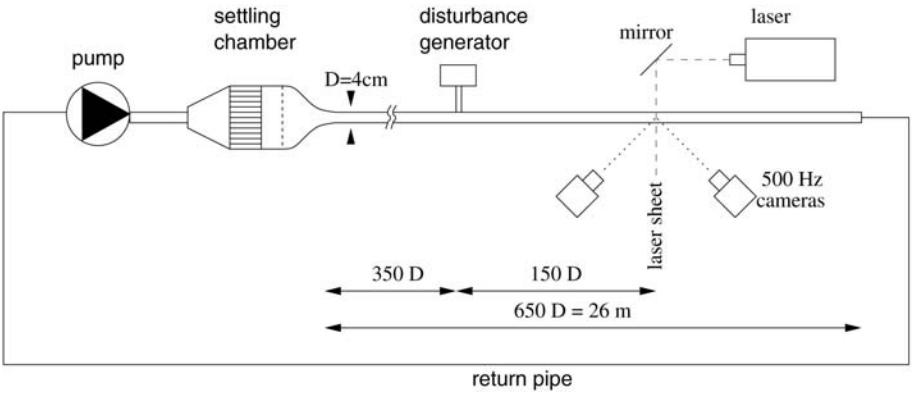

Figure 2. Schematic of the Delft pipe setup. See text for details.

3. STABILITY BOUNDARY

The stability boundary between the laminar and turbulent flow was investigated in the Manchester pipe by applying the single jet perturbation, described in Section 2, to the laminar base flow. The main difference to the study by Hof et al. (2003) is that in the present study the flow is perturbed by injection of a single jet rather than by six jets. For the six jet perturbation Hof et al. (2003) observed that the critical perturbation amplitude causing transition depended very strongly on the perturbation duration. For perturbations of short duration much larger amplitudes were required than for perturbations of long durations. For perturbations lasting longer than six non-dimensional time units the critical perturbation amplitude reached a constant level and was independent of the duration. Assuming that the disturbed flow is advected at the mean flow speed, the duration of six time units corresponds to a spread of the perturbation over six pipe diameters. In the following the non-dimensional length scale for the spread of the perturbation will be denoted by $l^* = Ut/D$, where U is the mean velocity in the pipe, t the time the perturbation is applied for and D the pipe diameter. The main observation of Hof et al. (2003) was that for perturbations either affecting a constant length l^* of fluid or affecting a length $l^* > 6$ D, the critical (non-dimensionalized) perturbation amplitude decays in proportion to $1/Re$. Our observations for the single jet perturbation confirm these results. In Figure 3 the dimensional critical amplitudes of a relatively short perturbation of $t = 0.2$ s (open circles) and for a perturbation of long duration with $t = 2$ s are plotted. The long perturbation always affects a sufficient length of the flow and shows a relatively constant critical amplitude. The 0.2 s perturbation on the other hand only acts over a relatively short length of $l^* = 1$ for $Re = 2000$ and the critical amplitude is much larger than the value observed for long perturbations. As the Reynolds number and therefore the spread of the perturbation l^*

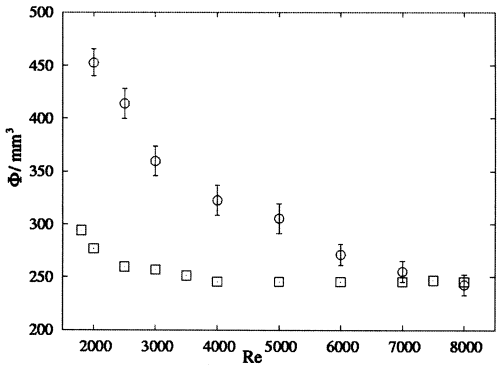

Figure 3. Critical perturbation amplitudes as a function of the Reynolds number. The circles mark the threshold for a short perturbation (0.2 s), the squares that for a perturbation with a longer duration time (8 s).

increases the critical amplitude decays and approaches the critical amplitude for the limiting case of long perturbations (open squares in Figure 3). The two curves meet at $Re = 8000$ where the 0.2 s perturbation spreads over four pipe diameters. Hence the minimum critical amplitude is reached when the perturbation affects at least four pipe diameters which is two pipe diameters shorter than the value observed for the six jet perturbation. These measurements confirm the observations of Hof et al. (2003), that in order to obtain a consistent scaling for the transition threshold the duration of the perturbation has to be scaled with Reynolds number or the perturbations have to extend over a long enough distance in the streamwise direction.

In Figure 4 the data for the 2 s perturbation is plotted on a double logarithmic scale and the amplitudes have been non-dimensionalized by the mean flow rate in the pipe. As in the case of the six jet perturbation (Hof et al., 2003) the critical amplitude decays in proportion to Re^{-1}. A small deviation to higher amplitudes is found as the lower limit of sustainable turbulence in pipe flow ($Re \approx 1800$) is approached. Such an increase in the critical Reynolds number had not been observed for the six jet perturbation (Hof et al., 2003).

A further difference to the six jet perturbation was observed for $Re < 2000$. As reported by Darbyshire and Mullin (1995) and Hof et al. (2003) close to the critical perturbation amplitude there is a relatively narrow margin where the threshold is of statistical nature. This means that for a given perturbation amplitude in this regime there is a certain probability that the flow will go turbulent. Following the suggestion by Darbyshire and Mullin (1995) the amplitude for which a 50% chance of transition is observed is defined as the critical amplitude. This statistical margin typically decreases for increasing Re. The measurements with the one jet perturbation showed that at Reynolds numbers smaller than 2000 this statistical interval increases very strongly and it is notably larger than that observed for the six jet perturbation. For Reynolds

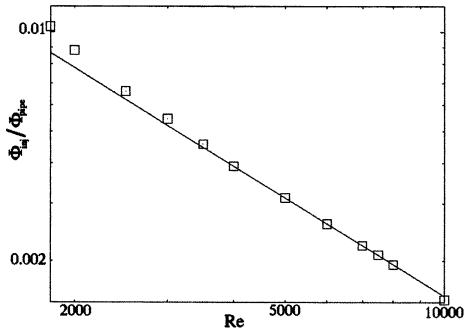

Figure 4. Double logarithmic plot of the critical perturbation amplitude for a single jet perturbation lasting 8 s. The line is fitted to the data points for $Re > 3500$ and has a slope of -1.

numbers as low as 1800 even perturbations 1.5 times the critical amplitude would occasionally fail to trigger turbulence.

4. GROWTH RATE OF PERTURBATIONS

Here I report on the evolution of a single pulse perturbation. The perturbation was applied sufficiently far downstream from the inlet of the pipe so that the flow at this point was fully developed. The perturbation consisted of six jets and the region of fluid initially perturbed could be varied as well as the amplitude of the applied jets. After the perturbation was applied the flow was investigated at several measurement stations downstream. Here flow visualization images were recorded by CCD cameras and stored on video tapes for later evaluation. Since flow visualization images give mainly qualitative information the analysis was restricted to measurements of the passage time of the turbulent region (i.e. turbulent puff) which again can be converted into a length scale by multiplication with the mean velocity in the pipe. In the investigated Reynolds number regime supercritical perturbations develop into turbulent puffs. Turbulent puffs typically consist of some wavy precursors at the leading edge which gradually evolve into the turbulent central part of the puff. The turbulence laminar interface at the trailing edge of the puff on the other hand is comparatively sharp. A detailed account of the structure of turbulent puffs can be found in Wygnanski and Champagne (1973). The length of a turbulent puff was determined as the distance between the points at the leading and trailing edge where the flow visualization images show clearly that the turbulent flow stretches across the entire pipe diameter. Hence the weaker precursors at the leading edge of the puff are not taken into consideration for these length measurements.

Only perturbation amplitudes larger than the critical values leading to transition were considered and here the magnitude of the perturbation was found to

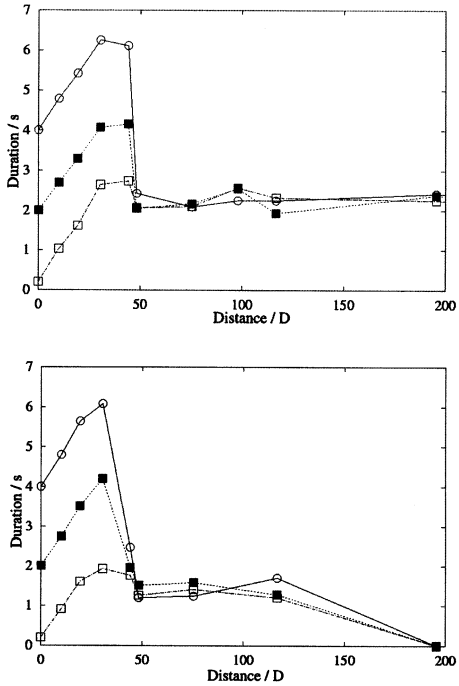

Figure 5. Passage time of the turbulent region measured at several positions downstream of the perturbation point for (a) $Re = 2000$ and (b) $Re = 1700$.

only have a small influence on the spread of the turbulent region downstream. The study was therefore restricted to an investigation of the effect of the perturbation duration on the growth rate of the turbulent flow. The amplitude of the jets was kept at 1.5 times the critical value. Perturbations lasting 0.2 s, 2 s and 4 s were considered which at $Re = 2000$ corresponds to a perturbation length of $1D$, $10D$ and $20D$ respectively. As shown in Figure 5(a) all three perturbations initially grow at the same rate in a more or less linear fashion up to a distance of approximately $40D$ from the perturbation point. Here the turbulent region starts to break up and typically only the region furthest upstream survives whereas the downstream parts relaminarize over the next ten pipe diameters. It is interesting to note that from 50 pipe diameters onwards all three initial perturbations result in a turbulent puff of equal length. It appears that in this Reynolds number regime longer turbulent structures cannot be sustained. The turbulent puff then travels with unchanged length for a further $450D$ downstream (the last $300D$ are not shown in the figure) until it reaches the end of the pipe. Similar observations were made for Reynolds numbers 1800 and 1900. Turbulent puffs travelling downstream at a constant length, so called equilibrium puffs, have previously been observed by Wygnanski and Champagne (1973).

In Figure 5(b) the evolution of flow perturbations at $Re = 1700$ is shown. The initial growth is almost identical to that observed at $Re = 2000$ The turbulent region then again breaks up approximately $40D$ from the perturbation point and results in a turbulent region slightly shorter than that at $Re = 2000$ as indicated by the shorter passage time. Interestingly at Reynolds 1700 the turbulent puffs are not sustained but disappear typically over the next 50 to 200 pipe diameters. Whereas in some instances the turbulent puff will disappear almost immediately after the initial growth period in other instances the turbulent region will progress several hundred pipe diameters before it suddenly disappears. The break up and relaminarisation of the puffs typically takes place over a distance smaller than $50D$ and there did not appear to be a notable difference between the flow visualization images taken upstream of those puffs which would disappear a short distance from the perturbation point and those which progressed further.

5. STREAMWISE VORTICITY OF A TURBULENT PUFF

Here I report on recent PIV measurements of the three component velocity fields during the passage of a turbulent puff at $Re = 2200$. These experiments were carried out in the Delft recirculation pipe. As reported in section two the fully developed pipe flow was perturbed by a single jet and the turbulent flow was investigated with a stereoscopic PIV system at 62.5 Hz, $150D$ downstream. A reconstruction of the streamwise vortex structure of the turbulent puff is shown in Figure 6. As discussed in the introduction streamwise vortices play an important role in the self sustaining mechanism as well as in transient growth.

The high spatial resolution (1024×1024 pixels) and the high sampling rate of the camera allowed us to measure the velocity field in the cross-sectional plane at very high spatial and temporal resolution. More than 1000 independent vectors were obtained in the plane. Assuming that the changes in the flow structures of the turbulent puff are relatively small while the puff travels through the measurement plane (Taylor's hypothesis), the full three dimensional velocity field of the puff can be reconstructed. The sampling frequency of 62.5 Hz then translates into a spatial resolutions of 47 cross-sectional velocity fields sampled per pipe diameter. From this data the streamwise vorticity can be calculated for the entire puff as shown in Figure 6. It is interesting to note that the vortices typically have a length of the order of 1 pipe diameter which is in good agreement with the length scale of streamwise vortices in unstable travelling wave solutions (Faisst, 2003).

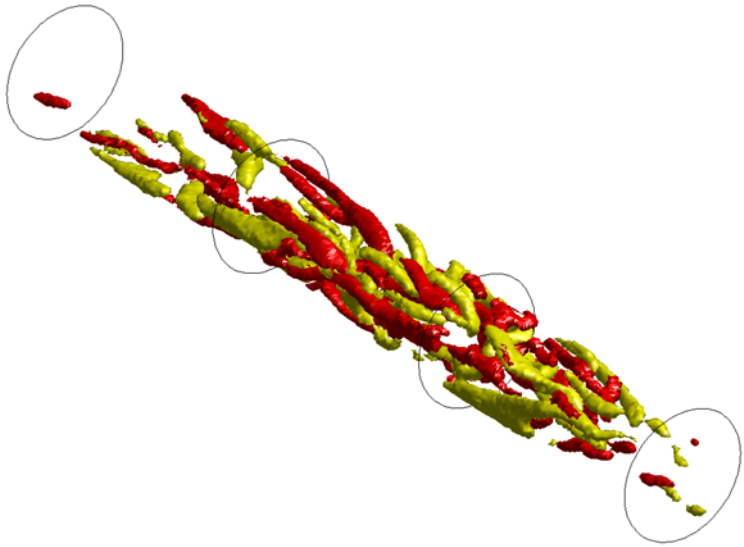

Figure 6. Reconstruction of the vortical structure of a turbulent puff at $Re = 2200$. The flow direction is from left to right and positive (negative) vorticity is shown in dark grey (light grey).

6. DISCUSSION AND CONCLUSION

The measurements of the stability boundary presented in Section 3 confirm the $1/Re$ scaling that has been observed for a different perturbation mechanism in an earlier study (Hof et al., 2003). A $1/Re$ scaling has previously also been found for a periodic blowing and suction mechanism (Draad et al., 1998) where fluid was injected over one half of the pipe perimeter and subtracted over the other through a porous wall. Also the DNS results of a periodic blowing and suction mechanism by Shan et al. (1998) and asymptotic models by Chapman (private communication) suggest a $1/Re$ scaling. Transient growth theories on the other hand have predicted a scaling exponent strictly smaller than -1 (Trefethen et al., 1993).

The initial streamwise growth of the localized perturbations reported in Section 4 is reminiscent to the algebraic growth observed in DNS of localized perturbations in channel flow (Henningson et al., 1993). In this study the largest transient growth was observed for small streamwise wavenumbers resulting in streamwise elongated structures.

The observation of long lived turbulent transients is in qualitative agreement with numerical calculations (Faisst and Eckhardt, 2004) where turbulence transients have been observed in the same Reynolds number regime ($1600 < Re < 2200$) and are believed to result from the existence of a chaotic saddle. Here the existence of transients and the exponential decay of their life-

times (Faisst and Eckhardt, 2004) have been seen as evidence for the existence of a turbulent saddle which evolves around unstable solutions as discussed in Section 1. More recently turbulence transients with exponential lifetimes have also been observed experimentally by Mullin and Peixinho (2005) and in my own experiments in the Delft pipe.

Finally the streamwise vortex structure of a turbulent puff was reconstructed. The average length of these vortices is in good agreement with that reported for the streamwise vortices in unstable travelling wave solutions (Faisst, 2003). The vortex-streak dynamics for these flows and the observation of vortex streak configurations closely resembling those of the unstable travelling waves have been reported in an earlier publication (Hof et al., 2004).

REFERENCES

Chapman, J., Private Communication.

Darbyshire, A. and Mullin, T. (1995). Transition turbulence in a constant-mass-flux pipe flow. *J. Fluid Mech.* **289**, 83–114.

Draad, A.A., Kuiken, G.D.C. and Nieuwstadt, F.T.M. (1998). Laminar-turbulent transition in pipe flow for Newtonian and non-Newtonian fluids. *J. Fluid Mech.* **377**, 261.

Drazin, P.G. and Reid, W.H. (1981). *Hydrodynamic Stability*. Cambridge University Press, Cambridge.

Faisst, H. (2003). Turbulence transition in pipe flow. PhD Thesis, Philipps Universität Marburg.

Faisst, H. and Eckhardt, B. (2003). Travelling waves in pipe flow. *Phys. Rev. Lett.* **91**, 224502.

Faisst, H. and Eckhardt, B. (2004). Sensitive dependence on initial conditions in transition to turbulence in pipe flow. *J. Fluid Mech.* **504**, 343–352.

Hamilton, J.M., Kim, J. and Waleffe, F. (1995). Regenaration mechanism of near-wall turbulence structures. *J. Fluid Mech.* **287**, 317.

Henningson, D.S., Lundbladh, A. and Johansson, A.V. (1993). A mechanism for bypass transition from localized disturbances in wall bounded shear flows. *J. Fluid Mech.* **250**, 169–207.

Hof, B., Juel, A. and Mullin, T. (2003). Scaling of the turbulence transition treshold in a pipe. *Phys. Rev. Lett.* **91**, 244502.

Hof, B., van Doorne, C.W.H., Westerweel, J., Nieuwstadt, F.T.M., Faisst, H., Eckhardt, B., Wedin, H., Kerswell, R.R. and Waleffe, F. (2004). Experimental observation of nonlinear traveling waves in turbulent pipe flow. *Science* **305**, 1594.

Mullin, T. and Peixinho, J. (2005). Recent observations in transition to turbulence in a pipe. In *Proceedings of the IUTAM Symposium in Laminar Turbulence Transition*, Bangalore, India, Springer, Dordrecht, forthcoming.

Reynolds, O. (1883). An experimental investigation of the circumstances which determine whether the motion of water shall be direct or sinuous and of the law of resistance in parallel channels. *Proc. R. Soc. Lond.* **35**, 84–99.

Shan, H., Zang, Z. and Nieuwstadt, F.T.M. (1998). Direct numerical simulation of transition in pipe flow under the influence of wall disturbances. *Int. J. Heat Fluid Flow* **19**, 320.

Trefethen, L.N., Trefethen, A.E. and Driscoll, T.A. (1993). Hydrodynamic stability without eigenvalues. *Science* **261**, 578–584.

Waleffe, F. (1997). On a self-sustaining mechanism in shear flows. *Phys. Fluids* **9**, 883.

Wedin, H. and Kerswell, R.R. (2004). Exact coherent solutions in pipe flow: Travelling wave solutions. *J. Fluid Mech.* **508**, 333.

Wygnanski, I.J. and Champagne, F.H. (1973). On transition in a pipe. Part 1. The origin of puffs and slugs and the flow in a turbulent slug. *J. Fluid Mech.* **59**, 281–335.

THRESHOLD AMPLITUDES IN SUBCRITICAL SHEAR FLOWS

Non-Linear Stability Bounds

Dan S. Henningson[1] and Gunilla Kreiss[2]
[1]*Department of Mechancis,* [2]*Numerical Analysis and Computer Science, KTH, SE-100 44 Stockholm, Sweden*
henning@mech.kth.se, gunillak@nada.kth.se

Abstract Non-linear stability bounds are derived for subcritical shear flows. First the methodology is exemplified using a model problem and then it is applied to plane Couette flow. The result is a lower bound which scales as Re^{-4}. Upper bounds based on numerical simulations are found to be about Re^{-1}, depending slightly on the transition scenario investigated. Bounds for plane Poiseuille flow are also presented.

Keywords: non-linear stability, subcritical transition, Couette flow.

1. INTRODUCTION

Stability of flows to finite amplitude disturbances has been the focus of numerous investigations. For parameter values allowing linear instability all perturbations, save for a few fulfilling certain symmetries, will lead to sustained non-vanishing solutions. On the other hand, for other parameter values it is possible to show that all disturbances vanish in some suitable metric. In between these values, in what for shear flows is called the subcritical Reynolds number regime, the stability depends both on the form and the amplitude of the perturbation. Here, very few results pertinent to anything but specific disturbances are available. We will here discuss results characterizing the threshold amplitudes needed for laminar-turbulent transition in plane shear flows in general and in plane Couette flow in particular.

T. Mullin and R.R. Kerswell (eds), Laminar Turbulent Transition and Finite Amplitude Solutions, 233–249.
© 2005 *Springer. Printed in the Netherlands.*

Table 1. Critical Reynolds numbers for a number of wall-bounded shear flows compiled from the literature (see e.g. Joseph, 1976; Drazin and Reid, 1981; Schmid and Henningson, 2001).

Flow	Re_E	Re_G	Re_T	Re_L
Hagen–Poiseuille	81.5	—	2000	∞
Plane Poiseuille	49.6	—	1000	5772
Plane Couette	20.7	125	360	∞

1.1 Disturbance equations and stability thresholds

The threshold bounds derived will be based on bounds of solutions to the linearized Navier–Stokes equations, where the non-linear terms are seen as forcing terms.

The non-linear disturbance equations can be written

$$\begin{aligned} \frac{\partial \mathbf{u}}{\partial t} &= L\mathbf{u} + G(\mathbf{u}) - \nabla p, \\ \nabla \cdot \mathbf{u} &= 0, \end{aligned} \tag{1}$$

Here

$$L\mathbf{u} = \frac{1}{\mathrm{Re}}\nabla^2\mathbf{u} - (\mathbf{U}\cdot\nabla)\mathbf{u} - (\mathbf{u}\cdot\nabla)\mathbf{U}, \quad G(\mathbf{u}) = (\mathbf{u}\cdot\nabla)\mathbf{u}. \tag{2}$$

where $\mathbf{u}$ and p are the disturbance velocity and the disturbance pressure, respectively, and the base flow $\mathbf{U}$, P, satisfies the Navier–Stokes equations.

The definitions of stability is usually based on the kinetic energy of the disturbance contained in a volume V, i.e.

$$E = \frac{1}{2}\int_V |\mathbf{u}|^2\, dV =: \frac{1}{2}\|\mathbf{u}\|^2. \tag{3}$$

We define a solution $\mathbf{U}$ as stable if $E \to 0$ as $t \to \infty$. If there exists a threshold energy δ such that $\mathbf{U}$ is stable when $E(0) < \delta$, then the solution $\mathbf{U}$ is conditionally stable and if $\delta \to \infty$ the solution is globally stable.

Based on the definitions of stability it is useful to introduce the critical Reynolds numbers Re_G, below which the flow is globally stable, and Re_L, above which the flow is unstable for any disturbance amplitude. Re_G may correspond to the lowest Reynolds number for which turbulence can be sustained. However, this does not hold in general, in which case it is necessary to introduce a separate critical Reynolds number Re_T below which the flow will relaminarize. This Reynolds number, which will be in the interval $\mathrm{Re}_G \le \mathrm{Re}_T \le \mathrm{Re}_L$, may be difficult to determine (see e.g. Faisst and Eckhardt, 2005). Examples of critical Reynolds numbers compiled from the literature are shown in Table 1.

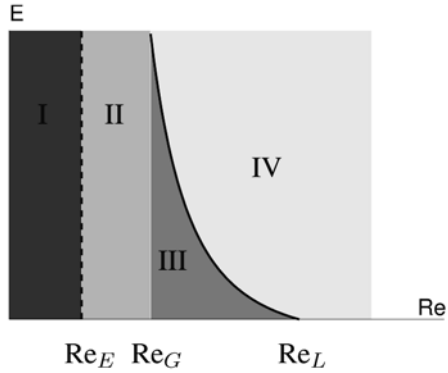

Figure 1. Sketch illustrating critical Reynolds numbers. Region I: monotonic stability; region II global stability, but not necessarily monotonic stability; between Re_G and Re_L: conditional stability; above Re_L: possible instability.

Here we have also noted Re_E, which is the Reynolds number below which disturbances decay monotonically.
Figure 1 gives a schematic view of the different Reynolds number regimes based on the preceding definitions. In region I, that is, for $\mathrm{Re} < \mathrm{Re}_E$, all disturbances exhibit monotonic decay. Region II is characterized by global, but not necessarily monotonic stability. In this region, disturbances may grow, but they will ultimately decay as time evolves. For $\mathrm{Re} > \mathrm{Re}_G$ we can encounter instabilities. For Re between Re_G and Re_L we have a conditionally stable flow: for energies below the curve separating regions III and IV the disturbance will decay; for energies above this curve we observe instabilities. The intersection of this curve with the Re-axis defines the Reynolds number above which there exist instabilities of infinitesimal disturbances. It is the nature and behavior of this threshold curve which is the subject of this paper.

1.2 Reynolds–Orr equations and linear growth mechanisms

Scalar multiplying the non-linear disturbance equations with u_i, integrating over a volume V, while assuming that the disturbance is localized or spatially periodic and divergence free, we find the Reynolds–Orr equation

$$\frac{dE}{dt} = -\int_V \mathbf{u}\cdot(\mathbf{u}\cdot\nabla)\mathbf{U}dV - \frac{1}{\mathrm{Re}}\int_V |\nabla\cdot\mathbf{u}|^2 dV. \tag{4}$$

Note that the non-linear terms have here dropped out and that the instantaneous growth rate, $\frac{1}{E}\frac{dE}{dt}$, is independent of the disturbance amplitude, for further discussion see e.g. Henningson (1996). In other words, the growth rate of a finite-amplitude disturbance can, at each instant of its evolution, be found from

an infinitesimal disturbance with an identical shape. Thus, the instantaneous growth rate of a finite-amplitude disturbance is given by mechanisms that are present in the linearized equations, and the total growth of a finite-amplitude disturbance can be regarded as a sum of growth rates associated with the linear mechanisms. This is a consequence of the conservative nature of the non-linear terms in the Navier–Stokes equations.

Since the non-linear growth possibilities critically depend on the behavior of the linearized equations, we here summarize their behavior for subcritical shear flows. We Fourier transform in the spanwise and streamwise directions. Then we can use the divergence constraint to eliminate the pressure to end up with the Orr–Sommerfeld–Squire equations governing the development of small perturbations. We have

$$\frac{\partial \hat{v}}{\partial t} = \underbrace{(D^2-k^2)^{-1}\left[-i\alpha U(D^2-k^2)+i\alpha U''+\frac{1}{\mathrm{Re}}(D^2-k^2)^2\right]}_{\mathcal{L}_{OS}}\hat{v} \quad (5)$$

$$\frac{\partial \hat{\eta}}{\partial t} = \underbrace{\left[-i\alpha U+\frac{1}{\mathrm{Re}}(D^2-k^2)\right]}_{\mathcal{L}_{SQ}}\hat{\eta} - \underbrace{i\beta U'}_{-\mathcal{L}_C}\hat{v} \quad (6)$$

Here $\hat{\eta}$ and $\hat{v}$ are the Fourier transforms of the normal vorticity and the normal velocity, respectively. Further, $k^2 = \alpha^2 + \beta^2$, where α and β are the wave numbers in the spanwise and streamwise directions, respectively. We can write these equations in the following form

$$\underbrace{\frac{d}{dt}\begin{pmatrix}\hat{v}\\ \hat{\eta}\end{pmatrix}}_{d\hat{u}/dt} = \underbrace{\begin{pmatrix}\mathcal{L}_{OS} & 0\\ \mathcal{L}_C & \mathcal{L}_{SQ}\end{pmatrix}}_{\mathcal{L}}\underbrace{\begin{pmatrix}\hat{v}\\ \hat{\eta}\end{pmatrix}}_{\hat{u}} \quad (7)$$

Two aspects of sub-critical growth in the linearized equations are of interest here. The maximum transient growth possible and the maximum response to forcing. The maximum transient growth is found by maximizing growth in solutions of the initial value problem

$$\frac{d\hat{u}}{dt} = \mathcal{L}\hat{u} \qquad \hat{u}(0) = \hat{u}_0 \quad (8)$$

We calculate

$$G(t) = \max_{\hat{u}_0 \neq 0} \frac{\|\hat{u}(t)\|^2}{\|\hat{u}_0\|^2} = \|e^{\mathcal{L}t}\|^2 \leq \kappa\, e^{2\Re\{\lambda_{\max}\}t} \quad (9)$$

where we use the energy norm defined earlier. We have also included a bound on the maximum growth, where the constant κ can be thought of the the condition number of the "matrix of eigenfunctions", which can be generalized to

Table 2. Maximum response for selected shear flows and the corresponding streamwise and spanwise wavenumbers (see e.g. Schmid and Henningson, 2001)).

Flow	$G_{\max}$ (10^{-3})	$t_{\max}$	α	β
Plane Poiseuille	0.20 Re^2	0.076 Re	0	2.04
Plane Couette	1.18 Re^2	0.117 Re	35/Re	1.6
Circular pipe	0.07 Re^2	0.048 Re	0	1

infinite dimensional operators (Trefethen, 1997). If $\mathcal{L}$ was a normal operator, or equivalently, if all of its eigenfunctions were orthogonal, this condition number would equal unity, i.e. $\kappa = 1$. It is streamwise independent disturbances or streaks, which experience the largest transient growth. Computations yield that $\kappa = \mathcal{O}(\mathrm{Re}^2)$, see Table 2. Physically, the growth is due to weak streamwise vortices which lift up low momentum fluid from the wall and bring down high momentum fluid close to the wall. This can create large amplitude streaks in the streamwise velocity.

Another consequence of a non-normal operator is that the corresponding linear system may show large response to forcing, although the forcing is not at a resonance condition. Let us consider that our linear system is driven by a complex frequency s, we have

$$\frac{d\hat{u}}{dt} = \mathcal{L}\hat{u} + \hat{u}_f e^{st} \tag{10}$$

If all of the eigenvalues are in the left half-plane the steady state solution is given by

$$\hat{u} = (sI - \mathcal{L})^{-1}\hat{u}_f \tag{11}$$

where $(sI - \mathcal{L})^{-1}$ is called the resolvent. The response can then be characterized by

$$R(s) = \max_{\hat{u}_f \neq 0} \frac{\|(sI - \mathcal{L})^{-1}\hat{u}_f\|^2}{\|\hat{u}_f\|^2} = \|(sI - \mathcal{L})^{-1}\|^2 \leq \frac{\kappa}{\min|\lambda - s|^2} \tag{12}$$

where $\min|\lambda - s|$ represents the closest distance between s and the spectrum of $\mathcal{L}$. For streamwise independent disturbances the distance between the real axis and the closest eigenvalue is $\mathcal{O}(1/\mathrm{Re})$, which together with the size of the condition number κ implies that the response is bounded by $\mathcal{O}(\mathrm{Re}^4)$, see Table 3.

1.3 Transition scenarios for subcritical shear flows

In the numerical simulations of transition thresholds by Kreiss et al. (1994) and Reddy et al. (1998), transition resulting from two main disturbances types

Table 3. Maximum transient growth for selected shear flows and the corresponding streamwise and spanwise wavenumbers (see e.g. Schmid and Henningson, 2001).

Flow	$\max_{\omega\in\mathcal{R}} R(i\omega)$	α	β
Plane Poiseuille	$(\mathrm{Re}/17.4)^4$	0	1.62
Plane Couette	$(\mathrm{Re}/8.12)^4$	0	1.18
Blasius boundary layer	$(\mathrm{Re}/1.83)^4$	0	0.21

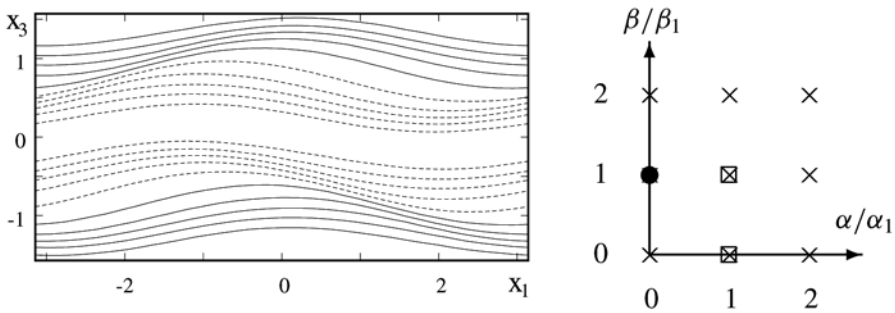

Figure 2. (a) Contours of streamwise velocity for a streak in Couette flow undergoing secondary instability. (b) Main active modes in transition scenario: filled circle: initial streak; squares: fundamental (sinuous) secondary instability modes. Crosses: modes with low amplitude noise. Adapted from Kreiss et al. (1994).

with large transient growth were considered: streak breakdown and oblique transition. We will here briefly describe those transition scenarios.

In Figure 2 we see contours of the streamwise velocity of a transitional streak in Couette flow. The scenario starts with a streamwise vortex which subsequently creates a streak in the streamwise velocity. If the streak amplitude is large enough it undergoes secondary instability, in this simulation triggered by low amplitude noise superimposed on the initial condition. In the figure a so called fundamental sinuous or symmetric mode can be seen superimposed on the streak. The main Fourier modes associated with this transition scenario are also depicted in the figure.

The other transition scenario can be seen in Figure 3, where the energy in selected Fourier components for oblique breakdown are shown. This scenario starts with an optimal pair of oblique waves, associated with $(1, \pm 1)$ in the streamwise and spanwise wavenumbers, respectively. The oblique modes interacts non-linearly to force energy in modes $(0, 0)$, $(0, 2)$, $(2, 0)$ and $(2, 2)$ by the quadratic non-linearity. Due to the sensitivity to forcing in the region of $(0, 2)$ it is seen that this Fourier component quickly reaches large amplitudes.

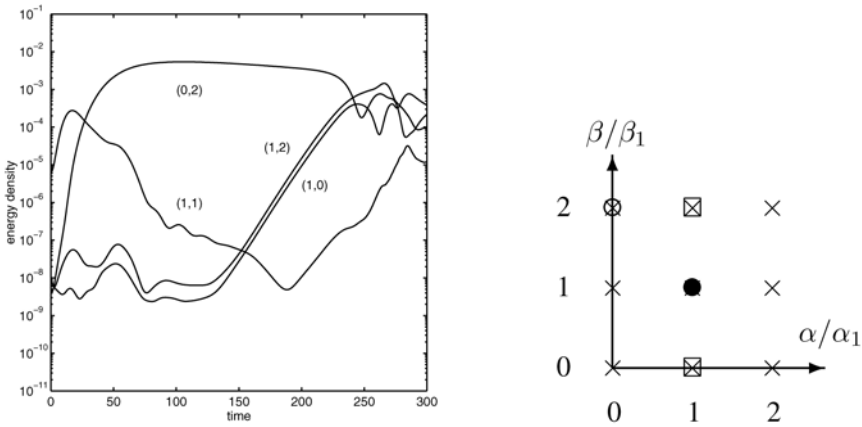

Figure 3. Energy in selected Fourier components for oblique breakdown. Filled circle: initial oblique waves; circle: non-linearly forced streak; squares: fundamental (sinuous) secondary instability modes. Adapted from Reddy et al. (1998).

This streak component subsequently undergoes sinuous secondary instability in a similar manner as for the pure streak breakdown case. The sinuous secondary instability is in this case associated with $(1, 0)$ and $(1, 2)$. These two scenarios have been found to be the two that require the least initial energy, i.e. have the lowest threshold values, see Reddy et al. (1998). In Section 4 we have compiled results from direct numerical simulations of these transition processes giving the dependence of the threshold energy needed for transition on the Reynolds number.

2. A MODEL PROBLEM

In this section we consider the following system of ordinary equations proposed by Waleffe (1995) as a model for subcritical transition

$$\frac{du}{dt} = Au + f(u), \quad u(0) = g_0.$$

Here u is a vector with 4 components and

$$A = \begin{pmatrix} -\lambda/\mathrm{Re} & 1 & 0 & 0 \\ 0 & -\mu/\mathrm{Re} & 0 & 0 \\ 0 & 0 & -\nu/\mathrm{Re} & 0 \\ 0 & 0 & 0 & -\sigma/\mathrm{Re} \end{pmatrix},$$

$$f(u) = \begin{pmatrix} -\gamma u_3^2 + u_2 u_4 \\ \delta u_3^2 \\ \gamma u_3 u_1 - \delta u_3 u_2 \\ -u_1 u_2 \end{pmatrix}.$$

where u_1 is modelling the amplitude of the streamwise streak forced by u_2, the amplitude by the streamwise vortex, and u_3 represents the secondary instability of the streak and u_4 the mean flow modification.

First we consider initial data corresponding to a small streamwise vortex,

$$u_1(0) = 0, \quad u_2(0) = \epsilon, \quad u_3(0) = 0, \quad u_4(0) = 0.$$

We will heuristically determine how large ϵ must be for the solution to grow. Due to the non-normality of the linear part u_1 will grow initially to at most $u_{1\,\max} \sim \epsilon \mathrm{Re}$. The physical interpretation is that a streak is generated by lift-up. If u_1 becomes sufficiently large the non-linear term $\gamma u_3 u_1$ will dominate over the linear term in the third equation. If $u_{1\,\max} > \frac{\nu}{\gamma \mathrm{Re}}$ we will have growth in u_3, which will also effect u_2 through the non-linear term δu_3^2 in the second equation. The physical interpretation of these steps is the energy from the streak feeds a stationary instability u_3, which regenerates the streamwise vortex. Thus there is a constant C such that a necessary condition for this scenario of growth is

$$|g_0| > \frac{C}{\mathrm{Re}^2}. \tag{13}$$

These arguments were used by Kreiss et al. (1994) and Baggett and Trefethen (1997) to determine thresholds for various model problems.

2.1 Linear bound

We will now mathematically derive a bound on the data that guarantees decay of the solution of the non-linear equation. We call this a threshold for stability. Consider

$$\frac{dv}{dt} = Av + f(v) + F(t), \qquad v(0) = 0. \tag{14}$$

The original initial value problem can be transformed into this form by subtracting a suitable decaying function, $v(t) = u(t) - e^{-t} g_0$ for example. Note that in this case F will decay exponentially with t. Note also that the non-linear term satisfies $|f(v)| \leq \bar{f}|v^2|$.

Let $|\cdot|$ denote the usual vector norm. The linear problem corresponding to (14) is after Laplace transform

$$s\tilde{v} \;=\; A\tilde{v} + \tilde{F}. \tag{15}$$

The solution operator for $\tilde{v}$ is the resolvent. In this case it is simply a matrix. With $\mathrm{Re} > 0$ the eigenvalues of L are negative and the resolvent is well defined in the entire right halfplane $R(s) \geq 0$. Let L be diagonalized by X, that is

$$A = X^{-1}\Lambda X.$$

The columns of X consist of the eigenvectors of L. Then

$$|(sI - A)^{-1}| = |X^{-1}(sI - \Lambda)X| \leq \kappa(X) \sup_{\lambda \in \sigma(A)} |s - \lambda|^{-1}.$$

Here $\sigma(A)$ denotes the set of eigenvalues of A and κ is the condition number of the diagonalizing matrix. Straightforward calculations yield

$$|(sI - A)^{-1}| \leq \tilde{C}\mathrm{Re}^2, \;\; R(s) \geq 0,$$

for some constant $\tilde{C}$. For a normal operator N, the diagonalizing matrix X_N is unitary. Hence $\kappa(X_N) = 1$ and if A were a normal operator the bound on the resolvent would only grow $\sim \mathrm{Re}$.

From the resolvent bound we have, using Parseval's identity, and the fact that future does not effect the past,

$$\int_0^T |v(t)|^2 dt \leq C\mathrm{Re}^4 \int_0^T |F(t)|^2 dt. \tag{16}$$

By using Equation (15) we also have

$$\frac{d}{dt}|v|^2 = 2\underbrace{(v, Av)}_{\leq \alpha |v|^2} + 2(v, F) \leq 2(\lambda + 1)|v|^2 + |F|^2. \tag{17}$$

Here $\alpha = 2$ is a bound of the numerical range of A. After integrating from 0 to T,

$$|v(T)|^2 \leq 2(\lambda + 1)\int_0^T |v(t)|^2 dt + \int_0^T |F(t)|^2 dt. \tag{18}$$

By combining (16) and (18) we have the following linear result

$$|v(T)|^2 + \int_0^T |v(t)|^2 dt \leq \tilde{c}\mathrm{Re}^4 \int_0^T |F(t)|^2 dt \tag{19}$$

Here $\tilde{c}$ is a constant.

2.2 Non-linear bound

As long as the solution of the non-linear problem (14) is bounded we can use the linear bound for the non-linear equation, yielding

$$|v(T)|^2 + \int_0^T |v(t)|^2 dt \leq \tilde{c}\mathrm{Re}^4 \int_0^T (\bar{f}^2 |v(t)|^4 + |F(t)|^2) dt. \tag{20}$$

We would like to show for all T that

$$|v(T)|^2 + \int_0^T |v|^2 dt < 2\tilde{c}\mathrm{Re}^4 \underbrace{\int_0^\infty |F|^2 dt}_{\bar{F}} \tag{21}$$

Since $v(0) = 0$ Equation (21) is true for sufficiently small T. There are two possibilities: (21) is true for all T or there is equality for at least some T. We shall prove that the second possibility is impossible if $\bar{F}$ is sufficiently small. Assume T_0 is the smallest value of T for which there is equality in (21). Then

$$\int_0^{T_0} |v|^4 dt \quad \leq \quad \max_{0\leq t\leq T_0} |v(t)|^2 \int_0^{T_0} |v|^2 dt \leq (2\tilde{c}\mathrm{Re}^4 \bar{F})^2$$

We see that if

$$4\bar{f}^2\tilde{c}^2\mathrm{Re}^8\bar{F} \leq \frac{1}{2} \quad \text{or equivalently} \quad \bar{F} \leq \frac{1}{8\bar{f}^2\tilde{c}^2\mathrm{Re}^8},$$

then

$$|v(T_0)|^2 + \int_0^{T_0} |v|^2 dt \quad \leq \quad \tilde{c}\mathrm{Re}^4(4\bar{f}^2\tilde{c}^2\mathrm{Re}^8\bar{F}^2 + \bar{F}) \leq 1.5\tilde{c}\mathrm{Re}^4\bar{F},$$

which is a contradiction. Hence if $\bar{F}$ is sufficiently small (21) is valid for all T, which implies

$$\lim_{t\to\infty} |v(t)| = 0.$$

We formulate the result as

Lemma 1. *There is a constant c such that if*

$$\int_0^\infty |F(t)|^2 dt \leq \frac{c}{Re^8} \tag{22}$$

then (14) has a bounded solution satisfying

$$\lim_{t\to\infty} |v(t)| = 0.$$

To be able to compare this result with the heuristic threshold for growth (13), we need to explicitly transform the initial value problem to the form (14). The suggested transformation yields a forcing

$$F(t) = (Lg_0 + g_0)e^{-t}. \tag{23}$$

From the condition (22) we obtain as a sufficient condition for non-linear stability,

$$|g_0| \leq \frac{c}{\mathrm{Re}^4} \tag{24}$$

When comparing with (13) we see that this condition is not sharp.

2.3 Improved threshold bound

To obtain a sharper result we introduce

$$\tau = \mathrm{Re}\, t, \quad \tilde{u}_1 = u_1, \quad \tilde{u}_2 = \mathrm{Re}\, u_2, \quad \tilde{u}_3 = \sqrt{\mathrm{Re}}\, u_3, \quad \tilde{u}_4 = u_4. \tag{25}$$

Then

$$\frac{d\tilde{u}}{d\tau} = \tilde{L}\tilde{u} + \tilde{f}(\tilde{u}), \quad \tilde{u}(0) = \tilde{g}_0$$

where

$$\tilde{L} = \begin{pmatrix} -\lambda & 1 & 0 & 0 \\ 0 & -\mu & 0 & 0 \\ 0 & 0 & -\nu & 0 \\ 0 & 0 & 0 & -\sigma \end{pmatrix}, \quad \tilde{f}(\tilde{u}) = \begin{pmatrix} -\gamma\tilde{u}_3^2 + \tilde{u}_1\tilde{u}_4 \\ \delta\mathrm{Re}\tilde{u}_3^2 \\ \gamma\tilde{u}_3\tilde{u}_1 - \frac{\delta}{\mathrm{Re}}\tilde{u}_3\tilde{u}_2 \\ -\frac{1}{\mathrm{Re}}\tilde{u}_1\tilde{u}_2 \end{pmatrix}$$

Clearly $\tilde{L}$ is independent of Re, and the corresponding resolvent can be bounded independently of Re. One can interpret the scaling (25) as the introduction of a new inner product and norm, with different weights for the different components. With respect to this inner product the degree of non-normality of the linear operator is independent of Re.

The heuristic arguments yield growth if $|\tilde{g}_0| > C\mathrm{Re}^{-1}$. If we introduce $\tilde{v} = \tilde{u} - e^{-\tau}\tilde{g}_0$ we obtain

$$\frac{d\tilde{v}}{d\tau} = \tilde{L}\tilde{v} + \tilde{f}(\tilde{v}) + \tilde{F}(t). \tag{26}$$

Now the non-linear term satisfies

$$|\tilde{f}(\tilde{v})| \leq \mathrm{Re}|\tilde{v}|^2.$$

Corresponding to (20) we have

$$|\tilde{v}(\tilde{T})|^2 + \int_0^{\tilde{T}} |\tilde{v}(\tau)|^2 d\tau \leq \kappa \int_0^{\tilde{T}} (\mathrm{Re}^2|v(t)|^4 + |\tilde{F}(t)|^2)dt. \tag{27}$$

Thus there exists a constant C such that we have decay if

$$\int_0^{\infty} |\tilde{F}|^2 d\tau \leq \frac{C}{\mathrm{Re}^2},$$

or equivalently, if the initial condition satisfies

$$|\tilde{g}_0| \leq \frac{c}{\mathrm{Re}},$$

which is sharp.

3. COUETTE FLOW

Using similar ideas as in the previous section, a bound of the resolvent can be used to prove a threshold for non-linear stability in plane Couette flow. In Kreiss et al. (1994) this idea was first explored. Consider (1) with the base flow being plane Couette flow. Let the initial perturbation be

$$\mathbf{u}(\cdot, 0) = \epsilon \mathbf{u}_0.$$

As before, we rewrite the initial value problem for the perturbation, on a form corresponding to (14), with forcing corresponding to (23). To prove non-linear decay we need linear estimates of the solution and its derivatives. Therefore the natural normalization is

$$\|L^2\mathbf{u_0} + L\mathbf{u_0}\| + \|L\mathbf{u_0} + \mathbf{u_0}\| = 1.$$

Here L is the linear operator, defined in (2) and the norm is defined in (3), and ϵ is a measure of the amplitude of the perturbation. The non-linear result is

Theorem 1. *Assume the resolvent condition*

$$\|(sI - L)^{-1}\|^2 \leq cRe^{\rho} \quad \Re s \geq 0, \tag{28}$$

is valid for some constants ρ and c. Then there exists a constant K such that plane Couette flow is non-linearly stable if

$$\epsilon \leq \frac{K}{Re^{\rho+5/4}}.$$

To obtain the linear estimate the resolvent equation is Fourier transformed in the spanwise and streamwise directions. The norm of the resolvent, $\|(sI - \mathcal{L})^{-1}\|$, where $\mathcal{L}$ is defined in (7) is computed numerically in parts of the parameter domain. The parameters are the Reynolds number, Re, the two wave numbers, α, β, and the Laplace transform parameter, s. For $\alpha\mathrm{Re} = 0$ an analytical result is given.

Theorem 2. *For $\alpha Re = 0$, $\Re s > 0$ the resolvent of plane Couette flow satisfies*

$$\max_{\Re(s)\geq 0} \|(sI - \mathcal{L})^{-1}\|^2 = cRe^4.$$

Numerical results presented in Kreiss et al. (1994) indicate that

$$\|(sI - \mathcal{L})^{-1}\|^2 \leq c\mathrm{Re}^4, \tag{29}$$

is valid for all parameter values. Thus $\rho = 4$ in (28), and Theorem 1 implies that the threshold is given by

$$\epsilon \leq \frac{K}{\mathrm{Re}^{21/4}}.$$

This result is not sharp, even though Theorem 2 shows that the linear result $\rho = 4$ cannot be improved. This is not unexpected since the disturbances for which the linear estimate is sharp are not the same as those for which the non-linear analysis is sharp.

Improvements have been achieved along two lines. The first idea is to scale the components as in the model problem. In Liefvendahl and Kreiss (2003), a new norm, $\|\cdot\|_m$, is introduced. The new norm weighs the different velocity components with coefficients depending on Re, and is defined by

$$\|\mathbf{u}\|_m^2 = \|u_1\|^2 + \mathrm{Re}^2\|u_2\|^2 + \|u_3\|^2.$$

Note that introducing the new norm corresponds to a rescaling of the velocity components. When measured in this norm the resolvent does not grow as fast with Re as when the standard norm is used. Computations indicate

$$\|(sI - L)^{-1}\|_m^2 \leq \tilde{c}\mathrm{Re}^2, \quad \Re(s) \geq 0.$$

In fact, since there are eigenvalues $\mathcal{L}$ with negative real part $\sim \mathrm{Re}^{-1}$, one can show that other weights cannot give a slower growth with Re than this.

Now we must use a different normalization of the initial perturbation. Let

$$\mathbf{u}(\cdot, t) = \varepsilon \mathbf{g}_0, \quad \|\mathbf{g}_0\|_{H^4,m} = 1.$$

The norm includes derivatives up to order 4, with a Re^2 weight of the normal velocity. In Liefvendahl and Kreiss (2002) the new norm is used to derive an improved non-linear result.

Theorem 3. *If*

$$\|(sI - L)^{-1}\|_m^2 \leq \tilde{c}Re^2,$$

then there exists a constant K such that plane Couette flow is non-linearly stable if

$$\epsilon \leq \frac{K}{Re^3}.$$

This implies that the threshold for the streamwise and spannwise velocity components is $\sim \mathrm{Re}^{-3}$ while the threshold for the normal velocity is $\sim \mathrm{Re}^{-4}$.

Secondly, the previously mentioned numerical results on the Reynolds number dependence of the resolvent are based on numerical computations in part

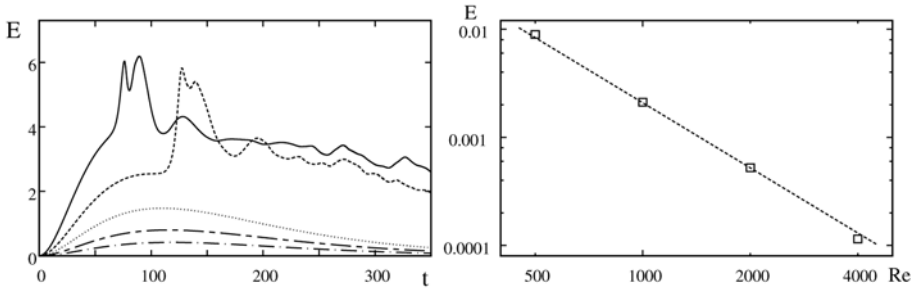

Figure 4. (a) Time evolution of energy of flow perturbations for the streamwise vortex scenario with different initial amplitudes. (b) Threshold energy density for transition from the streamwise vortex scenario in Couette flow. From Kreiss et al. (1994).

of the parameter domain. There are analytical results for certain wave numbers, see Liefvendahl and Kreiss (2003), but the numerical computations do not cover the remaining, infinite parameter domain. The mentioned papers do not discuss the behaviour of the resolvent for parameter values outside the domain were computations are done. In Åsen and Kreiss (2003) new analytical resolvent estimates are proved. Together with the old analytical estimates they cover all but a bounded part of the parameter domain. It is also shown how reliable computations of the resolvent in the remaining, bounded parameter domain can be achieved. The result is a proof of the resolvent bound (29).

4. UPPER THRESHOLD BOUNDS FROM NUMERICAL SIMULATIONS

In this section we discuss the numerical calculations from Kreiss et al. (1994) and Reddy et al. (1998) regarding the disturbance development resulting from particular initial conditions picked to achieve laminar-turbulent transition with low initial energy. By monitoring the energy of such disturbances and plotting them as a function of the Reynolds number, the upper bounds of the threshold curves are obtained.

4.1 Streak breakdown in Couette flow

Figure 4a gives the time history for the perturbation energy for some subcritical and supercritical amplitudes. We see that the subcritical simulations follows qualitatively the linear route of transient growth resulting from the forcing of the streaks by the vortex followed by viscous decay of the energy. For supercritical amplitudes we see four distinct phases: transient growth similar to that for subcritical amplitudes, a rapid secondary instability leading to a transient peak of high amplitude, a similarly rapid decay to a turbulent state and finally

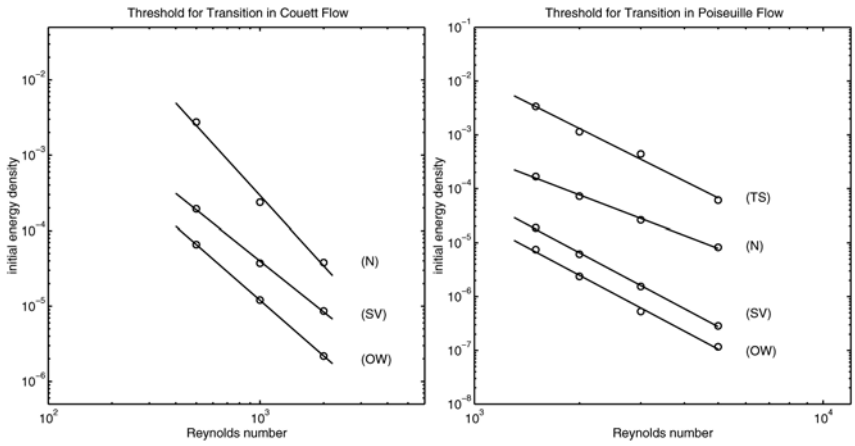

Figure 5. Threshold energy density for transition in Couette and Poiseuille flow and for the main scenarios, two-dimensional disturbances (TS), streamwise vorticies (SV), oblique waves (OW)and random three-dimensional noise (N). The circles correspond to data from simulations. The lines are fits to the data. Adapted from Reddy et al. (1998).

irregular amplitude variations as the turbulence relaxes towards a statistically steady state for large times.

To find the critical amplitude the simulations were continued until the energy in the wall normal velocity component rose to turbulent levels, or until a time of about three times that of the first peak in the energy. If turbulence was observed in this time the amplitude was considered supercritical and otherwise subcritical. In practise the solutions for supercritical amplitudes have a characteristic brief but rapid growth of the perturbation energy giving rise to a high transition peak as seen in Figure 4, which makes the determination of critical amplitude unambiguous. Figure 4 gives the critical perturbation energy for different Reynolds numbers. For the critical perturbation energy the result is $E \approx 2000/\mathrm{Re}^2$ which corresponds to a threshold amplitude $\sim \mathrm{Re}^{-1}$.

4.2 Thresholds in plane Couette and Poiseuille flows

The transition threshold has been determined not only for the streamwise vortex scenario (SV), but also for the oblique wave scenario (OW) discussed in section 1. In addition we have also determined the threshold for initial conditions only consisting of random noise (N). Figure 5a plots the threshold energy density for transition in Couette flow for these scenarios. The oblique wave scenario has the lowest threshold, closely followed by the streamwise vortex scenario. The random noise requires the largest energy to achieve transition in Couette flow. For the data collected, the threshold energy density scales like approximately $R^{-2.2}$, $R^{-2.5}$, $R^{-3.1}$ for the streamwise vortex, oblique wave,

Table 4. Transition threshold amplitude exponents compiled by Reddy et al. (1998). The values in parenthesis are those found by the asymptotic analysis of Chapman (2002).

Transition scenario	Couette flow	Poiseuille flow
TS-wave transition		–1.6
Noise transition	–1.55	–1.25
Streak transition	–1.10 (–1.0)	–1.25 (–1.5)
Oblique transition	–1.25 (–1.0)	–1.75 (–1.25)

and noise scenarios respectively. The result for (SV) corresponds to a threshold amplitude exponent of about -1.1, which is close to exponent of ≈ -1 found for streak breakdown by Kreiss et al. (1994), who did not consider an optimal streamwise vortex.

Figure 5b shows the threshold energy density for transition in Poiseuille flow for these scenarios discussed about, plus one consisting of an initial Tollmien–Schlichting wave (TS). A TS-wave is the least stable eigenmode of the Orr–Sommerfeld–Squire problem. The threshold transition energy for the initial oblique waves and the streamwise vortices are more than two orders of magnitude lower than for the Tollmien–Schlichting waves. The random initial perturbations have a threshold well below the one found for Tollmien–Schlichting waves.

The threshold exponents found from these calculations are compiled in Table 4, where they are also compared with the values found by Chapman (2002). Chapman used asymptotic analysis to calculate the threshold values and found that the Reynolds numbers that were used in the numerical simulations were not large enough to satisfy the assumptions made in the asymptotic analysis.

5. CONCLUSIONS

Non-linear stability bounds are derived for subcritical shear flows. First the methodology is exemplified using a model problem and then it is applied to plane Couette flow. A bound on the forced linear problem is derived, which is subsequently used on the non-linear problem with the non-linear terms used as forcing terms. The bounds are critically dependent on the behavior of the resolvent, which needs to be estimated in the whole parameter domain. The result of an improved analysis is a lower bound of Re^{-4}.

Upper bounds based on numerical simulations are found to be about Re^{-1}, depending slightly on the transition scenario investigated. Asymptotic analysis performed by Chapman (2002) gives similar bounds as the numerical simulations. For Couette flow we are thus left with the situation that the lower and upper bounds differ with the cube of the Reynolds number. Finally bounds for

plane Poiseuille flow are also presented. These bounds are valid for subcritical parameter regimes, or for cases in which the exponentially growing mode is removed or inactive.

The gap in the scaling exponents may be closed from both sides by more cleaver choice of initial disturbances and further development of the non-linear stability theory. One may speculate that for plane Couette flow the real threshold curve is slightly below -1 and that the major difference in threshold exponents between the upper bound from the computations and the lower bound from the non-linear stability theory could be bridged by further development of the non-linear theory. A possible approach would be to decompose the perturbation into parts with different length scales.

REFERENCES

Åsen, P.-O. and Kreiss, G. (2003). A rigorous resolvent estimate for plane Couette flow. Technical Report, TRITA-NA-0330.

Baggett, J.S. and Trefethen, L.N. (1997). Low-dimensional models of subcritical transition to turbulence. *Phys. Fluids* **9**, 1043–1053.

Chapman, S.J. (2002). Subcritical transition in shear flows. *J. Fluid Mech.* **451**, 35–97.

Drazin, P.G. and Reid, W.H. (1981). *Hydrodynamic Stability*, Cambridge University Press, Cambridge.

Faisst, H. and Eckhardt, B. (2005). Sensitive dependence on initial conditions in transition to turbulence in pipe flow. *J. Fluid Mech.* **504**, 343–352.

Henningson, D.S. (1996). Comment on "Transition in shear flows. Nonlinear normality versus non-normal linearity" [Phys. Fluids, 3060 (1995)]. *Phys. Fluids* **8**, 2257–2258.

Joseph, D.D. (1976). *Stability of Fluid Motions I*, Springer-Verlag, Berlin.

Kreiss, G., Lundblad, A. and Henningson, D.S. (1994). Bounds for threshold amplitudes in subcritical shear flow. *J. Fluid Mech.* **270**, 175–198.

Liefvendahl, M. and Kreiss, G. (2002) Bounds for the threshold amplitude for plane Couette flow. *J. Non-Linear Math. Phys.* **9**, 311–324.

Liefvendahl, M. and Kreiss, G. (2003). Analytical and numerical investigation of the resolvent for plane Couette flow. *SIAM J. Appl. Math.* **63**(3), 801–817.

Reddy, S.C., Schmid, P.J., Baggett, J.S. and Henningson, D.S. (1998). On stability of streamwise streaks and transition thresholds in plane channel flows. *J. Fluid Mech.* **365**, 269–303.

Schmid, P.J. and Henningson, D.S. (2001). *Stability and Transition in Shear Flows*, Applied Mathematical Sciences, Vol. 142, Spinger Verlag, Berlin.

Trefethen, L.N. (1997). Pseudospectra of linear operators. *SIAM Rev.* **39**, 383–406.

Waleffe, F. (1995). Transition in shear flows. Nonlinear normality versus non-normal linearity. *Phys. Fluids* **7**, 3060–3066.

NON-LINEAR OPTIMAL PERTURBATIONS IN SUBCRITICAL INSTABILITIES

Carlo Cossu
Laboratoire d'Hydrodynamique (LadHyX), École Polytechnique – CNRS, F-91128 Palaiseau Cedex, France
carlo.cossu@ladhyx.polytechnique.fr

Abstract Non-linear optimal perturbations are defined here as those of minimum energy leading to subcritical instability. We show that a necessary condition for an initial perturbation to be a non-linear optimal is that the initial perturbation energy growth is zero. The fulfillment of this condition does not depend on the disturbance amplitude but only on the linearized operator as long as the non-linearity conserves energy. Saddle point solutions and linear optimal perturbations leading to maximum transient growth both satisfy the non-linear optimality condition. We discuss these issues on low-dimensional models of subcritical transition for which non-linear optimals and the minimum threshold energy are computed.

Keywords: subcritical transition, non-linear stability, optimal perturbations, non-normality.

1. INTRODUCTION

The transition to turbulence in wall bounded shear flows has fascinated scientists since Reynolds' experiments in 1883 and is still not completely understood. Some of these flows, such as plane Couette flow and pipe Poiseuille flow, experience a transition to turbulence despite the linear stability of the laminar basic flow for all Reynolds numbers R. The fact that a turbulent state is observed for sufficiently large R is understood as an example of conditional stability, where asymptotic stability is guaranteed only if the energy of the perturbations $\mathcal{E}$ is lower than a threshold $\delta(R)$ which depend on the Reynolds number. For low values of the Reynolds number $R < R_G$, the threshold δ is infinite and the flow is said to be globally stable. However, for $R > R_G$, the threshold δ is finite and is thought to decrease with increasing R making the observation of the laminar basic flow less and less likely at large R. The direct computation of the curve $\delta(R)$, which is the scope of non-linear hydrodynamic stability theory, is currently out of reach. Different types of stability analyses

T. Mullin and R.R. Kerswell (eds), Laminar Turbulent Transition and Finite Amplitude Solutions, 251–266.
© 2005 *Springer. Printed in the Netherlands.*

have therefore provided, along the years, upper and lower bounds on R_G and/or on $\delta(R)$ itself or on its scaling with R as $R \to \infty$.

Energy theory (see Joseph, 1976, for a throughout account) provides a lower bound on R_G by providing sufficient conditions for monotonic stability. The idea is to start from the evolution equation for the energy of perturbations and then to maximize $d\mathcal{E}/dt$ over all admissible perturbations at given R. Through variational calculus it is possible to find a critical Reynolds number R_E such that if $R < R_E$ then $d\mathcal{E}/dt < 0\ \forall \mathbf{u}$. The lower bounds R_E given by this kind of theory can however be far below the observed values of R_G.

A 'global bifurcation' perspective, completely different from the classical non-linear stability analysis has emerged (Nagata, 1990; Clever and Busse, 1992, and many others thereafter) by looking for non-trivial solutions of the Navier–Stokes equations instead of examining the stability of the basic flow itself. In this approach, one usually looks for saddle-node bifurcations. Even if this kind of approach provide useful informations on the complexity of the phase space, for the moment it is not very effective in helping finding δ. The main problems are (a) that standard techniques only allow for the search of 'simple' limit sets such as fixed points or limit cycles and are therefore unable for instance to provide upper bounds for δ if the non-trivial attractors are not steady or periodic solutions, (b) that one is never sure to have found all the non-trivial attractors and (c) that to compute δ one should compute the envelope of all the basins of attraction of all the non-trivial attractors which may be more complicated than computing the basin of attraction of the laminar flow itself. This approach, appealing for the understanding of the structure of the turbulent flow itself, may be therefore less adapted to the determination of $\delta(R)$.

A complementary approach has emerged recently (see Schmid and Henningson, 2001, for a review) and has concentrated on the ability of linearly stable laminar shear flows, such as the Couette or Poiseuille solutions, to sustain, in the linear approximation, transient energy growths $\mathcal{E}_L(t)/\mathcal{E}(0)$ whose maximum value can attain values of order $O(R^2)$ (Gustavsson, 1991; Butler and Farrell, 1992). This huge potential for transient growth has been related to the strongly non-normal nature of the evolution operator linearized about the laminar basic flow (see Trefethen et al., 1993, for a review). Low-energy upper bounds on $\delta(R)$ have been obtained by direct numerical simulation using finite amplitude linear optimal perturbations plus noise as initial condition (Kreiss et al., 1994; Reddy et al., 1998).

The scaling of δ with the Reynolds number has been the subject of debate. Arguments based on the balance between linear/non-normal energy growth and non-linear energy feedback applied to model systems suggested a scaling of the type $\delta \sim R^{\gamma}$ with $\gamma < -1$ (Trefethen et al., 1993; Baggett and Trefethen, 1997), where the upper limit $\gamma = -1$ corresponds to the balance between non-linear terms and viscous diffusion (Waleffe, 1995). The scaling estimates

of γ provided by direct numerical simulation (Kreiss et al., 1994; Reddy et al., 1998) and asymptotic analyses (Chapman, 2002) for the Navier–Stokes equations are all near the -1 value when streamwise vortices or oblique waves are given as initial conditions in the plane Couette and the plane Poiseuille flow (for $R < 5772$). Recent experimental results (Hof et al., 2003) estimate $\gamma = -1$ for pipe Poiseuille flow. On the other hand, using estimates on the scaling of the resolvent norm with R, which is strongly related to the non-normal nature of the linear operator, lower bounds on the threshold $\delta(R)$ have been provided (Kreiss et al., 1994) as reviewed by Henningson and Kreiss (2005). These analyses provide a lower bound $\gamma > -4$ for the plane Couette flow.

Despite the great progress performed in recent years, an important gap still remains between lower bounds and upper estimates of the scaling exponent γ and of $\delta(R)$ itself. One therefore remains wondering if other initial conditions, not considered in the cited numerical simulations asymptotic analyses and experiments, would not be able to exhibit values of γ lower than its upper limit -1. Even if the computation of $\delta(R)$ seems still to be out of reach for the Navier–Stokes equations, it is not for model systems that have been used to mimic the subcritical transition and to propose new ideas for the Navier–Stokes case. The scope of the present contribution is to compute the non-linear stability threshold $\delta(R)$ itself and the associated non-linear optimal perturbations for some low-dimensional models of subcritical transition. It is expected that the comparison of these results with those issued by previously cited approaches could induce some progress in the computation of $\delta(R)$ in the Navier–Stokes case.

The setting and framework of the problem is laid down in Section 2 where a necessary condition for non-linear optimality is derived. Illustrative results, obtained for two representative low-dimensional model systems of subcritical transition are reported and commented in Section 3. Implications for the Navier–Stokes equations are briefly discussed and some conclusions are drawn in Section 4.

2. MATHEMATICAL FORMULATION

Framework. We are interested in the (non-linear) asymptotic stability of a linearly stable 'laminar basic state' $\mathbf{U}$ with respect to perturbations $\mathbf{u}$. The generic state being written as $\mathbf{U} + \mathbf{u}$, by substitution one obtains the evolution equation for the perturbations:

$$d\mathbf{u}/dt = \mathcal{L}_R\,\mathbf{u} + \mathcal{N}(\mathbf{u}), \tag{1}$$

where the 'laminar basic state' now corresponds to $\mathbf{u} = \mathbf{0}$. $\mathcal{L}_R$ is a linear operator depending on the real parameter R and on the basic flow $\mathbf{U}$ while

$\mathcal{N}$ is a non-linear operator that we assume to be homogeneous (i.e. such that $\mathcal{N}(\mathbf{0}) = \mathbf{0}$). The initial value problem for Equation (1) is solved by giving an initial condition $\mathbf{u}_0$ at $t = t_0$ and considering its evolution $\mathbf{u} = \mathbf{u}(t, \mathbf{u}_0, R)$ which depends on time, on the given initial condition and on the parameter R. The energy of the perturbations is defined in the standard way using a suitable inner product

$$\mathcal{E}[\mathbf{u}(t, \mathbf{u}_0, R)] = \frac{1}{2}\langle \mathbf{u}, \mathbf{u}\rangle. \tag{2}$$

We will denote the energy of the initial condition as $\mathcal{E}_0(\mathbf{u}_0) = \langle \mathbf{u}_0, \mathbf{u}_0\rangle/2$. The evolution equation for the perturbation energy is obtained by projection of Equation (1) on $\mathbf{u}$:

$$\frac{d\mathcal{E}}{dt} = \langle \mathbf{u}, \mathcal{L}_R\, \mathbf{u}\rangle + \langle \mathbf{u}, \mathcal{N}(\mathbf{u})\rangle. \tag{3}$$

We will call 'energy preserving non-linear terms' non-linear terms with the property that $\langle \mathbf{u}, \mathcal{N}(\mathbf{u})\rangle = 0\ \forall \mathbf{u}$. This is the case for Navier–Stokes equations and for most of low-dimensional models of subcritical transition. We will call 'amplitude' of $\mathbf{u}$ the norm $\|\mathbf{u}\|$ defined by the standard inner product (therefore $\|\mathbf{u}\| = \sqrt{2\,\mathcal{E}(\mathbf{u})}$) and 'shape' of $\mathbf{u}$ the direction of the corresponding vector in phase space i.e. $\mathbf{u}/\|\mathbf{u}\|$.

Minimum threshold energy and non-linear optimals. The basin of attraction $\mathcal{S}_R$ of the laminar basic flow $\mathbf{u} = \mathbf{0}$ at fixed R is given by the set of initial perturbations $\mathbf{u}_0$ such that $\lim_{t\to\infty} \mathcal{E}[\mathbf{u}(t, \mathbf{u}_0, R)]/\mathcal{E}_0 = 0$. As we assumed $\mathbf{U}$ linearly (strictly) stable, its basin of attraction has non-zero measure. The complementary set $\mathcal{U}_R$ is made of initial perturbations for which $\lim_{t\to\infty} \mathcal{E}[\mathbf{u}(t, \mathbf{u}_0, R)]/\mathcal{E}_0 \neq 0$; this set has zero measure as long as the laminar basic flow is globally stable. In the case in which $\mathcal{U}_R$ has non-zero measure, the *minimum threshold energy* can be defined as

$$\delta(R) = \min_{\mathbf{u}_0 \in \mathcal{U}_R} \mathcal{E}_0(\mathbf{u}_0). \tag{4}$$

The *non-linear optimal perturbation* (from now on abbreviated into NLOP) is the initial perturbation for which the minimum δ is attained.

A necessary condition of non-linear optimality. We now show that not all possible initial perturbations are suitable candidates to be non-linear optimals (NLOP) but only those that realize a local minimum for the perturbation energy along the trajectory selected by $\mathbf{u}_0$. In fact, in a neighborhood $\Delta t \ll 1$ of t_0, we can develop the perturbation energy as $\mathcal{E}[\mathbf{u}(t_0 + \Delta t, \mathbf{u}_0, R)] = \mathcal{E}_0 + \Delta t\,(d\mathcal{E}/dt)_0 + (\Delta t^2/2)\,(d^2\mathcal{E}/dt^2)_0 + O(\Delta t^3)$. If $\mathbf{u}_0 \in \mathcal{U}_R$ and $(d\mathcal{E}/dt)_0 < 0$

then $\mathbf{u}(t_0 + \Delta t, \mathbf{u}_0, R)$, with $\Delta t > 0$ would also belong to $\mathcal{U}_R$ and have a perturbation energy $\mathcal{E} < \mathcal{E}_0$, and therefore $\mathbf{u}_0$ cannot be the NLOP because it is not a minimum of $\mathcal{E}$. In the case $(d\mathcal{E}/dt)_0 > 0$ the same argument with $\Delta t < 0$ demonstrates that $\mathbf{u}_0$ is also not optimal. This proves that *a necessary condition for* $\mathbf{u}_0$ *to be a non-linear optimal perturbation is that* $(d\mathcal{E}/dt)(t_0, \mathbf{u}_0, R) = 0$. If this condition is satisfied an additional condition, by which we make sure to obtain a local minimum and not a maximum, is that $(d^2\mathcal{E}/dt^2)(t_0, \mathbf{u}_0, R) \geq 0$.

The $\mathcal{Z}_R$ set and some of its properties. The necessary condition of optimality allows to restrict the search of the non-linear optimals to the set $\mathcal{Z}_R$ of perturbations of zero energy growth $d\mathcal{E}/dt = 0$. By substitution in Equation (3), it is easily verified that these perturbations must satisfy the condition $\langle \mathbf{u}, \mathcal{L}_R\, \mathbf{u}\rangle + \langle \mathbf{u}, \mathcal{N}(\mathbf{u})\rangle = 0$. It is easy to verify[1] that all the non-trivial steady solutions $\mathbf{u}_e$ such as saddles or nodes necessarily belong to $\mathcal{Z}_R$. For systems with energy-conserving non-linear terms, the perturbations belonging to $\mathcal{Z}_R$ satisfy the simpler condition $\langle \mathbf{u}, \mathcal{L}_R\, \mathbf{u}\rangle = 0$. For these systems the $\mathcal{Z}_R$ set can therefore be determined by an analysis of the linear operator $\mathcal{L}_R$ and belonging to that set is a property independent of the amplitude, i.e. if $\mathbf{u}_0 \in \mathcal{Z}_R$ then $c\,\mathbf{u}_0 \in \mathcal{Z}_R$.

Linear optimal perturbations. Linear optimal perturbations are computed on the linear system $d\mathbf{u}^{(L)}/dt = \mathcal{L}_R\, \mathbf{u}^{(L)}$ by a suitable optimization on the initial conditions. We will denote by LOP1 the linear optimals maximizing the linear transient growth $\mathcal{E}^{(L)}/\mathcal{E}_0^{(L)}$ (e.g. Butler and Farrell, 1992; Trefethen et al., 1993). It can be shown[2] that these linear optimal perturbations satisfy the property $\langle \mathbf{u}, \mathcal{L}_R\mathbf{u}\rangle$. Linear optimals LOP1 therefore also belong to $\mathcal{Z}_R$ in the case of systems with energy preserving non-linear terms.

Another type of linear optimal, denoted as LOP2 in the following, can be defined by maximizing the initial energy growth rate $d\mathcal{E}^{(L)}/dt$. This second type of optimal initial condition has for instance been used as initial condition to compute the scaling laws of the critical threshold for low-dimensional model systems (Baggett and Trefethen, 1997). Unless the maximum energy growth rate is zero, this second type of linear optimal initial condition does not belong to $\mathcal{Z}_R$ in general.

3. APPLICATION TO LOW-DIMENSIONAL MODELS

Several low-dimensional models have been considered in order to discuss qualitative features of subcritical transitions. These models usually share properties of the Navier–Stokes equations that are thought to be relevant to the subcritical transition: (a) they admit the linearly stable laminar fixed point $\mathbf{u} = 0\ \forall R$; (b) the linear operator $\mathcal{L}_R$ is non-normal and is able to induce energy growths

of order R^2 for sufficiently large R; (c) non-linear terms conserve energy. In the following we will compute the minimum threshold energy and the associated non-linear optimal perturbations for two of these models. The first is a two-dimensional system proposed by Dauchot and Manneville (1997) and is briefly reviewed by Manneville in these proceedings. It has also been independently studied by Baggett and Trefethen (1997) as TTRD model from a different perspective. We use this simple two-dimensional model to introduce, in a simple case, the technique by which the non-linear optimals and threshold are computed. We then apply this technique to a four-dimensional model, proposed by Waleffe (1997), which is inspired by a low-dimensional projection of the Navier–Stokes equations.

3.1 A two-dimensional model

The model. The model is in the form of system (1) with

$$\mathbf{u} = \left\{ \begin{array}{c} u \\ v \end{array} \right\}; \quad \mathcal{L}_R = \left[\begin{array}{cc} -1/4R & 1 \\ 0 & -1/R \end{array} \right]; \quad \mathcal{N}(\mathbf{u}) = \left\{ \begin{array}{c} u\,v \\ -u^2 \end{array} \right\}. \tag{5}$$

where all the variables are real. Using the standard inner product for real vectors the perturbation energy is defined as $\mathcal{E} = (u^2 + v^2)/2$. The equation governing the perturbation energy is readily obtained as $d\mathcal{E}/dt = -u^2/4R + u\,v - v^2/R$. The linear operator $\mathcal{L}_R$ is non-normal and the non-linear terms conserve $\mathcal{E}$.

Global dynamics. Many of the properties of system (5) can be computed by hand and its phase space dynamics has already been described (Dauchot and Manneville, 1997; Manneville, 2005). The laminar basic flow is represented by the trivial solution $u = v = 0$, coinciding with the origin O in the phase plane, and is stable for all R. For $R < 1$ the laminar basic flow O is the sole attractor of the system and is therefore globally stable. At $R = 1$ two additional solutions, a stable node A and a saddle S appear through a saddle-node bifurcation at finite distance from the laminar fixed point so that for $R > 1$ the stability of laminar basic is only conditional because another attractor (the node A) exists.[3]

The $\mathcal{Z}_R$ and the computation of δ and the non-linear optimals. The states $\{u_0, v_0\}$ belonging to $\mathcal{Z}_R$ satisfy $\langle \phi, \mathcal{L}_R\,\phi \rangle = -u_0^2/4R + u_0\,v_0 - v_0^2/R = 0$ that gives the two solutions $v_0 = u_0 \left(R \pm \sqrt{R^2 - 1} \right)/2$. The $\mathcal{Z}_R$ is therefore defined only for $R > R_E = 1$ and corresponds to two straight lines in the phase space (respectively ${\mathcal{Z}_R}^+$ and ${\mathcal{Z}_R}^-$ for the $+$ or $-$ sign of the root). In order to find the minimum threshold energy one should in principle test the stability of all possible initial conditions with energy $(u_0^2 + v_0^2)/2 = \mathcal{E}_0$ starting from very

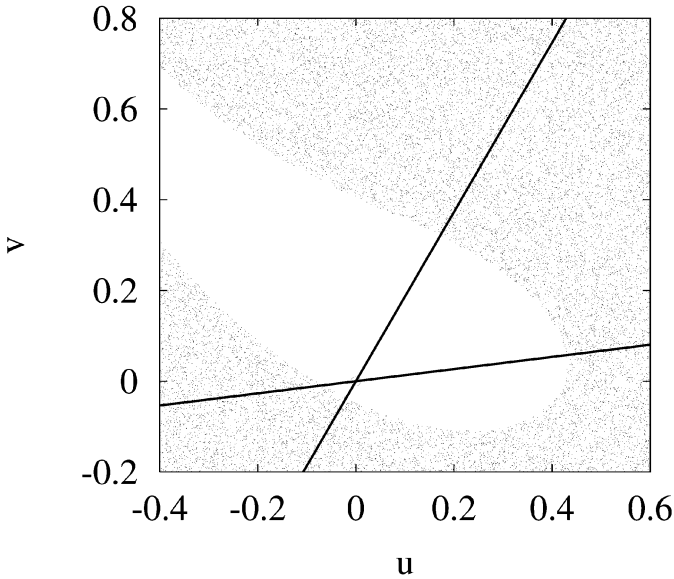

Figure 1. Phase space image of system (5) at $R = 2$. The two straight lines corresponding to the set $\mathcal{Z}_R$ are reported as solid lines; they cross each other in origin corresponding to the laminar basic flow solution. The basin of attraction $\mathcal{S}_R$ of the laminar basic flow is given by the white region sourrounding the origin while its complementary $\mathcal{U}_R$ is represented by the outside gray-shaded region. Iso-energy initial conditions lie on circles which are also reported in the figure.

low initial energy levels. These initial conditions corresponds to all the points on a circle in the phase space. When all the points of the circle corresponding to the given $\mathcal{E}_0$ lead to stability, a new, slightly larger, $\mathcal{E}_0$ can be considered and the computation repeated until the first initial condition leading to instability is encountered (see Figure 1). The necessary condition for optimality allows us instead to test the stability of only the four points on the circle which intersect the $\mathcal{Z}_R$ set. To compute the threshold δ and the corresponding non-linear optimals we therefore start at sufficiently low $\mathcal{E}_0$ and then we integrate up to $t_{\max} = 100\,R$ the equations giving as initial condition the 'potentially optimal' points of energy $\mathcal{E}_0$, on the set $\mathcal{Z}_R$ and with $(d^2\mathcal{E}/dt^2)_0 > 0$, which are the two points on the ${\mathcal{Z}_R}^+$ line. For low values of $\mathcal{E}_0$ the two initial conditions lead to asymptotic stability. The initial energy is therefore increased by small steps $\Delta\mathcal{E}_0$ and the computations repeated at each step. The minimum threshold δ is found as the minimum value of $\mathcal{E}_0$ for which no asymptotic decay of $\mathcal{E}$ is observed and the corresponding initial condition represent the non-linear optimal. This kind of computation has been repeated for values of R ranging from $R_E = 1$ to 100. The non-linear results are compared to the results that

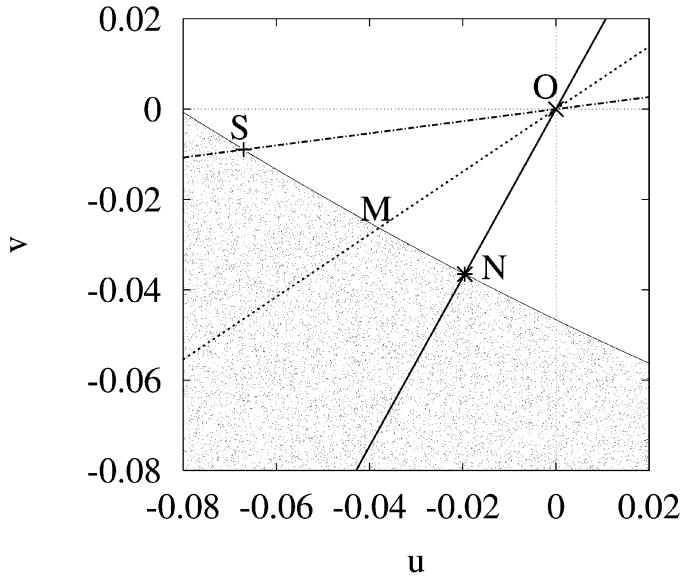

Figure 2. Phase space portrait of system (5) at $R = 2$. The laminar fixed point is denoted by O, the saddle by S and the non-linear optimal perturbation by N. The basin of attraction $\mathcal{S}_R$ is given by the white region sourrounding O. The two straight lines corresponding to $\mathcal{Z}_R{}^+$ and $\mathcal{Z}_R{}^-$ are reported respectively as the solid line and the dashed-dotted lines. The LOP2 linear optimal set is reported as a dotted line.

would have been found using linear optimization and saddle point tracking in the next paragraph.

Comparison with other results. The phase portrait of system (5) for $R = 2$ is shown in Figures 2 and 1. The linear optimal perturbations maximizing the energy growth (LOP1) lie on the $\mathcal{Z}_R{}^+$ line (as already remarked by Dauchot and Manneville, 1997) while the corresponding linear optimal response coincides with the $\mathcal{Z}_R{}^-$ line. The linear optimals maximizing the initial energy growth (LOP2) lie on the line reported in between $\mathcal{Z}_R{}^+$ and $\mathcal{Z}_R{}^-$ lines. The set of unstable initial conditions $\mathcal{U}_R$ had been numerically computed and appears as the external gray region while the set $\mathcal{S}_R$ is given by the inner white region sourrounding the laminar fixed point O. $\mathcal{U}_R$ and $\mathcal{S}_R$ are separated by the stable manifold of the saddle S (Dauchot and Manneville, 1997). From Figure 2 we therefore have a geometrical interpretations of the optimality condition: the minimum distance of $\mathcal{U}_R$ from the laminar fixed point O is realized by the non-linear optimal, denoted by N, which is situated on the $\mathcal{Z}_R{}^+$ line that is orthogonal to the boundary of the basin of attraction and therefore at the minimum distance (see also Figure 1). Furthermore, in the present case, the non-linear optimal and the linear optimal maximizing energy growth have the

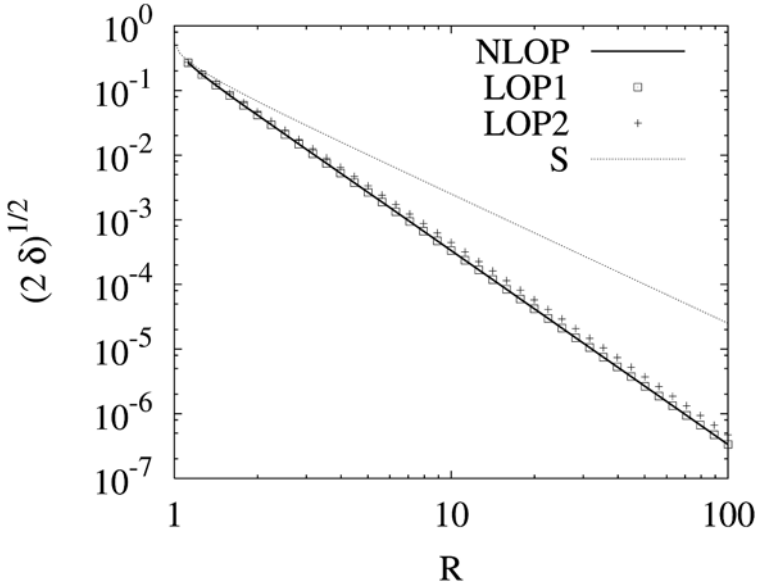

Figure 3. Dependence on the R of the (non-linear) minimum threshold amplitude $(2\,\delta(R))^{1/2}$ and of the critical amplitudes found using the other (LOP1,LOP2 and saddle point) strategies for system (5).

same shape. The same point N would have then been found by checking the stability threshold of linearly-optimal-shaped initial perturbations (LOP1) by increasing their amplitude (which is essentially the strategy followed by Reddy et al., 1998). The use of a strategy based on the linear optimals maximizing initial energy growth (Baggett and Trefethen, 1997), would have led to the critical point M, that, just like the saddle point S, is not only located farther from O, but also has a shape different from that of N. In Figure 3 we show the critical amplitudes corresponding to the described 'transition scenarios' as a function of R. The non-linear minimum threshold amplitude $\sqrt{2\delta(R)}$ and the critical amplitude found using the LOP1-strategy coincide, while the threshold amplitude found using the LOP2 strategy is slightly larger but they all scale as $\sim R^{-3}$ for $R > 10$, a scaling predicted by Baggett and Trefethen (1997) using non-normal/non-linear balance and by Dauchot and Manneville (1997) using geometrical considerations. The ratio u_0/v_0 scales as R^{-1} for the non-linear optimals (and therefore also for the LOP1 linear optimals), while it tends to a constant for the LOP2. The saddle solution S has both an amplitude scaling $\sim R^{-2}$ and a shape $u_0/v_0 \sim R$ which are completely different from the other critical perturbations therefore providing a less useful upper bound for critical thresholds.

Discussion. The coincidence of the shape of linear and non-linear optimal conditions is a general result for two-dimensional systems under the assumption of sufficiently low threshold energy.[4] Some of the conclusions that we may infer from the analysis of the two-dimensional model, however, may not extend to models of higher dimensions. In three dimensions for instance the set $\mathcal{Z}_R$ would not be given by two lines but by a cone and for instance the non-linear optimals and the linear LOP1 optimals could be on the same cone without necessarily being on the same line and therefore have the same 'shape'. This is why we now repeat our analysis on a four-dimensional model proposed by Waleffe (1997) which has also the advantage of including key physical ingredients of the subcritical transition in shear flows.

3.2 Waleffe's model

The model. The four-dimensional model of Waleffe (1997) is designed to mimic the subcritical instability of a Couette-like shear flow by a non-linear self-sustained process involving the amplitude of streamwise vortices v, of streamwise streaks u, of sinuous perturbations of the streaks w, and of the mean shear m induced by perturbations. The model can be recast in the form of system (1) with

$$\mathbf{u} = \left\{ \begin{array}{c} m \\ u \\ v \\ w \end{array} \right\}; \quad \mathcal{N}(\mathbf{u}) = \left\{ \begin{array}{c} \sigma_m\, w^2 - \sigma_u\, u\, v \\ -\sigma_w\, w^2 + \sigma_u\, m\, v \\ \sigma_v\, w^2 \\ (\sigma_w\, u - \sigma_m\, m - \sigma_v\, v)\, w \end{array} \right\}. \tag{6}$$

$$\mathcal{L}_R = \left[\begin{array}{cccc} -k_m^2/R & 0 & 0 & 0 \\ 0 & -k_u^2/R & \sigma_u & 0 \\ 0 & 0 & -k_v^2/R & 0 \\ 0 & 0 & 0 & -k_w^2/R - \sigma_m \end{array} \right]; \tag{7}$$

The same coefficients as those considered in Waleffe (1997) have been selected.[5] The linear operator becomes strongly non-normal when R is increased and the non-linear terms conserve energy.

Global bifurcations. The 'laminar basic flow' $m = u = v = w = 0$ is linearly stable for all R. For the parameters considered here, the phase space dynamics of the system has has already been investigated (Waleffe, 1997): the laminar basic flow is the only steady solution of the system up to $R = 104.84$ where a saddle node bifurcation takes place and two additional steady solutions appear. The 'lower branch' solution S is a saddle while the upper branch A is an unstable fixed point which become stable at $R_G = 138.06$ thus rendering the stability of the laminar basic flow only conditional for $R > R_G$.

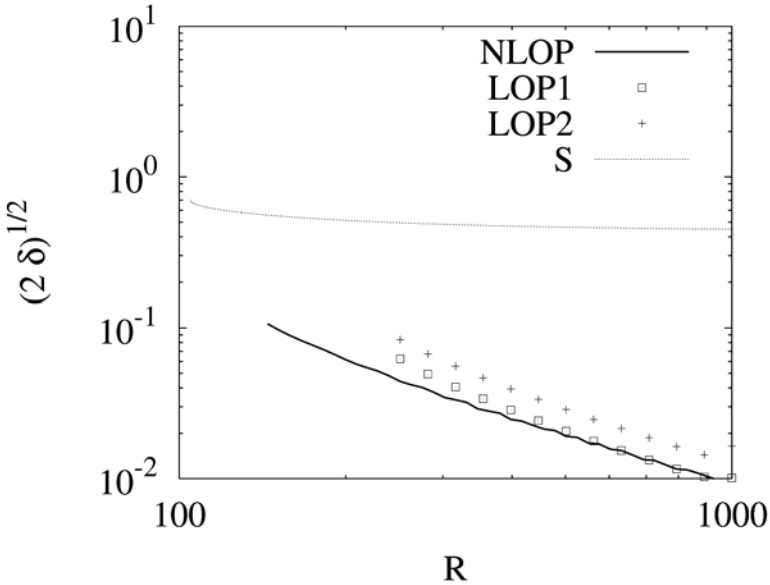

Figure 4. Dependence on the R of the (non-linear) minimum threshold amplitude $(2\,\delta(R))^{1/2}$ and of the critical amplitudes found using the other (LOP1, LOP2 and saddle point) strategies for system (7) with $\sigma_m = 0.31$.

The set $\mathcal{Z}_R$ and the computation of δ and of the NLOPs. The perturbation energy is defined through the standard inner product as $\mathcal{E} = (m^2 + u^2 + v^2 + w^2)/2$ and it is easily found that the vectors belonging to the set $\mathcal{Z}_R$ must satisfy $-(k_m^2 m_0^2 + k_u^2 u_0^2 + k_v^2 v_0^2)/R + \sigma_u u_0 v_0 - (\sigma_m + k_w^2/R) w_0^2 = 0$. Non-trivial solutions of the previous equation exist only when the monotonic stability is lost i.e. for $R \geq R_E = 2k_u k_v/\sigma_u = 4.89$ and $uv > 0$. To compute $\delta(R)$ only initial conditions in the $\mathcal{Z}_R$ set were considered by randomly selecting m_0, u_0 and w_0 and by then solving in v_0 the equation for $\mathcal{Z}_R$, which resulted in a second order equation. Real solutions for v_0 are found when the discriminant of the equation is non-negative, which strongly reduces the number of initial conditions to be investigated because in a large part of the phase space no solution belonging to $\mathcal{Z}_R$ exists. The minimum condition $(d^2\mathcal{E}/dt^2)_0 > 0$ was also checked, reducing the number of computations even more. Then, the same $\mathcal{E}_0$-marching procedure described above for the two-dimensional model, was used for the four-dimensional system. The minimum threshold energies and the corresponding non-linear optimals have then been computed for R ranging from $R_G = 138$ up to $R = 1000$, where an asymptotic regime seems to be attained. The results are reported in Figure 4 and in Table 1 and are compared to the linear optimals and to the saddle solution in the next paragraph.

Table 1. Asymptotic ($R > 500$) scaling of the non-linear optimal perturbations NLOP and of the critical LOP1 and LOP2-shaped perturbations for system (7). The variables whose amplitude is at almost constant noise level have been denoted by N.

Type	v	u	w	m	$(2\,\delta)^{1/2}$
NLOP	$15\,R^{-1.07}$	$89\,R^{-2.07}$	$0.00176\,e^{-0.026\,R}$	$35\,R^{-1.99}$	$15\,R^{-1.07}$
LOP1	$25\,R^{-1.14}$	$189\,R^{-2.18}$	N	N	$25\,R^{-1.14}$
LOP2	$1.9\,R^{-0.75}$	$8\,R^{-0.97}$	N	N	$11\,R^{-0.96}$

Comparison with other results. The linear optimal perturbations maximizing respectively the energy growth (LOP1) and the initial energy growth rate (LOP2) both systematically have $m_0 = w_0 = 0$. Like in the two-dimensional model previously considered, when R is sufficiently large, u_0/v_0 scales as R^{-1} for the linear optimal perturbations maximizing energy growth (LOP1) while it tends to a constant for the linear optimals maximizing energy growth rate (LOP2). The minimum threshold amplitude $\sqrt{2\delta(R)}$ and the critical amplitudes obtained using respectively the linear LOP1 and LOP2 optimals both with additional 10^{-9} noise as initial condition, are reported in Figure 4. The lower branch corresponding to the saddle node S amplitude is also shown for comparison. The initial LOP1-shaped perturbations have critical amplitudes converging to the non-linear minimum threshold for R sufficiently large, while the LOP2-shaped perturbations, even if leading to very low critical amplitudes, remain at finite distance from the minimum. The critical amplitudes all scale like $\sim R^{-1}$ but only for for $R > 500$. The saddle amplitude tends to a constant. This behaviour can be understood by examining the scalings observed for the critical perturbations for sufficiently large R ($R > 500$) that are reported in Table 1. The non-linear optimal is essentially made of a linear LOP1 perturbation (remark that the ratio u_0/v_0 is the same for the non-linear and for the linear LOP1 optimal) plus an algebraically small mean shear perturbation m_0 and an exponentially small w_0 that, at sufficiently large R, is of the same order of magnitude of the noise (10^{-9}) that is added to LOP1. The linear LOP2 initial condition is able to lead to so small critical amplitudes even if its shape is completely different from the NLOP shape.

The case $\sigma_m = 0$. The results for the considered systems could lead to the belief that the non-linear optimals (NLOP) always asymptotically approach the linear optimals maximizing transient growth (LOP1). A counter-example is found by setting $\sigma_m = 0$ in system (7), reverting to an older model of subcritical self-sustained process (Waleffe, 1995). The thresholds obtained using initial conditions with the shape of both types of linear optimals are now slightly larger than the minimum non-linear threshold and are reported in Figure 5.

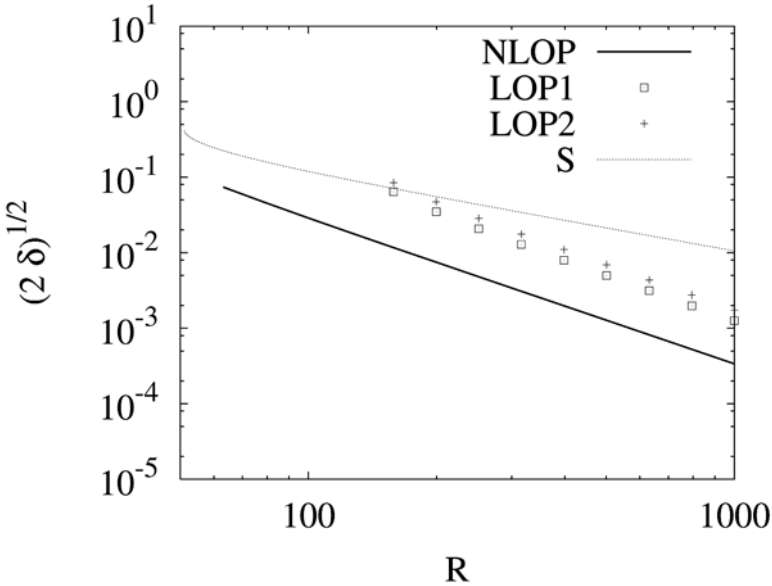

Figure 5. Same as in Figure 4 but in the case $\sigma_m = 0$.

Table 2. Asymptotic ($R > 500$) scaling of the non-linear optimal perturbations NLOP and of the critical LOP1- and LOP2-shaped perturbations for system (7) when $\sigma_m = 0$. The variables whose amplitude is at almost constant noise level have been denoted by N.

Type	v	u	w	m	$(2\,\delta)^{1/2}$
NLOP	$164\,R^{-1.9}$	$1337\,R^{-2.93}$	$115\,R^{-1.97}$	N	$194\,R^{-1.92}$
LOP1	$1309\,R^{-2.00}$	$7831\,R^{-3.00}$	N	N	$357\,R^{-1.81}$
LOP2	$1174\,R^{-1.99}$	$1200\,R^{-1.99}$	N	N	$1679\,R^{-1.99}$

This is explained by the fact that, in this case, the ratio w_0/v_0 of the non-linear optimal NLOP tends to a constant (see Table 2); even if the ratios u_0/v_0 are almost the same, the NLOP shape remains therefore asymptotically different from the shape of linear optimals for which $w_0/v_0 = 0$. Again, however, the non-linear optimal and the linear optimal strategies lead to the same asymptotic scaling of the critical amplitude $\sim R^{-2}$ for sufficiently large R, while the saddle S amplitude has very different scaling and shape.

4. SUMMARY AND CONCLUSIONS

The scope of this study was to compute the minimum energy threshold $\delta(R)$ and the associated non-linear optimal perturbations for low-dimensional systems of subcritical transition. The main results may be summarized as follows:

- A necessary condition for a perturbation to be non-linearly optimal, i.e., to be the one of minimum energy outside of the basin of attraction of the laminar basic flow, is that it realizes a local minimum for the perturbation energy i.e. $d\mathcal{E}/dt = 0$ and $d^2\mathcal{E}/dt^2 \geq 0$.

- For systems with energy preserving non-linear terms the first condition of optimality is equivalent to the condition $\langle \mathbf{u}, \mathcal{L}_R \mathbf{u} \rangle = 0$ which can be determined from the analysis of the linear operator $\mathcal{L}_R$ and does not depend on the amplitude of the perturbations.

- Linear optimal perturbations maximizing energy growth and steady non-trivial solutions such as saddles and nodes all necessarily belong to the set of perturbations satisfying the previous condition.

- Using these results it has been possible to demonstrate that in non-linear systems with two degrees of freedom and non-linear terms conserving energy, the non-linear optimal perturbations coincide in general with the linear optimal perturbations maximizing energy growth provided that the threshold energy is sufficiently small.

- This coincidence of linear and non-linear optimals is no longer necessary in systems with more than two degrees of freedom. However, the enforcement of the optimality condition allows one to reduce the extent of perturbations to be investigated for the determination of δ.

- The analysis of Waleffe's models, reveals that in general non-linear optimals do not have the same symmetries as the linear optimals. However, the projection of non-linear optimals in the subspace optimizing the linear growth has the same shape as the linear optimal. It is not clear if this result is general or peculiar to the considered systems.

- For the systems considered in this study, the minimum energy threshold asymptotically satisfy the R scalings predicted by dominant balance of non-normal growth and non-linear feedback (Trefethen et al., 1993; Baggett and Trefethen, 1997). The thresholds computed using both non-linear and linear optimal strategies are shown to reach the asymptotic scalings only for relatively large values of R.

The next extension of this study will probably be concerned with the analysis of the Navier–Stokes equations. In that case the necessary optimality condition still applies. If the perturbation energy is defined as $\mathcal{E} = \int_V (u_i' u_i'/2) dV$, where u_i denote the velocity components of the perturbations of a basic flow U_i and V is a control volume, then the necessary condition $\langle \mathbf{u}, \mathcal{L}_R \mathbf{u} \rangle = 0$ is

easily derived by making use of the Reynolds–Orr equation[6]

$$\int_V \left(-\frac{\partial U_i}{\partial x_j} u_i u_j - \frac{1}{R} \frac{\partial u_i}{\partial x_j} \frac{\partial u_i}{\partial x_j} \right) dV = 0. \tag{8}$$

Only perturbation satisfying the previous property are eligible to be non-linear optimals. The problem is that the number of perturbations to examine may be large. The previous condition should therefore be completed by an optimization algorithm and/or some supplementary condition. This is subject of current investigation.

ACKNOWLEDGEMENT

Stimulating discussions with Paul Manneville are kindly acknowledged.

NOTES

1. A non-trivial steady solution $\mathbf{u}_e$ must satisfy the equilibrium equation $\mathcal{L}_R\, \mathbf{u}_e + \mathcal{N}(\mathbf{u}_e) = 0$. By projecting this equation on $\mathbf{u}_e$ it follows that $\mathbf{u}_e \in \mathcal{Z}_{\mathcal{R}}$.

2. The linear optimal perturbations are the initial conditions for which the maximum transient growth of linear solutions $\mathbf{u}^{(L)}$ is reached: $G_{\max} = \max_t \max_{\mathbf{u}_0{}^{(L)}} \mathcal{E}[\mathbf{u}^{(L)}(t, \mathbf{u}_0{}^{(L)}, R)]/\mathcal{E}_0^{(L)}(\mathbf{u}_0{}^{(L)})$. The two maximizations (in time and over the initial condition) may be swapped and therefore one is reduced to a problem which is very similar to the non-linear one for the finding of δ, except that now we have to jointly maximize $\mathcal{E}^{(L)}$ and minimize $\mathcal{E}_0^{(L)}$ and the trajectories is phase space are given by the linear evolution operator. It is however clear that if $\mathbf{u}_0{}^{(L)}$ is not located at a local minimum of $\mathcal{E}^{(L)}$ along the trajectory then one could find another initial condition on the same trajectory with lowest $\mathcal{E}_0^{(L)}$ which therefore could realize a better growth. A necessary condition therefore for $\mathbf{u}_0{}^{(L)}$ to be a linear optimal is that at $t = 0$ $(d\mathcal{E}^{(L)}/dt)(0, \mathbf{u}_0{}^{(L)}, R) = 0$ and that if this condition is satisfied, furthermore $(d^2\mathcal{E}^{(L)}/dt^2)(0, \mathbf{u}_0{}^{(L)}, R) \geq 0$. As the evolution equation here is linear, the first condition can be recasted in the form $\langle \mathbf{u}_0{}^{(L)}, \mathcal{L}_R\, \mathbf{u}_0{}^{(L)} \rangle = 0$

3. The picture is essentially given by Figure 9 in the contribution by Manneville in these proceedings. In his notations, u is called X_1, v is X_2, the saddle point is denoted by M^+ and the stable node by M^-.

4. The non-linear optimal has to belong to the $\mathcal{Z}_R$ set which is formed of two lines. It therefore has essentially the choice between having the shape of the linear optimal maximizing energy growth (LOP1) or the shape of the linear optimal response. The linear optimal perturbation is distinguished from the optimal response by the sign of $d^2\mathcal{E}^{(L)}/dt^2$ which is positive for the optimal perturbation and negative for the optimal response. The non-linear optimal perturbation also has a positive $d^2\mathcal{E}/dt^2$ but now computed with the full non-linear equation. By deriving Equation (3) with respect to t and then eliminating $d\mathbf{u}/dt$ using Equation (1), it is possible to show that $d^2\mathcal{E}/dt^2 = d^2\mathcal{E}^{(L)}/dt^2 + O(\mathcal{E}^{1+\beta})$ where the order of the derivative computed with linear theory is proportional to $\mathcal{E}$ while the additional terms, due to the non-linear contributions, are of order $\mathcal{E}^{1+\beta}$ with $\beta > 0$ and therefore larger than $\mathcal{E}$. For sufficiently small $\mathcal{E}$ therefore the second derivative computed by including non-linear terms has the same sign as the second order derivative computed with the linear terms.

5. They correspond to a streamwise wavenumber $\alpha = 1.3$ and a spanwise wavenumber $\gamma = 2.28$ and are: $[k_m, k_u, k_v, k_w] = [1.57, 2.28, 2.77, 2.67]$, and $[\sigma_m, \sigma_u, \sigma_v, \sigma_w] = [0.31, 1.29, 0.22, 0.68]$.

6. Here one may want to assume *a priori* that the enstrophy of the non-linear optimals is finite so as to ensure, at finite R, the integrability of the dissipation term $\frac{1}{R}\frac{\partial u_i}{\partial x_j}\frac{\partial u_i}{\partial x_j}$ appearing in Equation (8).

REFERENCES

Baggett, J.S. and Trefethen, L.N. (1997). Low-dimensional models of subcritical transition to turbulence. *Phys. Fluids* **9**, 1043–1053.

Butler, K.M. and Farrell, B.F. (1992). Three-dimensional optimal perturbations in viscous shear flow. *Phys. Fluids A* **4**, 1637–1650.

Chapman, S.J. (2002). Subcritical transition in channel flows. *J. Fluid Mech.* **451**, 35–97.

Clever, R.M. and Busse, F.H. (1992). Three-dimensional convection in a horizontal fluid layer subjected to a constant shear. *J. Fluid Mech.* **234**, 511–527.

Dauchot, O. and Manneville, P. (1997). Local versus global concepts in hydrodynamic stability theory. *J. Phys. II France* **7**, 371–389.

Gustavsson, L.H. (1991). Energy growth of three-dimenisonal disturbances in plane Poiseuille flow. *J. Fluid Mech.* **224**, 241–260.

Henningson, D.S. and Kreiss, G. (2005). Threshold amplitudes in subcritical shear flows. In *Laminar Turbulent Transition and Finite Amplitude Solutions*, Proceedings of the IUTAM Symposium, Bristol, UK, 9–11 August 2004, T. Mullin and R.R. Kerswell (eds), Springer, Dordrecht, pp. 233–249 (*this volume*).

Hof, B., Juel, A. and Mullin, T. (2003). Scaling of the turbulence transition threshold in a pipe. *Phys. Rev. Lett.* **91**, 244502–1–4.

Joseph, D.D. (1976). *Stability of Fluid Motions*, Springer Tracts in Natural Philosophy, Vol. 27, Springer, New York.

Kreiss, G., Lundbladh, A. and Henningson, D.S. (1994). Bounds for threshold amplitudes in subcritical shear flows. *J. Fluid Mech.* **270**, 175–198.

Manneville, P. (2005). Modeling the direct transition to turbulence. In *Laminar Turbulent Transition and Finite Amplitude Solutions*, Proceedings of the IUTAM Symposium, Bristol, UK, 9–11 August 2004, T. Mullin and R.R. Kerswell (eds), Springer, Dordrecht, pp. 1–33 (*this volume*).

Nagata, M. (1990). Three-dimensional finite-amplitude solutions in plane Couette flow: Bifurcation from infinity. *J. Fluid Mech.* **217**, 519–527.

Reddy, S.C., Schmid, P.J., Baggett, J.S. and Henningson, D.S. (1998). On the stability of streamwise streaks and transition thresholds in plane channel flows. *J. Fluid Mech.* **365**, 269.

Schmid, P.J. and Henningson, D.S. (2001). *Stability and Transition in Shear Flows*, Springer, New York.

Trefethen, L.N., Trefethen, A.E., Reddy, S.C. and Driscoll, T.A. (1993). A new direction in hydrodynamic stability: Beyond eigenvalues. *Science* **261**, 578–584.

Waleffe, F. (1995). Transition in shear flows. Nonlinear normality versus non-normal linearity. *Phys. Fluids* **7**, 3060.

Waleffe, F. (1997). On a self-sustaining process in shear flows. *Phys. Fluids* **9**, 883–900.

A BYPASS SCENARIO OF LAMINAR-TURBULENT TRANSITION IN THE WIND-DRIVEN FREE-SURFACE BOUNDARY LAYER

Victor I. Shrira[1], Guillemette Caulliez[2] and Dmitry V. Ivonin[3]
[1]*Department of Mathematics, Keele University, Staffordshire ST5 5BG, UK*
[2]*IRPHE/IOA, 165 Av. de Luminy, Cedex 9, Marseille, France*
[3]*P.P. Shirshov Institute of Oceanology, Russian Academy of Sciences, Moscow, Russia*

Abstract The work is concerned with the theoretical and experimental study of laminar-turbulent transition in the wind induced boundary layer in water beneath the free surface. The mechanism of this transition has not been identified yet and the present work is aimed to fill this gap. The experiments in the wave tank showed that the first perturbations which emerge out of natural primordial noise are long compared to the boundary layer thickness, then they gradually grow, become more nonlinear until suddenly a strong localised instability occurs. This instability results in almost immediate breakdown of the laminar boundary layer and formation of localised 3D turbulent spots. The spots slowly expand downstream forming turbulent streaks having the shape of upstream pointed arrowheads marked by the wind generated capillary-gravity waves on the water surface. The streaks merge further downstream creating basin-wide turbulence zone. The notable feature of the observed transition is that there is no universal critical Reynolds number, although the results are reproducible for the same values of wind. The critical distance X_c where the turbulent spots first appear is found to be inversely proportional to the wind stress at the surface.

The theoretical study begins with the classical linear stability analysis carried out within the framework of Orr–Sommerfeld equation with the appropriate boundary conditions. In contrast to classical wall boundary layers, there are no linearly unstable modes. An analysis of weakly-nonlinear evolution of decaying perturbations under some unrestrictive assumptions suggests an unusual bypass scenario based on the explosive transverse instability of solitary waves as a plausible mechanism for the transition.

1. INTRODUCTION

Boundary layers ubiquitously induced by wind in natural basins play a key role in all exchange processes at the water-atmosphere interfaces. Despite their omnipresence and prime role in controlling cross-interface fluxes the present understanding of physical mechanisms of their formation is still quite poor. In

T. Mullin and R.R. Kerswell (eds), Laminar Turbulent Transition and Finite Amplitude Solutions, 267–288.
© 2005 *Springer. Printed in the Netherlands.*

particular, apart from the fact that the free-surface boundary layers commonly encountered in nature are as a rule turbulent, very little is known of their properties and, especially, of the mechanisms of their formation.

In the presence of a moderate wind, an initially laminar flow inevitably becomes turbulent. However neither the details of the processes, nor the physical mechanisms are known. The present work is aimed to fill this gap: the laminar-turbulent transition is investigated both theoretically and employing laboratory experiment. The problem is also of fundamental interest as an yet uncharted route to turbulence.

The laminar-turbulent transition in wind-driven flows was first identified by Okuda et al. (1976) and Kawai (1979) in experimental studies of a temporally developing boundary layer. The fundamental issue of separating the interfacial and boundary layer perturbations requires simultaneous study of both processes. It was shown by Caulliez et al. (1998) that, at least in spatially developing flow, it is the processes in the water which affect dynamics of the interfacial waves rather than the other way around. A detailed study of the evolution of the *temporally developing* boundary layer, its perturbations and wind waves focussed on Langmuir-type circulations in water was carried out by Melville et al. (1998) and Veron and Melville (2001). They attributed a considerable role in the transition to the surface wind-generated waves. However the question of the physical mechanisms of the transition remained open. Evolution of the spatially developing boundary layers in principle allows much better controlled experiments, and, although it is not a priory obvious whether the basic physics of the processes is the same, in the present paper we choose this route to attack the problem of laminar-turbulent transition in its laboratory part. We also address the role of the simultaneously unfolding interfacial wave instability. The early published work by Caulliez et al. (1998) was devoted primarily to the corresponding stages of evolution of wind-generated water waves. The experimental part of the present work is based on a related set of experiments, performed in the same facilities, and uses in part the same data; however, here we focussed on the processes in the water rather than its surface. The results by Caulliez et al. (1998) provide the present study with a remarkable observational tool: since the wind-induced ripples become visible after and due to flow transition it enables us to use these ripples as an ideal marker of spatial distribution of the transition.

Up to now, there has been no attempt to study this transition. The paper aims to fill this gap by studying the phenomenon both by means of a laboratory experiment and theoretically. The experimental part of the work describes the specifics of the bypass transition in the spatially developing free surface boundary layer observed in the wind wave tank; the theoretical part aims at providing a weakly nonlinear mathematical model of this particular transition.

2. EXPERIMENT

The observations were carried out in both the large (40 m long, 2.6 m wide and 1.0 m deep) and small ($8.0 \times 0.6 \times 0.2$ m^3) IRPHE-Luminy wind-wave facilities. Primarily the smaller facility was used since no discernible influence of the installation size on the observed phenomena has been found. The experimental setup is as follows: a steady wind ranging from 3 to 7 m/s generates a spatially developing steady boundary layer. No calibrated initial perturbation was introduced and what was studied was the development of the laminar-turbulent transition out of 'natural' noise. Therefore special measures were taken to minimise perturbations in the air and the water at the entrance of the tanks, in particular, the transition was made smooth by means of a weakly-inclined rough aluminium plate lengthened by a smooth floating plastic film. To minimise the effect of perturbations from the measuring devices the instruments were kept in the same fixed position relative to the tank during all experiments while all parameters were kept constant except for the length of the plastic strip which was changed from series to series as the most convenient and least intrusive way to vary the fetch. Hereinafter we will use the term 'fetch' which is common in studies of wind waves to refer to the distance to the end of plastic strip and, thus, to the tip of the boundary layer in the water. Spatio-temporal evolution of the boundary-layer perturbations resulting in laminar-turbulent transition was monitored in several different complementary ways which we briefly outline below. We focus our attention on the laminar-turbulent transition in the water boundary layer, while detailed measurements of the related processes and phenomena (surface waves, properties of turbulence in the air flow and in the water, etc.) are mentioned only to the extent necessary to provide the context for the phenomenon under consideration.

2.1 Observation techniques

2.1.1 Dye visualisation. Probably the most graphic way of getting an idea of the scenario of the laminar-turbulent transition is to employ a water flow visualisation. A dye trickle was carefully injected into the flow at a certain chosen depth within the boundary layer 30 cm upstream to the observation point. Evolution of such 'material lines' was monitored by the video-camera. A careful recording of the side view of evolution of a single dye line at different fetches and several initial depths was complemented by the plan view of evolution of two differently coloured 'material lines' separated initially 4 cm apart. Two types of dye were used: Rhodamin B in concentration 5 g per 30 cm^3 of water and a solution of latex particles diluted in proportion 1 ml of latex solution to 20 ml of water. Both solutions have densities and viscosities close to that of water.

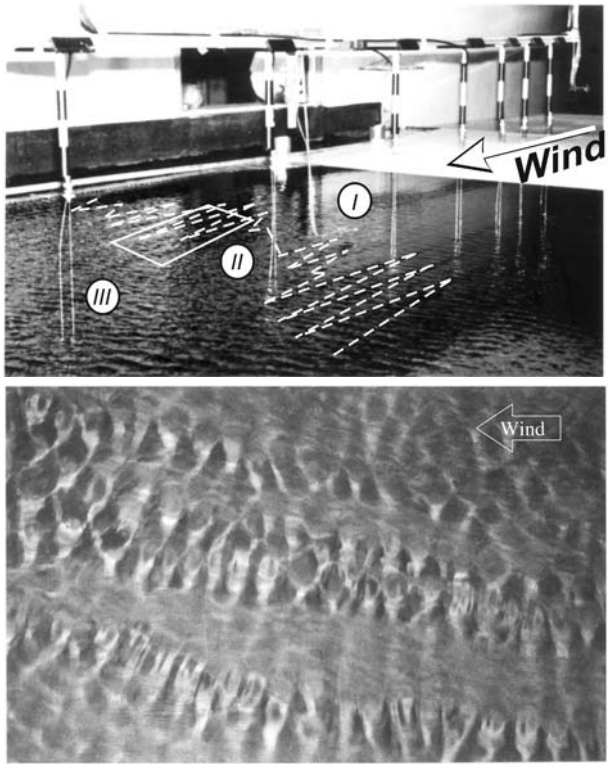

(a)

(b)

Figure 1. (a) The experimental setup. The turbulence is confined to the flow just beneath the longitudinal V-shaped streaks (in (a) their contours are emphasised). (b) The blowup of the streaks. The water surface is very smooth where the flow is still laminar. Turbulent areas are marked by the clearly visible capillary-gravity wind waves.

2.1.2 Laser Doppler Velocimeter. The local vertical structure of the drift current was explored by means of a two-component Laser Doppler Velocimeter (LDV) which provides point time records of the streamwise and vertical components of velocity taken simultaneously (Caulliez, 1987). To eliminate noise in the LDV signal, the frequencies above 60 Hz were filtered out. The continuous signal was then digitalised and recorded. The frequency range of LDV allows us to measure with desired accuracy both the mean flow, perturbations to the laminar flow and the turbulent fluctuations of the turbulent flow.

2.1.3 Visual observation. The naked eye observation of the water surface from above interpreted by exploiting the findings reported in Caulliez et al. (1998) prove to be remarkably informative. First, two very distinct types of the water surface are apparent. Just downstream of the air-water junction, the water surface looks very smooth. However, the careful measurements of

the water surface elevations reported in Caulliez et al. (1998) and partially repeated in the present study reveal the presence of tiny undulations (typical heights are $\sim 10^{-2}$ mm) hardly perceptible by naked eye. These undulations represent wind-generated capillary-gravity waves propagating primarily in the wind direction. These waves are found to be of no importance in the context of our study. Further downstream the first clearly visible wind waves suddenly appear. The striking feature of this appearance is that these waves occur only inside longitudinal V-shaped streaks with the tips pointed upstream (Figures 1a, b).

These streaks can appear or disappear, or move randomly crosswise. They mostly originate at a well-defined fetch. As it was shown by Caulliez et al. (1998) the tiny wind waves sharply increase their growth ('burst') and thus become visible as a result of the laminar-turbulent transition in the water boundary layer. These bursts occur where the surface velocity drops sharply, which happens where the laminar boundary layer breaks down and is replaced by a turbulent one. Hence the visible waves serve as perfect markers of the turbulent zones. This remarkable fact enables us to constantly monitor spatial distribution of turbulence and, in particular, to easily find the dependence on wind.

2.1.4 Supporting observations. **Airflow**. A set of the airflow parameters, including the mean flow vertical profile $U_{air}(z)$, fluctuations of streamwise and vertical velocity components $u_{air}(z)$, $v_{air}(z)$, the friction velocity $u^*_{air}(z)$ at different locations was monitored by hotwires and a Pitot tube in a standard manner. The temperature of the airflow was also controlled and kept constant during the experiments.

Surface velocity. The surface velocity was determined by filming small paper tracers by a video camera. The quantitative analysis of these tracers was confined to finding the *mean* surface current, while the potentially useful information on the statistics of the surface current fluctuations contained in these data requires a more sophisticated approach and remains to be analysed.

2.2 Observations

2.2.1 Qualitative picture. The water flow visualisation by means of differently coloured dye trickles recorded by video-camera provides a good qualitative picture of the transition. Samples of characteristic side views of flow evolution visualised by dye injected at depth 3 mm below the undisturbed water surface are shown in Figure 2. Although the time evolution was recorded by video-camera at a number of different fetches, here we provide just typical instantaneous shots taken at three characteristic fetches to illustrate the three different stages of flow evolution with fetch.

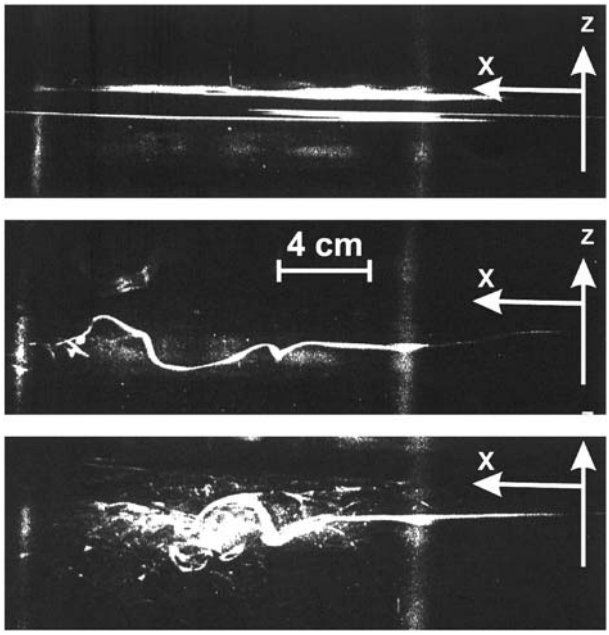

Figure 2. Side view of dyed streamline initially injected at depth $z = -3$ mm. Instantaneous flow visualisation at three different characteristic fetches X: (top) laminar zone; (middle and bottom) instantaneous shots of transition. The bottom box shows formation of a turbulent spot. The somewhat blurred image in the upper half-plane is due to light reflection from the free surface. The corruption of the upper image is due to the presence of wave perturbation on the water surface, the degree of corruption roughly corresponds to the intensity of the interfacial perturbations. Wind speed is kept constant (5 m/s).

First, in the initially laminar current, long wavy instabilities appear from time to time but they evolve to a very small extent before vanishing. The upper horizontal line is due to light reflection by the free surface. Then, further downstream there is a relatively long stage where the perturbations exhibit a consistent tendency to grow. The growth is slow and intermittent; its quantitative characteristics obtained by other means will be provided below. Noticeable variations in the thickness of the dyed streamline suggest that the variations in the streamwise velocity are strong compared to the vertical velocities manifested by small vertical displacements.

At a certain stage, the flow disturbances start to evolve quite rapidly, first developing instantaneous steep slopes, and then almost immediately overturning, creating a turbulent spot. Note that small-scale perturbations of the free surface become noticeable at the moment of breakdown of the laminar boundary layer. Further downstream the flow remains turbulent and the level of free surface perturbation does not seem to decrease, although certainly only rough

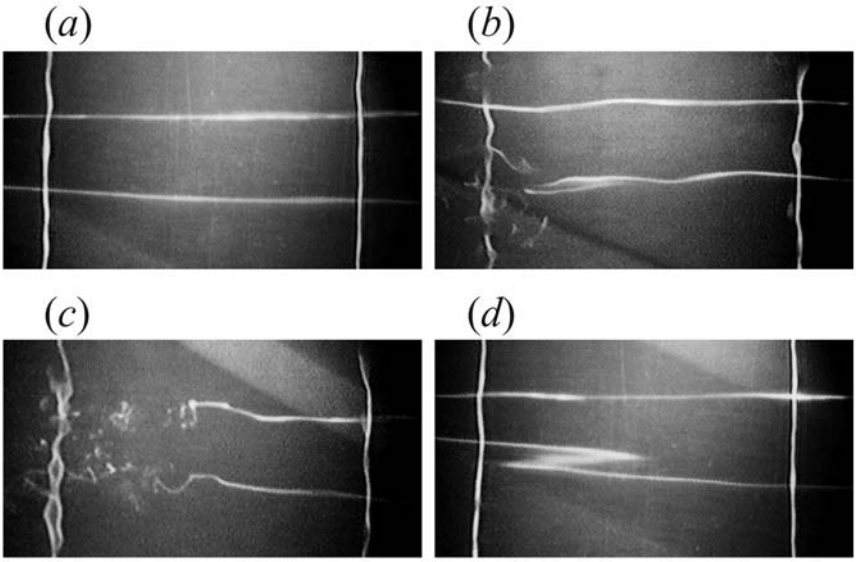

Figure 3. Plan view of instantaneous shots of flow evolution at different fetches for a fixed wind (The wind blows from the right to the left). The initial distance between the marked streamlines is 4 cm. Two vertical lines are drawn at the bottom of the tank and serve dual purpose: first, their distortion shows the intensity of the interface perturbations, second, they show the longitudinal scale (20 cm): (a) Laminar stage; (b, c) Growth of perturbations on the laminar stage, their breakdown and formation of turbulent spots; (d)Formation of short-lived Z-like patterns on the laminar stage.

qualitative judgements regarding the free surface can be made on the basis of the presented visualisation alone. The fetch at which the transition occurs for a particular wind speed varies widely, but the minimal fetch is well defined. Its dependence on wind will be summarised below. However, sometimes after the occurrence of streamline overturning the resulting turbulent spot disappears and the laminar flow is restored and then it again breaks down creating an intermittent pattern.

This picture of transition is complemented by analysis of plan view video records showing evolution of two differently coloured streamlines lying at the unperturbed depth 2 and 3 mms and separated by 4 cm laterally. A few characteristic samples for the same 5 m/s wind are presented in Figure 3. At small fetches we see practically no perturbations of the streamlines (Figure 3a). At a later stage variations of the trickle's width become noticeable along with small deviations from their initial positions (Figures 3b, c). This suggests smallness of the transverse velocities compared to the streamwise velocities. Note also the apparent lack of correlation in the motions of these streamlines separated by 4 cm, their transverse deviations and thickening and thinning of the two

lines do not occur simultaneously. Since the snapshots show that the transverse motions are weak, this suggests that the characteristic transverse scale of boundary layer perturbations does not exceed 4 cm, although for weaker winds this is not true. Further downstream there is a point where the laminar flow exhibits strong three-dimensional instability, and collapses almost immediately creating turbulent spots (Figures 3b, c), which, as a rule, persist further downstream. Often the collapse of the laminar flow affects only one of the streamlines suggesting that the transition is strongly transversely localised, the characteristic scale being smaller than 4 cm (Figure 3b). Note also the sharp increase of surface perturbations after laminar flow collapse, which is indicated by much stronger distortion of the image of the left vertical line compared to the upstream right line. The fetch at which the first non-vanishing turbulent spot appears is the same as that found from the analysis of the side view. Again, occasionally we can observe an intermittent cycle of the laminar flow breaking and regeneration resulting from slow transverse motion of the streaks. Compared to the side view observations there is another relatively rare event: formation of short-lived Z-like patterns as exemplified in (Figure 3d). We interpret such patterns as manifestations of transverse non-uniformity of the streamwise velocity (longitudinal streaks).

Observations of water surface. Based on the fact that the visible waves mark the areas of the flow where transition has already occurred, naked eye observations of water surface proved to be extremely helpful. A typical view of the surface illustrated in Figure 1 reveals a very important feature of the transition: it first occurs in strongly localised spots and hence has essentially 3D character. The V-shaped turbulent zones are relatively long-lived features. Their spacing is not particularly regular and shows a clear dependence on wind speed: it decreases with increase of of wind. The fetch at which the streaks originate, which we call the '*critical fetch*' also consistently decreases with increase of wind. In accordance with the dye visualisation observations the 'critical fetch' is $\sim$160 cm, 130 cm, 90 cm, 45 cm for the wind speeds, respectively, 3, 4, 5 and 6 m/s^{-1}.

Even by means of simple non-instrumental observations, we can immediately distinguish two qualitatively different states of the flow: the flow beneath the smooth surface which is laminar and the flow beneath the rough surface marked by visible gravity-capillary wind waves which is turbulent. Given the aforementioned pronounced spatial non-uniformity of the transition: at the same cross-section the flow might be laminar in one point, turbulent in another, and exhibit transition in a third one, it makes sense to speak of *transition zone* in a broader sense: from the appearance of the tips of the first V-streaks to homogeneous turbulent flow. In the transition zone thus defined, at any given point the flow might be either laminar, turbulent or in the stage of transition.

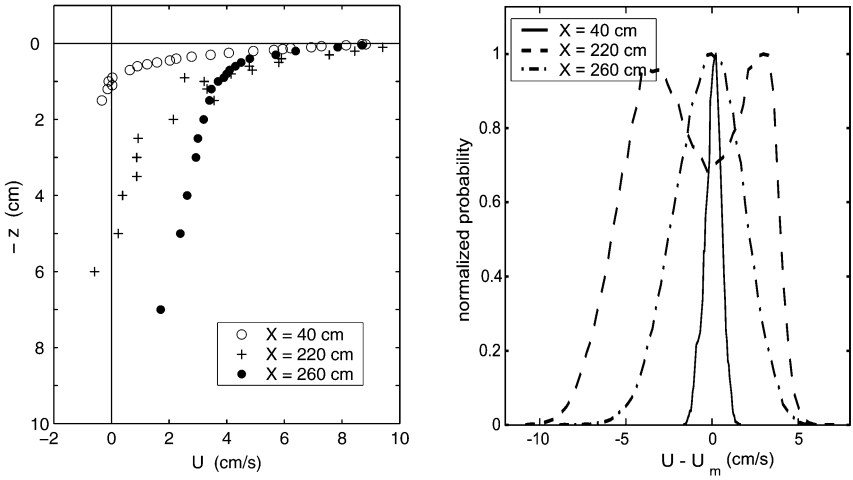

Figure 4. Main stages of development of mean flow profile for the wind speed 4 m/s. (a) Characteristic samples of vertical profile at three fetches; (b) Normalised probability distribution of instantaneous streamwise velocity at 3 mm depth.

We confine the use of the term *laminar zone* to the part of the laminar flow from the junction to the first tips of the V-streaks, and correspondingly reserve the use of the term *turbulent zone* to the part of the flow with transversely homogeneous turbulent flow where all streaks have already merged. In Figure 1a these zones are indicated by encircled Roman numbers 'I', 'II', 'III', respectively.

The overall qualitative picture provided by visual observations is complemented by various quantitative measurements discussed below.

2.2.2 The mean flow. The first task undertaken was to establish the behaviour of the *mean* flow vertical profile and its dependence on parameters. The main stages of development of mean flow profile for a fixed wind are illustrated by Figure 4. At the laminar stage, the surface velocity grows while the boundary layer thickness increases; after occurrence of the first turbulent spots the surface velocity sharply drops and the effective thickness increases. The stage of coexistence of turbulent and laminar patches is better seen in bimodal distributions of instantaneous streamwise velocity at 3 *mm* depth shown in Figure 4b. As expected, the smaller and broader peak corresponds to the already turbulent flow, while the higher and more narrow peak corresponds to the still laminar portion of the flow.

In self-similar variables introduced by Dupont and Caulliez (1993) all experimental points of vertical profiles measured at different fetches and at different winds corresponding to the laminar stage nicely collapse onto a single

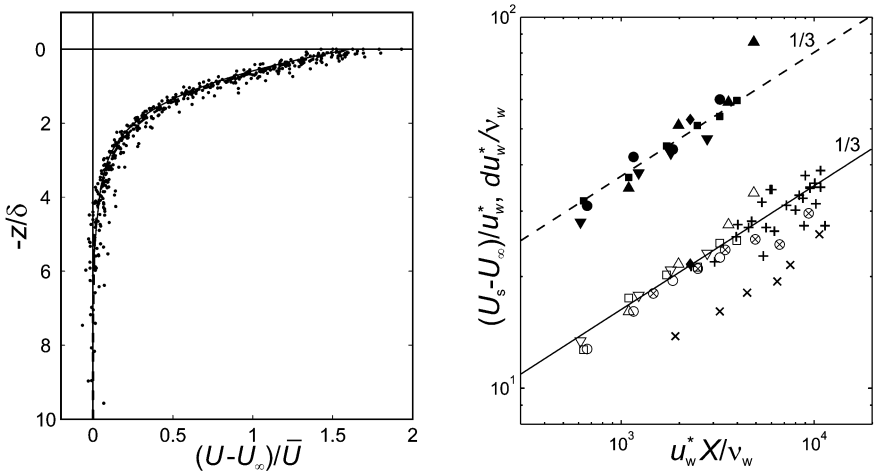

Figure 5. (a) Experimental laminar flow profile in self-similar variables. The measurements were taken at different fetches and wind speeds 3, 4, 5 and 6 m/s. (b) Evolution with fetch of the mean surface velocity U_s and the the boundary layer thickness d for the wind speeds 3, 4, 5 and 6 m/s. The thickness d is defined as the depth where the boundary layer velocity vanishes, $d \simeq 3.5\delta$.

curve (see Figure 5). This curve is compared to the solution of the Falkner–Skan equations for mean flow streamwise velocity U corresponding to the case when a constant tangential stress is applied to the upper surface of water occupying the quadrant $X > 0$, $z < 0$ (Dupont and Caulliez, 1993). The solution belongs to the family of the Falkner–Skan profiles (as well as the Blasius solution) and has the form

$$U = \overline{U} f'(z/\delta), \qquad (\overline{U} = u_w^* \mathrm{Re}_X^{1/3})$$

where $\overline{U}$ is the velocity self-similar scale, X is fetch, u_w^* is the friction velocity in water, $\delta = (\nu_w/u_w^*)\mathrm{Re}_X^{1/3}$ is a self-similar scale which can be roughly interpreted as a characteristic boundary layer thickness, ν_w is water viscosity, $\mathrm{Re}_X = u_* X/\nu_w$ is the fetch based Reynolds number. Function $f(\zeta)$ obeys the following nonlinear equation

$$-3f''' + 2ff'' - (f')^2 = 0 \tag{1}$$

and boundary conditions

$$f(\zeta = 0) = 0, \qquad f''(\zeta = 0) = 1, \qquad f'(\zeta \to -\infty) \to 0 \tag{2}$$

It was also checked that at the laminar stage the flow dependence on parameters behaves in accordance with the theoretical predictions: at fixed wind, the flow at the surface U_s accelerates with fetch X as $X^{1/3}$, while the thickness d of the boundary layer grows as $X^{1/3}$ (Figure 5b).

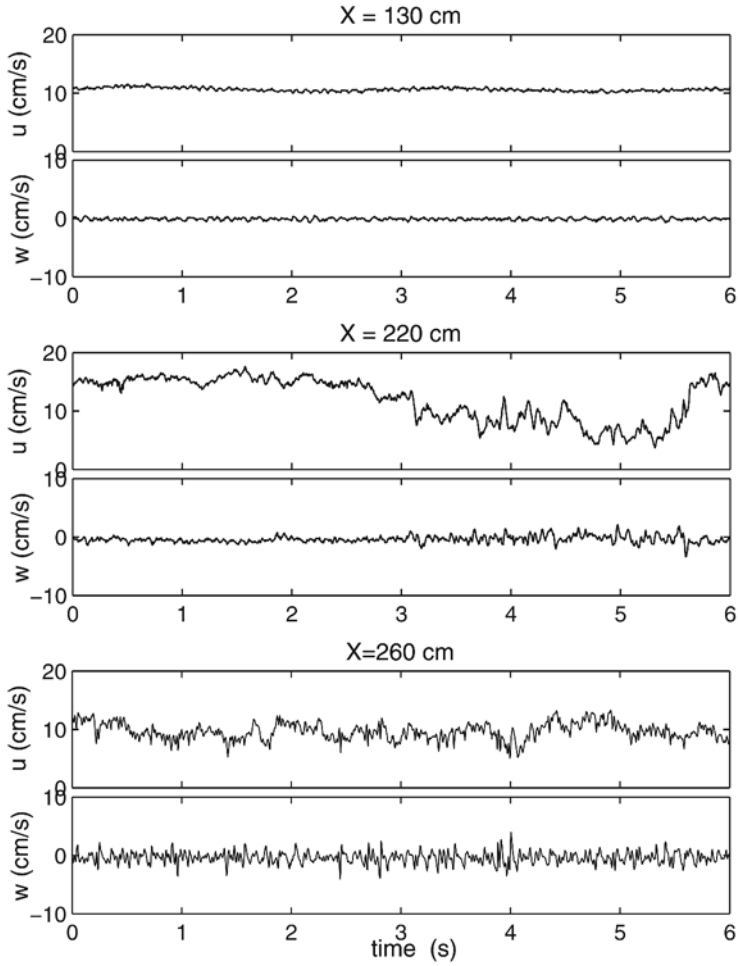

Figure 6. Samples of time records of streamwise $u(t)$ and vertical $w(t)$ velocities taken at depth 0.5 mm in (a) laminar, (b) transition and (c) turbulent zones, respectively. Wind speed is 4 m/s.

2.2.3 Evolution of perturbations. The LDV measurements show dramatic difference in behaviour of velocity perturbations in the three qualitatively different flow zones (laminar, transition, developed turbulence ones). Samples of typical records of velocity fluctuations are shown in Figure 6. The records of streamwise and vertical velocities are synchronous.

These raw samples suggest that the dynamical processes which cause the transition are of relatively low frequency. Note that the fluctuations of the streamwise velocity are much greater than the vertical ones. Figure 7 shows longer sample series of the streamwise velocity taken at the same values of

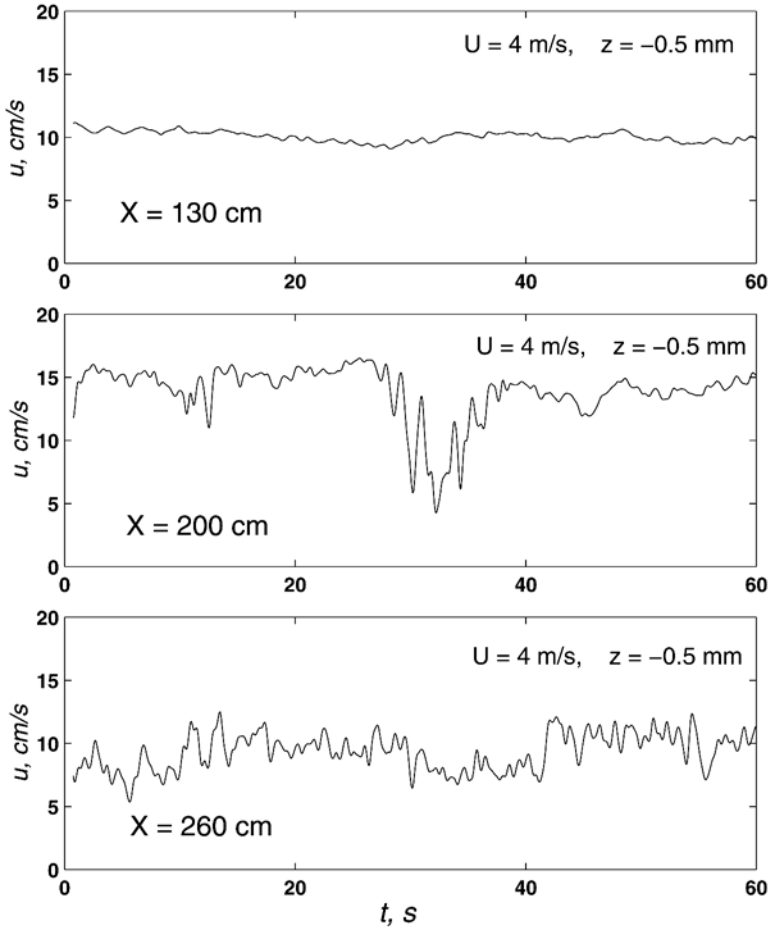

Figure 7. Samples of 80s records of the streamwise velocity u (1.3 s averaged) at depth 0.5 mm in the the laminar (top), transition and turbulent (bottom) zones, respectively. Wind speed is 4 m/s.

fetch as in Figure 6 with high-frequencies filtered out by applying averaging over 1.3 sec moving window. These records enable us to make some quantitative estimates of the typical perturbation parameters in different zones and arrive at important qualitative conclusions. In particular, we can see that at the laminar stage the dominant perturbations have finite amplitudes $\sim$ 1 cm/s. Without further processing of the signal it is very difficult to estimate the periods of dominant perturbations. However it is safe to say that the periods exceed $\sim$ 2 s, which corresponds to wavelengths $\sim$ 20 cm. (We use here the term '*amplitude*' as a half of maximal velocity variation, thus, the typical variations of flow velocity are about 20% of the mean surface velocity.) The perturbation

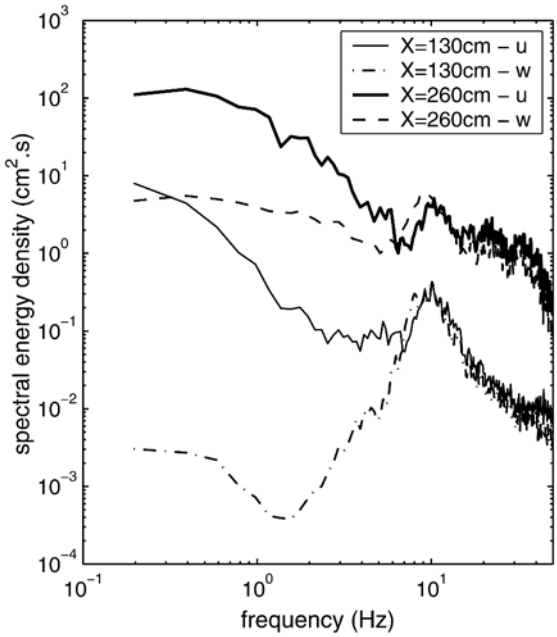

Figure 8. Typical spectra of streamwise and vertical velocity components for laminar and turbulent turbulent zones, respectively. Wind speed is 4 m/s.

amplitudes significantly increase prior to transition, reaching $\sim$ 5 cm/s, which corresponds to about 50% variations of the streamwise velocity.

In the turbulent zone, the level of velocity fluctuations becomes noticeably smaller in absolute terms. At the same time the *relative* level remains approximately the same as in the transition zone, because of the overall drop in the flow velocity.

These subjective rough estimates of the dominant scales and the principal conclusion about their essentially low-frequency and long-wave nature are supported by spectral analysis of the series presented in Figure 8. Indeed, most of the energy of streamwise fluctuations is concentrated in the low frequencies, and, since the energy of streamwise fluctuations far exceeds the energy of vertical ones, we can say that the most of the total energy is accumulated there. The tendency towards dominance of the streamwise (vs vertical) motions is more pronounced for the laminar motions.

The few samples of velocity measurements taken at fixed depth close to the free surface discussed above, on the basis of which the important preliminary conclusions were made, are in fact, representative. Unfiltered records taken in the laminar zone close to the critical transition fetch show that the low-

frequency perturbations penetrate the whole boundary layer, while the mean flow velocity and the high-frequency fluctuations related to wave motion noticeably decrease with depth.

2.3 Summary of the experimental evidence

We distinguish three main consecutive stages of the flow evolution from a practically undisturbed state to the fully turbulent one:

(i) Laminar flow: First, the basic flow is well described by the Falkner–Skan-type profile while the small perturbations are hardly visible to the unaided eye, then finite amplitude ondulations which are long compared to the boundary-layer thickness emerge and grow with fetch. These motions are *essentially longitudinal*: the perturbation streamwise component of velocity far exceeds both the spanwise and vertical velocities.

(ii) The flow is still laminar. The perturbations grow, show signs of nonlinear steepening and then suddenly collapse creating turbulent spots. The collapse is strongly laterally localised. *There is no critical Reynolds number* (no matter what definition of the Reynolds number is used). At the same time, the critical fetch X^* at which the turbulent spot first emerges, depends on the friction velocity u_* in a quite specific way:

$$X^* {u_*}^2 = \text{const.}$$

where $u_* = (\tau/\rho_a)^{1/2}$ and τ is the wind stress at the water surface, ρ_a is the air density, suggesting that in this context the work done by the wind stress might be a more important quantity than the Reynolds number.

(iii) Turbulent spots emerge at the point of collapse and slowly expand laterally, creating on the surface the V-shaped streaks pointed upstream. The flow between the streaks remains laminar. Further downstream the streaks coalesce and the flow becomes uniformly turbulent.

The experiments clearly show that there is not much noise produced at the air/water-flow junction and the unstable surface mode plays no role in the transition. Thus, the question of the physical mechanisms of the perturbation growth and their eventual collapse is open and represents the prime motivation of the theoretical study briefly outlined below.

3. MATHEMATICAL MODEL

We start with the Navier–Stokes equations (3) in the standard notation

$$\overline{\mathbf{u}}_t + (\overline{\mathbf{u}}\overline{\nabla})\overline{\mathbf{u}} = -\rho^{-1}\overline{\nabla} p + \nu^{a,w}\Delta\overline{\mathbf{u}}, \qquad \overline{\mathbf{u}} = (u, v, w) \tag{3}$$

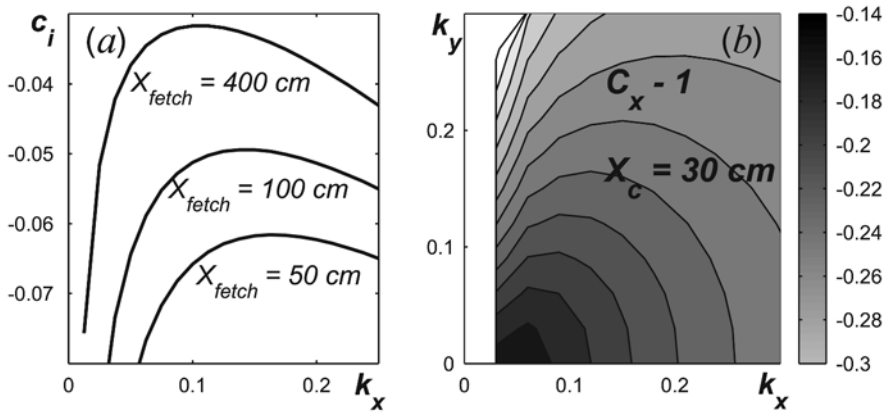

Figure 9. Analysis of linear stability: (a) Dimensionless decay rate c_i vs wavenumber $k_x h$ at fetch $X = 50, 100, 400$ cm. (b) Contour plot of phase velocity $c_x - 1$ at fetch $X = 30$ cm (note $\omega = c_x k_x$).

and the boundary conditions on the air-water interface of continuity of the normal and tangential stresses and the kinematic condition. Here, the superscripts a and w indicate the quantities for the air and water respectively. We look for solutions in water assuming the wind to be given and representing the motion as a steady shear basic flow and a perturbation of small but finite amplitude

$$\begin{aligned} \overline{\mathbf{u}} &= (U(x,y,z), V(x,y,z), W(x,y,z)) + \\ &\quad + \epsilon(u(x,y,z,t), v(x,y,z,t), w(x,z,t)), \end{aligned} \tag{4}$$

where ϵ is a small parameter characterising nonlinearity.

We focus our attention on the case of steady spatially accelerating basic flow induced by a constant tangential stress applied to the surface of water occupying the quadrant ($x > 0, z < 0$). Then, as we mentioned in the previous section the basic laminar flow is well described by the self-similar Falkner–Skan profile f given by (1, 2).

3.1 Analysis of linear stability

Following the classical route we first carry out a local analysis of the problem, i.e. we totally neglect the basic flow acceleration and assume $U = U(z)$, then we linearise the equations and boundary conditions and look for the solutions harmonic in x, y, t: $\mathbf{u}, p, \eta \sim e^{i(k_x x + k_y y - k_x ct)}$. The first neglected terms are $O(s, r^{-1})$: $s = \rho^a/\rho^w$, $\quad r = \nu^a/\nu^w$, $\quad (s \approx 10^{-3},\ r^{-1} \approx 10^{-2})$. Furthermore, we set the air density to be zero. Applying the Squire transformation and introducing streamfunction ψ for perturbations: $u = \partial\psi/\partial z$, $w = -\partial\psi/\partial x$, $\quad \psi = \phi(z)e^{ik(x-ct)}$, $k = (k_x^2 + k_y^2)^{1/2}$ we arrive at the Orr–

Sommerfeld equation

$$(U - c)(D^2 - k^2)\phi - U''\phi = (ikRe)^{-1}(D^2 - k^2)^2\phi \tag{5}$$

with some cumbersome boundary conditions. Although the boundary-value problem has been solved for the exact linearised boundary conditions, it was shown that due to the smallness of the Froude number ($Fr = U_s^2/g\delta$) in nature, the use of the simplified boundary conditions corresponding to $Fr = 0$

$$\phi = (U - c)\phi'' = 0 \tag{6}$$

is totally justified. The earlier analysis of this boundary-value problem (with full linearised boundary conditions) by Kawai (1979) was focussed on the unstable surface mode which has a much smaller spatial scale and, as our experiments suggest, is of no relevance to the flow instability under consideration.

We characterise the perturbations by real wavevector $\mathbf{k} = \{k_x, k_y\}$ and complex frequency $\omega(\mathbf{k})$ as well as by the complex phase velocity $\mathbf{c} = \{c_x, c_y\}$, where c_x is defined as ω/k_x.

The results of the linear stability analysis can be summarised as follows:

(i) *There are no linearly unstable modes.* This is also true for the non-stationary spatially uniform boundary layers which develop from rest when a constant tangential stress is suddenly applied to the water surface.

(ii) There are very weakly decaying Orr–Sommerfeld modes (see Figure 9). Their viscous decay is almost negligible for moderately small k, while the real part of the dispersion relation in the range of small k is very close to the asymptotics obtained in the limit of infinite Reynolds numbers (Shrira, 1989; Shrira and Sazonov, 2001)

$$\begin{aligned} \omega &= U_0(1 - h|\mathbf{k}|)k_x, \quad (U_0 \equiv U_s \equiv U(0)) \\ \mathbf{k} &= \{k_x, k_y\}, \qquad h = U_0/U_0'. \end{aligned} \tag{7}$$

3.2 Nonlinear evolution

Consider now evolution of a small but finite perturbation taking into account acceleration of the basic flow. In recent years in theoretical studies of flows characterised by the absence of unstable modes the paradigm of the '*non-modal transient growth*' has become dominant (e.g. Schmid and Henningson, 2001). Within the framework of this approach it is most common to focus attention on the 'optimal' perturbations, i.e. those which will attain maximal amplitude (in the linear setting) at some moment in time. Such motions are usually characterised by zero or nearly zero longitudinal wave numbers and

with time they give rise to streaky patterns in the laminar flow. The typical bypass scenario of transition in this approach is as follows: first the streaks evolve due to non-modal growth of the optimal perturbations, then the secondary instabilities of streaks cause the breakdown of the laminar flow and transition. However, the above scenario is based upon an implicit assumption that the nonlinearity turns on when the optimal perturbations attain (or approach) their maxima. In fact, there always exist oblique 'non-optimal' perturbations which could also exhibit noticeable growth (again, in the linear setting) and often grow much faster than the optimal ones. Such perturbations begin to decay earlier than the optimal ones and do not attain comparable amplitudes. This leaves room for other scenarios of transition, based upon '*bypass of bypass*': faster growing oblique perturbations which begin to decay earlier than the optimal ones and do not attain comparable amplitudes, nevertheless could become nonlinear well before the optimal streaky patterns get a chance to develop. Below we consider an alternative scenario based upon a very different approach, where these oblique perturbations might play an important role.

First we outline the main assumptions of our approach emphasising the points which remain to be worked through yet. Since there are no unstable Orr–Sommerfeld modes we *assume* that the least decaying modes play the dominant role in the field evolution or more precisely, that the evolution of the *generic* perturbation fields can be well described in terms of these mode dynamics. Furthermore, we assume that these modes are the finite Reynolds number continuations of the inviscid quasi-modes studied in Shrira (1989) and Shrira and Sazonov (2001). To support the latter assumption we have got some, but so far in no way exhaustive, numerical evidence. Regarding the conjecture on their dominant role in the field evolution we have the following arguments. First, note that in the context of 2D inviscid perturbations it has been rigorously proved that in the linear setting these modes are indeed absolute large-time asymptotics of generic initial perturbations (Sazonov and Shrira, 2003). To what extent this is true for 3D perturbations at large but finite Reynolds numbers is not clear, it is certainly not true for the streak-type motions. The second argument is that at least the asymptotic analysis we carried out below which is based upon this assumption did not result in any inconsistency.

Thus, we focus our attention on asymptotic description of the evolution of finite amplitude perturbations under the above assumptions. The main factors of their dynamics are *dispersion, nonlinearity and non-uniformity* (due to the accelerating character of the basic flow). The problem has natural small parameters. The dominant perturbations are quite long compared to the boundary layer thickness, which ensures *weakness of dispersion*:

$$\varepsilon_D = kh \approx 0.1.$$

Note that although we lack quantitative measurements of transverse motions it seems safe to assume that the streamwise scale far exceeds the spanwise scale: $k_x \ll k_y$ (see Figure 3), but in our derivation we do not exploit any small parameter based upon this disparity of scales.

Almost up to the point of 'breaking', the perturbations remain *weakly nonlinear*:

$$\varepsilon_N = u/U_0 \approx 0.1 - 0.2.$$

The flow *weak inhomogeneity* is characterised by the parameter

$$\varepsilon_{inh} = \partial_x U_0 / U_0 k_x \approx 0.1.$$

We assume the balance

$$\varepsilon_N \approx \varepsilon_D \approx \varepsilon_{inh} \approx \varepsilon$$

to hold, which ensures the distinguished limit.

We can describe evolution of generic perturbations by applying an asymptotic multiple-scale procedure similar to that of Shrira (1989) and Voronovich et al. (1998)

$$\{u, v, W, p\} = \sum_{n=0}^{\infty} \epsilon^n \{u_n, v_n, w_n, p_n\}.$$

We emphasise the presence of two vertical scales (z and Z): The fast independent vertical variable z varies at the scale of the boundary layer thickness, the slow vertical scale is of the order of longitudional wavelength and, thus, is ε^{-1} times larger. It is easy to find that separation of vertical and horizontal coordinates occurs only to leading order and only for the 'fast' vertical dependence:

$$D_t \partial_{zz}^2 w - U'' \partial_x w = \epsilon RHS; \quad D_t = (U - c)\partial_x + \epsilon \partial_\tau$$

To leading order the streamwise and vertical velocities are expressed in terms of amplitude $A(x, y, t)$ as follows

$$u(x, y, z, t) = -U'(z)(f * A(x, y, t))$$

where $*$ denotes convolution

$$(\varphi * \psi) = \int_{-\infty}^{+\infty} \int_{-\infty}^{+\infty} \varphi(\tilde{x}, \tilde{y}) \psi(x - \tilde{x}, y - \tilde{y}) \, \mathrm{d}\tilde{x} \, \mathrm{d}\tilde{y}.$$

$U'(z)$ provides the dependence on 'fast' z, while $f = f(x, y, Z)$ gives the dependence on slow scale $z = Z$ and is specified by the corresponding reduction of the Orr–Sommerfeld-type boundary value problem.

To leading order the streamwise and vertical velocities are expressed in terms of amplitude $A(x, y, t)$ as follows

$$u(x, y, z, t) = -A(x, y, t) U'(z), \exp(-|\mathbf{k}||z|)$$

$$w(x, y, z, t) = A(x, y, t)(U(z) - U_0) \exp(-|\mathbf{k}||z|)$$

Both the spanwise and vertical components $v, w \ll u$, even if $k_y \gg k_x$.

Finally, the asymptotic procedure leads to the following nonlinear evolution equation

$$\begin{gathered} A_t + U_0 A_x - r A A_x - s\hat{\mathsf{G}}[A_x] + \gamma A = 0 \\ r = U'|_{z=0} \quad s = U^2/U'|_{z=0} \quad \gamma = \partial_x U|_{z=0} + \gamma_0, \quad \gamma_0 = c_i k_x. \end{gathered} \tag{8}$$

The dispersion operator $\hat{\mathsf{G}}$ has the integral form

$$\hat{\mathsf{G}}[\varphi(\mathbf{r})] = \frac{1}{4\pi^2} \int_{-\infty}^{+\infty} \int_{-\infty}^{+\infty} |\mathbf{k}| \varphi(\mathbf{r}_1) \exp(\mathrm{i}\mathbf{k}(\mathbf{r} - \mathbf{r}_1))\, \mathrm{d}\mathbf{k}\, \mathrm{d}\mathbf{r}_1 \tag{9}$$

In the case $k_y \gg k_x$ it reduces to the Hilbert transform $\hat{\mathsf{H}}[\varphi]$ with respect to the spanwise coordinate y:

$$\hat{\mathsf{G}}[\varphi(\mathbf{r})] = \hat{\mathsf{H}}[\varphi(\mathbf{r})] = \frac{1}{\pi} \int_{-\infty}^{+\infty} \frac{\varphi(\mathsf{x}, \mathsf{y}_1, \mathsf{t})}{\mathsf{y}_1 - \mathsf{y}} \mathrm{d}\mathsf{y}_1.$$

The derivation also imposes certain conditions on the Reynolds number:

$$Re^{-1/2} \ll \varepsilon \ll Re^{-1/4}.$$

The condition ensures that, on the one hand, viscosity is strong enough and the critical layer dynamics is viscous rather than nonlinear, but that, on the other hand, the viscosity is small enough not to affect the dynamics to leading order, so that γ_0 in (8) can be neglected. The latter condition could be relaxed down to $Re^{-1/2} \sim \varepsilon$ (Voronovich et al., 1998). In the experiment $Re = U\delta/\nu_w$ is in the range $\sim 10^2$–10^3.

The evolution equation (8) with $\gamma = 0$ was first derived in Shrira (1989) and is well studied. In particular, it was found that the solitary-type solutions tend to blow up in finite time due to transverse focussing (D'yachenko and Kuznetsov, 1994; Pelinovsky and Shrira, 1995). However, since the collapse occurring in this equation is what we call 'critical collapse', the outcome of evolution of arbitrary initial perturbations in the conditions of our experiment, i.e. in the presence of the flow acceleration and viscous decay opposing the perturbation growth, could not have been predicted *a priori*. We simulated the evolution equation (8) numerically for a wide class of initial conditions. The perturbations of amplitudes exceeding a certain moderate threshold after a possible initial decay indeed exhibit transverse focussing and growth, invariably ending in finite time blowup. Then, obviously, the weakly nonlinear evolution equation soon ceases to be applicable and we can speak about the blowup only as a tendency.

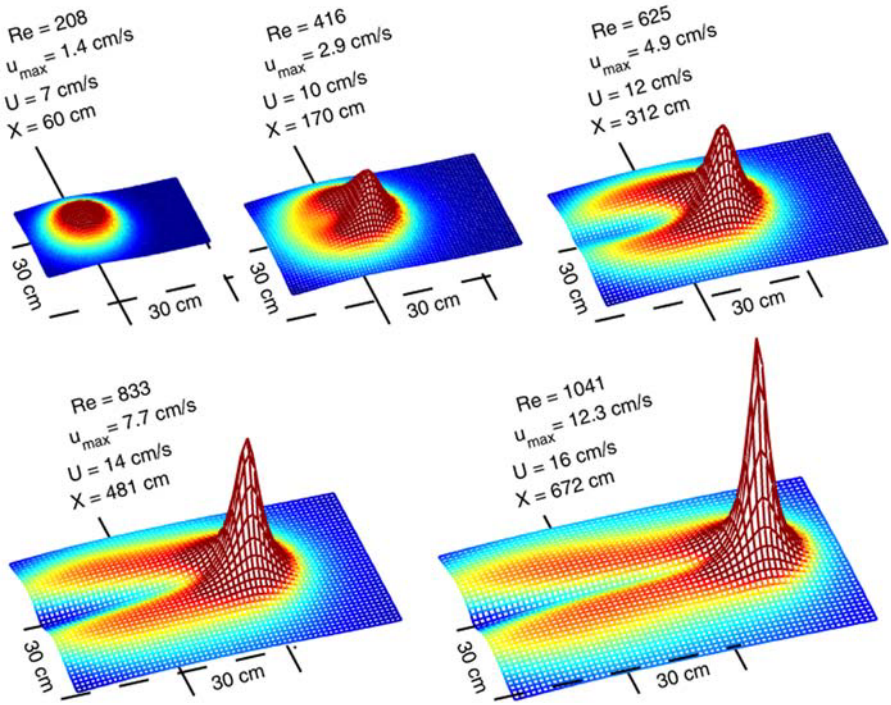

Figure 10. A sample of numerical simulation of evolution equation (8) for a Gaussian finite-amplitude initial disturbance: $u = 0.2 \cdot U_0 \cdot e^{-[(k\cdot(x-60))^2+(k\cdot y)^2]}$ with $k = 2\pi/150\ \mathrm{cm}^{-1}$ put into flow at fetch $X = 60$ cm characterised by mean surface velocity $U_0 = U = 7$ cm/s and $Re = 208$.

4. CONCLUDING REMARKS

We showed that the laminar-turbulent transition in the wind driven shear flows is essentially distinct from the classic scenario and this is where the certainty ends. There is an intriguing similarity with bypass scenarios found in a completely different context (see e.g. Wu et al., 1999) which remain to be explored.

We also suggested a plausible theoretical model of the transition which seems to explain qualitatively the main features we observed in the experiment (the effectively 1-D dynamics of the perturbations, their 'instability' and strongly localised blow-up), although we are unable to explain the crucial quantitative experimental finding: the inverse proportionality of the critical fetch to the wind stress. In contrast to most of studies on classical transition in our case both the basic flow itself and the characteristics of the initial perturbations in water are determined by the wind stress. Then, there is also an open question regarding the mechanism enabling the perturbations to attain the level exceeding certain moderate amplitude threshold, which is required for the con-

sidered mechanism of blowup to pick up. The most likely candidate for this role seems to be the transient growth of small amplitude oblique perturbations, although we do not exclude that other mechanisms might also play a role.

The essential assumptions we listed in Section 3.2 also require considerable effort to be verified.

A further advance in clarifying the mechanism of this challenging transition problem is certainly needed. At present, a DNS study seems to be the most promising way to advance our understanding.

ACKNOWLEDGEMENTS

The authors are grateful to the anonymous referee for helpful comments. The work was supported by INTAS 97-575 and 01-234.

REFERENCES

Caulliez, G. (1987). Measuring the wind-induced water surface flow by laser Doppler velocimetry. *Exp. in Fluids* **5**, 145–153.

Caulliez, G., Ricci, N. and Dupont, R. (1998). The generation of the first visible wind waves. *Phys. Fluids* **10**(4), 757–759.

Dupont, R. and Caulliez, G. (1993). Caractérisation de la couche limite laminaire générée par le vent sous une interface air-eau. In *Actes du 11é Congrès Français de Mécanique*, Vol. 3, pp. 257–260.

D'yachenko, A.E. and Kuznetsov, E.A. (1994). Instability and self-focusing of solitons in the boundary layer. *JETP Lett.* **59**(2), 108–113.

Kawai, S. (1979). Generation of initial wavelets by instability of a coupled shear flow and their evolution to wind waves. *J. Fluid Mech.* **93**(4), 661–703.

Melville, W.K., Shear, R. and Veron, F. (1998). Laboratory measurements of the generation and evolution of Langmuir circulations. *J. Fluid Mech.* **364**, 31–58.

Okuda, K., Kawai, M.S., Tokuda, M. and Toba Y. (1976). Detailed observation of the wind exerted surface flow by use of flow vizualization methods. *J. Oceanogr. Soc. Japan* **32**, 53–64.

Pelinovsky, D.E. and Shrira, V.I. (1995). Collapse transformation for self-focusing solitary waves in boundary-layer type shear flows. *Phys. Lett. A: Math. Gen.* **206**, 95–202.

Sazonov, I.A. and Shrira, V.I. (2003). Quasi-modes in the boundary-layer type shear flows. Part 2. *J. Fluid Mech.* **488**, 245–282.

Schmid, P.J. and Henningson, D.S. (2001). *Stability and Transition in Shear Flows*, Springer-Verlag, New-York.

Shrira, V.I. (1989). On the 'subsurface' waves in the oceanic upper mixed layer. *Dokl. Akad. Nauk SSSR* **308**, 732–736; Engl. translation: *Transactions (Doklady) USSR Academy of Sciences, Earth Science Section* **308**, 276–279.

Shrira, V.I. and Sazonov, I.A. (2001). Quasi-modes in the boundary-layer type shear flows. Part I. *J. Fluid Mech.* **446**, 133–171.

Veron, F. and Melville, W.K. (2001). Experiments on stability and transition of wind-driven water surfaces. *J. Fluid Mech.* **446**, 25–85.

Voronovich, V.V., Shrira, V.I. and Stepanyants, Yu.A. (1998). Two-dimensional models for nonlinear vorticity waves in shear flows. *Stud. Appl. Math.* **100**(1), 1–32.

Wu, X., Jacobs, R.G., Hunt, J.C.R. and Durbin, P. (1999). Simulation of boundary layer transition induced by periodically passing wakes. *J. Fluid Mech.* **398**, 109–153.

VISCOELASTIC NONLINEAR TRAVELING WAVES AND DRAG REDUCTION IN PLANE POISEUILLE FLOW

Wei Li, Philip A. Stone and Michael D. Graham*
*Department of Chemical and Biological Engineering, University of Wisconsin-Madison, Madison, WI 53706-1691, USA (*Corresponding author)*
graham@engr.wisc.edu

Abstract Nonlinear traveling wave solutions to the Navier–Stokes equations in the plane Poiseuille geometry (Waleffe, F. (2003), *Phys. Fluids* **15**, 1517–1534) come into existence through a saddle-node bifurcation at a Reynolds number of 977, very close to the experimentally observed Reynolds number of ~ 1000 for transition to turbulence in this geometry. These traveling waves are comprised of staggered counter-rotating streamwise vortices with a spanwise wavelength of 106 wall units, in good agreement with the experimentally observed value of ~ 100 wall units for buffer layer structures. In the present work, the effect of viscoelasticity on these states is examined, using the FENE-P constitutive model of polymer solutions. The changes to the velocity field for the viscoelastic traveling waves mirror those experimentally observed in fully turbulent flows of polymer solutions near the onset of turbulent drag reduction: drag is reduced, streamwise velocity fluctuations increase and wall-normal fluctuations decrease. The mechanism underlying theses changes is elucidated through an examination of the forces exerted by the polymer molecules on the fluid. The onset Weissenberg number (shear rate times polymer relaxation time) for drag reduction is insensitive to polymer extensibility or concentration. Above the onset Weissenberg number, there is a dramatic increase in the critical wall-normal length scale at which the nonlinear traveling waves can exist. This sharp increase in length scale directly correlates with the extensibility and concentration of the polymer molecules and is consistent with the observed shift to higher Reynolds numbers of the transition to turbulence in polymer solutions. The balance of turbulent kinetic energy for the nonlinear traveling waves shows the same qualititative changes as are found in full turbulence, as do the overall kinematics of stretching and rotation in the flow. These observations suggest that the mechanism of near-onset drag reduction in flow over smooth walls is captured by the effect of viscoelasticity on these nonlinear traveling waves.

T. Mullin and R.R. Kerswell (eds), Laminar Turbulent Transition and Finite Amplitude Solutions, 289–312.
© 2005 *Springer. Printed in the Netherlands.*

1. INTRODUCTION

The effect of polymer additives on turbulent flow has received much attention since the discovery in the 1940s that very small polymer concentrations, on the order of ten parts per million by weight, can lead to reductions in drag of 50% or greater (Virk, 1975; Lumley, 1969; McComb, 1990; Graham, 2004). At these small concentrations the properties of the solution measured in simple shear flows do not deviate appreciably from those of the pure solvent. However, in extensional flows, large stresses are generated due to the polymer contribution to the extensional viscosity. It is well-known that the extensional behavior of the polymers is key to the phenomenon of drag reduction, but a detailed knowledge of how polymer stretch and relaxation interact with turbulent structure is not available. The goal of the present work is to better understand this interaction, particularly in the context of near-wall turbulence.

In wall-bounded turbulent flows, the production and dissipation of turbulent kinetic energy peak in the buffer layer of the flow (Robinson, 1991). Observations of flows exhibiting drag reduction indicate that, at least near the onset Reynolds number for drag reduction, the effects of the polymer are confined primarily to this region (Virk, 1975; Donohue et al., 1972; Tiederman et al., 1985; Walker and Tiederman, 1990; Escudier et al., 1999). From experimental observations and direct numerical simulation (DNS) of turbulent flows, the dominant structures of this region are found to be pairs of counter-rotating, streamwise-aligned vortices (Robinson, 1991; Jeong et al., 1997; Holmes et al., 1996). These vortices pull slower moving fluid away from the wall, forming low-speed streaks – regions of low streamwise velocity that are highly elongated in the flow direction and with a statistically well-defined spacing in the spanwise direction. In flows exhibiting drag reduction, the structure of the buffer region is modified. Most notably, the wall-normal thickness of the buffer region increases (Virk, 1975), the coherent structures in this region shift to larger length scales (Donohue et al., 1972; Sureshkumar et al., 1997; den Toonder et al., 1997; Draad et al., 1998), and the bursting frequency decreases (Donohue et al., 1972). These structural changes are accompanied by changes in the root-mean-square (rms) velocity fluctuations and Reynolds stresses. Namely, the wall-normal and spanwise fluctuations are reduced while, at least at low to moderate degrees of drag reduction, the streamwise velocity fluctuations are enhanced (Lumley, 1973). Streamwise vorticity fluctuations are also decreased (Sureshkumar et al., 1997). Perhaps most importantly, the Reynolds shear stress decreases (Wei and Willmarth, 1992; Sureshkumar et al., 1997; Ptasinski et al., 2003). These changes become more pronounced as the extensional viscosity of the polymer solution is increased (Wei and Willmarth, 1992; Escudier et al., 1999; Dimitropoulos et al., 2001; Housiadas and Beris, 2003).

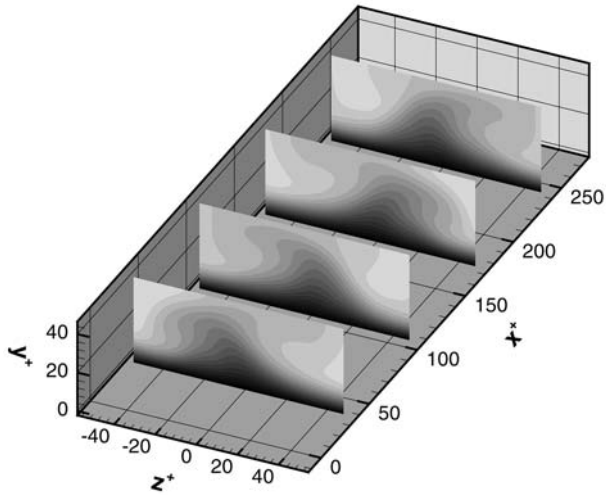

Figure 1. A nonlinear traveling wave state in the plane Poiseuille geometry; only the lower half of the channel is shown. "High drag" state at $Re = 977$ ($Re_\tau = 44.2$). The panels show contours of streamwise velocity, v_x (white for the highest velocity, black is zero).

The importance of the buffer layer structures in turbulence production and rheological drag reduction motivates the search for a better fundamental understanding of the nature and origin of these structures. A recent advance in this direction has come with the recognition that the Navier–Stokes equations support nonlinear traveling wave states, which we shall call "exact coherent states" or ECS, that capture the dominant buffer-region structure, namely counter-rotating, streamwise-aligned vortex pairs that flank streaks in the streamwise velocity (Robinson, 1991; Jeong et al., 1997; Waleffe, 2003). These states have been found by homotopy methods in plane Couette flow (Nagata, 1986, 1988, 1990; Clever and Busse, 1997), plane Poiseuille flow (Waleffe, 1998, 2001, 2003) and pipe flow (Faisst and Eckhardt, 2003; Wedin and Kerswell, 2004). The focus of the present work is the effect of viscoelasticity on these states in the plane Poiseuille geometry.

Figure 1 shows the velocity field for one of these states. The ECS are periodic in the streamwise (x) and spanwise (z) directions; for a given pair of wavelengths (L_x, L_z) they appear in pairs at finite amplitude in saddle-node bifurcations as the Reynolds number Re increases. While both of these solutions are unstable, one of these states, which we will call the "high drag" state due to its lower mean velocity at a given Reynolds number, has greater stability relative to the "low drag" ECS – the "high drag" solutions have one more stable direction in phase space than the "low drag" solutions. Recently, Waleffe and Wang have shown that these states are unconnected with the lam-

inar state even as the Reynolds number tends to infinity (Waleffe and Wang, 2005). For Couette flow with no-slip boundary conditions, the ECS first appear at $Re \approx 128$ (Waleffe, 2003) (i.e. this Reynolds number is the lowest for which an ECS solution can be found for any wavelength pair), where the Reynolds number is based on half the velocity difference between the walls and the half-channel height. For pipe flow, they appear at $Re \approx 1300$ (Faisst and Eckhardt, 2003), where the Reynolds number is based on the laminar centerline velocity and pipe radius, and in the case of interest here, plane Poiseuille flow, they appear at $Re = 977$, where the Reynolds number is based on the laminar centerline velocity and the half-channel height. An important feature of the ECS is that they presage transition to turbulence in all these geometries. In Couette flow, persistent turbulence is seen for $Re \gtrsim 325$ (Bottin et al., 1998), for pipe flow at $Re \gtrsim 2100$ (Bird et al., 2002) and for channel flow $Re \gtrsim 1000$ (Carlson et al., 1982).

Further evidence of the connection between ECS and near-wall turbulence can be found by a consideration of length scales (Waleffe, 2003). The friction Reynolds number $Re_\tau = \sqrt{2Re}$ at which the plane Poiseuille flow ECS appear is 44.2. This is simply the wall-normal extent of the ECS, expressed in wall units (i.e. in terms of the length scale ν/u_τ, where $u_\tau = \sqrt{\tau_w/\rho}$ is the friction velocity, τ_w is the average wall shear stress, ρ is the density and ν is the total, zero-shear-rate kinematic viscosity). The spanwise wavelength $L_z^+ = 105.6$ of the ECS at onset closely matches the streak spacing of ~ 100 wall-units widely observed in experiments over a large range of Reynolds numbers (Robinson, 1991). (Throughout this work, the $+$ superscript indicates a length expressed in the wall unit ν/u_τ.) Minimal channel flow, i.e., flow in the smallest computational domain that reproduces the velocity field statistics of near-wall turbulence, gives a range for the streamwise length L_x^+ of 250–350, compared to $L_x^+ = 273.7$ for the ECS, and a spanwise length that is again approximately 100 wall units (Jiménez and Moin, 1991). In the minimal channel flow the statistics of the near-wall region are faithfully captured up to a wall normal distance $y^+ \approx 40$, while again we note that the wall-normal size of the onset ECS is $L_y^+ = Re_\tau = 44.2$. It should be pointed out that this minimum channel contains a single wavelength of a wavy streak and a pair of quasi-streamwise vortices, which is the same structure seen in the ECS. Another approximately Reynolds-number-invariant length scale in near-wall turbulence is the peak in the production of turbulent kinetic energy at $y^+ \approx 12$ (Pope, 2000); the channel flow ECS also captures this length scale (Stone, 2004). The length scales at which the ECS first appear are in close agreement with the length scales of near-wall turbulence.

Beyond capturing the observed length scales of the buffer region structures, recent research also indicates that the ECS are saddle-points in phase space around which the strange attractor (Strogatz, 1994) of near-wall turbulence is

built. Recent studies by Kawahara and Kida (2001) and Toh and Itano (2003) find periodic solutions in minimal channel flows that are bifurcations of the ECS. The bursting trajectories in fully turbulent flows seem to be built around these periodic solutions. A further indication of this comes from a study by Jiménez and Simens (2001) that applies a numerical filter to DNS of channel flow to isolate the near-wall region from the main-stream turbulence. The simplest (nontrivial) flow structure, found when the numerical mask is at $y^+ \approx 50$, is a traveling-wave solution that has qualitatively the same structure as the ECS. The length scales of this traveling wave ($L_x^+ \approx 250$, $L_y^+ \approx 50$, and $L_z^+ \approx 150$) are similar to the optimum values for the channel flow ECS described above. As the mask moves further away from the wall, these traveling-wave solutions bifurcate into quasi-periodic solutions. These solutions then evolve into the bursts of full-scale turbulence with the flow being essentially turbulent when the numerical filter reaches $y^+ \approx 70$. These results along with the existence of the ECS indicate that staggered streamwise vortex traveling wave patterns are autonomous in wall-bounded shear flows and provide, at least in part, the foundation on which the near-wall turbulent fluctuations are built.

The self-sustaining process that underlies the ECS, making them autonomous, consists of three interacting, concurrent sub-processes: streak formation, streak instability, and vortex regeneration (Hamilton et al., 1995; Waleffe, 1997). The counter-rotating, streamwise-aligned vortex pairs pull fluid with low streamwise velocity up from near the wall while, at the opposite side of a vortex, higher velocity fluid is pulled toward the wall. This leads to a spanwise stratification of the streamwise velocity (*i.e.,* streaks in the streamwise velocity). The spanwise inflections in the streamwise velocity lead to a three-dimensional Kelvin–Helmholtz-like instability (Drazin and Reid, 1981) that concentrates wall-normal vorticity. This concentrated wall-normal vorticity, through a nonlinear interaction with the mean shear, is tilted and stretched in the streamwise direction, reenergizing the streamwise vortices. In studying the viscoelastic ECS, we aim to understand how the polymer modifies this mechanism.

We have previously studied viscoelastic ECS in the plane Couette geometry (Stone et al., 2002; Stone and Graham, 2003; Stone et al., 2004). That work provided some structural insight into the mechanism of drag reduction. The polymer molecules become highly elongated as they move through the streamwise streak. As they move out of the streak and into one of the vortices, the polymer molecules relax. This relaxation produces a polymer force that opposes the vortex motion. The polymer force thus weakens the vortex by slowing the fluid moving into it. The weakening of the vortices leads to collapse of the mechanism that sustains the ECS (Waleffe, 1997), and ultimately to a reduction in drag. Similar arguments, based on DNS results, are given by

Dubief et al. (2004). A related argument based on elastic energy arguments was proposed in a recent DNS study by Min et al. (2003). In their study, they find that during drag reduction turbulent energy is transformed into elastic energy by the stretching of the polymer near the wall. The vortices of the buffer region then lift this elastic energy up where it is released as turbulent kinetic energy or dissipated in the buffer and log regions.

The present work focuses on the effect of viscoelasticity on exact coherent states in the plane Poiseuille geometry. We illustrate the changes in the bifurcation diagram and the corresponding changes in the region of parameter space in which these solutions exist. These changes are then related to the physics of the interaction between the polymer dynamics and the flow field, to illustrate the physical mechanism by which viscoelasticity affects these states. The influence of viscoelasticity on these states very closely mirrors the effects of polymer additives observed in fully turbulent near-wall flows near the onset of drag reduction, suggesting that the essential mechanism of drag reduction, at least near its inception, is captured by the effect of viscoelasticity on these nonlinear traveling waves.

2. MATHEMATICAL FORMULATION AND SIMULATION DETAILS

Denoting the streamwise direction as x, the wall-normal direction as y, and the spanwise direction as z, we consider pressure-driven flow with no-slip boundary conditions at the wall

$$v_x = v_y = v_z = 0 \text{ at } y = -1, \tag{1}$$

where v_x, v_y, and v_z are streamwise, wall-normal, and spanwise components of the velocity, $\mathbf{v}$, respectively. We will only simulate half of the channel and apply reflection symmetry boundary conditions at the channel centerline $y = 0$:

$$\frac{\partial v_x}{\partial y} = v_y = \frac{\partial v_z}{\partial y} = 0. \tag{2}$$

The laminar centerline velocity, U, and the half-channel height, l, are used to scale velocity and position, respectively. Time, t, is scaled with l/U, and pressure, p, with ρU^2, where ρ is the fluid density. The stress due to the polymer, $\boldsymbol{\tau}_p$, is non-dimensionalized with the polymer elastic modulus, $G = \eta_p/\lambda$, where η_p is the polymer contribution to the viscosity and λ is the time constant for the polymer – the polymer model is described below. The momentum balance and the equation of continuity are

$$\frac{\partial \mathbf{v}}{\partial t} + \mathbf{v} \cdot \nabla \mathbf{v} = -\nabla p + \beta \frac{1}{Re} \nabla^2 \mathbf{v} + (1-\beta) \frac{2}{ReWi} (\nabla \cdot \boldsymbol{\tau}_p), \tag{3}$$

$$\nabla \cdot \mathbf{v} = 0, \tag{4}$$

where η_s is the solvent viscosity, $Wi = \lambda\dot{\gamma}_w$ is the Weissenberg number based on wall shear rate, $\dot{\gamma}_w = 2U/l$ and $\beta = \eta_s/(\eta_s + \eta_p)$ is the fraction of the total zero-shear viscosity that is due to the solvent. The Reynolds number, Re, is based on the total viscosity, $Re = \frac{\rho U l}{\eta_s+\eta_p}$. We seek "sinuous" traveling wave solutions that satisfy the shift-reflect symmetry

$$v_x(x, y, z) = v_x(x + L_x/2, y, -z), \tag{5}$$

$$v_y(x, y, z) = v_y(x + L_x/2, y, -z), \tag{6}$$

$$v_z(x, y, z) = -v_z(x + L_x/2, y, -z). \tag{7}$$

The polymer stress is computed with the widely-used FENE-P constitutive model, in which each polymer molecule consists of two beads, where the mass and drag of the molecule are concentrated, connected by a finitely extensible nonlinear elastic (FENE) spring. The governing equation for this model is (Bird et al., 1987):

$$\frac{\boldsymbol{\alpha}}{1 - \frac{tr\boldsymbol{\alpha}}{b}} + \frac{Wi}{2}\left(\frac{\partial\boldsymbol{\alpha}}{\partial t} + (\mathbf{v}\cdot\nabla\boldsymbol{\alpha}) - \{\boldsymbol{\alpha}\cdot\nabla\mathbf{v}\} - \{\boldsymbol{\alpha}\cdot\nabla\mathbf{v}\}^T\right) = \left(\frac{b}{b+2}\right)\boldsymbol{\delta}, \tag{8}$$

where $\boldsymbol{\alpha}$ is a non-dimensional conformation tensor and b is proportional to the maximum extension of the dumbbell – $tr\boldsymbol{\alpha}$ cannot exceed b. The polymer contribution to the stress is given by:

$$\boldsymbol{\tau}_p = \frac{b+5}{b}\left(\frac{\boldsymbol{\alpha}}{1 - \frac{tr\boldsymbol{\alpha}}{b}} - \left(1 - \frac{2}{b+2}\right)\boldsymbol{\delta}\right). \tag{9}$$

It is well-recognized that extensional rheology plays a key role in turbulent drag reduction. A simple measure of the importance of extensional polymer stress is the relative magnitude of the polymer and solvent contributions to the steady state extensional stress in uniaxial extension. We define the extensibility parameter

$$Ex \equiv \frac{\eta_\infty^+}{\eta_s}, \tag{10}$$

where η_∞^+ is the polymer contribution to the steady state uniaxial extensional viscosity of the fluid in the limit of high extension rate. For the FENE-P model this expression becomes:

$$Ex = \frac{2b(1-\beta)}{3\beta}. \tag{11}$$

Because $b \gg 1$ for a high molecular weight flexible polymer, the parameter Ex can be large even when the polymer contribution to the shear viscosity, $1-\beta$, is very small, as is usually the case for drag reducing solutions. For example, the case $Ex = 10$, $\beta = 0.97$ gives $b = 485$, a value which roughly corresponds to a solution of 25,000 MW polyethylene oxide (PEO) in water. Finally, we

note when $1 - \beta \ll 1$, the effect of shear-thinning on the flow is negligible, as the polymer only contributes a very small amount to the total shear viscosity of the solution.

The conservation and constitutive equations are solved through a Picard iteration. A Newtonian ECS, as computed in Waleffe (1998), is first used to calculate the polymer stress tensor, $\boldsymbol{\tau}_p$, by inserting the velocity field in the evolution equation for $\boldsymbol{\alpha}$ and integrating for a short length of time, usually one time unit (l/U). For this $\boldsymbol{\tau}_p$, a steady state of the momentum and continuity equations is found by Newton iteration. The resulting velocity field, $\mathbf{v}$, is used to compute the new $\boldsymbol{\tau}_p$, and the process is repeated until the velocity and polymer field converge to a steady state.

The momentum and continuity equations are discretized using a Fourier–Chebyshev formulation with typically a $9\times17\times9$ grid. The conformation tensor, $\boldsymbol{\alpha}$, is discretized with a third-order, compact upwind difference scheme (Lele, 1992; Min et al., 2001) in the x and z directions and Chebyshev collocation in the y direction. In this as in most previous computational studies of polymers in turbulent flows, we have found it necessary to add an artificial stress diffusivity $\frac{1}{ScRe}\nabla^2\boldsymbol{\alpha}$, to Equation (8) to achieve numerical stability. The Schmidt number, Sc, which is the ratio of the momentum diffusivity to stress diffusivity, is set to value of 1.0. This value of Sc, though artificially small, is greater than or of the same order of magnitude as that used in many DNS studies (Sureshkumar et al., 1997; Ptasinski et al., 2003; Sureshkumar and Beris, 1995; Sibilla and Baron, 2002). In the range of Sc where solutions can be obtained, the bifurcation diagrams shown below are insensitive to its value. The stress diffusion term is integrated implicitly by the Crank–Nicholson method with the other terms of the equation integrated using the Adams–Bashforth method. This equation is solved on a finer mesh than the momentum, contunity pair, typically $32\times33\times32$.

3. RESULTS

3.1 Existence of the ECS

Through this study, we analyze the Newtonian and viscoelastic exact coherent states at fixed streamwise and spanwise length (in outer units): $L_x = 2\pi/1.0148$ and $L_z = 2\pi/2.633$. This wavelength pair is where ECS first come into existence in the Newtonian case. The bifurcation diagram, which shows the solutions of Equations (3)–(9) as Re increases, is given in Figure 2. These solutions are plotted using the maximum in the rms wall-normal velocity fluctuations for the solution, $\langle\langle v_y'^2\rangle\rangle^{1/2}$. (Hereafter, double angle brackets indicate that the variable is averaged over the streamwise and spanwise directions.) The trivial base state in this geometry (laminar Poiseuille flow) exists at all Re and would appear as a horizonal line at max $\langle\langle v_y'^2\rangle\rangle^{1/2} = 0$ if it were plotted in

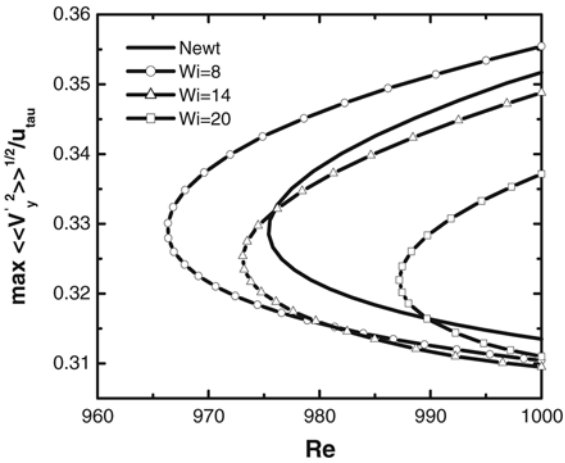

Figure 2. Bifurcation diagram for Newtonian and viscoelastic ECS with $L_x = 2\pi/1.0148$, $L_z = 2\pi/2.633$ and for viscoelastic solution, $Ex = 10$ ($b = 485$) and $\beta = 0.97$. Solid line, Newtonian; open circles, $Wi = 8$; open triangles, $Wi = 14$; open rectangles, $Wi = 20$.

Figure 2. At $Re \approx 977$ for the Newtonian flow (solid line), two new solutions that have nonzero wall-normal velocity appear via a saddle-node bifurcation. These are the ECS. The solutions with higher maximum wall-normal velocity at a given Re, i.e., solutions on the upper branch of the bifurcation diagram, we call "high drag" solutions due to their lower mean velocity at the centerline of the channel compared to the lower branch, or "low drag", solutions. While both solutions are unstable, the "high drag" state has greater stability relative to the "low drag" state - the "high drag" solutions have one more stable direction in phase space than the "low drag" solutions. All results should be assumed to be for the "high drag" states unless otherwise indicated. For the viscoelastic flow at $Wi = 8$, the open circles in Figure 2, the ECS again appear via a saddle node bifurcation. However, the bifurcation occurs at a Reynolds number, $Re_{\min} \approx 966$, that is lower than the Re for the appearance of the Newtonian ECS. As the Weissenberg number increases to $Wi = 14$ (open triangles) and $Wi = 20$ (open rectangles), the Re where the bifurcations occur likewise increase to $Re \approx 973$ and $Re \approx 987$, respectively. Accompanying this change in the Re at which the bifurcation occurs are changes to the flow field as indicated by the decrease in maximum of the rms wall-normal velocity fluctuations at a given Re as Wi increases. This change in the wall-normal velocity is more dramatic for the high drag state than for the low drag state.

To gain a better understanding of how the existence of the ECS is affected by the addition of polymer, we look at how the minimum value of Reynolds number at which the ECS can exist, $Re_{\min}$, (the bifurcation points in Figure 2) changes with Weissenberg number. This curve of $Re_{\min}$, given in Figure 3,

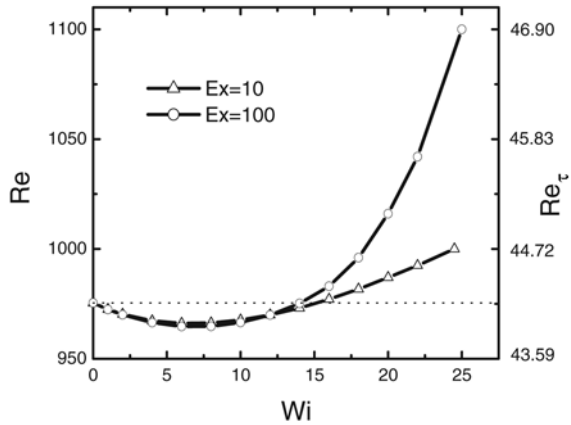

Figure 3. Changes in the minimum Re (left vertical axis) and $Re_\tau = \sqrt{2Re}$ (right vertical axis) as Wi increases. $L_x = 2\pi/1.0148$, $L_z = 2\pi/2.633$, $Ex = 10$, 100 and $\beta = 0.97$.

separates the region where the ECS can exist (above the curve) from the region where no ECS exist. At low Wi, there is a slight decrease in $Re_{\min}$ from the Newtonian value. A similar result is observed in the plane Couette flow case (Stone et al., 2004); its origin is unknown. At $Wi \approx 15$ the minimum Re for the viscoelastic ECS increases above that for the Newtonian. As Weissenberg number increases further, there is a dramatic increase in $Re_{\min}$. Recall that the Reynolds number is simply related to the wall-normal length scale of the structure measured in wall units, $Re = (L_y^+)^2/2$ (and in the present situation $L_y^+ = Re_\tau$, which is given on the right vertical axis of Figure 3). In experiments the thickness of the buffer region (the wall-normal extent of this region in wall units) is known to increase as drag reduction increases (Virk, 1975). The results for the viscoelastic ECS closely mirror this increase in L_y^+. For this reason, we will refer to the Wi above which the critical value of L_y^+ for the viscoelastic ECS is greater than for the Newtonian ECS as the onset Weissenberg number. As seen in Figure 3, $Wi_{onset} \approx 15$, which is insensitive to polymer extensibility or concentration. This agrees well with onset values from some DNS studies (Sureshkumar et al., 1997; Dimitropoulos et al., 1998) while is bigger by a factor of about two than found in two recent DNS studies of polymer drag reduction (Housiadas and Beris, 2003; Min et al., 2003). As mentioned previously, we add a small artificial stress diffusivity to polymer evolution equation, smearing out the steep gradients of polymer stress. This may result in less drag reduction at a given Weissenberg number and an increase in the onset value. Finally, there is also experimental evidence that the transition to turbulence in a polymer solution is delayed to higher Re than in the Newtonian case (Giles and Pettit, 1967; White and McEligot, 1970; Draad et

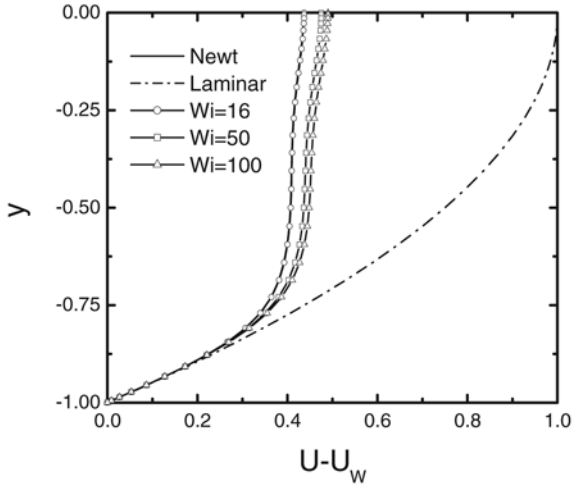

Figure 4. Mean streamwise velocity for Newtonian ECS and viscoelastic ECS, $Re = 1600$, $Ex = 10$, $\beta = 0.97$, $Wi = 16, 50, 100$.

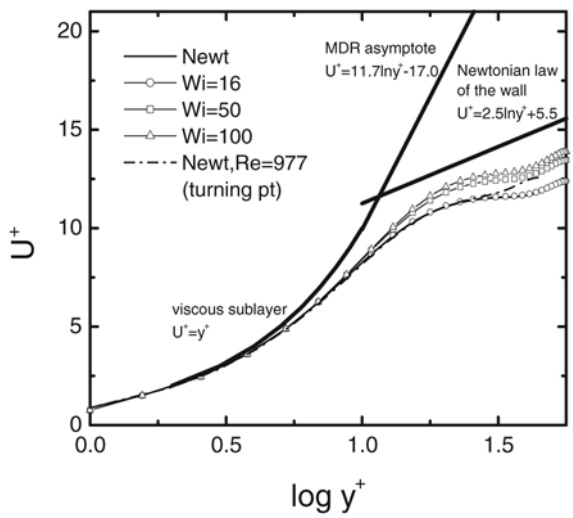

Figure 5. Mean streamwise velocity (velocity is scaled by friction velocity, u_τ, distance from the wall is scaled by wall units, ν/u_τ) for Newtonian ECS and viscoelastic ECS, $Re = 1600$, $Ex = 10$, $\beta = 0.97$, $Wi = 16, 50, 100$.

al., 1998; Escudier et al., 1999). The present results are completely consistent with that observation.

We now look at what happens to the ECS at constant Reynolds number as the Weissenberg increases. The mean velocity profiles for Newtonian and

viscoelastic flows at $Re = 1600$ are given in Figure 4. We observe that the maximum mean velocity in Newtonian ECS is reduced compared to the laminar state velocity due to the redistribution of streamwise momentum by the streamwise vortices. Above the onset Weissenberg number of about 15, the mean velocity profiles for the viscoelastic ECS are significantly higher than the Newtonian ECS, illustrating that the drag is reduced by the addition of polymer. Figure 5 shows the mean velocity profiles prepared in wall units. We observe a similar trend to that seen in both experimental and DNS results. Although the maximum drag reduction (MDR) regime is not approached in our simulations, we can still observe that there is a region with a nearly constant slope – a nearly-log-law region – that shifts upward with increasing Weissenberg number, though the slope for the ECS is slightly smaller than found experimentally (Virk, 1975).

Figure 6 shows a comparison of wall-normal and spanwise velocities (top) to their corresponding polymer forces $\mathbf{f} = \frac{2(1-\beta)}{ReWi}\nabla \cdot \boldsymbol{\tau}_p$ (bottom) on the flow. The upwelling and downwelling associated with the streamwise vortices are clearly seen in the wall-normal velocity plot. The regions where the wall-normal velocity is highest (white contours) is matched by the negative regions of the polymer force (black contours) and likewise, negative regions of wall-normal velocities correspond to positive polymer force. Similar results can also be observed in the spanwise velocity and polymer force. This anti-correlation of polymer force with the fluctuation velocity has also been found in DNS of drag reducing solutions (De Angelis et al., 2002) and more recently by Stone et al. (2004) in plane Couette flow ECS. Recalling the importance of these streamwise aligned vortices in the self-sustaining process in the redistribution of mean shear, these results indicate that the added polymer stress is working to suppress the mechanism of ECS.

Further insight into the influence of the polymers on the ECS can be gained by studying the spatial distribution of the polymer stress, $\boldsymbol{\tau_p}$. Figure 7 shows the distribution of $\mathrm{tr}\boldsymbol{\tau_p}$ in the channel for various Weissenberg numbers. Below the onset Weissenberg number of about 15, polymer molecules are only highly stretched in the near wall region due to the higher shear rate at the wall. After onset, the polymer stress is significantly increased both near the wall and close to the centerline of the channel. Furthermore, we see that highly stretched molecules are now getting "wrapped into" the streamwise vortices, where they relax – this relaxation generates the polymer forces that resist the streamwise vortex motions as shown in the previous paragraph. This process was also observed in our previous study in the plane Couette flow (Stone et al., 2004). The plane Poiseuille flow geometry is symmetric about centerline of the channel, which means the mean shear rate is zero at the centerline. Figure 7 shows a significant increase of the trace of polymer stress $\boldsymbol{\tau_p}$ at the centerline region af-

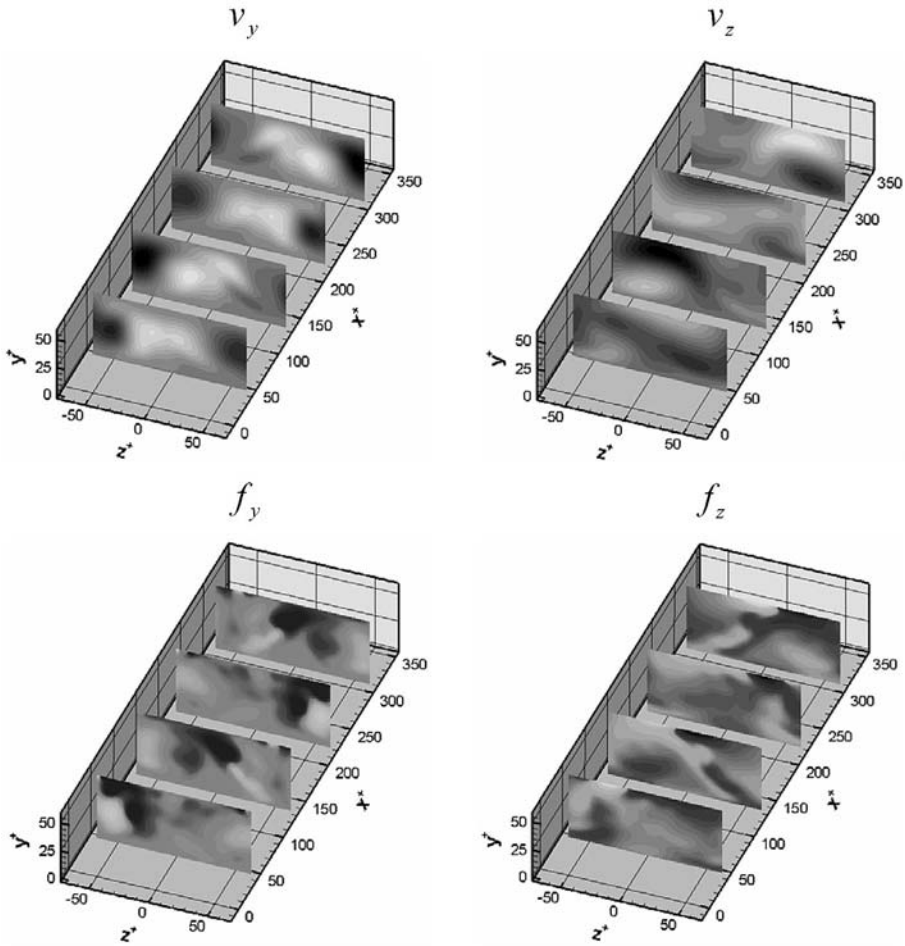

Figure 6. Contours of velocity and polymer force for the viscoelastic ECS with $Re = 1600$, $Wi = 24$, $Ex = 10$ and $\beta = 0.97$ Top left: v_y, range -0.054(black)–0.041(white); top right: v_z, range -0.13(black)–0.13(white); bottom left: f_y, range -0.0008(black)–0.0008(white); bottom right: f_z, range -0.004(black)–0.004(white).

ter onset, which indicates that in that region, the polymer molecules are highly stretched in spanwise direction.

The changes to the averaged streamwise, wall-normal and spanwise velocity fluctuations, each scaled by the friction velocity, u_τ, are given in Figure 8. For the Newtonian ECS (solid circles), the peak in $\langle\langle v_x'^2\rangle\rangle^{1/2}$ occurs at $y^+ \approx 12$ with peak value of about 2.5, both of which are very close to the values found in full channel DNS results (Pope, 2000). For the viscoelastic ECS (open rectangles and open triangles), this peak increases and shifts away from the wall monotonically with the increase of viscoelasticity. Away from the wall,

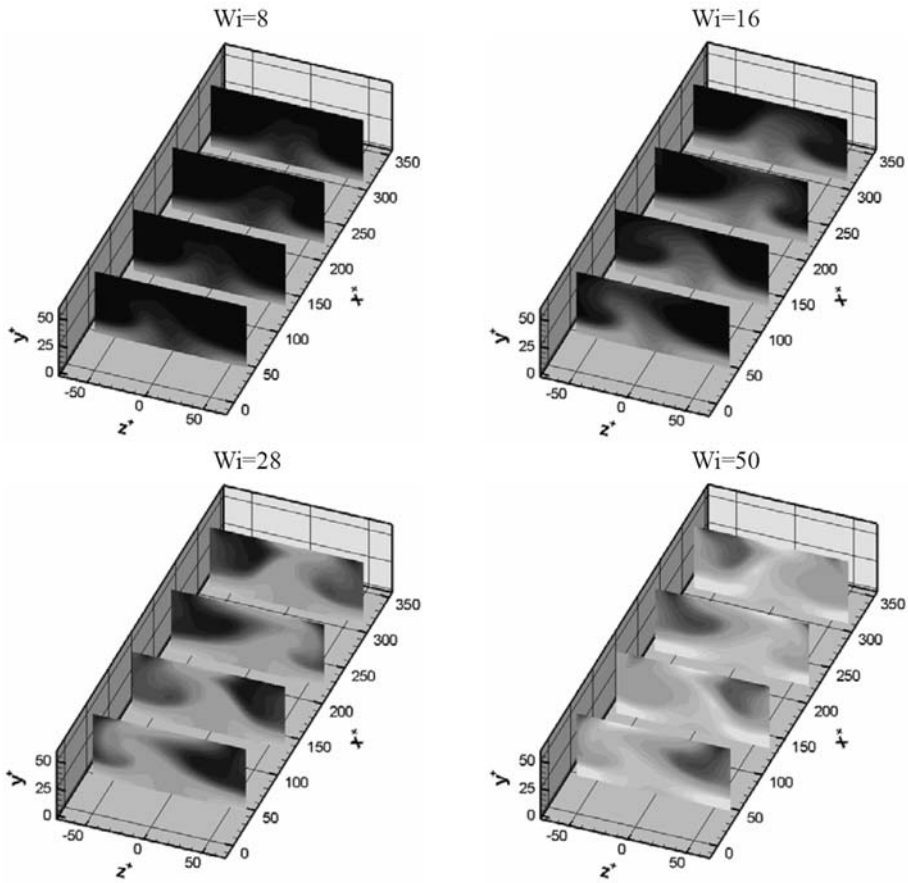

Figure 7. Trace of the polymer stress in the viscoelastic ECS. $Re = 1600$, $Ex = 10$, $\beta = 0.97$, $Wi = 8, 16, 28, 50$. Range 0 (black) - 900 (white).

the streamwise velocity fluctuations for the viscoelastic ECS increase significantly compared to the Newtonian. The wall-normal and spanwise velocity fluctuations decrease. All these results are consistent with experimental observations and DNS results (Virk, 1975; Sureshkumar et al., 1997). Given these changes in the velocity fluctuations, the Reynolds shear stress $-\rho\langle\langle v_x^{'} v_y^{'}\rangle\rangle$ should also be affected. Figure 9 shows the Reynolds shear stress for the ECS. The Reynolds shear stress is zero at the wall and the centerline since $v_y = 0$ is imposed on both boundaries. The Reynolds stress peaks in the buffer region as it does in experiments and DNS of fully turbulent flows. Throughout the channel, the Reynolds shear stress is significantly lower for the viscoelastic ECS (open rectangles and open triangles in Figure 9) than for the Newtonian (solid circles in Figure 9). Since the Reynolds shear stress is the wall-normal

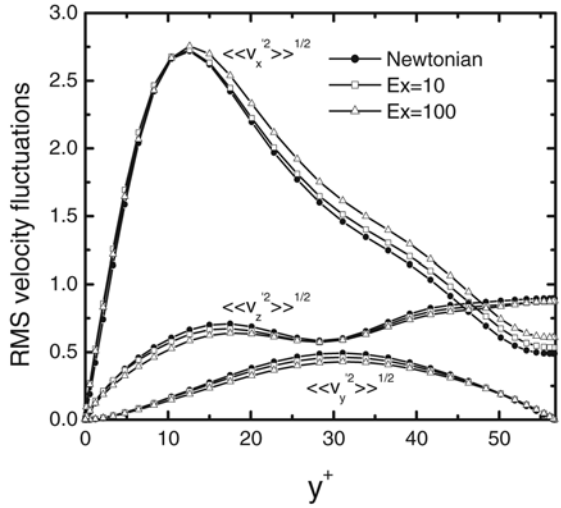

Figure 8. Fluctuations in the streamwise, wall-normal and spanwise velocitise: Newtonian (solid circles) viscoelastic (open rectangles and open triangles), $Re = 1600$, $Ex = 10, 100$, $\beta = 0.97$, $Wi = 24$.

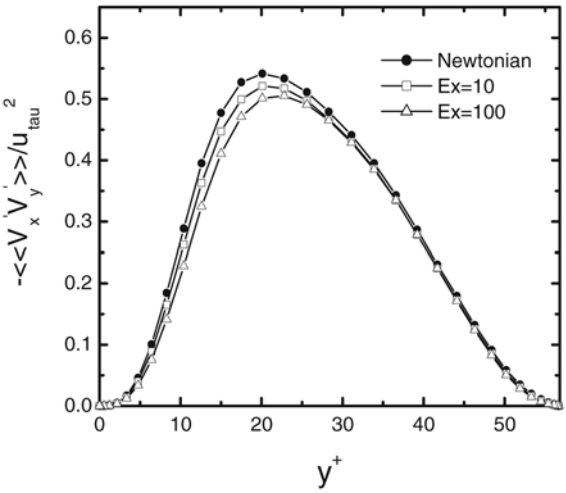

Figure 9. Reynolds shear stress: Newtonian (solid circles) viscoelastic (open rectangles and open open triangles), $Re = 1600$, $Ex = 10, 100$, $\beta = 0.97$, $Wi = 24$.

flux of streamwise momentum, this result provides a further indication of drag reduction in the viscoelastic ECS.

3.2 Kinetic energy budget, stress balance and local flow kinematics

Scaling the velocity fluctuations with u_τ and time with ν/u_τ^2, the budget equation for the kinetic energy of turbulence can be written as (Stone et al., 2004)

$$\frac{\partial(\frac{1}{2}\langle\langle v_i^{'} v_i^{'}\rangle\rangle)}{\partial t} + V_k \frac{\partial}{\partial x_k}(\frac{1}{2}\langle\langle v_i^{'} v_i^{'}\rangle\rangle) + T_{ii}^t = P_{ii} + D_{ii} + T_{ii}^p + \varepsilon_{ii} + E_{ii}. \quad (12)$$

Here the velocity, pressure, and force due to the polymer ($\mathbf{f} = \frac{2(1-\beta)}{ReWi}\nabla \cdot \boldsymbol{\tau}_p$) are written as sums of mean and fluctuating parts ($\mathbf{v} = \mathbf{V} + \mathbf{v}^{'}$, $p = P + p^{'}$, and $\mathbf{f} = \mathbf{F} + \mathbf{f}^{'}$). The terms

$$T_{ii}^t = \frac{1}{2}\frac{\partial}{\partial x_k}(\langle\langle v_i^{'} v_i^{'} v_k^{'}\rangle\rangle) \quad (13)$$

and

$$T_{ii}^p = -\frac{\partial}{\partial x_k}\langle\langle v_i^{'} p^{'}\rangle\rangle\delta_{ik} \quad (14)$$

are the transport of kinetic energy by the fluctuating velocities and the fluctuating pressure, respectively. The production term,

$$P_{ii} = -\langle\langle v_i^{'} v_k^{'}\rangle\rangle\frac{\partial V_i}{\partial x_k} \quad (15)$$

generates kinetic energy through interaction with the mean velocity gradient. The diffusion and dissipation of kinetic energy are given by

$$D_{ii} = \frac{1}{2}\frac{\beta}{Re}\frac{\partial^2}{\partial x_k \partial x_k}\langle\langle v_i^{'} v_i^{'}\rangle\rangle \quad (16)$$

$$\varepsilon_{ii} = -\frac{\beta}{Re}\langle\langle\frac{\partial v_i^{'}}{\partial x_k}\frac{\partial v_i^{'}}{\partial x_k}\rangle\rangle, \quad (17)$$

respectively. The direct contribution of the polymer stresses to the kinetic energy budgets is the velocity-polymer-force term,

$$E_{ii} = \langle\langle v_i^{'} f_i^{'}\rangle\rangle \quad (18)$$

Budget results are given in Figures 10 and 11. The maxima and minima associated with the various quantities display a pronounced monotonic decrease with the increase of viscoelasticity. The terms that show the most significant changes relative to Newtonian ECS are the production, dissipation and transport. Compared with Newtonian ECS, the production of the turbulent kinetic energy and the viscous dissipation of viscoelastic ECS are reduced. The transport term for the viscoelastic ECS is also at a lower level in most of the domain.

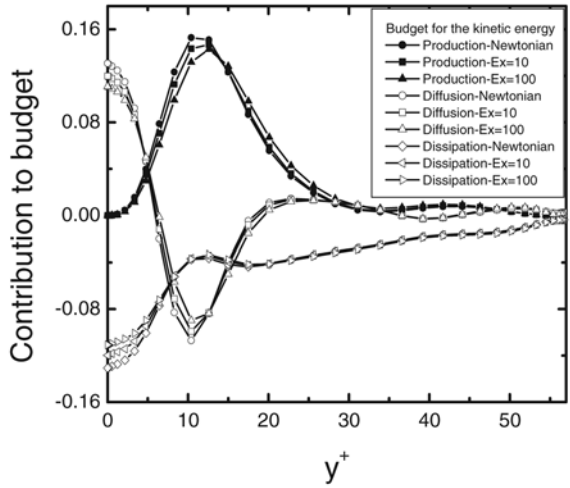

Figure 10. Budget for the kinetic energy of turbulence as a function of the distance from the wall for Newtonian and viscoelastic ECS, $Re = 1600$, $\beta = 0.97$, $Wi = 24$, $Ex = 10, 100$.

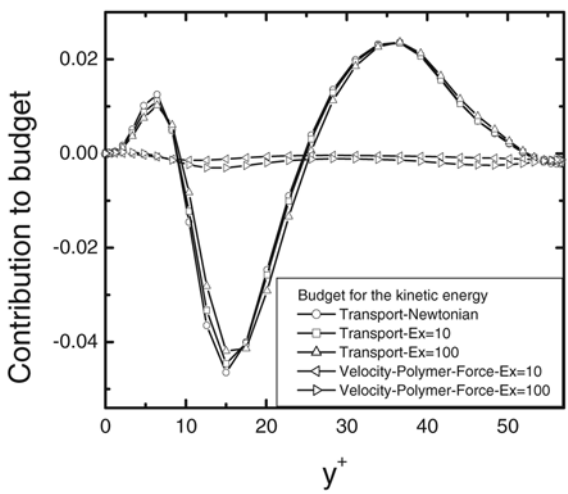

Figure 11. Budget for the kinetic energy of turbulence as a function of the distance from the wall for Newtonian and viscoelastic ECS, $Re = 1600$, $\beta = 0.97$, $Wi = 24$, $Ex = 10, 100$.

We also observe that the contribution of polymer stress appears as a weak sink term in most of the domain. In addition, a monotonic shift of maxima and minima further away from the wall is observed with the increase of viscoelasticity. This shift is consistent with the notion of the expansion of elastic sublayer as has been found experimentally (Virk, 1975), and all these results for the ECS mirror those found in DNS of full turbulence (Dimitropoulos et al., 2001). Our

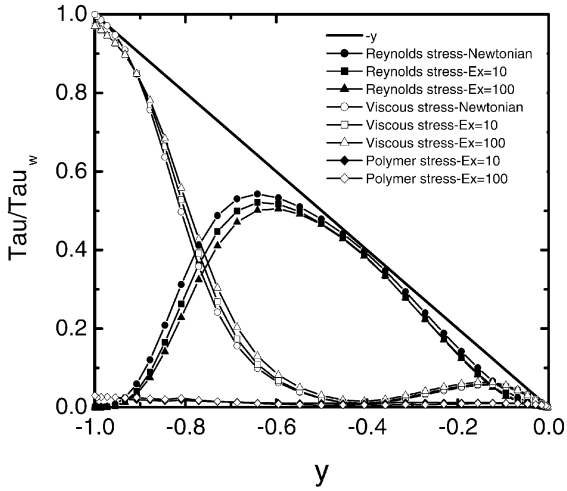

Figure 12. Stress balance for Newtonian and viscoelastic ECS, $Re = 1600$, $Ex = 10, 100$, $\beta = 0.97$, $Wi = 24$.

simulation results for Reynolds stress budgets show that the pressure-rate-of-strain term acts to redistribute energy from the streamwise velocity fluctuations to the wall-normal and spanwise velocity fluctuations and the Reynolds shear stress. The effect of polymer is to suppress the streamwise vorticity, leading to smaller pressure fluctuations. As a consequence, the pressure-rate-of-strain term decreases in magnitude. Transfer of energy from the streamwise fluctuations to the Reynolds shear stress diminishes and, therefore, drag is reduced. Again, these results are consistent with those found for the Couette flow ECS (Stone et al., 2004) and in DNS studies of full turbulence (Dimitropoulos et al., 2001).

Figure 12 shows the contributions to the mean shear stress as a function of distance from the wall. The stress balance is given by:

$$-y = \frac{\beta}{Re}\frac{1}{u_\tau^2}\frac{dV_x}{dy} - \frac{\langle\langle v_x v_y\rangle\rangle}{u_\tau^2} + \frac{2(1-\beta)}{ReWi}\frac{\langle\langle \tau_{p_{xy}}\rangle\rangle}{u_\tau^2}, \tag{19}$$

where the scaled Reynolds shear stress is $-\frac{\langle\langle v_x v_y\rangle\rangle}{u_\tau^2}$, the Newtonian viscous stress is $\frac{\beta}{Re}\frac{1}{u_\tau^2}\frac{dV_x}{dy}$ and the mean polymer stress is $\frac{2(1-\beta)}{ReWi}\frac{\langle\langle \tau_{p_{xy}}\rangle\rangle}{u_\tau^2}$. Again we observe qualitative agreement with DNS results (Sureshkumar et al., 1997; Ptasinski et al., 2003). Reynolds stresses for viscoelastic ECS (solid rectangles and solid triangles) decrease monotonically with the increase of viscoelasticity relative to Newtonian case (solid circles) throughout the whole channel. The average polymer shear stresses show a maximum at the wall.

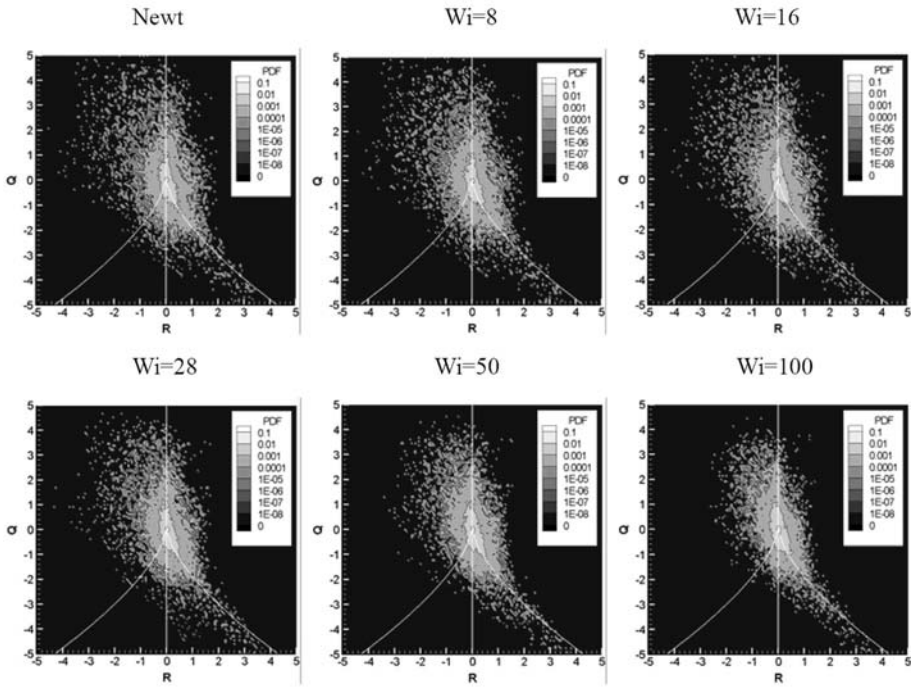

Figure 13. Distribution function of local flow topology for the ECS at various Weissenberg numbers, $Re = 1600$, $Ex = 10$, $\beta = 0.97$.

The local flow kinematics of an incompressible flow can be classified according to the eigenvalues of the velocity gradient tensor, $\nabla \mathbf{v}$ (Blackburn et al., 1996; Terrapon et al., 2004). For an incompressible flow, these eigenvalues, σ, are obtained as solutions of the characteristic equation

$$\sigma^3 + Q\sigma + R = 0, \tag{20}$$

with the tensor invariants Q and R given by

$$Q = -\frac{1}{2}\mathrm{tr}((\nabla \mathbf{v})^2), \tag{21}$$

$$R = -\det(\nabla \mathbf{v}). \tag{22}$$

The nature of the eigenvalues is determined by the discriminant $D = (27/4)R^2 + Q^3$. If $D > 0$, then there are one real and two complex-conjugate eigenvalues; $D < 0$ implies three real distinct eigenvalues and $D = 0$ (non-vertical white curves in Figure 13) corresponds to three real eigenvalues of which two are equal. A further classification can be made by the sign of R as follows: (R, Q) plane is divided into four regions separated by white curves

in Figure 13: in the upper right-hand region the local kinematics correspond to uniaxial compression along one eigenvector axis with outward spiraling along the plane defined by the other two eigenvectors; in the upper left-hand the behavior is reversed, so trajectories spiral inward on a plane while moving outward uniaxially; in the lower left-hand (third quadrant) region the flow has an unstable and two (real) stable directions; and in the lower right region there is a stable and two real unstable directions. Previous DNS studies (Chen et al., 1990; Soria et al., 1994) shows that in the turbulent buffer region, the kinematics are most likely to lie in the second (rotational flow with uniaxial extension) and fourth (biaxial extensional flow) regions of the (R, Q) plane, and the ECS kinematics reproduce this tendency. The distribution of points on this plane for the ECS at various Weissenberg number is shown in Figure 13. It is clearly seen that after the onset Weissenberg number of about 15, the preferences for the second and fourth quadrants are significantly reduced. Recalling the second quadrant represents strong rotational flow, this result is another indication that the effect of polymers is to suppress the streamwise vortices. The reduction of preference for the fourth quadrant or biaxial extensional flow indicates the importance of the extensional behavior of drag reduction, and the extensional polymer stress affects this behavior significantly.

4. CONCLUSIONS

The Navier–Stokes equations support nonlinear traveling wave solutions, or "exact coherent states" (ECS) that capture very well the length scales and dominant flow structures of near-wall (buffer layer) turbulence. In this work, we have studied in the plane Poiseuille geometry how these states are affected by viscoelasticity. The results are remarkably consistent with the experimentally observed effects of polymer additives on near-wall turbulence in the regime near the onset of drag reduction. Above a critical Weissenberg number, there is a dramatic increase in the minimum Reynolds number $Re_{\min}$ at which the ECS can exist. As the Reynolds number is related to the wall-normal scale of the flow structures, this result mirrors experimental observations of buffer region "thickening" in drag reducing flows. Furthermore, since evidence indicates that existence of the ECS is a prerequisite for transition to turbulence, the increase in minimum Reynods number with increasing viscoelasticity is also consistent with the experimental observed delay in transition for polymer solutions. The effect of viscoelasticity on the ECS lies primarily in its influence on the streamwise vortices that sustain the flow. The polymer molecules stretch near the wall and in the upwellings between vortices, and at sufficiently high *Wi*, they relax as they enter the vortices, resisting the vortex motion, and thus reducing drag. These effects can be seen in the kinetic energy budget, the mean shear stress balance and the distribution function for the invariants of

the velocity gradient tensor, all of which change in ways that are qualitatively identical to the changes found experimentally or via DNS.

Other additives, such as stiff polymers and fibers, are also drag reducers. They typically yield lower drag reduction for a given concentration than observed for flexible polymers. The effect of these additives on the ECS can be studied in the same way we have done here for polymer additives, by using the appropriate constitutive equation. Indeed, the ECS provide an ideal setting for such studies, as they allow the direct examination of the effect of rheology on what appear to be the canonical flow structures of transition and near-wall turbulence.

ACKNOWLEDGEMENTS

The authors are indebted to Fabian Waleffe for many illuminating discussions and for sharing his code for computation of the Newtonian exact coherent states. We also are grateful to Eric Shaqfeh for many discussions. This work was supported by the National Science Foundation, grant CTS-0328325, and the Petroleum Research Fund, administered by the American Chemical Society.

REFERENCES

Bird, R.B., Curtiss, C.F., Armstrong, R.C. and Hassager, O. (1987). *Dynamics of Polymeric Liquids*, 2nd edn., Vol. 2. Wiley, New York.

Bird, R.B., Stewart, W.E. and Lightfoot, E.N. (2002). *Transport Phenomena*, 2nd edn. Wiley, New York.

Blackburn, H.M., Mansour, N.N. and Cantwell, B.J. (1996). Topology of fine-scale motions in turbulent channel flow. *J. Fluid Mech.* **310**, 269–292 (1996).

Bottin, S., Dauchot, O., Daviaud, F. and Manneville, P. (1998). Experimental evidence of streamwise vorticies as finite amplitude solutions in transitional plane Couette flow. *Phys. Fluids* **10**, 2597–2607.

Carlson, D.R., Widnall, S.E. and Peeters, M.F. (1982). A flow-visualization study of transition in plane Poiseuille flow. *J. Fluid Mech.* **121**, 487–505.

Chen, J.H., Chong, M.S., Soria, J., Sondergaard, R., Perry, A.E., Rogers, M., Moser, R. and Cantwell, B.J. (1990). A study of the topology of dissipating motions in direct numerial simulations of time developing compressible and incompressible mixing layers. In *Proc. Center for Turbulence Research 1990 Summer Program*, pp. 141–164.

Clever, R.M. and Busse, F.H. (1997). Tertiary and quaternary solutions for plane Couette flow. *J. Fluid Mech.* **344**, 137–153.

De Angelis, E., Casciola, C.M. and Piva, R. (20020. DNS of wall turbulence: Dilute polymers and self-sustaining mechanisms. *Comput. & Fluids* **31**, 495–507.

den Toonder, J.M.J., Hulsen, M.A., Kuiken, G.D.C. and Nieuwstadt, F.T.M. (1997). Drag reduction by polymer additives in a turbulent pipe flow: Numerical and laboratory experiments. *J. Fluid Mech.* **337**, 193–231.

Dimitropoulos, C.D., Sureshkumar, R. and Beris, A.N. (1998). Direct numerical simulation of turbulent channel flow exhibiting drag reduction: Effect of the variation of rheological parameters. *J. Non-Newtonian Fluid Mech.* **79**, 433–468.

Dimitropoulos, C.D., Sureshkumar, R., Beris, A.N. and Handler, R.A. (2001). Budgets of Reynolds stress, kinetic energy and streamwise enstrophy in viscoelastic turbulent channel flow. *Phys. Fluids* **13**, 1016–1027.

Donohue, G.L., Tiederman, W.G. and Reischman, M.M. (1972). Flow visualization of the near-wall region in a drag-reducing channel flow. *J. Fluid Mech.* **50**, 559–575.

Draad, A.A., Kuiken, G.D.C. and Nieuwstadt, F.T.M. (1998). Laminar-turbulent transition in pipe flow for Newtonian and Non-Newtonian fluids. *J. Fluid Mech.* **377**, 267–312.

Drazin, P.G. and Reid, W.H. (1981). *Hydrodynamic Stability*. Cambridge University Press, New York.

Dubief, Y., White, C.M., Terrapon, V.E., Shaqfeh, E., Moin, P. and Lele, S.K. (2004). On the coherent drag-reducing and turbulence-enhancing behaviour of polymers in wall flows. *J. Fluid Mech.* **514**, 271–280.

Escudier, M.P., Presti, F. and Smith, S. (1999). Drag reduction in the turbulent pipe flow of polymers. *J. Non-Newtonian Fluid Mech.* **81**, 197–213.

Faisst, H. and Eckhardt, B. (2003). Traveling waves in pipe flow. *Phys. Rev. Lett.* **90**, 224502.

Giles, W.B. and Pettit, W.T. (1967). Stability of dilute viscoelastic flows. *Nature* **216**, 470–472.

Graham, M.D. (2004). Drag reduction in turbulent flow of polymer solutions. In *Rheology Reviews 2004*, D.M. Binding and K. Walters (eds), British Society of Rheology, pp. 143–170.

Hamilton, J.M., Kim, J. and Waleffe, F. (1995). Regeneration mechanisms of near-wall turbulent structures. *J. Fluid Mech.* **287**, 317–148.

Holmes, P., Lumley, J.L. and Berkooz, G. (1996). *Turbulence, Coherent Structures, Dynamical Systems and Symmetry*. Cambridge University Press, New York.

Housiadas, K.D. and Beris, A.N. (2003). Polymer-induced drag reduction: Effects of variations in elasticity and inertia in turbulent viscoelastic channel flow. *Phys. Fluids* **15**, 2369–2384.

Jeong, J., Hussian, F., Schoppa, W. and Kim, J. (1997). Coherent structures near the wall in a turbulent channel flow. *J. Fluid Mech.* **332**, 185–214.

Jiménez, J. and Moin, P. (1991). The minimal flow unit in near wall turbulence. *J. Fluid Mech.* **225**, 221–240.

Jiménez, J. and Simens, M.P. (2001). Low-dimensional dynamics of a turbulent wall flow. *J. Fluid Mech.* **435**, 81–91.

Kawahara, G. and Kida, S. (2001). Periodic motion embedded in plane Couette turbulence: Regeneration cycle and burst. *J. Fluid Mech.* **449**, 291–300.

Lele, S.K. (1992). Compact finite difference schemes with spectral-like resolution. *J. Comput. Phys.* **103**, 16–42.

Lumley, J.L. (1969). Drag reduction by additives. *Annu. Rev. Fluid Mech.* **1**, 367–384.

Lumley, J.L. (1973). Drag reduction in turbulent flow by polymer additives. *J. Polymer Sci.: Macromol. Rev.* **7**, 263–290.

McComb, W.D. (1990). *The Physics of Fluid Turbulence*. Oxford University Press, New York.

Min, T., Yoo, J.Y. and Choi, H. (2001). Effect of spatial discretization schemes on numerical solution of viscoelastic fluid flows. *J. Non-Newtonian Fluid Mech.* **100**, 27–47.

Min, T., Yoo, J.Y., Choi, H. and Joseph, D.D. (2003). Drag reduction by polymer additives in a turbulent channel flow. *J. Fluid Mech.* **486**, 213–238.

Nagata, M. (1986). Bifurcation in Couette flow between almost corotating cylinders. *J. Fluid Mech.* **169**, 229–250.

Nagata, M. (1988). On wavy instabilities of the Taylor-vortex flow between corotating cylinders. *J. Fluid Mech.* **188**, 585–598.

Nagata, M. (1990). Three-dimensional finite amplitude solutions in plane Couette flow: Bifurcation from infinity. *J. Fluid Mech.* **217**, 519–527.

Pope, S.B. (2000). *Turbulent Flows*. Cambridge University Press, New York.

Ptasinski, P.K., Boersma, B.J., Nieuwstadt, F.T.M., Hulsen, M.A., Brule, B.H.A.A.V.D. and Hunt, J.C.R. (2003). Turbulent channel flow near maximum drag reduction: Simulations, experiments and mechanisms. *J. Fluid Mech.* **490**, 251–291.

Robinson, S.K. (1991). Coherent motions in the turbulent boundary layer. *Annu. Rev. Fluid Mech.* **23**, 601–639.

Sibilla, S. and Baron, A. (2002). Polymer stress statistics in the near-wall turbulent flow of a drag-reducing solution. *Phys. Fluids* **14**, 1123–1136.

Soria, J., Sondergaard, R., Cantwell, B.J., Chong, M.S. and Perry, A.E. (1994). A study of the fine-scale motions of incompressible time-developing mixing layers. *Phys. Fluids* **6**, 871–884.

Stone, P.A. (2004). Ph.D. Thesis, University of Wisconsin-Madison.

Stone, P.A. and Graham, M.D. (2003). Polymer dynamics in a model of the turbulent buffer layer. *Phys. Fluids* **15**, 1247–1256.

Stone, P.A., Waleffe, F. and Graham, M.D. (2002). Toward a structural understanding of turbulent drag reduction: Nonlinear coherent states in viscoelastic shear flows. *Phys. Rev. Lett.* **89**, 208301.

Stone, P.A., Roy, A., Larson, R.G., Waleffe, F. and Graham, M.D. (2004). Polymer drag reduction in exact coherent structures of plane shear flow. *Phys. Fluids* **16**, 3470–3482.

Strogatz, S.H. (1994). *Nonlinear Dynamics and Chaos: With Applications to Physics, Biology, Chemistry and Engineering*. Addison Wesley, New York.

Sureshkumar, R. and Beris, A.N. (1995). Effect of artificial stress diffusivity on the stability of numerical calculations and the flow dynamics of time-dependent viscoelastic flows. *J. Non-Newtonian Fluid Mech.* **60**, 53–80.

Sureshkumar, R., Beris, A.N. and Handler, R. (1997). Direct numerical simulation of the turbulent channel flow of a polymer solution. *Phys. Fluids* **9**, 743–755.

Terrapon, V.E., Dubief, Y., Moin, P., Shaqfeh, E.S.G. and Lele, S.K. (2004). Simulated polymer stretch in a turbulent flow using Brownian dynamics. *J. Fluid Mech.* **504**, 61–71.

Tiederman, W.G., Luchik, T.S. and Bogard, D.G. (1985). Wall-layer structure and drag reduction. *J. Fluid Mech.* **156**, 419–437.

Toh, S. and Itano, T. (2003). A periodic-like solution in channel flow. *J. Fluid Mech.* **481**, 67–76.

Virk, P.S. (1975). Drag reduction fundamentals. *AIChE J.* **21**, 225–256.

Waleffe, F. (1997). On a self-sustaining process in shear flows. *Phys. Fluids* **9**, 883–900.

Waleffe, F. (1998). Three-dimensional coherent states in plane shear flows. *Phys. Rev. Lett.* **81**, 4140–4143.

Waleffe, F. (2001). Exact coherent structures in channel flow. *J. Fluid Mech.* **435**, 93–102.

Waleffe, F. (2003). Homotopy of exact coherent structures in plane shear flows. *Phys. Fluids* **15**, 1517–1534.

Waleffe, F. and Wang, J. (2005). Transition threshold and the self-sustaining process. In In *Laminar Turbulent Transition and Finite Amplitude Solutions*, Proceedings of the IUTAM Symposium, Bristol, UK, 9–11 August 2004, T. Mullin and R.R. Kerswell (eds), Springer, Dordrecht, pp. 85–106 (*this volume*).

Walker, D.T. and Tiederman, W.G. (1990). Turbulent structure in a channel flow with polymer injection at the wall. *J. Fluid Mech.* **218**, 377–403.

Wedin, H. and Kerswell, R.R. (2004). Exact coherent structures in pipe flow: Travelling wave solutions. *J. Fluid Mech.* **508**, 333–371.

Wei, T. and Willmarth, W.W. (1992). Modifying turbulent structure with drag-reducing polymer additives in turbulent channel flows. *J. Fluid Mech.* **245**, 619–641.

White, W.D. and McEligot, D.M. (1970). Transition of mixtures of polymers in a dilute aqueous solution. *ASME J. Basic Engrg.* **92**, 411–418.

SUBCRITICAL INSTABILITIES IN PLANE COUETTE FLOW OF VISCO-ELASTIC FLUIDS

Alexander N. Morozov and Wim van Saarloos
Instituut-Lorentz for Theoretical Physics, LION, Leiden University, P.O. Box 9506, 2300 RA Leiden, The Netherlands

Abstract A non-linear stability analysis of plane Couette flow of the Upper-Convected Maxwell model is performed. The amplitude equation describing time-evolution of a finite-size perturbation is derived. It is shown that above the critical Weissenberg number, a perturbation in the form of an eigenfunction of the linearized equations of motion becomes subcritically unstable, and the threshold value for the amplitude of the perturbation decreases as the Weissenberg number increases.

Keywords: visco-elastic flows, subcritical instabilities, amplitude equation.

1. INTRODUCTION

In the last decades, stability of flows of polymers, emulsions, colloids, etc., has attracted wide attention when it was discovered that such flows can exhibit hydrodynamic instabilities and even become turbulent at very small Reynolds numbers (Larson et al., 1990; McKinley et al., 1991; Groisman and Steinberg, 2000, 2004). Unlike Newtonian turbulence, where inertia plays a destabilizing role, this *elastic turbulence* or *turbulence without inertia* (Larson, 2000) has its origin in the visco-elastic properties of the fluid. It has become a challenge to find the mechanism of the elastic instabilities and transition to turbulence.

The non-Newtonian behaviour of complex fluids originates from the interaction between the flow and the internal structure of the fluid. In water, for example, external flows do not typically disturb molecular motion since the molecular and flow velocity- and time-scales are well separated, while in complex flows polymers get stretched, emulsion and colloidal clusters get deformed and break, vesicles change their shapes, etc. Since these interactions are partly reversible (e.g. the polymers return to their equilibrium conformation releasing accumulated stress) and depend on the deformation history, the fluid acquires memory and becomes visco-elastic. Naturally, this is reflected in the equations of motion for complex fluids: the Navier–Stokes equation (written in dimen-

T. Mullin and R.R. Kerswell (eds), Laminar Turbulent Transition and Finite Amplitude Solutions, 313–330.
© 2005 *Springer. Printed in the Netherlands.*

sionless units)

$$Re\left[\frac{\partial \mathbf{v}}{\partial t} + (\mathbf{v}\cdot\nabla)\,\mathbf{v}\right] = -\nabla p - \nabla\cdot\boldsymbol{\tau}$$

is supplemented by a *constitutive equation* – a relation between the stress tensor $\boldsymbol{\tau}$ and the velocity-gradient tensor $(\nabla\mathbf{v})$, which is no longer a linear Newtonian equation

$$\boldsymbol{\tau} = -\left[(\nabla\mathbf{v}) + (\nabla\mathbf{v})^{\dagger}\right],$$

but usually is a non-linear PDE in space and time;[1] the dagger † denotes the transposed matrix.

The main difference between Newtonian and visco-elastic equations of motion is the presence of additional non-linearity in the constitutive equation. The inertial non-linearity $Re\,(\mathbf{v}\cdot\nabla)\,\mathbf{v}$, which is responsible for instabilities and turbulence in Newtonian liquids, is of small significance for visco-elastic fluids (especially for dense polymer solutions and melts) since their large viscosity results in small Reynolds numbers $Re \sim 10^{-4}$–10^{1}. Therefore, the non-linear behaviour of the equations of motion is dominated by the elastic non-linearity, the strength of which is controlled by a dimensionless Weissenberg number $Wi = \dot{\gamma}\lambda$, where $\dot{\gamma}$ is the typical shear rate, and λ is the relaxation time of the fluid. When the Weissenberg number becomes comparable to unity, this non-linearity gives rise to non-trivial rheological phenomena: shear-rate dependent shear viscosity, and the normal-stress effect: in plane shear $v_x = \dot{\gamma}y$, the normal-stress difference $\tau_{yy} - \tau_{xx}$ is not zero as for Newtonian fluids, but grows as $\dot{\gamma}^2$ for small Wi. At larger Weissenberg numbers, the elastic non-linearity causes hydrodynamic instabilities and, possibly, transition to turbulence.

The mechanism of linear elastic instability was identified for flows with curved stream-lines (Larson et al., 1990; Joo and Shaqfeh, 1992). One of the classical examples of such a flow is realized in Taylor–Couette cell where fluid fills the gap between two coaxial cylinders made to rotate with respect to each other. In the laminar state, the fluid moves around the cylinder axis and the elastic or *hoop* stresses act on polymer molecules stretching them along the circular stream-lines and exerting extra pressure towards the inner cylinder in consequence of the normal-stress effect. When these stresses overcome viscous friction, the laminar state becomes linearly unstable – any infinitesimal perturbation will push a polymer from the circular stream-lines and create a secondary flow in the form of Taylor vortices. Pakdel and McKinley (1996) generalized this mechanism to arbitrary flows and proposed that there exists a universal relation between the properties of the fluid and the flow geometry which determines the conditions of the linear instability. They argued that the critical Weissenberg number is related to the characteristic curvature of the flow stream-lines and that the linear instability disappears when the curvature goes to zero. The known results on the visco-elastic instabilities in Taylor–

Couette (Larson et al., 1990), cone-and-plate and parallel plate (McKinley et al., 1991), Dean and Taylor–Dean (Joo and Shaqfeh, 1992) flows are in agreement with this *curved stream-lines – linear instability* paradigm.

The situation is different for visco-elastic parallel shear flows. There is no general agreement on whether flows like plane Couette or pipe flow do in fact become unstable. The only results available are on the linear stability of these flows. For essentially all studied visco-elastic models, laminar plane Couette flow is linearly stable (Gorodtsov and Leonov, 1967; Renardy and Renardy, 1986; Renardy, 1992; Wilson et al., 1999) (note the exception Grillet et al., 2002). In the case of pipe flow, the linear stability was demonstrated numerically by Ho and Denn (1978) for any value of the Weissenberg and Reynolds numbers. Therefore, it has become common knowledge that the parallel shear flows of fluids obeying simple visco-elastic models (UCM, Oldroyd-B, etc.) are linearly stable, in agreement with the *curved stream-lines – linear instability* paradigm. Clearly, if an instability does occur in practice, it has to be non-linear.

At the moment, there has been no experiment that would clearly establish the presence or absence of a bulk hydrodynamic instability in parallel visco-elastic shear flows. One of a few indirect indications that a bulk instability might occur in pipe flow comes from the famous melt-fracture problem (Petrie and Denn, 1976; Denn, 1990, 2001), which arises in extrusion of a dense polymer solution or melt through a thin capillary. There, when the extrusion rate exceeds some critical value, the surface of the extrudate becomes distorted and the extrudate might even break, giving the name to the phenomenon. It is possible that this is a manifestation of an instability taking place inside the capillary, though other mechanisms (such as stick-slip, influence of the inlet, etc.) have been proposed (Petrie and Denn, 1976; Denn, 1990, 2001). Recently, we presented arguments for the bulk instability being related to the melt-fracture phenomenon (Meulenbroek et al., 2003, 2004; Bertola et al., 2003), but the issue stays controversial. There is also some evidence for non-linear parallel shear flow instabilities from numerical simulations of visco-elastic hydrodynamic equations (Atalik and Keunings, 2002). Partly because the numerical schemes used to solve these equations are known to break down when elastic stresses become large ($Wi \gtrsim 1$) – the so-called *high Weissenberg number problem* (Owens and Phillips, 2002) – it is open to debate whether an observed phenomenon is due to a numerical or a true physical instability.

In this paper we argue that visco-elastic plane Couette flow does exhibit a subcritical instability as can be seen from the following argument. The laminar velocity profiles of the parallel shear flows have straight stream-lines, and, therefore, their linear stability is in agreement with the *curved stream-lines – linear instability* paradigm. The linear theory predicts that a small perturbation superimposed on top of the laminar flow will decay in time with the decay rate

depending on the Weissenberg number. When *Wi* becomes larger than one, the decay time becomes comparable with the elastic relaxation time λ, and the perturbation becomes long-living. Thus, on short time-scales, the superposition of the laminar flow and the slowly-decaying perturbation can be viewed as a new basis profile *with* curved stream-lines. Applying the same *curved stream-lines – linear instability* paradigm to the perturbed streamlines, we conclude that this new flow can become linearly unstable. The instability requires a subsequent creation of two perturbations, and thus is non-linear. Since the initial perturbation has to be strong enough to become unstable, there exists a finite-amplitude threshold for the transition, which becomes smaller as the Weissenberg number increases. This scenario resembles transition to turbulence in parallel shear flows of Newtonian fluids. There as well, one encounters the absence of the linear instability, and a subcritical transition with the threshold going down with the Reynolds number (Schmid and Henningson, 2001; Hof et al., 2003).

In order to check our hypothesis we perform the non-linear stability analysis of the Upper-Convected Maxwell (UCM) model. The method we employ is somewhat similar to what was used by Stuart (1960) and Herbert (1980) for Newtonian flows. We start from the laminar plane Couette flow and perturb it by a finite-size disturbance chosen to be in the form of an eigenmode of the linear part of the equations of motion. We then derive an amplitude equation that determines the time evolution of the disturbance. The instability is found for given eigenmode, if there is such an initial value of the amplitude of the disturbance that it will grow in time and, possibly, saturate. In the following sections we present the derivation and main results of our analysis.

2. ASYMPTOTIC EXPANSION

Let us consider plane Couette flow of a visco-elastic fluid. The fluid is confined in-between two plates a distance $2d$ apart moving with equal velocities v_0 in the opposite directions. We use the standard convention for the coordinates with x, y, and z referring to the streamwise, gradient, and spanwise directions, respectively. We define the Weissenberg $Wi = \lambda v_0/d$ and the Reynolds numbers $Re = \rho v_0 d/\eta$, where ρ is the density and η is the viscosity of the fluid; d is used as the unit of length, d/v_0 as the unit of time, and the stress tensor is scaled with $\eta v_0/d$.

The equations of motion include the Navier–Stokes equation

$$Re\left[\frac{\partial \mathbf{v}}{\partial t} + (\mathbf{v}\cdot\nabla)\,\mathbf{v}\right] = -\nabla p - \nabla\cdot\boldsymbol{\tau}, \tag{1}$$

and the incompressibility condition

$$\nabla\cdot\mathbf{v} = 0, \tag{2}$$

where p is the pressure, and $\boldsymbol{\tau}$ is the visco-elastic stress tensor. To close this system of equations one needs to specify the constitutive relation, and in this work we are going to use the Upper-Convected Maxwell (UCM) model

$$\boldsymbol{\tau} + Wi\left[\frac{\partial \boldsymbol{\tau}}{\partial t} + \mathbf{v}\cdot\nabla\boldsymbol{\tau} - (\nabla\mathbf{v})^{\dagger}\cdot\boldsymbol{\tau} - \boldsymbol{\tau}\cdot(\nabla\mathbf{v})\right] = -\left[(\nabla\mathbf{v}) + (\nabla\mathbf{v})^{\dagger}\right] \quad (3)$$

– one of the simplest non-linear models available. Although it does not reproduce realistic features of dense polymer solutions (Bird et al., 1987), it does predict the normal-stress effect, which is, as we have argued above, at the origin of the non-linear instabilities in parallel shear flows of visco-elastic fluids. Since our purpose is to demonstrate that such an instability *can* occur, this simple model will suffice.

As usually, we split the hydrodynamic fields $\mathbf{v}$ and $\boldsymbol{\tau}$ in two parts – the laminar value and the perturbation field:

$$\mathbf{v} = y\,\mathbf{e}_x + \mathbf{v}',$$
$$\tau_{ij} = -2\,Wi\;\delta_{ix}\delta_{jx} - (\delta_{ix}\delta_{jy} + \delta_{iy}\delta_{jx}) + \tau'_{ij}.$$

Next, we introduce the perturbation vector $V = \{v'_i, \tau'_{ij}, p\}^{\dagger}$ and rewrite the system (1)–(3) in the compact form

$$\hat{\mathcal{L}}\,V + \hat{A}\frac{\partial V}{\partial t} = N\,(V, V)\,, \quad (4)$$

where $\hat{\mathcal{L}}$ and N represent the linear operator and the quadratic non-linearity in (1)–(3), and $\hat{A}$ is a constant diagonal matrix. The explicit expressions for $\hat{\mathcal{L}}$, N and $\hat{A}$ are given in Appendix A.

Our stability analysis of Equation (4) is based on the eigenfunctions $V_0^{(n)}$ of the linear operator $\hat{\mathcal{L}}$:

$$\hat{\mathcal{L}}\left(e^{i(k_x x + k_z z)}V_0^{(n)}(y)\right) = -\lambda_n e^{i(k_x x + k_z z)}V_0^{(n)}(y). \quad (5)$$

The minus sign in the definition of the eigenvalues λ_n is chosen in such a way that $e^{\lambda_n t}e^{i(k_x x + k_z z)}V_0^{(n)}(y)$ is a solution of the linear problem $\left(\hat{\mathcal{L}} + \hat{A}\frac{\partial}{\partial t}\right)V = 0$. There are several kinds of eigenfunctions of the UCM plane Couette flow and their form and number will be discussed in Section 3. Here, we will focus on a particular eigenfunction $e^{i(k_x x + k_z z)}V_0(y)$ and assume that the non-linear dynamics of Equation (4) is dominated by V_0. Then, the solution to Equation (4) can be approximated by

$$V\,(\mathbf{r}, t) = \Phi(t)e^{i(k_x x + k_z z)}V_0(y) + \Phi^*(t)e^{-i(k_x x + k_z z)}V_0^*(y)$$
$$+U_0(y, t) + \sum_{n=2}^{\infty}\left[U_n(y, t)e^{in(k_x x + k_z z)} + U_n^*(y, t)e^{-in(k_x x + k_z z)}\right], \quad (6)$$

where we have introduced the time-dependent amplitude $\Phi(t)$; * denotes complex conjugation. Moreover, we notice that the higher order harmonics U_n can only be generated by at least n non-linear self-interactions of the linear mode and have, therefore, the following form:

$$\begin{aligned} U_0(y,t) &= |\Phi(t)|^2 u_0^{(2)}(y) + |\Phi(t)|^4 u_0^{(4)}(y) + \cdots, \\ U_2(y,t) &= \Phi^2(t) u_2^{(2)}(y) + \Phi^2(t)|\Phi(t)|^2 u_2^{(4)}(y) + \cdots, \\ U_3(y,t) &= \Phi^3(t) u_3^{(3)}(y) + \cdots, \\ &\cdots \end{aligned} \tag{7}$$

where $u_0^{(2)}(y)$, $u_0^{(4)}(y)$, etc., are unknown functions. Substituting the ansatz (6) into Equation (4) and separating the terms proportional to $e^{i(k_x x + k_z z)}$ we obtain

$$\begin{aligned} \left(\frac{d\Phi}{dt} - \lambda\Phi\right) e^{i(k_x x + k_z z)} V_0(y) &= \bar{N}\left(\Phi e^{i(k_x x + k_z z)} V_0(y), U_0(y,t)\right) \\ &+ \bar{N}\left(\Phi^* e^{-i(k_x x + k_z z)} V_0^*(y), e^{2i(k_x x + k_z z)} U_2(y,t)\right) \\ &+ \sum_{n=2}^{\infty} \bar{N}\left(e^{(n+1)i(k_x x + k_z z)} U_{n+1}(y,t), e^{-ni(k_x x + k_z z)} U_n^*(y,t)\right), \end{aligned} \tag{8}$$

where $\bar{N}(A,B) = N(A,B) + N(B,A)$. The evolution equation for the amplitude Φ can be derived with the help of the eigenmode of the adjoint operator $\hat{\mathcal{L}}^\dagger$, which is defined via

$$\langle V_1 | \hat{\mathcal{L}} V_2 \rangle = \langle \hat{\mathcal{L}}^\dagger V_1 | V_2 \rangle, \tag{9}$$

where the scalar product is given by

$$\langle V_1 | V_2 \rangle = \lim_{L_x, L_z \to \infty} \frac{1}{2L_x} \int_{-L_x}^{L_x} dx \, \frac{1}{2} \int_{-1}^{1} dy \, \frac{1}{2L_z} \int_{-L_z}^{L_z} dz \, \left(V_1^*, V_2\right), \tag{10}$$

and $(A,B) = \sum_i A_i B_i$. The eigenmodes of the adjoint operator

$$\hat{\mathcal{L}}^\dagger \left(e^{i(k_x x + k_z z)} W_0^{(m)}(y)\right) = -\lambda_m e^{i(k_x x + k_z z)} W_0^{(m)}(y) \tag{11}$$

are orthogonal to the eigenfunctions of the linear operator $\hat{\mathcal{L}}$ unless their eigenvalues coincide $\lambda_n = \lambda_m$ (see Equation (5)). Using this property, we project Equation (8) onto the eigenfunction V_0 to obtain the amplitude equation

$$\frac{d\Phi}{dt} = \lambda\Phi + C_3\Phi|\Phi|^2 + C_5\Phi|\Phi|^4 + C_7\Phi|\Phi|^6 + C_9\Phi|\Phi|^8 + \cdots, \tag{12}$$

where the coefficients are given by

$$\begin{aligned} C_3 = \frac{1}{\Delta} \Bigg\langle e^{i(k_x x + k_z z)} W_0(y) \Bigg| \bar{N}\left(e^{i(k_x x + k_z z)} V_0(y), u_0^{(2)}(y)\right) \\ + \bar{N}\left(e^{-i(k_x x + k_z z)} V_0^*(y), e^{2i(k_x x + k_z z)} u_2^{(2)}(y)\right) \Bigg\rangle, \end{aligned} \tag{13}$$

$$C_5 = \frac{1}{\Delta}\Bigg\langle e^{i(k_x x+k_z z)} W_0(y) \Bigg| \bar{N}\left(e^{i(k_x x+k_z z)} V_0(y), u_0^{(4)}(y)\right)$$
$$+\bar{N}\left(e^{-i(k_x x+k_z z)} V_0^*(y), e^{2i(k_x x+k_z z)} u_2^{(4)}(y)\right)$$
$$+\bar{N}\left(e^{-2i(k_x x+k_z z)} u_2^{(2)*}(y), e^{3i(k_x x+k_z z)} u_3^{(3)}(y)\right)\Bigg\rangle, \qquad (14)$$
$$\ldots$$

with $\Delta = \langle e^{i(k_x x+k_z z)} W_0(y) | e^{i(k_x x+k_z z)} V_0(y)\rangle$. The expressions for higher coefficients C_7, C_9, etc., are derived in the similar way. The equations for the unknown functions $u_0^{(2)}(y)$, $u_0^{(4)}(y)$ etc. are also derived by substituting the ansatz (6) into Equation (4) and are given in Appendix B.

In this work we are going to calculate the first five coefficients $C_3 - C_{11}$ of Equation (12) for plane Couette flow of a UCM fluid. In the next section we present the results for various eigenfunctions and discuss their non-linear stability.

3. RESULTS

Since our analysis is based on the eigenfunctions of the linear operator $\hat{\mathcal{L}}$, we first discuss the structure of the linear spectrum $\{\lambda_n\}$ for given Reynolds and Weissenberg numbers.

The eigenvalues of the UCM plane Couette flow problem can be separated in two groups: the "purely elastic" eigenvalues and "elastic-inertial" ones. The first group consists of a pair of complex conjugated eigenvalues and the so-called "continuous spectrum". The eigenvalues from this group are "purely elastic" in the sense that they exist even in the limit $Re = 0$. The pair was discovered by Gorodtsov and Leonov (1967) for two-dimensional purely elastic plane Couette flow and can be generalized to the three-dimensional case:

$$\lambda^{(GL)} = \epsilon \pm i\omega \qquad (15)$$
$$\epsilon = \frac{1}{D}\left[k_x\, k\, q\ \sin(2\, Wi\, k_x) - \frac{1}{2}\, Wi\, k_x^2 \sinh(2\, k) \sinh(2\, q)\right]$$
$$\omega^2 = -\epsilon^2 + k_x^2 - \frac{k_x^2}{D}\Big[2\, k\, q\ \cos(2\, Wi\, k_x) + q\ \cosh(2\, q) \sinh(2\, k)$$
$$-\frac{1}{2}\sinh(2\, q)\,(2\, k\ \cosh(2\, k) + \sinh(2\, k))\Big],$$

where

$$k = \sqrt{k_x^2 + k_z^2}\ , \qquad q = \sqrt{(1 + Wi^2)k_x^2 + k_z^2},$$
$$D = k\, q\Big(\cos 2\, Wi\, k_x - \cosh(2\, k) \cosh(2\, q)\Big) + q^2\ \sinh(2\, k) \sinh(2\, q)\ .$$

For small Reynolds numbers, the Gorodtsov–Leonov eigenvalues pick up corrections of order Re. This pair of eigenvalues corresponds to the three-dimensional vortices localized at the walls and traveling along them in opposite directions. An example of the velocity field generated by such an eigenmode is plotted in Figure 1 for $\lambda^{(GL)} = -0.9273 + 0.7279i$, $Wi = 1$, $Re = 0.1$, $k_x = 1$ and $k_z = 1$.

The continuous spectrum contains infinitely many eigenvalues in the form (Renardy and Renardy, 1986; Wilson et al., 1999)

$$\lambda^{(C)} = -\frac{1}{Wi} + i\,\omega\ , \qquad \omega \in [-k_x, k_x]. \tag{16}$$

and, as was shown by Graham (1998), is unphysical. It has its origin in the fact that polymers with non-linear relation between the degree of extension and the force necessary to achieve this extension behave as Hookean dumbbells upon linearization, while the latter can be infinitely stretched in extensional flow at finite Weissenberg numbers (Bird et al., 1987). Indeed, Graham (1998) has found that the stresses of the eigenmodes corresponding to $\lambda^{(C)}$ have singularities and are unrealistic. These eigenvalues will be discarded in our work.

The second group contains infinitely many eigenvalues that disappear in the limit of $Re \to 0$. The eigenvalues from this group have their real parts close to $1/2Wi$, while their imaginary parts scale as $1/\sqrt{Re}$; they can be ordered according to an integer n that gives the number of wiggles in the y-direction. The "elastic-inertial" eigenvalues can further be split in two infinite subsets, corresponding to two- and three-dimensional vortices. An example of the 3D vortices is given in Figure 2. The difference between the structure of the 2D and 3D vortices becomes apparent if $k_x = 0$: they reduce to the streamwise streaks and a combination of the streamwise streaks and vortices, respectively.

All of the eigenvalues discussed have negative real parts and are, therefore, linearly stable.

Now we turn to the non-linear stability analysis of the eigenmodes discussed above. For each eigenvalue λ we calculate the coefficients C's in Equation (12) with the help of Equations (13, 14, 11) and the equations from Appendix B. This calculation requires solution of several linear inhomogeneous ODEs of the fourth order. For the special case of the inertialess ($Re = 0$) Gorodtsov–Leonov eigenmode we were able to calculate the coefficients C_3 and C_5 analytically. The higher coefficients and the coefficients for the other eigenmodes involve long and cumbersome expressions and were treated numerically. Since the ODEs from Appendix B are very stiff, we solved them using the fourth-order Runge–Kutta method with reortonormalization performed at each step (Godunov, 1961; Conte, 1966). Our code was tested against the analytical result for the inertialess Gorodtsov–Leonov eigenmode.

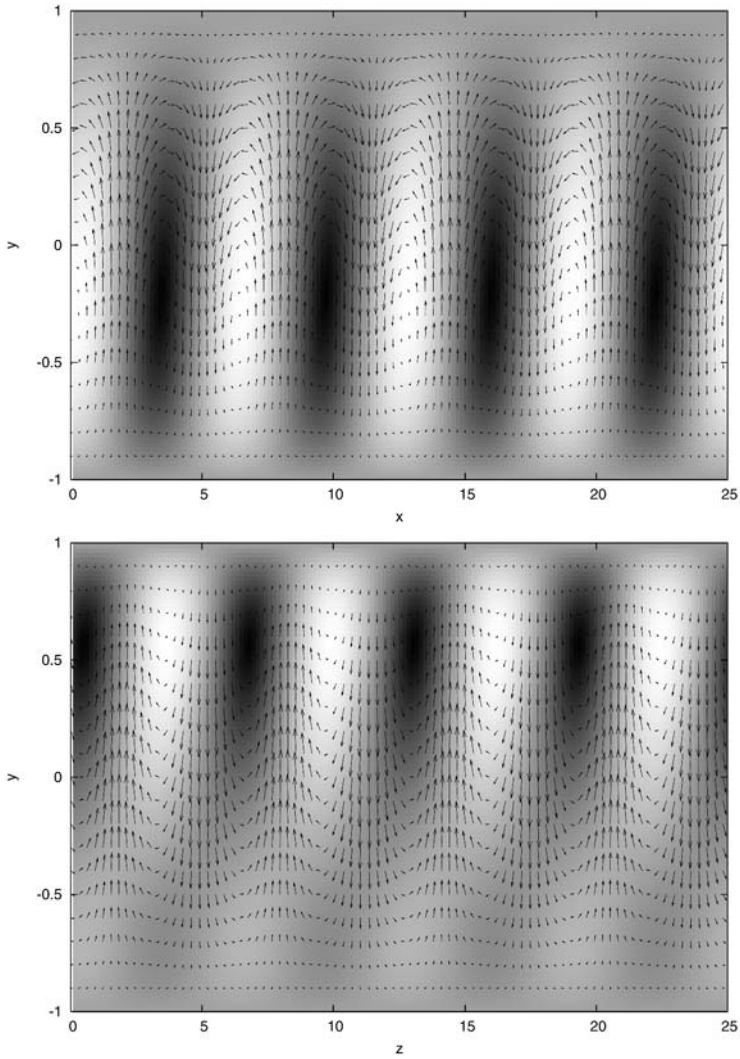

Figure 1. Velocity field of the Gorodtsov–Leonov eigenmode with $\lambda^{(GL)} = -0.9273 + 0.7279i$, $Wi = 1$, $Re = 0.1$, $k_x = 1$ and $k_z = 1$. The eigenmode is mostly localized near one wall, while the eigenmode with the complex-conjugated eigenvalue $\lambda^{(GL)} = -0.9273 - 0.7279i$ occupies the other. *Top:* velocity field in the xy-plane. The shade of gray represents the third velocity component; *Bottom:* The same in the yz-plane.

The instability threshold $|\Phi_*|$ is given by the amplitude of the traveling-wave solution, $\Phi(t) = |\Phi_*|\, e^{i\,\Omega\, t}$, of Equation (12)

$$S_m(|\Phi_*|) \equiv Re\left(\lambda + C_3|\Phi_*|^2 + \cdots + C_{2m+1}|\Phi_*|^{2m}\right) = 0. \qquad (17)$$

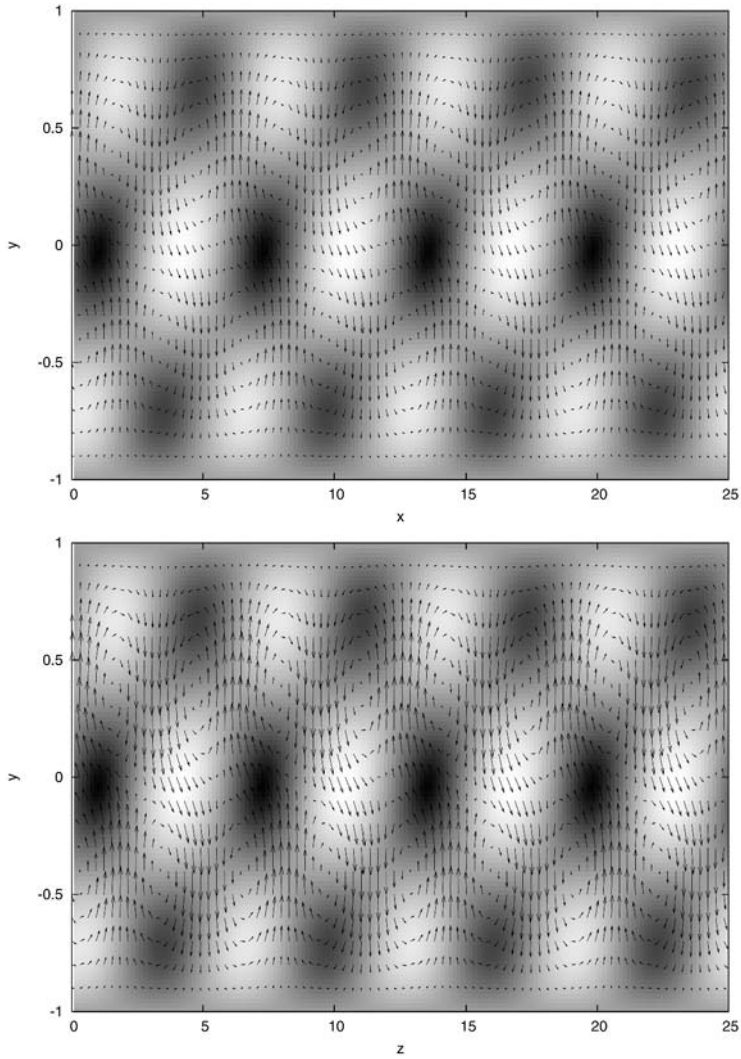

Figure 2. Velocity field of the "elastic-inertial" eigenmode with $\lambda = -0.4924 + 14.9384i$, $Wi = 1$, $Re = 0.1$, $k_x = 1$ and $k_z = 1$. *Top:* velocity field in the xy-plane. The shade of gray represents the third velocity component; *Bottom:* The same in the yz-plane.

However, one has to be careful because it is not guaranteed that the asymptotic series (17) converges. Thus, the amplitude expansion for the Newtonian channel flow was shown to suffer from convergence problems (Herbert, 1980). Therefore, we solve the sequence of equations $S_2 = 0, \ldots, S_5 = 0$ in order to check that their solutions do converge to some value $|\Phi_*|$.

The results for the Gorodtsov–Leonov eigenmodes are shown in Figures 3 and 4. The most important feature of these curves is that they show the ex-

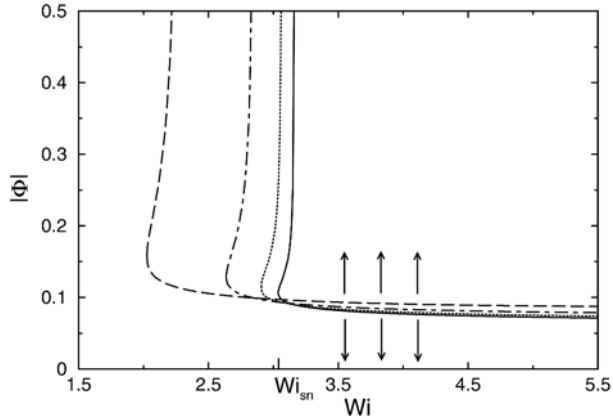

Figure 3. Steady-state amplitude Φ for $k_x = 1$ and $k_z = 1$ versus Weissenberg number Wi. The curves from left to right represent the solutions to $S_2 = 0, \ldots, S_5 = 0$, respectively. The ratio $Re = 10^{-3} Wi$ was kept constant.

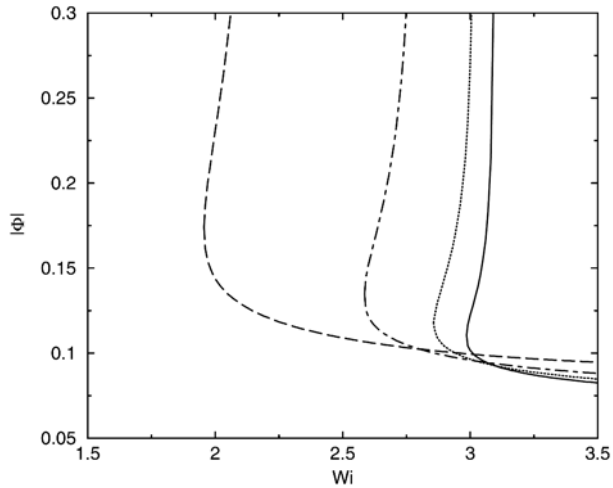

Figure 4. The same as Figure 3 for $k_x = 2$, $k_z = 2$, and $Re = 10^{-1} Wi$.

istence of a subcritical instability for Weissenberg numbers larger than the saddle-node value Wi_{sn}. As the arrows indicate, for $Wi > Wi_{\mathrm{sn}}$ the lower branch of the curves denotes the critical amplitude – amplitudes larger than this value will grow in time. Note that the instability threshold is small (consistent with the assumption $|\Phi| < 1$), and goes down as Wi increases. The inclusion of higher-order terms causes the whole curve to shift to the right, though the shift becomes roughly two times smaller with every coefficient included, suggesting convergence.

Table 1. Real parts of the coefficients C's for $k_x = 2$, $k_z = 2$, and $Re = 10^{-1}Wi$; ϵ and ω denote the real and imaginary parts of the Gorodtsov–Leonov eigenvalue, respectively.

Wi	ϵ	ω	C_3	$C_5 \times 10^{-2}$	$C_7 \times 10^{-5}$	$C_9 \times 10^{-7}$	$C_{11} \times 10^{-9}$
1.50	0.562	1.757	39.549	–21.322	–5.723	–7.617	–5.683
2.00	0.394	1.796	26.433	–3.571	–2.020	–3.169	–3.162
2.20	0.350	1.809	23.802	–0.011	–1.308	–2.344	–2.741
2.30	0.331	1.815	22.720	1.376	–1.019	–1.986	–2.495
2.80	0.259	1.841	18.642	5.740	–0.001	–0.517	–0.972
2.90	0.248	1.845	18.000	6.249	0.141	–0.276	–0.641
3.00	0.238	1.849	17.399	6.672	0.267	–0.053	–0.312
3.05	0.233	1.851	17.112	6.855	0.324	0.053	–0.149
3.10	0.228	1.853	16.833	7.021	0.378	0.155	0.012
5.50	0.113	1.912	9.096	6.926	1.112	2.243	4.802

While the lower branch of each curves gives the minimal amplitude of the disturbance sufficient to destabilize the laminar flow, the upper branch determines the saturated value of Φ after the transition. Surprisingly, it diverges in the vicinity of the saddle-node where the highest coefficient in the expansion changes sign (see Table 1). There could be several reasons for that. First, it may indicate that the non-linear state in the form of Equation (6) is unstable and will undergo a transition to another coherent state or to turbulence. Second, although we consider this unlikely, it may be that the UCM model cannot capture this state. Finally, and most likely, it may be that the upper branch lies beyond the radius of convergence of (12).

In Figure 5 we plot the lowest Weissenberg number for which the non-linear instability is possible, or the position of the saddle-node Wi_{sn}, as a function of the wave-vectors k_x and k_z. It clearly shows that the saddle-node position is only a weak function of the wave-vectors, and a large number of modes with different k_x's and k_z's is non-linearly unstable for given $Wi > 2.1$. Even if each individual mode saturates at a given value of Φ, we cannot predict the behaviour of the superposition of a large number of such modes. They might stabilize each other to form a three-dimensional coherent state, or they can become chaotic very close to or even at the instability.

Finally, we turn to the discussion of the "elastic-inertial" eigenmodes. We have performed calculations for the first ten of these modes and have found that for all of them the real parts of the coefficients C's are negative. Hence, we do not find a subcritical instability if the perturbation is chosen in the form of the "elastic-inertial" eigenmodes. An interesting question is whether these eigenmodes contribute to the visco-elastic exact coherent state (if such a state

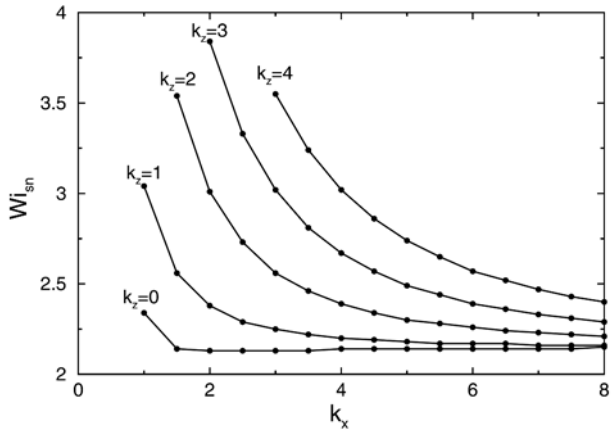

Figure 5. The saddle-node Weissenberg number versus k_x for different values of k_z; $Re = 10^{-3}Wi$.

exists!), or whether this state is a non-linear superposition of the Gorodtsov–Leonov eigenmodes only. To this moment, it remains an open question.

4. DISCUSSION

We have presented the non-linear stability analysis of the visco-elastic plane Couette flow of the UCM model. We have derived the amplitude equation describing the time-evolution of a perturbation chosen in the form of an eigenmode of the linear operator, and have shown that for the purely elastic Gorodtsov–Leonov eigenmodes, there exists a subcritical instability for the Weissenberg numbers $Wi > 2.1$. The other eigenmodes are found to be non-linearly stable.

As Figure 5 shows, the saddle-node Weissenberg number is a weak function of the wave-vectors k_x and k_z and an infinite number of the Gorodtsov–Leonov eigenmodes will become unstable for $Wi > 2.1$. The nature of the state that will result from the non-linear interactions of these modes is unknown. The possibilities include a turbulent state, a stable 3D coherent state and a linearly unstable 3D coherent state, in which case it will be a visco-elastic analog of the Newtonian Nagata solutions (Nagata, 1990). If such a state exists and is linearly unstable, there is an intriguing possibility that it will take part in the visco-elastic version of the self-sustaining cycle proposed by Waleffe (1997).

The previous studies of the visco-elastic plane Couette flow were inconclusive but might well be taken to be in agreement with our findings though they also were not able to capture the non-linear state after the instability. Atalik and Keunings (2002) performed 2D direct numerical simulations of the Oldroyd-B plane Couette flow, and have shown that it is stable for Weissenberg numbers

smaller than 2. Moreover, they reported appearance of numerical instabilities for Weissenberg numbers larger than 2. It is tempting to speculate that the numerical instability observed by Atalik and Keunings is a manifestation of the underlying physical instability. Ashrafi and Khayat (2000) have developed a low-dimensional Galerkin projection for the Johnson–Segalman fluid, and have shown that one-dimensional disturbances in x-direction become unstable. There as well, one cannot draw a conclusion about the resulting state in view of the special form of the perturbation and the very small number of modes included.

Finally, we want to make a general comment on the application of the amplitude expansion to the non-linear stability analysis of the visco-elastic flows. Surely, this method is crude for it (a) ignores interactions between various eigenmodes, (b) assumes "slaving" (see Section 3 for details), (c) requires amplitude of the perturbation to be small, etc. It is incomparable in conclusiveness and accuracy with the modern methods used in Newtonian instabilities. These methods, however, are difficult to employ for the visco-elastic instabilities as they rely heavily on the insights from numerical and experimental studies. Let us repeat that there has been no experimental or numerical study of the visco-elastic parallel shear flows. The low-dimensional models are also difficult to derive in the visco-elastic case, as we simply do not know what kind of coherent structures may get involved. Experiments in Taylor–Couette flow of Groisman and Steinberg (1997) and numerical study of Kumar and Graham (2000) suggest that the coherent structures in visco-elastic plane Couette flow may be different from the Newtonian counterparts. Therefore, the present study is a first step towards understanding visco-elastic instabilities in parallel shear flows.

APPENDIX A

As we have mentioned above, the equations of motion (1)–(3) can be written in the matrix form

$$\hat{\mathcal{L}}\, V + \hat{A}\frac{\partial V}{\partial t} = N\,(V, V)\,,$$

where $\hat{A}$ is a constant matrix

$$A_{ij} = \begin{cases} 0 & i \neq j \\ Re & i = j = 1 \ldots 3 \\ 0 & i = j = 4 \\ Wi & i = j = 5 \ldots 10 \end{cases}$$

and $\hat{\mathcal{L}}$ is the linear operator

$$\hat{\mathcal{L}} = \begin{pmatrix} \hat{K} & Re & 0 & \partial_x & \partial_y & \partial_z & 0 & 0 & 0 & \partial_x \\ 0 & \hat{K} & 0 & 0 & \partial_x & 0 & \partial_y & \partial_z & 0 & \partial_y \\ 0 & 0 & \hat{K} & 0 & 0 & \partial_x & 0 & \partial_y & \partial_z & \partial_z \\ \partial_x & \partial_y & \partial_z & 0 & 0 & 0 & 0 & 0 & 0 & 0 \\ 2\hat{X}_1 & 0 & 0 & \hat{L} & -2\,Wi & 0 & 0 & 0 & 0 & 0 \\ \partial_y & (1+2\,Wi^2)\,\partial_x & -Wi\,\partial_z & 0 & \hat{L} & 0 & -Wi & 0 & 0 & 0 \\ \partial_z & 0 & \hat{X}_1 & 0 & 0 & \hat{L} & 0 & -Wi & 0 & 0 \\ 0 & 2\hat{X}_2 & 0 & 0 & 0 & 0 & \hat{L} & 0 & 0 & 0 \\ 0 & \partial_z & \hat{X}_2 & 0 & 0 & 0 & 0 & \hat{L} & 0 & 0 \\ 0 & 0 & 2\,\partial_z & 0 & 0 & 0 & 0 & 0 & \hat{L} & 0 \end{pmatrix},$$

where $\hat{L} = 1 + Wi\,y\,\partial_x$, $\hat{K} = Re\,y\,\partial_x$, $\hat{X}_1 = (1+2\,Wi^2)\,\partial_x + Wi\,\partial_y$, and $\hat{X}_2 = Wi\,\partial_x + \partial_y$.

The bilinear form N represents the non-linear terms in Equations (1)–(3)

$$N\left(V^{(A)}, V^{(B)}\right) = -\left(\mathbf{v}^{(A)} \cdot \nabla\right) \hat{A} \cdot V^{(B)}$$
$$+ Wi \begin{pmatrix} 0 \\ 0 \\ 0 \\ 0 \\ 2\left[\tau_{xx}^{(A)}\partial_x v_x^{(B)} + \tau_{xy}^{(A)}\partial_y v_x^{(B)} + \tau_{xz}^{(A)}\partial_z v_x^{(B)}\right] \\ \tau_{xx}^{(A)}\partial_x v_y^{(B)} - \tau_{xy}^{(A)}\partial_z v_z^{(B)} + \tau_{xz}^{(A)}\partial_z v_y^{(B)} + \tau_{yy}^{(A)}\partial_y v_x^{(B)} + \tau_{yz}^{(A)}\partial_z v_x^{(B)} \\ \tau_{xx}^{(A)}\partial_x v_z^{(B)} + \tau_{xy}^{(A)}\partial_y v_z^{(B)} - \tau_{xz}^{(A)}\partial_y v_y^{(B)} + \tau_{yz}^{(A)}\partial_y v_x^{(B)} + \tau_{zz}^{(A)}\partial_z v_x^{(B)} \\ 2\left[\tau_{xy}^{(A)}\partial_x v_y^{(B)} + \tau_{yy}^{(A)}\partial_y v_y^{(B)} + \tau_{yz}^{(A)}\partial_z v_y^{(B)}\right] \\ \tau_{xy}^{(A)}\partial_x v_z^{(B)} + \tau_{xz}^{(A)}\partial_x v_y^{(B)} + \tau_{yy}^{(A)}\partial_y v_z^{(B)} - \tau_{yz}^{(A)}\partial_x v_x^{(B)} + \tau_{zz}^{(A)}\partial_z v_y^{(B)} \\ 2\left[\tau_{xz}^{(A)}\partial_x v_z^{(B)} + \tau_{yz}^{(A)}\partial_y v_z^{(B)} + \tau_{zz}^{(A)}\partial_z v_z^{(B)}\right] \end{pmatrix}.$$

Obviously, $N(A, B) \neq N(B, A)$.

APPENDIX B

The equations for the unknown functions $u_0^{(2)}(y)$, $u_0^{(4)}(y)$, etc., are derived by substituting the ansatz (6) into Equation (4). Requiring that the coefficients of

the harmonics $e^{in(k_x x+k_z z)}$ vanish for all n's one obtains

$$\begin{aligned}
&\hat{\mathcal{L}}\left(e^{2i\xi}u_2^{(2)}\right)+2\lambda e^{2i\xi}u_2^{(2)}=N\left(e^{i\xi}V_0,e^{i\xi}V_0\right)\\
&\hat{\mathcal{L}}\left(e^{2i\xi}u_2^{(4)}\right)+2\left(\lambda+\Re\lambda\right)e^{2i\xi}u_2^{(4)}\\
&\qquad\qquad=-2C_3e^{2i\xi}u_2^{(2)}+\bar{N}\left(e^{-i\xi}V_0^*,e^{3i\xi}u_3^{(3)}\right)\\
&\qquad\qquad+\bar{N}\left(u_0^{(2)},e^{2i\xi}u_2^{(2)}\right)\\
&\hat{\mathcal{L}}\left(u_0^{(2)}\right)+2\left(\Re\lambda\right)u_0^{(2)}=\bar{N}\left(e^{i\xi}V_0,e^{-i\xi}V_0^*\right)\\
&\hat{\mathcal{L}}\left(u_0^{(4)}\right)+4\left(\Re\lambda\right)u_0^{(4)}=-2\left(\Re C_3\right)u_0^{(2)}+N\left(u_0^{(2)},u_0^{(2)}\right)\\
&\qquad\qquad+\bar{N}\left(e^{2i\xi}u_2^{(2)},e^{-2i\xi}u_2^{(2)*}\right)\\
&\hat{\mathcal{L}}\left(e^{3i\xi}u_3^{(3)}\right)+3\lambda e^{3i\xi}u_3^{(3)}=\bar{N}\left(e^{i\xi}V_0,e^{2i\xi}u_2^{(2)}\right)
\end{aligned}$$

where $\xi = k_x x + k_z z$ and $\Re$ denotes the real part of a complex number. In deriving these equations one has to deal with the expressions like $\frac{\partial U_n(y,t)}{\partial t}$ or, in view of Equation (7), with $\frac{d\Phi(t)}{dt}$. This derivative is replaced by the r.h.s. of the amplitude equation (12) to assure self-consistency.

ACKNOWLEDGEMENT

The work by ANM is financially supported by the Dutch physics funding foundation FOM.

NOTE

1. Unfortunately, there is no unique constitutive equation for all visco-elastic systems and one has to choose between various standard models (Upper-Convected Maxwell model, Oldroyd-B, FENE-P, etc.) (Bird et al., 1987). This choice is usually guided by two requirements: (a) the model should (approximately) reproduce rheological properties of the visco-elastic system in question, (b) the model should be relatively simple to allow analytical or numerical analysis.

REFERENCES

Ashrafi, N. and Khayat, R.E. (2000). A low-dimensional approach to nonlinear plane-Couette flow of viscoelastic fluids. *Phys. Fluids* **12**, 345–365.

Atalik, K. and Keunings, R. (2002). Non-linear temporal stability analysis of viscoelastic plane channel flows using a fully-spectral method. *J. Non-Newtonian Fluid Mech.* **102**, 299–319.

Bertola, V., Meulenbroek, B., Wagner, C., Storm, C., Morozov, A.N., van Saarloos, W. and Bonn, D. (2003). Experimental evidence for an intrinsic route to polymer melt fracture phenomena: A nonlinear instability of viscoelastic Poiseuille flow. *Phys. Rev. Lett.* **90**, 114502.

Bird, R.B., Armstrong, R.C. and Hassager, O. (1987). *Dynamics of Polymeric Liquids*, volume 1, John Wiley & Sons, Inc., 2nd edition.

Conte, S.D. (1966). The numerical solution of linear boundary value problems. *SIAM Rev.* **8**, 309–321.

Denn, M.M. (1990). Issues in visco-elastic fluid-mechanics. *Annu. Rev. Fluid Mech.* **22**, 13–34.

Denn, M.M. (2001). Extrusion instabilities and wall slip. *Annu. Rev. Fluid Mech.* **33**, 265–287.

Godunov, S. (1961). On the numerical solution of boundary value problems for systems of linear ordinary differential equations. *Uspehi Mat. Nauk* **16**, 171–174.

Gorodtsov, V.A. and Leonov, A.I. (1967). On a linear instability of a parallel Couette flow of viscoelastic fluid. *J. Appl. Math. Mech.* **31**, 310–319.

Graham, M.D. (1998). Effect of axial flow on viscoelastic Taylor–Couette instability. *J. Fluid Mech.* **360**, 341–374.

Grillet, A.M., Bogaerds, A.C.B., Peters, G.W.M. and Baaijens, F.P.T. (2002). Stability analysis of constitutive equations for polymer melts in viscometric flows. *J. Non-Newtonian Fluid Mech.* **103**, 221–250.

Groisman, A. and Steinberg, V. (1997). Solitary vortex pairs in viscoelastic Couette flow. *Phys. Rev. Lett.* **78**, 1460–1463.

Groisman, A. and Steinberg, V. (2000). Elastic turbulence in a polymer solution flow. *Nature* **405**, 53.

Groisman, A. and Steinberg, V. (2004). Elastic turbulence in curvilinear flows of polymer solutions. *New J. Phys.* **6**, 29.

Herbert, T. (1980). Nonlinear stability of parallel flows by high-order amplitude expansions. *AIAA J.* **18**, 243–248.

Ho, T.C. and Denn, M.M. (1977/1978). Stability of plane Poiseuille flow of a highly elastic liquid. *J. Non-Newtonian Fluid Mech.* **3**, 179–195.

Hof, B., Juel, A. and Mullin, T. (2003). Scaling of the turbulence transition threshold in a pipe. *Phys. Rev. Lett.* **91**, 244502.

Joo, Y.L. and Shaqfeh, E.S.G. (1992). A purely elastic instability in Dean and Taylor–Dean flow. *Phys. Fluids A* **4**, 524.

Kumar, K.A. and Graham, M. (2000). Solitary coherent structures in viscoelastic shear flow: Computation and mechanism. *Phys. Rev. Lett.* **85**, 4056.

Larson, R. (2000). Turbulence without inertia. *Nature* **405**, 27.

Larson, R.G., Shaqfeh, E.S.G. and Muller, S.J. (1990). A purely elastic instability in Taylor–Couette flow. *J. Fluid Mech.* **218**, 573–600.

McKinley, G.H., Byars, J.A., Brown, R.A. and Armstrong, R.C. (1991). Observations on the elastic instability in cone-and-plate and parallel plate flows of a polyisobutylene Boger fluid. *J. Non-Newtonian Fluid Mech.* **40**, 201–229.

Meulenbroek, B., Storm, C., Bertola, V., Wagner, C., Bonn, D. and van Saarloos, W. (2003). Intrinsic route to melt fracture in polymer extrusion: A weakly nonlinear subcritical instability of viscoelastic Poiseuille flow. *Phys. Rev. Lett.* **90**, 024502.

Meulenbroek, B., Storm, C., Morozov, A.N. and van Saarloos, W. (2004). Weakly nonlinear subcritical instability of visco-elastic Poiseuille flow. *J. Non-Newtonian Fluid Mech.* **116**, 235–268.

Nagata, M. (1990). Three-dimensional finite-amplitude solutions in plane Couette flow: Bifurcation from infinity. *J. Fluid Mech.* **217**, 519–527.

Owens, R.G. and Phillips, T.N. (2002). *Computational Rheology*, Imperial College Press.

Pakdel, P. and McKinley, G.H. (1996). Elastic instability and curved streamlines. *Phys. Rev. Lett.* **77**, 2459.

Petrie, C.J.S. and Denn, M.M. (1976). Instabilities in polymer processing. *AICHE J.* **22**, 209–236.

Renardy, M. (1992). A rigorous stability proof for plane Couette flow of an upper convected Maxwell fluid at zero Reynolds number. *Eur. J. Mech. B* **11**, 511–516.

Renardy, M. and Renardy, Y. (1986). Linear stability of plane Couette flow of an upper convected Maxwell fluid. *J. Non-Newtonian Fluid Mech.* **22**, 23–33.

Schmid, P.J. and Henningson, D.S. (2001). *Stability and Transition in Shear Flows*, Springer-Verlag, New York.

Stuart, J.T. (1960). On the non-linear mechanics of wave disturbances in stable and unstable parallel flows. *J. Fluid Mech.* **9**, 353–370.

Waleffe, F. (1997). On a self-sustaining process in shear flows. *Phys. Fluids* **9**, 883–900.

Wilson, H.J., Renardy, M. and Renardy, Y. (1999). Structure of the spectrum in zero Reynolds number shear flow of the UCM and Oldroyd-B liquids. *J. Non-Newtonian Fluid Mech.* **80**, 251–268.

SUBJECT INDEX

basin of attraction 222, 254
bifurcation
  global 252, 260
  saddle-node 2
  subcritical 2
  supercritical 2, 61
channel flow, minimal 292
coherent states 41
coherent structures 146
conditional stability 251
constant mass flux 222
Coriolis force 173
co-supporting cycle 78
Couette apparatus 178
critical layer 93
destabilizing rotation 188
direct numerical simulations 80
directed percolation 20
dominant branches 76
drag reduction 290
elastic turbulence 2313
experiments 180, 197
finite amplitude solution 199, 201
Ginzburg–Landau equation 8, 20
growth
  rate 226
  sub-critical 236
  transient 163, 237, 252
homogeneous flow 182
intermittency regime 196
intermittent turbulence 119
kinetic energy of turbulence 304
laminar patch 118
laminar-turbulent coexistence 202
Landau theory 8
lifetime distributions 40
linear growth mechanisms 235
localized perturbation 200
low-dimensional models 255
lower branch 79
low-speed streaks 290
Lyapunov exponent 38
marginal stability curves 61
mean turbulent fraction 205
minimal flow unit 72, 146
minimum threshold energy 254
Navier–Stokes equation 130, 147, 316
near-wall region 146
non-linear bound 241
non-Newtonian 313
numerical simulation 214
oblique stripes 7
pipe flow 163, 221
PIV system 223
plane Couette apparatus 197
plane Couette flow 4, 52, 107, 129, 173, 174, 178, 316
plane Poiseuille flow 52
plane Poiseuille flow, rotating 59
polymer additives 290
polymer stress 295
proper orthogonal decomposition 151
recirculation pipe 223
reverse transition 195
Reynolds number 53, 176
roll-cell structures 190
rotation 173
rotation number 176
scaling 79
secondary instability 238
self-sustaining process 12, 87, 293
Smale horseshoe 36
spatio-temporal diagrams 211
spiral secondary disturbance 185
stability 234
streak 13
  breakdown 246
  streamwise 113
streamwise vortices 13
subcritical transition 135
Taylor–Couette apparatus 198
Taylor–Couette flows 129
tent map 18
threshold 203
transient algebraic growth 86
transition *from* turbulence 206

transition scenario 222
transition threshold 85, 90
travelling wave 46, 165
    nonlinear 291
turbulence 186
    featureless 108
    spiral 108
turbulent fraction 5
turbulent puffs 227
turbulent spot 6, 205
turbulent-laminar bands 112
visco-elastic equations 314
wavy structures 183
Weissenberg number 314
wind-driven flows 268

Mechanics

FLUID MECHANICS AND ITS APPLICATIONS

Series Editor: R. Moreau

Aims and Scope of the Series

The purpose of this series is to focus on subjects in which fluid mechanics plays a fundamental role. As well as the more traditional applications of aeronautics, hydraulics, heat and mass transfer etc., books will be published dealing with topics which are currently in a state of rapid development, such as turbulence, suspensions and multiphase fluids, super and hypersonic flows and numerical modelling techniques. It is a widely held view that it is the interdisciplinary subjects that will receive intense scientific attention, bringing them to the forefront of technological advancement. Fluids have the ability to transport matter and its properties as well as transmit force, therefore fluid mechanics is a subject that is particularly open to cross fertilisation with other sciences and disciplines of engineering. The subject of fluid mechanics will be highly relevant in domains such as chemical, metallurgical, biological and ecological engineering. This series is particularly open to such new multidisciplinary domains.

1. M. Lesieur: *Turbulence in Fluids.* 2nd rev. ed., 1990 ISBN 0-7923-0645-7
2. O. Métais and M. Lesieur (eds.): *Turbulence and Coherent Structures.* 1991 ISBN 0-7923-0646-5
3. R. Moreau: *Magnetohydrodynamics.* 1990 ISBN 0-7923-0937-5
4. E. Coustols (ed.): *Turbulence Control by Passive Means.* 1990 ISBN 0-7923-1020-9
5. A.A. Borissov (ed.): *Dynamic Structure of Detonation in Gaseous and Dispersed Media*. 1991 ISBN 0-7923-1340-2
6. K.-S. Choi (ed.): *Recent Developments in Turbulence Management.* 1991 ISBN 0-7923-1477-8
7. E.P. Evans and B. Coulbeck (eds.): *Pipeline Systems.* 1992 ISBN 0-7923-1668-1
8. B. Nau (ed.): *Fluid Sealing.* 1992 ISBN 0-7923-1669-X
9. T.K.S. Murthy (ed.): *Computational Methods in Hypersonic Aerodynamics.* 1992 ISBN 0-7923-1673-8
10. R. King (ed.): *Fluid Mechanics of Mixing*. Modelling, Operations and Experimental Techniques. 1992 ISBN 0-7923-1720-3
11. Z. Han and X. Yin: *Shock Dynamics.* 1993 ISBN 0-7923-1746-7
12. L. Svarovsky and M.T. Thew (eds.): *Hydroclones*. Analysis and Applications. 1992 ISBN 0-7923-1876-5
13. A. Lichtarowicz (ed.): *Jet Cutting Technology*. 1992 ISBN 0-7923-1979-6
14. F.T.M. Nieuwstadt (ed.): *Flow Visualization and Image Analysis*. 1993 ISBN 0-7923-1994-X
15. A.J. Saul (ed.): *Floods and Flood Management*. 1992 ISBN 0-7923-2078-6
16. D.E. Ashpis, T.B. Gatski and R. Hirsh (eds.): *Instabilities and Turbulence in Engineering Flows*. 1993 ISBN 0-7923-2161-8
17. R.S. Azad: *The Atmospheric Boundary Layer for Engineers.* 1993 ISBN 0-7923-2187-1
18. F.T.M. Nieuwstadt (ed.): *Advances in Turbulence IV.* 1993 ISBN 0-7923-2282-7
19. K.K. Prasad (ed.): *Further Developments in Turbulence Management.* 1993 ISBN 0-7923-2291-6
20. Y.A. Tatarchenko: *Shaped Crystal Growth.* 1993 ISBN 0-7923-2419-6
21. J.P. Bonnet and M.N. Glauser (eds.): *Eddy Structure Identification in Free Turbulent Shear Flows.* 1993 ISBN 0-7923-2449-8
22. R.S. Srivastava: *Interaction of Shock Waves*. 1994 ISBN 0-7923-2920-1
23. J.R. Blake, J.M. Boulton-Stone and N.H. Thomas (eds.): *Bubble Dynamics and Interface Phenomena*. 1994 ISBN 0-7923-3008-0

Mechanics

FLUID MECHANICS AND ITS APPLICATIONS

Series Editor: R. Moreau

24. R. Benzi (ed.): *Advances in Turbulence V.* 1995 ISBN 0-7923-3032-3
25. B.I. Rabinovich, V.G. Lebedev and A.I. Mytarev: *Vortex Processes and Solid Body Dynamics.* The Dynamic Problems of Spacecrafts and Magnetic Levitation Systems. 1994 ISBN 0-7923-3092-7
26. P.R. Voke, L. Kleiser and J.-P. Chollet (eds.): *Direct and Large-Eddy Simulation I.* Selected papers from the First ERCOFTAC Workshop on Direct and Large-Eddy Simulation. 1994 ISBN 0-7923-3106-0
27. J.A. Sparenberg: *Hydrodynamic Propulsion and its Optimization.* Analytic Theory. 1995 ISBN 0-7923-3201-6
28. J.F. Dijksman and G.D.C. Kuiken (eds.): *IUTAM Symposium on Numerical Simulation of Non-Isothermal Flow of Viscoelastic Liquids*. Proceedings of an IUTAM Symposium held in Kerkrade, The Netherlands. 1995 ISBN 0-7923-3262-8
29. B.M. Boubnov and G.S. Golitsyn: *Convection in Rotating Fluids*. 1995 ISBN 0-7923-3371-3
30. S.I. Green (ed.): *Fluid Vortices*. 1995 ISBN 0-7923-3376-4
31. S. Morioka and L. van Wijngaarden (eds.): *IUTAM Symposium on Waves in Liquid/Gas and Liquid/Vapour Two-Phase Systems*. 1995 ISBN 0-7923-3424-8
32. A. Gyr and H.-W. Bewersdorff: *Drag Reduction of Turbulent Flows by Additives.* 1995 ISBN 0-7923-3485-X
33. Y.P. Golovachov: *Numerical Simulation of Viscous Shock Layer Flows.* 1995 ISBN 0-7923-3626-7
34. J. Grue, B. Gjevik and J.E. Weber (eds.): *Waves and Nonlinear Processes in Hydrodynamics.* 1996 ISBN 0-7923-4031-0
35. P.W. Duck and P. Hall (eds.): *IUTAM Symposium on Nonlinear Instability and Transition in Three-Dimensional Boundary Layers.* 1996 ISBN 0-7923-4079-5
36. S. Gavrilakis, L. Machiels and P.A. Monkewitz (eds.): *Advances in Turbulence VI.* Proceedings of the 6th European Turbulence Conference. 1996 ISBN 0-7923-4132-5
37. K. Gersten (ed.): *IUTAM Symposium on Asymptotic Methods for Turbulent Shear Flows at High Reynolds Numbers.* Proceedings of the IUTAM Symposium held in Bochum, Germany. 1996 ISBN 0-7923-4138-4
38. J. Verhás: *Thermodynamics and Rheology.* 1997 ISBN 0-7923-4251-8
39. M. Champion and B. Deshaies (eds.): *IUTAM Symposium on Combustion in Supersonic Flows.* Proceedings of the IUTAM Symposium held in Poitiers, France. 1997 ISBN 0-7923-4313-1
40. M. Lesieur: *Turbulence in Fluids.* Third Revised and Enlarged Edition. 1997 ISBN 0-7923-4415-4; Pb: 0-7923-4416-2
41. L. Fulachier, J.L. Lumley and F. Anselmet (eds.): *IUTAM Symposium on Variable Density Low-Speed Turbulent Flows.* Proceedings of the IUTAM Symposium held in Marseille, France. 1997 ISBN 0-7923-4602-5
42. B.K. Shivamoggi: *Nonlinear Dynamics and Chaotic Phenomena.* An Introduction. 1997 ISBN 0-7923-4772-2
43. H. Ramkissoon, *IUTAM Symposium on Lubricated Transport of Viscous Materials*. Proceedings of the IUTAM Symposium held in Tobago, West Indies. 1998 ISBN 0-7923-4897-4
44. E. Krause and K. Gersten, *IUTAM Symposium on Dynamics of Slender Vortices.* Proceedings of the IUTAM Symposium held in Aachen, Germany. 1998 ISBN 0-7923-5041-3
45. A. Biesheuvel and G.J.F. van Heyst (eds.): *In Fascination of Fluid Dynamics.* A Symposium in honour of Leen van Wijngaarden. 1998 ISBN 0-7923-5078-2

Mechanics

FLUID MECHANICS AND ITS APPLICATIONS

Series Editor: R. Moreau

46. U. Frisch (ed.): *Advances in Turbulence VII.* Proceedings of the Seventh European Turbulence Conference, held in Saint-Jean Cap Ferrat, 30 June–3 July 1998. 1998 ISBN 0-7923-5115-0
47. E.F. Toro and J.F. Clarke: *Numerical Methods for Wave Propagation.* Selected Contributions from the Workshop held in Manchester, UK. 1998 ISBN 0-7923-5125-8
48. A. Yoshizawa: *Hydrodynamic and Magnetohydrodynamic Turbulent Flows*. Modelling and Statistical Theory. 1998 ISBN 0-7923-5225-4
49. T.L. Geers (ed.): *IUTAM Symposium on Computational Methods for Unbounded Domains*. 1998 ISBN 0-7923-5266-1
50. Z. Zapryanov and S. Tabakova: *Dynamics of Bubbles, Drops and Rigid Particles*. 1999 ISBN 0-7923-5347-1
51. A. Alemany, Ph. Marty and J.P. Thibault (eds.): *Transfer Phenomena in Magnetohydrodynamic and Electroconducting Flows*. 1999 ISBN 0-7923-5532-6
52. J.N. Sørensen, E.J. Hopfinger and N. Aubry (eds.): *IUTAM Symposium on Simulation and Identification of Organized Structures in Flows*. 1999 ISBN 0-7923-5603-9
53. G.E.A. Meier and P.R. Viswanath (eds.): *IUTAM Symposium on Mechanics of Passive and Active Flow Control*. 1999 ISBN 0-7923-5928-3
54. D. Knight and L. Sakell (eds.): *Recent Advances in DNS and LES*. 1999 ISBN 0-7923-6004-4
55. P. Orlandi: *Fluid Flow Phenomena*. A Numerical Toolkit. 2000 ISBN 0-7923-6095-8
56. M. Stanislas, J. Kompenhans and J. Westerveel (eds.): *Particle Image Velocimetry*. Progress towards Industrial Application. 2000 ISBN 0-7923-6160-1
57. H.-C. Chang (ed.): *IUTAM Symposium on Nonlinear Waves in Multi-Phase Flow*. 2000 ISBN 0-7923-6454-6
58. R.M. Kerr and Y. Kimura (eds.): *IUTAM Symposium on Developments in Geophysical Turbulence* held at the National Center for Atmospheric Research, (Boulder, CO, June 16–19, 1998) 2000 ISBN 0-7923-6673-5
59. T. Kambe, T. Nakano and T. Miyauchi (eds.): *IUTAM Symposium on Geometry and Statistics of Turbulence*. Proceedings of the IUTAM Symposium held at the Shonan International Village Center, Hayama (Kanagawa-ken, Japan November 2–5, 1999). 2001 ISBN 0-7923-6711-1
60. V.V. Aristov: *Direct Methods for Solving the Boltzmann Equation and Study of Nonequilibrium Flows*. 2001 ISBN 0-7923-6831-2
61. P.F. Hodnett (ed.): *IUTAM Symposium on Advances in Mathematical Modelling of Atmosphere and Ocean Dynamics.* Proceedings of the IUTAM Symposium held in Limerick, Ireland, 2–7 July 2000. 2001 ISBN 0-7923-7075-9
62. A.C. King and Y.D. Shikhmurzaev (eds.): *IUTAM Symposium on Free Surface Flows*. Proceedings of the IUTAM Symposium held in Birmingham, United Kingdom, 10–14 July 2000. 2001 ISBN 0-7923-7085-6
63. A. Tsinober: *An Informal Introduction to Turbulence*. 2001 ISBN 1-4020-0110-X; Pb: 1-4020-0166-5
64. R.Kh. Zeytounian: *Asymptotic Modelling of Fluid Flow Phenomena*. 2002 ISBN 1-4020-0432-X
65. R. Friedrich and W. Rodi (eds.): *Advances in LES of Complex Flows.* Prodeedings of the EUROMECH Colloquium 412, held in Munich, Germany, 4-6 October 2000. 2002 ISBN 1-4020-0486-9
66. D. Drikakis and B.J. Geurts (eds.): *Turbulent Flow Computation*. 2002 ISBN 1-4020-0523-7
67. B.O. Enflo and C.M. Hedberg: *Theory of Nonlinear Acoustics in Fluids*. 2002 ISBN 1-4020-0572-5

FLUID MECHANICS AND ITS APPLICATIONS

Series Editor: R. Moreau

68. I.D. Abrahams, P.A. Martin and M.J. Simon (eds.): *IUTAM Symposium on Diffraction and Scattering in Fluid Mechanics and Elasticity*. Proceedings of the IUTAM Symposium held in Manchester, (UK, 16-20 July 2000). 2002 ISBN 1-4020-0590-3
69. P. Chassaing, R.A. Antonia, F. Anselmet, L. Joly and S. Sarkar: *Variable Density Fluid Turbulence.* 2002 ISBN 1-4020-0671-3
70. A. Pollard and S. Candel (eds.): *IUTAM Symposium on Turbulent Mixing and Combustion.* Proceedings of the IUTAM Symposium held in Kingston, Ontario, Canada, June 3-6, 2001. 2002 ISBN 1-4020-0747-7
71. K. Bajer and H.K. Moffatt (eds.): *Tubes, Sheets and Singularities in Fluid Dynamics*. 2002 ISBN 1-4020-0980-1
72. P.W. Carpenter and T.J. Pedley (eds.): *Flow Past Highly Compliant Boundaries and in Collapsible Tubes*. IUTAM Symposium held at the Univerity of Warwick, Coventry, United Kingdom, 26-30 March 2001. 2003 ISBN 1-4020-1161-X
73. H. Sobieczky (ed.): *IUTAM Symposium Transsonicum IV.* Proceedings of the IUTAM Symposium held in Göttingen, Germany, 2-6 September 2002. 2003 ISBN 1-4020-1608-5
74. A.J. Smits (ed.): *IUTAM Symposium on Reynolds Number Scaling in Turbulent Flow*. Proceedings of the IUTAM Symposium held in Princeton, NJ, U.S.A., September 11-13, 2002. 2003 ISBN 1-4020-1775-8
75. H. Benaroya and T. Wei (eds.): *IUTAM Symposium on Integrated Modeling of Fully Coupled Fluid Structure Interactions Using Analysis, Computations and Experiments*. Proceedings of the IUTAM Symposium held in New Jersey, U.S.A., 2-6 June 2003. 2003 ISBN 1-4020-1806-1
76. J.-P. Franc and J.-M. Michel: *Fundamentals of Cavitation*. 2004 ISBN 1-4020-2232-8
77. T. Mullin and R.R. Kerswell (eds.): *IUTAM Symposium on Laminar Turbulent Transition and Finite Amplitude Solutions*. 2005 ISBN 1-4020-4048-2